P54/WGI-14 - Changes to the underlying scientific-technical assessment to ensure consistency with the approved SPM

These trickle backs will be implemented in the Chapter during copy-editing

SPM Page:Line	Chapter/Supp. Material	Chapter Page:Line	Summary of edit to be made
8: 48-51	7	6:36	Replace "**435 [325 to 545]**" with "**282 [177 to 387]**".
8: 48-51	7	6:36	Replace "**1971-2018**" with "**1971-2006**" .
8: 48-51	7	6:37-38	Replace "0.57 [0.43 to 0.72]" with "0.50 [0.32 to 0.69]".
8: 48-51	7	6:38	Replace "1971-2018" with "1971-2006".
8: 48-51	7	19:21	After the sentence that ends "… radiative forcing from greenhouse gases (*high confidence*)." insert "For the period 1971-2006 the total energy gain was 282 [177 to 387] ZJ, with an equivalent Earth energy imbalance of 0.50 [0.32 to 0.69] W m^{-2}."
4:17-22 footnote	7	32:40	Replace second last row of Table 7.5 by

Sum of HFCs (HFC-134a equivalent)	237.1	128.6	0.	0.	0.040	0.022	0.040	0.022
Sum of CFCs+HCFCs+other ozone depleting gases covered by the Montreal Protocol (CFC-12 equivalent)	1031.9	1050.1	0.	0.	0.354	0.362	0.354	0.362
Sum of PFCs (CF_4 equivalent)	109.4	98.9	34.0	34.0	0.007	0.006	0.007	0.006
Sum of HFCs (HFC-134a equivalent)	237.1	128.6	0.	0.	0.040	0.022	0.040	0.022
Sum of Halogenated species					0.408±0.078	0.394	0.408±0.078	0.394

AR6 WGI Report – List of corrigenda to be implemented

The corrigenda listed below will be implemented in the Chapter during copy-editing.

CHAPTER 7

Document (Chapter, Annex, Supp. Mat…)	Section	Page :Line (based on the final pdf FGD version)	Detailed info on correction to make
7	Executive Summary	6:37	Replace "153 [101 to 206]" with "152 [100 to 205]". (change reflects small bug in energy inventory calculation).
Chapter 7	Executive Summary	6:43	Replace "more confident" with "strengthened". (note that AR5 was also *high confidence*)
Chapter 7	7.2	14:53	Replace " and is a key element in energy budget framework" by ", which is a key element of the energy budget framework".
Chapter 7	7.2.1	16:13	Replace "Earth System Models (ESMs)" by "ESMs"
Chapter 7	7.2.2.2	18:24	Replace "a zero contribution" by "so a zero contribution".
Chapter 7	7.2.2.2	18:25	Replace "are based on" by "is based on".
Chapter 7	Table 7.1	18:40	Row 2 "Ocean", 5th column: replace "90.9" with "91.0" and replace "9.9" with "10.0" (change reflects small bug in energy inventory calculation)
Chapter 7	Table 7.1	18:40	Row 2 "Ocean", 7th column: replace "90.7" with "91.1", replace "49.3" with "49.5", and replace "32.4" with "32.6" (change reflects small bug in energy inventory calculation)
Chapter 7	Table 7.1	18:40	Row 4 "Cryosphere", 4th column: replace "10.6" with "10.5" (change reflects small bug in energy inventory calculation)
Chapter 7	Table 7.1	18:40	Row 4 "Cryosphere", 6th column: replace "5.4 [3.9 to 6.8]" with "4.7 [3.3 to 6.2]" (change reflects small bug in energy inventory calculation)
Chapter 7	Table 7.1	18:40	Row 4 "Cryosphere", 7th column: replace "3.5" with "3.1" (change reflects small bug in energy inventory calculation)
Chapter 7	Table 7.1	18:40	Row 6 "TOTAL", 2nd column: replace "545.5" with "545.3" (change reflects small bug in energy inventory calculation)
Chapter 7	Table 7.1	18:40	Row 6 "TOTAL", 3rd column: replace "358.2" with "358.1" (change reflects small bug in energy inventory calculation)
Chapter 7	Table 7.1	18:40	Row 6 "TOTAL", 4th column: replace "153.1 [100.6 to 205.5]" with "152.4 [100.0 to 204.9]" (change reflects small bug in energy inventory calculation)
Chapter 7	7.2.2.2	19:19	Remove "±"
Chapter 7	7.2.2.2	19:16	Replace "Box 7.2, Figure 1a" by "Box 7.2, Figure 1".
Chapter 7	7.2.2.2	19:22	Replace "rate of global energy" by "annual rate of global energy".
Chapter 7	7.2.2.2	19:6	Replace "about 3%" by "approximately 3%".
Chapter 7	7.2.2.2	19:7	Replace "about 1%" by "approximately 1%".
Chapter 7	7.2.2.2	19:8	Replace "about 8%" by "approximately 8%".
Chapter 7	7.2.2.2	19:24	Replace "ocean warming dominates the changes in total Earth system heating" by "this Report finds that ocean warming dominates the changes in the global energy inventory".
Chapter 7	7.2.2.3	19:48	Replace "as in Iran" by "as Iran".
Chapter 7	7.2.2.3	20:49	Remove erroneous strikethrough text so that the start of the line reads "variability, could further contribute …".
Chapter 7	Box 7.2	21:34	Replace "total climate feedback" by "climate system radiative response".
Chapter 7	Box 7.2	21:46	Replace "Earth's radiative response" by "the climate system radiative response".
|Chapter 7	Box 7.2	21:41	Replace "ERF since 1971" by "ERF for the period 1971-2018".
Chapter 7	Box 7.2	21:50	Replace "1971" by "for the period 1971-2018".
Chapter 7	Box 7.2	22:19	Add a full-stop at the end of the sentence.

Chapter 7	Figure 7.1	175	Add harmonised visual roadmap as a new panel to the current visual roadmap (1st). To make sure that CH7 has something consistent with the other chapters, while keeping the useful information put forward in the current visual abstract .
Chapter 7	Figure 7.1 caption	11:45 175:4	Change "A visual abstract of the chapter, illustrating why the Earth's energy budget matters and how it relates to the underlying chapter assessment. The methods used to assess processes and key new findings relative to AR5 are highlighted." to "Visual guide to chapter 7. (Panel A) Overview of the chapter. (Panel B) Visual abstract of the chapter, illustrating why the Earth's energy budget matters and how it relates to the underlying chapter assessment. The methods used to assess processes and key new findings relative to AR5 are highlighted."
Chapter 7	7.1	11 : 15	Replace "Collins et al., 2013a" by "M. Collins et al., 2013"
Chapter 7	7.2.1	15 : 46-47	Replace "Loeb et al., 2018a" by "Loeb et al., 2018b"
Chapter 7	7.2.1	16 : 2	Replace "Li et al., 2013b" by "J.-L.F. Li et al., 2013"
Chapter 7	7.2.1	16 : 19	Replace "Christensen et al., 2016a" by "Christensen et al., 2016b"
Chapter 7	7.2.1	16 : 38-39	Replace "Li et al., 2013b" by "J.-L.F. Li et al., 2013" Replace "Zang et al., 2018a" by "C. Zang et al., 2018"
Chapter 7	7.2.1	17 : 2 17 : 5 17 : 8-9 17 : 12	Replace "Loeb et al., 2018a" by "Loeb et al., 2018b"
Chapter 7	7.2.2.2	18 : 4	Replace "Allison et al., 2020a" by "Allison et al., 2020"
Chapter 7	7.2.2.3	19 : 41	Replace "Li et al., 2016b" by "Z. Li et al., 2016"
Chapter 7	7.2.2.3	20 : 1-2	Replace "Li et al., 2016b" by "Z. Li et al., 2016" Replace "He et al., 2018b" by "Y. He et al., 2018"
Chapter 7	7.2.2.3	20 : 25	Replace "Li et al., 2018a" by "J. Li et al., 2018"
Chapter 7	7.3	24 : 29-30 24 : 31 24 : 32 24 : 49 25 : 16 25 : 28	Replace "Smith et al., 2020a" by "Smith et al,. 2020b"
Chapter 7	7.3	24 : 55	Replace "Smith et al., 2020b" by "Smith et al,. 2020a"
Chapter 7	Table 7.2	25	Replace "Smith et al., 2020a" by "Smith et al,. 2020b"
Chapter 7	7.3.1	26 : 14	Replace "Smith et al., 2020a" by "Smith et al,. 2020b"
Chapter 7	7.3.2	27:24	Replace "by 25%" with "by approximately 25%"
Chapter 7	7.3.2.1	28 : 5-6	Replace "Smith et al., 2020a" by "Smith et al,. 2020b"
Chapter 7	7.3.2.1	28 : 9	Replace "Richardson et al., 2018b" by "T.B. Richardson et al., 2018"
Chapter 7	7.3.3.1.1	34 : 17	Replace "Bellouin et al. (2013b)" by "Bellouin et al. (2013a)"
Chapter 7	7.3.3.1.2	34 : 51	Replace "Andrews et al., 2017a" by "E. Andrews et al., 2017"
Chapter 7	7.3.3.1.2	35 : 34 35 : 37	Replace "Smith et al., 2020a" by "Smith et al,. 2020b"
Chapter 7	7.3.3.1.3	36 : 8	Replace "Smith et al., 2020a" by "Smith et al,. 2020b"
Chapter 7	7.3.3.1.3	36 : 10	Replace "Smith et al., 2020b" by "Smith et al,. 2020a"
Chapter 7	Table 7.7	37 38	Replace "Bellouin et al. (2013a)" by "Bellouin et al. (2013b)" Replace "McCoy et al. (2017a)" by "McCoy et al. (2017b)" Replace "Christensen et al. (2016b)" by "Christensen et al. (2016a)"
Chapter 7	7.3.3.2.1	38 : 28 38 : 33 38 : 37	Replace "Bellouin et al. (2013a)" by "Bellouin et al. (2013b)"
Chapter 7	7.3.3.2.1	38 : 30 38 : 33	Replace "McCoy et al. (2017a)" by "McCoy et al. (2017b)"
Chapter 7	7.3.3.2.1	38 : 35	Replace "Christensen et al. (2016b)" by "Christensen et al. (2016a)"

		38 : 40	
Chapter 7	7.3.3.2.1	39 : 12	Replace “Christensen et al. (2016a)” by “Christensen et al. (2016b)”
Chapter 7	7.3.3.2.2	40 : 40	Replace “Golaz et al., 2019a” by “Golaz et al., 2019”
Chapter 7	7.3.3.2.2	40 : 44	Replace “Smith et al., 2020a” by “Smith et al,. 2020b”
Chapter 7	7.3.3.4	43 : 52	Replace “Smith et al., 2020a” by “Smith et al,. 2020b”
Chapter 7	7.3.4.1	44 : 40 45 : 1	Replace “Andrews et al. (2017b)” by T. “Andrews et al. (2017)”
Chapter 7	7.3.4.1	44 : 46	Replace “Smith et al., 2020a” by “Smith et al,. 2020b”
Chapter 7	7.3.4.1	45 : 6	Replace “Zhu et al., 2019a” by “Zhu et al., 2019b”
Chapter 7	7.3.4.3	45 : 39-40	Replace “He et al. (2018a)” by “”C. He et al. (2018)”
Chapter 7	7.3.5.1	48:45-46	Replace “CO_2 radiative efficiency” by “forcing for doubling CO_2”
Chapter 7	7.3.5.1	48:47	Replace “by 25%” with “by approximately 25%”
Chapter 7	CCB 7.1	53 : 30	Replace “Collins et al., 2013a” by “M. Collins et al., 2013”
Chapter 7	7.4.1	60 : 20-21	Replace “Rugenstein et al., 2019a” by “Rugenstein et al., 2019”
Chapter 7	7.4.1	60:20	Replace “by about 10%” by “by about 15%”
Chapter 7	7.4.1	60:21	Replace “"small and cancel each other" by "small and approximately cancel each other"
Chapter 7	7.4.2.2	61 : 52 62 : 43-44 62 : 45	Replace “Sherwood et al., 2010b” by “Sherwood et al., 2010a”
Chapter 7	7.4.2.2	62 : 42 62 : 44	Replace “Po-Chedley et al., 2018a” by “Po-Chedley et al., 2018b”
Chapter 7	7.4.2.4.2	67 : 20	Replace “McCoy et al. (2017b)” by “McCoy et al. (2017a)”
Chapter 7	7.4.2.4.2	68 : 13	Replace “Li et al., 2018b” by “Y. Li et al., 2018”
Chapter 7	7.4.2.4.2	68 : 18	Replace “McCoy et al. (2017b)” by “McCoy et al. (2017a)”
Chapter 7	7.4.2.4.2	69 : 18-19	Replace “Zhang et al., 2018b” by “R. Zhang et al,. 2018”
Chapter 7	7.4.2.4	70:4	Replace “difference regimes” by “different regimes”
Chapter 7	7.4.2.5.2	71 : 38 71 : 51-52	Replace “Zhang et al., 2018c” by “W. Zhang et al., 2018”
Chapter 7	7.4.2.5.2	71 : 42	Replace “Collins et al., 2013a” by “M. Collins et al., 2013”
Chapter 7	7.4.2.6	73 : 17	Replace “Collins et al., 2013a” by “M. Collins et al., 2013”
Chapter 7	7.4.3	76 : 27	Replace “Hansen, 2005b” by “Hansen et al., 2005b”
Chapter 7	7.4.3.1	76 : 45 77 : 8	Replace “Zhu et al., 2019b” by “Zhu et al., 2019a”
Chapter 7	7.4.3.1	76 : 54-55	Replace “Zhu et al., 2019b” by “Zhu et al., 2019a” Replace “Sherwood et al., 2020b” by “Sherwood et al., 2020” Replace “Rugenstein et al., 2019b” by “Rugenstein et al., 2020”
Chapter 7	7.4.3.1	76:55	Replace “Sherwood et al., 2020b” with “Sherwood et al., 2020”
Chapter 7	7.4.3.1	77 : 1 77 : 11 77 : 28	Replace “Rugenstein et al., 2019b” by “Rugenstein et al., 2020”
Chapter 7	7.4.3.2	78 : 37	Replace “Rugenstein et al., 2019b” by “Rugenstein et al., 2020”
Chapter 7	7.4.3.3	78 : 48	Replace “Zhu et al., 2019b” by “Zhu et al., 2019a”
Chapter 7	7.4.4.1.1	80 : 54	Replace “Luo et al., 2017a” by “B. Luo et al., 2017”
Chapter 7	7.4.4.1.1	81 : 29-30	Replace “Po-Chedley et al., 2018a;” by “Po-Chedley et al., 2018b””
Chapter 7	7.4.4.1.1	82 : 2	Replace “Li et al., 2013a” by C. Li et al., 2013“”
Chapter 7	7.4.4.1.1	82 : 27	Replace “Liu et al., 2017a, 2017b” by “W. Liu et al., 2017; Y. Liu et al., 2017”
Chapter 7	7.4.4.1.2	84 : 11 84 : 41-42	Replace “Zhu et al., 2019b” by “Zhu et al., 2019a”
Chapter 7	7.4.4.2.1	85 : 49	Replace “Burls and Fedorov, 2014a” by “Burls and Fedorov, 2014b”
Chapter 7	7.4.4.2.1	86 : 7	Replace “Luo et al., 2017b” by “Y. Luo et al., 2017”
Chapter 7	7.4.4.2.1	86 : 26	Replace “Li et al., 2016a” by “X. Li et al., 2016”
Chapter 7	7.4.4.2.1	86 : 38	Replace “Watanabe et al., 2020a” by “Watanabe et al., 2020b”
Chapter 7	7.4.4.2.2	87 : 22-23	Replace “Burls and Fedorov, 2014b” by “Burls and Fedorov, 2014a”

Chapter 7	7.4.4.3	91 : 8	Replace "Loeb et al., 2018b" by "Loeb et al., 2018a"
Chapter 7	7.4.4.3	91 : 14	Replace "Li et al., 2013a" by "C. Li et al., 2013"
Chapter 7	7.5.1.2	94 : 23	Replace "Smith et al., 2020a" by "Smith et al,. 2020b"
Chapter 7	7.5.2.1	96 : 44 96 : 47-48	Replace "Sherwood et al., 2020b" by "Sherwood et al., 2020"
Chapter 7	7.5.2.1	96:44	Replace "Sherwood et al., 2020b" with "Sherwood et al., 2020"
Chapter 7	7.5.2.1	96:47	Replace "Sherwood et al., 2020b" with "Sherwood et al., 2020"
Chapter 7	7.5.2.1	97 : 9-10	Replace "Richardson et al., 2016, 2018a" by "M. Richardson et al., 2016, 2018"
Chapter 7	7.5.2.1	97 : 13 98 : 6	Replace "Collins et al., 2013a" by "M. Collins et al., 2013"
Chapter 7	7.5.3.1	101 : 49	Replace "Sherwood et al., 2020b" by "Sherwood et al., 2020"
Chapter 7	7.5.3.1	101:49	Replace "Sherwood et al., 2020b" with "Sherwood et al., 2020"
Chapter 7	7.5.3.3	102:49	Replace "Sherwood et al., 2020b" with "Sherwood et al., 2020"
Chapter 7	7.5.3.3	102 : 49	Replace "Sherwood et al., 2020b" by "Sherwood et al., 2020"
Chapter 7	7.5.3.4	103 : 20 103 : 21-22 103 : 26	Replace "Sherwood et al., 2020b" by "Sherwood et al., 2020"
Chapter 7	7.5.3.4	103:20	Replace "Sherwood et al., 2020b" with "Sherwood et al., 2020"
Chapter 7	7.5.3.4	103:21	Replace "Sherwood et al., 2020b" with "Sherwood et al., 2020"
Chapter 7	7.5.3.4	103:26	Replace "Sherwood et al., 2020b" with "Sherwood et al., 2020"
Chapter 7	Table 7.11	104	Replace "Annan and Hargreaves, Schneider von Deimling" by "Schneider von Deimling et al. (2006); Annan and Hargreaves (2013)" Annan and Hargreaves (2013) Doi:10.5194/cp-9-367-2013. Schneider von Deimling et al. (2006) Doi:10.1029/2006GL026484.
Chapter 7	7.5.3.4	104, Table 7.11, 3rd column, 4th row	Replace "Annan and Hargreaves, Schneider von Deimling" with "Annan and Hargreaves (2013), Schneider von Deimling et al. (2006)"
Chapter 7	7.5.4	106 : 60	Replace "Annan et al., 2020a" by "Annan et al., 2020"
Chapter 7	7.5.4.1	108 : 17 108 : 19	Replace "Po-Chedley et al., 2018b;" by "Po-Chedley et al., 2018a""
Chapter 7	7.5.4.1	108 : 23	Replace "Annan et al., 2020b" by "Annan et al., 2020"
Chapter 7	7.5.5	111 : 15	Replace "Collins et al., 2013a" by "M. Collins et al., 2013"
Chapter 7	7.5.5	111 : 20 111 : 25 111 : 39	Replace "Sherwood et al., 2020b" by "Sherwood et al., 2020"
Chapter 7	7.5.5	111:52	Replace "4°C "by "4.5°C"
Chapter 7	7.5.5	111:39	Replace "Sherwood et al., 2020b" with "Sherwood et al., 2020"
Chapter 7	7.5.6	113 : 23	Replace "Sherwood et al., 2020b" by "Sherwood et al., 2020"
Chapter 7	7.5.6	115 : 10	Replace "Golaz et al., 2019b" by "Golaz et al., 2019"
Chapter 7	7.5.7	116 : 48	Replace "Po-Chedley et al., 2018a;" by "Po-Chedley et al., 2018b""
Chapter 7	7.5.7	117 : 30	Replace "Watanabe et al. (2020b)" by "Watanabe et al. (2020a)"
Chapter 7	7.6.1.1	119:13	Replace "1.36×10^{-5}, 3.77×10^{-4} and 3.11×10^{-3}" with "1.33×10^{-5}, 3.89×10^{-4} and 3.19×10^{-3}"
Chapter 7	7.6.1.1	119:15	Delete "re-evaluated radiative properties and"
Chapter 7	7.6.1.1	119:16	Replace "balance" by "do not quite balance"
Chapter 7	7.6.1.2	120 : 28 120 : 50	Replace "Collins et al., 2013b" by "W.J. Collins et al., 2013"
Chapter 7	7.6.1.3	120 : 53	Replace "Collins et al., 2013a" by "W.J. Collins et al., 2013"
Chapter 7	7.6.1.3	121 : 27	Replace "Collins et al., 2013b" by "W.J. Collins et al., 2013"

Chapter 7	References	163,50	Add reference: “Schneider von Deimling, T., A. Ganopolski, H. Held, and S. Rahmstorf, 2006: How cold was the Last Glacial Maximum?, Geophys. Res. Lett., 33, L14709, doi:10.1029/2006GL026484”
Chapter 7	References	165:35-38	Remove duplicate Sherwood et al. 2020b reference and replace “2020a” with “2020” on line 35
Chapter 7	References	135,23	Add reference: “Annan, J. D., and J. C. Hargreaves, 2013: A new global reconstruction of temperature changes at the Last Glacial Maximum, Clim. Past, 9, 367–376, doi:10.5194/cp-9-367-2013.”

Chapter 7: The Earth's energy budget, climate feedbacks, and climate sensitivity

Coordinating Lead Authors:
Piers Forster (United Kingdom), Trude Storelvmo (Norway)

Lead Authors:
Kyle Armour (United States of America), William Collins (United Kingdom), Jean-Louis Dufresne (France), David Frame (New Zealand), Daniel J. Lunt (United Kingdom), Thorsten Mauritsen (Sweden/Denmark), Matthew D. Palmer (United Kingdom), Masahiro Watanabe (Japan), Martin Wild (Switzerland), Hua Zhang (China)

Contributing Authors:
Kari Alterskjær (Norway), Chris Smith (United Kingdom), Govindasamy Bala (India/United States of America), Nicolas Bellouin (United Kingdom/France), Terje Berntsen (Norway), Fábio Boeira Dias (Finland/Brazil), Sandrine Bony (France), Natalie J. Burls (United States of America/South Africa), Michelle Cain (United Kingdom), Catia M. Domingues (Australia, United Kingdom/Brazil), Aaron Donohoe (United States of America), Mark Flanner (United States of America), Jan S. Fuglestvedt (Norway), Lily C. Hahn (United States of America), Glen R. Harris (United Kingdom/New Zealand, United Kingdom), Christopher Jones (United Kingdom), Seiji Kato (United States of America), Jared Lewis (Australia/New Zealand), Zhanqing Li (United States of America), Mike Lockwood (United Kingdom), Norman Loeb (United States of America), Jochem Marotzke (Germany), Malte Meinshausen (Australia/Germany), Sebastian Milinski (Germany), Zebedee R. J. Nicholls (Australia), Ryan S. Padron Flasher (Switzerland/Ecuador, United States of America), Anna Possner (Germany), Cristian Proistosescu (Romania), Johannes Quaas (Germany), Joeri Rogelj (United Kingdom/Belgium), Daniel Rosenfeld (Israel), Bjørn H. Samset (Norway), Abhishek Savita (Australia/India), Jessica Vial (France), Karina von Schuckmann (France/Germany), Mark Zelinka (United States of America), Shuyun Zhao (China)

Review Editors:
Robert Colman (Australia), Damon H. Matthews (Canada), Venkatachalam Ramaswamy (United States of America)

Chapter Scientists:
Kari Alterskjær (Norway), Chris Smith (United Kingdom)

This Chapter should be cited as:
Forster, P., T. Storelvmo, K. Armour, W. Collins, J. L. Dufresne, D. Frame, D. J. Lunt, T. Mauritsen, M. D. Palmer, M. Watanabe, M. Wild, H. Zhang, 2021, The Earth's Energy Budget, Climate Feedbacks, and Climate Sensitivity. In: *Climate Change 2021: The Physical Science Basis. Contribution of Working Group I to the Sixth Assessment Report of the Intergovernmental Panel on Climate Change* [Masson-Delmotte, V., P. Zhai, A. Pirani, S. L. Connors, C. Péan, S. Berger, N. Caud, Y. Chen, L. Goldfarb, M. I. Gomis, M. Huang, K. Leitzell, E. Lonnoy, J.B.R. Matthews, T. K. Maycock, T. Waterfield, O. Yelekçi, R. Yu and B. Zhou (eds.)]. Cambridge University Press. In Press.

Date: August 2021

This document is subject to copy-editing, corrigenda and trickle backs.

Table of Content

Executive Summary

This chapter assesses the present state of knowledge of Earth's energy budget, that is, the main flows of energy into and out of the Earth system, and how these energy flows govern the climate response to a radiative forcing. Changes in atmospheric composition and land use, like those caused by anthropogenic greenhouse gas emissions and emissions of aerosols and their precursors, affect climate through perturbations to Earth's top-of-atmosphere energy budget. The effective radiative forcings (ERFs) quantify these perturbations, including any consequent adjustment to the climate system (but excluding surface temperature response). How the climate system responds to a given forcing is determined by climate feedbacks associated with physical, biogeophysical and biogeochemical processes. These feedback processes are assessed, as are useful measures of global climate response, namely equilibrium climate sensitivity (ECS) and the transient climate response (TCR). This chapter also assesses emission metrics, which are used to quantify how the climate response due to the emission of different greenhouse gases compares to the response to the emission of carbon dioxide (CO_2). This chapter builds on the assessment of carbon cycle and aerosol processes from Chapters 5 and 6, respectively, to quantify non-CO_2 biogeochemical feedbacks and the ERF for aerosols. Chapters 3, 4, 5, 6 and 9 use the assessment of ERF, ECS and TCR from this chapter to help understand historical and future temperature changes, the response to cumulative emissions, the remaining carbon budget and sea level rise respectively. This chapter builds on findings from the IPCC Fifth Assessment Report (AR5), the Special Report on Global Warming of 1.5°C (SR1.5), the Special Report on Ocean and Cryosphere in a Changing Climate (SROCC) and the Special Report on Climate Change and Land (SRCCL). *Very likely* ranges are presented unless otherwise indicated.

Earth's Energy Budget

Since AR5, the accumulation of energy in the Earth system, quantified by changes in the global energy inventory for all components of the climate system, has become established as a robust measure of the rate of global climate change on interannual-to-decadal timescales. Compared to changes in global surface air temperature (GSAT), the global energy inventory exhibits less variability, which can mask underlying climate trends. Compared to AR5, there is increased confidence in the quantification of changes in the global energy inventory due to improved observational records and closure of the sea level budget. Energy will continue to accumulate in the Earth system until at least the end of the 21st century, even under strong mitigation scenarios, and will primarily be manifest through ocean warming and associated with continued sea level rise through thermal expansion. (*high confidence*) {7.2.2, Box 7.2, Table 7.1, Chapter 9 Cross-Chapter Box 9.1, Table 9.5, 9.2.2, 9.6.3}

The global energy inventory increased by 435 [325 to 545] Zettajoules (ZJ) for the period 1971–2018 and 153 [101 to 206] ZJ for the period 2006–2018. This corresponds to an Earth energy imbalance of 0.57 [0.43 to 0.72] W m^{-2} for the period 1971–2018, increasing to 0.79 [0.52 to 1.06] W m^{-2} for the period 2006–2018, expressed per unit area of Earth's surface. Ocean heat uptake is by far the largest contribution and accounts for 91% of the total energy change. Compared to AR5, the contribution from land heating has been revised upwards from about 3% to about 5%. Melting of ice and warming of the atmosphere account for about 3% and 1% of the total change respectively. More comprehensive analysis of inventory components and cross-validation of satellite and in situ-based global heating rates lead to a more confident assessment relative to AR5. (*high confidence*) {Box 7.2, 7.2.2, Table 7.1, 7.5.2.3}

Improved quantification of effective radiative forcing, the climate system radiative response, and the observed energy increase in the Earth system for the period 1971–2018 demonstrate improved closure of the global energy budget compared to AR5. Combining the *likely* range of ERF with the central estimate of radiative response gives an expected energy gain of 340 [47 to 662] ZJ. Combining the *likely* range of climate response with the central estimate of ERF gives an expected energy gain of 340 [147 to 527] ZJ. Both estimates are consistent with an independent observation-based assessment of the global energy increase of 284 [96 to 471] ZJ, (*very likely range*) expressed relative to the estimated 1850-1900 Earth energy imbalance. (*high confidence*) {7.2.2, Box 7.2, 7.3.5, 7.5.2}

Since AR5, additional evidence for a widespread decline (or dimming) in solar radiation reaching the

surface is found in the observational records between the 1950s and 1980s, with a partial recovery (brightening) at many observational sites thereafter (*high confidence*). These trends are neither a local phenomenon nor a measurement artefact (*high confidence*). Multi-decadal variation in anthropogenic aerosol emissions are thought to be a major contributor (*medium confidence*), but multi-decadal variability in cloudiness may also have played a role. The downward and upward thermal radiation at the surface has increased in recent decades, in line with increased greenhouse gas concentrations and associated surface and atmospheric warming and moistening (*medium confidence*). {7.2.2}

Effective Radiative Forcing

For carbon dioxide, methane, nitrous oxide and chlorofluorocarbons, there is now evidence to quantify the effect on ERF of tropospheric adjustments (e.g., from changes in atmospheric temperatures, clouds and water vapour). The assessed ERF for a doubling of carbon dioxide compared to 1750 levels (3.93 ± 0.47 W m^{-2}) is larger than in AR5. Effective radiative forcings (ERF), introduced in AR5, have been estimated for a larger number of agents and shown to be more closely related to the temperature response than the stratospheric-temperature adjusted radiative forcing. For carbon dioxide, the adjustments include the physiological effects on vegetation. (*high confidence*) {7.3.2}

The total anthropogenic ERF over the industrial era (1750–2019) was 2.72 [1.96 to 3.48] W m^{-2}. This estimate has increased by 0.43 W m^{-2} compared to AR5 estimates for 1750–2011. This increase includes a +0.34 W m^{-2} from increases in atmospheric concentrations of well-mixed greenhouse gases (including halogenated species) since 2011, a +0.15 W m^{-2} from upwards revisions of their radiative efficiencies and a +0.10 W m^{-2} from re-evaluation of the ozone and stratospheric water vapour ERF. The 0.59 W m^{-2} increase in ERF from greenhouse gases is partly offset by a better-constrained assessment of total aerosol ERF that is more strongly negative than in AR5, based on multiple lines of evidence (*high confidence*). Changes in surface reflectance from land-use change, deposition of light-absorbing particles on ice and snow, and contrails and aviation-induced cirrus have also contributed to the total anthropogenic ERF over the industrial era, with –0.20 [–0.30 to –0.10] W m^{-2} (*medium confidence*), +0.08 [0 to 0.18] W m^{-2} (*low confidence*) and +0.06 [0.02 to 0.10] W m^{-2} (*low confidence*), respectively. {7.3.2, 7.3.4, 7.3.5}

Anthropogenic emissions of greenhouse gases (GHGs) and their precursors contribute an ERF of 3.84 [3.46 to 4.22] W m^{-2} over the industrial era (1750–2019). Most of this total ERF, 3.32 [3.03 to 3.61] W m^{-2}, comes from the well-mixed greenhouse gases, with changes in ozone and stratospheric water vapour (from methane oxidation) contributing the remainder. The ERF of GHGs is composed of 2.16 [1.90 to 2.41] W m^{-2} from carbon dioxide, 0.54 [0.43 to 0.65] W m^{-2} from methane, 0.41 [0.33 to 0.49] W m^{-2} from halogenated species, and 0.21 [0.18 to 0.24] W m^{-2} from nitrous oxide. The ERF for ozone is 0.47 [0.24 to 0.71] W m^{-2}. The estimate of ERF for ozone has increased since AR5 due to revised estimates of precursor emissions and better accounting for effects of tropospheric ozone precursors in the stratosphere. The estimated ERF for methane has slightly increased due to a combination of increases from improved spectroscopic treatments being somewhat offset by accounting for adjustments. (*high confidence*) {7.3.2, 7.3.5}

Aerosols contribute an ERF of –1.3 [–2.0 to –0.6] W m^{-2} over the industrial era (1750–2014) (*medium confidence*). The ERF due to aerosol–cloud interactions (ERFaci) contributes most to the magnitude of the total aerosol ERF (*high confidence*) and is assessed to be –1.0 [–1.7 to –0.3] W m^{-2} (*medium confidence*), with the remainder due to aerosol–radiation interactions (ERFari), assessed to be –0.3 [–0.6 to 0.0] W m^{-2} (*medium confidence*). There has been an increase in the estimated magnitude but a reduction in the uncertainty of the total aerosol ERF relative to AR5, supported by a combination of increased process-understanding and progress in modelling and observational analyses. ERF estimates from these separate lines of evidence are now consistent with each other, in contrast to AR5, and support the assessment that it is *virtually certain* that the total aerosol ERF is negative. Compared to AR5, the assessed magnitude of ERFaci has increased, while the magnitude of ERFari has decreased. The total aerosol ERF over the period 1750–2019 is less certain than the headline statement assessment. It is also assessed to be smaller in magnitude at –1.1 [–1.7 to –0.4] W m^{-2}, primarily due to recent emission changes (*medium confidence*). {7.3.3, 7.3.5, 2.2.6}

Climate Feedbacks and Sensitivity

The net effect of changes in clouds in response to global warming is to amplify human-induced warming, that is, the net cloud feedback is positive (*high confidence*). Compared to AR5, major advances in the understanding of cloud processes have increased the level of confidence and decreased the uncertainty range in the cloud feedback by about 50%. An assessment of the low-altitude cloud feedback over the subtropical oceans, which was previously the major source of uncertainty in the net cloud feedback, is improved owing to a combined use of climate model simulations, satellite observations, and explicit simulations of clouds, altogether leading to strong evidence that this type of cloud amplifies global warming. The net cloud feedback, obtained by summing the cloud feedbacks assessed for individual regimes, is 0.42 [–0.10 to 0.94] W m^{-2} $°C^{-1}$. A net negative cloud feedback is *very unlikely*. (*high confidence*) {7.4.2, Figure 7.10, Table 7.10}

The combined effect of all known radiative feedbacks (physical, biogeophysical, and non-CO_2 biogeochemical) is to amplify the base climate response, also known as the Planck temperature response (*virtually certain*). Combining these feedbacks with the base climate response, the net feedback parameter based on process understanding is assessed to be –1.16 [–1.81 to –0.51] W m^{-2} $°C^{-1}$, which is slightly less negative than that inferred from the overall ECS assessment. The combined water vapour and lapse rate feedback makes the largest single contribution to global warming, whereas the cloud feedback remains the largest contribution to overall uncertainty. Due to the state-dependence of feedbacks, as evidenced from paleoclimate observations and from models, the net feedback parameter will increase (become less negative) as global temperature increases. Furthermore, on long time scales the ice sheet feedback parameter is *very likely* positive, promoting additional warming on millennial time scales as ice sheets come into equilibrium with the forcing. (*high confidence*) {7.4.2, 7.4.3, 7.5.7}

Radiative feedbacks, particularly from clouds, are expected to become less negative (more amplifying) on multi-decadal timescales as the *spatial pattern* of surface warming evolves, leading to an ECS that is higher than was inferred in AR5 based on warming over the instrumental record. This new understanding, along with updated estimates of historical temperature change, ERF, and Earth's energy imbalance, reconciles previously disparate ECS estimates (*high confidence*). However, there is currently insufficient evidence to quantify a *likely* range of the magnitude of future changes to current climate feedbacks. Warming over the instrumental record provides robust constraints on the lower end of the ECS range (*high confidence*), but owing to the possibility of future feedback changes it does not, on its own, constrain the upper end of the range, in contrast to what was reported in AR5. {7.4.4, 7.5.2, 7.5.3}

Based on multiple lines of evidence the best estimate of ECS is 3°C, the *likely* range is 2.5°C to 4°C, and the *very likely* range is 2°C to 5°C. It is *virtually certain* that ECS is larger than 1.5°C. Substantial advances since AR5 have been made in quantifying ECS based on feedback process understanding, the instrumental record, paleoclimates and emergent constraints. There is a high level of agreement among the different lines of evidence. All lines of evidence help rule out ECS values below 1.5°C, but currently it is not possible to rule out ECS values above 5 °C. Therefore, the 5°C upper end of the *very likely* range is assessed to have *medium confidence* and the other bounds have *high confidence*. {7.5.5}

Based on process understanding, warming over the instrumental record, and emergent constraints, the best estimate of TCR is 1.8°C, the *likely* range is 1.4°C to 2.2°C and the *very likely* range is 1.2°C to 2.4°C (*high confidence*). {7.5.5}

On average, CMIP6 models have higher mean ECS and TCR values than the CMIP5 generation of models. They also have higher mean values and wider spreads than the assessed best estimates and *very likely* ranges within this Report. These higher ECS and TCR values can, in some models, be traced to changes in extra-tropical cloud feedbacks that have emerged from efforts to reduce biases in these clouds compared to satellite observations (*medium confidence*). The broader ECS and TCR ranges from CMIP6 also lead the models to project a range of future warming that is wider than the assessed warming range, which is based on multiple lines of evidence. However, some of the high-sensitivity CMIP6 models are less consistent with observed recent changes in global warming and with paleoclimate proxy data than models with ECS within the *very likely* range. Similarly, some of the low-sensitivity models are less consistent with the paleoclimate data. The CMIP models with the highest ECS and TCR values provide insights into high-risk, low-likelihood futures, which cannot be excluded based on currently-available evidence. (*high confidence*) {4.3.1, 4.3.4, 7.4.2, 7.5.6}

Climate Response

The total human-forced GSAT change from 1750–2019 is calculated to be 1.29 [0.99 to 1.65] °C. This calculation is an emulator-based estimate, constrained by the historic GSAT and ocean heat content changes from Chapter 2 and the ERF, ECS and TCR from this chapter. The calculated GSAT change is composed of a well-mixed greenhouse gas warming of 1.58 [1.17 to 2.17] °C (*high confidence*), a warming from ozone changes of 0.23 [0.11 to 0.39] °C (*high confidence*), a cooling of –0.50 [–0.22 to –0.96] °C from aerosol effects (*medium confidence*), and a –0.06 [–0.15 to +0.01] °C contribution from surface reflectance changes from land-use change and light absorbing particles on ice and snow (*medium confidence*). Changes in solar and volcanic activity are assessed to have together contributed a small change of –0.02 [–0.06 to +0.02] °C since 1750 (*medium confidence*). {7.3.5}

Uncertainties regarding the true value of ECS and TCR are the dominant source of uncertainty in global temperature projections over the 21st century under moderate to high GHG emission scenarios. For scenarios that reach net zero carbon dioxide emissions, the uncertainty in the ERF values of aerosol and other short-lived forcings contribute substantial uncertainty in projected temperature. Global ocean heat uptake is a smaller source of uncertainty in centennial-time-scale surface warming. (*high confidence*) {7.5.7}

The assessed historical and future ranges of GSAT change in this Report are shown to be internally consistent with the Report's assessment of key physical-climate indicators: greenhouse gas ERFs, ECS and TCR. When calibrated to match the assessed ranges within the assessment, physically based emulators can reproduce the best estimate of GSAT change over 1850–1900 to 1995–2014 to within 5% and the *very likely* range of this GSAT change to within 10%. Two physically based emulators match at least two-thirds of the Chapter 4-assessed projected GSAT changes to within these levels of precision. When used for multi-scenario experiments, calibrated physically based emulators can adequately reflect assessments regarding future GSAT from Earth system models and/or other lines of evidence. (*high confidence*) {Cross-Chapter Box 7.1}

It is now well understood that the Arctic warms more quickly than the Antarctic due to differences in radiative feedbacks and ocean heat uptake between the poles, but that surface warming will eventually be amplified in both poles (*high confidence*). The causes of this polar amplification are well understood, and the evidence is stronger than at the time of AR5, supported by better agreement between modelled and observed polar amplification during warm paleo time periods (*high confidence*). The Antarctic warms more slowly than the Arctic owing primarily to upwelling in the Southern Ocean, and even at equilibrium is expected to warm less than the Arctic. The rate of Arctic surface warming will continue to exceed the global average over this century (*high confidence*). There is also *high confidence* that Antarctic amplification will emerge as the Southern Ocean surface warms on centennial time scales, although only *low confidence* regarding whether the feature will emerge during the 21st century. {7.4.4}

The assessed global warming potentials (GWP) and global temperature-change potentials (GTP) for methane and nitrous oxide are slightly lower than in AR5 due to revised estimates of their lifetimes and updated estimates of their indirect chemical effects (*medium confidence*). The assessed metrics now also include the carbon-cycle response for non-CO_2 gases. The carbon cycle estimate is lower than in AR5, but there is *high confidence* in the need for its inclusion and in the quantification methodology. Metrics for methane from fossil fuel sources account for the extra fossil CO_2 that these emissions contribute to the atmosphere and so have slightly higher emission metric values than those from biogenic sources (*high confidence*). {7.6.1}

New emission metric approaches such as GWP* and the combined-GTP (CGTP) are designed to relate emission rates of short-lived gases to cumulative emissions of CO_2. These metric approaches are well suited to estimate the GSAT response from aggregated emissions of a range of gases over time, which can be done by scaling the cumulative CO_2 equivalent emissions calculated with these metrics by the transient climate response to cumulative emissions of carbon dioxide. For a given multi-gas emission pathway, the estimated contribution of emissions to surface warming is improved by either using these new metric approaches or by treating short- and long-lived GHG emission pathways separately, as compared to approaches that aggregate emissions of GHGs using standard GWP or GTP emission metrics. By contrast, if emissions are weighted by their 100-year GWP or GTP values, different multi-gas emission pathways with the same aggregated CO_2 equivalent emissions rarely lead to the same estimated temperature outcome. (*high confidence*) {7.6.1, Box 7.3}

The choice of emission metric affects the quantification of net zero GHG emissions and therefore the resulting temperature outcome after net zero emissions are achieved. In general, achieving net zero CO_2 emissions and declining non-CO_2 radiative forcing would be sufficient to prevent additional human-caused warming. Reaching net zero GHG emissions as quantified by GWP-100 typically results in global temperatures that peak and then decline after net zero GHGs emissions are achieved, though this outcome depends on the relative sequencing of mitigation of short-lived and long-lived species. In contrast, reaching net zero GHG emissions when quantified using new emission metrics such as CGTP or GWP* would lead to approximate temperature stabilization (*high confidence*) {7.6.2}

7.1 Introduction, conceptual framework, and advances since AR5

This chapter assesses the major physical processes that affect the evolution of Earth's energy budget and the associated changes in surface temperature and the broader climate system, integrating elements that were dealt with separately in previous reports.

The top-of-atmosphere (TOA) energy budget determines the net amount of energy entering or leaving the climate system. Its time variations can be monitored in three ways, using: (i) satellite observations of the radiative fluxes at the TOA; (ii) observations of the accumulation of energy in the climate system; and (iii) observations of surface energy fluxes. When the TOA energy budget is changed by a human or natural cause (a radiative forcing), the climate system responds by warming or cooling (i.e., the system gains or loses energy). Understanding of changes in the Earth's energy flows helps understanding of the main physical processes driving climate change. It also provides a fundamental test of climate models and their projections.

This chapter principally builds on AR5 (Boucher, 2012; Church et al., 2013; Collins et al., 2013a; Flato et al., 2013; Hartmann et al., 2013; Myhre et al., 2013b; Rhein et al., 2013). It also builds on the subsequent SR1.5 (IPCC, 2018), SROCC (IPCC, 2019a) and SRCCL (IPCC, 2019b), as well as community-led assessments (e.g., Bellouin et al. (2019) covering aerosol radiative forcing and Sherwood et al. (2020) covering equilibrium climate sensitivity).

Throughout this chapter, global surface air temperature (GSAT) is used to quantify surface temperature change (see Cross-Chapter Box 2.3, Chapter 4 Section 4.3.4). The total energy accumulation in the Earth system represents a metric of global change that is complementary to GSAT but shows considerably less variability on interannual-to-decadal timescales (Section 7.2.2). Research and new observations since AR5 have improved scientific confidence in the quantification of changes in the global energy inventory and corresponding estimates of Earth's energy imbalance (Section 7.2). Improved understanding of adjustments to radiative forcing and of aerosol-cloud interactions have led to revisions of forcing estimates (Section 7.3). New approaches to the quantification and treatment of feedbacks (Section 7.4) have improved the understanding of their nature and time-evolution, leading to a better understanding of how these feedbacks relate to Equilibrium Climate Sensitivity (ECS). This has helped to reconcile disparate estimates of ECS from different lines of evidence (Section 7.5). Innovations in the use of emission metrics have clarified the relationships between metric choice and temperature policy goals (Section 7.6), linking this chapter to WGIII which provides further information on metrics, their use, and policy goals beyond temperature. *Very likely* (5% to 95%) ranges are presented unless otherwise indicated. In particular, the addition of (one standard deviation) indicates that the range represents one standard deviation.

In Box 7.1 an energy budget framework is introduced, which forms the basis for the discussions and scientific assessment in the remainder of this chapter and across the report. The framework reflects advances in the understanding of the Earth system response to climate forcing since the publication of AR5. A schematic of this framework and the key changes relative to the science reported in AR5 are provided in Figure 7.1.

[START FIGURE 7.1 HERE]

Figure 7.1: A visual abstract of the chapter, illustrating why the Earth's energy budget matters and how it relates to the underlying chapter assessment. The methods used to assess processes and key new findings relative to AR5 are highlighted.

[END FIGURE 7.1 HERE]

A simple way to characterise the behaviour of multiple aspects of the climate system at once is to summarise them using global-scale metrics. This report distinguishes between "climate metrics" (e.g., ECS, TCR) and "emission metrics" (such as the global warming potential; GWP, or global temperature potential; GTP), but this distinction is not definitive. Climate metrics are generally used to summarise aspects of the surface temperature response (Box 7.1). Emission metrics are generally used to summarise the relative effects of emissions of different forcing agents, usually greenhouse gases (see Section 7.6). The climate metrics used in this report typically evaluate how the Earth system response varies with atmospheric gas concentration or change in radiative forcing. Emission metrics evaluate how radiative forcing or a key climate variable (such as GSAT) is affected by the emissions of a certain amount of gas. Emission-related metrics are sometimes used in mitigation policy decisions such as trading greenhouse gas reduction measures and life cycle analysis. Climate metrics are useful to gauge the range of future climate impacts for adaptation decisions under a given emission pathway. Metrics such as the transient climate response to cumulative emissions of carbon dioxide (TCRE) are used in both adaptation and mitigation contexts: for gauging future global surface temperature change under specific emission scenarios, and to estimate remaining carbon budgets that are used to inform mitigation policies (see Chapter 5, Section 5.5).

Given that TCR and ECS are metrics of GSAT response to a theoretical doubling of atmospheric CO_2 (Box 7.1), they do not directly correspond to the warming that would occur under realistic forcing scenarios that include time-varying CO_2 concentrations and non-CO_2 forcing agents (such as aerosols and land-use changes). It has been argued that TCR, as a metric of transient warming, is more policy-relevant than ECS (Frame et al., 2006; Schwartz, 2018). However, as detailed in Chapter 4, both established and recent results (Forster et al., 2013; Gregory et al., 2015; Marotzke and Forster, 2015; Grose et al., 2018; Marotzke, 2019) indicate that TCR and ECS help explain variation across climate models both over the historical period and across a range of concentration-driven future scenarios. In emission-driven scenarios the carbon cycle response is also important (Smith et al., 2019). The proportion of variation explained by ECS and TCR varies with scenario and the time period considered, but both past and future surface warming depend on these metrics (Section 7.5.7).

Regional changes in temperature, rainfall, and climate extremes have been found to correlate well with the forced changes in GSAT within Earth System Models (ESMs) (Giorgetta et al., 2013; Tebaldi and Arblaster, 2014; Seneviratne et al., 2016; Chapter 4, Section 4.6.1). While this so-called 'pattern scaling' has important limitations arising from, for instance, localized forcings, land-use changes, or internal climate variability (Deser et al., 2012; Luyssaert et al., 2014), changes in GSAT nonetheless explain a substantial fraction of inter-model differences in projections of regional climate changes over the 21st century (Tebaldi and Knutti, 2018). This Chapter's assessments of TCR and ECS thus provide constraints on future global and regional climate change (Chapter 4 and Chapter 11).

[START BOX 7.1 HERE]

BOX 7.1: The energy budget framework – forcing and response

The forcing and response energy budget framework provides a methodology to assess the effect of individual drivers of global mean surface temperature response, and to facilitate the understanding of the key phenomena that set the magnitude of this temperature response. The framework used here is developed from that adopted in previous IPCC reports (see Ramaswamy et al., 2019 for a discussion). *Effective Radiative Forcing* (ERF), introduced in AR5 (Boucher et al., 2013; Myhre et al., 2013b) is more explicitly defined in this report and is employed as the central definition of radiative forcing (Sherwood et al. 2015, Box 7.1, Figure 1a). The framework has also been extended to allow variations in feedbacks over different timescales and with changing climate state (Section 7.4.4; Section 7.4.3).

The GSAT response to perturbations that give rise to an energy imbalance is traditionally approximated by the following linear energy budget equation, in which ΔN represents the change in the top-of-atmosphere (TOA) net energy flux, ΔF is an ***effective radiative forcing*** perturbation to the TOA net energy flux, α is the net ***feedback parameter*** and ΔT is the change in ***GSAT***:

$$\Delta N = \Delta F + \alpha \Delta T \qquad \text{Box 7.1, Equation (7.1)}$$

ERF is the TOA energy budget change resulting from the perturbation, excluding any radiative response related to a change in GSAT (i.e., ΔT =0). Climate feedbacks (α) represent those processes that change the TOA energy budget in response to a given ΔT.

[START BOX 7.1, FIGURE 1 HERE]

Box 7.1, Figure 1: Schematics of the forcing-feedback framework adopted within the assessment, following Equation 7.1. Illustrated is how the Earth's TOA net energy flux might evolve for a hypothetical doubling of atmospheric CO_2 concentration above preindustrial levels, where an initial positive energy imbalance (energy entering the Earth system, shown on the y-axis) is gradually restored towards equilibrium as the surface temperature warms (shown on the x-axis). a) illustrates the definitions of ERF for the special case of a doubling of atmospheric CO_2 concentration, the feedback parameter and the ECS. b) illustrates how approximate estimates of these metrics are made within the chapter and how these approximations might relate to the exact definitions adopted in panel a).

[END BOX 7.1, FIGURE 1 HERE]

The ***effective radiative forcing, ERF*** (ΔF; units: W m^{-2}) quantifies the change in the net TOA energy flux of the Earth system due to an imposed perturbation (e.g., changes in greenhouse gas or aerosol concentrations, in incoming solar radiation, or land-use change). ERF is expressed as a change in net downward radiative flux at the TOA following adjustments in both tropospheric and stratospheric temperatures, water vapour, clouds, and some surface properties, such as surface albedo from vegetation changes, that are uncoupled to any GSAT change (Smith et al., 2018b). These adjustments affect the TOA energy balance and hence the ERF. They are generally assumed to be linear and additive (Section 7.3.1). Accounting for such processes gives an estimate of ERF that is more representative of the climate change response associated with forcing agents than stratospheric-temperature-adjusted radiative forcing (SARF) or the instantaneous radiative forcing (IRF) (Section 7.3.1). Adjustments are processes that are independent of GSAT change, whereas feedbacks refer to processes caused by GSAT change. Although adjustments generally occur on timescales of hours to several months, and feedbacks respond to ocean surface temperature changes on timescales of a year or more, timescale is not used to separate the definitions. ERF has often been approximated as the TOA energy balance change due to an imposed perturbation in climate model simulations with sea-surface temperature and sea-ice concentrations set to their pre-industrial climatological values (e.g., Forster et al., 2016). However, to match the adopted forcing-feedback framework, the small effects of any GSAT change from changes in land surface temperatures need to be removed from the TOA energy balance in such simulations to give an approximate measure of ERF (Box 7.1, Figure 1b and Section 7.3.1).

The ***feedback parameter, α***, (units: W m^{-2} °C^{-1}) quantifies the change in net energy flux at the TOA for a given change in GSAT. Many climate variables affect the TOA energy budget, and the feedback parameter can be decomposed, to first order, into a sum of terms $\alpha = \sum_x \frac{\partial N}{\partial x}\frac{dx}{dT}$], where x represents a variable of the Earth system that has a direct effect on the energy budget at the TOA. The sum of the feedback terms (i.e., α in Equation 7.1) governs Earth's equilibrium GSAT response to an imposed ERF. In previous assessments, α and the related ECS have been associated with a distinct set of physical processes (Planck response and changes in water vapour, lapse rate, surface albedo, and clouds) (Charney et al., 1979). In this assessment, a more general definition of α and ECS is adopted such that they include additional Earth system processes that act across many timescales (e.g., changes in natural aerosol emissions or vegetation). Because, in our assessment, these additional processes sum to a near-zero value, including these additional processes does not change the assessed central value of ECS but does affect its assessed uncertainty range (Section 7.4.2). Note that there is no standardised notation or sign convention for the feedback parameter in the literature. Here the convention is used that the sum of all feedback terms (the net feedback parameter, α) is negative for a stable climate that radiates additional energy to space with a GSAT increase, with a more negative value of α corresponding to a stronger radiative response and thus a smaller GSAT change required to balance a change in ERF (Equation 7.1). A change in process x amplifies the temperature response to a forcing when the associated feedback parameter α_x is positive (positive feedback) and dampens the temperature response when α_x is negative (negative feedback). New research since AR5 emphasises how feedbacks can vary over different timescales (Section 7.4.4) and with climate state (Section 7.4.3), giving rise to the concept of an *effective feedback parameter* that may be different from the equilibrium value of the feedback parameter governing ECS (Section 7.4.3).

The ***equilibrium climate sensitivity***, ***ECS*** (units: °C), is defined as the equilibrium value of ΔT in response to a sustained doubling of atmospheric CO_2 concentration from a pre-industrial reference state. The value of ERF for this scenario is denoted by ΔF_{2xCO2}, giving $ECS = -\Delta F_{2xCO2}/\alpha$ from Equation (7.1) applied at equilibrium (see Box 7.1, Figure 1a and Section 7.5). Equilibrium refers to a steady state where ΔN averages to zero over a multi-century period. ECS is representative of the multi-century to millennial ΔT response to ΔF_{2xCO2}, and is based on a CO_2 concentration change so any feedbacks that affect the atmospheric concentration of CO_2 do not influence its value. As employed here, ECS also excludes the long-term response of the ice sheets (Section 7.4.2.6) which may take multiple millennia to reach equilibrium, but includes all other feedbacks. Due to a number of factors, studies rarely estimate ECS or α at equilibrium or under CO_2 forcing alone. Rather, they give an *effective feedback parameter* (Section 7.4.1 and Box 7.1, Figure 1b) or an *effective ECS* (Section 7.5.1 and Box 7.1, Figure 1b), which represent approximations to the true values of α or ECS. The *effective ECS* represents the equilibrium value of ΔT in response to a sustained doubling of atmospheric CO_2 concentration that would occur assuming the *effective feedback parameter* applied at that equilibrium state. For example, a feedback parameter can be estimated from the linear slope of ΔN against ΔT over a set number of years within ESM simulations of an abrupt doubling or quadrupling of atmospheric CO_2 ($2\times CO_2$ or $4\times CO_2$, respectively), and the ECS can be estimated from the intersect of this regression line with $\Delta N = 0$ (see Box 7.1, Figure 1b). To infer ECS from a given estimate of effective ECS necessitates that assumptions are made for how ERF varies with CO_2 concentration (Section 7.3.2) and how the slope of ΔN against ΔT relates to the slope of the straight line from ERF to ECS (see Section 7.5 and Box 7.1, Figure 1b). Care has to be taken when comparing results across different lines of evidence to translate their estimates of the effective ECS into the ECS definition used here (Section 7.5.5).

The ***transient climate response, TCR*** (units: °C), is defined as the ΔT for the hypothetical scenario in which CO_2 increases at 1% yr^{-1} from a pre-industrial reference state to the time of a doubling of atmospheric CO_2 concentration (year 70) (Section 7.5). TCR is based on a CO_2 concentration change, so any feedbacks that affect the atmospheric concentration of CO_2 do not influence its value. It is a measure of transient warming accounting for the strength of climate feedbacks and ocean heat uptake. The ***transient climate response to cumulative emissions of carbon dioxide*** (***TCRE***) is defined as the transient ΔT per 1000 Gt C of cumulative CO_2 emission increase since preindustrial. TCRE combines information on the airborne fraction of cumulative CO_2 emissions (the fraction of the total CO_2 emitted that remains in the atmosphere at the time of doubling, which is determined by carbon cycle processes) with information on the TCR. TCR is assessed in this chapter, whereas TCRE is assessed in Chapter 5, Section 5.5.

[END BOX 7.1 HERE]

7.2 Earth's energy budget and its changes through time

Earth's energy budget encompasses the major energy flows of relevance for the climate system (Figure 7.2). Virtually all the energy that enters or leaves the climate system does so in the form of radiation at the TOA. The TOA energy budget is determined by the amount of incoming solar (shortwave) radiation and the outgoing radiation that is composed of reflected solar radiation and outgoing thermal (longwave) radiation emitted by the climate system. In a steady state climate, the outgoing and incoming radiative components are essentially in balance in the long-term global mean, although there are still fluctuations around this balanced state that arise through internal climate variability (Brown et al., 2014; Palmer and McNeall, 2014). However, anthropogenic forcing has given rise to a persistent imbalance in the global mean TOA radiation budget that is often referred to as Earth's energy imbalance (e.g., Trenberth et al., 2014; von Schuckmann et al., 2016) and is a key element in energy budget framework (*N*, Box 7.1, Equation 7.1) and an important metric of the rate of global climate change (Hansen et al., 2005a; von Schuckmann et al., 2020). In addition to the TOA energy fluxes, Earth's energy budget also includes the internal flows of energy within the climate system, which characterize the climate state. The surface energy budget consists of the net solar and thermal radiation as well as the non-radiative components such as sensible, latent and ground heat fluxes (Figure 7.2 upper panel). It is a key driver of the global water cycle, atmosphere and ocean dynamics, as well as a variety of surface processes.

7.2.1 Present-day energy budget

Figure 7.2 (upper panel) shows a schematic representation of Earth's energy budget for the early 21st century, including globally-averaged estimates of the individual components (Wild et al., 2015). Clouds are important modulators of the global energy fluxes. Thus, any perturbations in the cloud fields, such as forced by aerosol-cloud interactions (Section 7.3) or through cloud feedbacks (Section 7.4) can have a strong influence on the energy distribution in the climate system. To illustrate the overall effects that clouds exert on the energy fluxes, Figure 7.2 (lower panel) also shows the energy budget in the absence of clouds, with otherwise identical atmospheric and surface radiative properties. It has been derived by taking into account information contained in both in-situ and satellite radiation measurements taken under cloud-free conditions (Wild et al., 2019). A comparison of the upper and lower panels in Figure 7.2 shows that without clouds, 47 W m^{-2} less solar radiation is reflected back to space globally (53 ± 2 W m^{-2} instead of 100 ± 2 W m^{-2}), while 28 W m^{-2} more thermal radiation is emitted to space (267 ± 3 W m^{-2} instead of 239 ± 3 W m^{-2}). As a result, there is a 20 W m^{-2} radiative imbalance at the TOA in the clear-sky energy budget (Figure 7.2 lower panel), suggesting that the Earth would warm substantially if there were no clouds.

[START FIGURE 7.2 HERE]

Figure 7.2: Schematic representation of the global mean energy budget of the Earth (upper panel), and its equivalent without considerations of cloud effects (lower panel). Numbers indicate best estimates for the magnitudes of the globally averaged energy balance components in W m^{-2} together with their uncertainty ranges in parentheses (5–95 % confidence range), representing climate conditions at the beginning of the 21st century. Note that the cloud-free energy budget shown in the lower panel is not the one that Earth would achieve in equilibrium when no clouds could form. It rather represents the global mean fluxes as determined solely by removing the clouds but otherwise retaining the entire atmospheric structure. This enables the quantification of the effects of clouds on the Earth energy budget and corresponds to the way clear-sky fluxes are calculated in climate models. Thus, the cloud-free energy budget is not closed and therefore the sensible and latent heat fluxes are not quantified in the lower panel. Adapted from Wild et al. (2015, 2019).

[END FIGURE 7.2 HERE]

AR5 (Church et al., 2013; Hartmann et al., 2013; Myhre et al., 2013b) highlighted the progress in quantifying the TOA radiation budget following new satellite observations that became available in the early 21st Century (Clouds and the Earth's Radiant Energy System, CERES; Solar Radiation and Climate Experiment, SORCE). Progress in the quantification of changes in incoming solar radiation at the TOA is discussed in Chapter 2, Section 2.2. Since AR5, the CERES Energy Balance EBAF Ed4.0 product was released, which includes algorithm improvements and consistent input datasets throughout the record (Loeb et al., 2018a). However, the overall precision of these fluxes (uncertainty in global mean TOA flux 1.7% (1.7 W m^{-2}) for reflected solar and 1.3% (3.0 W m^{-2}) for outgoing thermal radiation at the 90% confidence level) is not sufficient to quantify the Earth's energy imbalance in absolute terms. Therefore, adjustments within the uncertainty ranges of the CERES reflected solar and emitted thermal TOA fluxes were applied to the entire EBAF record to ensure that the net TOA flux for July 2005–June 2015 was consistent with the estimated Earth's energy imbalance for the same period based on ocean heat content (OHC) measurements and energy uptake estimates for the land, cryosphere and atmosphere (Johnson et al., 2016; Riser et al., 2016; Section 7.2.2.2). ESMs typically show good agreement with global mean TOA fluxes from CERES-EBAF. However, as some ESMs are known to calibrate their TOA fluxes to CERES or similar data (Hourdin et al., 2017), this is not necessarily an indication of model accuracy, especially as ESMs show significant discrepancies on regional scales, often related to their representation of clouds (Trenberth and Fasullo, 2010; Donohoe and Battisti, 2012; Hwang and Frierson, 2013; Li et al., 2013b; Dolinar et al., 2015; Wild et al., 2015).

The radiation components of the surface energy budget are associated with substantially larger uncertainties than at the TOA, since they are less directly measured by passive satellite sensors from space and require retrieval algorithms and ancillary data for their estimation (Raschke et al., 2016; Kato et al., 2018; Huang et al., 2019). Confidence in the quantification of the global mean surface radiation components has increased recently, as independent estimates now converge to within a few W m^{-2} (Wild, 2017). Current best estimates for downward solar and thermal radiation at Earth's surface are near 185 W m^{-2} and 342 W m^{-2}, respectively (Figure 7.2). These estimates are based on complementary approaches that make use of satellite products from active and passive sensors (L'Ecuyer et al., 2015; Kato et al., 2018) and information from surface observations and Earth System Models (ESMs) (Wild et al., 2015). Inconsistencies in the quantification of the global mean energy and water budgets discussed in AR5 (Hartmann et al., 2013) have been reconciled within the (considerable) uncertainty ranges of their individual components (Wild et al., 2013, 2015; L'Ecuyer et al., 2015). However, on regional scales, the closure of the surface energy budgets remains a challenge with satellite-derived datasets (Loeb et al., 2014; L'Ecuyer et al., 2015; Kato et al., 2016). Nevertheless, attempts have been made to derive surface energy budgets over land and ocean (Wild et al., 2015), over the Arctic (Christensen et al., 2016a) and over individual continents and ocean basins (L'Ecuyer et al., 2015; Thomas et al., 2020). Since AR5, the quantification of the uncertainties in surface energy flux datasets has improved. Uncertainties in global monthly mean downward solar and thermal fluxes in the CERES-EBAF surface dataset are, respectively, 10 W m^{-2} and 8 W m^{-2} (converted to 5% to 95% ranges) (Kato et al., 2018). The uncertainty in the surface fluxes for polar regions is larger than in other regions (Kato et al., 2018) due to the limited number of surface sites and larger uncertainty in surface observations (Previdi et al., 2015). The uncertainties in ocean mean latent and sensible heat fluxes are approximately 11 W m^{-2} and 5 W m^{-2} (converted to 5% to 95% ranges), respectively (L'Ecuyer et al., 2015). A recent review of the latent and sensible heat flux accuracies over the period 2000 to 2007 highlights significant differences between several gridded products over ocean, where root mean squared differences between the multi-product ensemble and data at more than 200 moorings reached up to 25 W m^{-2} for latent heat and 5 W m^{-2} for sensible heat (Bentamy et al., 2017). This uncertainty stems from the retrieval of flux-relevant meteorological variables, as well as from differences in the flux parameterizations (Yu, 2019). Estimating the uncertainty in sensible and latent heat fluxes over land is difficult because of the large temporal and spatial variability. The flux values over land computed with three global datasets vary by 10% to 20% (L'Ecuyer et al., 2015).

ESMs also show larger discrepancies in their surface energy fluxes than at the TOA due to weaker observational constraints, with a spread of typically 10-20 W m^{-2} in the global average, and an even greater spread at regional scales (Li et al., 2013b; Wild et al., 2013; Boeke and Taylor, 2016; Wild, 2017; Zhang et al., 2018a; Wild, 2020). Differences in the land-averaged downward thermal and solar radiation in CMIP5 ESMs amount to more than 30 and 40 W m^{-2}, respectively (Wild et al., 2015). However, in the global multi-model mean, the magnitudes of the energy budget components of the CMIP6 ESMs generally show better agreement with reference estimates than previous model generations (Wild, 2020).

In summary, since AR5, the magnitudes of the global mean energy budget components have been quantified more accurately, not only at the TOA, but also at the Earth's surface, where independent estimates of the radiative components have converged (*high confidence*). Considerable uncertainties remain in regional surface energy budget estimates as well as their representation in climate models.

7.2.2 Changes in Earth's energy budget

7.2.2.1 Changes in Earth's TOA energy budget

Since 2000, changes in the TOA energy fluxes can be tracked from space using CERES satellite observations (Figure 7.3). The variations in TOA energy fluxes reflect the influence of internal climate variability, particularly that of ENSO, in addition to radiative forcing of the climate system and climate feedbacks (Allan et al., 2014; Loeb et al., 2018a). For example, globally, the reduction in both outgoing thermal and reflected solar radiation during La Niña conditions in 2008/2009 led to an energy gain for the climate system, whereas enhanced outgoing thermal and reflected solar radiation caused an energy loss during the El Niños of 2002/2003 and 2009/2010 (Figure 7.3; Loeb et al., 2018a). An ensemble of CMIP6 models is able to track the variability in the global mean TOA fluxes observed by CERES, when driven with prescribed sea-surface temperatures (SSTs) and sea-ice concentrations (Figure 7.3; Loeb et al., 2020). Under cloud-free conditions, the CERES record shows a near zero trend in outgoing thermal radiation (Loeb et al., 2018a), which combined with an increasing surface upwelling thermal flux implies an increasing clear-sky greenhouse effect (Raghuraman et al., 2019). Conversely, clear-sky solar reflected TOA radiation in the CERES record covering March 2000 to September 2017 shows a decrease due to reductions in aerosol optical depth in the Northern Hemisphere and sea-ice fraction (Loeb et al., 2018b; Paulot et al., 2018).

An effort to reconstruct variations in the net TOA fluxes back to 1985, based on a combination of satellite data, atmospheric reanalysis and high-resolution climate model simulations (Allan et al., 2014; Liu et al., 2020), exhibits strong interannual variability associated with the volcanic eruption of Mt Pinatubo in 1991 and the ENSO events before 2000. The same reconstruction suggests that Earth's energy imbalance increased by several tenths of a W m^{-2} between the periods 1985–1999 and 2000–2016, in agreement with the assessment of changes in the global energy inventory (Section 7.2.2.2, Box 7.2, Figure 1). Comparisons of year-to-year variations in Earth's energy imbalance estimated from CERES and independent estimates based on ocean heat content change are significantly correlated with similar phase and magnitude (Johnson et al., 2016; Meyssignac et al., 2019), promoting confidence in both satellite and in situ-based estimates (Section 7.2.2.2).

In summary, variations in the energy exchange between Earth and space can be accurately tracked since the advent of improved observations since the year 2000 (*high confidence*), while reconstructions indicate that the Earth's energy imbalance was larger in the 2000s than in the 1985–1999 period (*high confidence*).

[START FIGURE 7.3 HERE]

Figure 7.3: Anomalies in global mean all-sky TOA fluxes from EBAF Ed4.0 (solid black lines) and various CMIP6 climate models (coloured lines) in terms of (a) reflected solar, (b) emitted thermal and (c) net TOA fluxes. The multi-model means are additionally depicted as dotted black lines. Model fluxes stem from simulations driven with prescribed SSTs and all known anthropogenic and natural forcings. Shown are anomalies of 12-month running means. All flux anomalies are defined as positive downwards, consistent with the sign convention used throughout this chapter. The correlations between the multi-model means (dotted black lines) and the CERES records (solid black lines) for 12-month running means are 0.85, 0.73 and 0.81 for the global mean reflected solar, outgoing thermal and net TOA radiation, respectively. Adapted from Loeb et al. (2020). Further details on data sources and processing are available in the chapter data table (Table 7.SM.14).

[END FIGURE 7.3 HERE]

7.2.2.2 *Changes in the global energy inventory*

The global energy inventory quantifies the integrated energy gain of the climate system associated with global ocean heat uptake, warming of the atmosphere, warming of the land, and melting of ice. Due to energy conservation, the rate of accumulation of energy in the Earth system (Section 7.1) is equivalent to the Earth energy imbalance (*N* in Box 7.1, Equation 7.1). On annual and longer timescales, changes in the global energy inventory are dominated by changes in global OHC (Rhein et al., 2013; Palmer and McNeall, 2014; Johnson et al., 2016). Thus, observational estimates and climate model simulations of OHC change are critical to the understanding of both past and future climate change (Chapter 2, Section 2.3.3.1, Chapter 3, Section 3.5.1.3, Chapter 4, Section 4.5.2.1, Chapter 9, Section 9.2.2.1).

Since AR5, both modelling and observational-based studies have established Earth's energy imbalance (characterised by OHC change) as a more robust metric of the rate of global climate change than GSAT on interannual-to-decadal timescales (Palmer and McNeall, 2014; von Schuckmann et al., 2016; Wijffels et al., 2016; Cheng et al., 2018; Allison et al., 2020a). This is because GSAT is influenced by large unforced variations, for example linked to ENSO and Pacific decadal variability (Roberts et al., 2015; Yan et al., 2016; Cheng et al., 2018). Measuring OHC change more comprehensively over the full ocean depth results in a higher signal-to-noise ratio and a timeseries that increases steadily over time (Box7.2, Figure 1; Allison et al., 2020). In addition, understanding of the potential effects of historical ocean sampling on estimated global ocean heating rates has improved (Durack et al., 2014; Good, 2017; Allison et al., 2019) and there are now more estimates of OHC change available that aim to mitigate the effect of limited observational sampling in the Southern Hemisphere (Lyman and Johnson, 2008; Cheng et al., 2017; Ishii et al., 2017).

The assessment of changes in the global energy inventory for the periods 1971-2018, 1993-2018 and 2006–2018 draws upon the latest observational timeseries and the assessments presented in other chapters of this report. The estimates of OHC change come directly from the assessment presented in Chapter 2, Section 2.3.3.1. The assessment of land and atmospheric heating comes from von Schuckmann et al. (2020), based on the estimates of Cuesta-Valero et al. (2021) and Steiner et al. (2020), respectively. Heating of inland waters, including lakes, reservoirs and rivers, is estimated to account for < 0.1 % of the total energy change, and is therefore neglected from this assessment (Vanderkelen et al., 2020). The cryosphere contribution from melting of grounded ice is based on the mass loss assessments presented in Chapter 9, Sections 9.4.1 (Greenland ice sheet), 9.4.2 (Antarctic ice sheet) and 9.5.1 (glaciers). Following AR5, the estimate of heating associated with loss of Arctic sea ice is based on a reanalysis (Schweiger et al., 2011), following the methods described by Slater et al. (2021). Chapter 9, Section 9.3.2 finds no significant trend in Antarctic sea ice area over the observational record, a zero contribution is assumed. Ice melt associated with the calving and thinning of floating ice shelves are based on the decadal rates presented in Slater et al. (2021). For all cryospheric components, mass loss is converted to heat input using a latent heat of fusion of 3.34×10^5 J Kg^{-1} C^{-1} with the second-order contributions from variations associated with ice type and warming of ice from sub-freezing temperatures neglected, as in AR5. The net change in energy, quantified in Zetta Joules (1 ZJ = 10^{21} Joules), is computed for each component as the difference between the first and last year of each period (Table 7.1). The uncertainties in the depth-interval contributions to OHC are summed to get the uncertainty in global OHC change. All other uncertainties are assumed to be independent and added in quadrature.

[START TABLE 7.1 HERE]

Table 7.1: Contributions of the different components of the global energy inventory for the periods 1971 to 2018, 1993 to 2018 and 2006 to 2018 (Box 7.2, Cross-chapter box 9.1). Energy changes are computed as the difference between annual mean values or year mid-points. The total heating rates correspond to Earth's energy imbalance and are expressed per unit area of Earth's surface.

Component	1971 to 2018		1993 to 2018		2006 to 2018	
	Energy Gain (ZJ)	%	Energy Gain (ZJ)	%	Energy Gain (ZJ)	%
Ocean	396.0 [285.7 to 506.2]	91.0	263.0 [194.1 to 331.9]	90.9	138.8 [86.4 to 191.3]	90.7
0-700 m	241.6 [162.7 to 320.5]	55.6	151.5 [114.1 to 188.9]	52.4	75.4 [48.7 to 102.0]	49.3
700-2000 m	123.3 [96.0 to 150.5]	28.3	82.8 [59.9 to 105.6]	28.6	49.7 [29.0 to 70.4]	32.4
> 2000 m	31.0 [15.7 to 46.4]	7.1	28.7 [14.5 to 43.0]	9.9	13.8 [7.0 to 20.6]	9.0
Land	21.8 [18.6 to 25.0]	5.0	13.7 [12.4 to 14.9]	4.7	7.2 [6.6 to 7.8]	4.7
Cryosphere	11.5 [9.0 to 14.0]	2.7	8.8 [7.0 to 10.6]	3.0	5.4 [3.9 to 6.8]	3.5
Atmosphere	5.6 [4.6 to 6.7]	1.3	3.8 [3.2 to 4.3]	1.3	1.6 [1.2 to 2.1]	1.1
TOTAL	**434.9 [324.5 to 545.5] ZJ**		**289.2 [220.3 to 358.2] ZJ**		**153.1 [100.6 to 205.5] ZJ**	

Heating Rate	**0.57 [0.43 to 0.72] W m^{-2}**	**0.72 [0.55 to 0.89] W m^{-2}**	**0.79 [0.52 to 1.06] W m^{-2}**

[END TABLE 7.1 HERE]

For the period 1971–2010, AR5 (Rhein et al., 2013) found an increase in the global energy inventory of 274 [196 to 351] ZJ with a 93% contribution from total OHC change, about 3% for both ice melt and land heating, and about 1% for warming of the atmosphere. For the same period, this Report finds an upwards revision of OHC change for the upper (< 700 m depth) and deep (> 700 m depth) ocean of about 8% and 20% compared to AR5 and a modest increase in the estimated uncertainties associated with the ensemble approach of Palmer et al. (2021). The other substantive change compared to AR5 is the updated assessment of land heating, with values approximately double those assessed previously, based on a more comprehensive analysis of the available observations (von Schuckmann et al., 2020; Cuesta-Valero et al., 2021). The result of these changes is an assessed energy gain of 329 [224 to 434] ZJ for the period 1971–2010, which is consistent with AR5 within the estimated uncertainties, despite the systematic increase.

The assessed changes in the global energy inventory (Box 7.2, Figure 1a; Table 7.1) yields an average value for Earth's energy imbalance (*N*, Box 7.1, Equation 7.1) of 0.57 [0.43 to 0.72] W m^{-2} for the period 1971 to 2018, expressed relative to Earth's surface area (*high confidence*). The estimates for the periods 1993 to 2018 and 2006 to 2018 yield substantially larger values of 0.72 [0.55 to 0.89] W m^{-2} and 0.79 ± [0.52 to 1.06] W m^{-2}, respectively, consistent with the increased radiative forcing from greenhouse gases (*high confidence*). To put these numbers in context, the 2006–2018 average Earth system heating is equivalent to approximately 20 times the rate of global energy consumption in 2018[1].

Consistent with AR5 (Rhein et al., 2013), ocean warming dominates the changes in total Earth system heating (*high confidence*), accounting for 91% of the observed change for all periods considered (Table 7.1). The contributions from the other components across all periods are approximately 5% from land heating, 3% for cryosphere heating and 1% associated with warming of the atmosphere (*high confidence*). The assessed percentage contributions are similar to the recent study by von Schuckmann et al. (2020) and the total heating rates are consistent within the assessed uncertainties. Cross-validation of heating rates based on satellite and in situ observations (Section 7.2.2.1) and closure of the global sea-level budget using consistent datasets (Cross-Chapter Box 9.1; Chapter 9, Table 9.5) strengthen scientific confidence in the assessed changes in the global energy inventory relative to AR5.

7.2.2.3 Changes in Earth's surface energy budget

AR5 (Hartmann et al., 2013) reported pronounced changes in multi-decadal records of in situ observations of surface solar radiation, including a widespread decline between the 1950s and 1980s, known as "global dimming", and a partial recovery thereafter, termed "brightening" (see also Chapter 12, Section 12.4). Over the past decades, these changes have interacted with closely-related elements of climate change, such as global and regional warming rates (Li et al., 2016b; Wild, 2016; Du et al., 2017; Zhou et al., 2018a), glacier melt (Ohmura et al., 2007; Huss et al., 2009), the intensity of the global water cycle (Wild, 2012) and terrestrial carbon uptake (Mercado et al., 2009). These observed changes have also been used as emergent constraints to quantify aerosol effective radiative forcing (see Section 7.3.3.3).

Since AR5, additional evidence for dimming and/or subsequent brightening up to several percent per decade, based on direct surface observations, has been documented in previously less studied areas of the globe, such as in Iran, Bahrain, Tenerife, Hawaii, the Taklaman desert and the Tibetan Plateau (Elagib and Alvi, 2013; You et al., 2013; Garcia et al., 2014; Longman et al., 2014; Rahimzadeh et al., 2015). Strong decadal trends in surface solar radiation remain evident after careful data quality assessment and homogenization of long-

[1] https://ourworldindata.org/energy, accessed 13 April 2021

term records (Sanchez-Lorenzo et al., 2013; Manara et al., 2015; Sanchez-Lorenzo et al., 2015; Wang et al., 2015; Li et al., 2016b; Manara et al., 2016; Wang and Wild, 2016; He et al., 2018b; Yang et al., 2018). Since AR5, new studies on the potential effects of urbanization on solar radiation trends indicate that these effects are generally small, with the exception of some specific sites in Russia and China (Wang et al., 2014; Imamovic et al., 2016; Tanaka et al., 2016). Also, surface-based solar radiation observations have been shown to be representative over large spatial domains of up to several degrees latitude/longitude on monthly and longer timescales (Hakuba et al., 2014; Schwarz et al., 2018). Thus, there is *high confidence* that the observed dimming between the 1950s and 1980s and subsequent brightening are robust and do not arise from measurement artefacts or localised phenomena.

As noted in AR5 (Hartmann et al., 2013) and supported by recent studies, the trends in surface solar radiation are less spatially coherent since the beginning of the 21st century, with evidence for continued brightening in parts of Europe and the USA, some stabilization in China and India, and dimming in other areas (Augustine and Dutton, 2013; Sanchez-Lorenzo et al., 2015; Manara et al., 2016; Soni et al., 2016; Wang and Wild, 2016; Jahani et al., 2018; Pfeifroth et al., 2018; Yang et al., 2018; Schwarz et al., 2020). The CERES-EBAF satellite-derived dataset of surface solar radiation (Kato et al., 2018) does not indicate a globally significant trend over the short period 2001–2012 (Zhang et al., 2015), whereas a statistically significant increase in surface solar radiation of +3.4 W m^{-2} per decade over the period 1996–2010 has been found in the Satellite Application Facility on Climate Monitoring (CM SAF) record of the geostationary satellite Meteosat, which views Europe, Africa and adjacent ocean (Posselt et al., 2014).

Since AR5 there is additional evidence that strong decadal changes in surface solar radiation have occurred also under cloud-free conditions, as shown for long term observational records in Europe, USA, China, India and Japan (Xu et al., 2011; Gan et al., 2014; Manara et al., 2016; Soni et al., 2016; Tanaka et al., 2016; Kazadzis et al., 2018; Li et al., 2018a; Yang et al., 2019; Wild et al., 2021). This suggests that changes in the composition of the cloud-free atmosphere, primarily in aerosols, contributed to these variations, particularly since the second half of the 20th century (Wild, 2016). Water vapour and other radiatively active gases seem to have played a minor role (Wild, 2009; Mateos et al., 2013; Posselt et al., 2014; Yang et al., 2019). For Europe and East Asia, modelling studies also point to aerosols as an important factor for dimming and brightening by comparing simulations that include/exclude variations in anthropogenic aerosol and aerosol-precursor emissions (Golaz et al., 2013; Nabat et al., 2014; Persad et al., 2014; Folini and Wild, 2015; Turnock et al., 2015; Moseid et al., 2020). Moreover, decadal changes in surface solar radiation have often occurred in line with changes in anthropogenic aerosol emissions and associated aerosol optical depth (Streets et al., 2006; Wang and Yang, 2014; Storelvmo et al., 2016; Wild, 2016; Kinne, 2019). However, further evidence for the influence of changes in cloudiness on dimming and brightening is emphasized in some studies (Augustine and Dutton, 2013; Parding et al., 2014; Stanhill et al., 2014; Pfeifroth et al., 2018; Antuña-Marrero et al., 2019). Thus, the contribution of aerosol and clouds to dimming and brightening is still debated. The relative influence of cloud-mediated aerosol effects versus direct aerosol radiative effects on dimming and brightening in a specific region may depend on the prevailing pollution levels (Wild, 2016; Section 7.3.3).

ESMs and reanalyses often do not reproduce the full extent of observed dimming and brightening (Wild and Schmucki, 2011; Allen et al., 2013; Zhou et al., 2017a; Storelvmo et al., 2018; Moseid et al., 2020; Wohland et al., 2020), potentially pointing to inadequacies in the representation of aerosol mediated effects or related emission data. The inclusion of assimilated aerosol optical depth inferred from satellite retrievals in the MERRA2 reanalysis (Buchard et al., 2017; Randles et al., 2017) helps to improve the accuracy of the simulated surface solar radiation changes in China (Feng and Wang, 2019). However, non-aerosol related deficiencies in model representations of clouds and circulation, and/or an underestimation of natural variability, could further contribute to the lack of dimming and brightening in ESMs (Wild, 2016; Storelvmo et al., 2018).

AR5 reported evidence for an increase in surface downward thermal radiation based on different studies covering in total 1964–2008, in line with expectation from an increased radiative forcing from greenhouse gases and the warming and moistening of the atmosphere. Updates of the longest observational records from the Baseline Surface Radiation Network continue to show an increase at the majority of the sites, in line with an overall increase predicted by ESMs on the order of 2 W m^{-2} $decade^{-1}$ (Wild, 2016). Upward longwave radiation at the surface is rarely measured but expected to have increased over the same period due to rising surface temperatures.

Turbulent fluxes of latent and sensible heat are also an important part of the surface energy budget (Figure 7.2). Large uncertainties in measurements of surface turbulent fluxes continue to prevent the determination of their decadal changes. Nevertheless, over the ocean, reanalysis-based estimates of linear trends from 1948 to 2008 indicate high spatial variability and seasonality. Increases in magnitudes of 4 to 7 W m^{-2} $decade^{-1}$ for latent heat and 2 to 3 W m^{-2} $decade^{-1}$ for sensible heat in the western boundary current regions are mostly balanced by decreasing trends in other regions (Gulev and Belyaev, 2012). Over land, the terrestrial latent heat flux is estimated to have increased in magnitude by 0.09 W m^{-2} $decade^{-1}$ from 1989 to 1997, and subsequently decreased by 0.13 W m^{-2} $decade^{-1}$ from 1998 to 2005 due to soil moisture limitation mainly in the Southern Hemisphere (derived from Mueller et al. (2013)). These trends are small in comparison to the uncertainty associated with satellite-derived and in-situ observations, as well as from land surface models forced by observations and atmospheric reanalyses. Ongoing advances in remote sensing of evapotranspiration from space (Mallick et al., 2016; Fisher et al., 2017; McCabe et al., 2017b, 2017a), as well as terrestrial water storage (Rodell et al., 2018) may contribute to future constraints on changes in latent heat flux.

In summary, since AR5, multidecadal trends in surface solar radiation up to several percent per decade have been detected at many more locations also in remote areas. There is *high confidence* that these trends are widespread, and not localised phenomena or measurement artefacts. The origin of these trends is not fully understood, although there is evidence that anthropogenic aerosols have made a substantial contribution (*medium confidence*). There is *medium confidence* that downward and upward thermal radiation has increased since the 1970s, while there remains *low confidence* in the trends in surface sensible and latent heat.

[START BOX 7.2 HERE]

BOX 7.2: The Global Energy Budget

This box assesses the present knowledge of the global energy budget for the period 1971–2018, i.e. the balance between radiative forcing, the total climate feedback and observations of the changes in the global energy inventory (Box 7.2, Figure 1a, d).

The net ERF of the Earth system since 1971 has been positive (Box 7.2, Figure 1b, e; Section 7.3), mainly as a result of increases in atmospheric greenhouse gas concentrations (Chapter 2, Section 2.2.8 and Section 7.3.2). The ERF of these positive forcing agents have been partly offset by that of negative forcing agents, primarily due to anthropogenic aerosols (Section 7.3.3), which dominate the overall uncertainty. The net energy inflow to the Earth system from ERF since 1971 is estimated to be 937 ZJ (1 ZJ = 10^{21} J) with a *likely* range of 644 to 1259 ZJ (Box 7.2, Figure 1b).

The ERF-induced heating of the climate system results in increased thermal radiation to space via the Planck response, but the picture is complicated by a variety of climate feedbacks (Box 7.1; Section 7.4.2) that also influence Earth's radiative response (Box 7.2, Figure 1c). The total radiative response is estimated by multiplying the assessed net feedback parameter, α, from process-based evidence (Section 7.4.2, Table 7.10) with the observed GSAT change for the period (Chapter 2, Cross Chapter Box 2.3) and time-integrating (Box 7.2, Figure 1c). The net energy outflow from the Earth system associated with the integrated radiative response 1971 is estimated to be 621 ZJ with a *likely* range of 419 to 823 ZJ. Assuming a pattern effect (Section 7.4.4) on α of -0.5 W m^{-2} C^{-1} would lead to a systematically larger energy outflow by about 250 ZJ.

Combining the *likely* range of integrated radiative forcing (Box 7.2, Figure 1b) with the central estimate of integrated radiative response (Box 7.2, Figure 1c) gives a central estimate and *likely* range of 340 [47 to 662] ZJ (Box 7.2, Figure 1f). Combining the *likely* range of integrated radiative response with the central estimate

of integrated radiative forcing gives a *likely* range of 340 [147 to 527] ZJ (Box 7.2, Figure 1f). Both calculations yield an implied energy gain in the climate system that is consistent with an independent observation-based assessment of the increase in the global energy inventory expressed relative to the estimated 1850-1900 Earth energy imbalance (Box 7.2, Figure 1a; Section 7.5.2) with a central estimate and *very likely* range of 284 [96 to 471] ZJ (*high confidence*) (Box 7.2, Figure 1d; Table 7.1). Estimating the total uncertainty associated with radiative forcing and radiative response remains a scientific challenge and depends on the degree of correlation among the two (Box 7.2, Figure 1f). However, the central estimate of observed energy change falls well with the estimated *likely* range assuming either correlated or uncorrelated uncertainties. Furthermore, the energy budget assessment would accommodate a substantial pattern effect (Section 7.4.4.3) during 1971–2018 associated with systematically larger values of radiative response (Box 7.2, Figure 1c), and potentially improved closure of the global energy budget. For the period 1970-2011, AR5 reported that the global energy budget was closed within uncertainties (*high confidence*) and consistent with the *likely* range of assessed climate sensitivity (Church et al., 2013). This report provides a more robust quantitative assessment based on additional evidence and improved scientific understanding.
In addition to new and extended observations (Section 7.2.2), confidence in the observed accumulation of energy in the Earth system is strengthened by cross-validation of heating rates based on satellite and in situ observations (Section 7.2.2.1) and closure of the global sea-level budget using consistent datasets (Cross-Chapter Box 9.1; Chapter 9, Table 9.5). Overall, there is *high confidence* that the global energy budget is closed for 1971–2018 with improved consistency compared to AR5

[START BOX 7.2, FIGURE 1 HERE]

Box 7.2, Figure 1: Estimates of the net cumulative energy change (ZJ = 10^{21} Joules) for the period 1971–2018 associated with: (a) observations of changes in the Global Energy Inventory (b) Integrated Radiative Forcing; (c) Integrated Radiative Response. Black dotted lines indicate the central estimate with *likely* and *very likely* ranges as indicated in the legend. The grey dotted lines indicate the energy change associated with an estimated pre-industrial Earth energy imbalance of 0.2 W m^{-2} (panel a) and an illustration of an assumed pattern effect of –0.5 W m^{-2} °C^{-1} (panel c). Background grey lines indicate equivalent heating rates in W m^{-2} per unit area of Earth's surface. Panels (d) and (e) show the breakdown of components, as indicated in the legend, for the Global Energy Inventory and Integrated Radiative Forcing, respectively. Panel (f) shows the Global Energy Budget assessed for the period 1971–2018, i.e. the consistency between the change in the Global Energy Inventory relative to pre-industrial and the implied energy change from Integrated Radiative Forcing plus Integrated Radiative Response under a number of different assumptions, as indicated in the figure legend, including assumptions of correlated and uncorrelated uncertainties in Forcing plus Response. Shading represents the *very likely* range for observed energy change relative to pre-industrial and *likely* range for all other quantities. Forcing and Response timeseries are expressed relative to a baseline period of 1850–1900. Further details on data sources and processing are available in the chapter data table (Table 7.SM.14).

[END BOX 7.2, FIGURE 1 HERE]

[END BOX 7.2 HERE]

7.3 Effective radiative forcing

Effective radiative forcing (ERF) quantifies the energy gained or lost by the Earth system following an imposed perturbation (for instance in greenhouse gases, aerosols or solar irradiance). As such it is a fundamental driver of changes in the Earth's TOA energy budget. ERF is determined by the change in the net downward radiative flux at the TOA (see Box 7.1) after the system has adjusted to the perturbation but excluding the radiative response to changes in surface temperature. This section outlines the methodology for ERF calculations in Section 7.3.1 and then assesses the ERF due to greenhouse gases in Section 7.3.2, aerosols in Section 7.3.3 and other natural and anthropogenic forcing agents in Section 7.3.4. These are brought together in Section 7.3.5 for an overall assessment of the present-day ERF and its evolution over the historical time period since 1750 until 2019. The same section also evaluates the surface temperature response to individual ERFs.

7.3.1 Methodologies and representation in models; overview of adjustments

As introduced in Box 7.1, AR5 (Boucher et al., 2013; Myhre et al., 2013b) recommended ERF as a more useful measure of the climate effects of a physical driver than the stratospheric-temperature-adjusted radiative forcing (SARF) adopted in earlier assessments. AR5 assessed that the ratios of surface temperature change to forcing resulting from perturbations of different forcing agents were more similar between species using ERF than SARF. ERF extended the SARF concept to account for not only adjustments to stratospheric temperatures, but also responses in the troposphere and effects on clouds and atmospheric circulation, referred to as "adjustments". For more details see Box 7.1. Since circulation can be affected, these responses are not confined to the locality of the initial perturbation (unlike the traditional stratospheric-temperature adjustment).

This chapter defines "adjustments" as those changes caused by the forcing agent that are independent of changes in surface temperature, rather than defining a specific timescale. AR5 used the terminology "rapid adjustment", but in this assessment the definition is based on the independence from surface temperature rather than the rapidity. The definition of ERF in Box 7.1 aims to have a clean separation between forcing (energy budget changes that are not mediated by surface temperature) and feedbacks (energy budget changes that are mediated by surface temperature). This means that changes in land or ocean surface temperature patterns (for instance as identified by Rugenstein et al. (2016b)) are not included as adjustments. As in previous assessments (Forster et al., 2007; Myhre et al., 2013b) ERFs can be attributed simply to changes in the forcing agent itself or attributed to components of emitted gases (see Chapter 6, Figure 6.12). Because ERFs can include chemical and biospheric responses to emitted gases, they can be attributed to precursor gases even if those gases do not have a direct radiative effect themselves. Similar chemical and biospheric responses to forcing agents can also be included in the ERF in addition to their direct effects.

Instantaneous Radiative Forcing (IRF) is defined here as the change in the net TOA radiative flux following a perturbation, excluding any adjustments. SARF is defined here as the change in the net radiative flux at TOA following a perturbation including the response to stratospheric temperature adjustments. These differ from AR5 where these quantities were defined at the tropopause (Myhre et al., 2013b). The net IRF values will be different using the TOA definition. The net SARF values will be the same as with the tropopause definition, but will have a different partitioning between the longwave and shortwave. Defining all quantities at the TOA enables consistency in breaking down the ERF into its component parts.

The assessment of ERFs in AR5 was preliminary because ERFs were only available for a few forcing agents, so for many forcing agents the report made the assumption that ERF and SARF were equivalent. A body of work published since AR5 is discussed in this section that has computed ERFs across many more forcing agents and models, closely examined the methods of computation, quantified the processes involved in causing adjustments and examined how well ERFs predict the ultimate temperature response. This work is assessed to have led to a much-improved understanding and increased confidence in the quantification of radiative forcing across the Report. These same techniques allow for an evaluation of radiative forcing within Earth System Models (ESMs) as a key test of their ability to represent both historical and future temperature changes (Chapter 3, Section 3.3.1 and Chapter 4, Section 4.3.4).

The ERF for a particular forcing agent is the sum of the IRF and the contribution from the adjustments, so in principle this could be constructed bottom-up by calculating the IRF and adding in the adjustment contributions one-by-one or together. However, there is no simple way to derive the global tropospheric adjustment terms or adjustments related to circulation changes without using a comprehensive climate model (e.g., CMIP5/6). There have been two main modelling approaches used to approximate the ERF definition in Box 7.1. The first approach is to use the assumed linearity (Equation 7.1) to regress the net change in the TOA radiation budget (ΔN) against change in global mean surface temperature (ΔT) following a step change in the forcing agent (Gregory et al., 2004; Box 7.1, Figure 1). The ERF (ΔF) is then derived from ΔN when

ΔT=0. Regression-based estimates of ERF depend on the temporal resolution of the data used (Modak et al., 2016, 2018). For the first few months of a simulation both surface temperature change and stratospheric temperature adjustment occur at the same time, leading to misattribution of the stratospheric temperature adjustment to the surface temperature feedback. Patterns of sea-surface temperature change also affect estimates of the forcing obtained by regression methods (Andrews et al., 2015). At multidecadal timescales the curvature of the relationship between net TOA radiation and surface temperature can also lead to biases in the ERF estimated from the regression method (Armour et al., 2013; Andrews et al., 2015; Knutti et al., 2017; Section 7.4). The second modelling approach to estimate ERF is to set the ΔT term in Box 7.1 (Equation 7.1) to zero. It is technically difficult to constrain land surface temperatures in ESMs (Shine et al., 2003; Ackerley and Dommenget, 2016; Andrews et al., 2021), so most studies reduce the ΔT term by prescribing the SSTs and sea-ice concentrations in a pair of "fixed-SST" (fSST) simulations with and without the change in forcing agent (Hansen et al., 2005b). An approximation to ERF (ΔF_{fsst}) is then given by the difference in ΔN_{fsst} between the simulations. The fSST method has less noise due to internal variability than the regression method. Nevertheless a 30-year fSST integration or 10 × 20-year regression ensemble needs to be conducted in order to reduce the 5–95% confidence range to 0.1 W m^{-2} (Forster et al., 2016), thus neither method is practical for quantifying the ERF of agents with forcing magnitudes of order 0.1 W m^{-2} or smaller. The internal variability in the fSST method can be further constrained by nudging winds towards a prescribed climatology (Kooperman et al., 2012). This allows the determination of the ERF of forcing agents with smaller magnitudes but excludes adjustments associated with circulation responses (Schmidt et al., 2018). There are insufficient studies to assess whether these circulation adjustments are significant.

Since the near-surface temperature change over land, ΔT_{land}, is not constrained in the fSST method, this response needs to be removed for consistency with the Section 7.1 definition. These changes in the near-surface temperature will also induce further responses in the tropospheric temperature and water vapour that should also be removed to conform with the physical definition of ERF. The radiative response to ΔT_{land} can be estimated through radiative transfer modelling in which a kernel, k, representing the change in net TOA radiative flux per change in unit near-surface temperature change over land (or an approximation using land surface temperature), is precomputed (Smith et al., 2018b; Richardson et al., 2019; Tang et al., 2019; Smith et al., 2020a). Thus ERF ≈ $\Delta F_{\mathrm{fsst}} - k\,\Delta T_{\mathrm{land}}$. Since k is negative this means that ΔF_{fsst} underestimates the ERF. For 2×CO_2 this term is around 0.2 W m^{-2} (Smith et al., 2018b, 2020a). There have been estimates of the corrections due to tropospheric temperature and water vapour (Tang et al., 2019; Smith et al., 2020a) showing additional radiative responses of comparable magnitude to those directly from ΔT_{land}. An alternative to computing the response terms directly is to use the feedback parameter, α, (Hansen et al., 2005b; Sherwood et al., 2015; Tang et al., 2019). This gives approximately double the correction compared to the kernel approach (Tang et al., 2019). The response to land surface temperature change varies with location and even for GSAT change k is not expected to be the same as α (Section 7.4). One study where land-surface temperatures are constrained in a model (Andrews et al., 2021) finds this constraint adds +1.0 W m^{-2} to ΔF_{fsst} for 4×CO_2, thus confirming the need for a correction in calculations where this constraint is not applied. For this assessment the correction is conservatively based only on the direct radiative response kernel to ΔT_{land} as this has a strong theoretical basis to support it. While there is currently insufficient corroborating evidence to recommend including tropospheric temperature and water vapour corrections in this assessment, it is noted that the science is progressing rapidly on this topic.

TOA radiative flux changes due to the individual adjustments can be calculated by perturbing the meteorological fields in a climate model's radiative transfer scheme (partial radiative perturbation approach) (Colman, 2015; Mülmenstädt et al., 2019) or by using precomputed radiative kernels of sensitivities of the TOA radiation fluxes to changes in these fields (as done for near-surface temperature change above) (Vial et al., 2013; Zelinka et al., 2014; Zhang and Huang, 2014; Smith et al., 2018b, 2020a). The radiative kernel approach is easier to implement through post-processing of output from multiple ESMs, whereas it is recognized that the partial radiation perturbation approach gives a more accurate estimate of the adjustments within the setup of a single model and its own radiative transfer code. There is little difference between using a radiative kernel from the same or a different model when calculating the adjustment terms, except for stratospheric temperature adjustments where it is important to have sufficient vertical resolution in the stratosphere in the model used to derive the kernel (Smith et al., 2018b, 2020b).

For comparison with offline radiative transfer calculations the SARFs can be approximated by removing the adjustment terms (apart from stratospheric temperature) from the ERFs using radiative kernels to quantify the adjustment for each meteorological variable. Kernel analysis by Chung and Soden (2015) suggested a large spread in CO_2 SARF across climate models, but their analysis was based on regressing variables in a coupled-ocean experiment rather than using a fSST approach which leads to a large spread due to natural variability (Forster et al., 2016). Adjustments computed from radiative kernels are shown for seven different climate drivers (using a fSST approach) in Figure 7.4. Table 7.2 shows the estimates of SARF, ΔF_{fsst} and ERF (corrected for land surface temperature change) for 2×CO_2 from the nine climate models analysed in Smith et al. (2018b). The SARF shows a smaller spread over previous studies (Pincus et al., 2016; Soden et al., 2018) and most estimates are within 10% of the multi-model mean and the assessment of 2×CO_2 SARF in Section 7.3.2 (3.75 W m^{-2}). It is not possible from these studies to determine how much of this reduction in spread is due to convergence in the model radiation schemes or the meteorological conditions of the model base states; nevertheless the level of agreement in this and earlier intercomparisons gives *medium confidence* in ESM's ability to represent radiative forcing from CO_2. The 4×CO_2 CMIP6 fSST experiments (Smith et al., 2020a) in Table 7.2 include ESMs with varying levels of complexity in aerosols and reactive gas chemistry. The CMIP6 experimental setup allows for further climate effects of CO_2 (including on aerosols and ozone) depending on model complexity. The chemical effects are adjustments to CO_2 but are not separable from the SARF in the diagnosis in Table 7.2. In these particular models, this leads to higher SARF than when only CO_2 varies, however there are insufficient studies to make a formal assessment of composition adjustments to CO_2.

[START TABLE 7.2 HERE]

Table 7.2: SARF, ΔF_{fsst}, and ERF diagnosed from ESMs for fSST CO_2 experiments. 2×CO_2 data taken from fixed atmospheric composition experiments (Smith et al., 2018b). 4×CO_2 data taken from CMIP6 experiments with interactive aerosols (and interactive gas phase chemistry in some) (Smith et al., 2020a). The radiative forcings from the 4×CO_2 experiments are scaled by 0.476 for comparison with 2×CO_2 (Meinshausen et al., 2020). SARF is approximated by removing the (non-stratospheric temperature) adjustment terms from the ERF. In Smith et al. (2018b) separation of temperature adjustments into tropospheric and stratospheric contributions is approximate based on a fixed tropopause of 100 hPa at the equator, varying linearly in latitude to 300 hPa at the poles. In Smith et al. (2020b) this separation is based on the model-diagnosed tropopause. ERF is approximated by removing the response to land surface temperature change from ΔF_{fsst}. The confidence range is based on the inter-model standard deviation.

.

2 × CO_2 (W m^{-2}) (Smith et al., 2018b)	SARF	ΔF_{fsst}	ERF
HadGEM2-ES	3.45	3.37	3.58
NorESM1	3.67	3.50	3.70
GISS-E2-R	3.98	4.06	4.27
CanESM2	3.68	3.57	3.77
MIROC-SPRINTARS	3.89	3.62	3.82
NCAR-CESM1-CAM5	3.89	4.08	4.39
HadGEM3	3.48	3.64	3.90
IPSL-CM5A	3.50	3.39	3.61
MPI-ESM	4.27	4.14	4.38
NCAR-CESM1-CAM4	3.50	3.62	3.86
Multi-model Mean and 5-95% confidence range	3.73 ± 0.44	3.70 ± 0.44	3.93 ± 0.48
0.476 × 4×CO_2 (W m^{-2}) (Smith et al., 2020a)			
ACCESS-CM2	3.56	3.78	3.98
CanESM5	3.67	3.62	3.82
CESM2	3.56	4.24	4.48

CNRM-CM6-1	3.99	3.81	4.01
CNRM-ESM2-1	3.99	3.77	3.94
EC-Earth3		3.85	4.04
GFDL-CM4	3.65	3.92	4.10
GFDL-ESM4	3.27	3.68	3.85
GISS-E2-1-G	3.78	3.50	3.69
HadGEM3-GC31-LL	3.61	3.85	4.07
IPSL-CM6A-LR	3.84	3.81	4.05
MIROC6	3.63	3.48	3.69
MPI-ESM1-2-LR	3.74	3.97	4.20
MRI-ESM2-0	3.76	3.64	3.80
NorESM2-LM	3.58	3.88	4.10
NorESM2-MM	3.62	3.99	4.22
UKESM1-0-LL	3.49	3.78	4.01
Multi-model Mean and 5-95% confidence range	3.67 ± 0.29	3.80 ± 0.30	4.00 ± 0.32

[END TABLE 7.2 HERE]

[START FIGURE 7.4 HERE]

Figure 7.4: Radiative adjustments at top of atmosphere for seven different climate drivers as a proportion of forcing. Tropospheric temperature (orange), stratospheric temperature (yellow), water vapour (blue), surface albedo (green), clouds (grey) and the total adjustment (black) is shown. For the greenhouse gases (carbon dioxide, methane, nitrous oxide, CFC-12) the adjustments are expressed as a percentage of SARF, whereas for aerosol, solar and volcanic forcing they are expressed as a percentage of IRF. Land surface temperature response (outline red bar) is shown, but included in the definition of forcing. Data from Smith et al. (2018b) for carbon dioxide and methane, Smith et al. (2018b) and Gray et al. (2009) for solar, Hodnebrog et al. (2020b) for nitrous oxide and CFC-12, Smith et al. (2020a) for aerosol, and Marshall et al. (2020) for volcanic. Further details on data sources and processing are available in the chapter data table (Table 7.SM.14).

[END FIGURE 7.4 HERE]

ERFs have been found to yield more consistent values of GSAT change per unit forcing than SARF, i.e. α shows less variation across different forcing agents (Rotstayn and Penner, 2001; Shine et al., 2003; Hansen et al., 2005b; Marvel et al., 2016; Richardson et al., 2019). Having a consistent relationship between forcing and response is advantageous when making climate projections using simple models (Cross-Chapter Box 7.1) or emission-metrics (Section 7.6). The definition of ERF used in this assessment, which excludes the radiative response to land surface temperature changes, brings the α values into closer agreement than when SARF is used (Richardson et al., 2019), although for individual models there are still variations particularly for more geographically localised forcing agents. However, even for ERF, studies find that α is not identical across all forcing agents (Shindell, 2014; Shindell et al., 2015; Modak et al., 2018; Modak and Bala, 2019; Richardson et al., 2019). Section 7.4.4 discusses the effect of different SST response patterns on α. Analysis of the climate feedbacks (Kang and Xie, 2014; Gregory et al., 2016, 2020; Marvel et al., 2016; Duan et al., 2018; Persad and Caldeira, 2018; Stuecker et al., 2018; Krishnamohan et al., 2019) suggests a weaker feedback (i.e., less-negative α) and hence larger sensitivity for forcing of the higher latitudes (particularly the Northern Hemisphere). Nonetheless, as none of these variations are robust across models, the ratio of $1/\alpha$ from non-CO_2 forcing agents (with approximately global distributions) to that from doubling CO_2 is within 10% of unity.

In summary, this Report adopts an estimate of ERF based on the change in TOA radiative fluxes in the absence of GSAT changes. This allows for a theoretically cleaner separation between forcing and feedbacks in terms of factors respectively unrelated and related to GSAT change (Box 7.1). ERF can be computed from prescribed SST and sea-ice experiments after removing the TOA energy budget change associated with the land surface temperature response. In this assessment this is removed using a kernel accounting only for the direct radiative effect of the land surface temperature response. To compare these results with sophisticated high spectral resolution radiative transfer models the individual tropospheric adjustment terms can be removed to leave the SARF. SARFs for $2\times CO_2$ calculated by ESMs from this method agree within 10% with the more sophisticated models. The new studies highlighted above suggest that physical feedback parameters computed within this framework have less variation across forcing agents. There is *high confidence* that an α based on ERF as defined here varies by less (less than variation 10% across a range of forcing agents with global distributions), than α based on SARF. For geographically localised forcing agents there are fewer studies and less agreement between them, resulting in *low confidence* that ERF is a suitable estimator of the resulting global mean near-surface temperature response.

7.3.2 Greenhouse Gases

High spectral resolution radiative transfer models provide the most accurate calculations of radiative perturbations due to greenhouse gases (GHGs) with errors in the IRF of less than 1% (Mlynczak et al., 2016; Pincus et al., 2020). They can calculate IRFs with no adjustments, or SARFs by accounting for the adjustment of stratospheric temperatures using a fixed dynamical heating. It is not possible with offline radiation models to account for other adjustments. The high resolution model calculations of SARF for carbon dioxide, methane and nitrous oxide have been updated since AR5, which were based on Myhre et al. (1998). The new calculations include the shortwave forcing from methane and updates to the water vapour continuum (increasing the total SARF of methane by 25%) and account for the absorption band overlaps between carbon dioxide and nitrous oxide (Etminan et al., 2016). The associated simplified expressions, from a re-fitting of the Etminan et al. (2016) results by Meinshausen et al. (2020), are given in Supplementary Table 7.SM.1. The shortwave contribution to the IRF of methane has been confirmed independently (Collins et al., 2018). Since they incorporate known missing effects we assess the new calculations as being a more appropriate representation than Myhre et al. (1998).

As described in Section 7.3.1, ERFs can be estimated using ESMs, however the radiation schemes in climate models are approximations to high spectral resolution radiative transfer models with variations and biases in results between the schemes (Pincus et al., 2015). Hence ESMs alone are not sufficient to establish ERF best estimates for the well-mixed GHGs (WMGHGs). This assessment therefore estimates ERFs from a combined approach that uses the SARF from radiative transfer models and adds the tropospheric adjustments derived from EMSs.

In AR5, the main information used to assess components of ERFs beyond SARF was from Vial et al. (2013) who found a near-zero non-stratospheric adjustment (without correcting for near-surface temperature changes over land) in $4\times CO_2$ CMIP5 model experiments, with an uncertainty of ±10% of the total CO_2 ERF. No calculations were available for other WMGHGs, so ERF was therefore assessed to be approximately equal to SARF (within 10%) for all WMGHGs.

The effect of WMGHGs in ESMs can extend beyond their direct radiative effects to include effects on ozone and aerosol chemistry and natural emissions of ozone and aerosol precursors, and in the case of CO_2 to vegetation cover through physiological effects. In some cases these can have significant effects on the overall radiative budget changes from perturbing WMGHGs within ESMs (Myhre et al., 2013b; Zarakas et al., 2020; O'Connor et al., 2021; Thornhill et al., 2021a). These composition adjustments are further discussed in Chapter 6 (Section 6.4.2).

7.3.2.1 Carbon Dioxide

The SARF for CO_2 has been slightly revised due to updates to spectroscopic data and inclusion of the absorption band overlaps between N_2O and CO_2 (Etminan et al., 2016). The formulae fitting to the Etminan et al. (2016) results in Meinshausen et al. (2020) are used. This increases the SARF due to doubling CO_2 slightly from 3.71 W m^{-2} in AR5 to 3.75 W m^{-2}. Tropospheric responses to CO_2 in fSST experiments have been found to lead to an approximate balance in their radiative effects between an increased radiative forcing due to water vapour, cloud and surface albedo adjustments and a decrease due to increased tropospheric temperature and land surface temperature response (Vial et al., 2013; Zhang and Huang, 2014; Smith et al., 2018b, 2020a; Table 7.3). The ΔF_{fsst} includes any effects represented within the ESMs on tropospheric adjustments due to changes in evapotranspiration or leaf area (mainly affecting surface and boundary layer temperature, low cloud amount and albedo) from the CO_2-physiological effects (Doutriaux-Boucher et al., 2009; Cao et al., 2010; Richardson et al., 2018b). The effect on surface temperature (negative longwave response) is consistent with the expected physiological responses and needs to be removed for consistency with the ERF definition. The split between surface and tropospheric temperature responses was not reported in Vial et al. (2013) or Zhang and Huang (2014) but the total of surface and tropospheric temperature response agrees with Smith et al. (2018b, 2020b) giving *medium confidence* in this decomposition. Doutriaux-Boucher et al. (2009) and Andrews et al. (2021) (using the same land surface model) find a 13% and 10% increase respectively in ERF due to the physiological responses to CO_2. The physiological adjustments are therefore assessed to make a substantial contribution to the overall tropospheric adjustment for CO_2 (*high confidence*), but there is insufficient evidence to provide a quantification of the split between physiological and thermodynamic adjustments. These forcing adjustments due to the effects of CO_2 on plant physiology differ from the biogeophysical feedbacks due to the effects of temperature changes on vegetation discussed in Section 7.4.2.5. The adjustment is assumed to scale with the SARF in the absence of evidence for non-linearity. The tropospheric adjustment is assessed from Table 7.3 to be +5% of the SARF with an uncertainty of 5%, which is added to the Meinshausen et al. (2020) formula for SARF. Due to the agreement between the studies and the understanding of the physical mechanisms there is *medium confidence* in the mechanisms underpinning the tropospheric adjustment, but *low confidence* in its magnitude.

[START TABLE 7.3 HERE]

Table 7.3: Adjustments to the TOA CO_2 forcing due to changes in stratospheric temperature, surface and tropospheric temperatures, water vapour, clouds and surface albedo, as a fraction of the SARF. ERF is defined in this report as excluding the surface temperature response.

Percentage of SARF	Surface temp	Trop. temp	Strat. temp	Surface albedo	Water vapour	Clouds	Troposphere (inc. surface)	Troposphere (excl. surface)
Vial et al. (2013)	–20%			2%	6%	11%	–1%	
Zhang and Huang (2014)	–23%		26%		6%	16%	–1%	
Smith et al. (2018b)	–6%	–16%	30%	3%	6%	12%	–1%	+5%
Smith et al. (2020b)	–6%	–15%	35%	3%	6%	15%	+3%	+9%

[END TABLE 7.3 HERE]

The ERF from doubling CO_2 ($2\times CO_2$) from the 1750 level (278 ppm Chapter 2, Section 2.2.3.3) is assessed to be 3.93 ± 0.47 W m^{-2} (*high confidence*). Its assessed components are given in Table 7.4. The combined spectroscopic and radiative transfer modelling uncertainties give an uncertainty in the CO_2 SARF of around 10% or less (Etminan et al., 2016; Mlynczak et al., 2016). The overall uncertainty in CO_2 ERF is assessed as ±12%, as the more uncertain adjustments only account for a small fraction of the ERF (Table 7.3). The $2\times CO_2$ ERF estimate is 0.2 W m^{-2} larger than using the AR5 formula (Myhre et al., 2013b) due to the combined effects of tropospheric adjustments which were assumed to be zero in AR5. CO_2 concentrations have increased from 278 ppm in 1750 to 410 ppm in 2019 (Chapter 2, Section 2.2.3.3). The historical ERF estimate from CO_2 is revised upwards from the AR5 value of 1.82 ± 0.38 W m^{-2} (1750 to 2011) to 2.16 ±0.26 W m^{-2} (1750 to 2019) in this assessment, from a combination of the revisions described above (0.06 W m^{-2}) and the 19 ppm rise in atmospheric concentrations between 2011 and 2019 (0.27 W m^{-2}). The ESM estimates of 2×CO_2 ERF (Table 7.2) lie within ±12% of the assessed value (apart from CESM2). The definition of ERF can also include further physiological effects for instance on dust, natural fires and biogenic emissions from the land and ocean, but these are not typically included in the modelling set up for 2×CO_2 ERF.

[START TABLE 7.4 HERE]

Table 7.4: Assessed ERF, SARF and tropospheric adjustments to 2×CO_2 change since preindustrial times compared to the AR5 assessed range (Myhre et al., 2013b). Adjustments are due to changes in tropospheric temperatures, water vapour, clouds and surface albedo and land cover and are taken from Smith et al. (2018b) and assessed as a percentage of SARF (Table 7.3). Uncertainties are based on multi-model spread in Smith et al. (2018b). Note some of the uncertainties are anticorrelated, which means that they do not sum linearly.

2×CO_2 forcing	AR5 SARF/ ERF	SARF (W m^{-2})	Tropospheric temperature adjustment (W m^{-2})	Water vapour adjustment (W m^{-2})	Cloud adjustment (W m^{-2})	Surface albedo and land cover adjustment (W m^{-2})	Total tropospheric adjustment (W m^{-2})	ERF (W m^{-2})
2×CO_2 ERF components	3.71	3.75	–0.60	0.22	0.45	0.11	0.18	3.93
5%–95% uncertainty ranges as percentage of ERF	10% (SARF) 20% (ERF)	<10%	±6%	±4%	±7%	±2%	±7%	±12%

[END TABLE 7.4 HERE]

7.3.2.2 Methane

The SARF for methane (CH_4) has been substantially increased due to updates to spectroscopic data and inclusion of the shortwave absorption (Etminan et al., 2016). Adjustments have been calculated in nine climate models by Smith et al. (2018b). Since CH_4 is found to absorb in the shortwave near infrared, only adjustments from those models including this absorption are taken into account. For these models the adjustments act to reduce the ERF because the shortwave absorption leads to tropospheric heating and reductions in upper tropospheric cloud amounts. The adjustment is –14% ± 15% which counteracts much of the increase in SARF identified by Etminan et al. (2016). Modak et al. (2018) also found negative forcing adjustments from a methane perturbation including shortwave absorption in the NCAR CAM5 model, in agreement with the above assessment. The uncertainty in the shortwave component leads to a higher radiative modelling uncertainty (14%) than for CO_2 (Etminan et al., 2016). When combined with the uncertainty in the adjustment, this gives an overall uncertainty of ± 20%. There is *high confidence* in the spectroscopic revision but only *medium confidence* in the adjustment modification. CH_4 concentrations have increased from 729 ppb in 1750 to 1866 ppb in 2019 (Chapter 2, Section 2.2.3.3). The historical ERF estimate from AR5 of 0.48 ± 0.10 W m^{-2} (1750 to 2011) is revised to 0.54 ± 0.11 W m^{-2} (1750 to 2019) in this assessment from a combination of spectroscopic radiative efficiency revisions (+0.12 W m^{-2}), adjustments (–0.08 W m^{-2}) and the 63 ppb rise in atmospheric CH_4 concentrations between 2011 and 2019 (+0.03 W m^{-2}). As the adjustments are assessed to be small, there is *high confidence* in the overall assessment of ERF from methane. Increased methane leads to tropospheric ozone production and increased stratospheric water vapour, so that an attribution of forcing to methane emissions gives a larger effect than that directly from the methane concentration itself. This is discussed in detail in Chapter 6, Section 6.4.2 and shown in Figure 6.12.

7.3.2.3 Nitrous oxide

The tropospheric adjustments to nitrous oxide (N_2O) have been calculated from 5 ESMs as 7% ± 13% of the SARF (Hodnebrog et al., 2020b). This value is therefore taken as the assessed adjustment, but with *low confidence*. The radiative modelling uncertainty is ± 10% (Etminan et al., 2016), giving an overall uncertainty of ± 16%. Nitrous oxide concentrations have increased from 270 ppb in 1750 to 332 ppb in 2019 (Chapter 2, Section 2.2.3.3). The historical ERF estimate from N_2O is revised upwards from 0.17 ± 0.06 W m^{-2} (1750 to 2011) in AR5 to 0.21 ± 0.03 W m^{-2} (1750 to 2019) in this assessment, of which 0.02 W m^{-2} is due to the 7 ppb increase in concentrations, and 0.02 W m^{-2} to the tropospheric adjustment. As the adjustments are assessed to be small there remains *high confidence* in the overall assessment.

Increased nitrous oxide leads to ozone depletion in the upper stratosphere which will make a positive contribution to the direct ERF here (Chapter 6, Section 6.4.2, Figure 6.12) when considering emission-based estimates of ERF.

7.3.2.4 Halogenated species

The stratospheric-temperature adjusted radiative efficiencies (SARF per ppb increase in concentration) for halogenated compounds are reviewed extensively in Hodnebrog et al. (2020a), an update to those used in AR5. Many halogenated compounds have lifetimes short enough that they can be considered short-lived climate forcers (Table 6.1). As such, they are not completely "well-mixed" and their vertical distributions are taken into account when determining their radiative efficiencies. The WMO (World Meteorological Organization, 2018) updated the lifetimes of many halogenated compounds and these were used in Hodnebrog et al. (2020a).

The tropospheric adjustments to chlorofluorocarbons (CFCs), specifically CFC-11 and CFC-12, have been quantified as 13% ± 10% and 12% ± 14% of the SARF respectively (Hodnebrog et al., 2020b). The assessed adjustment to CFCs is therefore 12 % ± 13% with *low confidence* due to the lack of corroborating studies. There have been no calculations for other halogenated species so for these the tropospheric adjustments are therefore assumed to be 0 ± 13% with *low confidence.* The radiative modelling uncertainties are 14% and 24% for compounds with lifetimes greater than and less than 5 years respectively (Hodnebrog et al., 2020a). The overall uncertainty in the ERFs of halogenated compounds is therefore assessed to be 19% and 26% depending on the lifetime. The ERF from CFCs is slowly decreasing, but this is compensated for by the increased forcing from the replacement species (HCFCs and HFCs). The ERF from HFCs has increased by 0.028 ± 0.05 W m^{-2}. Thus, the concentration changes mean that the total ERF from halogenated compounds has increased since AR5 from 0.360 ± 0.036 W m^{-2} to 0.408 ± 0.078 W m^{-2} (Table 7.5). Of this 0.034 W m^{-2} is due to increased radiative efficiencies and tropospheric adjustments, and 0.014 W m^{-2} due to increases in concentrations. As the adjustments are assessed to be small there remains *high confidence* in the overall assessment.

Halogenated compounds containing chlorine and bromine lead to ozone depletion in the stratosphere which will reduce the associated ERF (Morgenstern et al., 2020). Chapter 6, Section 6.4 and Figure 6.12 assess the ERF contributions due to the chemical effects of reactive gases.

7.3.2.5 Ozone

Estimates of the pre-industrial to present-day tropospheric ozone radiative forcing are based entirely on models. The lack of pre-industrial ozone measurements prevents an observational determination. There have been limited studies of ozone ERFs (MacIntosh et al., 2016; Xie et al., 2016; Skeie et al., 2020). Skeie et al. (2020) found little net contribution to the ERF from tropospheric adjustment terms for 1850-2000 change in ozone (tropospheric and stratospheric ozone combined), although MacIntosh et al. (2016) suggested that increases in stratospheric or upper tropospheric ozone reduces high cloud and increases low cloud, whereas an increase in lower tropospheric ozone reduces low cloud. Further studies suggest that changes in circulation due to decreases in stratospheric ozone affect Southern Hemisphere clouds and the atmospheric levels of sea salt aerosol that would contribute additional adjustments, possibly of comparable magnitude to the SARF from stratospheric ozone depletion (Grise et al., 2013, 2014, Xia et al., 2016, 2020). ESM responses to changes in ozone depleting substances (ODS) in CMIP6 show a much more negative ERF than would be expected from offline calculations of SARF (Morgenstern et al., 2020; Thornhill et al., 2021b) again suggesting a negative contribution from adjustments. However there is insufficient evidence available to quantify this effect.

Without sufficient information to assess whether the ERFs differ from SARF, this assessment relies on offline radiative transfer calculations of SARF for both tropospheric and stratospheric ozone. Checa-Garcia et al. (2018) found SARF of 0.30 W m^{-2} for changes in ozone (1850–1860 to 2009–2014). These were based on precursor emissions and ODS concentrations from the Coupled Chemistry Model Initiative (CCMI) project (Morgenstern et al., 2017). Skeie et al. (2020) calculated an ozone SARF of 0.41 ± 0.12 W m^{-2} (1850 to 2010) (from five climate models and one chemistry transport model) using CMIP6 precursor emissions and ODS concentrations (excluding models without fully interactive ozone chemistry and one model with excessive ozone depletion). The ozone precursor emissions are higher in CMIP6 than in CCMI which explains much of the increase compared to Checa-Garcia et al. (2018).

Previous assessments have split the ozone forcing into tropospheric and stratospheric components. This does not correspond to the division between ozone production and ozone depletion and is sensitive to the choice of tropopause (Myhre et al., 2013b) (*high confidence*). The contributions to total SARF in CMIP6 (Skeie et al., 2020) are 0.39 ± 0.07 and 0.02 ± 0.07 W m^{-2} for troposphere and stratosphere respectively (using a 150 ppb ozone tropopause definition). This small positive (but with uncertainty encompassing negative values) stratospheric ozone SARF is due to contributions from ozone precursors to lower stratospheric ozone and some of the CMIP6 models showing ozone depletion in the upper stratosphere, where depletion contributes a positive radiative forcing *(medium confidence)*.

As there is insufficient evidence to quantify adjustments, for total ozone the assessed central estimate for ERF is assumed to be equal to SARF (*low confidence*) and follows Skeie et al. (2020) since that study uses the most recent emission data. The dataset is extended over the entire historical period following Skeie et al. (2020) with a SARF for 1750 to 1850 of 0.03 W m^{-2} and for 2010 to 2018 of 0.03 W m^{-2}, to give 0.47 [0.24 to 0.70] W m^{-2} for 1750 to 2019. This maintains the 50% uncertainty (5%–95% range) from AR5 which is largely due to the uncertainty in pre-industrial emissions (Rowlinson et al., 2020). There also *high confidence* that this range includes uncertainty due to the adjustments. The CMIP6 SARF is more positive than the AR5 value of 0.31 W m^{-2} for the period 1850 to 2011 (Myhre et al., 2013b) which was based on the Atmospheric Chemistry and Climate Intercomparison Project (ACCMIP) (Shindell et al., 2013). The assessment is sensitive to the assumptions on precursor emissions used to drive the models, which are larger in CMIP6 than ACCMIP.

In summary, although there is insufficient evidence to quantify adjustments, there is *high confidence* in the assessed range of ERF for ozone changes over the 1750 to 2019 period, giving an assessed ERF of 0.47 [0.24 to 0.70] W m^{-2}.

7.3.2.6 Stratospheric water vapour

This section considers direct anthropogenic effects on stratospheric water vapour by oxidation of methane. Since AR5 the SARF from methane-induced stratospheric water vapour changes has been calculated in two models (Winterstein et al., 2019; O'Connor et al., 2021), both corresponding to 0.09 W m^{-2} (1850 to 2014, by scaling the Winterstein et al., 2019 study). This is marginally larger than the AR5 assessed value of 0.07 ± 0.05 W m^{-2} (Myhre et al., 2013b). However, O'Connor et al. (2021) found the ERF to be approximately zero due to a negative cloud adjustment. Wang and Huang (2020) quantified the adjustment terms to a stratospheric water vapour change equivalent to that from a 2×CO_2 warming (which has different vertical profile, though also largest in the lower stratosphere). They found that the ERF was less than 50% of the SARF due to high cloud decrease and upper tropospheric warming. The assessed ERF is therefore 0.05±0.05 W m^{-2} with a lower limit reduced to zero and the central value and upper limit reduced to allow for adjustment terms. This still encompasses the two recent SARF studies. There is *medium confidence* in the SARF from agreement with the recent studies and AR5. There is *low confidence* in the adjustment terms.

Stratospheric water vapour may also change as an adjustment to species that warm or cool the upper troposphere-lower stratosphere region (Forster and Joshi, 2005; Stuber et al., 2005), in which case it should be included as part of the ERF for that compound. Changes in GSAT are also associated with changes in stratospheric water vapour as part of the water vapour climate feedback (Section 7.4.2.2).

7.3.2.7 Synthesis

The GHGs (excluding ozone and stratospheric water vapour) ERF over 1750 to 2019 is assessed to be 3.32 ± 0.29 W m^{-2}. It has increased by 0.49 W m^{-2} compared to AR5 (reference year 2011) *(high confidence)*. Most of this has been due to an increase in CO_2 concentration since 2011 [0.27 ± 0.03 W m^{-2}], with concentration increases in CH_4, N_2O and halogenated compounds adding 0.02, 0.02 and 0.01 W m^{-2} respectively (Table 7.5). Changes in the radiative efficiencies (including adjustments) of CO_2, CH_4, N_2O and halogenated compounds have increased the ERF by an additional 0.15 W m^{-2} compared to the AR5 values (*high confidence*). Note that the ERFs in this section do not include chemical effects of GHGs on production or destruction of ozone or aerosol formation (see Chapter 6, Section 6.2.2). The ERF for ozone is considerably increased compared to AR5 due to an increase in the assumed ozone precursor emissions in CMIP6 compared to CMIP5, and better accounting for the effects of both ozone precursors and ODSs in the stratosphere. The ERF for stratospheric water vapour is slightly reduced. The combined ERF from ozone and stratospheric water vapour has increased since AR5 by 0.10 ± 0.50 W m^{-2} (*high confidence*), although the uncertainty ranges still include the AR5 values.

[START TABLE 7.5 HERE]

Table 7.5: Present-day mole fractions in ppt (pmol mol^{-1}) (except where specified) and ERF (in W m^{-2}) for the WMGHGs. Data taken from Chapter 2, Section 2.2.3. The data for 2011 (the time of the AR5 estimates) are also shown. Some of the concentrations vary slightly from those reported in AR5 owing to averaging different data sources. Individual species are reported where 1750-2019 ERF is at least 0.001 W m^{-2}. Radiative efficiencies for the minor gases are given in Supplementary Table 7.SM.7. Uncertainties in the ERF for all gases are dominated by the uncertainties in the radiative efficiencies. Tabulated global mixing ratios of all well mixed GHGs and ERFs from 1750-2019 are provided in Annex III.

	Concentration				ERF with respect to 1850		ERF with respect to 1750	
	2019	2011	1850	1750	2019	2011	2019	2011
CO_2 (ppm)	409.9	390.5	285.5	278.3	2.012±0.241	1.738	2.156±0.259	1.882
CH_4 (ppb)	1866.3	1803.3	807.6	729.2	0.496±0.099	0.473	0.544±0.109	0.521
N_2O (ppb)	332.1	324.4	272.1	270.1	0.201±0.030	0.177	0.208±0.031	0.184
HFC-134a	107.6	62.7	0.	0.	0.018	0.010	0.018	0.010
HFC-23	32.4	24.1	0.	0.	0.006	0.005	0.006	0.005
HFC-32	20.0	4.7	0.	0.	0.002	0.001	0.002	0.001
HFC-125	29.4	10.3	0.	0.	0.007	0.002	0.007	0.002
HFC-143a	24.0	12.0	0.	0.	0.004	0.002	0.004	0.002
SF_6	10.0	7.3	0.	0.	0.006	0.004	0.006	0.004
CF_4	85.5	79.0	34.0	34.0	0.005	0.004	0.005	0.004

C_2F_6	4.8	4.2	0.	0.	0.001	0.001	0.001	0.001
CFC-11	226.2	237.3	0.	0.	0.066	0.070	0.066	0.070
CFC-12	503.1	528.6	0.	0.	0.180	0.189	0.180	0.189
CFC-113	69.8	74.6	0.	0.	0.021	0.022	0.021	0.022
CFC-114	16.0	16.3	0.	0.	0.005	0.005	0.005	0.005
CFC-115	8.7	8.4	0.	0.	0.002	0.002	0.002	0.002
HCFC-22	246.8	213.2	0.	0.	0.053	0.046	0.053	0.046
HCFC-141b	24.4	21.4	0.	0.	0.004	0.003	0.004	0.003
HCFC-142b	22.3	21.2	0.	0.	0.004	0.004	0.004	0.004
CCl_4	77.9	86.1	0.	0.	0.013	0.014	0.013	0.014
Sum of CFCs					0.276	0.289	0.276	0.289
Sum of HCFCs					0.061	0.053	0.061	0.053
Sum of HFCs					0.040	0.022	0.040	0.022
Sum of Halogenated species					0.408±0.078	0.394	0.408±0.078	0.394
Total					3.118±0.258	2.782	3.317±0.278	2.981

[END TABLE 7.5 HERE]

7.3.3 Aerosols

Anthropogenic activity, and particularly burning of biomass and fossil fuels, has led to a substantial increase in emissions of aerosols and their precursors, and thus to increased atmospheric aerosol concentrations since pre-industrial times (Chapter 2, Section 2.2.6 and Figure 2.9; Chapter 6, Section 6.3.5). This is particularly true for sulphate and carbonaceous aerosols (Chapter 6, Section 6.3.5). This has in turn led to changes in the scattering and absorption of incoming solar radiation, and also affected cloud micro- and macro-physics and thus cloud radiative properties. Aerosol changes are heterogeneous in both space and time and have impacted not just Earth’s radiative energy budget but also air quality (Chapter 6, Section 6.1.1 and 6.6.2). Here, the assessment is focused exclusively on the global mean effects of aerosols on Earth’s energy budget, while regional changes and changes associated with individual aerosol compounds are assessed in Chapter 6, Sections 6.4.1 and 6.4.2.

Consistent with the terminology introduced in Box 7.1, the ERF due to changes from direct aerosol-radiation interactions (ERFari) is equal to the sum of the instantaneous TOA radiation change (IRFari) and the subsequent adjustments. Likewise, the ERF following interactions between anthropogenic aerosols and clouds (ERFaci, referred to as “indirect aerosol effects” in previous assessment reports) can be divided into an instantaneous forcing component (IRFaci) due to changes in cloud droplet (and indirectly also ice crystal) number concentrations and sizes, and the subsequent adjustments of cloud water content or extent. While these changes are thought to be induced primarily by changes in the abundance of cloud condensation nuclei (CCN), a change in the number of ice nucleating particles (INPs) in the atmosphere may also have occurred, and thereby contributed to ERFaci by affecting properties of mixed-phase and cirrus (ice) clouds. In the following, an assessment of IRFari and ERFari (Section 7.3.3.1) focusing on observation-based (Section 7.3.3.1.1) as well as model-based (Section 7.3.3.1.2) evidence is presented. The same lines of evidence are presented for IRFaci and ERFaci in Section 7.3.3.2. These lines of evidence are then compared with TOA energy budget constraints on the total aerosol ERF (Section 7.3.3.3) before an overall assessment of the total aerosol ERF is given in Section 7.3.3.4. For the model-based evidence, all estimates are generally valid for 2014 relative to 1750 (the time period spanned by CMIP6 historical simulations), while for observation-based evidence the assessed studies use slightly different end points, but they all generally fall within a decade (2010-2020).

7.3.3.1 Aerosol-radiation interactions

Since AR5, deeper understanding of the processes that govern aerosol radiative properties, and thus IRFari, has emerged. Combined with new insights into adjustments to aerosol forcing, this progress has informed new observation- and model-based estimates of ERFari and associated uncertainties.

7.3.3.1.1 Observation-based lines of evidence

Estimating IRFari requires an estimate of industrial-era changes in Aerosol Optical Depth (AOD) and absorption AOD, which are often taken from global aerosol model simulations. Since AR5, updates to methods of estimating IRFari based on aerosol remote sensing or data-assimilated reanalyses of atmospheric composition have been published. Ma et al. (2014) applied the method of Quaas et al. (2008) to updated broadband radiative flux measurements from CERES, MODIS-retrieved AODs, and modelled anthropogenic aerosol fractions to find a clear-sky IRFari of −0.6 W m^{-2}. This would translate into an all-sky estimate of about −0.3 W m^{-2} based on the clear-to-all-sky ratio implied by Kinne (2019). Rémy et al. (2018) applied the methods of Bellouin et al. (2013b) to the reanalysis by the Copernicus Atmosphere Monitoring Service, which assimilates MODIS total AOD. Their estimate of IRFari varies between −0.5 W m^{-2} and −0.6 W m^{-2} over the period 2003–2018, and they attribute those relatively small variations to variability in biomass-burning activity. Kinne (2019) provided updated monthly total AOD and absorption AOD climatologies, obtained by blending multi-model averages with ground-based sun-photometer retrievals, to find a best estimate of IRFari of −0.4 W m^{-2}. The updated IRFari estimates above are all scattered around the midpoint of the IRFari range of −0.35 ± 0.5 W m^{-2} assessed by AR5 (Boucher et al., 2013).

The more negative estimate of Rémy et al. (2018) is due to neglecting a small positive contribution from absorbing aerosols above clouds and obtaining a larger anthropogenic fraction than Kinne (2019). Rémy et al. (2018) also did not update their assumptions on black carbon anthropogenic fraction and its contribution to absorption to reflect recent downward revisions (Section 7.3.3.1.2). Kinne (2019) made those revisions, so more weight is given to that study to assess the central estimate of satellite-based IRFari to be only slightly stronger than reported in AR5 at –0.4 W m^{-2}. While uncertainties in the anthropogenic fraction of total AOD remain, improved knowledge of anthropogenic absorption results in a slightly narrower *very likely* range here than in AR5. The assessed best estimate and *very likely* IRFari range from observation-based evidence is therefore –0.4 ± 0.4 W m^{-2} , but with *medium confidence* due to the limited number of studies available.

7.3.3.1.2 Model-based lines of evidence

While observation-based evidence can be used to estimate IRFari, global climate models are needed to calculate the associated adjustments and the resulting ERFari, using the methods described in Section 7.3.1. A range of developments since AR5 affect model-based estimates of IRFari. Global emissions of most major aerosol compounds and their precursors are found to be higher in the current inventories, and with increasing trends. Emissions of the sulphate precursor SO_2 are a notable exception; they are similar to those used in AR5 and approximately time-constant in recent decades (Hoesly et al., 2018). Myhre et al. (2017) showed, in a multi-model experiment, that the net result of these revised emissions is an IRFari trend that is relatively flat in recent years (post-2000), a finding confirmed by a single-model study by Paulot et al. (2018).

In AR5, the assessment of the black carbon (BC) contribution to IRFari was markedly strengthened in confidence by the review by Bond et al. (2013), where a key finding was a perceived model underestimate of atmospheric absorption when compared to Aeronet observations (Boucher et al., 2013). This assessment has since been revised considering new knowledge on the effect of the temporal resolution of emission inventories (Wang et al., 2016), the representativeness of Aeronet sites (Wang et al., 2018), issues with comparing absorption retrieval to models (Andrews et al., 2017a), and the ageing (Peng et al., 2016), lifetime (Lund et al., 2018b) and average optical parameters (Zanatta et al., 2016) of BC. Consistent with these updates, Lund et al. (2018a) estimated the net IRFari in 2014 (relative to 1750) to be –0.17 W m^{-2}, using CEDS emissions (Hoesly et al., 2018) as input to a chemical transport model. They attributed the weaker estimate relative to AR5 (–0.35 ± 0.5 W m^{-2}; Myhre et al., 2013a) to stronger absorption by organic aerosol, updated parameterization of BC absorption, and slightly reduced sulphate cooling. Broadly consistent with Lund et al. (2018a), another single-model study by Petersik et al. (2018) estimated an IRFari of –0.19 W m^{-2}. Another single-model study by Lurton et al. (2020) reported a more negative estimate at –0.38 W m^{-2}, but is given less weight here because the model lacked interactive aerosols and instead used prescribed climatological aerosol concentrations.

The above estimates support a less negative central estimate and a slightly narrower range compared to those reported for IRFari from ESMs in AR5 of –0.35 [–0.6 to –0.13] W m^{-2}. The assessed central estimate and *very likely* IRFari range from model-based evidence alone is therefore –0.2 ± 0.2 W m^{-2} for 2014 relative to 1750, with *medium confidence* due to the limited number of studies available. Revisions due to stronger organic aerosol absorption, further developed BC parameterizations and somewhat reduced sulphate emissions in recent years.

Since AR5 considerable progress has been made in the understanding of adjustments in response to a wide range of climate forcings, as discussed in Section 7.3.1. The adjustments in ERFari are principally caused by cloud changes, but also by lapse rate and atmospheric water vapour changes, all mainly associated with absorbing aerosols like BC. Stjern et al. (2017) found that for BC, about 30% of the (positive) IRFari is offset by adjustments of clouds (specifically, an increase in low clouds and decrease in high clouds) and lapse rate, by analysing simulations by five Precipitation Driver Response Model Intercomparison Project (PDRMIP) models. Smith et al. (2018b) considered more models participating in PDRMIP and suggested that about half the IRFari was offset by adjustments for BC, a finding generally supported by single-model studies (Takemura and Suzuki, 2019; Zhao and Suzuki, 2019). Thornhill et al. (2021b) also reported a negative adjustment for BC based on AerChemMIP (Collins et al., 2017) but found it to be somewhat smaller in magnitude than those reported in Smith et al. (2018b) and Stjern et al. (2017). In contrast, Allen et al. (2019) found a positive adjustment for BC and suggested that most models simulate negative adjustment for BC because of a misrepresentation of aerosol atmospheric heating profiles.

Zelinka et al. (2014) used the Approximate Partial Radiation Perturbation technique to quantify the ERFari in 2000 relative to 1860 in nine CMIP5 models; they estimated the ERFari (accounting for a small contribution from longwave radiation) to be –0.27 ± 0.35 W m^{-2}. However, it should be noted that in Zelinka et al. (2014) adjustments of clouds caused by absorbing aerosols through changes in the thermal structure of the atmosphere (termed the semidirect effect of aerosols in AR5) are not included in ERFari but in ERFaci. The corresponding estimate emerging from the Radiative Forcing Model Intercomparison Project (RFMIP, Pincus et al., 2016) is –0.25 ± 0.40 W m^{-2} (Smith et al., 2020a), which is generally supported by single-model studies published post-AR5 (Zhang et al., 2016; Fiedler et al., 2017; Nazarenko et al., 2017; Zhou et al., 2017c; Grandey et al., 2018; Zhou et al., 2018b). A 5% inflation is applied to the CMIP5 and CMIP6 fixed-SST derived estimates of ERFari from Zelinka et al. (2014) and (Smith et al., 2020a) to account for land surface cooling (Table 7.6). Based on the above, ERFari from model-based evidence is assessed to be –0.25 ± 0.25 W m^{-2}.

7.3.3.1.3 Overall assessment of IRFari and ERFari

The observation-based assessment of IRFari of –0.4 ± 0.4 W m^{-2} and the corresponding model-based assessment of –0.2 ± 0.2 W m^{-2} can be compared to the range of –0.45 W m^{-2} to –0.05 W m^{-2} that emerged from a comprehensive review in which an observation-based estimate of anthropogenic AOD was combined with model-derived ranges for all relevant aerosol radiative properties (Bellouin et al., 2019). Based on the above, IRFari is assessed to be –0.25 ± 0.2 W m^{-2} (*medium confidence*).

ERFari from model-based evidence is –0.25 ± 0.25 W m^{-2}, which suggests a small negative adjustment relative to the model-based IRFari estimate, consistent with the literature discussed in 7.3.3.1.2. Adding this small adjustment to our assessed IRFari estimate of –0.25 W m^{-2}, and accounting for additional uncertainty in the adjustments, ERFari is assessed to –0.3 ± 0.3 (*medium confidence*). This assessment is consistent with the 5% to 95 % confidence range for ERFari in Bellouin et al. (2019) of –0.71 to –0.14 W m^{-2}, and notably implies that it is *very likely* that ERFari is negative. Differences relative to Bellouin et al. (2019) reflect the range of estimates in Table 7.6 and the fact that a more negative ERFari than -0.6 W m^{-2} would require adjustments that considerably augment the assessed IRFari, which is not supported by the assessed literature.

[START TABLE 7.6 HERE]

Table 7.6: Present-day ERF due to changes in aerosol-radiation interactions (ERFari) and changes in aerosol-cloud interactions (ERFaci), and total aerosol ERF (ERFari+aci) from GCM CMIP6 (2014 relative to 1850) (Smith et al., 2020a and later model results) and CMIP5 (year 2000 relative to 1860) (Zelinka et al., 2014). CMIP6 results are simulated as part of RFMIP (Pincus et al., 2016). An additional 5% is applied to the CMIP5 and CMIP6 model results to account for land-surface cooling (Smith et al., 2020b; Figure 7.4).

Models	ERFari ($W m^{-2}$)	ERFaci ($W m^{-2}$)	ERFari+aci ($W m^{-2}$)
ACCESS-CM2	–0.24	–0.93	–1.17
ACCESS-ESM1-5	–0.07	–1.19	–1.25
BCC-ESM1	–0.79	–0.69	–1.48
CanESM5	–0.02	–1.09	–1.11
CESM2	+0.15	–1.65	–1.50
CNRM-CM6-1	–0.28	–0.86	–1.14
CNRM-ESM2-1	–0.15	–0.64	–0.79
EC-Earth3	–0.39	–0.50	–0.89
GFDL-CM4	–0.12	–0.72	–0.84
GFDL-ESM4	–0.06	–0.84	–0.90
GISS-E2-1-G (physics_version=1)	–0.55	–0.81	–1.36
GISS-E2-1-G (physics_version=3)	–0.64	–0.39	–1.02
HadGEM3-GC31-LL	–0.29	–0.87	–1.17
IPSL-CM6A-LR	–0.39	–0.29	–0.68
IPSL-CM6A-LR-INCA	–0.45	–0.35	–0.80
MIROC6	–0.22	–0.77	–0.99
MPI-ESM-1-2-HAM	+0.10	–1.40	–1.31
MRI-ESM2-0	–0.48	–0.74	–1.22
NorESM2-LM	–0.15	–1.08	–1.23
NorESM2-MM	–0.03	–1.26	–1.29
UKESM1-0-LL	–0.20	–0.99	–1.19
CMIP6 average and 5 to 95% confidence range (2014–1850)	–0.25 ± 0.40	–0.86 ± 0.57	–1.11 ± 0.38
CMIP5 average and 5 to 96% confidence range (2000–1860)	–0.27 ± 0.35	–0.96 ± 0.55	–1.23 ± 0.48

[END TABLE 7.6 HERE]

7.3.3.2 Aerosol-cloud interactions

Anthropogenic aerosol particles primarily affect water clouds by serving as additional cloud condensation nuclei (CCN) and thus increasing cloud drop number concentration (N_d) (Twomey, 1959). Increasing N_d while holding liquid water content constant reduces cloud drop effective radius (r_e), increases the cloud albedo, and induces an instantaneous negative radiative forcing (IRFaci). The clouds are thought to subsequently adjust by a slowing of the drop coalescence rate, thereby delaying or suppressing rainfall. Rain generally reduces cloud lifetime and thereby liquid water path (LWP, i.e., the vertically integrated cloud water) and/or cloud fractional coverage (Cf) (Albrecht, 1989), thus any aerosol-induced rain delay or suppression would be expected to increase LWP and/or Cf. Such adjustments could potentially lead to an ERFaci considerably larger in magnitude than the IRFaci alone. However, adding aerosols to non-precipitating clouds has been observed to have the opposite effect (i.e., a reduction in LWP and/or Cf) (Lebsock et al., 2008; Christensen and Stephens, 2011). These findings have been explained by enhanced evaporation of the smaller droplets in the aerosol-enriched environments, and resultant enhanced mixing with ambient air, leading to cloud dispersal.

A small subset of aerosols can also serve as ice nucleating particles (INPs) that initiate the ice phase in supercooled water clouds, and thereby alter cloud radiative properties and/or lifetimes. However, the ability of anthropogenic aerosols (specifically BC) to serve as INPs in mixed-phase clouds has been found to be negligible in recent laboratory studies (e.g., Vergara-Temprado et al. (2018)). No assessment of the contribution to ERFaci from cloud phase changes induced by anthropogenic INPs will therefore be presented.

In ice (cirrus) clouds (cloud temperatures less than –40° C), INPs can initiate ice crystal formation at relative humidity much lower than that required for droplets to freeze spontaneously. Anthropogenic INPs can thereby influence ice crystal numbers and thus cirrus cloud radiative properties. At cirrus temperatures, certain types of BC have in fact been demonstrated to act as INPs in laboratory studies (Ullrich et al., 2017; Mahrt et al., 2018), suggesting a non-negligible anthropogenic contribution to INPs in cirrus clouds. Furthermore, anthropogenic changes to drop number also alter the number of droplets available for spontaneous freezing, thus representing a second pathway through which anthropogenic emissions could affect cirrus clouds.

7.3.3.2.1 Observation-based evidence

Since AR5, the analysis of observations to investigate aerosol-cloud interactions has progressed along several axes: (i) The framework of forcing and adjustments introduced rigorously in AR5 has helped better categorize studies; (ii) the literature assessing statistical relationships between aerosol- and cloud in satellite retrievals has grown, and retrieval uncertainties are better characterized; (iii) advances have been made to infer causality in aerosol-cloud relationships.

[START TABLE 7.7 HERE]

Table 7.7: Studies quantifying aspects of the global ERFaci that are mainly based on satellite retrievals and were published since AR5. All forcings/adjustments as global annual mean values in W m^{-2}. Most studies split the ERFaci into IRFaci and adjustments in LWP and cloud fraction separately. All published studies only considered liquid clouds. Some studies assessed the IRFaci and the LWP adjustment together and called this "intrinsic forcing"(Christensen et al., 2017) and the cloud fraction adjustment "extrinsic forcing". Published uncertainty ranges are converted to 5%–95 % confidence intervals, and "n/a" indicates that the study did not provide an estimate for the relevant IRF/ERF.

IRFaci	LWP adjustment	Cloud fraction adjustment	Reference
–0.6±0.6	n/a	n/a	Bellouin et al. (2013a)
–0.4 [–0.2 to –1.0]	n/a	n/a	Gryspeerdt et al. (2017)
–1.0±0.4	n/a	n/a	McCoy et al. (2017a)
n/a	n/a	–0.5 [–0.1 to –0.6]	Gryspeerdt et al. (2016)
n/a	+0.3 to 0	n/a	Gryspeerdt et al. (2019)
–0.8±0.7	n/a	n/a	Rémy et al. (2018)
–0.53	+0.15	n/a	Toll et al. (2019)
–1.14 [–1.72 to –0.84]	n/a	n/a	Hasekamp et al. (2019)
–1.2 to -0.6	n/a	n/a	McCoy et al. (2020)
–0.69 [–0.99 to –0.44]	n/a	n/a	Diamond et al. (2020)
"intrinsic forcing"			

–0.5 ± 0.5	–0.5 ± 0.5	Chen et al. (2014)
–0.4 ± 0.3	n/a	Christensen et al. (2016b)
–0.3 ± 0.4	–0.4 ± 0.5	Christensen et al. (2017)

[END TABLE 7.7 HERE]

In AR5 the statistical relationship between cloud microphysical properties and aerosol index (AI; AOD multiplied by Ångström exponent) was used to make inferences about IRFaci were assessed alongside other studies which related cloud quantities to AOD. However, it is now well-documented that the latter approach leads to low estimates of IRFaci since AOD is a poor proxy for cloud-base CCN (Penner et al., 2011; Stier, 2016). Gryspeerdt et al. (2017) demonstrated that the statistical relationship between droplet concentration and AOD leads to an inferred IRFaci that is underestimated by at least 30%, while the use of AI leads to estimates of IRFaci to within ±20%, if the anthropogenic perturbation of AI is known.

Further, studies assessed in AR5 mostly investigated linear relationships between cloud droplet concentration and aerosol (Boucher et al., 2013). Since in most cases the relationships are not linear, this leads to a bias (Gryspeerdt et al., 2016). Several studies did not relate cloud droplet concentration, but cloud droplet effective radius to the aerosol (Brenguier et al., 2000). This is problematic since then, in order to infer IRFaci, stratification by cloud LWP is required (McComiskey and Feingold, 2012). Where LWP positively co-varies with aerosol retrievals (which is often the case), IRFaci inferred from such relationships is biased towards low values. Also, it is increasingly evident that different cloud regimes show different sensitivities to aerosols (Stevens and Feingold, 2009). Averaging statistics over regimes thus bias the inferred IRFaci (Gryspeerdt et al., 2014b). AR5 concluded that IRFaci estimates tied to satellite studies generally show weak IRFaci (Boucher et al., 2013), but when correcting for the biases discussed above, this is no longer the case.

Since AR5, several studies assessed the global IRFaci from satellite observations using different methods (Table 7.7). All studies relied on statistical relationships between aerosol- and cloud quantities to infer sensitivities. Four studies inferred IRFaci by estimating the anthropogenic perturbation of N_d. For this, Bellouin et al. (2013a) and Rémy et al. (2018) made use of regional-seasonal regressions between satellite-derived N_d and AOD following Quaas et al. (2008), while Gryspeerdt et al. (2017) used AI instead of AOD in the regression to infer IRFaci. McCoy et al. (2017a) instead used the sulphate specific mass derived in the MERRA aerosol reanalysis that assimilated MODIS AOD (Rienecker et al., 2011). All approaches have in common the need to identify the anthropogenic perturbation of the aerosol to assess IRFaci. Gryspeerdt et al. (2017) and Rémy et al. (2018) used the same approach as Bellouin et al. (2013a), while McCoy et al. (2017a) used an anthropogenic fraction from the AEROCOM multi-model ensemble (Schulz et al., 2006). Chen et al. (2014), Christensen et al. (2016b) and Christensen et al. (2017) derived the combination of IRFaci and the LWP adjustment to IRFaci ("intrinsic forcing" in their terminology). They relate AI and cloud albedo statistically and use the anthropogenic aerosol fraction from Bellouin et al. (2013a). This was further refined by Hasekamp et al. (2019) who used additional polarimetric satellite information over ocean to obtain a better proxy for CCN. They derived an IRFaci of –1.14 [–1.72 to –0.84] W m^{-2}. The variant by Christensen et al. (2017) is an update compared to the Chen et al. (2014) and Christensen et al. (2016b) studies in that it better accounts for ancillary influences on the aerosol retrievals such as aerosol swelling and 3D radiative effects. McCoy et al. (2020) used the satellite-observed hemispheric difference in N_d as an emergent constraint on IRFaci as simulated by GCMs to obtain a range of –1.2 to –0.6 W m^{-2} (95% confidence interval). Diamond et al. (2020) analysed the difference in clouds affected by ship emissions with unperturbed clouds and based on this inferred a global IRFaci of –0.69 [–0.99 to –0.44] W m^{-2}.

Summarising the above findings related to statistical relationships and causal aerosol effects on cloud properties, there is *high confidence* that anthropogenic aerosols lead to an increase in cloud droplet concentrations. Taking the average across the studies providing IRFaci estimates discussed above and considering the general agreement among estimates (Table 7.7), IRFaci is assessed to be –0.7 ± 0.5 W m^{-2} (*medium confidence*).

Multiple studies have found a positive relationship between cloud fraction and/or cloud LWP and aerosols (e.g., Nakajima et al., 2001; Kaufman and Koren, 2006; Quaas et al., 2009). Since AR5, however, it has been documented that factors independent of causal aerosol-cloud interactions heavily influence such statistical relationships. These include the swelling of aerosols in the high relative humidity in the vicinity of clouds (Grandey et al., 2013) and the contamination of aerosol retrievals next to clouds by cloud remnants and cloud-side scattering (Várnai and Marshak, 2015; Christensen et al., 2017). Stratifying relationships by possible influencing factors such as relative humidity (Koren et al., 2010) does not yield satisfying results since observations of the relevant quantities are not available at the resolution and quality required. Another approach to tackle this problem was to assess the relationship of cloud fraction with droplet concentration (Gryspeerdt et al., 2016; Michibata et al., 2016; Sato et al., 2018). The relationship between satellite-retrieved cloud fraction and N_d was found to be positive (Christensen et al., 2016b, 2017; Gryspeerdt et al., 2016), implying an overall adjustment that leads to a more negative ERFaci. However, since retrieved N_d is biased low for broken clouds this result has been called into question (Grosvenor et al., 2018). Zhu et al. (2018) proposed to circumvent this problem by considering N_d of only continuous thick cloud covers, on the basis of which Rosenfeld et al. (2019) still obtained a positive cloud fraction – N_d relationship.

The relationship between LWP and cloud droplet number is debated. Most recent studies (primarily based on MODIS data) find negative statistical relationships (Michibata et al., 2016; Toll et al., 2017; Sato et al., 2018; Gryspeerdt et al., 2019), while Rosenfeld et al. (2019) obtained a modest positive relationship. To increase confidence that observed relationships between aerosol emissions and cloud adjustments are causal, known emissions of aerosols and aerosol precursor gases into otherwise pristine conditions have been exploited. Ship exhaust is one such source. Goren and Rosenfeld (2014) suggested that both LWP and Cf increase in response to ship emissions, contributing approximately 75% to the total ERF_{aci} in mid-latitude stratocumulus. Christensen and Stephens (2011) found that such strong adjustments occur for open-cell stratocumulus regimes, while adjustments are comparatively small in closed-cell regimes. Volcanic emissions have been identified as another important source of information (Gassó, 2008). From satellite observations, Yuan et al. (2011) documented substantially larger Cf, higher cloud tops, reduced precipitation likelihood, and increased albedo in cumulus clouds in the plume of the Kilauea volcano. Ebmeier et al. (2014) confirmed the increased LWP and albedo for other volcanoes. In contrast, for the large Holuhraun eruption, Malavelle et al. (2017) did not find any large-scale change in LWP in satellite observations. However, when accounting for meteorological conditions, McCoy et al. (2018) concluded that for cyclonic conditions, the extra Holuhraun aerosol did enhance LWP. Toll et al. (2017) examined a large sample of volcanoes and found a distinct albedo effect, but only modest LWP changes on average. Gryspeerdt et al. (2019) demonstrated that the negative LWP – Nd relationship becomes very small when conditioned on a volcanic eruption, and therefore concluded that LWP adjustments are small in most regions. Similarly, Toll et al. (2019) studied clouds downwind of various anthropogenic aerosol sources using satellite observations and inferred an IRFaci of –0.52 W m^{-2} that was partly offset by 29% due to aerosol-induced LWP decreases.

Apart from adjustments involving LWP and Cf, several studies have also documented a negative relationship between cloud-top temperature and AOD/AI in satellite observations (e.g., Koren et al., 2005). Wilcox et al. (2016) proposed that this could be explained by BC absorption reducing boundary layer turbulence, which in turn could lead to taller clouds. However, it has been demonstrated that the satellite-derived relationships are affected by spurious co-variation (Gryspeerdt et al., 2014a), and it therefore remains unclear whether a systematic causal effect exists.

Identifying relationships between INP concentrations and cloud properties from satellites is intractable because the INPs generally represent a very small subset of the overall aerosol population at any given time or location. For ice clouds, only few satellite studies have investigated responses to aerosol perturbations so far. Gryspeerdt et al. (2018) find a positive relationship between aerosol and ice crystal number for cold cirrus under strong dynamical forcing, which could be explained by an overall larger number of solution droplets available for homogeneous freezing in polluted regions. Zhao et al. (2018) conclude that the sign of the ice crystal size – aerosol relationship depends on humidity. While these studies support modelling results finding that ice clouds do respond to anthropogenic aerosols (Section 7.3.3.2.2), no quantitative conclusions about IRFaci or ERFaci for ice clouds can be drawn based on satellite observations.

Only a handful of studies have estimated the LWP and Cf adjustments that are needed for satellite-based estimates of ERFaci. Chen et al. (2014) and Christensen et al. (2017) used the relationship between cloud fraction and AI to infer the cloud fraction adjustment. Gryspeerdt et al. (2017) used a similar approach but tried to account for non-causal aerosol – cloud fraction correlations by using N_d as a mediating factor. These three studies together suggest a global Cf adjustment that augments ERFaci relative to IRFaci by –0.5 ± 0.4 W m^{-2} (*medium confidence*). For global estimates of the LWP adjustment, evidence is even scarcer. Gryspeerdt et al. (2019) derived an estimate of the LWP adjustment using a method similar to Gryspeerdt et al. (2016). They estimated that the LWP adjustment offsets 0 to 60% of the (negative) IRFaci (0 to +0.3 W m^{-2}). Supporting an offsetting LWP adjustment, Toll et al. (2019) estimated a moderate LWP adjustment of 29% (+0.15 W m^{-2}). The adjustment due to LWP is assessed to be small, with a central estimate and *very likely* range of 0.2 ± 0.2 W m^{-2} , but with *low confidence* due to the limited number of studies available.

Combining IRFaci and the associated adjustments in Cf and LWP (adding uncertainties in quadrature), considering only liquid-water clouds and evidence from satellite observations alone, the central estimate and *very likely* range for ERFaci is assessed to be –1.0 ± 0.7 W m^{-2} (*medium confidence*). The confidence level and wider range for ERFaci compared to IRFaci reflect the relatively large uncertainties that remain in the adjustment contribution to ERFaci.

7.3.3.2.2 Model-based evidence

As in AR5, the representation of aerosol-cloud interactions in ESMs remains a challenge, due to the limited representation of important sub-gridscale processes, from the emissions of aerosols and their precursors to precipitation formation. ESMs that simulate ERFaci typically include aerosol-cloud interactions in liquid stratiform clouds only, while very few include aerosol interactions with mixed-phase-, convective-, and ice clouds. Adding to the spread in model-derived estimates of ERFaci is the fact that model configurations and assumptions vary across studies, for example when it comes to the treatment of oxidants, which influence aerosol formation, and their changes through time (Karset et al., 2018).

In AR5, ERFaci was assessed as the residual of the total aerosol ERF and ERFari, as the total aerosol ERF was easier to calculate based on available model simulations (Boucher et al., 2013). The central estimates of total aerosol ERF and ERFari in AR5 were –0.9 W m^{-2} and –0.45 W m^{-2}, respectively, yielding an ERFaci estimate of –0.45 W m^{-2}. This value is much less negative than the bottom-up estimate of ERFaci from ESMs presented in AR5 (–1.4 W m^{-2}) and efforts have been made since to reconcile this difference. Zelinka et al. (2014) estimated ERFaci to be –0.96 ± 0.55 W m^{-2} (including semi-direct effects, and with land-surface cooling effect applied) based on nine CMIP5 models (Table 7.6). The corresponding ERFaci estimate based on 17 RFMIP models from CMIP6 is slightly less negative at –0.86 ± 0.57 W m^{-2} (Table 7.6). Other post-AR5 estimates of ERFaci based on single model studies are either in agreement with or slightly larger in magnitude than the CMIP6 estimate (Gordon et al., 2016; Fiedler et al., 2017; Neubauer et al., 2017; Karset et al., 2018; Regayre et al., 2018; Zhou et al., 2018b; Fiedler et al., 2019; Golaz et al., 2019a; Diamond et al., 2020).

The adjustment contribution to the CMIP6 ensemble mean ERFaci is –0.20 W m^{-2}, though with considerable differences between the models (Smith et al., 2020a). Generally, this adjustment in ESMs arises mainly from LWP changes (e.g., Ghan et al., 2016), while satellite observations suggest that cloud cover adjustments dominate and that aerosol effects on LWP are over-estimated in ESMs (Bender et al., 2019). Large-eddy-simulations also tend to suggest an over-estimated aerosol effect on cloud lifetime in ESMs, but some report an aerosol-induced decrease in cloud cover that is at odds with satellite observations (Seifert et al., 2015). Despite this potential disagreement when it comes to the dominant adjustment mechanism, a substantial negative contribution to ERFaci from adjustments is supported both by observational and modelling studies.

Contributions to ERFaci from anthropogenic aerosols acting as INPs are generally not included in CMIP6 models. Two global modelling studies incorporating parameterizations based on recent laboratory studies both found a negative contribution to ERFaci (Penner et al., 2018; McGraw et al., 2020), with central estimates of –0.3 and –0.13 W m^{-2}, respectively. However, previous studies have produced model estimates of opposing signs (Storelvmo, 2017). There is thus *limited evidence* and *medium agreement* for a small negative contribution to ERFaci from anthropogenic INP-induced cirrus modifications (*low confidence*).

Similarly, aerosol effects on deep convective clouds are typically not incorporated in ESMs. However, cloud-resolving modelling studies support non-negligible aerosol effects on the radiative properties of convective clouds and associated detrained cloud anvils (Tao et al., 2012). While global ERF estimates are currently not available for these effects, the fact that they are missing in most ESMs adds to the uncertainty range for the model-based ERFaci.

From model-based evidence, ERFaci is assessed to –1.0 ± 0.8 W m^{-2} (*medium confidence*). This assessment uses the mean ERFaci in Table 7.6 as a starting point, but further allows for a small negative ERF contribution from cirrus clouds. The uncertainty range is based on those reported in Table 7.6, but widened to account for uncertain but *likely* non-negligible processes currently unaccounted for in ESMs.

7.3.3.2.3 Overall assessment of ERFaci

The assessment of ERFaci based on observational evidence alone (–1.0 ± 0.7 W m^{-2}) is very similar to the one based on model-evidence alone (–1.0 ± 0.8 W m^{-2}), in strong contrast to what was reported in AR5. This reconciliation of observation-based and model-based estimates is the result of considerable scientific progress and reflects comparable revisions of both model-based and observation-based estimates. The strong agreement between the two largely independent lines of evidence increases confidence in the overall assessment of the central estimate and *very likely* range for ERFaci of –1.0 ± 0.7 W m^{-2} (*medium confidence*). The assessed range is consistent with but narrower than that reported by the review of Bellouin et al. (2019) of –2.65 to –0.07 W m^{-2}. The difference is primarily due to a wider range in the adjustment contribution to ERFaci in Bellouin et al. (2019), however adjustments reported relative to IRFaci ranging from 40% to 150% in that study are fully consistent with the ERFaci assessment presented here.

7.3.3.3 Energy budget constraints on the total aerosol ERF

Energy balance models of reduced complexity have in recent years increasingly been combined with Monte Carlo approaches to provide valuable "top-down" (also called inverse) observational constraints on the total aerosol ERF. These top-down approaches report ranges of aerosol ERF that are found to be consistent with the global mean temperature record and, in some cases, also observed ocean heat uptake. However, the total aerosol ERF is also used together with the historical temperature record in Section 7.5 to constrain ECS and TCR. Using top-down estimates as a separate line of evidence also for the total aerosol ERF would therefore be circular. Nevertheless, it is useful to examine the development of these estimates since AR5 and the degree to which these estimates are consistent with the upper and lower bounds of the assessments of total aerosol ERF (ERFari+ERFaci).

When the first top-down estimates emerged (e.g., Knutti et al., 2002), it became clear that some of the early ("bottom-up") ESM estimates of total aerosol ERF were inconsistent with the plausible top-down range. However, as more inverse estimates have been published, it has increasingly become clear that they too are model-dependent and span a wide range of ERF estimates, with confidence intervals that in some cases do not overlap (Forest, 2018). It has also become evident that these methods are sensitive to revised estimates of other forcings and/or updates to observational data sets. A recent review of 19 such estimates reported a mean of –0.77 W m^{-2} for the total aerosol ERF, and a 95% confidence interval of –1.15 W m^{-2} to –0.31 W m^{-2} (Forest, 2018). Adding to that review, a more recent study using the same approach reported an estimate of total aerosol ERF of –0.89 [–1.82 to –0.01] W m^{-2} (Skeie et al., 2018). However, in the same study, an alternative way of incorporating ocean heat content in the analysis produced a total aerosol ERF estimate of –1.34 [–2.20 to –0.46] W m^{-2}, illustrating the sensitivity to the manner in which observations are included. A new approach to inverse estimates took advantage of independent climate radiative response estimates from eight prescribed SST and sea-ice concentration simulations over the historical period to estimate the total anthropogenic ERF. From this a total aerosol ERF of –0.8 [–1.6 to +0.1] W m^{-2} was derived (valid for near-present relative to the late 1800s). This range was found to be more invariant to parameter choices than earlier inverse approaches (Andrews and Forster, 2020).

Beyond the inverse estimates described above, other efforts have been made since AR5 to constrain the total aerosol ERF. For example, Stevens (2015) used a simple (1-dimensional) model to simulate the historical total aerosol ERF evolution consistent with the observed temperature record. Given the lack of temporally extensive cooling trends in the 20th century record and the fact that the historical evolution of greenhouse gas forcing is relatively well constrained, the study concluded that a more negative total aerosol ERF than –1.0 W m^{-2} was incompatible with the historical temperature record. This was countered by Kretzschmar et al. (2017), who argued that the model employed in Stevens (2015) was too simplistic to account for the effect of geographical redistributions of aerosol emissions over time. Following the logic of Stevens (2015), but basing their estimates on a subset of CMIP5 models as opposed to a simplified modelling framework, they argued that a total aerosol ERF as negative as –1.6 W m^{-2} was consistent with the observed temperature record. Similar arguments were put forward by Booth et al. (2018), who emphasized that the degree of non-linearity of the total aerosol ERF with aerosol emission is a central assumption in Stevens (2015).

The historical temperature record was also the key observational constraint applied in two additional studies (Rotstayn et al., 2015; Shindell et al., 2015) based on a subset of CMIP5 models. Rotstayn et al. (2015) found a strong temporal correlation (> 0.9) between the total aerosol ERF and the global surface temperature. They used this relationship to produce a best estimate for the total aerosol ERF of –0.97 W m^{-2}, but with considerable unquantified uncertainty, in part due to uncertainties in the TCR. Shindell et al. (2015) came to a similar best estimate for the total aerosol ERF of –1.0 W m^{-2} and a 95% confidence interval of –1.4 to –0.6 W m^{-2} but based this on spatial temperature and ERF patterns in the models in comparison with observed spatial temperature patterns.

A separate observational constraint on the total ERF was proposed by Cherian et al. (2014), who compared trends in downward fluxes of solar radiation observed at surface stations across Europe (described in Section 7.2.2.3) to those simulated by a subset of CMIP5 models. Based on the relationship between solar radiation trends and the total aerosol ERF in the models, they inferred a total aerosol ERF of –1.3 W m^{-2} and a standard deviation of ± 0.4 W m^{-2}.

Based solely on energy balance considerations or other observational constraints, it is *extremely likely* that the total aerosol ERF is negative (*high confidence*), but *extremely unlikely* that the total aerosol ERF is more negative than –2.0 W m^{-2} (*high confidence*).

7.3.3.4 Overall assessment of total aerosol ERF

In AR5 (Boucher et al., 2013), the overall assessment of total aerosol ERF (ERFari+aci) used the median of all ESM estimates published prior to AR5 of –1.5 [–2.4 to –0.6] W m^{-2} as a starting point, but placed more confidence in a subset of models that were deemed more complete in their representation of aerosol-cloud interactions. These models, which included aerosol effects on mixed-phase, ice and/or convective clouds, produced a smaller estimate of –1.38 W m^{-2}. Likewise, studies that constrained models with satellite observations (five in total), which produced a median estimate of –0.85 W m^{-2}, were given extra weight. Furthermore, a longwave ERFaci of 0.2 W m^{-2} was added to studies that only reported shortwave ERFaci values. Finally, based on higher resolution models, doubt was raised regarding the ability of ESMs to represent the cloud adjustment component of ERFaci with fidelity. The expert judgement was therefore that aerosol effects on cloud lifetime were too strong in the ESMs, further reducing the overall ERF estimate. The above lines of argument resulted in a total aerosol assessment of –0.9 [–1.9 to –0.1] W m^{-2} in AR5.

Here, the best estimate and range is revised relative to AR5 (Boucher et al., 2013), partly based on updates to the above lines of argument. Firstly, the studies that included aerosol effects on mixed-phase clouds in AR5 relied on the assumption that anthropogenic black carbon (BC) could act as INPs in these clouds, which has since been challenged by laboratory experiments (Kanji et al., 2017; Vergara-Temprado et al., 2018). There is no observational evidence of appreciable ERFs associated with aerosol effects on mixed-phase and ice clouds (Section 7.3.3.2.1), and modelling studies disagree when it comes to both their magnitude and sign

(Section 7.3.3.2.2). Likewise, very few ESMs incorporate aerosol effects on deep convective clouds, and cloud-resolving modelling studies report different effects on cloud radiative properties depending on environmental conditions (Tao et al., 2012). Thus, it is not clear whether omitting such effects in ESMs would lead to any appreciable ERF biases, or if so, what the sign of such biases would be. As a result, all ESMs are given equal weight in this assessment. Furthermore, there is now a considerably expanded body of literature which suggests that early modelling studies that incorporated satellite observations may have resulted in overly conservative estimates of the magnitude of ERFaci (Section 7.3.3.2.1). Finally, based on an assessment of the longwave ERFaci in the CMIP5 models, the offset of +0.2 W m^{-2} applied in AR5 appears to be too large (Heyn et al., 2017). As in AR5, there is still reason to question the ability of ESMs to simulate adjustments in LWP and cloud cover in response to aerosol perturbation, but it is not clear that this will result in biases that exclusively increase the magnitude of the total aerosol ERF (Section 7.3.3.2.2).

The assessment of total aerosol ERF here uses the following lines of evidence: satellite-based evidence for IRFari, model-based evidence for IRFari and ERFari, satellite-based evidence of IRF/ERFaci, and finally model-based evidence for ERFaci. Based on this, ERFari and ERFaci for 2014 relative to 1750 are assessed to –0.3 ± 0.3 W m^{-2} and –1.0 ± 0.7 W m^{-2}, respectively. There is thus strong evidence for a substantive negative total aerosol ERF, which is supported by the broad agreement between observation-based and model-based lines of evidence for both ERFari and ERFaci that has emerged since AR5 (Gryspeerdt et al., 2020). However, considerable uncertainty remains, particularly with regards to the adjustment contribution to ERFaci, as well as missing processes in current ESMs, notably aerosol effects on mixed-phase, ice and convective clouds. This leads to a *medium confidence* in the estimate of ERFari+aci and a slight narrowing of the uncertainty range. Because the estimates informing the different lines of evidence are generally valid for approximately 2014 conditions, the total aerosol ERF assessment is considered valid for 2014 relative to 1750.

Combining the lines of evidence and adding uncertainties in quadrature, the ERFari+aci estimated for 2014 relative to 1750 is assessed to be –1.3 [–2.0 to –0.6] W m^{-2} *(medium confidence).* The corresponding range from Bellouin et al. (2019) is –3.15 to –0.35 W m^{-2}, thus there is agreement for the upper bound while the lower bound assessed here is less negative. A lower bound more negative than -2.0 W m^{-2} is not supported by any of the assessed lines of evidence. There is *high confidence* that ERFaci contributes most (75–80%) to the total aerosol effect (ERFari+aci). In contrast to AR5 (Boucher et al., 2013), it is now *virtually certain* that the total aerosol ERF is negative. Figure 7.5 depicts the aerosol ERFs from the different lines of evidence along with the overall assessments.

As most modelling and observational estimates of aerosol ERF have end points in 2014 or earlier, there is limited evidence available for the assessment of how aerosol ERF has changed from 2014 to 2019. However, based on a general reduction in global mean AOD over this period (Chapter 2, Section 2.2.6, Figure 2.9), combined with a reduction in emissions of aerosols and their precursors in updated emission inventories (Hoesly et al., 2018), the aerosol ERF is assessed to have decreased in magnitude from about 2014 to 2019 *(medium confidence)*. Consistent with Chapter 2, Figure 2.10, the change in aerosol ERF from about 2014 to 2019 is assessed to be +0.2 W m^{-2}, but with *low confidence* due to limited evidence. Aerosols are therefore assessed to have contributed an ERF of –1.1 [–1.7 to –0.4] W m^{-2} over 1750–2019 (*medium confidence*).

[START FIGURE 7.5 HERE]

Figure 7.5: Net aerosol effective radiative forcing from different lines of evidence. The headline AR6 assessment of –1.3 [–2.0 to –0.6] W m^{-2} is highlighted in purple for 1750–2014 and compared to the AR5 assessment of –0.9 [–1.9 to –0.1] W m^{-2} for 1750–2011. The evidence comprising the AR6 assessment is shown below this: energy balance constraints (–2 to 0 W m^{-2} with no best estimate), observational evidence from satellite retrievals of –1.4 [–2.2 to –0.6] W m^{-2}, and climate model-based evidence of –1.25 [–2.1 to –0.4] W m^{-2}. Estimates from individual CMIP5 (Zelinka et al., 2014) and CMIP6 (Smith et al., 2020a and Table 7.6) models are depicted by blue and red crosses respectively. For each line of evidence the assessed best-estimate contributions from ERFari and ERFaci are shown with darker and paler shading respectively. The observational assessment for ERFari is taken from the IRFari. Uncertainty ranges are given in black bars for the total aerosol ERF and depict *very likely* ranges. Further details on data sources

and processing are available in the chapter data table (Table 7.SM.14).

[END FIGURE 7.5 HERE]

7.3.4 Other agents

In addition to the large anthropogenic ERFs associated with WMGHGs and atmospheric aerosols assessed in Sections 7.3.2 and 7.3.3, land use change, contrails and aviation-induced cirrus and light absorbing particles deposited on snow and ice have also contributed to the overall anthropogenic ERF and are assessed in Sections 7.3.4.1, 7.3.4.2 and 7.3.4.3. Changes in solar irradiance, galactic cosmic rays and volcanic eruptions since pre-industrial times combined represent the natural contribution to the total (anthropogenic + natural) ERF and are discussed in Sections 7.3.4.4, 7.3.4.5 and 7.3.4.6.

7.3.4.1 Land use

Land use forcing is defined as those changes in land surface properties directly caused by human activity rather than by climate processes (see also Chapter 2, Section 2.2.7). Land use change affects the surface albedo. For example, deforestation typically replaces darker forested areas with brighter cropland, and thus imposes a negative radiative forcing on climate, while afforestation and reforestation can have the opposite effect. Precise changes depend on the nature of the forest, crops and underlying soil. Land use change also affects the amount of water transpired by vegetation (Devaraju et al., 2015). Irrigation of land directly affects the evaporation (Sherwood et al., 2018) causing a global increase of 32 500 m^3 s^{-1} due to human activity. Changes in evaporation and transpiration affect the latent heat budget, but do not directly affect the top-of-atmosphere radiative fluxes. The lifetime of water vapour is so short that the effect of changes in evaporation on the greenhouse contribution of water vapour are negligible (Sherwood et al., 2018). However, evaporation can affect the ERF through adjustments, particularly through changes in low cloud amounts. Land management affects the emissions or removal of greenhouse gases from the atmosphere (such as CO_2, CH_4, N_2O). These emission changes have the greatest effect on climate (Ward et al., 2014), however they are already included in greenhouse gas inventories. Land use change also affects the emissions of dust and biogenic volatile organic compounds (BVOCs), which form aerosols and affect the atmospheric concentrations of ozone and methane (Chapter 6, Section 6.2.2). The effects of land use on surface temperature and hydrology were recently assessed in SRCCL (Jia et al., 2019).

Using the definition of ERF from Section 7.1, the adjustment in land surface temperature is excluded from the definition of ERF, but changes in vegetation and snow cover (resulting from land use change) are included (Boisier et al., 2013). Land use change in the mid-latitudes induces a substantial amplifying adjustment in snow cover. Few climate model studies have attempted to quantify the ERF of land use change. Andrews et al. (2017b) calculated a very large surface albedo ERF (–0.47 W m^{-2}) from 1860 to 2005 in the HadGEM2-ES model although they did not separate out the surface albedo change from snow cover change. HadGEM2-ES is known to overestimate the amount of boreal trees and shrubs in the unperturbed state (Collins et al., 2011) so will tend to overestimate the ERF associated with land use change. The increases in dust in HadGEM2-ES contributed an extra –0.25 W m^{-2}, whereas cloud cover changes added a small positive adjustment (0.15 W m^{-2}) consistent with a reduction in transpiration. A multi-model quantification of land use forcing in CMIP6 models (excluding one outlier) (Smith et al., 2020a) found an IRF of –0.15 ± 0.12 W m^{-2} (1850 to 2014), and an ERF (correcting for land surface temperature change) of -0.11 ± 0.09 W m^{-2}. This shows a small positive adjustment term (mainly from a reduction in cloud cover. CMIP5 models show an IRF of –0.11 [–0.16 to –0.04] W m^{-2} (1850 to 2000) after excluding unrealistic models (Lejeune et al., 2020).

The contribution of land use change to albedo changes has recently been investigated using MODIS and AVHRR to attribute surface albedo to geographically-specific land cover types (Ghimire et al., 2014). When combined with a historical land use map (Hurtt et al., 2011) this gives a 1700 to 2005 SARF of –0.15 ± 0.01 W m^{-2} (of which –0.12 W m^{-2} is from 1850). This study accounted for correlations between vegetation type and snow cover, but not the adjustment in snow cover identified in (Andrews et al., 2017b).

The indirect contributions of land use change through biogenic emissions is very uncertain. Decreases in biogenic volatile organic compounds (BVOCs) reduce ozone and methane (Unger, 2014), but also reduce the formation of organic aerosols and their effects of clouds Scott et al. (2017). Adjustments through changes in aerosols and chemistry are model dependent (Zhu et al., 2019a; Zhu and Penner, 2020), and it is not yet possible to make an assessment based on a limited number of studies.

The contribution of irrigation (mainly to low cloud amount) is assessed as –0.05 [–0.1 to 0.05] W m^{-2} for the historical period (Sherwood et al., 2018).

Since the CMIP5 and CMIP6 modelling studies are in agreement with Ghimire et al. (2014), that study is used as the assessed albedo ERF. Adding the irrigation effect to this gives an overall assessment of the ERF from land use change of –0.20 ± 0.10 W m^{-2} (*medium confidence*). Changes in ERF since 2014 are assumed to be small compared to the uncertainty, so this ERF applies to the period 1750 to 2019. The uncertainty range includes uncertainties in the adjustments.

7.3.4.2 Contrails and aviation-induced cirrus

ERF from contrails and aviation-induced cirrus is taken from the assessment of Lee et al. (2020), at 0.057 [0.019 to 0.098] W m^{-2} in 2018 (see Chapter 6, Section 6.6.2 for an assessment of the total effects of aviation). This is rounded up to address its *low confidence* and the extra year of air traffic to give an assessed ERF over 1750–2019 of 0.06 [0.02 to 0.10]. This assessment is given *low confidence* due to the potential for missing processes to affect the magnitude of contrails and aviation-induced cirrus ERF.

7.3.4.3 Light absorbing particles on snow and ice

In AR5, it was assessed that the effects of light absorbing particles (LAPs) did probably not significantly contribute to recent reductions in Arctic ice and snow (Vaughan et al., 2013). The SARF from LAPs on snow and ice was assessed to +0.04 [+0.02 to +0.09] W m^{-2} (Boucher et al., 2013), a range appreciably lower than the estimates given in AR4 (Forster et al., 2007). This effect was assessed to be *low confidence* (*medium evidence, low agreement*) (Table 8.5 in Myhre et al., 2013b).

Since AR5 there has been progress in the understanding of the physical state and processes in snow that governs the albedo reduction by black carbon (BC). The SROCC (IPCC, 2019a) assessed that there is *high confidence* that darkening of snow by deposition of BC and other light absorbing aerosol species increases the rate of snow melt (Section 2.2 in Hock et al., 2019; Section 3.4 in Meredith et al., 2019). He et al. (2018a) found that taking into account the non-spherical shape of snow grains and internal mixing of BC in snow both significantly altered the effects of BC on snow albedo. The reductions of snow albedo by dust and black carbon have been measured and characterised in the Arctic, the Tibetan Plateau, and mid latitude regions subject to seasonal snowfall including North America and Northern and Eastern Asia (Qian et al., 2015).

Since AR5, two further studies of global IRF from black carbon on snow deposition are available, with best estimates of 0.01 W m^{-2} and 0.04 W m^{-2} (Lin et al., 2014; Namazi et al., 2015). Organic carbon deposition on snow and ice has been estimated to contribute a small positive IRF of 0.001 to 0.003 W m^{-2} (Lin et al., 2014). No comprehensive global assessments of mineral dust deposition on snow are available, although the effects are potentially large in relation to the total LAPs on snow and ice forcing (Yasunari et al., 2015).

Most radiative forcing estimates have a regional emphasis. The regional focus makes estimating a global mean radiative forcing from aggregating different studies challenging, and the relative importance of each region is expected to change if the global pattern of emission sources changes (Bauer et al., 2013). The lower bound of the assessed range of black carbon on snow and ice is extended to zero to encompass Lin et al.

(2014), with the best estimate unchanged resulting in 0.04 [0.00 to 0.09] W m^{-2}. The efficacy of black carbon on snow forcing was estimated to be 2 to 4 times as large as for an equivalent CO_2 forcing as the effects are concentrated at high latitudes in the cryosphere (Bond et al., 2013). However, it is unclear how much of this effect is due to radiative adjustments leading to a higher ERF, and how much comes from a less negative feedback α due the high latitude nature of the forcing. To estimate the overall ERF, the IRF is doubled assuming that part of the increased efficacy is due to adjustments. This gives an overall assessed ERF of +0.08 [0.00 to 0.18] W m^{-2}, with *low confidence*.

7.3.4.4 Solar

Variations in the total solar irradiance (TSI) represent a natural external forcing agent. The dominant cycle is the solar 11-year activity cycle, which is superimposed on longer cycles (Chapter 2, Section 2.2). Over the last three 11-year cycles, the peak-to-trough amplitude in TSI has differed by about 1 W m^{-2} between solar maxima and minima (Chapter 2, Figure 2.2).

The fractional variability in the solar irradiance, over the solar cycle and between solar cycles, is much greater at short wavelengths in the 200–400 nm band than for the broad visible/IR band that dominates TSI (Krivova et al., 2006). The IRF can be derived simply by ΔTSI × (1 – albedo)/4 irrespective of wavelength, where the best estimate of the planetary albedo is usually taken to be 0.29 and ΔTSI represents the change in total solar irradiance (Stephens et al., 2015). (The factor 4 arises because TSI is per unit area of Earth cross section presented to the Sun and IRF is per unit area of Earth's surface). The adjustments are expected to be wavelength dependent. Gray et al. (2009) determined a stratospheric temperature adjustment of –22% to spectrally resolved changes in the solar radiance over one solar cycle. This negative adjustment is due to stratospheric heating from increased absorption by ozone at the short wavelengths, increasing the outgoing longwave radiation to space. A multi-model comparison (Smith et al., 2018b) calculated adjustments of –4% due to stratospheric temperatures and –6% due to tropospheric processes (mostly clouds), for a change in TSI across the spectrum (Figure 7.4). The smaller magnitude of the stratospheric temperature adjustment is consistent with the broad spectral change rather than the shorter wavelengths characteristic of solar variation. A single model study also found an adjustment that acts to reduce the forcing (Modak et al., 2016). While there has not yet been a calculation based on the appropriate spectral change, the –6% tropospheric adjustment from Smith et al. (2018b) is adopted along with the Gray et al. (2009) stratospheric temperature adjustment. The ERF due to solar variability over the historical period is therefore represented by 0.72 × ΔTSI × (1 – albedo)/4 using the TSI timeseries from Chapter 2, Section 2.2.1.

AR5 (Myhre et al., 2013b) assessed solar SARF from around 1750 to 2011 to be 0.05 [0.00 to 0.10] W m^{-2} which was computed from the seven-year mean around the solar minima in 1745 (being closest to 1750) and 2008 (being the most recent solar minimum). The inclusion of tropospheric adjustments that reduce ERF (compared to SARF in AR5) has a negligible effect on the overall forcing. Prior to the satellite era, proxy records are used to reconstruct historical solar activity. In AR5, historical records were constructed using observations of solar magnetic features. In this assessment historical time series are constructed from radiogenic compounds in the biosphere and in ice cores that are formed from cosmic rays (Steinhilber et al., 2012).

In this assessment the TSI from the Paleoclimate Model Intercomparison Project Phase 4 (PMIP4) reconstruction is used (Jungclaus et al., 2017; Chapter 2, Section 2.2.1). Proxies constructed from the ^{14}C and ^{10}Be radiogenic records for the SATIRE-M model (Vieira et al., 2011) and ^{14}C record for the PMOD model (Shapiro et al., 2011) for the 1745 solar minimum provide 1745 to 2008 ERFs of –0.01, –0.02 and 0.00 W m^{-2} respectively. An independent dataset from the National Oceanic and Atmospheric Administration's Climate Data Record (Coddington et al., 2016; Lean, 2018) provides a 1745 to 2008 ERF of +0.03 W m^{-2}. One substantially higher ERF estimate of +0.35 W m^{-2} derived from TSI reconstructions is provided by Egorova et al. (2018). However, the estimate from Egorova et al. (2018) hinges on assumptions about long-term changes in the quiet Sun for which there is no observed evidence. Lockwood and Ball (2020) analysed the relationship of observed changes in cosmic ray fluxes and recent, more accurate, TSI data and derived ERF between –0.01 and +0.02 W m^{-2} and Yeo et al. (2020) modelling showed the maximum possible ERF to be 0.26 ± 0.09 W m^{-2}. Hence the Egorova et al. (2018) estimate is not explicitly taken into account in the assessment presented in this section.

In contrast to AR5, the solar ERF in this assessment uses full solar cycles rather than solar minima. The pre-industrial TSI is defined as the mean from all complete solar cycles from the start of the ^{14}C SATIRE-M proxy record in 6755 BCE to 1744 CE. The mean TSI from solar cycle 24 (2009–2019) is adopted as the assessment period for 2019. The best estimate solar ERF is assessed to be 0.01 W m^{-2}, using the ^{14}C reconstruction from SATIRE-M, with a *likely* range of –0.06 to +0.08 W m^{-2} (*medium confidence*). The uncertainty range is adopted from the evaluation of Lockwood and Ball (2020) using a Monte Carlo analysis of solar activity from the Maunder Minimum to 2019 from several datasets, leading to an ERF of –0.12 to +0.15 W m^{-2}. The Lockwood and Ball (2020) full uncertainty range is halved as the period of reduced solar activity in the Maunder Minimum had ended by 1750 *(medium confidence)*.

7.3.4.5 Galactic Cosmic Rays

Variations in the flux of galactic cosmic rays (GCR) reaching the atmosphere are modulated by solar activity and affect new particle formation in the atmosphere through their link to ionization of the troposphere (Lee et al., 2019). It has been suggested that periods of high GCR flux correlate with increased aerosol and CCN concentrations and therefore also with cloud properties (e.g., Dickinson, 1975; Kirkby, 2007).

Since AR5, the link between GCR and new particle formation has been more thoroughly studied, particularly by experiments in the CERN CLOUD chamber (Cosmics Leaving OUtdoor Droplets) (Dunne et al., 2016; Kirkby et al., 2016; Pierce, 2017). By linking the GCR-induced new particle formation from CLOUD experiments to CCN, Gordon et al. (2017) found the CCN concentration for low clouds to differ by 0.2% to 0.3% between solar maximum and solar minimum of the solar cycle. Combined with relatively small variations in the atmospheric ion concentration over centennial time scales (Usoskin et al., 2015), it is therefore unlikely that cosmic ray intensity affects present day climate via nucleation (Yu and Luo, 2014; Dunne et al., 2016; Pierce, 2017; Lee et al., 2019).

Studies continue to seek a relationship between GCR and properties of the climate system based on correlations and theory. Svensmark et al. (2017) proposed a new mechanism for ion-induced increase in aerosol growth rate and subsequent influence on the CCN concentration. The study does not include an estimate of the resulting effect on atmospheric CCN concentration and cloud radiative properties. Furthermore, Svensmark et al. (2009, 2016) find correlations between GCRs and aerosol and cloud properties in satellite and ground based data. Multiple studies investigating this link have challenged such correlations (Kristjánsson et al., 2008; Calogovic et al., 2010; Laken, 2016).

AR5 concluded that the GCR effect on CCN is too weak to have any detectable effect on climate and no robust association was found between GCR and cloudiness (Boucher et al., 2013). Published literature since then robustly support these conclusions with key laboratory, theoretical and observational evidence. There is *high confidence* that GCRs contribute a negligible ERF over the period 1750 to 2019.

7.3.4.6 Volcanic aerosols

There is large episodic negative radiative forcing associated with SO_2 being ejected into the stratosphere from explosive volcanic eruptions, accompanied by more frequent smaller eruptions (Chapter 2, Figure 2.2; Cross-Chapter Box 4.1). From SO_2 gas, reflective sulphate aerosol is formed in the stratosphere where it may persist for months, reducing the incoming solar radiation. The volcanic SARF in AR5 (Myhre et al., 2013b) was derived by scaling the stratospheric aerosol optical depth (SAOD) by a factor of –25 W m^{-2} per unit SAOD from Hansen et al. (2005b). Quantification of the adjustments to SAOD perturbations from climate model simulations have determined a significant positive adjustment driven by a reduction in cloud amount (Marshall et al., 2020; Figure 7.4). Analysis of CMIP5 models provide a mean ERF of –20 W m^{-2} per unit SAOD (Larson and Portmann, 2016). Single model studies with successive generations of Hadley Centre climate models produce estimates between –17 and –19 W m^{-2} per unit SAOD (Gregory et al., 2016; Marshall et al., 2020), with some evidence that ERF may be non-linear with SAOD for large eruptions (Marshall et al., 2020). Analysis of the volcanically active periods of 1982-1985 and 1990-1994 using the CESM1(WACCM) aerosol-climate model provided an SAOD to ERF relationship of –21.5 (± 1.1) W m^{-2} per unit SAOD (Schmidt et al., 2018). Volcanic SO_2 emissions may contribute a positive forcing through effects on upper tropospheric ice clouds, due to additional ice nucleation on volcanic sulphate particles (Friberg et al., 2015; Schmidt et al., 2018), although one observational study found no significant effect (Meyer et al., 2015). Due to *limited agreement*, the contribution to volcanic ERF due to sulphate aerosol effects on ice clouds is not included in the overall assessment.

Non-explosive volcanic eruptions generally yield negligible global ERFs due to the short atmospheric lifetimes (a few weeks) of volcanic aerosols in the troposphere. However, as discussed in Section 7.3.3.2, the massive fissure eruption in Holuhraun, Iceland persisted for months in 2014 and 2015 and did in fact result in a marked and persistent reduction in cloud droplet radii and a corresponding increase in cloud albedo regionally (Malavelle et al., 2017). This shows that non-explosive fissure eruptions can lead to strong regional and even global ERFs, but because the Holuhraun eruption occurred in NH winter, solar insolation was weak and the observed albedo changes therefore did not result in an appreciable global ERF (Gettelman et al., 2015).

The ERF for volcanic stratospheric aerosols is assessed to be –20 ± 5 W m^{-2} per unit SAOD (*medium confidence*) based on the CMIP5 multi-model mean from the Larson and Portmann (2016) SAOD forcing efficiency calculations combined with the single-model results of Gregory et al. (2016), Schmidt et al. (2018) and Marshall et al. (2020). This is applied to the SAOD timeseries from Chapter 2, Section 2.2.2 to generate a timeseries of ERF and temperature response shown in Chapter 2, Figure 2.2 and Figure 7.8 respectively. The period from 500 BC to 1749, spanning back to the start of the record of Toohey and Sigl (2017), is defined as the pre-industrial baseline and the volcanic ERF is calculated using an SAOD anomaly from this long-term mean. As in AR5, a pre-industrial to present-day ERF assessment is not provided due to the episodic nature of volcanic eruptions.

7.3.5 Synthesis of Global Mean Radiative Forcing, Past and Future

7.3.5.1 Major changes in forcing since IPCC AR5

AR5 introduced the concept of ERF and radiative adjustments, and made a preliminary assessment that the tropospheric adjustments were zero for all species other than the effects of aerosol-cloud interaction and black carbon. Since AR5, new studies have allowed for a tentative assessment of values for tropospheric adjustments to CO_2, CH_4, N_2O, some CFCs, solar forcing, and stratospheric aerosols, and to place a tighter constraint on adjustments from aerosol-cloud interaction (Sections 7.3.2, 7.3.3, 7.3.4). In AR6, the definition of ERF explicitly removes the land-surface temperature change as part of the forcing, in contrast to AR5 where only sea-surface temperatures were fixed. The ERF is assessed to be a better predictor of modelled equilibrium temperature change (i.e. less variation in feedback parameter) than SARF (Section 7.3.1).

As discussed in Section 7.3.2, the radiative efficiencies for CO_2, CH_4 and N_2O have been updated since AR5 (Etminan et al., 2016). There has been a small (1%) increase in the stratospheric-temperature adjusted CO_2 radiative efficiency, and a +5% tropospheric adjustment has been added. The stratospheric-temperature adjusted radiative efficiency for CH_4 is increased by 25% (*high confidence*). The tropospheric adjustment is tentatively assessed to be –14% *(low confidence*). A +7% tropospheric adjustment has been added to the radiative efficiency for N_2O and +12% to CFC-11 and CFC-12 (*low confidence*).

For aerosols there has been a convergence of model and observational estimates of aerosol forcing, and the partitioning of the total aerosol ERF has changed. Compared to AR5 a greater fraction of the ERF is assessed to come from ERFaci compared to the ERFari. It is now assessed as *virtually certain* that the total aerosol ERF (ERFari+aci) is negative.

7.3.5.2 Summary ERF assessment

Figure 7.6 shows the industrial-era ERF estimates for 1750 to 2019 for the concentration change in different forcing agents. The assessed uncertainty distributions for each individual component are combined with a 100,000-member Monte Carlo simulation that samples the different distributions, assuming they are independent, to obtain the overall assessment of total present-day ERF (Supplementary Material 7.SM.1). The corresponding emissions based ERF figure is shown in Chapter 6, Figure 6.12.

[START FIGURE 7.6 HERE]

Figure 7.6: Change in effective radiative forcing from 1750 to 2019 by contributing forcing agents (carbon dioxide, other well-mixed greenhouse gases (WMGHGs), ozone, stratospheric water vapour, surface albedo, contrails and aviation-induced cirrus, aerosols, anthropogenic total, and solar). Solid bars represent best estimates, and *very likely* (5–95%) ranges are given by error bars. Non-CO_2 WMGHGs are further broken down into contributions from methane (CH_4), nitrous oxide (N_2O) and halogenated compounds. Surface albedo is broken down into land use changes and light absorbing particles on snow and ice. Aerosols are broken down into contributions from aerosol-cloud interactions (ERFaci) and aerosol-radiation interactions (ERFari). For aerosols and solar, the 2019 single-year values are given (Table 7.8) that differ from the headline assessments in both cases. Volcanic forcing is not shown due to the episodic nature of volcanic eruptions. Further details on data sources and processing are available in the chapter data table (Table 7.SM.14).

[END FIGURE 7.6 HERE]

[START TABLE 7.8 HERE]

Table 7.8: Summary table of ERF estimates for AR6 and comparison with the four previous IPCC assessment reports. Prior to AR5 values are SARF. For AR5 ari and aci are ERF, all other values assume ERF equals SARF. 5% to 95% ranges are shown. Volcanic ERF is not added to the table due to the episodic nature of volcanic eruptions which makes it difficult to compare to the other forcing mechanisms. Solar ERF is based on TSI and not spectral variation.

	Global Mean Effective Radiative Forcing (W m^{-2})					
Driver	***SAR (1750–1993)***	***TAR (1750–1998)***	***AR4 (1750–2005)***	***AR5 (1750–2011)***	**AR6 (1750–2019)**	***Comment***
CO_2	1.56 [1.33 to 1.79]	1.46 [1.31 to 1.61]	1.66 [1.49 to 1.83]	1.82 (1.63 to 2.01)	2.16 [1.90 to 2.41]	Increases in concentrations. Changes to radiative efficiencies. Inclusion of tropospheric adjustments.
CH_4	0.47 [0.40 to 0.54	0.48 [0.41 to 0.55]	0.48 [0.43 to 0.53]	0.48 [0.43 to 0.53]	0.54 [0.43 to 0.65]	
N_2O	0.14 [0.12 to 0.16]	0.15 [0.14 to 0.16]	0.16 [0.14 to 0.18]	0.17 [0.14 to 0.20]	0.21 [0.18 to 0.24]	
Halogenated species	0.26 [0.22 to 0.30]	0.36 [0.31 to 0.41]	0.33 [0.30 to 0.36]	0.36 [0.32 to 0.40]	0.41 [0.33 to 0.49]	
Tropospheric ozone	0.4 [0.2 to 0.6]	0.35 [0.20 to 0.50]	0.35 [0.25 to 0.65]	0.40 [0.20 to 0.60]	0.47 [0.24 to 0.71]	Revised precursor emissions. No tropospheric
Stratospheric	–0.1 [–0.2 to	–0.15	–0.05	–0.05 [–		

ozone	–0.05]	[–0.25 to –0.05]	[–0.15 to 0.05]	0.15 to 0.05]		adjustment assessed. No trop-strat separation.
Stratospheric water vapour	Not estimated	[0.01 to 0.03]	0.07 [0.02 to 0.1])	0.07 [0.02 to 0.12]	0.05 [0.00 to 0.10]	Downward revision due to adjustments.
Aerosol–radiation interactions	–0.5 [–0.25 to –1.0]	Not estimated	–0.50 [–0.90 to –0.10]	–0.45 [–0.95 to 0.05]	–0.22 [–0.47 to 0.04]	ERFari magnitude reduced by about 50% compared to AR5, based on agreement between observation-based and modelling-based evidence
Aerosol–cloud interactions	[–1.5 to 0.0] (sulphate only)	[–2.0 to 0.0] (all aerosols)	–0.7 [–1.8 to –0.3] (all aerosols)	–0.45 [–1.2 to 0.0]	–0.84 [–1.45 to –0.25]	ERFaci magnitude increased by about 85% compared to AR5, based on agreement between observation-based and modelling-based lines of evidence
Land use	Not estimated	–0.2 [–0.4 to 0.0]	–0.2 [–0.4 to 0.0]	–0.15 [–0.25 to –0.05]	–0.20 [–0.30 to –0.10]	Includes irrigation.
Surface albedo (black+organic carbon aerosol on snow and ice)	Not estimated	Not estimated	0.10 [0.00 to 0.20]	0.04 [0.02 to 0.09]	0.08 [0.00 to 0.18]	Increased since AR5 to better account for temperature effects
Combined contrails and aviation-induced cirrus	Not estimated	[0.00 to 0.04]	Not estimated	0.05 [0.02 to 0.15]	0.06 [0.02 to 0.10]	Narrower range since AR5
Total anthropogenic	Not estimated	Not estimated	1.6 [0.6 to 2.4]	2.3 [1.1 to 3.3]	**2.72 [1.96 to 3.48]**	Increase due to greenhouse gases, compensated slightly by aerosol ERFaci
Solar irradiance	0.3 [0.1 to 0.5]	0.3 [0.1 to 0.5]	0.12 [0.06 to 0.30]	0.05 [0.0 to 0.10]	0.01 [–0.06 to 0.08]	Revised historical TSI estimates and methodology

[END TABLE 7.8 HERE]

The total anthropogenic ERF over the industrial era (1750–2019) is estimated as 2.72 [1.96 to 3.48] W m^{-2} (Table 7.8; Annex III) (*high confidence).* This represents a 0.43 W m^{-2} increase over the assessment made in AR5 (Myhre et al., 2013b) for the period 1750–2011. This increase is a result of compensating effects. Atmospheric concentration increases of greenhouse gases since 2011 and upwards revisions of their forcing estimates have led to a 0.59 W m^{-2} increase in their ERF. Whereas, the total aerosol ERF is assessed to be more negative compared to AR5, due to revised estimates rather than trends *(high confidence)*.

Greenhouse gases, including ozone and stratospheric water vapour from methane oxidation, are estimated to contribute an ERF of 3.84 [3.46 to 4.22] W m^{-2} over 1750–2019. Carbon dioxide continues to contribute the largest part (56 ± 16 %) of this GHG ERF (*high confidence*).

As discussed in Section 7.3.3, aerosols have in total contributed an ERF of –1.1 [–1.7 to –0.4] W m^{-2} over 1750-2019 (*medium confidence*). Aerosol-cloud interactions contribute approximately 75–80% to this ERF with the remainder due to aerosol-radiation interactions (Table 7.8).

For the purpose of comparing forcing changes with historical temperature change (Section 7.5.2), longer averaging periods are useful. The change in ERF from the second half of the 19th century (1850–1900) compared with a recent period (2006–2019) is 2.20 [1.53 to 2.91] W m^{-2}, of which 1.71 [1.51 to 1.92] W m^{-2} is due to CO_2.

7.3.5.3 Temperature Contribution of forcing agents

The estimated contribution of forcing agents to the 2019 global surface air temperature (GSAT) change relative to 1750 is shown in Figure 7.7. These estimates were produced using concentration-derived ERF timeseries presented in Chapter 2, Figure 2.10 and described in Supplementary Material 7.SM.1.3. The resulting GSAT changes over time are shown in Figure 7.8. The historical timeseries of ERFs for the WMGHGs can be derived by applying the ERF calculations of Section 7.3.2 to the observed timeseries of WMGHG concentrations in Chapter 2, Section 2.2.

These ERF timeseries are combined with a two-layer emulator (Cross-Chapter Box 7.1, Supplementary Material 7.SM.2) using a 2,237-member constrained Monte Carlo sample of both forcing uncertainty (by sampling ERF ranges) and climate response (by sampling ECS, TCR and ocean heat capacity ranges). The net model warming over the historical period is matched to the assessment of historical GSAT warming from 1850–1900 to 1995–2014 of 0.85 [0.67 to 0.98]°C (Chapter 2, Cross-Chapter Box 2.3) and ocean heat content change from 1971 to 2018 (Section 7.2.2.2), therefore the model gives the breakdown of the GSAT trend associated with different forcing mechanisms that are consistent with the overall GSAT change. The model assumes that there is no variation in feedback parameter across forcing mechanism (see Section 7.3.1) and variations in the effective feedback parameter over the historical record (Section 7.4.4). The distribution of ECS was informed by Section 7.5.5 and chosen to approximately maintain the best estimate and *likely/very likely* ranges assessed in that section (see also Supplementary Material 7.SM.2). The TCR has an ensemble median value of 1.81°C, in good agreement with Section 7.5.5. Two error bars are shown in Figure 7.7. The dashed error bar shows the contribution of ERF uncertainty (as assessed in the Section 7.3 subsections) employing the best estimate of climate response with an ECS of 3.0 °C. The solid bar is the total response uncertainty using the Section 7.5.5 assessment of ECS. The uncertainty in the historic temperature contributions for the different forcing agents are mostly due to uncertainties in ERF, yet for the WMGHG the uncertainty is dominated by the climate response as its ERF is relatively well known (Figure 7.7). From the assessment of emulator responses in Cross-Chapter Box 7.1, there is *high confidence* that calibrated emulators such as the one employed here can represent the historical GSAT change from 1850-1900 to 1995–2014 to within 5% for the best estimate and 10% for the *very likely* range (Supplementary Table 7.SM.4). This gives *high confidence* in the overall assessment of GSAT change for the response to ERFs over 1750–2019 derived from the emulator.

The total human forced GSAT change from 1750–2019 is calculated to be 1.29 [1.00 to 1.65] °C (*high confidence*). Although the total emulated GSAT change has *high confidence*, the confidence of the individual contributions matches those given for the ERF assessment in Section 7.3 subsections. The calculated GSAT change is comprised of a well-mixed greenhouse gas warming of 1.58 [1.17 to 2.17] °C (*high confidence*), a warming from ozone changes of 0.23 [0.11 to 0.39] °C (*high confidence*), a cooling of –0.50 [–0.22 to –0.96] °C from aerosol effects (*medium confidence*). The aerosol cooling has considerable regional time dependence (Chapter 6, Section 6.4.3) but has weakened slightly over the last 20 years in the global mean (Figure 7.8 and Chapter 2, Figure 2.10). There is also a –0.06 [–0.15 to +0.01] °C contribution from surface reflectance changes which dominated by land-use change (*medium confidence*). Changes in solar and volcanic activity are assessed to have together contributed a small change of –0.02 [–0.06 to +0.02] °C since

1750 (*medium confidence*).

The total (anthropogenic plus natural) emulated GSAT between 1850–1900 and 2010–2019 is 1.14 [0.89 to 1.45]°C, compared to the assessed GSAT of 1.06 [0.88 to 1.21] °C (Section 2.3.1; Cross Chapter Box 2.3). The emulated response is slightly warmer than the observations and has a larger uncertainty range. As the emulated response attempts to constrain to multiple lines of evidence (Supplementary Material 7.SM.2), only one of which is GSAT, they should not necessarily be expected to exactly agree. The larger uncertainty range in the emulated GSAT compared to the observations is reflective of the uncertainties in ECS, TCR and ERF (particularly the aerosol ERF) which drive the emulator response.

The emulator gives a range of GSAT response for the 1750 to the 1850–1900 period of 0.09 [0.04 to 0.14] °C from a anthropogenic ERFs. These results are used as a line of evidence for the assessment of this change in Chapter 1 (Cross-Chapter Box 1.2), which gives an overall assessment of 0.1 °C [*likely* range -0.1 to 0.3] °C.

[START FIGURE 7.7 HERE]

Figure 7.7: The contribution of forcing agents to 2019 temperature change relative to 1750 produced using the two-layer emulator (Supplementary Material 7.SM.2), constrained to assessed ranges for key climate metrics described in Cross-Chapter Box 7.1. The results are from a 2,237-member ensemble. Temperature contributions are expressed for carbon dioxide, other well-mixed greenhouse gases (WMGHGs), ozone, stratospheric water vapour, surface albedo, contrails and aviation-induced cirrus, aerosols, solar, volcanic, and total. Solid bars represent best estimates, and *very likely* (5–95%) ranges are given by error bars. Dashed error bars show the contribution of forcing uncertainty alone, using best estimates of ECS (3.0°C), TCR (1.8°C) and two-layer model parameters representing the CMIP6 multi-model mean. Solid error bars show the combined effects of forcing and climate response uncertainty using the distribution of ECS and TCR from Tables 7.13 and 7.14, and the distribution of calibrated model parameters from 44 CMIP6 models. Non-CO_2 WMGHGs are further broken down into contributions from methane (CH_4), nitrous oxide (N_2O) and halogenated compounds. Surface albedo is broken down into land use changes and light absorbing particles on snow and ice. Aerosols are broken down into contributions from aerosol-cloud interactions (ERFaci) and aerosol-radiation interactions (ERFari). Further details on data sources and processing are available in the chapter data table (Table 7.SM.14).

[END FIGURE 7.7 HERE]

Figure 7.8 presents the GSAT timeseries using ERF timeseries for individual forcing agents rather than their aggregation. It shows that for most of the historical period the long timescale total GSAT trend estimate from the emulator closely follows the CO_2 contribution. The GSAT estimate from non-CO_2 greenhouse gas forcing (from other WMGHGs and ozone) has been approximately cancelled out in the global average by a cooling GSAT trend from aerosol. However, since 1980 the aerosol cooling trend has stabilised and may have started to reverse so over the last few decades the long-term warming has been occurring at a faster rate than that expected by CO_2 alone (*high confidence,* see also Chapter 2, Section 2.2.6 and 2.2.8). Throughout the record, but especially prior to 1930, periods of volcanic cooling dominate decadal variability. These estimates of the forced response are compared with model simulations and attributable warming estimates in Chapter 3, Section 3.3.1.

[START FIGURE 7.8 HERE]

Figure 7.8: Attributed global surface air temperature change (GSAT) from 1750 to 2019 produced using the two-layer emulator (Supplementary Material 7.SM.2), forced with ERF derived in this chapter (displayed in Chapter 2, Figure 2.10) and climate response constrained to assessed ranges for key climate metrics described in Cross-Chapter Box 7.1. The results shown are the medians from a 2,237-member ensemble that encompasses uncertainty in forcing and climate response (year-2019 best

estimates and uncertainties are shown in Figure 7.7 for several components). Temperature contributions are expressed for carbon dioxide, methane, nitrous oxide, other well-mixed greenhouse gases (WMGHGs), ozone, aerosols, other anthropogenic forcings, total anthropogenic, solar, volcanic, and total. Shaded uncertainty bands show *very likely* ranges. Further details on data sources and processing are available in the chapter data table (Table 7.SM.14).

[END FIGURE 7.8 HERE]

[START CROSS-CHAPTER BOX 7.1 HERE]

Cross-Chapter Box 7.1: Physical emulation of Earth System Models for scenario classification and knowledge integration in AR6

Contributors: Zebedee Nicholls (Australia), Malte Meinshausen (Australia/Germany), Piers Forster (UK), Kyle Armour (USA), Terje Berntsen (Norway), William Collins (UK), Christopher Jones (UK), Jared Lewis (Australia/New Zealand), Jochem Marotzke (Germany), Sebastian Milinski (Germany), Joeri Rogelj (Austria/Belgium), Chris Smith (UK)

Climate model emulators are simple physically-based models that are used to approximate large-scale climate responses of complex Earth System Models (ESMs). Due to their low computational cost they can populate or span wide uncertainty ranges that ESMs cannot. They need to be calibrated to do this and, once calibrated, they can aid inter-ESM comparisons and act as ESM extrapolation tools to reflect and combine knowledge from ESMs and many other lines of evidence (Geoffroy et al., 2013a; Good et al., 2013; Smith et al., 2018a). In AR6, the term 'climate model emulator' (or simply emulator) is preferred over 'simple' or 'reduced-complexity climate model' to reinforce their use as specifically calibrated tools (Cross-Chapter Box 7.1, Figure 1). Nonetheless, simple physically-based climate models have a long history of use in previous IPCC reports (Chapter 1, Section 1.5.3.4). Climate model emulators can include carbon and other gas cycles and can combine uncertainties along the cause-effect chain from emissions to temperature response. AR5(Collins et al., 2013a) used the MAGICC6 emulator (Meinshausen et al., 2011a) in a probabilistic setup (Meinshausen et al., 2009) to explore the uncertainty in future projections. A simple impulse response emulator (Good et al., 2011) was also used to ensure a consistent set of ESM projections could be shown across a range of scenarios. AR5 WGI Chapter 8 (Myhre et al., 2013b) employed a two-layer emulator for quantifying Global Temperature Potentials (GTP). In AR5 WGIII (Clarke et al., 2014), MAGICC6 was also used for the classification of scenarios, and in AR5 Synthesis Report (IPCC, 2014) this information was used to estimate carbon budgets. In SR1.5, two emulators were used to provide temperature projections of scenarios: the MAGICC6 model, which was used for the scenario classification, and the FaIR1.3 model (Millar et al., 2017; Smith et al., 2018a).

SR1.5 found that the physically-based emulators produced different projected non-CO_2 forcing and identified the largely unexplained differences between the two emulators used as a key knowledge gap (Forster et al., 2018). This led to a renewed effort to test the skill of various emulators. The Reduced Complexity Model Intercomparison Project (RCMIP; Nicholls et al. (2020)) found that the latest generation of the emulators can reproduce key characteristics of the observed changes in global surface air temperature (GSAT) together with other key responses of ESMs (Cross-Chapter Box 7.1, Figure 1a). In particular, despite their reduced structural complexity, some emulators are able to replicate the non-linear aspects of ESM GSAT response over a range of scenarios. GSAT emulation has been more thoroughly explored in the literature than other types of emulation. Structural differences between emulation approaches lead to different outcomes and there are problems with emulating particular ESMs. In conclusion, there is *medium confidence* that emulators calibrated to single ESM runs can reproduce ESM projections of the forced GSAT response to other similar emissions scenarios to within natural variability (Meinshausen et al., 2011b; Geoffroy et al., 2013a; Dorheim et al., 2020; Nicholls et al., 2020; Tsutsui, 2020), although larger differences can remain for scenarios with very different forcing characteristics. For variables other than GSAT there has not yet been a comprehensive effort to evaluate the performance of emulators.

Application of emulators in AR6 WGI

Cross-Chapter Box 7.1 Table 1 shows the use of emulators within the WGI Report. The main use of emulation in the Report is to estimate GSAT change from Effective Radiative Forcing (ERF) or concentration changes, where various versions of a two layer energy budget emulator are used. The two-layer emulator is equivalent to a two-timescale impulse response model (Geoffroy et al., 2013b, Supplementary Material 7.SM.2). Both a single configuration version and probabilistic forms are used. The emulator is an extension of the energy budget equation (Equation 7.1) and allows for heat exchange between the upper- and deeper-ocean layers, mimicking the ocean heat uptake that reduces the rate of surface warming under radiative forcing (Gregory, 2000; Held et al., 2010; Winton et al., 2010; Armour, 2017; Mauritsen and Pincus, 2017; Rohrschneider et al., 2019). Although the same energy budget emulator approach is used, different calibrations are employed in various sections, to serve different purposes and keep lines of evidence as independent as possible. Chapter 9 additionally employs projections of ocean heat content from the Chapter 7 two-layer emulator to estimate the thermostatic component to future sea-level rise (see Chapter 9, Section 9.6.3 and Supplementary Material 7.SM.2).

Emission-driven emulators, as opposed to ERF- or concentration-driven emulators are also used in the Report. In Chapter 4 (Section 4.6) MAGICC7 is used to emulate GSAT beyond 2100 since its long-term response has been assessed to be fit-for-purpose to represent the behaviour of ESMs. In Chapter 5 (Section 5.5) MAGICC7 is used to explore the non-CO_2 GSAT contribution in emissions scenarios. In Chapter 6 and Chapter 7 (Section 7.6), two-layer model configurations were tuned to match the probabilistic GSAT responses of FaIRv1.6.2 and MAGICC7 emission-driven emulators. For Chapter 6 the two median values from FaIRv1.6.2 and MAGICC7 emulators are averaged and then matched to the best-estimate ECS of 3°C and TCR of 1.8 °C (Table 7.13 and Table 7.14) under the best-estimate ERF due to a doubling of CO_2 of 3.93 W m^{-2} (Table 7.4). For Section 7.6 a distribution of responses are used from the two emulators to estimate uncertainties in Global Temperature-change Potentials.

[START CROSS-CHAPTER BOX 7.1, TABLE 1 HERE]

Cross-Chapter Box 7.1, Table 1: Use of emulation within the WGI report

Chapter (Ch) and Section	Application and emulator type	Emulated Variables
Ch1, Cross Chapter-Box 1.2	Estimate anthropogenic temperature change pre-1850, based on radiative forcing time series from Chapter 7. Uses the Chapter 7 calibrated 2-layer emulator: a two-layer energy budget emulator, probabilistically calibrated to AR6 ECS, TCR, historical warming and ocean heat uptake ranges, driven by the Chapter 7 concentration based ERFs.	GSAT
Ch 3, Section 3.3 Ch 7, Section 7.3	Investigation of the historical temperature response to individual forcing mechanisms to compliment detection and attribution results. Uses the Chapter 7 calibrated two-layer emulator.	GSAT
Ch 4, Box 4.1	Understanding the spread in global surface air temperature increase of CMIP6 models and comparison to other assessments; assessment of contributions to projected temperature uncertainty. Uses a two-layer emulator calibrated to the Chapter 7 ECS and TCR	GSAT

	assessment driven by Chapter 7 best-estimate ERFs.	
Ch 4, Section 4.6	Emulators used to assess differences in radiative forcing and GSAT response between RCP and SSP scenarios. Uses the Chapter 7 ERF timeseries and the MAGICC7 probabilistic emission-driven emulator for GSAT calibrated to the WGI assessment.	ERF, GSAT
Ch 4, Section 4.7	Emulator used for long-term GSAT projections (post-2100) to complement the small number of ESMs with data beyond 2100. Uses the MAGICC7 probabilistic emission-driven emulator calibrated to the WGI assessment.	GSAT
Ch 5, Section 5.5	Estimated non-CO_2 warming contributions of mitigation scenarios at the time of their net zero CO_2 emissions for integration in the assessment of remaining carbon budgets. Uses the MAGICC7 probabilistic emission-driven emulator calibrated to the WGI assessment.	GSAT
Ch 6, Section 6.6 Ch 6, Section 6.7	Estimated contributions to future warming from SLCFs across SSP scenarios based on ERF timeseries. Uses a single two-layer emulator configuration derived from the medians of MAGICC7 and FaIRv1.6.2 AR6 WG1 GSAT probabilistic responses and the best-estimate of ECS and TCR.	GSAT
Ch.7, Section 7.5	Estimating a process based TCR from a process based ECS. Uses a two-layer emulator in probabilistic form calibrated to process based estimates from Chapter 7; a different calibration compared to the main Chapter 7 emulator.	TCR
Ch 7, Section 7.6	Deriving emission metrics. Uses two-layer emulator configurations derived from MAGICC7 and FaIRv1.6.2 AR6 WG1 probabilistic GSAT responses.	Global Temperature-change Potentials and their uncertainty
Ch 9, Section 9.6	Deriving global mean sea level projections. Uses the Chapter 7 calibrated two-layer emulator for GSAT and ocean heat content, where GSAT drives regional statistical emulators of ice sheets and glaciers.	Sea level and ice loss
Ch 11, Section 11.2 and Cross-Chapter	Regional patterns of response are compared to global mean trends. Assessed literature includes projections with	Various regional

Box 11.1	a regional pattern scaling and variability emulator.	information

[END CROSS-CHAPTER BOX 7.1, TABLE 1 HERE]

Emission-driven emulators for scenario classification in AR6 WGIII

As in AR5 and SR1.5, emission-driven emulators are used to communicate outcomes of the physical climate science assessment and uncertainties to quantify the temperature outcome associated with different emission scenarios. In particular, the computational efficiency of these emulators allows the analysis of a large number of multi-gas emissions scenarios in terms of multiple characteristics, e.g., year of peak temperature or the 2030 emission levels in line with keeping global warming to below 1.5°C or 2.0 ºC.

Four emission-driven emulators have been considered as tools for WGIII to explore the range of GSAT response to multiple scenarios beyond those assessed in WGI. The four emulators are CICERO-SCM (Skeie et al., 2017, 2021), FaIRv1.6.2 (Millar et al., 2017; Smith et al., 2018a), MAGICC7 (Meinshausen et al., 2009) and OSCARv3.1.1 (Gasser et al., 2017a, 2020). Each emulator's probabilistic distribution has been calibrated to capture the relationship between emissions and GSAT change. The calibration is informed by the WGI assessed ranges of ECS, TCR, historical GSAT change, ERF, carbon cycle metrics and future warming projections under the (concentration-driven) SSP scenarios. The emulators are then provided as a tool for WGIII to perform a GSAT-based classification of mitigation scenarios consistent with the physical understanding assessed in WGI.. The calibration step reduced the emulator differences identified in SR1.5. Note that evaluation of both central and range estimates of each emulator’s probabilistic projections is important to assess the fitness-for-purpose for the classification of scenarios in WGIII based on information beyond the central estimate of GSAT warming.

[START CROSS-CHAPTER BOX 7.1, FIGURE 1 HERE]

Cross-Chapter Box 7.1, Figure 1: A comparison between the global-mean surface air temperature response of various calibrated simple climate models, assessed ranges and Earth System Models. The top panels compare the assessed historical GSAT time series (Chapter 2, Cross Chapter Box 2.3) with four multi-gas emulators calibrated to replicate numerous assessed ranges (Cross-Chapter Box 7.1, Table 2 below) (panel a) and also compares idealized CO_2-only concentration scenario response for one ESM (IPSL CM6A-LR) and multiple emulators which participated in RCMIP Phase 1 (Nicholls et al., 2020) calibrated to that single ESM (panel b). The bottom panels compare this Report’s assessed ranges for GSAT warming (Chapter 4, Box 4.1) under the multi-gas scenario SSP1-2.6 with the same calibrated emulators as in panel a (panel c and d). For context, a range of CMIP6 ESM results are also shown (thin lines in bottom-left panel c and open circles in bottom-right panel d). Panel b) adapted from Nicholls et al. (2020). Further details on data sources and processing are available in the chapter data table (Table 7.SM.14).

[END CROSS-CHAPTER BOX 7.1, FIGURE 1 HERE]

MAGICC7 and FaIRv1.6.2 emission based emulators are able to represent the WGI assessment to within small differences (defined here as within typical rounding precisions of ±5% for central estimates and ±10% for ranges) across more than 80% of metric ranges (Cross-Chapter Box 7.1, Table 2 below). Both calibrated emulators are consistent with assessed ranges of ECS, historical GSAT, historical ocean heat uptake, total greenhouse gas ERF, methane ERF and the majority of the assessed SSP warming ranges. FaIRv1.6.2 also matches the assessed central value of TCRE and airborne fraction. Whereas, MAGICC7 matches the assessed TCR ranges as well as providing a closer fit to the SSP warming ranges for the lower emission scenarios. In the evaluation framework considered here, CICERO-SCM represents historical warming to within 2% of the assessed ranges and also represents future temperatures ranges across the majority of the assessment although it lacks the representation of the carbon cycle. In this framework, OSCARv3.1.1 is less able to represent the assessed projected GSAT ranges although it matches the range of airborne fraction estimates closely and the assessed historical GSAT *likely* range to within 0.5%. Despite these identified limitations, both CICERO-SCM and OSCARv3.1.1 provide additional information for evaluating the sensitivity of scenario classification to model choice.

How emulators match the assessed ranges used for the evaluation framework is summarised here and in Table 2. The first is too low projections in 2081–2100 under SSP1-1.9 (8% or 15% too low for the central estimate and 15% or 25% too low for the lower end in the case of MAGICC7 or FaIRv1.6.2, respectively). The second is the representation of the aerosol effective radiative forcing (both MAGICC7 and FaIRv1.6.2 are greater than 8% less negative than the central assessed range and greater than 10% less negative for the lower assessed range), as energy balance models struggle to reproduce an aerosol ERF with a magnitude as strong as the assessed best estimate and still match historical warming estimates. Both emulators have medium to large differences compared to the TCRE and airborne fraction ranges (see note of Table 2). Finally, there is also a slight overestimate of the low-end of the assessed historical GSAT range.

Overall, there is *high confidence* that emulated historical and future ranges of GSAT change can be calibrated to be internally-consistent with the assessment of key physical-climate indicators in this Report: greenhouse gas ERFs, ECS and TCR. When calibrated to match the assessed ranges of GSAT and multiple physical climate indicators, physically-based emulators can reproduce the best estimate of GSAT change over 1850–1900 to 1995–2014 to within 5% and *very likely* range of this GSAT change to within 10%. MAGICC7 and FaIRv1.6.2 match at least two-thirds of the Chapter 4 assessed projected GSAT changes to within these levels of precision.

[START CROSS-CHAPTER BOX 7.1, TABLE 2 HERE]

Cross-Chapter Box 7.1, Table 2: Percentage differences between the emulator value and the WGI assessed best estimate and range for key metrics. Values are given for four emulators in their respective AR6-calibrated probabilistic setups. Absolute values of these indicators are shown in Supplementary Table 7.SM.4.

Emulator		**CICERO-SCM**			**FaIRv1.6.2**			**MAGICC7**			**OSCARv3.1.1**		
Assessed range		**Lower**	**Central**	**Upper**	**Lower**	**Central**	**Upper**	**Lower**	**Central**	**Upper**	**Lower**	**Central**	**Upper**
Key metrics													
ECS (°C)		26%	2%	–18%	3%	–2%	1%	–3%	–1%	–3%	–8%	–15%	–22%
TCRE (°C per 1000 Gt C)**					29%	–7%	–21%	37%	5%	–5%	50%	–8%	–20%
TCR (°C)		15%	–5%	–3%	14%	0%	3%	6%	4%	9%	26%	1%	–14%
Historical warming and Effective Radiative Forcing													
GSAT warming (°C)	1995–2014 rel. 1850–1900	2%	0%	0%	7%	3%	4%	7%	1%	–1%	–0%	–8%	–0%
Ocean heat content change (ZJ)*	1971–2018	–24%	–27%	–29%	5%	–4%	–9%	–1%	–3%	–6%	–47%	–39%	10%
Total Aerosol ERF (W m^{-2})	2005–2014 rel. 1750	36%	37%	10%	16%	12%	0%	10%	8%	8%	38%	15%	–31%
GHG ERF (W m^{-2})	2019 rel. 1750	4%	–5%	–13%	1%	2%	1%	2%	1%	–0%	1%	3%	–3%
Methane ERF (W m^{-2})	2019 rel.	31%	4%	–13%	3%	3%	3%	0%	–0%	3%	8%	–1%	–5%

	1750												
Carbon Cycle metrics													
Airborne Fraction *1pctCO2* (dimensionless)*	2×CO_2				8%	–3%	–11%	12%	6%	–1%	1%	–0%	8%
Airborne Fraction *1pctCO2* (dimensionless)*	4×CO_2				12%	1%	–9%	15%	4%	–6%	5%	–1%	–1%
Future warming (GSAT) relative to 1995–2014													
SSP1-1.9 (ºC)	2021–2040	10%	–4%	10%	3%	1%	11%	2%	–0%	4%	12%	–9%	–25%
	2041–2060	8%	–9%	7%	–11%	–8%	6%	–1%	–1%	7%	12%	–8%	–31%
	2081–2100	–12%	–25%	–2%	–25%	–15%	4%	–15%	–8%	3%	7%	–10%	–31%
SSP1-2.6 (ºC)	2021–2040	7%	–5%	5%	2%	1%	8%	–1%	–2%	–0%	9%	–9%	–28%
	2041–2060	8%	–6%	2%	–2%	–2%	5%	0%	1%	2%	15%	–6%	–28%
	2081–2100	–2%	–14%	–5%	–8%	–7%	1%	–6%	–1%	1%	17%	–9%	–29%
SSP2-4.5 (ºC)	2021–2040	8%	–5%	5%	7%	–1%	2%	3%	–3%	–2%	–5%	–14%	–30%
	2041–2060	4%	–4%	3%	1%	–1%	2%	1%	1%	2%	8%	–8%	–28%
	2081–2100	–1%	–10%	–3%	–2%	–3%	1%	–2%	1%	3%	8%	–4%	–25%
SSP3-7.0 (ºC)	2021–2040	11%	–4%	1%	14%	1%	–1%	10%	1%	–0%	–5%	–15%	–29%
	2041–2060	4%	–5%	–0%	6%	0%	–1%	7%	4%	1%	7%	–8%	–26%
	2081–2100	–0%	–8%	–3%	3%	–1%	–1%	6%	3%	6%	5%	–6%	–25%
SSP5-8.5 (ºC)	2021–2040	5%	–7%	2%	9%	2%	4%	7%	1%	2%	1%	–14%	–30%
	2041–2060	2%	–8%	–1%	4%	0%	4%	3%	2%	4%	10%	–6%	–24%
	2081–2100	4%	–7%	–3%	6%	–0%	1%	8%	4%	7%	9%	–4%	–25%

Notes. Metrics calibrated against are equilibrium climate sensitivity, ECS (Section 7.5); transient climate response to cumulative emissions of carbon dioxide, TCRE (Chapter 5, Section 5.5); transient climate response, TCR (Section 7.5), historical GSAT change (Chapter 2, Section 2.3), ocean heat uptake (Section 7.2 and Chapter 2, Section 2.3) and effective radiative forcing, ERF (Section 7.3), carbon cycle metrics, namely airborne fractions of idealized CO_2 scenarios (taking the *likely* range as twice the standard deviation across the models analysed in Arora et al. (2020), see also Chapter 5, Table 5.7, cross-AR6 lines of evidence row) and GSAT projections under the concentration-driven SSP scenarios for the near-term (2021–2040), mid-term (2041–2060) and long-term (2081–2100) relative to 1995–2014 (Chapter 4, Table 4.2). See Supplementary Table 7.SM.4 for a version of this table with the absolute values rather than percentage differences. The columns labelled “upper” and “lower” indicate 5% to 95% ranges, except for the variables demarcated with an asterisk or double asterisk (* or **), where they denote *likely* ranges from 17% to 83%. Note that the TCRE assessed range (**) is wider than the combination of the TCR and airborne fraction to account for uncertainties related to model limitations (Chapter 5, Table 5.7) hence it is expected that the emulators are too narrow on this. particular metric and/or too wide on TCR and airborne fraction. For illustrative purposes, the cells are coloured as follows: white cells indicate small differences (up to ±5% for the central value and +10% for the ranges), light blue and light teal cells indicate medium differences (up to +10% and -10% for light blue and light teal for central values, respectively; up to ±20% for the ranges) and darker cells indicate larger positive (blue) or negative (teal) differences (note that values are rounded after the colours are applied).

[END CROSS-CHAPTER BOX 7.1, TABLE 2 HERE]

[END CROSS-CHAPTER BOX 7.1 HERE]

7.4 Climate feedbacks

The magnitude of global surface temperature change primarily depends on the strength of the radiative forcings and feedbacks, the latter defined as the changes of the net energy budget at the top of atmosphere (TOA) in response to a change in the GSAT (Box 7.1, Equation 7.1). Feedbacks in the Earth system are numerous, and it can be helpful to categorise them into three groups: (1) physical feedbacks; (2) biogeophysical and biogeochemical feedbacks; and (3) long-term feedbacks associated with ice sheets. The physical feedbacks (for example, associated with changes in lapse-rate, water vapour, surface albedo, or clouds; Sections 7.4.2.1-7.4.2.4) and biogeophysical/biogeochemical feedbacks (for example, associated with changes in methane, aerosols, ozone, or vegetation; Section 7.4.2.5) act both on time scales that are used to estimate the equilibrium climate sensitivity (ECS) in models (typically 150 years, see Box 7.1) and on longer time scales required to reach equilibrium. Long-term feedbacks associated with ice sheets (Section 7.4.2.6) are relevant primarily after several centuries or more. The feedbacks associated with biogeophysical/biogeochemical processes and ice sheets, often collectively referred to as Earth system feedbacks, had not been included in conventional estimates of the climate feedback (e.g., Hansen et al., 1984), but the former can now be quantified and included in the assessment of the total (net) climate feedback. Feedback analysis represents a formal framework for the quantification of the coupled interactions occurring within a complex Earth system in which everything influences everything else (e.g., Roe, 2009). As used here and presented in Section 7.4.1, its primary objective is to identify and understand the key processes that determine the magnitude of the surface temperature response to an external forcing. For each feedback, the basic underlying mechanisms and their assessment are presented in Section 7.4.2.

Up until AR5, process understanding and quantification of feedback mechanisms were based primarily on global climate models. Since AR5, the scientific community has undertaken a wealth of different alternative approaches, including observational and fine-scale modelling approaches. This has in some cases led to more constrained feedbacks and, on the other hand, uncovered shortcomings in global climate models, which are starting to be corrected. Consequently, AR6 achieves a more robust assessment of feedbacks in the climate system that is less reliant on global climate models than in earlier assessment reports.

It has long been recognized that the magnitude of climate feedbacks can change as the climate state evolves over time (Manabe and Bryan, 1985; Murphy, 1995), but the implications for projected future warming have been investigated only recently. Since AR5, progress has been made in understanding the key mechanisms behind this time- and state-dependence. Specifically, the state-dependence is assessed by comparing climate feedbacks between warmer and colder climate states inferred from paleoclimate proxies and model simulations (Section 7.4.3). The time-dependence of the feedbacks is evident between the historical period and future projections and is assessed to arise from the evolution of the surface warming pattern related to changes in zonal and meridional temperature gradients (Section 7.4.4).

7.4.1 Methodology of the feedback assessment

The global surface temperature changes of the climate system are generally analysed with the classical forcing-feedback framework as described in Box 7.1 (Equation 7.1). In this equation α is the net feedback parameter (W m^{-2} °C^{-1}). As surface temperature changes in response to the TOA energy imbalance, many other climate variables also change, thus affecting the radiative flux at the TOA. The aggregate feedback parameter can then be decomposed into an approximate sum of terms $\alpha = \sum_x \alpha_x$, where x is a vector representing variables that have a direct effect on the net TOA radiative flux N and $\alpha_x = \frac{\partial N}{\partial x}\frac{dx}{dT}$. Following the conventional definition, the physical climate feedbacks are here decomposed into terms associated with a vertically uniform temperature change (Planck response, P), changes in the water vapour plus temperature lapse rate (WV+LR), surface albedo (A) and clouds (C). The water vapour plus temperature lapse rate feedback is further decomposed using two different approaches, one based on changes in specific humidity, the other on changes in relative humidity. Biogeochemical feedbacks arise due to changes in aerosols and atmospheric chemical composition in response to changes in surface temperature, and Gregory et al. (2009) and Raes et al. (2010) show that they can be analysed using the same framework as for the physical climate feedbacks (see Chapter 5, Section 5.4 and Chapter 6, Section 6.4.5 Similarly, feedbacks associated with biogeophysical and ice sheet changes can also be incorporated.

In global climate models, the feedback parameters α_x in global warming conditions are often estimated as the mean differences in the radiative fluxes between atmosphere-only simulations in which the change in SST is prescribed (Cess et al., 1990), or as the regression slope of change in radiation flux against change in global-mean surface air temperature using atmosphere-ocean coupled simulations with abrupt CO_2 changes (*abrupt4xCO2*) for 150 years (Gregory et al., 2004; Andrews et al., 2012; Caldwell et al., 2016; see Box 7.1). Neither method is perfect, but both are useful and yield consistent results (Ringer et al., 2014). In the regression method, the radiative effects of land warming are excluded from the effective radiative forcing due to doubling of CO_2 (Section 7.3.2), which may overestimate feedback values by about 10%. At the same time, the feedback calculated using the regression over years 1–150 ignores its state-dependence on multi-centennial time scales (Section 7.4.3), probably giving an underestimate of α by about 10% (Rugenstein et al., 2019a). These effects are both small and cancel each other in the ensemble mean, justifying the use of regression over 150 years as an approximation to feedbacks in ESMs.

The change of the TOA radiative flux N as a function of the change of a climate variable x (such as water vapour) is commonly computed using the 'radiative kernel' method (Soden et al., 2008). In this method, the kernel $\partial N/\partial x$ is evaluated by perturbing x within a radiation code. Then multiplying the kernel by $\mathrm{d}x/\mathrm{d}T$ inferred from observations, meteorological analysis or GCMs produces a value of α_x.

Feedback parameters from lines of evidence other than global models are estimated in various ways. For example, observational data combined with GCM simulations could produce an emergent constraint on a particular feedback (Hall and Qu, 2006; Klein and Hall, 2015), or the observed interannual fluctuations in the global-mean TOA radiation and the surface air temperature, to which the linear regression analysis is applied, could generate a direct estimate of the climate feedback assuming that the feedback associated with internal climate variability at short time scales can be a surrogate of the feedback to CO_2-induced warming (Dessler, 2013; Loeb et al., 2016). The assumption is not trivial, but can be justified given that the climate feedbacks are fast enough to occur at the interannual time scale. Indeed, a broad agreement has been obtained in estimates of individual physical climate feedbacks based on interannual variability and longer climate change timescales in GCMs (Zhou et al., 2015; Colman and Hanson, 2017). This means that the climate feedbacks estimated from the observed interannual fluctuations are representative of the longer-term feedbacks (decades to centuries). Care must be taken for these observational estimates because they can be sensitive to details of the calculation such as data sets and periods used (Dessler, 2013; Proistosescu et al., 2018). In particular, there would be a dependence of physical feedbacks on the surface warming pattern at the interannual time scale due, for example, to El Niño-Southern Oscillation. However, this effect both amplifies and suppresses the feedback when data include the positive and negative phases of the interannual fluctuation, and therefore the net bias will be small.

In summary, the classical forcing-feedback framework has been extended to include biogeophysical and non-CO_2-biogeochemical feedbacks in addition to the physical feedbacks. It has also been used to analyse seasonal and interannual to decadal climate variations in observations and ESMs, in addition to long-term climate changes as seen in *abrupt4xCO2* experiments. These developments allow an assessment of the feedbacks based on a larger variety of lines of evidence compared to AR5.

7.4.2 Assessing climate feedbacks

This section provides an overall assessment of individual feedback parameters, α_x, by combining different lines of evidence from observations, theory, process models and ESMs. To achieve this, we review the understanding of the key processes governing the feedbacks, why the feedback estimates differ among models, studies or approaches, and the extent to which these approaches yield consistent results. The individual terms assessed are the Planck response (Section 7.4.2.1) and feedbacks associated with changes in water vapour and lapse rate (Section 7.4.2.2), surface albedo (Section 7.4.2.3), clouds (Section 7.4.2.4), biogeophysical and non-CO_2 biogeochemical processes (Section 7.4.2.5), and ice sheets (Section 7.4.2.6). A synthesis is provided in Section 7.4.2.7. Climate feedbacks in CMIP6 models are then evaluated in Section 7.4.2.8, with an explanation of how they have been incorporated into the assessment.

7.4.2.1 Planck response

The Planck response represents the additional thermal or longwave (LW) emission to space arising from vertically uniform warming of the surface and the atmosphere. The Planck response α_P, often called the Planck feedback, plays a fundamental stabilizing role in Earth's climate and has a value that is strongly negative: a warmer planet radiates more energy to space. A crude estimate of α_P can be made using the normalized greenhouse effect $\tilde{g}$, defined as the ratio between the greenhouse effect G and the upwelling LW flux at the surface (Raval and Ramanathan, 1989). Current estimates (Section 7.2, Figure 7.2) give G = 159 W m^{-2} and $\tilde{g} \approx 0.4$. Assuming $\tilde{g}$ is constant, one obtains for a surface temperature T_s = 288K, $\alpha_P = (\tilde{g} - 1)\ 4\ \sigma\ T_s^3 \approx -3.3$ W m^{-2} °C^{-1}, where σ is the Stefan-Boltzmann constant. This parameter α_P is estimated more accurately using kernels obtained from meteorological reanalysis or climate simulations (Soden and Held, 2006; Dessler, 2013; Vial et al., 2013; Caldwell et al., 2016; Colman and Hanson, 2017; Zelinka et al., 2020). Discrepancies among estimates primarily arise because differences in cloud distributions make the radiative kernels differ (Kramer et al., 2019). Using six different kernels, Zelinka et al. (2020) obtained a spread of ±0.1 W m^{-2} °C^{-1} (one standard deviation). Discrepancies among estimates secondarily arise from differences in the pattern of equilibrium surface temperature changes among ESMs. For the CMIP5 and CMIP6 models this introduces a spread of ±0.04 W m^{-2} °C^{-1} (one standard deviation). The multi-kernel and multi-model mean of α_P is equal to –3.20 W m^{-2} °C^{-1} for the CMIP5 and –3.22 W m^{-2} °C^{-1} for the CMIP6 models (Supplementary Table 7.SM.5). Overall, there is *high confidence* in the estimate of the Planck response, which is assessed to be α_P = –3.22 W m^{-2} °C^{-1} with a *very likely* range of –3.4 to –3.0 W m^{-2} °C^{-1} and a *likely range* of –3.3 to –3.1 W m^{-2} °C^{-1}.

The Planck temperature response ΔT_P is the equilibrium temperature change in response to a forcing ΔF when the net feedback parameter is equal to the Planck response parameter: $\Delta T_P = -\Delta F / \alpha_P$.

7.4.2.2 Water vapour and temperature lapse rate feedbacks

Two decompositions are generally used to analyse the feedbacks associated with a change in the water vapour and temperature lapse rate in the troposphere. As in any system, many feedback decompositions are possible, each of them highlighting a particular property or aspect of the system (Ingram, 2010; Held and Shell, 2012; Dufresne and Saint-Lu, 2016). The first decomposition considers separately the changes (and therefore feedbacks) in the lapse rate (LR) and specific humidity (WV). The second decomposition considers changes in the lapse rate assuming constant relative humidity (LR*) separately from changes in relative humidity (RH).

The specific humidity (WV) feedback, also known as the water vapour feedback, quantifies the change in radiative flux at the TOA due to changes in atmospheric water vapour concentration associated with a change in global mean air surface temperature. According to theory, observations and models, the water vapour increase approximately follows the Clausius-Clapeyron relationship at the global scale with regional differences dominated by dynamical processes (Chapter 8, Section 8.2.1; Sherwood et al., 2010b; Chung et al., 2014; Romps, 2014; Liu et al., 2018; Schröder et al., 2019). Greater atmospheric water vapour content, particularly in the upper troposphere, results in enhanced absorption of LW and SW radiation and reduced outgoing radiation. This is a positive feedback. Atmospheric moistening has been detected in satellite records

(Chapter 2, Section 2.3.1.3.3), is simulated by climate models (Chapter 3, Section 3.3.2.1), and the estimates agree within model and observational uncertainty (Soden et al., 2005; Dessler, 2013; Gordon et al., 2013; Chung et al., 2014). The estimate of this feedback inferred from satellite observations is $\alpha_{WV} = 1.85 \pm 0.32$ W m^{-2} °C^{-1} (Liu et al., 2018). This is consistent with the value $\alpha_{WV} = 1.77 \pm 0.20$ W m^{-2} °C^{-1} (one standard deviation) obtained with CMIP5 and CMIP6 models (Zelinka et al., 2020).

The lapse rate (LR) feedback quantifies the change in radiative flux at the TOA due to a non-uniform change in the vertical temperature profile. In the tropics, the vertical temperature profile is mainly driven by moist convection and is close to a moist adiabat. The warming is larger in the upper troposphere than in the lower troposphere (Manabe and Wetherald, 1975; Santer et al., 2005; Bony et al., 2006), leading to a larger radiative emission to space and therefore a negative feedback. This larger warming in the upper troposphere than at the surface has been observed over the last twenty years thanks to the availability of sufficiently accurate observations (Chapter 2, Section 2.3.1.2.2). In the extra-tropics, the vertical temperature profile is mainly driven by a balance between radiation, meridional heat transport and ocean heat uptake (Rose et al., 2014). Strong wintertime temperature inversions lead to warming that is larger in the lower troposphere (Payne et al., 2015; Feldl et al., 2017a) and a positive lapse rate feedback in polar regions (Manabe and Wetherald, 1975; Bintanja et al., 2012; Pithan and Mauritsen, 2014; Section 7.4.4.1). However, the tropical contribution dominates, leading to a negative global mean lapse rate feedback (Soden and Held, 2006; Dessler, 2013; Vial et al., 2013; Caldwell et al., 2016). The LR feedback has been estimated at interannual time scales using meteorological reanalysis and satellite measurements of TOA fluxes (Dessler, 2013). These estimates from climate variability are consistent between observations and ESMs (Dessler, 2013; Colman and Hanson, 2017). The mean and standard deviation of this feedback under global warming based on the cited studies are $\alpha_{LR} = -0.50 \pm 0.20$ W m^{-2} °C^{-1} (Dessler, 2013; Caldwell et al., 2016; Colman and Hanson, 2017; Zelinka et al., 2020).

The second decomposition was proposed by Held and Shell (2012) to separate the response that would occur under the assumption that relative humidity remains constant from that due to the change in relative humidity. The feedback is decomposed into three: (1) change in water vapour due to an identical temperature increase at the surface and throughout the troposphere assuming constant relative humidity, which will be called the Clausius-Clapeyron (CC) feedback here; (2) change in lapse rate assuming constant relative humidity (LR*); (3) change in relative humidity (RH). Since AR5 it has been clarified that by construction, the sum of the temperature lapse rate and specific humidity (LR+WV) feedbacks is equal to the sum of the Clausius-Clapeyron, lapse rate assuming constant relative humidity, and changes in relative humidity (CC+LR*+RH) feedbacks. Therefore, each of these two sums may simply be referred to as the "water vapour plus lapse rate" feedback.

The CC feedback has a large positive value due to well understood thermodynamic and radiative processes: $\alpha_{CC} = 1.36 \pm 0.04$ W m^{-2} °C^{-1} (one standard deviation) (Held and Shell, 2012; Zelinka et al., 2020). The lapse rate feedback assuming a constant relative humidity LR* in CMIP6 models has small absolute values ($\alpha_{LR*} = -0.10 \pm 0.07$ W m^{-2} °C^{-1} (one standard deviation)), as expected from theoretical arguments (Ingram, 2010, 2013). It includes the pattern effect of surface warming that modulates the lapse rate and associated specific humidity changes (Po-Chedley et al., 2018a). The relative humidity feedback is close to zero ($\alpha_{RH} = 0.00 \pm 0.06$ W m^{-2} °C^{-1} (one standard deviation)) and the spread among models is confined to the tropics (Sherwood et al., 2010a; Vial et al., 2013; Takahashi et al., 2016; Po-Chedley et al., 2018a). The change in upper tropospheric RH is closely related to model representation of current climate (Sherwood et al., 2010a; Po-Chedley et al., 2019), and a reduction in model RH biases is expected to reduce the uncertainty of the RH feedback. At inter-annual time scales, it has been shown that the change in RH in the tropics is related to the change of the spatial organisation of deep convection (Holloway et al., 2017; Bony et al., 2020).

Both decompositions allow estimates of the sum of the lapse rate and specific humidity feedbacks α_{LR+WV}. The multi-kernel and multi-model mean of α_{LR+WV} is equal to 1.24 and 1.26 W m^{-2} °C^{-1} respectively for CMIP5 and CMIP6 models, with a standard deviation of 0.10 W m^{-2} °C^{-1} (Zelinka et al., 2020). These values are larger than the recently assessed value of 1.15 W m^{-2} °C^{-1} by Sherwood et al. (2020) as a larger set of kernels, including those obtained from meteorological reanalysis, are used here.

Since AR5, the effect of the water vapour increase in the stratosphere with global warming has been investigated by different studies. This increase produces a positive feedback between 0.1 and 0.3 W m^{-2} °C^{-1} if the stratospheric radiative response is computed assuming temperatures that are adjusted with fixed dynamical heating (Dessler et al., 2013; Banerjee et al., 2019). However, various feedbacks reduce this temperature adjustment and the overall physical (water vapour, temperature and dynamical) stratospheric feedback becomes much smaller (0.0 to 0.1 W m^{-2} °C^{-1}) (Huang et al., 2016, 2020; Li and Newman, 2020), with uncertainty arising from limitations of current ESMs in simulating stratospheric processes. The total stratospheric feedback is assessed at 0.05 ± 0.1 W m^{-2} °C^{-1} (one standard deviation).

The combined water vapour plus lapse rate feedback is positive. The main physical processes that drive this feedback are well understood and supported by multiple lines of evidence including models, theory and observations. The combined water vapour plus lapse rate feedback parameter is assessed to be α_{LR+WV} = 1.30 W m^{-2} °C^{-1}, with a *very likely* range of 1.1 to 1.5 W m^{-2} °C^{-1} and a *likely* range of 1.2 to 1.4 W m^{-2} °C^{-1} with *high confidence.*

7.4.2.3 Surface albedo feedback

Surface albedo is determined primarily by reflectance at Earth's surface, but also by the spectral and angular distribution of incident solar radiation. Changes in surface albedo result in changes in planetary albedo that are roughly reduced by two-thirds, owing to atmospheric absorption and scattering, with variability and uncertainty arising primarily from clouds (Bender, 2011; Donohoe and Battisti, 2011; Block and Mauritsen, 2013). Temperature change induces surface albedo change through several direct and indirect means. In the present climate and at multidecadal time scales, the largest contributions by far are changes in the extent of sea ice and seasonal snow cover, as these media are highly reflective and are located in regions that are close to the melting temperature (Chapter 2, Sections 2.3.2.1 and 2.3.2.2). Reduced snow cover on sea ice may contribute as much to albedo feedback as reduced extent of sea ice (Zhang et al., 2019). Changes in the snow metamorphic rate, which generally reduces snow albedo with warmer temperature, and warming-induced consolidation of light absorbing impurities near the surface, also contribute secondarily to the albedo feedback (Flanner and Zender, 2006; Qu and Hall, 2007; Doherty et al., 2013; Tuzet et al., 2017). Other contributors to albedo change include vegetation state (assessed separately in Section 7.4.2.5), soil wetness, and ocean roughness.

Several studies have attempted to derive surface albedo feedback from observations of multidecadal changes in climate, but only over limited spatial and inconsistent temporal domains, inhibiting a purely observational synthesis of global α_A. Flanner et al. (2011) applied satellite observations to determine that the northern hemisphere (NH) cryosphere contribution to global α_A over 1979–2008 was 0.48 [*likely* range 0.29 to 0.78] W m^{-2} °C^{-1}, with roughly equal contributions from changes in land snow cover and sea ice. Since AR5, and over similar periods of observation, Crook and Forster (2014) found an estimate of 0.8 ± 0.3 W m^{-2} °C^{-1} (one standard deviation) for the total NH extratropical surface albedo feedback, when averaged over global surface area. For the Arctic sea ice alone, Pistone et al. (2014) and Cao et al. (2015) estimated the contribution to global α_A to be 0.31 ± 0.04 W m^{-2} °C^{-1} (one standard deviation) and 0.31 ± 0.08 W m^{-2} °C^{-1} (one standard deviation), respectively, whereas Donohoe et al. (2020) estimated it to be only 0.16 ± 0.04 W m^{-2} °C^{-1} (one standard deviation). Much of this discrepancy can be traced to different techniques and data used for assessing the attenuation of surface albedo change by Arctic clouds. For the NH land snow, Chen et al. (2016) estimated that observed changes during 1982–2013 contributed (after converting from NH temperature change to global mean temperature change) by 0.1 W m^{-2} °C^{-1} to global α_A, smaller than the estimate of 0.24 W m^{-2} °C^{-1} from Flanner et al. (2011). The contribution of the southern hemisphere (SH) to global α_A is expected to be small because seasonal snow cover extent in the SH is limited, and trends in SH sea ice extent are relatively flat over much of the satellite record (Chapter 2, Section 2.3.2).

CMIP5 and CMIP6 models show moderate spread in global α_A determined from century timescale changes (Qu and Hall, 2014; Schneider et al., 2018; Thackeray and Hall, 2019; Zelinka et al., 2020), owing to variations in modelled sea-ice loss and snow cover response in boreal forest regions. The multi-model mean global-scale α_A (from all contributions) over the 21st century in CMIP5 models under the RCP8.5 scenario was derived by Schneider et al. (2018) to be 0.40 ± 0.10 W m^{-2} °C^{-1} (one standard deviation). Moreover, they found that modelled α_A does not decline over the 21st century, despite large losses of snow and sea ice, though a weakened feedback is apparent after 2100. Using the idealized *abrupt4xCO2* as for the other feedbacks, the estimate of the global-scale albedo feedback in the CMIP5 models is 0.35± 0.08 W m^{-2}°C^{-1} (one standard deviation) (Vial et al., 2013; Caldwell et al., 2016). The CMIP6 multi-model mean varies from 0.3 to 0.5 W m^{-2}°C^{-1} depending on the kernel used (Zelinka et al., 2020). Donohoe et al. (2020) derived a multi-model mean α_A and its inter-model spread of 0.37 ± 0.19 W m^{-2} °C^{-1} from the CMIP5 *abrupt4xCO2* ensemble, employing model-specific estimates of atmospheric attenuation and thereby avoiding bias associated with use of a single radiative kernel.

The surface albedo feedback estimates using centennial changes have been shown to be highly correlated to those using seasonal regional changes for NH land snow (Qu and Hall, 2014) and Arctic sea ice (Thackeray and Hall, 2019). For the NH land snow, the physics underpinning this relationship being credible, this opens the possibility to use it as an emergent constraint (Qu and Hall, 2014). Considering only the 8 models whose seasonal cycle of albedo feedback falls within the observational range does not change the multi-model mean contribution to global α_A (0.08 W m^{-2}°C^{-1}) but decreases the inter-model spread by a factor of two (from ± 0.03 to ± 0.015 W m^{-2}°C^{-1}) (Qu and Hall, 2014). For the Arctic sea-ice, Thackeray and Hall (2019) show that the seasonal cycle also provides an emergent constraint, at least until mid-century when the relationship degrades. They find that the CMIP5 multi-model mean of the Arctic sea-ice contribution to α_A is 0.13 W m^{-2} °C^{-1} and that the inter-model spread is reduced by a factor of two (from ± 0.04 to ± 0.02 W m^{-2} °C^{-1}) when the emergent constraint is used. This model estimate is smaller than observational estimates (Pistone et al., 2014; Cao et al., 2015) except those of Donohoe et al. (2020). This can be traced to CMIP5 models generally underestimating the rate of Arctic sea ice loss during recent decades (Stroeve et al., 2012; Flato et al., 2013; Chapter 9, Section 9.3.1), though this may also be an expression of internal variability, since the observed behaviour is captured within large ensemble simulations (Notz, 2015). CMIP6 models better capture the observed Arctic sea ice decline (Chapter 3, Section 3.4.1). In the SH the opposite situation is observed. Observations show relatively flat trends in SH sea ice over the satellite era (Chapter 2, Section 2.3.2.1) whereas CMIP5 models simulate a small decrease (Chapter 3, Section 3.4.1). SH α_A is presumably larger in models than observations but only contribute to about one quarter of the global α_A. Thus, we assess that α_A estimates are consistent, at global scale, in CMIP5 and CMIP6 models and satellite observations, though hemispheric differences and the role of internal variability need to be further explored.

Based on the multiple lines of evidence presented above that include observations, CMIP5 and CMIP6 models and theory, the global surface albedo feedback is assessed to be positive with *high confidence*. The basic phenomena that drive this feedback are well understood and the different studies cover a large variety of hypotheses or behaviours, including how the evolution of clouds affects this feedback. The value of the global surface albedo feedback is assessed to be α_A = 0.35 W m^{-2} °C^{-1}, with a *very likely* range from 0.10 to 0.60 W m^{-2} °C^{-1} and a *likely* range from 0.25 to 0.45 W m^{-2} °C^{-1} with *high confidence*.

7.4.2.4 Cloud feedbacks

7.4.2.4.1 Decomposition of clouds into regimes

Clouds can be formed almost anywhere in the atmosphere when moist air parcels rise and cool, enabling the water vapour to condense. The cloud droplets, ice crystals frozen from small water droplets, and their mixture may further grow into large particles of rain, snow, or drizzle. These microphysical processes interact with aerosols, radiation and atmospheric circulation, resulting in a highly complex set of processes governing cloud formation and lifecycles that operate across a wide range of spatial and temporal scales.

Clouds have various types, from optically thick convective clouds to thin stratus and cirrus clouds, depending upon thermodynamic conditions and large-scale circulation (Figure 7.9). Over the equatorial warm pool and inter-tropical convergence zone (ITCZ) regions, high SSTs stimulate the development of deep convective cloud systems, which are accompanied by anvil and cirrus clouds near the tropopause where the convective air outflows. The large-scale circulation associated with these convective clouds leads to subsidence over the subtropical cool ocean, where deep convection is suppressed by a lower tropospheric inversion layer maintained by the subsidence and promoting the formation of shallow cumulus and stratocumulus clouds. In the extratropics, mid-latitude storm tracks control cloud formation, which occurs primarily in the frontal bands of extratropical cyclones. Since liquid droplets do not freeze spontaneously at temperatures warmer than approximately –40°C and ice nucleating particles that can aid freezing at warmer temperatures are scarce (see Section 7.3.3), extratropical clouds often consist both of super-cooled liquid and ice crystals, resulting in mixed-phase clouds.

In the global energy budget at TOA, clouds affect SW radiation by reflecting sunlight due to their high albedo (cooling the climate system) and also LW radiation by absorbing the energy from the surface and emitting at a lower temperature to space, i.e., contributing to the greenhouse effect, warming the climate system. In general, the greenhouse effect of clouds strengthens with height whereas the SW reflection depends on the cloud optical properties. The effects of clouds on Earth's energy budget are measured by the cloud radiative effect (CRE), which is the difference in the TOA radiation between clear and all skies (see Section 7.2.1). In the present climate, the SW CRE tends to be compensated by the LW CRE over the equatorial warm pool, leading to the net CRE pattern showing large negative values over the eastern part of the subtropical ocean and the extratropical ocean due to the dominant influence of highly reflective marine low clouds.

In a first attempt to systematically evaluate ECS based on fully coupled GCMs in AR4, diverging cloud feedbacks were recognized as a dominant source of uncertainty. An advance in understanding the cloud feedback was to assess feedbacks separately for different cloud regimes (Gettelman and Sherwood, 2016). A thorough assessment of cloud feedbacks in different cloud regimes was carried out in AR5 (Boucher et al., 2013), which assigned *high* or *medium confidence* for some cloud feedbacks but *low* or *no confidence* for others (Table 7.9). Many studies that estimate the net cloud feedback using CMIP5 simulations (Vial et al., 2013; Caldwell et al., 2016; Zelinka et al., 2016; Colman and Hanson, 2017) show different values depending on the methodology and the set of models used, but often report a large inter-model spread of the feedback, with the 90% confidence interval spanning both weak negative and strong positive net feedbacks. Part of this diversity arises from the dependence of the model cloud feedbacks on the parameterization of clouds and their coupling to other sub-grid scale processes (Zhao et al., 2015).

Since AR5, community efforts have been undertaken to understand and quantify the cloud feedbacks in various cloud regimes coupled with large-scale atmospheric circulation (Bony et al., 2015). For some cloud regimes, alternative tools to ESMs, such as observations, theory, high-resolution cloud resolving models (CRMs), and Large Eddy Simulations (LES), help quantify the feedbacks. Consequently, the net cloud feedback derived from ESMs has been revised by assessing the regional cloud feedbacks separately and summing them with weighting by the ratio of fractional coverage of those clouds over the globe to give the global feedback, following an approach adopted in Sherwood et al. (2020). This "bottom-up" assessment is explained below with a summary of updated confidence of individual cloud feedback components (Table 7.9). Dependence of cloud feedbacks on evolving patterns of surface warming will be discussed in Section 7.4.4 and is not explicitly taken into account in the assessment presented in this section.

[START FIGURE 7.9 HERE]

Figure 7.9: Schematic cross section of diverse cloud responses to surface warming from the tropics to polar regions. Thick solid and dashed curves indicate the tropopause and the subtropical inversion layer in the current climate, respectively. Thin grey text and arrows represent robust responses in the thermodynamic structure to greenhouse warming, of relevance to cloud changes. Text and arrows in red, orange and green show the major cloud responses assessed with *high*, *medium* and *low confidence*, respectively, and the sign of their feedbacks to the surface warming is indicated in the parenthesis. Major advances since AR5 are listed in a box.

[END FIGURE 7.9 HERE]

7.4.2.4.2 Assessment for individual cloud regimes

High-cloud altitude feedback.

It has long been argued that cloud top altitude rises under global warming, concurrent with the rising of the tropopause at all latitudes (Marvel et al., 2015; Thompson et al., 2017). This increasing altitude of high clouds was identified in early generation GCMs and the tropical high-cloud altitude feedback was assessed to be positive with *high confidence* in AR5 (Boucher et al., 2013). This assessment is supported by a theoretical argument called the fixed anvil temperature mechanism, which ensures that the temperature of the convective detrainment layer does not change when the altitude of high-cloud tops increases with the rising tropopause (Hartmann and Larson, 2002). Because the cloud top temperature does not change significantly with global warming, cloud longwave emission does not increase even though the surface warms, resulting in an enhancement of the high-cloud greenhouse effect (a positive feedback; Yoshimori et al. (2020)). The upward shift of high clouds with surface warming is detected in observed interannual variability and trends in satellite records for recent decades (Chepfer et al., 2014; Norris et al., 2016; Saint-Lu et al., 2020). The observational detection is not always successful (Davies et al., 2017), but the cloud altitude shifts similarly in many CRM experiments (Khairoutdinov and Emanuel, 2013; Tsushima et al., 2014; Narenpitak et al., 2017). The high-cloud altitude feedback was estimated to be 0.5 W m^{-2}°C^{-1} based on GCMs in AR5, but is revised, using a recent re-evaluation that excludes aliasing effects by reduced low-cloud amounts, downward to 0.22 ± 0.12 W m^{-2} °C^{-1} (one standard deviation) (Zhou et al., 2014; Zelinka et al., 2020). In conclusion, there is *high confidence* in the positive high-cloud altitude feedback simulated in ESMs as it is supported by theoretical, observational, and process modelling studies.

Tropical high-cloud amount feedback.

Updrafts in convective plumes lead to detrainment of moisture at a level where the buoyancy diminishes, and thus deep convective clouds over high SSTs in the tropics are accompanied by anvil and cirrus clouds in the upper troposphere. These clouds, rather than the convective plumes themselves, play a substantial role in the global TOA radiation budget. In the present climate, the net CRE of these clouds is small due to a cancellation between the SW and LW components (Hartmann et al., 2001). However, high clouds with different optical properties could respond to surface warming differently, potentially perturbing this radiative balance and therefore leading to a non-zero feedback.

A thermodynamic mechanism referred to as the 'stability iris effect' has been proposed to explain that the anvil cloud amount decreases with surface warming (Bony et al., 2016). In this mechanism, a temperature-mediated increase of static stability in the upper troposphere, where convective detrainment occurs, acts to balance a weakened mass outflow from convective clouds, and thereby reduce anvil cloud areal coverage (Figure 7.9). The reduction of anvil cloud amount is accompanied by enhanced convective aggregation that causes a drying of the surrounding air and thereby increases the LW emission to space that acts as a negative feedback (Bony et al., 2020). This phenomenon is found in many CRM simulations (Emanuel et al., 2014; Wing and Emanuel, 2014; Wing et al., 2020) and also identified in observed interannual variability (Stein et al., 2017; Saint-Lu et al., 2020).

Despite the reduction of anvil cloud amount supported by several lines of evidence, estimates of radiative feedback due to high-cloud amount changes is highly uncertain in models. The assessment presented here is guided by combined analyses of TOA radiation and cloud fluctuations at interannual time scale using multiple satellite data sets. The observationally based local amount feedback associated with optically thick high clouds is negative, leading to its global contribution (by multiplying the mean tropical anvil cloud fraction of about 8%) of –0.24 ± 0.05 W m^{-2} °C^{-1} (one standard deviation) for LW (Vaillant de Guélis et al., 2018). Also, there is a positive feedback due to increase of optically thin cirrus clouds in the tropopause layer, estimated to be 0.09 ± 0.09 W m^{-2} °C^{-1} (one standard deviation) (Zhou et al., 2014). The negative LW feedback due to reduced amount of thick high clouds is partly compensated by the positive SW feedback (due to less reflection of solar radiation), so that the tropical high-cloud amount feedback is assessed to be equal to or smaller than their sum. Consistently, the net high cloud feedback in the tropical convective regime, including a part of the altitude feedback, is estimated to have the global contribution of –0.13 ± 0.06 W m^{-2} °C^{-1} (one standard deviation) (Williams and Pierrehumbert, 2017). The negative cloud LW feedback is considerably biased in CMIP5 GCMs (Mauritsen and Stevens, 2015; Su et al., 2017; Li et al., 2019) and highly uncertain primarily due to differences in the convective parameterization (Webb et al., 2015).

Furthermore, high-resolution CRM simulations cannot alone be used to constrain uncertainty because the results depend on parametrized cloud microphysics and turbulence (Bretherton et al., 2014; Ohno et al., 2019). Therefore, the tropical high-cloud amount feedback is assessed as negative but with *low confidence* given the lack of modelling evidence. Taking observational estimates altogether and methodological uncertainty into account, the global contribution of the high-cloud amount feedback is assessed to –0.15 ± 0.2 W m^{-2} °C^{-1} (one standard deviation).

Subtropical marine low-cloud feedback.
It has long been argued that the response of marine boundary layer clouds over the subtropical ocean to surface warming was the largest contributor to the spread among GCMs in the net cloud feedback (Boucher et al., 2013). However, uncertainty of the marine low-cloud feedback has been reduced considerably since AR5 through combined knowledge from theoretical, modelling, and observational studies (Klein et al., 2017). Processes that control the low clouds are complex and involve coupling with atmospheric motions on multiple scales, from the boundary layer turbulence to the large-scale subsidence, which may be represented by a combination of shallow and deep convective mixing (Sherwood et al., 2014).

In order to disentangle the large-scale processes that cause the cloud amount either to increase or decrease in response to the surface warming, the cloud feedback has been expressed in terms of several 'cloud controlling factors' (Qu et al., 2014, 2015; Zhai et al., 2015; Brient and Schneider, 2016; Myers and Norris, 2016; McCoy et al., 2017b). The advantage of this approach over conventional calculation of cloud feedbacks is that the temperature-mediated cloud response can be estimated without using information of the simulated cloud responses that are less well-constrained than the changes in the environmental conditions. Two dominant factors are identified for the subtropical low clouds: a thermodynamic effect due to rising SST that acts to reduce low cloud by enhancing cloud-top entrainment of dry air, and a stability effect accompanied by an enhanced inversion strength that acts to increase low cloud (Qu et al., 2014, 2015; Kawai et al., 2017). These controlling factors compensate with a varying degree in different ESMs, but can be constrained by referring to the observed seasonal or interannual relationship between the low-cloud amount and the controlling factors in the environment as a surrogate. The analysis leads to a positive local feedback that has the global contribution of 0.14–0.36 W m^{-2} °C^{-1} (Klein et al., 2017), to which the feedback in the stratocumulus regime dominates over the feedback in the trade cumulus regime (Cesana et al., 2019; Radtke et al., 2020). The stratocumulus feedback may be underestimated because explicit simulations using LES show a larger local feedback of up to 2.5 W m^{-2} °C^{-1}, corresponding to the global contribution of 0.2 W m^{-2} °C^{-1} by multiplying the mean tropical stratocumulus fraction of about 8% (Bretherton, 2015). Supported by different lines of evidence, the subtropical marine low-cloud feedback is assessed as positive with *high confidence*. Based on the combined estimate using LESs and the cloud controlling factor analysis, the global contribution of the feedback due to marine low clouds equatorward of 30° is assessed to be 0.2 ± 0.16 W m^{-2} °C^{-1} (one standard deviation), for which the range reflects methodological uncertainties.

Land cloud feedback.
Intensification of the global hydrological cycle is a robust feature of global warming, but at the same time, many land areas in the subtropics will experience drying at the surface and in the atmosphere (Chapter 8, Section 8.2.2). This occurs due to a limited water availability in these regions, where the cloudiness is consequently expected to decrease. Reduction in clouds over land are consistently identified in the CMIP5 models and also in a GCM with explicit convection (Bretherton et al., 2014; Kamae et al., 2016). Because low clouds make up the majority of subtropical land clouds, this reduced amount of low clouds reflects less solar radiation and leads to a positive feedback similar to the marine low clouds. The mean estimate of the global land cloud feedback in CMIP5 models is smaller than the marine low cloud feedback, 0.08 ± 0.08 W m^{-2} °C^{-1} (Zelinka et al., 2016). These values are nearly unchanged in CMIP6 (Zelinka et al., 2020). However, ESMs still have considerable biases in the climatological temperature and cloud fraction over land and the magnitude of this feedback has not yet been supported by observational evidence. Therefore, the feedback due to decreasing land clouds is assessed to be 0.08 ± 0.08 W m^{-2} °C^{-1} (one standard deviation) with *low confidence*.

Mid-latitude cloud amount feedback.
Poleward shifts in the mid-latitude jets are evident since the 1980s (Chapter 2, Section 2.3.1.4.3) and are a

feature of the large-scale circulation change in future projections (Chapter 4, Section 4.5.1.6). Because mid-latitude clouds over the North Pacific, North Atlantic, and Southern Ocean are induced mainly by extratropical cyclones in the storm tracks along the jets, it has been suggested that the jet shifts should be accompanied by poleward shifts in the mid-latitude clouds, which would result in a positive feedback through the reduced reflection of insolation (Boucher et al., 2013). However, studies since AR5 have revealed that this proposed mechanism does not apply in practice (Ceppi and Hartmann, 2015). While a poleward shift of mid-latitude cloud maxima in the free troposphere has been identified in satellite and ground-based observations (Bender et al., 2012; Eastman and Warren, 2013), associated changes in net CRE are small because the responses in high and low clouds to the jet shift act to cancel each other (Grise and Medeiros, 2016; Tselioudis et al., 2016; Zelinka et al., 2018). This cancellation is not well captured in ESMs (Lipat et al., 2017), but the above findings show that the mid-latitude cloud feedback is not dynamically driven by the poleward jet shifts, which are rather suggested to occur partly in response to high cloud changes (Li et al., 2018b).

Thermodynamics play an important role in controlling extratropical cloud amount equatorward of about 50° latitude. Recent studies showed using observed cloud controlling factors that the mid-latitude low cloud fractions decrease with rising SST, which also acts to weaken stability of the atmosphere unlike the subtropics (McCoy et al., 2017b). ESMs consistently show a decrease of cloud amounts and a resultant positive shortwave feedback in the 30°–40° latitude bands, which can be constrained using observations of seasonal migration of cloud amount (Zhai et al., 2015). Based on the qualitative agreement between observations and ESMs, the mid-latitude cloud amount feedback is assessed as positive with *medium confidence.* Following these emergent constraint studies using observations and CMIP5/6 models, the global contribution of net cloud amount feedback over 30°–60° ocean areas, covering 27% of the globe, is assigned 0.09 ± 0.1 W m^{-2} °C^{-1} (one standard deviation), in which the uncertainty reflects potential errors in models' low cloud response to changes in thermodynamic conditions.

Extratropical cloud optical depth feedback.
Mixed-phase clouds that consist of both liquid and ice are dominant over the Southern Ocean (50°–80°S), which accounts for 20% of the net CRE in the present climate (Matus and L'Ecuyer, 2017). It has been argued that the cloud optical depth (opacity) will increase over the Southern Ocean as warming drives the replacement of ice-dominated clouds with liquid-dominated clouds (Tan et al., 2019). Liquid clouds generally consist of many small cloud droplets, while the crystals in ice clouds are orders of magnitudes fewer in number and much larger, causing the liquid clouds to be optically thicker and thereby resulting in a negative feedback (Boucher et al., 2013). However, this phase change feedback works effectively only below freezing temperature (Lohmann and Neubauer, 2018; Terai et al., 2019) and other processes that increase or decrease liquid water path (LWP) may also affect the optical depth feedback (McCoy et al., 2019).

Due to insufficient amounts of super-cooled liquid water in the simulated atmospheric mean state, many CMIP5 models overestimated the conversion from ice to liquid clouds with climate warming and the resultant negative phase change feedback (Kay et al., 2016a; Tan et al., 2016; Lohmann and Neubauer, 2018). This feedback can be constrained using satellite-derived LWP observations over the past 20 years that enable estimates of both long-term trends and the interannual relationship with SST variability (Gordon and Klein, 2014; Ceppi et al., 2016; Manaster et al., 2017). The observationally-constrained SW feedback ranges from –0.91 to –0.46 W m^{-2} °C^{-1} over 40°–70°S depending on the methodology (Ceppi et al., 2016; Terai et al., 2016). In some CMIP6 models, representation of super-cooled liquid water content has been improved, leading to weaker negative optical depth feedback over the Southern Ocean closer to observational estimates (Bodas-Salcedo et al., 2019; Gettelman et al., 2019). This improvement at the same time results in a positive optical depth feedback over other extratropical ocean where LWP decreased in response to reduced stability in those CMIP6 models (Zelinka et al., 2020). Given the accumulated observational estimates and an improved agreement between ESMs and observations, the extratropical optical depth feedback is assessed to be small negative with *medium confidence.* Quantitatively, the global contribution of this feedback is assessed to have a value of -0.03 ± 0.05 W m^{-2} °C^{-1} (one standard deviation) by combining estimates based on observed interannual variability and the cloud controlling factors.

Arctic cloud feedback.

Clouds in polar regions, especially over the Arctic, form at low altitude above or within a stable to neutral boundary layer and are known to co-vary with sea-ice variability beneath. Because the clouds reflect sunlight during summer but trap longwave radiation throughout the year, seasonality plays an important role for cloud effects on Arctic climate (Kay et al., 2016b). AR5 assessed that Arctic low cloud amount will increase in boreal autumn and winter in response to declining sea ice in a warming climate, due primarily to an enhanced upward moisture flux over open water. The cloudier conditions during these seasons result in more downwelling longwave radiation, acting as a positive feedback on surface warming (Kay and Gettelman, 2009). Over recent years, further evidence of the cloud contribution to the Arctic amplification has been obtained (Goosse et al., 2018; Section 7.4.4.1). Space-borne lidar observations show that the cloud response to summer sea-ice loss is small and cannot overcome the cloud effect in autumn (Taylor et al., 2015; Morrison et al., 2018). The seasonality of the cloud response to sea-ice variability is reproduced in GCM simulations (Laîné et al., 2016; Yoshimori et al., 2017). The agreement between observations and models indicates that the Arctic cloud feedback is positive at the surface. This leads to an Arctic cloud feedback at TOA that is *likely* positive, but very small in magnitude as found in some climate models (Pithan and Mauritsen, 2014; Morrison et al., 2018). The observational estimates are sensitive to the analysis period and the choice of reanalysis data, and a recent estimate of the TOA cloud feedback over 60°–90°N using atmospheric reanalysis data and CERES satellite observations suggests a regional value ranging from –0.3 to 0.5 W m^{-2} °C^{-1}, which corresponds to a global contribution of –0.02 to 0.03 W m^{-2} °C^{-1} (Zhang et al., 2018b). Based on the overall agreement between ESMs and observations, the Arctic cloud feedback is assessed small positive and has the value of 0.01 ± 0.05 W m^{-2} °C^{-1} (one standard deviation). The assessed range indicates that a negative feedback is almost as probable as a positive feedback, and the assessment that the Arctic cloud feedback is positive is therefore given *low confidence*.

7.4.2.4.3 Synthesis for the net cloud feedback

The understanding of the response of clouds to warming and associated radiative feedback has deepened since AR5 (Figure 7.9, FAQ7.2). Particular progress has been made in the assessment of the marine low-cloud feedback, which has historically been a major contributor to the cloud feedback uncertainty but is no longer the largest source of uncertainty. Multiple lines of evidence (theory, observations, emergent constraints and process modelling) are now available in addition to ESM simulations, and the positive low-cloud feedback is consequently assessed with *high confidence*.

The best estimate of net cloud feedback is obtained by summing feedbacks associated with individual cloud regimes and assessed to be α_C = 0.42 W m^{-2} °C^{-1}. By assuming that uncertainty of individual cloud feedbacks is independent of each other, their standard deviations are added in quadrature, leading to the *likely* range of 0.12 to 0.72 W m^{-2} °C^{-1} and the *very likely* range of –0.10 to 0.94 W m^{-2} °C^{-1} (Table 7.10). This approach potentially misses feedbacks from cloud regimes that are not assessed, but almost all the major cloud regimes were taken into consideration (Gettelman and Sherwood, 2016) and therefore additional uncertainty will be small. This argument is also supported by an agreement between the net cloud feedback assessed here and the net cloud feedback directly estimated using observations. The observational estimate, which is sensitive to the period considered, based on two atmospheric reanalyses (ERA-Interim and MERRA) and TOA radiation budgets derived from the CERES satellite observations for the years 2000–2010 is 0.54 ± 0.7 W m^{-2} °C^{-1} (one standard deviation) (Dessler, 2013) and overlaps with the assessed range of the net cloud feedback. The assessed *very likely* range is reduced by about 50% compared to AR5, but is still wide compared to those of other climate feedbacks (Table 7.10). The largest contribution to this uncertainty range is the estimate of tropical high-cloud amount feedback which is not yet well quantified using models.

In reality, different types of cloud feedback may occur simultaneously in one cloud regime. For example, an upward shift of high clouds associated with the altitude feedback could be coupled to an increase/decrease of cirrus/anvil cloud fractions associated with the cloud amount feedback. Alternatively, slowdown of the tropical circulation with surface warming (Chapter 4, Section 4.5.3; Figure 7.9) could affect both high and low clouds so that their feedbacks are co-dependent. Quantitative assessments of such covariances require further knowledge about cloud feedback mechanisms, which will further narrow the uncertainty range.

In summary, deepened understanding of feedback processes in individual cloud regimes since AR5 leads to an assessment of the positive net cloud feedback with *high confidence*. A small probability (less than 10%) of a net negative cloud feedback cannot be ruled out, but this would require an extremely large negative feedback due to decreases in the amount of tropical anvil clouds or increases in optical depth of extratropical clouds over the Southern Ocean; neither is supported by current evidence.

[START TABLE 7.9 HERE]

Table 7.9: Assessed sign and confidence level of cloud feedbacks in difference regimes, compared between AR5 and AR6. For some cloud regimes, the feedback was not assessed in AR5, indicated by N/A.

Feedback	AR5	AR6
High-cloud altitude feedback	Positive (*high confidence*)	Positive (*high confidence*)
Tropical high-cloud amount feedback	N/A	Negative (*low confidence*)
Subtropical marine low-cloud feedback	N/A (*low confidence*)	Positive (*high confidence*)
Land cloud feedback	N/A	Positive (*low confidence*)
Mid-latitude cloud amount feedback	Positive (*medium confidence*)	Positive (*medium confidence*)
Extratropical cloud optical depth feedback	N/A	Small negative (*medium confidence*)
Arctic cloud feedback	Small positive (*very low confidence*)	Small positive (*low confidence*)
Net cloud feedback	Positive (*medium confidence*)	Positive (*high confidence*)

[END TABLE 7.9 HERE]

7.4.2.5 Biogeophysical and non-CO_2 biogeochemical feedbacks

The feedbacks presented in the previous sections (Sections 7.4.2.1–7.4.2.4) are directly linked to physical climate variables (for example temperature, water vapour, clouds, or sea ice). The central role of climate feedbacks associated with these variables has been recognised since early studies of climate change. However, in addition to these physical climate feedbacks, the Earth system includes feedbacks for which the effect of global mean surface temperature change on the TOA energy budget is mediated through other mechanisms, such as the chemical composition of the atmosphere, or by vegetation changes. Among these additional feedbacks, the most important is the CO_2 feedback that describes how a change of the global surface temperature affects the atmospheric CO_2 concentration. In ESM simulations in which CO_2 emissions are prescribed, changes in surface carbon fluxes affect the CO_2 concentration in the atmosphere, the TOA radiative energy budget, and eventually the global mean surface temperature. In ESM simulations in which the CO_2 concentration is prescribed, changes in the carbon cycle allow compatible CO_2 emissions to be calculated, i.e., the CO_2 emissions that are compatible with both the prescribed CO_2 concentration and the representation of the carbon cycle in the ESM. The CO_2 feedback is assessed in Chapter 5, Section 5.4. The framework presented in this chapter assumes that the CO_2 concentration is prescribed, and our assessment of the net feedback parameter, α, does not include carbon-cycle feedbacks on the atmospheric CO_2 concentration (Section 7.1; Box 7.1). However, our assessment of α does include non-CO_2 biogeochemical feedbacks (Section 7.4.2.5.1; including effects due to changes in atmospheric methane concentration) and biogeophysical feedbacks (Section 7.4.2.5.2). A synthesis of the combination of biogeophysical and non-CO_2 biogeochemical feedbacks is given in Section 7.4.2.5.3.

7.4.2.5.1 Non-CO_2 biogeochemical feedbacks

The chemical composition of the atmosphere (beyond CO_2 and water vapour changes) is expected to change in response to a warming climate. These changes in greenhouse gases (CH_4, N_2O, and ozone) and aerosol amount (including dust) have the potential to alter the TOA energy budget and are collectively referred to as non-CO_2 biogeochemical feedbacks. CH_4 and N_2O feedbacks arise partly from changes in their emissions from natural sources in response to temperature change; these are assessed in Chapter 5, Section 5.4.7 (see also Figure 5.29c). Here we exclude the permafrost CH_4 feedback (Chapter 5, Section 5.4.9.1.2) because, although associated emissions are projected to increase under warming on multi-decadal to centennial timescales, on longer timescales these emissions would eventually substantially decline as the permafrost carbon pools were depleted (Schneider von Deimling et al., 2012, 2015). This leaves the wetland CH_4, land N_2O, and ocean N_2O feedbacks, the assessed mean values of which sum to a positive feedback parameter of +0.04 [0.02 to 0.06] W m^{-2} °C^{-1} (Chapter 5, Section 5.4.7). Other non-CO_2 biogeochemical feedbacks that are relevant to the net feedback parameter are assessed in Chapter 6, Section 6.4.5 (Table 6.8). These feedbacks are associated with sea salt, dimethyl sulphide, dust, ozone, biogenic volatile organic compounds, lightning, and CH_4 lifetime, and sum to a negative feedback parameter of –0.20 [–0.41 to +0.01] W m^{-2} °C^{-1}. The overall feedback parameter for non-CO_2 biogeochemical feedbacks is obtained by summing the Chapter 5 and Chapter 6 assessments, which gives –0.16 [–0.37 to +0.05] W m^{-2} °C^{-1}. However, there is *low confidence* in the estimates of both the individual non-CO_2 biogeochemical feedbacks as well as their total effect, as evident from the large range in the magnitudes of α from different studies, which can be attributed to diversity in how models account for these feedbacks and limited process-level understanding.

7.4.2.5.2 Biogeophysical feedbacks

Biogeophysical feedbacks are associated with changes in the spatial distribution and/or biophysical properties of vegetation, induced by surface temperature change and attendant hydrological cycle change. These vegetation changes can alter radiative fluxes directly via albedo changes, or via surface momentum or moisture flux changes and hence changes in cloud properties. However, the direct physiological response of vegetation to changes in CO_2, including changes in stomatal conductance, is considered part of the CO_2 effective radiative forcing rather than a feedback (Section 7.3.2.1). The timescale of response of vegetation to climate change is relatively uncertain but can be from decades to hundreds of years (Willeit et al., 2014), and could occur abruptly or as a tipping point (Chapter 5, Section 5.4.9.1.1; Chapter 8, Sections 8.6.2.1 and 8.6.2.2); equilibrium only occurs when the soil system and associated nutrient and carbon pools equilibrate, which can take millennia (Brantley, 2008; Sitch et al., 2008). The overall effects of climate-induced vegetation changes may be comparable in magnitude to those from anthropogenic land-use and land cover change (Davies-Barnard et al., 2015). Climate models that include a dynamical representation of vegetation (e.g., Reick et al., 2013; Harper et al., 2018) are used to explore the importance of biogeophysical feedbacks (Notaro et al., 2007; Brovkin et al., 2009; O'ishi et al., 2009; Port et al., 2012; Willeit et al., 2014; Alo and Anagnostou, 2017; Zhang et al., 2018c; Armstrong et al., 2019). In AR5, it was discussed that such model experiments predicted that expansion of vegetation in the high latitudes of the Northern Hemisphere would enhance warming due to the associated surface albedo change, and that reduction of tropical forests in response to climate change would lead to regional surface warming, due to reduced evapotranspiration (Collins et al., 2013a), but there was no assessment of the associated feedback parameter. SRCCL stated that regional climate change can be dampened or enhanced by changes in local land cover, but that this depends on the location and the season; however, in general the focus was on anthropogenic land cover change, and no assessment of the biogeophysical feedback parameter was carried out. There are also indications of a marine biogeophysical feedback associated with surface albedo change due to changes in phytoplankton (Frouin and Iacobellis, 2002; Park et al., 2015), but there is not currently enough evidence to quantitatively assess this feedback.

Since AR5, several studies have confirmed that a shift from tundra to boreal forests and the associated albedo change leads to increased warming in Northern Hemisphere high latitudes (Willeit et al., 2014; Zhang et al., 2018c; Armstrong et al., 2019) (*high confidence*). However, regional modelling indicates that vegetation feedbacks may act to cool climate in the Mediterranean (Alo and Anagnostou, 2017), and in the tropics and subtropics the regional response is in general not consistent across models. On a global scale, several modelling studies have either carried out a feedback analysis (Stocker et al., 2013; Willeit et al.,

2014) or presented simulations that allow a feedback parameter to be estimated (O'ishi et al., 2009; Armstrong et al., 2019), in such a way that the physiological response can be accounted for as a forcing rather than a feedback. The central estimates of the biogeophysical feedback parameter from these studies range from close to zero (Willeit et al., 2014) to +0.13 W m^{-2} °C^{-1} (Stocker et al., 2013). An additional line of evidence comes from the mid-Pliocene warm period (MPWP, Chapter 2, Cross-Chapter Box 2.1), for which paleoclimate proxies provide evidence of vegetation distribution and CO_2 concentrations. Model simulations that include various combinations of modern versus MPWP vegetation and CO_2 allow an associated feedback parameter to be estimated, as long as account is also taken of the orographic forcing (Lunt et al., 2010, 2012b). This approach has the advantage over pure modelling studies in that the reconstructed vegetation is based on (paleoclimate) observations, and is in equilibrium with the CO_2 forcing. However, there are uncertainties in the vegetation reconstruction in regions with little or no proxy data, and it is uncertain how much of the vegetation change is associated with the physiological response to CO_2. This paleoclimate approach gives an estimate for the biogeophysical feedback parameter of +0.3 W m^{-2} °C^{-1}.

Given the limited number of studies, we take the full range of estimates discussed above for the biogeophysical feedback parameter, and assess the *very likely* range to be from zero to +0.3 W m^{-2} °C^{-1}, with a central estimate of +0.15 W m^{-2} °C^{-1} (*low confidence*). Although this assessment is based on evidence from both models and paleoclimate proxies, and the studies above agree on the sign of the change, there is nonetheless *limited evidence*. Higher confidence could be obtained if there were more studies that allowed calculation of a biogeophysical feedback parameter (particularly from paleoclimates), and if the partitioning between biogeophysical feedbacks and physiological forcing were clearer for all lines of evidence.

7.4.2.5.3 Synthesis of biogeophysical and non-CO_2 biogeochemical feedbacks

The non-CO_2 biogeochemical feedbacks are assessed in Section 7.4.2.5.1 to be –0.16 [–0.37 to +0.05] W m^{-2} °C^{-1} and the biogeophysical feedbacks are assessed in Section 7.4.2.5.2 to be +0.15 [0 to +0.3] W m^{-2} °C^{-1}. The sum of the biogeophysical and non-CO_2 biogeochemical feedbacks is assessed to have a central value of -0.01 W m^{-2} °C^{-1} and a *very likely* range from –0.27 to +0.25 W m^{-2} °C^{-1} (see Table 7.10). Given the relatively long timescales associated with the biological processes that mediate the biogeophysical and many of the non-CO_2 biogeochemical feedbacks, in comparison with the relatively short timescale of many of the underlying model simulations, combined with the small number of studies for some of the feedbacks, and the relatively small signals, this overall assessment has *low confidence*.

Some supporting evidence for this overall assessment can be obtained from the CMIP6 ensemble, which provides some pairs of instantaneous 4×CO_2 simulations carried out using related models with and without biogeophysical and non-CO_2 biogeochemical feedbacks. This is not a direct comparison because these pairs of simulations may differ by more than just their inclusion of these additional feedbacks; furthermore, not all biogeophysical and non-CO_2 biogeochemical feedbacks are fully represented. However, a comparison of the pairs of simulations does provide a first-order estimate of the magnitude of these additional feedbacks. Séférian et al. (2019) find a slightly more negative feedback parameter in CNRM-ESM2-1 (with additional feedbacks) then in CNRM-CM6-1 (a decrease of 0.02 W m^{-2} °C^{-1}, using the linear regression method from years 10-150). Andrews et al. (2019) also find a slightly more negative feedback parameter when these additional feedbacks are included (a decrease of 0.04 W m^{-2}°C^{-1} in UKESM1 compared with HadGEM3-GC3.1). Both of these studies suggest a small but slightly negative feedback parameter for the combination of biogeophysical and non-CO_2 biogeochemical feedbacks, but with relatively large uncertainty given (a) interannual variability and (b) that feedbacks associated with natural terrestrial emissions of CH_4 and N_2O were not represented in either pair.

7.4.2.6 Long term radiative feedbacks associated with ice sheets

Although long-term radiative feedbacks associated with ice sheets are not included in our definition of ECS (Box 7.1), the relevant feedback parameter is assessed here because the timescales on which these feedbacks act are relatively uncertain, and the long-term temperature response to CO_2 forcing of the entire Earth system may be of interest.

Earth's ice sheets (Greenland and Antarctica) are sensitive to climate change (Chapter 9, Section 9.4; Pattyn et al., 2018). Their time evolution is determined by both their surface mass balance and ice dynamic processes, with the latter being particularly important for the West Antarctic Ice Sheet. Surface mass balance depends on the net energy and hydrological fluxes at their surface, and there are mechanisms of ice sheet instability that depend on ocean temperatures and basal melt rates (Chapter 9, Section 9.4.1.1). The presence of ice sheets affects Earth's radiative budget, hydrology, and atmospheric circulation due to their characteristic high albedo, low roughness length, and high altitude, and they influence ocean circulation through freshwater input from calving and melt (e.g., Fyke et al., 2018). Ice sheet changes also modify surface albedo through the attendant change in sea level and therefore land area (Abe-Ouchi et al., 2015). The timescale for ice sheets to reach equilibrium is on the order of thousands of years (Clark et al., 2016). Due to the long timescales involved, it is a major challenge to run coupled climate-ice sheet models to equilibrium, and as a result, long-term simulations are often carried out with lower complexity models, and/or are asynchronously coupled.

In AR5, it was described that both the Greenland and Antarctic ice sheets would continue to lose mass in a warming world (Collins et al., 2013a), with a continuation in sea level rise beyond the year 2500 assessed as *virtually certain*. However, there was *low confidence* in the associated radiative feedback mechanisms, and as such, there was no assessment of the magnitude of long-term radiative feedbacks associated with ice sheets. That assessment is consistent with SROCC, wherein it was stated that 'with limited published studies to draw from and no simulations run beyond 2100, firm conclusions regarding the net importance of atmospheric versus ocean melt feedbacks on the long-term future of Antarctica cannot be made.'

The magnitude of the radiative feedback associated with changes to ice sheets can be quantified by comparing the global mean long-term equilibrium temperature response to increased CO_2 concentrations in simulations that include interactive ice sheets with that of simulations that do not include the associated ice-sheet climate interactions (Swingedouw et al., 2008; Vizcaíno et al., 2010; Goelzer et al., 2011; Bronselaer et al., 2018; Golledge et al., 2019). These simulations indicate that on multi-centennial timescales, ice sheet mass loss leads to fresh water fluxes that can modify ocean circulation (Swingedouw et al., 2008; Goelzer et al., 2011; Bronselaer et al., 2018; Golledge et al., 2019). This leads to reduced surface warming (by about 0.2°C in the global mean after 1000 years; Goelzer et al., 2011; see also Section 7.4.4.1.1), although other work suggests no net global temperature effect of ice sheet mass loss (Vizcaíno et al., 2010). However, model simulations in which the Antarctic ice sheet is removed completely in a paleoclimate context indicate a positive global mean feedback on multi-millennial timescales due primarily to the surface albedo change (Goldner et al., 2014a; Kennedy-Asser et al., 2019); in Chapter 9 (Section 9.6.3) it is assessed that such ice-free conditions could eventually occur given 7–13°C of warming. This net positive feedback due to ice sheets on long timescales is also supported by model simulations of the mid-Pliocene warm period (MPWP, Chapter 2, Cross-chapter Box 2.1) in which the volume and area of the Greenland and West Antarctic ice sheets are reduced in model simulations in agreement with geological data (Chandan and Peltier, 2018), leading to surface warming. As such, overall, on multi-centennial timescales the feedback parameter associated with ice sheets is *likely* negative (*medium confidence*), but on multi-millennial timescales by the time the ice sheets reach equilibrium, the feedback parameter is *very likely* positive (*high confidence*; see Table 7.10). However, a relative lack of models carrying out simulations with and without interactive ice sheets over centennial to millennial timescales means that there is currently not enough evidence to quantify the magnitude of these feedbacks, or the timescales on which they act.

7.4.2.7 Synthesis

Table 7.10 summarises the estimates and the assessment of the individual and the net feedbacks presented in the above sections. The uncertainty range of the net climate feedback was obtained by adding standard deviations of individual feedbacks in quadrature, assuming that they are independent and follow the Gaussian distribution. It is *virtually certain* that the net climate feedback is negative, primarily due to the Planck temperature response, indicating that climate acts to stabilise in response to radiative forcing imposed to the system. Supported by the level of confidence associated with the individual feedbacks, it is also *virtually certain* that the sum of the non-Planck feedbacks is positive. Based on Table 7.10 these climate feedbacks amplify the Planck temperature response by about 2.8 [1.9 to 5.9] times. Cloud feedback remains the largest contributor to uncertainty of the net feedback, but the uncertainty is reduced compared to AR5. A secondary contribution to the net feedback uncertainty is the biogeophysical and non-CO_2 biogeochemical feedbacks, which together are assessed to have a central value near zero and thus do not affect the central estimate of ECS. The net climate feedback is assessed to be –1.16 W m^{-2} °C^{-1}, *likely* from –1.54 to –0.78 W m^{-2} °C^{-1}, and *very likely* from –1.81 to –0.51 W m^{-2}°C^{-1}.

Feedback parameters in climate models are calculated assuming that they are independent of each other, except for a well-known co-dependency between the WV and LR feedbacks. When the inter-model spread of the net climate feedback is computed by adding in quadrature the inter-model spread of individual feedbacks, it is 17% wider than the spread of the net climate feedback directly derived from the ensemble. This indicates that the feedbacks in climate models are partly co-dependent. Two possible co-dependencies have been suggested (Huybers, 2010; Caldwell et al., 2016). One is a negative covariance between the LR and longwave cloud feedbacks, which may be accompanied by a deepening of the troposphere (O'Gorman and Singh, 2013; Yoshimori et al., 2020) leading both to greater rising of high clouds and a larger upper-tropospheric warming. The other is a negative covariance between albedo and shortwave cloud feedbacks, which may originate from the Arctic regions: a reduction in sea ice enhances the shortwave cloud radiative effect because the ocean surface is darker than sea ice (Gilgen et al., 2018). This covariance is reinforced as the decrease of sea-ice leads to an increase in low-level clouds (Mauritsen et al., 2013). However, the mechanism causing these co-dependences between feedbacks is not well understood yet and a quantitative assessment based on multiple lines of evidence is difficult. Therefore, this synthesis assessment does not consider any co-dependency across individual feedbacks.

The assessment of the net climate feedback presented above is based on a single approach (i.e., process understanding) and directly results in a value for ECS given in Section 7.5.1; this is in contrast to the synthesis assessment of ECS in Section 7.5.5 which combines multiple approaches. The total (net) feedback parameter consistent with the final synthesis assessment of the ECS and Equation 7.1 is provided there.

[START TABLE 7.10 HERE]

Table 7.10: Synthesis assessment of climate feedbacks (central estimate shown by boldface). The mean values and their 90% ranges in CMIP5/6 models, derived using multiple radiative kernels (Zelinka et al., 2020), are also presented for comparison.

Feedback parameter α_x (W m^{-2} °C^{-1})	CMIP5 GCMs	CMIP6 ESMs	AR6 assessed ranges			
	Mean and the 5–95% interval	Mean and the 5–95% interval	Central estimate	*Very likely* interval	*Likely* interval	Level of confidence
Planck	–3.20 [–3.3 to –3.1]	–3.22 [–3.3 to –3.1]	**–3.22**	–3.4 to –3.0	–3.3 to –3.1	*high*
WV+LR	1.24 [1.08 to 1.35]	1.25 [1.14 to 1.45]	**1.30**	1.1 to 1.5	1.2 to 1.4	*high*
Surface albedo	0.41 [0.25 to 0.56]	0.39 [0.26 to 0.53]	**0.35**	0.10 to 0.60	0.25 to 0.45	*medium*
Clouds	0.41 [–0.09 to 1.1]	0.49 [–0.08 to 1.1]	**0.42**	–0.10 to 0.94	0.12 to 0.72	*high*
Biogeophysical and non-CO_2 biogeochemical	Not evaluated	Not evaluated	**–0.01**	–0.27 to 0.25	–0.16 to 0.14	*low*
Residual of kernel estimates	0.06 [–0.17 to 0.29]	0.05 [–0.18 to 0.28]				
Net (i.e., relevant for ECS)	–1.08 [–1.61 to –0.68]	–1.03 [–1.54 to –0.62]	**–1.16**	–1.81 to –0.51	–1.54 to –0.78	*medium*
Long-term ice				> 0.0		*high*

sheet feedbacks (millennial scale)		

[END TABLE 7.10 HERE]

7.4.2.8 Climate feedbacks in ESMs

Since AR5, many modelling groups have newly participated in CMIP experiments, leading to an increase in the number of models in CMIP6 (Chapter 1, Section 1.5.4). Other modelling groups that contributed to CMIP5 also updated their ESMs for carrying out CMIP6 experiments. While some of the CMIP6 models share components and are therefore not independent, they are analysed independently when calculating climate feedbacks. This, and more subtle forms of model inter-dependence, creates challenges when determining appropriate model weighting schemes (Chapter 1, Section 1.5.4). Additionally, it must be kept in mind that the ensemble sizes of the CMIP5 and CMIP6 models are not sufficiently large to sample the full range of model uncertainty.

The multi-model mean values of all physical climate feedbacks are calculated using the radiative kernel method (Section 7.4.1) and compared with the assessment in the previous sections (Figure 7.10). For CMIP models, there is a discrepancy between the net climate feedback calculated directly using the time evolutions of ΔT and ΔN in each model and the accumulation of individual feedbacks, but it is negligibly small (Supplementary Material 7.SM.4). Feedbacks due to biogeophysical and non-CO_2 biogeochemical processes are included in some models but neglected in the kernel analysis. In the AR6, biogeophysical and non-CO_2 biogeochemical feedbacks are explicitly assessed (Section 7.4.2.5).

All the physical climate feedbacks apart from clouds are very similar to each other in CMIP5 and CMIP6 model ensembles (see also Table 7.10). These values, where possible supported by other lines of evidence, are used for assessing feedbacks in Sections 7.4.2.1–7.4.2.3. A difference found between CMIP5 and CMIP6 models is the net cloud feedback, which is larger in CMIP6 by about 20%. This change is the major cause of less-negative values of the net climate feedback in CMIP6 than in CMIP5 and hence an increase in modelled ECS (Section 7.5.1).

A remarkable improvement of cloud representation in some CMIP6 models is the reduced error of the too weak negative SW CRE over the Southern Ocean (Bodas-Salcedo et al., 2019; Gettelman et al., 2019) due to a more realistic simulation of supercooled liquid droplets and associated cloud optical depths that were biased low commonly in CMIP5 models (McCoy et al. 2014a; 2014b). Because the negative cloud optical depth feedback occurs due to ‘brightening’ of clouds via phase change from ice to liquid cloud particles in response to surface warming (Cesana and Storelvmo, 2017), the extratropical cloud SW feedback tends to be less negative or even slightly positive in models with reduced errors (Bjordal et al., 2020; Zelinka et al., 2020). The assessment of cloud feedbacks in Section 7.4.2.4 incorporates estimates from these improved ESMs. Yet, there still remain other shared model errors such as in the subtropical low clouds (Calisto et al., 2014) and tropical anvil clouds (Mauritsen and Stevens, 2015), hampering an assessment of feedbacks associated with these cloud regimes based only on ESMs (Section 7.4.2.4).

[START FIGURE 7.10 HERE]

Figure 7.10: Global-mean climate feedbacks estimated in *abrupt4xCO2* simulations of 29 CMIP5 models (light blue) and 49 CMIP6 models (orange), compared with those assessed in this Report (red). Individual feedbacks for CMIP models are averaged across six radiative kernels as computed in Zelinka et al. (2020). The white line, black box and vertical line indicate the mean, 66% and 90% ranges, respectively. The shading represents the probability distribution across the full range of GCM/ESM values and for the 2.5-97.5 percentile range of the AR6 normal distribution. The unit is W m^{-2} °C^{-1}. Feedbacks associated with biogeophysical and non-CO_2 biogeochemical processes are assessed in AR6, but they are not explicitly estimated from GCMs/ESMs in CMIP5 and CMIP6. Further details on data sources and processing are available in the chapter data table (Table 7.SM.14).

[END FIGURE 7.10 HERE]

7.4.3 Dependence of feedbacks on climate mean state

In the standard framework of forcings and feedbacks (Section 7.4.1; Box 7.1), the approximation is made that the strength of climate feedbacks is independent of the background global surface mean temperature. More generally, the individual feedback parameters, α_x, are often assumed to be constant over a range of climate states, including those reconstructed from the past (encompassing a range of states warmer and colder than today, with varying continental geographies) or projected for the future. If this approximation holds, then the equilibrium global surface temperature response to a fixed radiative forcing will be constant, regardless of the climate state to which that forcing is applied.

This approximation will break down if climate feedbacks are not constant, but instead vary as a function of, e.g., background temperature (Roe and Baker, 2007; Zaliapin and Ghil, 2010; Roe and Armour, 2011; Bloch-Johnson et al., 2015), continental configuration (Farnsworth et al., 2019), or configuration of ice sheets (Yoshimori et al., 2009). If the real climate system exhibits this state dependence, then the future equilibrium temperature change in response to large forcing may be different from that inferred using the standard framework, and/or different to that inferred from paleoclimates. Such considerations are important for the assessment of ECS (Section 7.5). Climate models generally include representations of feedbacks that allow state-dependent behaviour, and so model results may also differ from the predictions from the standard framework.

In AR5 (Boucher et al., 2013), there was a recognition that climate feedbacks could be state dependent (Colman and McAvaney, 2009), but modelling studies that explored this (e.g., Manabe and Bryan, 1985; Voss and Mikolajewicz, 2001; Stouffer and Manabe, 2003; Hansen, 2005b) were not assessed in detail. Also in AR5 (Masson-Delmotte et al., 2013), it was assessed that some models exhibited weaker sensitivity to Last Glacial Maximum (LGM, Cross-Chapter Box 2.1) forcing than to $4\times CO_2$ forcing, due to state-dependence in shortwave cloud feedbacks.

Here, recent evidence for state-dependence in feedbacks from modelling studies (Section 7.4.3.1) and from the paleoclimate record (Section 7.4.3.2) are assessed, with an overall assessment in Section 7.4.3.3. The focus is on temperature-dependence of feedbacks when the system is in equilibrium with the forcing; evidence for transient changes in the net feedback parameter associated with evolving spatial patterns of warming is assessed separately in Section 7.4.4.

7.4.3.1 State-dependence of feedbacks in models

There are several modelling studies since AR5 in which ESMs of varying complexity have been used to explore temperature dependence of feedbacks, either under modern (Hansen et al., 2013; Jonko et al., 2013; Meraner et al., 2013; Good et al., 2015; Duan et al., 2019; Mauritsen et al., 2019; Rohrschneider et al., 2019; Rugenstein et al., 2019b; Stolpe et al., 2019; Bloch-Johnson et al., 2020) or paleo (Caballero and Huber, 2013; Zhu et al., 2019b) climate conditions, typically by carrying out multiple simulations across successive CO_2 doublings. A non-linear temperature response to these successive doublings may be partly due to forcing that increases more (or less) than expected from a purely logarithmic dependence (Section 7.3.2; Etminan et al., 2016), and partly due to state-dependence in feedbacks; however, not all modelling studies have partitioned the non-linearities in temperature response between these two effects. Nonetheless, there is general agreement amongst ESMs that the net feedback parameter, α, increases (i.e., becomes less negative) as temperature increases from pre-industrial levels (i.e., sensitivity to forcing increases as temperature increases; e.g., Meraner et al., 2013; see Figure 7.11). The associated increase in sensitivity to forcing is, in most models, due to the water vapour (Section 7.4.2.2) and cloud (Section 7.4.2.4) feedback parameters increasing with warming (Caballero and Huber, 2013; Meraner et al., 2013; Rugenstein et al., 2019b; Zhu et al., 2019b; Sherwood et al., 2020b). These changes are offset partially by the surface albedo feedback parameter decreasing (Jonko et al., 2013; Meraner et al., 2013; Rugenstein et al., 2019b), as a consequence of a reduced amount of snow and sea ice cover in a much warmer climate. At the same time, there is little change in the Planck response (Section 7.4.2.1), which has been shown in one model to be due to competing effects from increasing Planck emission at warmer temperatures and decreasing planetary emissivity due to increased CO_2 and water vapour (Mauritsen et al., 2019). Analysis of the spatial patterns of the non-linearities in temperature response (Good et al., 2015) suggests that these patterns are linked to a reduced weakening of the AMOC, and changes to evapotranspiration. The temperature dependence of α is also found in model simulations of high-CO_2 paleoclimates (Caballero and Huber, 2013; Zhu et al., 2019b). The temperature dependence is not only evident at very high CO_2 concentrations in excess of $4\times CO_2$, but also apparent in the difference in temperature response to a $2\times CO_2$ forcing compared with to a $4\times CO_2$ forcing (Mauritsen et al., 2019; Rugenstein et al., 2019b), and as such is relevant for interpreting century-scale climate projections.

Despite the general agreement that α increases as temperature increases from pre-industrial levels (Figure 7.11), other modelling studies have found the opposite (Duan et al., 2019; Stolpe et al., 2019). Modelling studies exploring state dependence in climates colder than today, including in cold paleoclimates such as the LGM, provide conflicting evidence of either decreased (Yoshimori et al., 2011) or increased (Kutzbach et al., 2013; Stolpe et al., 2019) temperature response per unit forcing during cold climates compared to the modern era.

In contrast to most ESMs, the majority of Earth system models of intermediate complexity (EMICs) do not exhibit state dependence, or have a net feedback parameter that decreases with increasing temperature (Pfister and Stocker, 2017). This is unsurprising since EMICs usually do not include process-based representations of water vapour and cloud feedbacks. Although this shows that care must be taken when interpreting results from current generation EMICs, Pfister and Stocker (2017) also suggest that non-linearities in feedbacks can take a long time to emerge in model simulations due slow adjustment timescales associated with the ocean; longer simulations also allow better estimates of equilibrium warming (Bloch-Johnson et al., 2020). This implies that multi-century simulations (Rugenstein et al., 2019b) could increase confidence in ESM studies examining state dependence.

The possibility of more substantial changes in climate feedbacks, sometimes accompanied by hysteresis and/or irreversibility, has been suggested from some theoretical and modelling studies. It has been postulated that such changes could occur on a global scale and across relatively narrow temperature changes (Popp et al., 2016; von der Heydt and Ashwin, 2016; Steffen et al., 2018; Schneider et al., 2019; Ashwin and von der Heydt, 2020; Bjordal et al., 2020). However, the associated mechanisms are highly uncertain, and as such there is *low confidence* as to whether such behaviour exists at all, and in the temperature thresholds at which it might occur.

Overall, the modelling evidence indicates that there is *medium confidence* that the net feedback parameter, α, increases (i.e., becomes less negative) with increasing temperature (i.e., that sensitivity to forcing increases with increasing temperature), under global surface background temperatures at least up to 40°C (Meraner et al., 2013; Seeley and Jeevanjee, 2021), and *medium confidence* that this temperature dependence primarily derives from increases in the water vapour and shortwave cloud feedbacks. This assessment is further supported by recent analysis of CMIP6 model simulations (Bloch-Johnson et al., 2020) in the framework of nonlinMIP (Good et al., 2016), which showed that out of ten CMIP6 models, seven of them showed an increase of the net feedback parameter with temperature, primarily due to the water vapour feedback.

7.4.3.2 State-dependence of feedbacks in the paleoclimate proxy record

Several studies have estimated ECS from observations of the glacial-interglacial cycles of the last approximately 2 million years, and found a state dependence, with more-negative α (i.e., lower sensitivity to forcing) during colder periods of the cycles and less-negative α during warmer periods (von der Heydt et al., 2014; Köhler et al., 2015, 2017; Friedrich et al., 2016; Royer, 2016; Snyder, 2019); see summaries in Skinner (2012) and von der Heydt et al. (2016). However, the nature of the state dependence derived from these observations is dependent on the assumed ice sheet forcing (Köhler et al., 2015; Stap et al., 2019), which is not well known, due to a relative lack of proxy indicators of ice sheet extent and distribution prior to the LGM (Cross-Chapter Box 2.1). Furthermore, many of these glacial-interglacial studies estimate a very strong temperature-dependence of *α* (Figure 7.11) that is hard to reconcile with the other lines of evidence, including proxy estimates from warmer paleoclimates. However, if the analysis excludes time periods when the temperature and CO_2 data are not well correlated, which occurs in general at times when sea level is falling and obliquity is decreasing, the state-dependence reduces (Köhler et al., 2018). Despite these uncertainties, due to the agreement in the sign of the temperature-dependence from all these studies, there is *medium confidence* from the paleoclimate proxy record that the net feedback parameter, α, was less negative in the warm periods than in the cold periods of the glacial-interglacial cycles.

Paleoclimate proxy evidence from past high-CO_2 time periods much warmer than present (the early Eocene and PETM; Cross-Chapter Box 2.1) show that the feedback parameter increases as temperature increases (Anagnostou et al., 2016, 2020; Shaffer et al., 2016). However, such temperature-dependence of feedbacks was not found in the warm Pliocene relative to the cooler Pleistocene (Martínez-Botí et al., 2015), although the temperature changes are relatively small at this time, making temperature-dependence challenging to detect given the uncertainties in reconstructing global mean temperature and forcing. Overall, the paleoclimate proxy record provides *medium confidence* that the net feedback parameter, α, was less negative in these past warm periods than in the present day.

7.4.3.3 Synthesis of state-dependence of feedbacks from modelling and paleoclimate records

Overall, independent lines of evidence from models (Section 7.4.3.1) and from the paleoclimate proxy record (Section 7.4.3.2) lead to *high confidence* that the net feedback parameter, α, increases (i.e., becomes less negative) as temperature increases; i.e., that sensitivity to forcing increases as temperature increases; see Figure 7.11. This temperature-dependence should be considered when estimating ECS from ESM simulations in which CO_2 is quadrupled (Section 7.5.5) or from paleoclimate observations from past time periods colder or warmer than today (Section 7.5.4). Although individual lines of evidence give only *medium confidence*, the overall high confidence comes from the multiple models that show the same sign of the temperature-dependence of α, the general agreement in evidence from the paleo proxy and modelling lines of evidence, and the agreement between proxy evidence from both cold and warm past climates. However, due to the large range in estimates of the magnitude of the temperature-dependence of α across studies (Figure 7.11), a quantitative assessment cannot currently be given, which provides a challenge for including this temperature-dependence in emulator-based future projections (Cross-Chapter Box 7.1). Greater confidence in the modelling lines of evidence could be obtained from simulations carried out for several hundreds of years (Rugenstein et al., 2019b), substantially longer than in many studies, and from more models carrying out simulations at multiple CO_2 concentrations. Greater confidence in the paleoclimate lines of evidence would be obtained from stronger constraints on atmospheric CO_2 concentrations, ice sheet forcing, and temperatures, during past warm climates.

[START FIGURE 7.11 HERE]

Figure 7.11: Feedback parameter, α (W m^{-2} °C^{-1}), as a function of global mean surface air temperature anomaly relative to preindustrial, for ESM simulations (red circles and lines) (Caballero and Huber, 2013; Jonko et al., 2013; Meraner et al., 2013; Good et al., 2015; Duan et al., 2019; Mauritsen et al., 2019; Stolpe et al., 2019; Zhu et al., 2019b), **and derived from paleoclimate proxies (grey squares and lines)** (von der Heydt et al., 2014; Anagnostou et al., 2016, 2020; Friedrich et al., 2016; Royer, 2016; Shaffer et al., 2016; Köhler et al., 2017; Snyder, 2019; Stap et al., 2019). For the ESM simulations, the value on the *x*-axis refers to the average of the temperature before and after the system has equilibrated to a forcing (in most cases a CO_2 doubling), and is expressed as an anomaly relative to an associated pre-industrial global mean temperature from that model. The light blue shaded square extends across the assessed range of α (Table 7.10) on the *y*-axis, and on the *x*-axis extends across the approximate temperature range over which the assessment of α is based (taken as from zero to the assessed central value of ECS (Table 7.13). Further details on data sources and processing are available in the chapter data table (Table 7.SM.14).

[END FIGURE 7.11 HERE]

7.4.4 Relationship between feedbacks and temperature patterns

The large-scale patterns of surface warming in observations since the 19th century (Chapter 2, Section 2.3.1) and climate model simulations (Chapter 4, Section 4.3.1; Figure 7.12a) share several common features. In particular, surface warming in the Arctic is greater than for the global average and greater than in the southern hemisphere (SH) high latitudes; and surface warming is generally greater over land than over the ocean. Observations and climate model simulations also show some notable differences. ESMs generally simulate a weakening of the equatorial Pacific Ocean zonal (east-west) SST gradient on multi-decadal to centennial timescales, with greater warming in the east than the west, but this trend has not been seen in observations (Chapter 2, Figure 2.11b; Chapter 9, Section 9.2.1).

Chapter 4, Section 4.5.1 discusses patterns of surface warming for 21st century climate projections under the Shared Socioeconomic Pathways (SSP) scenarios. Chapter 9, Section 9.2.1 assesses historical SST trends and the ability of coupled ESMs to replicate the observed changes. Chapter 4, Section 4.5.1 discusses the processes that cause the land to warm more than the ocean (land-ocean warming contrast). This section assesses process understanding of the large-scale patterns of surface temperature response from the perspective of a regional energy budget. It then assesses evidence from the paleoclimate proxy record for patterns of surface warming during past time periods associated with changes in atmospheric CO_2 concentrations. Finally, it assesses how radiative feedbacks depend on the spatial pattern of surface temperature, and thus how they can change in magnitude as that pattern evolves over time, with implications for the assessment of ECS based on historical warming (Sections 7.4.4.3 and 7.5.2.1).

7.4.4.1 Polar amplification

Polar amplification describes the phenomenon where surface temperature change at high latitudes exceeds the global average surface temperature change in response to radiative forcing of the climate system. Arctic amplification, often defined as the ratio of Arctic to global surface warming, is a ubiquitous emergent feature of climate model simulations (Holland and Bitz, 2003; Pithan and Mauritsen, 2014; Chapter 4, Section 4.5.1; Figure 7.12a) and is also seen in observations (Chapter 2, Section 2.3.1). However, both climate models and observations show relatively less warming of the SH high latitudes compared to the northern hemisphere (NH) high latitudes over the historical record (Chapter 2, Section 2.3.1); a characteristic that is projected to continue over the 21st century (Chapter 4, Section 4.5.1). Since AR5 there is a much-improved understanding of the processes that drive polar amplification in the NH and delay its emergence in the SH (Section 7.4.4.1.1). Furthermore, the paleoclimate record provides evidence for polar amplification from multiple time periods associated with changes in CO_2 (Hollis et al., 2019; Cleator et al., 2020; McClymont et al., 2020; Tierney et al., 2020b), and allows an evaluation of polar amplification in model simulations of these periods (Section 7.4.4.1.2). Research since AR5 identifies changes in the degree of polar amplification over time, particularly in the SH, as a key factor affecting how radiative feedbacks may evolve in the future (Section 7.4.4.3).

[START FIGURE 7.12 HERE]

Figure 7.12: Contributions of effective radiative forcing, ocean heat uptake, atmospheric heat transport, and radiative feedbacks to regional surface temperature changes at year 100 of *abrupt4xCO2* simulations of CMIP6 ESMs. (a) Pattern of near-surface air temperature change. (b-d) Contributions to net Arctic (>60°N), tropical (30°S – 30°N), and Antarctic (<60°S) warming calculated by dividing regional-average energy inputs by the magnitude of the regional-average Planck response. The contributions from radiative forcing, changes in moist, dry-static, and total atmospheric energy transport, ocean heat uptake, and radiative feedbacks (orange bars) all sum to the value of net warming (grey bar). Inset shows regional warming contributions associated with individual feedbacks, all summing to the

total feedback contribution. Uncertainties show the interquartile range (25th and 75th percentiles) across models. The warming contributions (units of °C) for each process are diagnosed by calculating the energy flux (units of W m^{-2}) that each process contributes to the atmosphere over a given region, either at the TOA or surface, then dividing that energy flux by the magnitude of the regional Planck response (around 3.2 W m^{-2} °C^{-1} but varying with region). By construction, the individual warming contributions sum to the total warming in each region. Radiative kernel methods (see Section 7.4.1) are used to decompose the net energy input from radiative feedbacks into contributions from changes in atmospheric water vapour, lapse-rate, clouds, and surface albedo (Zelinka et al. (2020) using the Huang et al. (2017) radiative kernel). The CMIP6 models included are those analysed by Zelinka et al. (2020) and the warming contribution analysis is based on that of Goosse et al. (2018). Further details on data sources and processing are available in the chapter data table (Table 7.SM.14).

[END FIGURE 7.12 HERE]

7.4.4.1.1 Critical processes driving polar amplification

Several processes contribute to polar amplification under greenhouse gas forcing including the loss of sea ice and snow (an amplifying surface-albedo feedback), the confinement of warming to near the surface in the polar atmosphere (an amplifying lapse-rate feedback), and increases in poleward atmospheric and oceanic heat transport (Pithan and Mauritsen, 2014; Goosse et al., 2018; Dai et al., 2019; Feldl et al., 2020). Modelling and process studies since AR5 have led to an improved understanding of the combined effect of these different processes in driving polar amplification and how they differ between the hemispheres.

Idealized modelling studies suggest that polar amplification would occur even in the absence of any amplifying polar surface-albedo or lapse-rate feedbacks owing to changes in poleward atmospheric heat transport under global warming (Hall, 2004; Alexeev et al., 2005; Graversen and Wang, 2009; Alexeev and Jackson, 2013; Graversen et al., 2014; Roe et al., 2015; Merlis and Henry, 2018; Armour et al., 2019). Poleward heat transport changes reflect compensating changes in the transport of latent energy (moisture) and dry-static energy (sum of sensible and potential energy) by atmospheric circulations (Alexeev et al., 2005; Held and Soden, 2006; Hwang and Frierson, 2010; Hwang et al., 2011; Kay et al., 2012; Huang and Zhang, 2014; Feldl et al., 2017a; Donohoe et al., 2020). ESMs project that within the mid-latitudes, where eddies dominate the heat transport, an increase in poleward latent energy transport arises from an increase in the equator-to-pole gradient in atmospheric moisture with global warming, with moisture in the tropics increasing more than at the poles as described by the Clausius-Clapeyron relation (Chapter 8, Section 8.2). This change is partially compensated by a decrease in dry-static energy transport arising from a weakening of the equator-to-pole temperature gradient as the polar regions warm more than the tropics.

Energy balance models that approximate atmospheric heat transport in terms of a diffusive flux down the meridional gradient of near-surface moist static energy (sum of dry-static and latent energy) are able to reproduce the atmospheric heat transport changes seen within ESMs (Flannery, 1984; Hwang and Frierson, 2010; Hwang et al., 2011; Rose et al., 2014; Roe et al., 2015; Merlis and Henry, 2018), including the partitioning of latent and dry-static energy transports (Siler et al., 2018b; Armour et al., 2019). These models suggest that polar amplification is driven by enhanced poleward latent heat transport and that the magnitude of polar amplification can be enhanced or diminished by the latitudinal structure of radiative feedbacks. Amplifying polar feedbacks enhance polar warming and in turn cause a decrease in the dry-static energy transport to high latitudes (Alexeev and Jackson, 2013; Rose et al., 2014; Roe et al., 2015; Bonan et al., 2018; Merlis and Henry, 2018; Armour et al., 2019; Russotto and Biasutti, 2020). Poleward latent heat transport changes act to favour polar amplification and inhibit tropical amplification (Armour et al., 2019), resulting in a strongly polar-amplified warming response to polar forcing and a more latitudinally-uniform warming response to tropical forcing within ESMs (Alexeev et al., 2005; Rose et al., 2014; Stuecker et al., 2018). The important role for poleward latent energy transport in polar amplification is supported by studies of atmospheric reanalyses and ESMs showing that episodic increases in latent heat transport into the Arctic can enhance surface downwelling radiation and drive sea-ice loss on sub-seasonal timescales (Woods and Caballero, 2016; Gong et al., 2017; Lee et al., 2017; Luo et al., 2017a), however this may be a smaller driver of sea-ice variability than atmospheric temperature fluctuations (Olonscheck et al., 2019).

Regional energy budget analyses are commonly used to diagnose the relative contributions of radiative feedbacks and energy fluxes to polar amplification as projected by ESMs under increased CO_2 concentrations (Figure 7.12; Feldl and Roe, 2013; Pithan and Mauritsen, 2014; Goosse et al., 2018; Stuecker et al., 2018). These analyses suggest that a primary cause of amplified Arctic warming in ESMs is the latitudinal structure of radiative feedbacks, which warm the Arctic more than the tropics (Figure 7.12b), and enhanced latent energy transport into the Arctic. That net atmospheric heat transport into the Arctic does not change substantially within ESMs, on average, under CO_2 forcing (Figure 7.12b) reflects a compensating decrease in poleward dry-static energy transport as a response to polar amplified warming (Hwang et al., 2011; Armour et al., 2019; Donohoe et al., 2020). The latitudinal structure of radiative feedbacks primarily reflects that of the surface-albedo and lapse-rate feedbacks, which preferentially warm the Arctic (Graversen et al., 2014; Pithan and Mauritsen, 2014; Goosse et al., 2018). Latitudinal structure in the lapse-rate feedback reflects weak radiative damping to space with surface warming in polar regions, where atmospheric warming is constrained to the lower troposphere owing to stably stratified conditions, and strong radiative damping in the tropics, where warming is enhanced in the upper troposphere owing to moist convective processes. This is only partially compensated by latitudinal structure in the water vapour feedback (Taylor et al., 2013), which favours tropical warming (Pithan and Mauritsen, 2014). While cloud feedbacks have been found to play little role in Arctic amplification in CMIP5 models (Pithan and Mauritsen, 2014; Goosse et al., 2018; Figure 7.12b), less-negative cloud feedbacks at high latitude as seen within some CMIP6 models (Zelinka et al., 2020) tend to favour stronger polar amplification (Dong et al., 2020). A weaker Planck response at high latitudes, owing to less efficient radiative damping where surface and atmospheric temperatures are lower, also contributes to polar amplification (Pithan and Mauritsen, 2014). The effective radiative forcing of CO_2 is larger in the tropics than at high latitudes, suggesting that warming would be tropically amplified if not for radiative feedbacks and poleward latent heat transport changes (Stuecker et al., 2018; Figure 7.12b-d).

While the contributions to regional warming can be diagnosed within ESM simulations (Figure 7.12), assessment of the underlying role of individual factors is limited by interactions inherent to the coupled climate system. For example, polar feedback processes are coupled and influenced by warming at lower latitudes (Screen et al., 2012; Alexeev and Jackson, 2013; Graversen et al., 2014; Graversen and Burtu, 2016; Rose and Rencurrel, 2016; Feldl et al., 2017a; Yoshimori et al., 2017; Garuba et al., 2018; Po-Chedley et al., 2018a; Stuecker et al., 2018; Dai et al., 2019; Feldl et al., 2020), while atmospheric heat transport changes are in turn influenced by the latitudinal structure of regional feedbacks, radiative forcing, and ocean heat uptake (Hwang et al., 2011; Zelinka and Hartmann, 2012; Feldl and Roe, 2013; Huang and Zhang, 2014; Merlis, 2014; Rose et al., 2014; Roe et al., 2015; Feldl et al., 2017b; Stuecker et al., 2018; Armour et al., 2019). The use of different feedback definitions, such as a lapse-rate feedback partitioned into upper and lower tropospheric components (Feldl et al., 2020) or including the influence of water vapour at constant relative humidity (Held and Shell, 2012; Section 7.4.2), would also change the interpretation of which feedbacks contribute most to polar amplification.

The energy budget analyses (Figure 7.12) suggest that greater surface warming in the Arctic than the Antarctic under greenhouse gas forcing arises from two main processes. The first is large surface heat uptake in the Southern Ocean (Figure 7.12c) driven by the upwelling of deep waters that have not yet felt the effects of the radiative forcing; the heat taken up is predominantly transported away from Antarctica by northward-flowing surface waters (Marshall et al., 2015; Armour et al., 2016; Chapter 9, Section 9.2.1). Strong surface heat uptake also occurs in the subpolar North Atlantic Ocean under global warming (Chapter 9, Section 9.2.1). However, this heat is partially transported northward into the Arctic which leads to increased heat fluxes into the Arctic atmosphere (Rugenstein et al., 2013; Jungclaus et al., 2014; Koenigk and Brodeau, 2014; Marshall et al., 2015; Nummelin et al., 2017; Singh et al., 2017; Oldenburg et al., 2018; Figure 7.12b). The second main process contributing to differences in Arctic and Antarctic warming is the asymmetry in radiative feedbacks between the poles (Yoshimori et al., 2017; Goosse et al., 2018). This primarily reflects the weaker lapse-rate and surface-albedo feedbacks and more-negative cloud feedbacks in the SH high latitudes (Figure 7.12). However, note the SH cloud feedbacks are uncertain due to possible biases in the treatment of mixed phase clouds (Hyder et al., 2018). Idealized modelling suggests that the asymmetry in the polar lapse-rate feedback arises from the height of the Antarctic ice sheet precluding the formation of deep atmospheric inversions that are necessary to produce the stronger positive lapse-rate feedbacks seen in the Arctic (Salzmann, 2017; Hahn et al., 2020). ESM projections of the equilibrium response to CO_2 forcing show polar amplification in both hemispheres, but generally with less warming in the Antarctic than the Arctic (Li et al., 2013a; Yoshimori et al., 2017).

Because multiple processes contribute to polar amplification, it is a robust feature of the projected long-term response to greenhouse gas forcing in both hemispheres. At the same time, contributions from multiple processes make projections of the magnitude of polar warming inherently more uncertain than global mean warming (Holland and Bitz, 2003; Roe et al., 2015; Bonan et al., 2018; Stuecker et al., 2018). The magnitude of Arctic amplification ranges from a factor of two to four in ESM projections of 21st century warming (Chapter 4, Section 4.5.1). While uncertainty in both global and tropical warming under greenhouse gas forcing is dominated by cloud feedbacks (Vial et al., 2013; Section 7.5.7), uncertainty in polar warming arises from polar surface-albedo, lapse-rate, and cloud feedbacks, changes in atmospheric and oceanic poleward heat transport, and ocean heat uptake (Hwang et al., 2011; Mahlstein and Knutti, 2011; Pithan and Mauritsen, 2014; Bonan et al., 2018).

The magnitude of polar amplification also depends on the type of radiative forcing applied (Stjern et al., 2019; Chapter 4, Section 4.5.1.1), with Chapter 6, Section 6.4.3 discussing changes in sulphate aerosol emissions and the deposition of black carbon aerosols on ice and snow as potential drivers of amplified Arctic warming. The timing of the emergence of SH polar amplification remains uncertain due to insufficient knowledge of the timescales associated with Southern Ocean warming and the response to surface wind and freshwater forcing (Bintanja et al., 2013; Kostov et al., 2017, 2018; Pauling et al., 2017; Purich et al., 2018). ESM simulations indicate that freshwater input from melting ice shelves could reduce Southern Ocean warming by up to several tenths of a °C over the 21st century by increasing stratification of the surface ocean around Antarctica (Bronselaer et al., 2018; Golledge et al., 2019; Lago and England, 2019; Section 7.4.2.6; Chapter 9, Section 9.2.1 and Box 9.3) (*low confidence* due to *medium agreement* but *limited evidence*). However, even a large reduction in the Atlantic meridional overturning circulation (AMOC) and associated northward heat transport due, for instance, to greatly increased freshwater runoff from Greenland would be insufficient to eliminate Arctic amplification (Liu et al., 2017a, 2017b; Wen et al., 2018) (*medium confidence* based on to *medium agreement* and *medium evidence*).

Arctic amplification has a distinct seasonality with a peak in early winter (Nov–Jan) owing to sea-ice loss and associated increases in heat fluxes from the ocean to the atmosphere resulting in strong near-surface warming (Pithan and Mauritsen, 2014; Dai et al., 2019). Surface warming may be further amplified by positive cloud and lapse-rate feedbacks in autumn and winter (Burt et al., 2016; Morrison et al., 2018; Hahn et al., 2020). Arctic amplification is weak in summer owing to surface temperatures remaining stable as excess energy goes into thinning the summertime sea-ice cover, which remains at the melting point, or into the ocean mixed layer. Arctic amplification can also be interpreted through changes in the surface energy budget (Burt et al., 2016; Woods and Caballero, 2016; Boeke and Taylor, 2018; Kim et al., 2019), however such analyses are complicated by the finding that a large portion of the changes in downward longwave radiation can be attributed to the lower troposphere warming along with the surface itself (Vargas Zeppetello et al., 2019).

7.4.4.1.2 Polar amplification from proxies and models during past climates associated with CO_2 change

Paleoclimate proxy data provide observational evidence of large-scale patterns of surface warming in response to past forcings, and allow an evaluation of the modelled response to these forcings (Chapter 3, Section 3.3.1.1; Section 3.8.2.1). In particular, paleoclimate data provide evidence for long-term changes in polar amplification during time periods in which the primary forcing was a change in atmospheric CO_2, although data sparsity means that for some time periods this evidence may be limited to a single hemisphere or ocean basin, or the evidence may come primarily from the mid-latitudes as opposed to the polar regions. In this context, there has been a modelling and data focus on the Last Glacial Maximum (LGM) in the context of PMIP4 (Cleator et al., 2020; Tierney et al., 2020b; Kageyama et al., 2021), the mid-Pliocene warm period (MPWP) in the context of PlioMIP2 (Chapter 2, Cross-Chapter Box 2.4; Salzmann et al., 2013; Haywood et al., 2020; McClymont et al., 2020), the early Eocene climatic optimum (EECO) in the context of DeepMIP (Hollis et al., 2019; Lunt et al., 2021), and there is growing interest in the Miocene (Goldner et al., 2014b; Steinthorsdottir et al., 2020) (for definitions of time periods see Chapter 2, Cross-Chapter Box 2.1).

For all these time periods, in addition to the CO_2 forcing there are long-term feedbacks associated with ice sheets (Section 7.4.2.6), and in particular for the early Eocene there is a forcing associated with paleogeographic change (Farnsworth et al., 2019). However, because these non-CO_2 effects can all be included as boundary conditions in model simulations, these time periods allow an assessment of the patterns of modelled response to known forcing (although uncertainty in the forcing increases further back in time). Because these changes to boundary conditions can be complex to implement in models, and because long simulations (typically >500 years) are required to approach equilibrium, these simulations have been carried out mostly by pre-CMIP6 models, with relatively few (or none for the early Eocene) fully coupled CMIP6 models in the ensembles.

At the time of AR5, polar amplification was evident in proxy reconstructions of paleoclimate SST and SAT from the LGM, MPWP and the early Eocene, but uncertainties associated with proxy calibrations (Waelbroeck et al., 2009; Dowsett et al., 2012; Lunt et al., 2012a) and the role of orbital forcing (for the MPWP; Lisiecki and Raymo, 2005) meant that the degree of polar amplification during these time periods was not accurately known. Furthermore, although some models (CCSM3; Winguth et al., 2010; Huber and Caballero, 2011) at that time were able to reproduce the strong polar amplification implied by temperature proxies of the early Eocene, this was achieved at higher CO_2 concentrations (>2000 ppm) than those indicated by CO_2 proxies (<1500 ppm; Beerling and Royer, 2011).

Since AR5 there has been progress in improving the accuracy of proxy temperature reconstructions of the LGM (Cleator et al., 2020; Tierney et al., 2020b), the MPWP (McClymont et al., 2020), and the early Eocene (Hollis et al., 2019) time periods. In addition, reconstructions of the MPWP have been focused on a short time slice with an orbit similar to modern-day (isotopic stage KM5C; Haywood et al., 2013, 2016b). Furthermore, there are more robust constraints on CO_2 concentrations from the MPWP (Martínez-Botí et al., 2015; de la Vega et al., 2020) and the early Eocene (Anagnostou et al., 2016, 2020). As such, polar amplification during the LGM, MPWP, and early Eocene time periods can now be better quantified than at the time of AR5, and the ability of climate models to reproduce this pattern can be better assessed; model-data comparisons for SAT and SST for these three time periods are shown in Figure 7.13.

[START FIGURE 7.13 HERE]

Figure 7.13: Polar amplification in paleo proxies and models of the early Eocene climatic optimum (EECO), the mid-Pliocene warm period (MPWP), and the Last Glacial Maximum (LGM). Temperature anomalies compared with pre-industrial (equivalent to CMIP6 simulation *piControl*) are shown for the high-CO_2 EECO and MPWP time periods, and for the low-CO_2 LGM (expressed as pre-industrial minus LGM). (a,b,c) Modelled near-surface air temperature anomalies for ensemble-mean simulations of the (a) EECO (Lunt et al., 2021), (b) MPWP (Haywood et al., 2020; Zhang et al., 2021), and (c) LGM (Kageyama et al., 2021; Zhu et al., 2021). Also shown are proxy near-surface air temperature anomalies (coloured circles). (d,e,f) Proxy near-surface air temperature anomalies (grey circles), including published uncertainties (grey vertical bars), model ensemble mean zonal mean anomaly (solid red line) for the same model ensembles as in (a,b,c), light red lines show the modelled temperature anomaly for the individual models that make up each ensemble (LGM, N=9; MPWP, N=17; EECO, N=5). Black dashed lines show the average of the proxy values in each latitude bands 90°S to 30°S, 30°S to 30°N, and 30°N to 90°N. Red dashed lines show the same banded average in the model ensemble mean, calculated from the same locations as the proxies. Black and red dashed lines are only shown if there are 5 or more proxy points in that band. Mean differences between the 90°S/N to 30°S/N and 30°S to 30°N bands are quantified for the models and proxies in each plot. Panels (g,h,i) are like panels (d,e,f) but for SST instead of near-surface air temperature. Panels (j,k,l) are like panels (a,b,c) but for SST instead of near-surface air temperature. For the EECO maps (a,j), the anomalies are relative to the zonal mean of the pre-industrial, due to the different continental configuration. Proxy datasets are (a,d) Hollis et al. (2019), (b,e) Salzmann et al. (2013); Vieira et al. (2018), (c,f) Cleator et al. (2020) at the sites defined in Bartlein et al. (2011), (g,j)) Hollis et al. (2019), (h,k) McClymont et al. (2020) (i,l) Tierney et al. (2020b). Where there are multiple proxy estimations at a single site, a mean is taken. Model ensembles are (a,d,g,j) DeepMIP (only model simulations carried out with a mantle-frame paleogeography, and carried out under CO_2 concentrations within the range assessed in Chapter 2, Table 2.2, are shown), (b,e,h,k) PlioMIP, and (c,f,i,l) PMIP4. Further details on data sources and processing are available in the chapter data table (Table 7.SM.14).

[END FIGURE 7.13 HERE]

Since AR5, there has been progress in the simulation of polar amplification by paleoclimate models of the early Eocene. Initial work indicated that changes to model parameters associated with aerosols and/or clouds could increase simulated polar amplification and improve agreement between models and paleoclimate data (Kiehl and Shields, 2013; Sagoo et al., 2013), but such parameter changes were not physically based. In support of these initial findings, a more recent (CMIP5) climate model, that includes a process-based representation of cloud microphysics, exhibits polar amplification in better agreement with proxies when compared to the models assessed in AR5 (Zhu et al., 2019b). Since then, some other CMIP3 and CMIP5 models in the DeepMIP multi-model ensemble (Lunt et al., 2021) have obtained polar amplification for the EECO that is consistent with proxy indications of both polar amplification and CO_2. Although there is a lack of tropical proxy SAT estimates, both proxies and DeepMIP models show greater terrestrial warming in the high latitudes than the mid-latitudes in both Hemispheres (Figure 7.13a,d). SST proxies also exhibit polar amplification in both Hemispheres, but the magnitude of this polar amplification is too low in the models, in particular in the southwest Pacific (Figure 7.13g,j).

For the MPWP, model simulations are now in better agreement with proxies than at the time of AR5 (Haywood et al., 2020; McClymont et al., 2020). In particular, in the tropics new proxy reconstructions of SSTs are warmer and in better agreement with the models, due in part to the narrower time window in the proxy reconstructions. There is also better agreement at higher latitudes (primarily in the North Atlantic), due in part to the absence of some very warm proxy SSTs due to the narrower time window (McClymont et al., 2020), and in part to a modified representation of Arctic gateways in the most recent Pliocene model simulations (Otto-Bliesner et al., 2017), which have resulted in warmer modelled SSTs in the North Atlantic (Haywood et al., 2020). Furthermore, as for the Eocene, improvements in the representation of aerosol-cloud interactions has also led to improved model-data consistency at high latitudes (Feng et al., 2019). Although all PlioMIP2 models exhibit polar amplification of SAT, due to the relatively narrow time window there are insufficient terrestrial proxies to assess this (Figure 7.13b,e). However, polar SST amplification in the PlioMIP2 ensemble mean is in reasonably good agreement with that from SST proxies in the Northern Hemisphere (Figure 7.13h,k).

The Last Glacial Maximum (LGM) also gives an opportunity to evaluate model simulation of polar amplification under CO_2 forcing, albeit under colder conditions than today (Kageyama et al., 2021). Terrestrial SAT and marine SST proxies exhibit clear polar amplification in the Northern Hemisphere, and the PMIP4 models capture this well (Figure 7.13c,f,i,l), in particular for SAT. There is less proxy data in the mid to high latitudes of the Southern Hemisphere, but here the models exhibit polar amplification of both SST and SAT. LGM regional model-data agreement is also assessed in Chapter 3, Section 3.8.2.

Overall, the proxy reconstructions give *high confidence* that there was polar amplification in the LGM, MPWP and EECO, and this is further supported by model simulations of these time periods (Zhu et al., 2019b; Haywood et al., 2020; Kageyama et al., 2021; Lunt et al., 2021; Figure 7.13). For both the MPWP and EECO, models are more consistent with the temperature and CO_2 proxies than at the time of AR5 (*high confidence*). For the LGM Northern Hemisphere, which is the region with the most data and the time period with the least uncertainty in model boundary conditions, polar amplification in the PMIP4 ensemble mean is in good agreement with the proxies, especially for SAT (*medium confidence*). Overall, the confidence in the ability of models to accurately simulate polar amplification is higher than at the time of AR5, but a more complete model evaluation could be carried out if there were more CMIP6 paleoclimate simulations included in the assessment.

7.4.4.1.3 Overall assessment of polar amplification

Based on mature process understanding of the roles of poleward latent heat transport and radiative feedbacks in polar warming, a high degree of agreement across a hierarchy of climate models, observational evidence, paleoclimate proxy records of past climates associated with CO_2 change, and ESM simulations of those past climates, there is *high confidence* that polar amplification is a robust feature of the long-term response to greenhouse gas forcing in both hemispheres. Stronger warming in the Arctic than in the global average has already been observed (Chapter 2, Section 2.3.1) and its causes are well understood. It is *very likely* that the warming in the Arctic will be more pronounced than on global average over the 21st century (*high confidence*) (Chapter 4, Section 4.5.1.1). This is supported by models' improved ability to simulate polar amplification during past time periods, compared with at the time of AR5 (*high confidence*); although this is based on an assessment of mostly non-CMIP6 models.

Southern Ocean SSTs have been slow to warm over the instrumental period, with cooling since about 1980 owing to a combination of upper-ocean freshening from ice-shelf melt, intensification of surface westerly winds from ozone depletion, and variability in ocean convection (Chapter 9, Section 9.2.1). This stands in contrast to the equilibrium warming pattern either inferred from the proxy record or simulated by ESMs under CO_2 forcing. There is *high confidence* that the SH high latitudes will warm more than the tropics on centennial timescales as the climate equilibrates with radiative forcing and Southern Ocean heat uptake is reduced. However, there is only *low confidence* that this feature will emerge this century.

7.4.4.2 Tropical Pacific sea-surface temperature gradients

Research published since AR5 identifies changes in the tropical Pacific Ocean zonal SST gradient over time as a key factor affecting how radiative feedbacks may evolve in the future (Section 7.4.4.3). There is now a much-improved understanding of the processes that govern the tropical Pacific SST gradient (Section 7.4.4.2.1) and the paleoclimate record provides evidence for its equilibrium changes from time periods associated with changes in CO_2 (Section 7.4.4.2.2).

7.4.4.2.1 Critical processes determining changes in tropical Pacific sea-surface temperature gradients

A weakening of the equatorial Pacific Ocean east-west SST gradient, with greater warming in the East than the west, is a common feature of the climate response to greenhouse gas forcing as projected by ESMs on centennial and longer timescales (e.g., Figure 7.14b) (Chapter 4, Section 4.5.1). There are thought to be several factors contributing to this pattern. In the absence of any changes in atmospheric or oceanic circulations, the east-west surface temperature difference is theorized to decrease owing to weaker evaporative damping, and thus greater warming in response to forcing, where climatological temperatures are lower in the eastern Pacific cold tongue (Xie et al., 2010; Luo et al., 2015). Within atmospheric ESMs coupled to mixed-layer ocean, this gradient in damping has been linked to the rate of change with warming of the saturation specific humidity, which is set by the Clausius-Clapeyron relation (Merlis and Schneider, 2011). Gradients in low-cloud feedbacks may also favour eastern equatorial Pacific warming (DiNezio et al., 2009).

In the coupled climate system, changes in atmospheric and oceanic circulations will influence the east-west temperature gradient as well. It is expected that as global temperature increases and as the east-west temperature gradient weakens, east-west sea-level pressure gradients and easterly trade winds (characterizing the Walker circulation) will weaken as well (Vecchi et al., 2006, 2008; Figure 7.14b; Chapter 8, Sections 8.2.2.2 and 8.4.2.3; Chapter 4, Section 4.5.3). This would, in turn, weaken the east-west temperature gradient through a reduction of equatorial upwelling of cold water in the east Pacific and a reduction in the transport of warmer water to the western equatorial Pacific and Indian Ocean (England et al., 2014; Dong and McPhaden, 2017; Li et al., 2017; Maher et al., 2018).

Research published since AR5 (Burls and Fedorov, 2014a; Fedorov et al., 2015; Erfani and Burls, 2019) has built on an earlier theory (Liu and Huang, 1997; Barreiro and Philander, 2008) linking the east-west temperature gradient to the north-south temperature gradient. In particular, model simulations suggest that a reduction in the equator-to-pole temperature gradient (polar amplification) increases the temperature of water subducted in the extra-tropics, which in turn is upwelled in the eastern Pacific. Thus, polar amplified warming, with greater warming in the mid-latitudes and subtropics than in the deep tropics, is expected to contribute to the weakening of the east-west equatorial Pacific SST gradient on decadal to centennial timescales.

The transient adjustment of the equatorial Pacific SST gradient is influenced by upwelling waters which delay surface warming in the east since they have not been at the surface for years-to-decades to experience the greenhouse gas forcing. This 'thermostat mechanism' (Clement et al., 1996; Cane et al., 1997) is not thought to persist to equilibrium since it does not account for the eventual increase in temperatures of upwelled waters (Liu et al., 2005; Xie et al., 2010; Luo et al., 2017b) which will occur as the subducting waters in mid-latitudes warm by more than the tropics on average as polar amplification emerges. An individual CMIP5 ESM (GFDL's ESM2M) has been found to exhibit a La Niña–like pattern of Pacific temperature change through the 21st century, similar to the SST trends seen over the historical record (Chapter 9, Section 9.2.1; Figure 7.14a), owing to a weakening asymmetry between El Niño and La Niña events (Kohyama et al., 2017), but this pattern of warming may not persist to equilibrium (Paynter et al., 2018).

Since 1870, observed SSTs in the tropical western Pacific Ocean have increased while those in the tropical eastern Pacific Ocean have changed less (Figure 7.14a; Chapter 9, Section 9.2.1). Much of the resultant strengthening of the equatorial Pacific temperature gradient has occurred since about 1980 due to strong warming in the west and cooling in the east (Chapter 2, Figure 2.11b) concurrent with an intensification of the surface equatorial easterly trade winds and Walker Circulation (England et al., 2014; Chapter 3, Section 3.3.3.1, Section 3.7.6, Figure 3.16f, Figure 3.39f; Chapter 8, Section 8.3.2.3; Chapter 9, Section 9.2). This temperature pattern is also reflected in regional ocean heat content trends and sea level changes observed from satellite altimetry since 1993 (Bilbao et al., 2015; Richter et al., 2020). The observed changes may have been influenced by one or a combination of temporary factors including sulphate aerosol forcing (Smith et al., 2016; Takahashi and Watanabe, 2016; Hua et al., 2018), internal variability within the Indo-Pacific Ocean (Luo et al., 2012; Chung et al., 2019), teleconnections from multi-decadal tropical Atlantic SST trends (Kucharski et al., 2011, 2014, 2015; McGregor et al., 2014; Chafik et al., 2016; Li et al., 2016a; Kajtar et al., 2017; Sun et al., 2017), teleconnections from multi-decadal Southern Ocean SST trends (Hwang et al., 2017), and coupled ocean–atmosphere dynamics which slow warming in the equatorial eastern Pacific (Clement et al., 1996; Cane et al., 1997; Seager et al., 2019). CMIP3 and CMIP5 ESMs have difficulties replicating the observed trends in the Walker Circulation and Pacific Ocean SSTs over the historical record (Sohn et al., 2013; Zhou et al., 2016; Coats and Karnauskas, 2017), possibly due to model deficiencies including insufficient multi-decadal Pacific Ocean SST variability (Laepple and Huybers, 2014; Bilbao et al., 2015; Chung et al., 2019), mean state biases affecting the forced response or the connection between Atlantic and Pacific basins (Kucharski et al., 2014; Kajtar et al., 2018; Luo et al., 2018; McGregor et al., 2018; Seager et al., 2019), and/or a misrepresentation of radiative forcing (Chapter 9, Section 9.2.1 and Chapter 3, Section 3.7.6). However, the observed trends in the Pacific Ocean SSTs are still within the range of internal variability as simulated by large initial condition ensembles of CMIP5 and CMIP6 models (Olonscheck et al., 2020; Watanabe et al., 2020a). Because the causes of observed equatorial Pacific temperature gradient and Walker circulation trends are not well understood (Chapter 3, Section 3.3.3.1), there is *low confidence* in their attribution to anthropogenic influences (Chapter 8, Section 8.3.2.3), while there is *medium confidence* that the observed changes have resulted from internal variability (Chapter 8, Section 8.2.2.2; Chapter 3, Section 3.7.6).

7.4.4.2.2 Tropical Pacific temperature gradients in past high-CO_2 climates

AR5 stated that paleoclimate proxies indicate a reduction in the longitudinal SST gradient across the equatorial Pacific during the mid-Pliocene warm period (MPWP; Cross-Chapter Box 2.1; Cross-Chapter Box 2.4; Masson-Delmotte et al., 2013). This assessment was based on SST reconstructions between two sites situated very close to the equator in the heart of the western Pacific warm pool and eastern Pacific cold tongue, respectively. Multiple SST reconstructions based on independent paleoclimate proxies generally agreed that during the Pliocene the SST gradient between these two sites was reduced compared with the modern long-term mean (Wara et al., 2005; Dekens et al., 2008; Fedorov et al., 2013).

Since AR5, the generation of new SST records has led to a variety of revised gradient estimates, specifically the generation of a new record for the warm pool (Zhang et al., 2014), the inclusion of SST reconstructions from sites in the South China Sea as warm pool estimates (O'Brien et al., 2014; Zhang et al., 2014), and the inclusion of several new sites from the eastern Pacific as cold tongue estimates (Zhang et al., 2014; Fedorov et al., 2015). Published estimates of the reduction in the longitudinal SST difference for the Late Pliocene, relative to either Late Quaternary (0-0.5Ma) or pre-industrial values, include 1 to 1.5°C (Zhang et al., 2014), 0.1 to 1.9°C (Tierney et al., 2019), and about 3°C (Ravelo et al., 2014; Fedorov et al., 2015; Wycech et al., 2020). All of these studies report a further weakening of the longitudinal gradient based on records extending into the Early Pliocene. While these revised estimates differ in magnitude due to differences in the sites and SST proxies used, they all agree that the longitudinal gradient was weaker, and this is supported by the probabilistic approach of Tierney et al. (2019). However, given that there are currently relatively few western equatorial Pacific records from independent site locations, and due to uncertainties associated with the proxy calibrations (Haywood et al., 2016a), there is only *medium confidence* that the average longitudinal gradient in the tropical Pacific was weaker during the Pliocene than during the Late Quaternary.

To avoid the influence of local biases, changes in the longitudinal temperature difference within Pliocene model simulations are typically evaluated using domain-averaged SSTs within chosen east and west Pacific regions and as such there is sensitivity to methodology. Unlike the reconstructed estimates, longitudinal gradient changes simulated by the Pliocene Model Intercomparison Project Phase 1 (PlioMIP1) models do not agree on the change in sign and are reported as spanning approximately –0.5 to 0.5 °C by Brierley et al. (2015) and approximately –1 to 1 °C by Tierney et al. (2019). Initial PlioMIP Phase 2 (PlioMIP2) analysis suggests responses similar to PlioMIP1 (Feng et al., 2019; Haywood et al., 2020). Models that include hypothetical modifications to cloud albedo or ocean mixing are required to simulate the substantially weaker longitudinal differences seen in reconstructions of the early Pliocene (Fedorov et al., 2013; Burls and Fedorov, 2014b).

While more western Pacific warm pool temperature reconstructions are needed to refine estimates of the longitudinal gradient, several Pliocene SST reconstructions from the east Pacific indicate enhanced warming in the centre of the eastern equatorial cold tongue upwelling region (Liu et al., 2019). This enhanced warming in the east Pacific cold tongue appears to be dynamically consistent with reconstruction of enhanced subsurface warming (Ford et al., 2015) and enhanced warming in coastal upwelling regions, suggesting that the tropical thermocline was deeper and/or less stratified during the Pliocene. The Pliocene data therefore suggests that the observed cooling trend over the last 60 years in parts of the eastern equatorial Pacific (Seager et al., 2019; Chapter 9, Section 9.2.1.1; Figure 9.3), whether forced or due to internal variability, involves transient processes that are probably distinct from the longer-timescale process (Burls and Fedorov, 2014a, 2014b; Luo et al., 2015; Heede et al., 2020) that maintained warmer eastern Pacific SST during the Pliocene.

7.4.4.2.3 Overall assessment of tropical Pacific sea-surface temperature gradients under CO_2 forcing

The paleoclimate proxy record and ESM simulations of the MPWP, process understanding, and ESM projections of climate response to CO_2 forcing provide medium evidence and a medium degree of agreement and thus *medium confidence* that equilibrium warming in response to elevated CO_2 will be characterized by a weakening of the east-west tropical Pacific SST gradient.

Overall the observed pattern of warming over the instrumental period, with a warming minimum in the eastern tropical Pacific Ocean (Figure 7.14a), stands in contrast to the equilibrium warming pattern either inferred from the MPWP proxy record or simulated by ESMs under CO_2 forcing. There is *medium confidence* that the observed strengthening of the east-west SST gradient is temporary and will transition to a weakening of the SST gradient on centennial timescales. However, there is only *low confidence* that this transition will emerge this century owing to a low degree of agreement across studies about the factors driving the observed strengthening of the east-west SST gradient and how those factors will evolve in the future. These trends in tropical Pacific SST gradients reflect changes in the climatology, rather than changes in ENSO amplitude or variability, which are assessed in Chapter 4, Section 4.3.3.

7.4.4.3 Dependence of feedbacks on temperature patterns

The expected time-evolution of the spatial pattern of surface warming in the future has important implications for values of ECS inferred from the historical record of observed warming. In particular, changes in the global TOA radiative energy budget can be induced by changes in the regional variations of surface temperature, even without a change in the global mean temperature (Zhou et al., 2016; Ceppi and Gregory, 2019). Consequently, the global radiative feedback, characterizing the net TOA radiative response to global surface warming, depends on the *spatial pattern* of that warming. Therefore, if the equilibrium warming pattern under CO_2 forcing (similar to CMIP6 projections in Fig. 7.12a) is distinct from that observed over the historical record or indicated by paleoclimate proxies (Sections 7.4.4.1 and 7.4.4.2), then ECS will be different from the effective ECS (Box 7.1) that is inferred from those periods. Accounting for the dependence of radiative feedbacks on the spatial pattern of warming has helped to reconcile values of ECS inferred from the historical record with values of ECS based on other lines of evidence and simulated by climate models (Armour, 2017; Proistosescu and Huybers, 2017; Andrews et al., 2018; Section 7.5.2.1) but has not yet been examined in the paleoclimate context.

This temperature "pattern effect" (Stevens et al., 2016) can result from both internal variability and radiative forcing of the climate system. Importantly, it is distinct from potential radiative feedback dependencies on the global surface temperature, which are assessed in Section 7.4.3. While changes in global radiative feedbacks under transient warming have been documented in multiple generations of climate models (Williams et al., 2008; Andrews et al., 2015; Ceppi and Gregory, 2017; Dong et al., 2020), research published since AR5 has developed a much-improved understanding of the role of evolving SST patterns in driving feedback changes (Armour et al., 2013; Andrews et al., 2015, 2018, Zhou et al., 2016, 2017b; Gregory and Andrews, 2016; Proistosescu and Huybers, 2017; Ceppi and Gregory, 2017; Haugstad et al., 2017; Andrews and Webb, 2018; Silvers et al., 2018; Marvel et al., 2018; Dong et al., 2019, 2020). This section assesses process understanding of the pattern effect, which is dominated by the evolution of SSTs. Section 7.5.2.1 describes how potential feedback changes associated with the pattern effect are important to interpreting ECS estimates based on historical warming.

The radiation changes most sensitive to warming patterns are those associated with the low-cloud cover (affecting global albedo) and the tropospheric temperature profile (affecting thermal emission to space) (Ceppi and Gregory, 2017; Zhou et al., 2017b; Andrews et al., 2018; Dong et al., 2019). The mechanisms and radiative effects of these changes are illustrated in Figure 7.14a,b. SSTs in regions of deep convective ascent (e.g., in the western Pacific warm pool) govern the temperature of the tropical free troposphere and, in turn, affect low clouds through the strength of the inversion that caps the boundary layer (i.e., the lower-tropospheric stability) in subsidence regions (Wood and Bretherton, 2006; Klein et al., 2017). Surface warming within ascent regions thus warms the free troposphere and increases low-cloud cover, causing an increase in emission of thermal radiation to space and a reduction in absorbed solar radiation. In contrast, surface warming in regions of overall descent preferentially warms the boundary layer and enhances convective mixing with the dry free troposphere, decreasing low-cloud cover (Bretherton et al., 2013; Qu et al., 2014; Zhou et al., 2015). This leads to an increase in absorption of solar radiation but little change in thermal emission to space. Consequently, warming in tropical ascent regions results in negative lapse-rate and cloud feedbacks while warming in tropical descent regions results in positive lapse-rate and cloud feedbacks (Figure 7.14; Rose and Rayborn, 2016; Zhou et al., 2017b; Andrews and Webb, 2018; Dong et al., 2019). Surface warming in mid-to-high latitudes causes a weak radiative response owing to compensating changes in thermal emission (Planck and lapse-rate feedbacks) and absorbed solar radiation (shortwave cloud and surface-albedo feedbacks) (Rose and Rayborn, 2016; Dong et al., 2019), however this compensation may weaken due to less-negative shortwave cloud feedbacks at high warming (Frey and Kay, 2018; Bjordal et al., 2020; Dong et al., 2020).

[START FIGURE 7.14 HERE]

Figure 7.14: Illustration of tropospheric temperature and low-cloud response to observed and projected Pacific Ocean sea-surface temperature trends; adapted from Mauritsen (2016). (a) Atmospheric response to linear sea-surface temperature trend observed over 1870–2019 (HadISST1 dataset; Rayner et al., 2003).

(b) Atmospheric response to linear sea-surface temperature trend over 150 years following *abrupt4xCO2* forcing as projected by CMIP6 ESMs (Dong et al., 2020). Relatively large historical warming in the western tropical Pacific has been communicated aloft (a shift from grey to red atmospheric temperature profile), remotely warming the tropical free troposphere and increasing the strength of the inversion in regions of the tropics where warming has been slower, such as the eastern equatorial Pacific. In turn, an increased inversion strength has increased the low-cloud cover (Zhou et al., 2016) causing an anomalously-negative cloud and lapse-rate feedbacks over the historical record (Andrews et al., 2018; Marvel et al., 2018). Relatively large projected warming in the eastern tropical Pacific is trapped near the surface (shift from grey to red atmospheric temperature profile), decreasing the strength of the inversion locally. In turn, a decreased inversion strength combined with surface warming is projected to decrease the low-cloud cover, causing the cloud and lapse-rate feedbacks to become less negative in the future. Further details on data sources and processing are available in the chapter data table (Table 7.SM.14).

[END FIGURE 7.14 HERE]

The spatial pattern of SST changes since 1870 shows relatively little warming in key regions of less-negative radiative feedbacks, including the eastern tropical Pacific Ocean and Southern Ocean (Sections 7.4.4.1 and 7.4.4.2; Figure 7.14a; Chapter 2, Figure 2.11b). Cooling in these regions since 1980 has occurred along with an increase in the strength of the capping inversion in tropical descent regions, resulting in an observed increase in low-cloud cover over the tropical eastern Pacific (Zhou et al., 2016; Ceppi and Gregory, 2017; Fueglistaler and Silvers, 2021; Figure 7.14a). Thus, tropical low-cloud cover increased over recent decades even as global surface temperature increased, resulting in a negative low-cloud feedback which is at odds with the positive low-cloud feedback expected for the pattern of equilibrium warming under CO_2 forcing (Section 7.4.2.4; Figure 7.14b).

Andrews et al. (2018) analysed available CMIP5/6 ESM simulations (six in total) comparing effective feedback parameters diagnosed within atmosphere-only ESMs using prescribed historical SST and sea-ice concentration patterns with the equilibrium feedback parameters as estimated within coupled ESMs (using identical atmospheres) driven by abrupt $4\times CO_2$ forcing. The atmosphere-only ESMs show pronounced multi-decadal variations in their effective feedback parameters over the last century, with a trend toward strongly negative values since about 1980 owing primarily to negative shortwave cloud feedbacks driven by warming in the western equatorial Pacific Ocean and cooling in the eastern equatorial Pacific Ocean (Zhou et al., 2016; Andrews et al., 2018; Marvel et al., 2018; Dong et al., 2019). Yet, all six models show a less-negative net feedback parameter under *abrupt4xCO2* than for the historical period (based on regression since 1870 following Andrews et al., 2018). The average change in net feedback parameter between the historical period and the equilibrium response to CO_2 forcing, denoted here as α', for these simulations is α' = +0.6 W $m^{-2}\,°C^{-1}$ (+0.3 to +1.0 W $m^{-2}\,°C^{-1}$ range across models) (Figure 7.15b). These feedback parameter changes imply that the value of ECS may be substantially larger than that inferred from the historical record (Section 7.5.2.1). These findings can be understood from the fact that, due to a combination of internal variability and transient response to forcing (Section 7.4.4.2), historical sea-surface warming has been relatively large in regions of tropical ascent (Figure 7.14a), leading to an anomalously large net negative radiative feedback; however, future warming is expected to be largest in tropical descent regions, such as the eastern equatorial Pacific, and at high latitudes (Sections 7.4.4.1 and 7.4.4.2; Figure 7.14b), leading to a less-negative net radiative feedback and higher ECS.

A similar behaviour is seen within transient simulations of coupled ESMs, which project SST warming patterns that are initially characterised by relatively large warming rates in the western equatorial Pacific Ocean on decadal timescales and relatively large warming in the eastern equatorial Pacific and Southern Ocean on centennial timescales (Andrews et al., 2015; Proistosescu and Huybers, 2017; Dong et al., 2020). Recent studies based on simulations of 1% yr^{-1} CO_2 increase (*1pctCO2*) or *abrupt4xCO2* as analogues for historical warming suggest characteristic values of α' = +0.05 W $m^{-2}\,°C^{-1}$ (–0.2 to +0.3 W $m^{-2}\,°C^{-1}$ range across models) based on CMIP5 and CMIP6 ESMs (Armour 2017, Lewis and Curry 2018, Dong et al. 2020). Using historical simulations of one CMIP6 ESM (HadGEM3-GC3.1-LL), Andrews et al., (2019) find an average feedback parameter change of α' = +0.2 W $m^{-2}\,°C^{-1}$(–0.2 to +0.6 W $m^{-2}\,°C^{-1}$ range across four ensemble members). Using historical simulations from another CMIP6 ESM (GFDL CM4.0), Winton et al.

(2020) find an average feedback parameter change of α' = +1.5 W m^{-2} °C^{-1}(+1.2 to +1.7 W m^{-2} °C^{-1} range across three ensemble members). This value is larger than the α' = +0.7 W m^{-2} °C^{-1} within GFDL CM4.0 for historical CO_2 forcing only, suggesting that the value of α' may depend on historical non-CO_2 forcings such as those associated with tropospheric and stratospheric aerosols (Marvel et al., 2016; Gregory et al., 2020; Winton et al., 2020).

The magnitude of the net feedback parameter change α' found within coupled CMIP5 and CMIP6 ESMs is generally smaller than that found when prescribing observed warming patterns within atmosphere-only ESMs (Andrews et al., 2018; Figure 7.15). This arises from the fact that the forced spatial pattern of warming within transient simulations of most coupled ESMs are distinct from observed warming patterns over the historical record in key regions such as the equatorial Pacific Ocean and Southern Ocean (Sections 7.4.4.1 and 7.4.4.2), while being more similar to the equilibrium pattern simulated under *abrupt4xCO2*. However, historical simulations with HadGEM3-GC3.1-LL (Andrews et al., 2019) and GFDL CM4.0 (Winton et al., 2020) show substantial spread in the value of α' across ensemble members, indicating a potentially important role for internal variability in setting the magnitude of the pattern effect over the historical period. Using the 100-member historical simulation ensemble of MPI- ESM1.1, Dessler et al. (2018) find that internal climate variability alone results in a 0.5 W m^{-2} °C^{-1} spread in the historical effective feedback parameter, and thus also in the value of α'. Estimates of α' using prescribed historical warming patterns provide a more realistic representation of the historical pattern effect because they account for the net effect of the transient response to historical forcing and internal variability in the observed record (Andrews et al., 2018).

The magnitude of α', as quantified by ESMs, depends on the accuracy of both the projected patterns of SST and sea-ice concentration changes in response to CO_2 forcing and the radiative response to those patterns (Andrews et al., 2018). Model biases that affect the long-term warming pattern (e.g., SST and relative humidity biases in the equatorial Pacific cold tongue as suggested by Seager et al. (2019)) will affect the value of α'. The value of α' also depends on the accuracy of the historical SST and sea-ice concentration conditions prescribed within atmosphere-only versions of ESMs to quantify the historical radiative feedback (Figure 7.15b). Historical SSTs are particularly uncertain for the early portion of the historical record (Chapter 2, Section 2.3.1), and there are few constraints on sea-ice concentration prior to the satellite era. Using alternative SST datasets, Andrews et al. (2018) found little change in the value of α' within two models (HadGEM3 and HadAM3), while Lewis and Mauritsen (2020) found a smaller value of α' within two other models (ECHAM6.3 and CAM5). The sensitivity of results to the choice of dataset represents a major source of uncertainty in the quantification of the historical pattern effect using atmosphere-only ESMs that has yet to be systematically explored, but the preliminary findings of Lewis and Mauritsen (2020) and Fueglistaler and Silvers (2021) suggest that α' could be smaller than the values reported in Andrews et al. (2018).

[START FIGURE 7.15 HERE]

Figure 7.15: Relationship between *historical* and *abrupt4xCO2* net radiative feedbacks in ESMs. (a) Radiative feedbacks in CMIP6 ESMs estimated under historical forcing (values for GFDL CM4.0 and HadGEM3-CG3.1-LL from Winton et al. (2020) and Andrews et al. (2019), respectively); horizontal lines show the range across ensemble members. The other points show effective feedback values for 29 ESMs estimated using regression over the first 50 years of *abrupt4xCO2* simulations as an analogue for historical warming (Dong et al., 2020). (b) Historical radiative feedbacks estimated from atmosphere-only ESMs with prescribed observed sea-surface temperature and sea-ice concentration changes (Andrews et al. 2018) based on a linear regression of global TOA radiation against global near-surface air temperature over the period 1870–2010 (pattern of warming similar to Figure 7.14a) and compared with equilibrium feedbacks in a *abrupt4xCO2* simulations of coupled versions of the same ESMs (pattern of warming similar to Figure 7.14b). In all cases, the equilibrium feedback magnitudes are estimated as CO_2 ERF divided by ECS where ECS is derived from regression over years 1–150 of *abrupt4xCO2* simulations (Box 7.1); similar results are found if the equilibrium feedback is estimated directly from the slope of the linear regression. Further details on data sources and processing are available in the chapter data table (Table 7.SM.14).

[END FIGURE 7.15 HERE]

While there are not yet direct observational constraints on the magnitude of the pattern effect, satellite measurements of variations in TOA radiative fluxes show strong co-variation with changing patterns of SSTs, with a strong dependence on SST changes in regions of deep convective ascent (e.g., in the western Pacific warm pool) (Loeb et al., 2018b; Fueglistaler, 2019). Cloud and TOA radiation responses to observed warming patterns in atmospheric models have been found to compare favourably with those observed by satellite (Zhou et al., 2016; Loeb et al., 2020; Section 7.2.2.1; Figure 7.3). This observational and modelling evidence indicates the potential for a strong pattern effect in nature that will only be negligible if the observed pattern of warming since pre-industrial levels persists to equilibrium – an improbable scenario given that Earth is in a relatively early phase of transient warming and that reaching equilibrium would take multiple millennia (Li et al., 2013a). Moreover, paleoclimate proxies, ESM simulations, and process understanding indicate that strong warming in the eastern equatorial Pacific Ocean (with *medium confidence*) and Southern Ocean (with *high confidence*) will emerge on centennial timescales as the response to CO_2 forcing dominates temperature changes in these regions (Sections 7.4.4.1; 7.4.4.2; Chapter 9, Section 9.2.1). However, there is *low confidence* that these features, which have been largely absent over the historical record, will emerge this century (Sections 7.4.4.1; 7.4.4.2; Chapter 9, Section 9.2.1). This leads to *high confidence* that radiative feedbacks will become less negative as the CO_2-forced pattern of surface warming emerges ($\alpha' > 0$ W m^{-2} °C^{-1}), but *low confidence* that these feedback changes will be realized this century. There is also substantial uncertainty in the magnitude of the net radiative feedback change between the present warming pattern and the projected equilibrium warming pattern in response to CO_2 forcing owing to the fact that its quantification currently relies solely on ESM results and is subject to uncertainties in historical SST patterns. Thus, based on the pattern of warming since 1870, α' is estimated to be in the range 0.0 to 1.0 W m^{-2} °C^{-1} but with a *low confidence* in the upper end of this range. A value of $\alpha' = +0.5 \pm 0.5$ W m^{-2} °C^{-1} is used to represent this range in Box 7.2 and Section 7.5.2, which respectively assess the implications of changing radiative feedbacks for Earth's energy imbalance and estimates of ECS based on the instrumental record. The value of α' is larger if quantified based on the observed pattern of warming since 1980 (Chapter 2, Figure 2.11b) which is more distinct from the equilibrium warming pattern expected under CO_2 forcing (similar to CMIP6 projections shown in Figure 7.12a) (Andrews et al., 2018) (*high confidence*).

7.5 Estimates of ECS and TCR

Equilibrium climate sensitivity (ECS) and transient climate response (TCR) are metrics of the global surface air temperature (GSAT) response to forcing, as defined in Section 7.1; Box 7.1. ECS is the magnitude of the long-term GSAT increase in response to a doubling of atmospheric CO_2 concentration after the planetary energy budget is balanced, though leaving out feedbacks associated with ice sheets; whereas the TCR is the magnitude of GSAT increase at year 70 when CO_2 concentration is doubled in a 1% yr^{-1} increase scenario. Both are idealised quantities, but can be inferred from paleoclimate or observational records or estimated directly using climate simulations, and are strongly correlated with the climate response in realistic future projections (Grose et al., 2018; Chapter 4, Section 4.3.4; Section 7.5.7).

TCR is always smaller than ECS because ocean heat uptake acts to reduce the rate of surface warming. Yet, TCR is related with ECS across CMIP5 and CMIP6 models (Grose et al., 2018; Flynn and Mauritsen, 2020) as expected since TCR and ECS are inherently measures of climate response to forcing; both depend on effective radiative forcing (ERF) and the net feedback parameter, α. The relationship between TCR and ECS is, however, non-linear and becomes more so for higher ECS values (Hansen et al., 1985; Knutti et al., 2005; Millar et al., 2015; Flynn and Mauritsen, 2020; Tsutsui, 2020) owing to ocean heat uptake processes and surface temperature pattern effects temporarily reducing the rate of surface warming. When α is small in magnitude, and correspondingly ECS is large (recall that ECS is inversely proportional to α), these temporary effects are increasingly important in reducing the ratio of TCR to ECS.

Before the AR6, the assessment of ECS relied on either CO_2-doubling experiments using global atmospheric models coupled with mixed-layer ocean or standardized CO_2-quadrupling (*abrupt4xCO2*) experiments using fully coupled ocean-atmosphere models or Earth system models (ESMs). The TCR has similarly been diagnosed from ESMs in which the CO_2 concentration is increased at 1% yr^{-1} (*1pctCO2*, an approximately linear increase in ERF over time) and is in practice estimated as the average over a 20–year period centred at the time of atmospheric CO_2 doubling, i.e., year 70. In the AR6, the assessments of ECS and TCR are made based on multiple lines of evidence, with ESMs representing only one of several sources of information. The constraints on these climate metrics are based on radiative forcing and climate feedbacks assessed from process understanding (Section 7.5.1), climate change and variability seen within the instrumental record (Section 7.5.2), paleoclimate evidence (Section 7.5.3), emergent constraints (Section 7.5.4), and a synthesis of all lines of evidence (Section 7.5.5). In AR5, these lines of evidence were not explicitly combined in the assessment of climate sensitivity, but as demonstrated by Sherwood et al. (2020) their combination narrows the uncertainty ranges of ECS compared to that assessed in AR5. ECS values found in CMIP6 models, some of which exhibit values higher than 5 °C (Meehl et al., 2020; Zelinka et al., 2020), are discussed in relation to the AR6 assessment in section 7.5.6.

7.5.1 Estimates of ECS and TCR based on process understanding

This section assesses the estimates of ECS and TCR based on process understanding of the ERF due to a doubling of CO_2 concentration and the net climate feedback (Sections 7.3.2 and 7.4.2). This process-based assessment is made in Section 7.5.1.1 and applied to TCR in Section 7.5.1.2.

7.5.1.1 ECS estimated using process-based assessments of the forcing and feedbacks

The process-based assessment is based on the global energy budget equation (Box 7.1, Equation 7.1), where the ERF (ΔF) is set equal to the effective radiative forcing due to a doubling of CO_2 concentration (denoted as $\Delta F_{2\times CO2}$) and the climate state reaches a new equilibrium, i.e., Earth's energy imbalance averages to zero ($\Delta N = 0$). ECS is calculated as the ratio between the ERF and the net feedback parameter: ECS = $-\Delta F_{2\times CO2}/\alpha$. Estimates of $\Delta F_{2\times CO2}$ and α are obtained separately based on understanding of the key processes that determine each of these quantities. Specifically, $\Delta F_{2\times CO2}$ is estimated based on instantaneous radiative forcing that can be accurately obtained using line-by-line calculations, to which uncertainty due to adjustments are added (Section 7.3.2). The range of α is derived by aggregating estimates of individual climate feedbacks based not only on ESMs but also on theory, observations, and high-resolution process modelling (Section 7.4.2).

The effective radiative forcing of CO_2 doubling is assessed to be $\Delta F_{2\times CO2}$ = 3.93 ± 0.47 W m^{-2} (Section 7.3.2.1), while the net feedback parameter is assessed to be α = –1.16 ± 0.40 W m^{-2} $°C^{-1}$ (Section 7.4.2.7, Table 7.10), where the ranges indicate one standard deviation. These values are slightly different from those directly calculated from ESMs because more information is used to assess them, as explained above. Assuming $\Delta F_{2\times CO2}$ and α each follow an independent normal distribution, the uncertainty range of ECS can be obtained by substituting the respective probability density function into the expression of ECS (red curved bar in Figure 7.16). Since α is in the denominator, the normal distribution leads to a long tail in ECS toward high values, indicating the large effect of uncertainty in α in estimating the likelihood of a high ECS (Roe and Baker, 2007; Knutti and Hegerl, 2008).

The wide range of the process-based ECS estimate is not due solely to uncertainty in the estimates of $\Delta F_{2\times CO2}$ and α, but is partly explained by the assumption that $\Delta F_{2\times CO2}$ and α are independent in this approach. In CMIP5 and CMIP6 ensembles, $\Delta F_{2\times CO2}$ and α are negatively correlated when they are calculated using linear regression in *abrupt4xCO2* simulations (r^2 = 0.34) (Andrews et al., 2012; Webb et al., 2013; Zelinka et al., 2020). The negative correlation leads to compensation between the inter-model spreads of these quantities, thereby reducing the ECS range estimated directly from the models. If the process-based ECS distribution is reconstructed from probability distributions of $\Delta F_{2\times CO2}$ and α assuming that they are correlated as in CMIP model ensembles, the range of ECS will be narrower by 14% (pink curved bar in Figure 7.16). If, however, the covariance between $\Delta F_{2\times CO2}$ and α is not adopted, there is no change in the mean, but the wide range still applies.

A significant correlation between $\Delta F_{2\times CO2}$ and α also occurs when the two parameters are estimated separately from AGCM fixed-SST experiments (Section 7.3.1) or fixed CO_2 concentration experiments (Ringer et al., 2014; Chung and Soden, 2018; Section 7.4.1). Hence the relationship is not expected to be an artefact of calculating them using linear regression in *abrupt4xCO2* simulations. A possible physical cause of the correlation may be a compensation between the cloud adjustment and the cloud feedback over the tropical ocean (Ringer et al., 2014; Chung and Soden, 2018). It has been shown that the change in the hydrological cycle is a controlling factor for the low-cloud adjustment (Dinh and Fueglistaler, 2019) and for the low-cloud feedback (Watanabe et al., 2018), and therefore the responses of these clouds to the direct CO_2 radiative forcing and to the surface warming may not be independent. However, robust physical mechanisms are not yet established, and furthermore, the process-based assessment of the tropical low-cloud feedback is only indirectly based on ESMs given that physical processes which control the low clouds are not sufficiently well-simulated in models (Section 7.4.2.4). For these reasons, the co-dependency between $\Delta F_{2\times CO2}$ and α is assessed to have *low confidence* and, therefore, the more conservative assumption that they are independent for the process-based assessment of ECS is retained.

In summary, the ECS based on the assessed values of $\Delta F_{2\times CO2}$ and α is assessed to have a median value of 3.4°C with a *likely* range of 2.5–5.1 °C and *very likely* range of 2.1–7.7 °C. To this assessed range of ECS, the contribution of uncertainty in α is approximately three times as large as the contribution of uncertainty in $\Delta F_{2\times CO2}$.

[START FIGURE 7.16 HERE]

Figure 7.16: Probability distributions of ERF to CO_2 doubling ($\Delta F_{2\times CO2}$, top) and the net climate feedback (α, right), derived from process-based assessments in Sections 7.3.2 and 7.4.2. Middle panel shows the joint probability density function calculated on a two-dimensional plane of $\Delta F_{2\times CO2}$ and α (red), on which the 90% range shown by an ellipse is imposed to the background theoretical values of ECS (colour shading). The white dot, thick and thin curves in the ellipse represent the mean, *likely* and *very likely* ranges of ECS. An alternative estimation of the ECS range (pink) is calculated by assuming that $\Delta F_{2\times CO2}$ and α have a covariance. The assumption about the co-dependence between $\Delta F_{2\times CO2}$ and α does not alter the mean estimate of ECS but affects its uncertainty. Further details on data sources and processing are available in the chapter data table (Table 7.SM.14).

[END FIGURE 7.16 HERE]

7.5.1.2 Emulating process-based ECS to TCR

ECS estimated using the ERF due to a doubling of CO_2 concentration and the net feedback parameter (ECS = $-\Delta F_{2\times CO2}/\alpha$) can be translated into the TCR so that both climate sensitivity metrics provide consistent information about the climate response to forcing. Here a two-layer energy budget emulator is used to transfer the process-based assessment of forcing, feedback, efficacy and heat uptake to TCR (Supplementary Material 7.SM.2.1, Cross-Chapter Box 7.1). The emulator can reproduce the transient surface temperature evolution in ESMs under *1pctCO2* simulations and other climate change scenarios, despite the very low number of degrees of freedom (Held et al., 2010; Geoffroy et al., 2012, 2013a; Palmer et al., 2018). Using this model with parameters given from assessments in the previous sections, TCR is assessed based on the process-based understanding.

In the two-layer energy balance emulator, additional parameters are introduced: heat capacities of the upper and deep ocean, heat uptake efficiency (γ), and the so-called efficacy parameter (ε) that represents the dependence of radiative feedbacks and heat uptake on the evolving SST pattern under CO_2 forcing alone (Section 7.4.4). In the real world, natural internal variability and aerosol radiative forcing also affect the efficacy parameter, but these effects are excluded for the current discussion.

The analytical solution of the energy balance emulator reveals that the global surface temperature change to abrupt increase of the atmospheric CO_2 concentration is expressed by a combination of a fast adjustment of the surface components of the climate system and a slow response of the deep ocean, with time scales of several years and several centuries, respectively (grey curves in Figure 7.17). The equilibrium response of upper ocean temperature, approximating SST and the surface air temperature response, depends, by definition, only on the radiative forcing and the net feedback parameter. Uncertainty in α dominates (80–90%) the corresponding uncertainty range for ECS in CMIP5 models (Vial et al., 2013), and also an increase of ECS in CMIP6 models (Section 7.5.5) is attributed by about 60–80% to a change in α (Zelinka et al., 2020). For the range of TCR, the contribution from uncertainty in α is reduced to 50–60% while uncertainty in $\Delta F_{2\times CO2}$ becomes relatively more important (Geoffroy et al., 2012; Lutsko and Popp, 2019). TCR reflects the fast response occurring approximately during the first 20 years in the *abrupt4xCO2* simulation (Held et al., 2010), but the fast response is not independent of the slow response because there is a nonlinear co-dependence between them (Andrews et al., 2015). The nonlinear relationship between ECS and TCR indicates that the probability of high TCR is not very sensitive to changes in the probability of high ECS (Meehl et al., 2020).

Considering an idealized time evolution of ERF (1% increase per year until CO_2 doubling and held fixed afterwards, see Figure 7.17a), the TCR defined by the surface temperature response at year 70 is derived by substituting the process-based ECS into the analytical solution of the emulator (Figure 7.17b, see also Supplementary Material 7.SM.2.1). When additional parameters in the emulator are prescribed by using CMIP6 multi-model mean values of those estimates (Smith et al., 2020a), this calculation translates the range of ECS in Section 7.5.2.1 to the range of TCR. The transient temperature response, in reality, varies with different estimates of the ocean heat uptake efficiency (γ) and efficacy (ε). When the emulator was calibrated to the transient responses in CMIP5 models, it shows that uncertainty in heat capacities is negligible and differences in γ and ε explain 10–20% of the inter-model spread of TCR among GCMs (Geoffroy et al., 2012). Specifically, their product, $\kappa = \gamma\varepsilon$, appearing in a simplified form of the solution, i.e., TCR $\cong -\Delta F_{2\times CO2}/(\alpha - \kappa)$, gives a single parameter quantifying the damping effects of heat uptake (Jiménez-de-la-Cuesta and Mauritsen, 2019). This parameter is positive and acts to slow down the temperature response in a similar manner to the 'pattern effect' (Sections 7.4.4.3 and 7.5.2.1). The ocean heat uptake in nature is controlled by multiple processes associated with advection and mixing (Exarchou et al., 2014; Kostov et al., 2014; Kuhlbrodt et al., 2015) but is simplified to be represented by a single term of heat exchange between the upper- and deep-ocean in the emulator. Therefore, it is challenging to constrain γ and ε from process-based understanding (Section 7.5.2). Because the estimated values are only weakly correlated across models, the mean value and one standard deviation of κ are calculated as $\kappa = 0.84 \pm 0.38$ W m^{-2} °C^{-1} (one standard deviation) by ignoring their covariance (the mean value is very similar to that used for Chapter 4, Box 4.1, Figure 1) (see Supplementary Material 7.SM.2.1). By incorporating this inter-model spread in κ, the range of TCR is widened by about 10% (blue bar in Figure 7.17b). Yet, the dominant contribution to the uncertainty range of TCR arises from the net feedback parameter α, consistent with analyses of CMIP6 models (Williams et al., 2020), and this assessment remains unchanged from AR5 stating that uncertainty in ocean heat uptake is of secondary importance.

In summary, the process-based estimate of TCR is assessed to have the central value of 2.0°C with the *likely* range from 1.6 to 2.7°C and the *very likely* range from 1.3 to 3.1°C (*high confidence*). The upper bound of the assessed range was slightly reduced from AR5 but can be further constrained using multiple lines of evidence (Section 7.5.5).

[START FIGURE 7.17 HERE]

Figure 7.17: (a) Time evolution of the effective radiative forcing (ERF) to the CO_2 concentration increased by 1% per year until the year 70 (equal to the time of doubling) and kept fixed afterwards (white line). The *likely* and *very likely* ranges of ERF indicated by light and dark orange have been assessed in Section 7.3.2.1. (b) Surface temperature response to the CO_2 forcing calculated using the emulator with a given

value of ECS, considering uncertainty in $\Delta F_{2\times CO2}$, α, and κ associated with the ocean heat uptake and efficacy (white line). The *likely* and *very likely* ranges are indicated by cyan and blue. For comparison, the temperature response to abrupt doubling of the CO_2 concentration is displayed by a grey curve. The mean, *likely* and *very likely* ranges of ECS and TCR are shown at the right (the values of TCR also presented in the panel). Further details on data sources and processing are available in the chapter data table (Table 7.SM.14).

[END FIGURE 7.17 HERE]

7.5.2 Estimates of ECS and TCR based on the instrumental record

This section assesses the estimates of ECS and TCR based on the instrumental record of climate change and variability with an emphasis on new evidence since AR5. Several lines of evidence are assessed including the global energy budget (Section 7.5.2.1), the use of simple climate models evaluated against the historical temperature record (Section 7.5.2.2), and internal variability in global temperature and TOA radiation (Section 7.5.2.3). Section 7.5.2.4 provides an overall assessment of TCR and ECS based on these lines of evidence from the instrumental record.

7.5.2.1 Estimates of ECS and TCR based on the global energy budget

The GSAT change from 1850–1900 to 2006–2019 is estimated to be 1.03 [0.86 to 1.18] °C (Cross-chapter Box 2.3). Together with estimates of Earth's energy imbalance (Section 7.2.2) and the global ERF that has driven the observed warming (Section 7.3), the instrumental temperature record enables global energy budget estimates of ECS and TCR. While energy budget estimates use instrumental data, they are not based purely on observations. A conceptual model typically based on the global-mean forcing and response energy budget framework (Box 7.1) is needed to relate ECS and TCR to the estimates of global warming, ERF and Earth's energy imbalance (Forster, 2016; Knutti et al., 2017). Moreover, ESM simulations partly inform estimates of the historical ERF (Section 7.3) as well as Earth's energy imbalance in the 1850-1900 climate (the period against which changes are measured) (Forster, 2016; Lewis and Curry, 2018). ESMs are also used to estimate uncertainty due the internal climate variability that may have contributed to observed changes in temperature and energy imbalance (e.g., Palmer and McNeall, 2014; Sherwood et al., 2020). Research since AR5 has shown that global energy budget estimates of ECS may be biased low when they do not take into account how radiative feedbacks depend on the spatial pattern of surface warming (Section 7.4.4.3) or when they do not incorporate improvements in the estimation of global surface temperature trends which take better account of data-sparse regions and are more consistent in their treatment of surface temperature data (Chapter 2, Section 2.3.1). Together with updated estimates of global ERF and Earth's energy imbalance, these advances since AR5 have helped to reconcile energy budget estimates of ECS with estimates of ECS from other lines of evidence.

The traditional global-mean forcing and response energy budget framework (Gregory et al., 2002; Section 7.4.1; Box 7.1) relates the difference between the ERF (ΔF) and the radiative response to observed global warming ($\alpha\Delta T$) to the Earth's energy imbalance (ΔN): $\Delta N = \alpha\Delta T + \Delta F$. Given the relationship ECS = $-\Delta F_{2\times CO2}/\alpha$, where $\Delta F_{2\times CO2}$ is the ERF from CO_2 doubling, ECS can be estimated from historical estimates of ΔT, ΔF, ΔN and $\Delta F_{2\times CO2}$: ECS = $\Delta F_{2\times CO2}\,\Delta T/(\Delta F - \Delta N)$. Since TCR is defined as the temperature change at the time of CO_2 doubling under an idealized 1% yr^{-1} CO_2 increase, it can be inferred from the historical record as: TCR = $\Delta F_{2\times CO2}\,\Delta T/\Delta F$, under the assumption that radiative forcing increases quickly compared to the adjustment timescales of the deep ocean, but slowly enough and over a sufficiently long time that the upper ocean is adjusted, so that ΔT and ΔN increases approximately in proportion to ΔF. Because ΔN is positive, TCR is always smaller than ECS, reflecting weaker transient warming than equilibrium warming. TCR is better constrained than ECS owing to the fact that the denominator of TCR, without the quantity ΔN, is more certain and further from zero than is the denominator of ECS. The upper bounds of both TCR and ECS estimated from historical warming are inherently less certain than their lower bounds because ΔF is uncertain and in the denominator.

The traditional energy budget framework lacks a representation of how radiative feedbacks depend on the spatial pattern of warming. Thus, studies employing this framework (Otto et al., 2013; Lewis and Curry, 2015, 2018; Forster, 2016) implicitly assume that the net radiative feedback has a constant magnitude, producing an estimate of the effective ECS (defined as the value of ECS that would occur if α does not change from its current value) rather than of the true ECS. As summarized in Section 7.4.4.3, there are now multiple lines of evidence providing *high confidence* that the net radiative feedback will become less negative as the warming pattern evolves in the future (the pattern effect). This arises because historical warming has been relatively larger in key negative feedback regions (e.g., western tropical Pacific Ocean) and relatively smaller in key positive feedback regions (e.g., eastern tropical Pacific Ocean and Southern Ocean) than is projected in the near-equilibrium response to CO_2 forcing (Held et al., 2010; Proistosescu and Huybers, 2017; Dong et al., 2019; Section 7.4.4.3), implying that the true ECS will be larger than the effective ECS inferred from historical warming. This section first assesses energy budget constraints on TCR and the effective ECS based on updated estimates of historical warming, ERF, and Earth's energy imbalance. It then assesses what these energy budget constraints imply for values of ECS once the pattern effect is accounted for.

Energy budget estimates of TCR and ECS have evolved in the literature over recent decades. Prior to AR4, the global energy budget provided relatively weak constraints, primarily due to large uncertainty in the tropospheric aerosol forcing, giving ranges of the effective ECS that typically included values above 10°C (Forster, 2016; Knutti et al., 2017). Revised estimates of aerosol forcing together with a larger greenhouse-gas forcing by the time of AR5 led to an estimate of ΔF that was more positive and with reduced uncertainty relative to AR4. Using energy budget estimates and radiative forcing estimates updated to 2009, Otto et al. (2013) estimated that TCR was 1.3 [0.9 to 2.0] °C, and that the effective ECS was 2.0 [1.2 to 3.9] °C. This AR5-based energy budget estimate of ECS was lower than estimates based on other lines of evidence, leading AR5 to expand the assessed *likely* range of ECS to include lower values relative to AR4. Studies since AR5 using similar global energy budget methods have produced similar or slightly narrower ranges for TCR and effective ECS (Forster, 2016; Knutti et al., 2017).

Energy budget estimates of TCR and ECS assessed here are based on improved observations and understanding of global surface temperature trends extended to the year 2020 (Chapter 2, Section 2.3.1), revised estimates of Earth's energy imbalance (Section 7.2), and revised estimates of ERF (Section 7.3). Accurate, in situ-based estimates of Earth's energy imbalance can be made from around 2006 based on near-global ocean temperature observations from the ARGO array of autonomous profiling floats (Chapter 2 Section 2.3, Section 7.2). Over the period 2006 to 2018 the Earth's energy imbalance is estimated to be 0.79 ± 0.27 W m^{-2} (Section 7.2) and it is assumed that this value is also representative for the period 2006 to 2019. Anomalies are taken with respect to the baseline period 1850-1900, although other baselines could be chosen to avoid major volcanic activity (Otto et al., 2013; Lewis and Curry, 2018). Several lines of evidence, including ESM simulations (Lewis and Curry, 2015), energy balance modelling (Armour, 2017), inferred ocean warming given observed SSTs using ocean models (Gebbie and Huybers, 2019; Zanna et al., 2019), and ocean warming reconstructed from noble gas thermometry (Baggenstos et al., 2019) suggest a 1850-1900 Earth energy imbalance of 0.2 ± 0.2 W m^{-2}. Combined with estimates of internal variability in Earth's energy imbalance, calculated using periods of equivalent lengths of years as used in unforced ESM simulations (Palmer and McNeall, 2014; Sherwood et al., 2020b), the anomalous energy imbalance between 1850–1900 and 2006–2019 is estimated to be ΔN = 0.59 ± 0.35 W m^{-2}. GSAT change between 1850–1900 and 2006–2019 is estimated to be ΔT = 1.03°C ± 0.20 °C (Chapter 2, Cross-Chapter Box 2.3; Box 7.2) after accounting for internal temperature variability derived from unforced ESM simulations (Sherwood et al., 2020b). The ERF change between 1850–1900 and 2006–2019 is estimated to be ΔF = 2.20 [1.53 to 2.91] W m^{-2} (Section 7.3.5) and the ERF for a doubling of CO_2 is estimated to be $\Delta F_{2\times CO2}$ = 3.93 ± 0.47 W m^{-2} (Section 7.3.2). Employing these values within the traditional global energy balance framework described above (following the methods of Otto et al. (2013) and accounting for correlated uncertainties between ΔF and $\Delta F_{2\times CO2}$) produces a TCR of 1.9 [1.3 to 2.7]°C and an effective ECS of 2.5 [1.6–4.8] °C. These TCR and effective ECS values are higher than those in the recent literature (Otto et al., 2013; Lewis and Curry, 2015, 2018) but are comparable to those of Sherwood et al. (2020) who also used updated estimates of observed warming, Earth's energy imbalance, and ERF.

The trend estimation method applied to global surface temperature affects derived values of ECS and TCR from the historical record. In this Report, the effective ECS is inferred from estimates that use global coverage of GSAT to estimate the surface temperature trends. The GSAT trend is assessed to have the same best estimate as the observed global mean surface temperature (GMST), although the GSAT trend is assessed to have larger uncertainty (see Cross-Chapter Box 2.3). Many previous studies have relied on HadCRUT4 GMST estimates that used the blended observations and did not interpolate over regions of incomplete observational coverage such as the Arctic. As a result, the ECS and TCR derived from these studies has smaller ECS and TCR values than those derived from model-inferred estimates (Richardson et al., 2016, 2018a). The energy budget studies assessing ECS in AR5 employed HadCRUT4 or similar measures of GMST trends. As other lines of evidence in that report used GSAT trends, this could partly explain why AR5-based energy budget estimates of ECS were lower than those estimated from other lines of evidence, adding to the overall disparity in Collins et al. (2013a). In this report, GSAT is chosen as the standard measure of global surface temperature to aid comparison with previous model and process-based estimates of ECS, TCR and climate feedbacks (see Cross-Chapter Box 2.3).

The traditional energy budget framework has been evaluated within ESM simulations by comparing the effective ECS estimated under historical forcing with the ECS estimated using regression methods (Box 7.1) under *abrupt4xCO2* (Andrews et al., 2019; Winton et al., 2020). For one CMIP6 model (GFDL-CM4.0), the value of effective ECS derived from historical energy budget constraints is 1.8°C while ECS is estimated to be 5.0°C (Winton et al., 2020). For another model (HadGEM3-GC3.1-LL) the effective ECS derived from historical energy budget constraints is 4.1°C (average of four ensemble members) while ECS is estimated to be 5.5°C (Andrews et al., 2019). These modelling results suggest that the effective ECS under historical forcing could be lower than the true ECS owing to differences in radiative feedbacks induced by the distinct patterns of historical and equilibrium warming (Section 7.4.4.3). Using GFDL-CM4, Winton et al. (2020) also find that the value of TCR estimated from energy budget constraints within a historical simulation (1.3°C) is substantially lower than the true value of TCR (2.1°C) diagnosed within a *1pctCO₂* simulation owing to a combination of the pattern effect and differences in the efficiency of ocean heat uptake between historical and *1pctCO₂* forcing. This section next considers how the true ECS can be estimated from the historical energy budget by accounting for the pattern effect. However, owing to limited evidence this section does not attempt to account for these effects in estimates of TCR.

Research since AR5 has introduced extensions to the traditional energy budget framework that account for the feedback dependence on temperature patterns by allowing for multiple radiative feedbacks operating on different timescales (Armour et al., 2013; Geoffroy et al., 2013a; Armour, 2017; Proistosescu and Huybers, 2017; Goodwin, 2018; Rohrschneider et al., 2019), by allowing feedbacks to vary with the spatial pattern or magnitude of ocean heat uptake (Winton et al., 2010; Rose et al., 2014; Rugenstein et al., 2016a), or by allowing feedbacks to vary with the type of radiative forcing agent (Kummer and Dessler, 2014; Shindell, 2014; Marvel et al., 2016; Winton et al., 2020). A direct way to account for the pattern effect is to use the relationship $ECS = \Delta F_{2\times CO2}/(-\alpha + \alpha')$, where $\alpha = (\Delta N - \Delta F)/\Delta T$ is the effective feedback parameter (Box 7.1) estimated from historical global energy budget changes and α' represents the change in the feedback parameter between the historical period and the equilibrium response to CO_2 forcing, which can be estimated using ESMs (Armour, 2017; Andrews et al., 2018, 2019; Lewis and Curry, 2018; Dong et al., 2020; Winton et al., 2020; Section 7.4.4.3).

The net radiative feedback change between the historical warming pattern and the projected equilibrium warming pattern in response to CO_2 forcing (α') is estimated to be in the range 0.0 to 1.0 W m^{-2} $°C^{-1}$ (Figure 7.15). Using the value $\alpha' = +0.5 \pm 0.5$ W m^{-2} $°C^{-1}$ to represent this range illustrates the effect of changing radiative feedbacks on estimates of ECS. While the effective ECS inferred from historical warming is 2.5 [1.6–4.8] °C , $ECS = \Delta F_{2\times CO2}/(-\alpha + \alpha')$ is 3.5 [1.7–13.8] °C. For comparison, values of α' derived from the response to historical and idealized CO_2 forcing within coupled climate models (Armour, 2017; Lewis and Curry, 2018; Andrews et al., 2019; Dong et al., 2020; Winton et al., 2020) can be approximated as $\alpha' = +0.1 \pm 0.3$ W m^{-2} $°C^{-1}$ (Section 7.4.4.3), corresponding to a value of ECS of 2.7 [1.7–5.9] °C. In both cases, the low end of the ECS range is similar to that of the effective ECS inferred using the traditional energy balance model framework that assumes $\alpha' = 0$, reflecting a weak dependence on the value of α' when ECS is small

(Armour, 2017; Andrews et al., 2018); the low end of the ECS range is robust even in the hypothetical case that α' is slightly negative. However, the high end of the ECS range is substantially larger than that of the effective ECS and strongly dependent on the value of α'.

The values of ECS obtained from the techniques outlined above are all higher than those estimated from both AR5 and recently published estimates (Collins et al., 2013a; Otto et al., 2013; Lewis and Curry, 2015; Forster, 2016; Lewis and Curry, 2018). Four revisions made in this Report are responsible for this increase: (1) An upwards revision of historic global surface temperature trends from newly published trend estimates (Chapter 2, Section 2.3.1); (2) An 8% increase in the ERF for $\Delta F_{2\times CO2}$ (Section 7.3.2); (3) A more negative central estimate of aerosol ERF, which acts to reduce estimates of historical ERF trends; and (4) Accounting for the pattern effect in ECS estimates. Values of ECS provided here are similar to those based on the historical energy budget found in Sherwood et al. (2020), with small differences owing to methodological differences and the use of different estimates of observed warming, Earth's energy imbalance, and ERF.

Overall, there is *high confidence* that the true ECS is higher than the effective ECS as inferred from the historical global energy budget, but there is substantial uncertainty in how much higher because of *limited evidence* regarding how radiative feedbacks may change in the future. While several lines of evidence indicate that α' > 0, the quantitative accuracy of feedback changes is not known at this time (Section 7.4.4.3). Global energy budget constraints thus provide *high confidence* in the lower bound of ECS which is not sensitive to the value of α': ECS is *extremely unlikely* to be less than 1.6°C. Estimates of α' that are informed by idealized CO_2 forcing simulations of coupled ESMs (Armour, 2017; Lewis and Curry, 2018; Andrews et al., 2019; Dong et al., 2020; Winton et al., 2020) indicate a median value of ECS of around 2.7°C while estimates of α' that are informed by observed historical sea surface temperature patterns (Andrews et al., 2018) indicate a median value of ECS of around 3.5°C. Owing to large uncertainties in future feedback changes, the historical energy budget currently provides little information about the upper end of the ECS range.

7.5.2.2 Estimates of ECS and TCR based on climate model emulators

Energy budget emulators are far less complex than comprehensive ESMs (see Chapter 1, Section 1.5.3 and Cross-Chapter Box 7.1). For example, an emulator could represent the atmosphere, ocean, and land using a small number of connected boxes (e.g., Goodwin, 2016), or it could represent the global mean climate using two connected ocean layers (e.g., Cross-Chapter Box 7.1, Supplementary Material 7.SM.2). The numerical efficiency of emulators means that they can be empirically constrained by observations: a large number of possible parameter values (e.g., feedback parameter, aerosol radiative forcing, and ocean diffusivity) are randomly drawn from prior distributions; forward integrations of the model are performed with these parameters and weighted against observations of surface or ocean warming, producing posterior estimates of quantities of interest such as TCR, ECS and aerosol forcing (see Section 7.3). Owing to their reduced complexity, emulators lack full representations of the spatial patterns of sea surface temperature and radiative responses to changes in those patterns (discussed in Section 7.4.4.3) and many represent the net feedback parameter using a constant value. The ranges of ECS reported by studies using emulators are thus interpreted here as representative of the effective ECS over the historical record rather than of the true ECS.

Improved estimates of ocean heat uptake over the past two decades (Section 7.2) have diminished the role of ocean diffusivity in driving uncertainty in ECS estimates, leaving the main trade-off between posterior ranges in ECS and aerosol radiative forcing (Forest, 2002; Knutti et al., 2002; Frame et al., 2005). AR5 (Bindoff et al., 2013) assessed a variety of estimates of ECS based on emulators and found that they were sensitive to the choice of prior parameter distributions and temperature datasets used, particularly for the upper end of the ECS range, though priors can be chosen to minimize the effect on results (e.g., Lewis, 2013). Emulators generally produced estimates of effective ECS between 1°C and 5°C and ranges of TCR between 0.9°C and 2.6°C. Padilla et al. (2011) use a simple global-average emulator with two timescales (see Supplementary Material 7.SM.2 and Section 7.5.1.2) to estimate a TCR of 1.6 [1.3 to 2.6] °C. Using the same model, Schwartz (2012) finds TCR in the range 0.9–1.9°C while Schwartz (2018) finds that an effective ECS of 1.7°C provides the best fit to the historical global surface temperature record while also finding a median aerosol forcing that is smaller than that assessed in Section 7.3. Using an eight-box representation of the atmosphere–ocean–terrestrial system constrained by historical warming, Goodwin (2016) found an effective ECS of 2.4 [1.4 to 4.4] °C while Goodwin (2018) found effective ECS to be in the range 2–4.3°C when using a prior for ECS based on paleoclimate constraints.

Using an emulator comprised of northern and southern hemispheres and an upwelling-diffusive ocean (Aldrin et al., 2012), with surface temperature and ocean heat content datasets updated to 2014, Skeie et al. (2018) estimate a TCR of 1.4 [0.9 to 2.0] °C and a median effective ECS of 1.9 [1.2 to 3.1] °C. Using a similar emulator comprised of land and ocean regions and an upwelling-diffusive ocean, with global surface temperature and ocean heat content datasets through 2011, Johansson et al. (2015) find an effective ECS of 2.5 [2.0 to 3.2] °C. The estimate is found to be sensitive to the choice of dataset endpoint and the representation of internal variability meant to capture the El Niño–Southern Oscillation and Pacific Decadal Variability. Differences between these two studies arise, in part, from their different global surface temperature and ocean heat content datasets, different radiative forcing uncertainty ranges, different priors for model parameters, and different representations of internal variability. This leads to different estimates of effective ECS, with the median estimate of Skeie et al. (2018) lying below the 5% to 95% range of effective ECS from Johansson et al. (2015). Moreover, while the Skeie et al. (2018) emulator has a constant value of the net feedback parameter, the Johansson et al. (2015) emulator allows distinct radiative feedbacks for land and ocean, contributing to the different results.

The median estimates of TCR and effective ECS inferred from emulator studies generally lie within the 5% to 95% ranges of the those inferred from historical global energy budget constraints (1.3 to 2.7°C for TCR and 1.6 to 4.8°C for effective ECS). Their estimates would be consistent with still higher values of ECS when accounting for changes in radiative feedbacks as the spatial pattern of global warming evolves in the future (Section 7.5.2.1). Cross-Chapter Box 7.1 and references therein show that four very different physically-based emulators can be calibrated to match the assessed ranges of historical GSAT change, ERF, ECS and TCR from across the report. Therefore, the fact that the emulator effective ECS values estimated from previous studies tend to lie at the lower end of the range inferred from historical global energy budget constraints may reflect that the energy budget constraints in Section 7.5.2.1 use updated estimates of Earth's energy imbalance, GSAT trends and ERF, rather than any methodological differences between the lines of evidence. The 'emergent constraints' on ECS based on observations of climate variability used in conjunction with comprehensive ESMs are assessed in Section 7.5.4.1.

7.5.2.3 Estimates of ECS based on variability in Earth's top-of-atmosphere radiation budget

While continuous satellite measurements of TOA radiative fluxes (Figure 7.3) do not have sufficient accuracy to determine the absolute magnitude of Earth's energy imbalance (Section 7.2.1), they provide accurate estimates of its variations and trends since the year 2002 that agree well with estimates based on observed changes in global ocean heat content (Loeb et al., 2012; Johnson et al., 2016; Palmer, 2017). When combined with global surface temperature observations and simple models of global energy balance, satellite measurements of TOA radiation afford estimates of the net feedback parameter associated with recent climate variability (Tsushima and Manabe, 2013; Donohoe et al., 2014; Dessler and Forster, 2018). These feedback estimates, derived from the regression of TOA radiation on surface temperature variability, imply values of ECS that are broadly consistent with those from other lines of evidence (Forster, 2016; Knutti et al., 2017). A history of regression-based feedbacks and their uncertainties is summarized in (Bindoff et al., 2013; Forster, 2016; Knutti et al., 2017).

Research since AR5 has noted that regression-based feedback estimates depend on whether annual- or monthly-mean data are used and on the choice of lag employed in the regression, complicating their interpretation (Forster, 2016). The observed lead-lag relationship between global TOA radiation and global surface temperature, and its dependence on sampling period, is well replicated within unforced simulations of ESMs (Dessler, 2011; Proistosescu et al., 2018). These features arise because the regression between global TOA radiation and global surface temperature reflects a blend of different radiative feedback processes associated with several distinct modes of variability acting on different time scales (Annex IV), such as monthly atmospheric variability and inter-annual El Niño–Southern Oscillation (ENSO) variability (Lutsko and Takahashi, 2018; Proistosescu et al., 2018). Regression-based feedbacks thus provide estimates of the radiative feedbacks that are associated with internal climate variability (e.g., Brown et al., 2014), and do not provide a direct estimate of ECS (*high confidence*). Moreover, variations in global surface temperature that do not directly affect TOA radiation may lead to a positive bias in regression-based feedback, although this bias appears to be small, particularly when annual-mean data are used (Murphy and Forster, 2010; Spencer and Braswell, 2010, 2011; Proistosescu et al., 2018). When tested within ESMs, regression-based feedbacks have been found to be only weakly correlated with values of ECS (Chung et al., 2010), although cloudy-sky TOA radiation fluxes have been found to be moderately correlated with ECS at ENSO timescales within CMIP5 models (Lutsko and Takahashi, 2018).

Finding such correlations within models requires simulations that span multiple centuries, suggesting that the satellite record may not be of sufficient length to produce robust feedback estimates. However, correlations between regression-based feedbacks and long-term feedbacks have been found to be higher when focused on specific processes or regions, such as for cloud or the water vapour feedback (Dessler, 2013; Zhou et al., 2015; Section 7.4.2). Assessing the global radiative feedback in terms of the more stable relationship between tropospheric temperature and TOA radiation offers another potential avenue for constraining ECS. The 'emergent constraints' on ECS based on variability in the TOA energy budget are assessed in Section 7.5.4.1.

7.5.2.4 Estimates of ECS based on the climate response to volcanic eruptions

A number of studies consider the observed climate response to volcanic eruptions over the 20th century (Knutti et al., 2017; Chapter 3 Section 3.3.1, Cross-Chapter Box 4.1). However, the direct constraint on ECS is weak, particularly at the high end, because the temperature response to short-term forcing depends only weakly on radiative feedbacks and because it can take decades of a sustained forcing before the magnitude of temperature changes reflects differences in ECS across models (Geoffroy et al., 2013b; Merlis et al., 2014). It is also a challenge to separate the response to volcanic eruptions from internal climate variability in the years that follow them (Wigley et al., 2005). Based on ESM simulations, radiative feedbacks governing the global surface temperature response to volcanic eruptions can be substantially different than those governing long-term global warming (Merlis et al., 2014; Marvel et al., 2016; Ceppi and Gregory, 2019). Estimates based on the response to volcanic eruptions agree with other lines of evidence (Knutti et al., 2017), but they do not constitute a direct estimate of ECS (*high confidence*). The 'emergent constraints' on ECS based on climate variability, including volcanic eruptions, are summarized in Section 7.5.4.1.

7.5.2.5 Assessment of ECS and TCR based on the instrumental record

Evidence from the instrumental temperature record, including estimates using global energy budget changes (Section 7.5.2.1), climate emulators (Section 7.5.2.2), variability in the TOA radiation budget (Section 7.5.2.3), and the climate response to volcanic eruptions (Section 7.5.2.4) produce median ECS estimates that range between 2.5°C and 3.5°C, but a best estimate value cannot be given owing to a strong dependence on assumptions about how radiative feedbacks will change in the future. However, there is *robust evidence* and *high agreement* across the lines of evidence that ECS is *extremely likely* greater than 1.6°C (*high confidence*). There is *robust evidence* and *medium agreement* across the lines of evidence that ECS is *very likely* greater than 1.8°C and *likely* greater than 2.2°C (*high confidence)*. These ranges of ECS correspond to estimates based on historical global energy budget constraints (Section 7.5.2.1) under the assumption of no feedback dependence on evolving SST patterns (i.e., $\alpha' = 0$) and thus represent an underestimate of the true ECS ranges that can be inferred from this line of evidence (*high confidence*). Historical global energy budget changes do not provide constraints on the upper bound of ECS, while the studies assessed in Section 7.5.2.3 based on climate variability provide *low confidence* in its value owing to *limited evidence*.

Global energy budget constraints indicate a central estimate (median) TCR value of 1.9°C and that TCR is *likely* in the range 1.5°C to 2.3°C and *very likely* in the range 1.3°C to 2.7°C (*high confidence*). Studies that constrain TCR based on the instrumental temperature record used in conjunction with ESM simulations are summarized in Section 7.5.4.3.

7.5.3 Estimates of ECS based on paleoclimate data

Estimates of ECS based on paleoclimate data are complementary to, and largely independent from, estimates based on process-based studies (Section 7.5.1) and the instrumental record (Section 7.5.2). The strengths of using paleoclimate data to estimate ECS include: (1) the estimates are based on observations of a real-world Earth system response to a forcing, in contrast to using estimates from process-based modelling studies or directly from models; (2) the forcings are often relatively large (similar in magnitude to a CO_2 doubling or more), in contrast to data from the instrumental record; (3) the forcing often changes relatively slowly so the system is close to equilibrium; as such, all individual feedback parameters, α_x, are included, and complications associated with accounting for ocean heat uptake are reduced or eliminated, in contrast to the instrumental record. However, there can be relatively large uncertainties on estimates of both the paleo forcing and paleo global surface temperature response, and care must be taken to account for long-term feedbacks associated with ice sheets (Section 7.4.2.6), which often play an important role in the paleoclimate response to forcing, but which are not included in the definition of ECS. Furthermore, the state-dependence of feedbacks (Section 7.4.3) means that climate sensitivity during Earth's past may not be the same as it is today, which should be accounted for when interpreting paleoclimate estimates of ECS.

AR5 stated that data and modelling of the Last Glacial Maximum (LGM, Cross-Chapter Box 2.1) indicated that it was *very unlikely* that ECS lay outside the range 1–6°C (Masson-Delmotte et al., 2013). Furthermore, AR5 reported that climate records of the last 65 million years indicated an ECS 95% confidence interval of 1.1–7.0°C.

Compared with AR5, there are now improved constraints on estimates of ECS from paleoclimate evidence. The strengthened understanding and improved lines of evidence come in part from the use of high-resolution paleoclimate data across multiple glacial-interglacial cycles, taking into account state-dependence (von der Heydt et al., 2014; Köhler et al., 2015, 2017, 2018; Friedrich et al., 2016; Snyder, 2019; Stap et al., 2019; Section 7.4.3) and better constrained pre-ice core estimates of atmospheric CO_2 concentrations (Martínez-Botí et al., 2015; Anagnostou et al., 2016, 2020; de la Vega et al., 2020) and surface temperature (Hollis et al., 2019; Inglis et al., 2020; McClymont et al., 2020).

Overall, the paleoclimate lines of evidence regarding climate sensitivity can be broadly categorised into two types: estimates of radiative forcing and temperature response from paleo proxy measurements, and emergent constraints on paleoclimate model simulations. This section focuses on the first type only; the second type (emergent constraints) are discussed in Section 7.5.4.

In order to provide estimates of ECS, evidence from the paleoclimate record can be used to estimate forcing (ΔF) and global surface temperature response (ΔT) in Equation 7.1, Box 7.1, under the assumption that the system is in equilibrium (i.e. ΔN=0). However, there are complicating factors when using the paleoclimate record in this way, and these challenges and uncertainties are somewhat specific to the time period being considered.

7.5.3.1 Estimates of ECS from the Last Glacial Maximum

The LGM (Cross-Chapter Box 2.1) has been used to provide estimates of ECS (Sherwood et al., 2020b; Tierney et al., 2020b) (see Table 7.11 for estimates since AR5). The major forcings and feedback processes that led to the cold climate at that time (e.g., CO_2, non-CO_2 greenhouse gases, and ice sheets) are relatively well-known (Chapter 5, Section 5.1), orbital forcing relative to pre-industrial was negligible, and there are relatively high spatial resolution and well-dated paleoclimate temperature data available for this time period (Chapter 2, Section 2.3.1). Uncertainties in deriving global surface temperature from the LGM proxy data arise partly from uncertainties in the calibration from the paleoclimate data to local annual mean surface temperature, and partly from uncertainties in the conversion of the local temperatures to an annual mean global surface temperature. Overall, the global mean LGM cooling relative to pre-industrial is assessed to be *very likely* from 5–7°C (Chapter 2, Section 2.3.1). The LGM climate is often assumed to be in full equilibrium with the forcing, such that ΔN in Equation 7.1, Box 7.1, is zero. A calculation of sensitivity using solely CO_2 forcing, and assuming that the LGM ice sheets were in equilibrium with that forcing, would give an Earth System Sensitivity (ESS) rather than an ECS (see Box 7.1). In order to calculate an ECS, which is defined here to include all feedback processes except ice sheets, the approach of Rohling et al. (2012) can be used. This approach introduces an additional forcing term in Equation 7.1, Box 7.1, that quantifies the resulting forcing associated with the ice sheet feedback (primarily an estimate of the radiative forcing associated with the change in surface albedo). However, differences between studies as to which processes are considered as forcings (for example, some studies also include vegetation and/or aerosols, such as dust, as forcings), means that published estimates are not always directly comparable. Additional uncertainty arises from the magnitude of the ice sheet forcing itself (Stap et al., 2019; Zhu and Poulsen, 2021), which is often estimated using ESMs. Furthermore, the ECS at the LGM may differ from that of today due to state-dependence (see Section 7.4.3). Here, only studies that report values of ECS that have accounted for the long-term feedbacks associated with ice sheets, and therefore most closely estimate ECS as defined in this chapter, are assessed here (see Table 7.11).

7.5.3.2 Estimates of ECS from glacial-interglacial cycles

Since AR5, several studies have extended the Rohling et al. (2012) approach (described above for the LGM) to the glacial-interglacial cycles of the last ~1 to 2 million years (von der Heydt et al., 2014; Köhler et al., 2015; Friedrich et al., 2016; Royer, 2016; Köhler et al., 2017, 2018; Snyder, 2019; Stap et al., 2019; Friedrich and Timmermann, 2020; Table 7.11). Compared to the LGM, uncertainties in the derived ECS from these periods are in general greater, due to greater uncertainty in global surface temperature (due to fewer individual sites with proxy temperature records), ice sheet forcing (due to a lack of detailed ice sheet reconstructions), and CO_2 forcing (for those studies that include the pre-ice core period, where CO_2 reconstructions are substantially more uncertain). Furthermore, accounting for varying orbital forcing in the traditional global-mean forcing and response energy budget framework (Box 7.1) is challenging (Schmidt et al., 2017b), due to seasonal and latitudinal components of the forcing that, despite a close-to-zero orbital forcing in the global annual mean, can directly result in responses in annual mean global surface temperature (Liu et al., 2014), ice volume (Abe-Ouchi et al., 2013), and feedback processes such as those associated with methane (Singarayer et al., 2011). In addition, for time periods in which the forcing relative to the modern era is small (interglacials), the inferred ECS has relatively large uncertainties because the forcing and temperature response (ΔF and ΔT in Equation 7.1 in Box 7.1) are both close to zero.

7.5.3.3 Estimates of ECS from warm periods of the pre-Quaternary

In the pre-Quaternary (prior to about 2.5 million years ago), the forcings and response are generally of the same sign and similar magnitude as future projections of climate change (Burke et al., 2018; Tierney et al., 2020a). Similar uncertainties as for the LGM apply, but in this case a major uncertainty relates to the forcing, because prior to the ice core record there are only indirect estimates of CO_2 concentration. However, advances in pre-ice-core CO_2 reconstruction (e.g., Foster and Rae, 2016; Super et al., 2018; Witkowski et al., 2018) mean that the estimates of pre-Quaternary CO_2 have less uncertainty than at the time of AR5, and these time periods can now contribute to an assessment of climate sensitivity (see Table 7.11). The mid-Pliocene warm period (MPWP; Cross-Chapter Box 2.1; Cross-Chapter Box 2.4) has been targeted for constraints on ECS (Martínez-Botí et al., 2015; Sherwood et al., 2020b), due to the fact that CO_2 concentrations were relatively high at this time (350–425 ppm) and because the MPWP is sufficiently recent that topography and continental configuration are similar to modern-day. As such, a comparison of the MPWP with the pre-industrial climate provides probably the closest natural geological analogue for the modern day that is useful for assessing constraints on ECS, despite the effects of different geographies not being negligible (global surface temperature patterns; ocean circulation). Furthermore, the global surface temperature of the MPWP was such that non-linearities in feedbacks (Section 7.4.3) were relatively modest.

Within the MPWP, the KM5c interglacial has been identified as a particularly useful time period for assessing ECS (Haywood et al., 2013, 2016b) because Earth's orbit during that time was very similar to that of the modern-day.

Further back in time, in the early Eocene (Cross-Chapter Box 2.1), uncertainties in forcing and temperature change become larger, but the signals are generally larger too (Anagnostou et al., 2016, 2020; Shaffer et al., 2016; Inglis et al., 2020). Caution must be applied when estimating ECS from these time periods, due to differing continental position and topography/bathymetry (Farnsworth et al., 2019), and due to temperature-dependence of feedbacks (Section 7.4.3). On even longer timescales of the last 500 million years (Royer, 2016) the temperature and CO_2 measurements are generally asynchronous, presenting challenges in using this information for assessments of ECS.

7.5.3.4 Synthesis of ECS based on paleo radiative forcing and temperature

The lines of evidence directly constraining ECS from paleoclimates are summarised in Table 7.11. Although some of the estimates in Table 7.11 are not independent because they use similar proxy records to each other (e.g., von der Heydt et al., 2014; Köhler et al., 2015, 2017; Stap et al., 2019), there are still multiple independent lines of paleoclimate evidence regarding ECS, from differing past time periods (LGM (Sherwood et al., 2020b; Tierney et al., 2020b); glacial-interglacial (Royer, 2016; Köhler et al., 2017; Snyder, 2019; Friedrich and Timmermann, 2020), Pliocene (Martínez-Botí et al., 2015; Sherwood et al., 2020b) and the Eocene (Anagnostou et al., 2016, 2020; Shaffer et al., 2016; Inglis et al., 2020), with differing proxies for estimating forcing (e.g., CO_2 from ice cores or boron isotopes) and response (e.g., global surface temperature from $\delta^{18}O$, Mg/Ca or Antarctic δD). Furthermore, although different studies have uncertainty estimates that account for differing sources of uncertainty, some studies (Snyder, 2019; Inglis et al., 2020; Sherwood et al., 2020b; Tierney et al., 2020b) do consider many of the uncertainties discussed in Sections 7.5.3.1-7.5.3.3. All the studies based on glacial-interglacial cycles account for some aspects of the state-dependence of climate sensitivity (Section 7.4.3) by considering only the warm phases of the Pleistocene, although what constitutes a warm phase is defined differently across the studies.

[START TABLE 7.11 HERE]

Table 7.11: Estimates of ECS derived from paleoclimates; from AR5 (above double lines) and from post-AR5 studies (below double lines). Many studies provide an estimate of ECS that includes only CO_2 and the ice sheet feedback as forcings, providing an estimate of $S_{[CO2, LI]}$ using the notation of Rohling et al. (2012), which is equivalent to our definition of ECS (Box 7.1). However, some studies provide estimates of other types of sensitivity (column 4). Different studies (column 1) focus on different time periods (column 2) and use a variety of different paleoclimate proxies and models (column 3) to give a best estimate (column 5) and/or a range (column 5). The published ranges given account for varying sources of uncertainty (column 6). See Cross-Chapter Box 2.1 for definition of time periods. All temperature values in column (5) are shown to a precision of 1 decimal place.

(1) Study	(2) Time period	(3) Proxies/models used for CO_2, temperature (T), and global scaling (GS).	(4) Climate sensitivity classification according to Rohling et al. (2012).	(5) Published best estimate of ECS [and/or range]	(6) Range accounts for:
AR5 (Masson-Delmotte et al., 2013)	LGM	Assessment of multiple lines of evidence	S^a = ECS	[*very likely* > 1.0 ; very unlikely > 6.0 °C]	Multiple sources of uncertainty
AR5	Cenozoic (last 65	Assessment of	$S_{[CO2,LI]}$	[95% range:	Multiple

(Masson-Delmotte et al., 2013)	million years)	multiple lines of evidence		1.1 to 7.0 °C]	sources of uncertainty
Tierney et al. (2020b)	LGM	CO_2: ice core T: multiproxy	$S_{[CO2,LI,CH4,N2O]}$	3.8 °C [68% range: 3.3 to 4.3°C]	Multiple sources of uncertainty
Sherwood et al. (2020)	LGM	CO_2: ice core T: multiple lines of evidence	$S_{[CO2, LI, CH4, N2O, dust, VG]}$	maximum likelihood: 2.6 °C [*likely* range depends on chosen prior; 0.6 likelihood: 1.6 to 4.4°C]	Multiple sources of uncertainty
von der Heydt et al. (2014)	Warm states of glacial-interglacial cycles of last 800 kyrs.	CO_2: ice core T: ice core δD, benthic $\delta^{18}O$. GS: Annan and Hargreaves, Schneider von Deimling	$S_{[CO2,LI]}$	3.5°C [range: 3.1 to 5.4°C]*	Varying LGM global mean temperatures used for scaling.
Köhler et al. (2015)	Warm states of glacial-interglacial cycles of last 2 Myrs.	CO_2: ice core alkenones and boron isotopes T: benthic $\delta^{18}O$ GS: PMIP LGM and PlioMIP MPWP	$S_{[CO2,LI]}$	5.7 °C [68% range: 3.7 to 8.1 °C]*	Temporal variability in records.
Köhler et al. (2017)	Warm states of glacial-interglacial cycles of last 2 Myrs.	CO_2: boron isotopes T: benthic $\delta^{18}O$ GS: PMIP LGM and PlioMIP MPWP	$S_{[CO2,LI]}$	5.6 °C [16^{th} to 84^{th} percentile: 3.6 to 8.1 °C]*	Temporal variability in records.
Köhler et al. (2018)	Warm states of glacial-interglacial cycles of last 800 kyrs, excluding those for which CO_2 and T diverge.	CO_2: ice cores T: benthic $\delta^{18}O$, alkenone, Mg/Ca, MAT, and faunal SST GS: PMIP3 LGM	$S_{[CO2, LI]}$	[range: 3.0 to 5.9 °C]*	Varying temperature reconstructions.
(Stap et al., 2019)	States of glacial-interglacial cycles of last 800 kyrs for which forcing is zero compared with modern, excluding those for which CO_2 and T diverge.	CO_2: ice cores T: benthic $\delta^{18}O$ GS: PMIP LGM and PlioMIP MPWP	$S_{[CO2, LI]}$	[range: 6.1 to 11.0 °C]*	Varying efficacies of ice sheet forcing
Friedrich et al. (2016)	Warm states of glacial-interglacial cycles of last 780 kyrs.	CO_2: ice cores T: alkenone, Mg/Ca, MAT, and faunal SST GS: PMIP3 LGM.	$S_{[GHG,LI,AE]}$	4.9 °C [*Likely* range: 4.3 to 5.4°C]*	Varying LGM global mean temperatures, aerosol forcing.

Friedrich and Timmermann (2020)	Last glacial-interglacial cycle	CO_2: ice cores T: alkenone, Mg/Ca, MAT	$S_{[GHG,LI,AE]}$	4.2°C [range: 3.4 to 6.2°C]*	Varying aerosol forcings
Snyder (2019)	Interglacial periods and intermediate glacial climates of last 800 kyrs	CO_2: ice cores T: alkenone, Mg/Ca, species assemblages GS: PMIP models	$S_{[GHG,LI,AE,VG]}$	3.1°C [67% range : 2.6 to 3.7 °C]*	Multiple sources of uncertainty
Royer (2016)	Glacial-interglacial cycles of the Pliocene (3.4 to 2.9 Ma)	CO_2: boron isotopes T: benthic $\delta^{18}O$	$S_{[CO2,LI]}$	10.2°C [68% range: 8.1 to 12.3°C]	Temporal variability in records.
Martínez-Botí et al. (2015)	Pliocene	CO_2: boron isotopes T: benthic $\delta^{18}O$	$S_{[CO2,LI]}$	3.7 °C [68% range: 3.0 to 4.4°C]*	Pliocene sea level, temporal variability in records.
Sherwood et al. (2020)	Pliocene	CO_2: boron isotopes T: multiple lines of evidence	$S_{[CO2, LI,N2O,CH4,VG]}$	maximum likelihood: 3.2°C [*likely* range depends on chosen prior; 0.6 likelihood: 1.8 to 5.2°C]	Multiple sources of uncertainty
Anagnostou et al. (2016)	Early Eocene	CO_2: boron isotopes T: various terrestrial MAT, Mg/Ca, TEX, $\delta^{18}O$ SST.	$S_{[CO2,LI]}$	3.6 °C [66% range: 2.1 to 4.6 °C]	Varying calibrations for temperature and CO_2.
Anagnostou et al. (2020)	Late Eocene (41.2 to 33.9 Ma)	CO_2: boron isotopes T: one SST record GS: CESM1	$S_{[CO2,LI]}$	3.0 °C [68% range: 1.9 to 4.1 °C]	Temporal variability in records.
Shaffer et al. (2016)	Pre-PETM	CO_2: mineralogical, carbon cycling, and isotope constraints T: various terrestrial MAT, Mg/Ca, TEX, $\delta^{18}O$ SST.	$S_{[GHG,AE,VG,LI]}$	[range: 3.3 to 5.6 °C]	Varying calibration of temperature and CO_2.
Inglis et al. (2020)	Mean of EECO, PETM, and latest Paleocene	CO_2: boron isotopes T: multiproxy SST and SAT GS: EoMIP models	$S_{[CO2,LI, VG,AE]}$	3.7 °C [*likely* range : 2.2 to 5.3°C]	Multiple sources of uncertainty

Notes:
(Note 1) S^a in this table denotes a classification of climate sensitivity following (Rohling et al., 2012).
(Note 2) * = Although our assessed value of ERF due to CO_2 doubling is 3.93 W m^{-2} (Section 7.3.2.1), for these studies the best estimate and range of temperature is calculated from the published estimate of sensitivity in units of °C (W m^{-2})$^{-1}$ using an ERF of 3.7 W m^{-2}, for consistency with the typical value used in the studies to estimate the paleo CO_2 forcing.

[END TABLE 7.11 HERE]

None of the post-AR5 studies in Table 7.11 have an estimated lower range for ECS below 1.6 °C. As such, based solely on the paleoclimate record, it is assessed to be *very likely* that ECS is greater than 1.5°C (*high confidence*).

In general, it is the studies based on the warm periods of the glacial-interglacial cycles (Section 7.5.3.2) that give the largest values of ECS. Given the large uncertainties associated with estimating the magnitude of the ice sheet forcing during these intervals (Stap et al., 2019), and other uncertainties discussed in Section 7.5.3.2, in particular the direct effect of orbital forcing on estimates of ECS, there is only *low confidence* in estimates from the studies based on glacial-interglacial periods. This *low confidence* also results from the temperature-dependence of the net feedback parameter, α, resulting from several of these studies (Figure 7.10), that is hard to reconcile with the other lines of evidence for α, including proxy estimates from warmer paleoclimates (Section 7.4.3.2). A central estimate of ECS, derived from the LGM (Section 7.5.3.1) and warm periods of the pre-Quaternary (Section 7.5.3.3), that takes into account some of the interdependencies between the different studies, can be obtained by averaging across studies within each of these two time periods, and then averaging across the two time periods; this results in a central estimate of 3.4°C. This approach of focussing on the LGM and warm climates was also taken by Sherwood et al. (2020) in their assessment of ECS from paleoclimates. An alternative method is to average across all studies, from all periods, that have considered multiple sources of uncertainty (Table 7.11); this approach leads to a similar central estimate of 3.3°C. Overall, we assess *medium confidence* for a central estimate of 3.3–3.4°C.

There is more variation in the upper bounds of ECS than in the lower bounds. Estimates of ECS from pre-Quaternary warm periods have an average upper range of 4.9 °C, and from the LGM of 4.4°C; taking into account the independence of the estimates from these two time periods, and accounting for state-dependence (Section 7.4.3) and other uncertainties discussed in Section 7.5.3, the paleoclimate record on its own indicates that ECS is *likely* less than 4.5 °C. Given the higher values from many glacial-interglacial studies, this value has only *medium confidence*. Despite the large variation in individual studies at the extreme upper end, all except two studies (both of which are from glacial-interglacial time periods associated with *low confidence*) have central estimates that are below 6 °C; overall we assess that it is *extremely likely* that ECS is below 8 °C (*high confidence*).

7.5.4 Estimates of ECS and TCR based on emergent constraints

ESMs exhibit substantial spread in ECS and TCR (Section 7.5.7). Numerous studies have leveraged this spread in order to narrow estimates of Earth's climate sensitivity by employing methods known as "emergent constraints" (Chapter 1, Section 1.5.4). These methods establish a relationship between an observable and either ECS or TCR based on an ensemble of models, and combine this information with observations to constrain the probability distribution of ECS or TCR. Most studies of this kind have clearly benefitted from the international efforts to coordinate the CMIP and other multi-model ensembles.

A number of considerations must be taken into account when assessing the diverse literature on ECS and TCR emergent constraints. For instance, it is important to have physical and theoretical basis for the connection between the observable and modelled ECS or TCR since in model ensembles thousands of relationships that pass statistical significance can be found simply by chance (Caldwell et al., 2014). It is also important that the underlying model ensemble does not exhibit a shared bias that influences the simulation of the observable quantity on which the emergent constraint is based. Also, correctly accounting for uncertainties in both the observable (including measurement uncertainty and natural variability) and the emergent constraint statistical relationship can be challenging, in particular in cases where the latter is not expected to be linear (Annan et al., 2020a). A number of proposed emergent constraints leverage variations in modelled ECS arising from tropical low clouds, which was the dominant source of inter-model spread in the CMIP5 ensemble used in most emergent constraint studies. Since ECS is dependent on the sum of individual feedbacks (Section 7.5.1) these studies implicitly assume that all other feedback processes in models are unbiased and should therefore rather be thought of as constraints on tropical low-cloud feedback (Klein and Hall, 2015; Qu et al., 2018; Schlund et al., 2020). The following sections go through a range of emergent constraints and assess their strengths and limitations.

7.5.4.1 Emergent constraints using global or near-global surface temperature change

Perhaps the simplest class of emergent constraints regress past equilibrium paleoclimate temperature change against modelled ECS to obtain a relationship that can be used to translate a past climate change to ECS. The advantage is that these are constraints on the sum of all feedbacks, and furthermore unlike constraints on the instrumental record they are based on climate states that are at, or close to, equilibrium. So far, these emergent constraints have been limited to the Last Glacial Maximum (LGM; Cross-Chapter Box 2.1) cooling (Hargreaves et al., 2012; Schmidt et al., 2014; Renoult et al., 2020) and warming in the mid-Pliocene Warm Period (MPWP, Hargreaves and Annan, 2016; Renoult et al., 2020; Cross-Chapter Box 2.1; Cross-Chapter Box 2.4) due to the availability of sufficiently large multi-model ensembles for these two cases. The paleoclimate emergent constraints are limited by structural uncertainties in the proxy-based global surface temperature and forcing reconstructions (Section 7.5.3), possible differences in equilibrium sea-surface temperature patterns between models and the real world, and a small number of model simulations participating, which has led to divergent results. For example, Hopcroft and Valdes (2015) repeated the study based on the LGM by Hargreaves et al. (2012) using another model ensemble and found that the emergent constraint was not robust, whereas studies using multiple available ensembles retain useful constraints (Schmidt et al., 2014; Renoult et al., 2020). Also, the results are somewhat dependent on the applied statistical methods (Hargreaves and Annan, 2016). However, Renoult et al. (2020) explored this and found 95th percentiles of ECS below 6°C for LGM and Pliocene individually, regardless of statistical approach, and by combining the two estimates the 95th percentile dropped to 4.0°C. The consistency between the cold LGM and warm MPWP emergent constraint estimates increases confidence in these estimates, and further suggests that the dependence of feedback on climate mean state (Section 7.4.3) as represented in PMIP models used in these studies is reasonable.

Various emergent constraint approaches using global warming over the instrumental record have been proposed. These benefit from more accurate data compared with paleoclimates, but suffer from the fact that the climate is not in equilibrium, thereby assuming that ESMs on average accurately depict the ratio of short term to long term global warming. Global warming in climate models over 1850 to the present day exhibits no correlation with ECS, which is partly due to a substantial number of models exhibiting compensation between a high climate sensitivity with strong historical aerosol cooling (Kiehl, 2007; Forster et al., 2013; Nijsse et al., 2020). However, the aerosol cooling increased up until the 1970s when air quality regulations reduced the emissions from Europe and North America whereas other regions saw increases resulting in a subsequently reduced pace of global mean aerosol ERF increase (Chapter 2, Section 2.2.8, Figure 2.10). Energy balance considerations over the 1970–2010 period gave a best estimate ECS of 2.0°C (Bengtsson and Schwartz, 2013), however this estimate did not account for pattern effects. To address this limitation an emergent constraint on 1970–2005 global warming was demonstrated to yield a best estimate ECS of 2.83 [1.72 to 4.12] °C (Jiménez-de-la-Cuesta and Mauritsen, 2019). The study was followed up using CMIP6 models yielding a best estimate ECS of 2.6 [1.5 to 4.0] °C based on 1975–2019 global warming (Nijsse et al., 2020), thereby confirming the emergent constraint. Internal variability and forced or unforced pattern effects may influence the results (Jiménez-de-la-Cuesta and Mauritsen, 2019; Nijsse et al., 2020). For instance the Atlantic Multidecadal Oscillation changed from negative to positive anomaly, while the Indo-Pacific Oscillation changed less over the 1970–2005 period, potentially leading to high-biased results (Jiménez-de-la-Cuesta and Mauritsen, 2019), whereas during the later period 1975–2019 these anomalies roughly cancel (Nijsse et al., 2020). Pattern effects may have been substantial over these periods (Andrews et al., 2018), however the extent to which TOA radiation anomalies influenced surface temperature may have been dampened by the deep ocean (Hedemann et al., 2017; Newsom et al., 2020). It is therefore deemed *more likely than not* that these estimates based on post-1970s global warming are biased low by internal variability.

A study that developed an emergent constraint based on the response to the Mount Pinatubo 1991 eruption yielded a best estimate of 2.4 [*likely* range 1.7–4.1] °C (Bender et al., 2010). When accounting for ENSO variations they found a somewhat higher best estimate of 2.7°C, which is in line with results of later studies that suggest ECS inferred from periods with substantial volcanic activity are low-biased due to strong pattern effects (Gregory et al., 2020) and that the short-term nature of volcanic forcing could exacerbate possible underestimates of modelled pattern effects.

Lagged-correlations present in short term variations in the global surface temperature can be linked to ECS through the fluctuation-dissipation theorem which is derived from a single heat reservoir model (Einstein, 1905; Hasselmann, 1976; Schwartz, 2007; Cox et al., 2018a). From this it follows that the memory carried by the heat capacity of the ocean results in low-frequency global temperature variability (red noise) arising from high frequency (white noise) fluctuations in the radiation balance, e.g., caused by weather. Initial attempts to apply the theorem to observations yielded a fairly low median ECS estimate of 1.1°C (Schwartz, 2007), a result that was disputed (Foster et al., 2008; Knutti et al., 2008). Recently it was proposed by Cox et al. (2018a) to use variations in the historical experiments of the CMIP5 climate models as an emergent constraint giving a median ECS estimate of 2.8 [1.6 to 4.0] °C. A particular challenge associated with these approaches is to separate short-term from long-term variability, and slightly arbitrary choices regarding the methodology of separating these in the global surface temperature from long-term signals in the historical record, omission of the more strongly forced period after 1962, as well as input data choices, can lead to median ECS estimates ranging from 2.5–3.5°C (Brown et al., 2018; Po-Chedley et al., 2018b; Rypdal et al., 2018). Calibrating the emergent constraint using CMIP5 modelled internal variability as measured in historical control simulations (Po-Chedley et al., 2018b) will inevitably lead to an overestimated ECS due to externally forced short term variability present in the historical record (Cox et al., 2018b). Contrary to constraints based on paleoclimates or global warming since the 1970s, when based on CMIP6 models a higher, yet still well-bounded ECS estimate of 3.7 [2.6 to 4.8] °C is obtained (Schlund et al., 2020). A more problematic issue is raised by (Annan et al., 2020b) who showed that the upper bound on ECS estimated this way is less certain when considering deep ocean heat uptake. In conclusion, even if not inconsistent, these limitations prevents us from directly using this type of constraint in the assessment.

Short term variations in the TOA energy budget, observable from satellites, arising from variations in the tropical tropospheric temperature has been linked to ECS through models, either as a range of models consistent with observations (those with ECS values between 2.0°C and 3.9°C) (Dessler et al., 2018) or as a formal emergent constraint by deriving further model-based relationships to yield a median of 3.3 [2.4 to 4.5] °C (Dessler and Forster, 2018). There are major challenges associated with short term variability in the energy budget, in particular how it relates to the long-term forced response of clouds (Colman and Hanson, 2017; Lutsko and Takahashi, 2018), and variations in the surface temperature that are not directly affecting the radiation balance lead to an overestimated ECS when using linear regression techniques where it appears as noise in the independent variable (Proistosescu et al., 2018; Gregory et al., 2020). The latter issue is largely overcome when using the tropospheric mean or mid-tropospheric temperature (Trenberth et al., 2015; Dessler et al., 2018).

7.5.4.2 Emergent constraints focused on cloud feedbacks and present-day climate

A substantial number of emergent constraint studies focus on observables that are related to tropical low-cloud feedback processes (Volodin, 2008; Sherwood et al., 2014; Zhai et al., 2015; Brient and Schneider, 2016; Brient et al., 2016). These studies yield median ECS estimates of 3.5–4°C and in many cases indicate low likelihoods of values below 3°C. The approach has attracted attention since most of the spread in climate sensitivity seen in CMIP5, and earlier climate model ensembles, arises from uncertainty in low cloud feedbacks (Bony and Dufresne, 2005; Wyant et al., 2006; Randall et al., 2007; Vial et al., 2013). Nevertheless, this approach assumes that all other feedback processes are unbiased (Klein and Hall, 2015; Qu et al., 2018; Schlund et al., 2020), for instance the possibly missing negative anvil area feedback or the possibly exaggerated mixed-phase cloud feedback (Section 7.4.2.4). Thus, the subset of emergent constraints that focus on low-level tropical clouds are not necessarily inconsistent with other emergent constraints of ECS. Related emergent constraints that focus on aspects of the tropical circulation and ECS have led to conflicting results (Su et al., 2014; Tian, 2015; Lipat et al., 2017; Webb and Lock, 2020), possibly because these processes are not the dominant factors in causing the inter-model spread (Caldwell et al., 2018).

The fidelity of models in reproducing aspects of temperature variability or the radiation budget has also been proposed as emergent constraints on ECS (Covey et al., 2000; Knutti et al., 2006; Huber et al., 2010; Bender et al., 2012; Brown and Caldeira, 2017; Siler et al., 2018a). Here indices based on spatial or seasonal variability are linked to modelled ECS, and overall the group of emergent constraints yields best estimates of 3.3°C to 3.7°C. Nevertheless, the physical relevance of present-day biases to the sum of long-term climate change feedbacks is unclear and therefore these constraints on ECS are not considered reliable.

7.5.4.3 Assessed ECS and TCR based on emergent constraints

The available emergent constraint studies have been divided into two classes: (i) those that are based on global or near-global indices, such as global surface temperature and the TOA energy budget; and (ii) those that are more focussed on physical processes, such as the fidelity of phenomena related to low-level cloud feedbacks or present-day climate biases. The former class is arguably superior in representing ECS, since it is a global surface temperature or energy budget change, whereas the latter class is perhaps best thought of as providing constraints on individual climate feedbacks, e.g., the determination that low-level cloud feedbacks are positive. The latter result is consistent with and confirms process-based estimates of low cloud feedbacks (Section 7.4.2.4), but are potentially biased as a group by missing or biased feedbacks in ESMs and is accordingly not taken into account here. A limiting case here is Dessler and Forster (2018) which is focused on monthly co-variability in the global TOA energy budget with mid-tropospheric temperature, at which time scale the surface albedo feedback is unlikely to operate thus implicitly assuming it is unbiased in the model ensemble.

In the first group of emergent constraints there is broad agreement on the best estimate of ECS ranging from 2.4–3.3°C. At the lower end, nearly all studies find lower bounds (5th percentiles) around 1.5°C, whereas several studies indicate 95th percentiles as low as 4°C. Considering both classes of studies, none of them yield upper *very likely* bounds above 5°C. Since several of the emergent constraints can be considered nearly independent one could assume that emergent constraints provide very strong evidence on ECS by combining them. Nevertheless, this is not done here because there are sufficient cross-dependencies, as for instance models are re-used in many of the derived emergent constraints, and furthermore the methodology has not yet reached a sufficient level of maturity since systematic biases may not have been accounted for. Uncertainty is therefore conservatively added to reflect these potential issues. This leads to the assessment that ECS inferred from emergent constraints is *very likely* 1.5 to 5°C with *medium confidence*.

Emergent constraints on TCR with a focus on the instrumental temperature record, though less abundant, have also been proposed. These can be influenced by internal variability and pattern effects as discussed in Section 7.5.4.1, although the influence is smaller because uncertainty in forced pattern effects correlate between transient historical warming and TCR. In the simplest form Gillett et al. (2012) regressed the response of one model to individual historical forcing components to obtain a tight range of 1.3–1.8°C, but later when an ensemble of models was used the range was widened to 0.9–2.3°C (Gillett et al., 2013), and updated by Schurer et al. (2018). A related data-assimilation based approach that accounted also for uncertainty in response patterns gave 1.33–2.36°C (Ribes et al., 2021), but is dependent on the choice of prior ensemble distribution (CMIP5 or CMIP6). Another study used the response to the Pinatubo volcanic eruption to obtain a range of 0.8–2.3°C (Bender et al., 2010). A tighter range, notably at the lower end, was found in an emergent constraint focusing on the post-1970s warming exploiting the lower spread in aerosol forcing change over this period (Jiménez-de-la-Cuesta and Mauritsen, 2019). Their estimate was 1.67 [1.17 to 2.16] °C. Two studies tested this idea: Tokarska et al. (2020) estimates TCR was 1.60 [0.90 to 2.27] °C based on CMIP6 models, whereas Nijsse et al. (2020) found 1.68 [1.0 to 2.3] °C, and in both cases there was a small sensitivity to choice of ensemble with CMIP6 models yielding slightly lower values and ranges. Combining these studies gives a best estimate of 1.7°C and a *very likely* range of TCR of 1.1–2.3°C with *high confidence*.

[START TABLE 7.12 HERE]

Table 7.12: Emergent constraint studies used in the assessment of ECS. These are studies that rely on global or near-global temperature change as the observable.

Study	Emergent constraint description	Published best estimate and uncertainty (°C)	Uncertainty estimate:
(Bender et al., 2010)	Pinatubo integrated forcing normalized by CMIP3 models own forcing versus temperature change regressed against ECS	2.4 [1.7 to 4.1]	5% to 95%
(Dessler and Forster, 2018)	Emergent constraint on TOA radiation variations linked to mid-tropospheric temperature in CMIP5 models	3.3 [2.4 to 4.5]	17% to 83%
(Hargreaves et al., 2012)	Last Glacial Maximum tropical SSTs in PMIP2 models	2.5 [1.3 to 4.2]	5% to 95%
(Hargreaves and Annan, 2016)	Pliocene tropical SSTs in PlioMIP models	[1.9 to 3.7]	5% to 95%
(Jiménez-de-la-Cuesta and Mauritsen, 2019)	Post–1970s global warming, 1995–2005 relative to 1970–1989, CMIP5 models	2.83 [1.72 to 4.12]	5% to 95%
(Nijsse et al., 2020)	Post–1970s global warming, 2009–2019 relative to 1975–1985, CMIP6 models	2.6 [1.5 to 4.0]	5% to 95%
(Renoult et al., 2020)	Combined Last Glacial Maximum and Pliocene tropical SSTs in PMIP2, PMIP3, PMIP4, PlioMIP and PlioMIP2 models	2.5 [0.8 to 4.0]	5% to 95%

[END TABLE 7.12 HERE]

7.5.5 Combined assessment of ECS and TCR

Substantial quantitative progress has been made in interpreting evidence of Earth's climate sensitivity since AR5, through innovation, scrutiny, theoretical advances and a rapidly evolving data base from current, recent and paleo climates. It should be noted that, unlike AR5 and earlier reports, our assessment of ECS is not directly informed by ESM simulations (Section 7.5.6). The assessments of ECS and TCR are focussed on the following lines of evidence: process-understanding; the instrumental record of warming; paleoclimate evidence; and emergent constraints. ESMs remain essential tools throughout establishing these lines of evidence, for instance for estimating part of the feedback parameters and radiative forcings, and emergent constraints rely on substantial model spread in ECS and TCR (Section 7.5.6).

A key advance over the AR5 assessment is the broad agreement across multiple lines of evidence. These support a central estimates of ECS close to, or at least not inconsistent with, 3°C. This advance is foremost following improvements in the understanding and quantification of Earth's energy imbalance, the instrumental record of global temperature change, and the strength of anthropogenic radiative forcing. Further advances include increased understanding of how the pattern effect influences ECS inferred from historical global warming (Sections 7.4.4 and 7.5.3), improved quantification of paleo climate change from proxy evidence and a deepened understanding of how feedback mechanisms increase ECS in warmer climate states (Sections 7.4.3, 7.4.4 and 7.5.4), and also an improved quantification of individual cloud feedbacks (Sections 7.4.2 and 7.5.4.2). The assessment findings for ECS and TCR are summarized in Table 7.13 and Table 7.14, respectively, and also visualized in Figure 7.18.

[START FIGURE 7.18 HERE]

Figure 7.18: Summary of the equilibrium climate sensitivity (ECS) and transient climate response (TCR)

assessments using different lines of evidence. Assessed ranges are taken from Tables 7.13 and 7.14 for ECS and TCR respectively. Note that for the ECS assessment based on both the instrumental record and paleoclimates, limits (i.e. one-sided distributions) are given, which have twice the probability of being outside the maximum/minimum value at a given end, compared to ranges (i.e. two tailed distributions) which are given for the other lines of evidence. For example, the *extremely likely* limit of greater than 95% probability corresponds to one side of the *very likely* (5% to 95%) range. Best estimates are given as either a single number or by a range represented by grey box. CMIP6 model values are not directly used as a line of evidence but presented on the Figure for comparison. ECS values are taken from Schlund et al. (2020) and TCR values from Meehl et al. (2020), see Supplementary Material 7.SM.4. Further details on data sources and processing are available in the chapter data table (Table 7.SM.14).

[END FIGURE 7.18 HERE]

AR5 assessed ECS to have a *likely* range from 1.5 to 4.5°C (Collins et al., 2013a) based on the majority of studies and evidence available at the time. The broader evidence base presented in this Report and the general agreement among different lines of evidence means that they can be combined to yield a narrower range of ECS values. This can be done formally using Bayesian statistics, though such a process is complex and involves formulating likelihoods and priors (Annan and Hargreaves, 2006; Stevens et al., 2016; Sherwood et al., 2020b). However, it can be understood that if two lines of independent evidence each give a low probability of an outcome being true, e.g., that ECS is less than 2.0°C, then the combined probability that ECS is less than 2.0°C is lower than that of either line of evidence. On the contrary, if one line of evidence is unable to rule out an outcome, but another is able to assign a low probability, then there is a low probability that the outcome is true (Stevens et al., 2016). This general principle applies even when there is some dependency between the lines of evidence (Sherwood et al., 2020b), for instance between historical energy budget constraints (Section 7.5.2.1) and those emergent constraints that use the historically observed global warming (Section 7.5.4.1). Even in this case the combined constraint will be closer to the narrowest range associated with the individual lines of evidence.

In the process of providing a combined and self-consistent ECS assessment across all lines of evidence, the above principles were all considered. As in earlier reports, a 0.5°C precision is used. Starting with the *very likely* lower bound, there is broad support for a value of 2.0°C, including process understanding and the instrumental record (Table 7.13). For the *very likely* upper bound, emergent constraints give a value of 5.0°C whereas the three other lines of evidence are individually less tightly constrained. Nevertheless, emergent constraints are a relatively recent field of research, in part taken into account by adding uncertainty to the upper bound (Section 7.5.4.3), and the underlying studies use, to a varying extent, information that is also used in the other three lines of evidence causing statistical dependencies. However, omitting emergent constraints and statistically combining the remaining lines of evidence likewise yields 95th percentiles close to 5.0°C (Sherwood et al., 2020b). Information for the *likely* range is partly missing or one-sided, however it must necessarily reside inside the *very likely* range and is therefore supported by evidence pertaining to both the *likely* and *very likely* ranges. Hence, the upper *likely* bound is assessed to be about halfway between the best estimate and the upper *very likely* bound while the lower *likely* bound is assessed to be about halfway between the best estimate and the lower *very likely* bound. In summary, based on multiple lines of evidence the best estimate of ECS is 3°C, it is *likely* within the range 2.5 to 4°C and *very likely* within the range 2 to 5°C. It is *virtually certain* that ECS is larger than 1.5°C. Whereas there is *high confidence* based on mounting evidence that supports the best estimate, *likely* range and *very likely* lower end, a higher ECS than 5°C cannot be ruled out, hence there is *medium confidence* in the upper end of the *very likely* range. Note that the best estimate of ECS made here corresponds to a feedback parameter of -1.3 W m^{-2} °C^{-1} which is slightly more negative than the feedback parameter from process based evidence alone that is assessed in Section 7.4.2.7).

There has long been a consensus (Charney et al., 1979) supporting an ECS estimates of 1.5 to 4°C. In this regard it is worth remembering the many debates challenging an ECS of this magnitude. These started as early as Ångström (1900) criticizing the results of Arrhenius (1896) arguing that the atmosphere was already saturated in infrared absorption such that adding more CO_2 would not lead to warming. The assertion of Ångström was understood half a century later to be incorrect. History has seen a multitude of studies (e.g., Svensmark, 1998; Lindzen et al., 2001; Schwartz, 2007) mostly implying lower ECS than the range assessed as *very likely* here. However, there are also examples of the opposite such as very large ECS estimates based on the Pleistocene records (Snyder, 2016), which has been shown to be overestimated due to a lack of accounting for orbital forcing and long term ice sheet feedbacks (Schmidt et al., 2017b), or suggestions that global climate instabilities may occur in the future (Steffen et al., 2018; Schneider et al., 2019). There is, however, no evidence for unforced instabilities of such magnitude occurring in the paleo record temperatures of the past 65 million years (Westerhold et al., 2020), possibly short of the PETM excursion (Chapter 5, Section 5.3.1.1) that occurred at more than 10°C above present (Anagnostou et al., 2020). Looking back, the resulting debates have led to a deeper understanding, strengthened the consensus, and have been scientifically valuable.

In the climate sciences, there are often good reasons to consider representing deep uncertainty, or what is sometimes referred to as unknown unknowns. This is natural in a field that considers a system that is both complex and at the same time challenging to observe. For instance, since emergent constraints represent a relatively new line of evidence, important feedback mechanisms may be biased in process-level understanding, pattern effects and aerosol cooling may be large and paleo evidence inherently builds on indirect and incomplete evidence of past climate states, there certainly can be valid reasons to add uncertainty to the ranges assessed on individual lines of evidence. This has indeed been addressed throughout Sections 7.5.1–7.5.4. Since it is neither probable that all lines of evidence assessed here are collectively biased nor is the assessment sensitive to single lines of evidence, deep uncertainty it is not considered as necessary to frame the combined assessment of ECS.

[START TABLE 7.13 HERE]

Table 7.13: Summary of ECS assessment

Equilibrium Climate Sensitivity (ECS)	Central value	*Likely*	*Very likely*	*Extremely likely*
Process understanding (7.5.1)	3.4°C	2.5 to 5.1 °C	2.1 to 7.7 °C	
Warming over instrumental record (7.5.2)	2.5 to 3.5 °C	> 2.2°C	> 1.8 °C	> 1.6 °C
Paleoclimates (7.5.3)	3.3 to 3.4°C	< 4.5 °C	> 1.5°C	< 8 °C
Emergent constraints (7.5.4)	2.4 to 3.3°C		1.5 to 5.0 °C	
Combined assessment	3°C	2.5 to 4.0 °C	2.0 to 5.0 °C	

[END TABLE 7.13 HERE]

The evidence for TCR is less abundant than for ECS, and focuses on the instrumental temperature record (Sections 7.5.2 and 7.5.6), emergent constraints (Section 7.5.4.3) and process understanding (Section 7.5.1). AR5 assessed a *likely* range of 1.0 to 2.5°C. TCR and ECS are related, though, and in any case TCR is less than ECS (see Section 7.5 introduction). Furthermore, estimates of TCR from the historical record are not as strongly influenced by externally forced surface temperature pattern effects as estimates of ECS are since both historical transient warming and TCR are affected by this phenomenon (Section 7.4.4). A slightly higher weight is given to instrumental record warming and emergent constraints since these are based on observed transient warming, whereas the process understanding estimate relies on pattern effects and ocean heat uptake efficiency from ESMs to represent the transient dampening effects of the ocean. If these effects are underestimated by ESMs then the resulting TCR would be lower. Given the interdependencies of the other two lines of evidence, a conservative approach to combining them as reflected in the assessment is adopted. Since uncertainty is substantially lower than in AR5 a 0.1°C precision is therefore used here. Otherwise the same methodology for combining the lines of evidence as applied to ECS is used for TCR. Based on process understanding, warming over the instrumental record and emergent constraints the best estimate TCR is 1.8°C, it is *likely* 1.4 to 2.2°C and *very likely* 1.2 to 2.4°C. The assessed ranges are all assigned *high confidence* due to the high level of agreement among the lines of evidence.

[START TABLE 7.14 HERE]

Table 7.14: Summary of TCR assessment

Transient Climate Response (TCR)	Central value	*Likely* range	*Very likely* range
Process understanding (7.5.1)	2.0 °C	1.6 to 2.7 °C	1.3 to 3.1 °C
Warming over instrumental record (7.5.2)	1.9 °C	1.5 to 2.3°C	1.3 to 2.7 °C
Emergent constraints (7.5.4)	1.7 °C		1.1 to 2.3°C
Combined assessment	1.8 °C	1.4 to 2.2°C	1.2 to 2.4°C

[END TABLE 7.14 HERE]

7.5.6 Considerations on the ECS and TCR in global climate models and their role in the assessment

Coupled climate models, such as those participating in CMIP, have long played a central role in assessments of ECS and TCR. In reports up to and including TAR, climate sensitivities derived directly from ESMs were the primary line of evidence. However, since AR4, historical warming and paleoclimate information provided useful additional evidence and it was noted that assessments based on models alone were problematic (Knutti, 2010). As new lines of evidence have evolved, in AR6 various numerical models are used where they are considered accurate, or in some cases the only available source of information, and thereby support all four lines of evidence (Sections 7.5.1-7.5.4). However, AR6 differs from previous IPCC reports in excluding direct estimates of ECS and TCR from ESMs in the assessed ranges (Section 7.5.5), following several recent studies (Annan and Hargreaves, 2006; Stevens et al., 2016; Sherwood et al., 2020b). The purpose of this section is to explain why this approach has been taken and to provide a perspective on the interpretation of the climate sensitivities exhibited in CMIP6 models.

The primary consideration that led to excluding ECS and TCR directly derived from ESMs is that information from these models is incorporated in the lines of evidence used in the assessment: ESMs are partly used to estimate historical- and paleoclimate ERFs (Sections 7.5.2 and 7.5.3); to convert from local to global mean paleo temperatures (Section 7.5.3), to estimate how feedbacks change with SST patterns (Section 7.4.4.3); and to establish emergent constraints on ECS (Section 7.5.4). They are also used as important evidence in the process understanding estimates of the temperature, water vapour, albedo, biogeophysical, and non-CO_2 biogeochemical feedbacks, whereas other evidence is primarily used for cloud feedbacks where the climate model evidence is weak (Section 7.4.2). One perspective on this is that the process understanding line of evidence builds on and replaces ESM estimates.

The ECS of a model is the net result of the model's effective radiative forcing from a doubling of CO_2 and the sum of the individual feedbacks and their interactions. It is well known that most of the model spread in ECS arises from cloud feedbacks, and particularly the response of low-level clouds (Bony and Dufresne, 2005; Zelinka et al., 2020). Since these clouds are small-scale and shallow, their representation in climate models is mostly determined by sub-grid scale parameterizations. It is sometimes assumed that parameterization improvements will eventually lead to convergence in model response and therefore a decrease in the model spread of ECS. However, despite decades of model development, increases in model resolution and advances in parametrization schemes, there has been no systematic convergence in model estimates of ECS. In fact, the overall inter model spread in ECS for CMIP6 is larger than for CMIP5; ECS and TCR values are given for CMIP6 models in Supplementary Material 7.SM.4 based on Schlund et al. (2020) for ECS and Meehl et al. (2020) for TCR, see also Figure 7.18 and FAQ 7.3. The upward shift does not apply to all models traceable to specific modelling centres, but a substantial subset of models have seen an increase in ECS between the two model generations. The increased ECS values, as discussed in Section 7.4.2.8, are partly due to shortwave cloud feedbacks (Flynn and Mauritsen, 2020) and it appears that in some models extra-tropical clouds with mixed ice and liquid phases are central to the behaviour (Zelinka et al., 2020), probably borne out of a recent focus on biases in these types of clouds (McCoy et al., 2016; Tan et al., 2016). These biases have recently been reduced in many ESMs, guided by process understanding from laboratory experiments, field measurements, and satellite observations (Lohmann and Neubauer, 2018; Bodas-Salcedo et al., 2019; Gettelman et al., 2019). However, this and other known model biases are already factored into the process-level assessment of cloud feedback (Section 7.4.2.4), and furthermore the emergent constraints used here focus on global surface temperature change, which are less susceptible to shared model biases in individual feedback parameters than emergent constraints that focus on specific physical processes (Section 7.5.4). The high values of ECS and TCR in some CMIP6 models lead to higher levels of surface warming than CMIP5 simulations and also the AR6 projections based on the assessed ranges of ECS, TCR and ERF (Chapter 4, Box 4.1; FAQ 7.3; Forster et al., 2019).

It is generally difficult to determine which information enters the formulation and development of parameterizations used in ESMs. Climate models frequently share code components and in some cases entire sub-model systems are shared and slightly modified. Therefore, models cannot be considered independent developments, but rather families of models with interdependencies (Knutti et al., 2013). It is therefore difficult to interpret the collection of models (Knutti, 2010), and it cannot be ruled out that there are common limitations and therefore systematic biases to model ensembles that are reflected in the distribution of ECS as derived from them. Although ESMs are typically well-documented, in ways that increasingly include information on critical decisions regarding tuning (Mauritsen et al., 2012; Hourdin et al., 2017; Schmidt et al., 2017a; Mauritsen and Roeckner, 2020), the full history of development decisions could involve both process-understanding and sometimes also other information such as historical warming. As outlying or poorly performing models emerge from the development process, they can become re-tuned, reconfigured or discarded and so might not see publication (Hourdin et al., 2017; Mauritsen and Roeckner, 2020). In the process of addressing such issues, modelling groups may, whether intentional or not, modify the modelled ECS.

[START FIGURE 7.19 HERE]

Figure 7.19: Global mean temperature anomaly in models and observations from 5 time periods. (a) Historical (CMIP6 models), (b) post 1975 (CMIP6 models), (c) Last Glacial Maximum (LGM; Cross-Chapter Box 2.1; PMIP4 models; (Kageyama et al., 2021; Zhu et al., 2021), (d) mid Pliocene warm period (MPWP; Cross-Chapter Box 2.4; PlioMIP models; Haywood et al., 2020; Zhang et al., 2021), (e) early Eocene climatic optimum (EECO; Cross-Chapter Box 2.1; DeepMIP models; Zhu et al., 2020; Lunt et al., 2021). Grey circles show models with ECS in the assessed *very likely* range; models in red have an ECS greater than the assessed *very likely* range (>5°C), models in blue have an ECS lower than the assessed *very likely* range (<2°C). Black ranges show the assessed temperature anomaly derived from observations (Chapter 2, Section 2.3). The Historical anomaly in models and observations is calculated as the difference between 2005–2014 and 1850–1900, and the post 1975 anomaly is calculated as the difference between 2005–2014 and 1975–1984. For the LGM, MPWP, and EECO, temperature anomalies are compared with pre-industrial (equivalent to CMIP6 simulation *piControl*). All model simulations of the MPWP and LGM were carried out with atmospheric CO_2 concentrations of 400 and 190 ppm respectively. However, CO_2 during the EECO is relatively more uncertain, and model simulations were carried out at either 1120ppm or 1680 ppm (except for the one high-ECS EECO simulation which was carried out at 560 ppm; Zhu et al., 2020). The one low-ECS EECO simulation was carried out at 1680 ppm. Further details on data sources and processing are available in the chapter data table (Table 7.SM.14).

[END FIGURE 7.19 HERE]

It is problematic and not obviously constructive to provide weights for, or rule out, individual CMIP6 model ensemble members based solely on their ECS and TCR values. Rather these models must be tested in a like-with-like way against observational evidence. Based on the currently published CMIP6 models we provide such an analysis, marking models with ECS above and below the assessed *very likely* range (Figure 7.19). In the long term historical warming (Figure 7.19a) both low and high ECS models are able to match the observed warming, presumably in part as a result of compensating aerosol cooling (Kiehl, 2007; Forster et al., 2013; Wang et al., 2021). In several cases of high ECS models that apply strong aerosol cooling it is found to result in surface warming and ocean heat uptake evolutions that are inconsistent with observations (Golaz et al., 2019b; Andrews et al., 2020; Winton et al., 2020). Modelled warming since the 1970s is less influenced by compensation between climate sensitivity and aerosol cooling (Jiménez-de-la-Cuesta and Mauritsen, 2019; Nijsse et al., 2020) resulting in the high ECS models in general warming more than observed, whereas low sensitivity models mostly perform better (Figure 7.19b); a result that may also have been influenced by temporary pattern effects (Sections 7.4.4 and 7.5.4). Paleoclimates are not influenced by such transient pattern effects, but are limited by structural uncertainties in the proxy-based temperature and forcing reconstructions as well as possible differences in equilibrium sea-surface temperature patterns between models and the real world (Section 7.5.4). Across the LGM, MPWP and EECO (Figure 7.19c-e), the few high ECS models that simulated these cases were outside the observed *very likely* ranges; see also (Feng et al., 2020; Renoult et al., 2020; Zhu et al., 2020). Also the low ECS model is either outside or on the edge of the observed *very likely* ranges.

As a result of the above considerations, in this Report projections of global surface temperature are produced using climate model emulators that are constrained by the assessments of ECS, TCR and ERF. In reports up to and including AR5, ESM values of ECS did not fully encompass the assessed *very likely* range of ECS, raising the possibility that past multi-model ensembles underestimated the uncertainty in climate change projections that existed at the times of those reports (e.g., Knutti, 2010). However, due to an increase in the modelled ECS spread and a decrease in the assessed ECS spread based on improved knowledge in multiple lines of evidence, the CMIP6 ensemble encompasses the *very likely* range of ECS (2–5°C) assessed in Section 7.5.5. Models outside of this range are useful for establishing emergent constraints on ECS and TCR and provide useful examples of "tail risk" (Sutton, 2018), producing dynamically consistent realisations of future climate change to inform impacts studies and risk assessments.

In summary, the distribution of CMIP6 models have higher average ECS and TCR values than the CMIP5 generation of models and the assessed values of ECS and TCR in Section 7.5.5. The high ECS and TCR values can in some CMIP6 models be traced to improved representation of extra-tropical cloud feedbacks (*medium confidence*). The ranges of ECS and TCR from the CMIP6 models are not considered robust samples of possible values and the models are not considered a separate line of evidence for ECS and TCR. Solely based on its ECS or TCR values an individual ESM cannot be ruled out as implausible, though some models with high (greater than 5°C) and low (less than 2°C) ECS are less consistent with past climate change (*high confidence*). High model climate sensitivity leads to generally higher projected warming in CMIP6 compared to both CMIP5 and that assessed based on multiple lines of evidence (Chapter 4, Sections 4.3.1 and 4.3.4; FAQ 7.3).

7.5.7 Processes underlying uncertainty in the global temperature response to forcing

While the magnitude of global warming by the end of the 21st century is dominated by future greenhouse gas emissions, the uncertainty in warming for a given ERF change is dominated by the uncertainty in ECS and TCR (Chapter 4, Section 4.3.4). The proportion of variation explained by ECS and TCR varies with scenario and the time period considered, but within CMIP5 models around 60% to 90% of the globally averaged projected surface warming range in 2100 can be explained by the model range of these metrics (Grose et al., 2018). Uncertainty in the long-term global surface temperature change can further be understood in terms of the processes affecting the global TOA energy budget, namely the ERF, the radiative feedbacks which govern the efficiency of radiative energy loss to space with surface warming, and the increase in the global energy inventory (dominated by ocean heat uptake) which reduces the transient surface warming. A variety of studies evaluate the effect of each of these processes on surface changes within coupled ESM simulations by diagnosing so-called 'warming contributions' (Dufresne and Bony, 2008; Crook et al., 2011; Feldl and Roe, 2013; Vial et al., 2013; Pithan and Mauritsen, 2014; Goosse et al., 2018). By construction, the individual warming contributions sum to the total global surface warming (Figure 7.19b). For long-term warming in response to CO_2 forcing in CMIP5 models, the energy added to the climate system by radiative feedbacks is larger than the ERF of CO_2 (Figure 7.19a), implying that feedbacks more than double the magnitude of global warming (Figure 7.19b). Radiative kernel methods (see Section 7.4.1) can be used to decompose the net energy input from radiative feedbacks into its components. The water-vapour, cloud and surface-albedo feedbacks enhance global warming, while the lapse-rate feedback reduces global warming. Ocean heat uptake reduces the rate of global surface warming by sequestering heat at depth away from the ocean surface. Section 7.4.4.1 shows the warming contributions from these factors at the regional scale.

[START FIGURE 7.20 HERE]

Figure 7.20: Contributions of effective radiative forcing, ocean heat uptake and radiative feedbacks to global atmospheric energy input and near-surface air temperature change at year 100 of *abrupt4xCO2* simulations of CMIP6 models. (a) The energy flux to the global atmosphere associated with the effective CO_2 forcing, global ocean heat uptake, Planck response, and radiative feedbacks, which together sum to zero. The inset shows energy input from individual feedbacks, summing to the total feedback energy input. (b) Contributions to net global warming are calculated by dividing the energy inputs by the *magnitude* of the global Planck response (3.2 W m^{-2} °C^{-1}), with the contributions from radiative forcing, ocean heat uptake, and radiative feedbacks (orange bars) summing to the value of net warming (grey bar). The inset shows warming contributions associated with individual feedbacks, summing to the total feedback contribution. Uncertainties show the interquartile range (25% and 75% percentiles) across models. Radiative kernel methods (see Section 7.4.1) were used to decompose the net energy input from radiative feedbacks into contributions from changes in atmospheric water vapour, lapse-rate, clouds, and surface albedo (Zelinka et al. (2020) using the Huang et al. (2017) radiative kernel). The CMIP6 models included are those analysed by Zelinka et al. (2020) and the warming contribution analysis is based on that of Goosse et al. (2018). Further details on data sources and processing are available in the chapter data table (Table 7.SM.14).

[END FIGURE 7.20 HERE]

Differences in projected transient global warming across ESMs are dominated by differences in their radiative feedbacks, while differences in ocean heat uptake and radiative forcing play secondary roles (Figure 7.20b; Vial et al., 2013). The uncertainty in projected global surface temperature change associated with inter-model differences in cloud feedbacks is the largest source of uncertainty in CMIP5 and CMIP6 models (Figure 7.20b), just as they were for CMIP3 models (Dufresne and Bony, 2008). Extending this energy budget analysis to equilibrium surface warming suggests that about 70% of the inter-model differences in ECS arises from uncertainty in cloud feedbacks, with the largest contribution to that spread coming from shortwave low-cloud feedbacks (Vial et al., 2013; Zelinka et al., 2020).

Interactions between different feedbacks within the coupled climate system pose a challenge to our ability to understand global warming and its uncertainty based on energy budget diagnostics (Section 7.4.2). For example, water-vapour and lapse-rate feedbacks are correlated (Held and Soden, 2006) owing to their joint dependence on the spatial pattern of warming (Po-Chedley et al., 2018a). Moreover, feedbacks are not independent of ocean heat uptake because the uptake and transport of heat by the ocean influences the SST pattern on which global feedbacks depend (Section 7.4.4.3). However, alternative decompositions of warming contributions that better account for correlations between feedbacks produce similar results (Caldwell et al., 2016). The key role of radiative feedbacks in governing the magnitude of global warming is also supported by the high correlation between radiative feedbacks (or ECS) and transient 21st century warming within ESMs (Grose et al., 2018).

Another approach to evaluating the roles of forcing, feedbacks, and ocean heat uptake in projected warming employs idealized energy balance models that emulate the response of ESMs, and which preserve the interactions between system components. One such emulator, used in Section 7.5.1.2, resolves the heat capacity of both the surface components of the climate system and the deep ocean (Held et al., 2010; Geoffroy et al., 2013a, 2013b; Kostov et al., 2014; Armour, 2017). Using this emulator, Geoffroy et al. (2012) find that: under an idealized 1% per year increase in atmospheric CO_2, radiative feedbacks constitute the greatest source of uncertainty (about 60% of variance) in transient warming beyond several decades; ERF uncertainty plays a secondary but important role in warming uncertainty (about 20% of variance) that diminishes beyond several decades; and ocean heat uptake processes play a minor role in warming uncertainty (less than 10% of variance) at all timescales.

More computationally intensive approaches evaluate how the climate response depends on perturbations to key parameter or structural choices within ESMs. Large 'perturbed parameter ensembles' wherein a range of parameter settings associated with cloud physics are explored within atmospheric ESMs produce a wide range of ECS due to changes in cloud feedbacks, but often produce unrealistic climate states (Joshi et al., 2010). Rowlands et al. (2012) generated a ESM perturbed-physics ensemble of several thousand members by perturbing model parameters associated with radiative forcing, cloud feedbacks, and ocean vertical diffusivity (an important parameter for ocean heat uptake). After constraining the ensemble to have a reasonable climatology and to match the observed historical surface warming, they found a wide range of projected warming by the year 2050 under the SRES A1B scenario (1.4–3°C relative to the 1961–1990 average) that is dominated by differences in cloud feedbacks. The finding that cloud feedbacks are the largest source of spread in the net radiative feedback has since been confirmed in perturbed parameter ensemble studies using several different ESMs (Gettelman et al., 2012; Tomassini et al., 2015; Kamae et al., 2016; Rostron et al., 2020; Tsushima et al., 2020). By swapping out different versions of the atmospheric or oceanic components in a coupled ESM, Winton et al. (2013) found that TCR and ECS depend on which atmospheric component was used (using two versions with different atmospheric physics), but that only TCR is sensitive to which oceanic component of the model was used (using two versions with different vertical coordinate systems, among other differences); TCR and ECS changed by 0.4°C and 1.4°C, respectively, when the atmospheric model component was changed, while TCR and ECS changed by 0.3°C and less than 0.05°C, respectively, when the oceanic model component was changed. By perturbing ocean vertical diffusivities over a wide range, Watanabe et al. (2020b) found that TCR changed by 0.16°C within the model MIROC5.2 while Krasting et al. (2018) found that ECS changed by about 0.6°C within the model GFDL-ESM2G, with this difference linked to different radiative feedbacks associated with different spatial patterns of sea-surface warming (see Section 7.4.4.3). By comparing simulations of CMIP6 models with and without the effects of CO_2 on vegetation, (Zarakas et al., 2020) find a physiological contribution to TCR of 0.12°C (range 0.02–0.29°C across models) owing to physiological adjustments to the CO_2 ERF (Section 7.3.2.1).

There is *robust evidence* and *high agreement* across a diverse range of modelling approaches and thus *high confidence* that radiative feedbacks are the largest source of uncertainty in projected global warming out to 2100 under increasing or stable emissions scenarios, and that cloud feedbacks in particular are the dominant source of that uncertainty. Uncertainty in radiative forcing plays an important but generally secondary role. Uncertainty in global ocean heat uptake plays a lesser role in global warming uncertainty, but ocean circulation could play an important role through its effect on sea-surface warming patterns which in turn project onto radiative feedbacks through the pattern effect (Section 7.4.4.3).

The spread in historical surface warming across CMIP5 ESMs shows a weak correlation with inter-model differences in radiative feedback or ocean heat uptake processes but a high correlation with inter-model differences in radiative forcing owing to large variations in aerosol forcing across models (Forster et al., 2013). Likewise, the spread in projected 21st century warming across ESMs depends strongly on emissions scenario (Hawkins and Sutton, 2012; Chapter 4, Section 4.3.1). Strong emissions reductions would remove aerosol forcing (Chapter 6, Section 6.7.2) and this could dominate the uncertainty in near-term warming projections (Armour and Roe, 2011; Mauritsen and Pincus, 2017; Schwartz, 2018; Smith et al., 2019). On post 2100 timescales carbon cycle uncertainty such as that related to permafrost thawing could become increasingly important, especially under high emission scenarios (Chapter 5, Figure 5.30).

In summary, there is *high confidence* that cloud feedbacks are the dominant source of uncertainty for late 21st century projections of transient global warming under increasing or stable emissions scenarios, whereas uncertainty is dominated by aerosol ERF in strong mitigation scenarios. Global ocean heat uptake is a smaller source of uncertainty in long-term surface warming. (*high confidence*).

7.6 Metrics to evaluate emissions

Emission metrics are used to compare the relative effect of emissions of different gases over time in terms of radiative forcing, global surface temperature or other climate effects. They are introduced in Chapter 1, Box 1.3. Chapter 8 of AR5 (Myhre et al., 2013b) comprehensively discussed different emission metrics so this section focuses on updates since that report. Section 7.6.1 updates the physical assessment. Section 7.6.2 assesses developments in the comparison of emissions of short- and long-lived gases. Box 7.3 assesses physical aspects of emission metric use within climate policy.

7.6.1 Physical description of metrics

This section discusses metrics that relate emissions to physical changes in the climate system. Other metrics, for instance relating to economic costs or 'damage' are discussed in WG III Chapter 2. The same Chapter also assesses literature examining to what extent different physical metrics are linked to cost-benefit and cost-effectiveness metrics. One metric, the 100-year Global Warming Potential (GWP-100), has extensively been employed in climate policy to report emissions of different greenhouse gases on the same scale. Other physical metrics exist, which are discussed in this section.

Emission metrics can be quantified as the magnitude of the effect a unit mass of emission of a species has on a key measure of climate change. This section focuses on physical measures such as the radiative forcing, GSAT change, global average precipitation change, and global mean sea level rise (Myhre et al., 2013b; Sterner et al., 2014; Shine et al., 2015). When used to represent a climate effect, the metrics are referred to as absolute metrics and expressed in units of effect per kg (e.g., Absolute Global Warming Potential, AGWP or Absolute Global Temperature-change Potential, AGTP). More commonly, these are compared with a reference species (almost always CO_2 in kg(CO_2)), to give a dimensionless factor (written as e.g., Global Warming Potential (GWP) or Global Temperature-change Potential (GTP)). The unit mass is usually taken as a 1 kg instantaneous "pulse" (Myhre et al., 2013b), but can also refer to a "step" in emission rate of 1 kg yr^{-1}.

There is a cause-effect chain that links human activity to emissions, then from emissions to radiative forcing, climate response, and climate impacts (Fuglestvedt et al., 2003). Each step in the causal chain requires an inference or modelling framework that maps causes to effects. Emission metrics map from emissions of some compound to somewhere further down the cause and effect chain, radiative forcing (e.g., GWP) or temperature (e.g., GTP) or other effects (such as sea-level rise or socioeconomic impacts). While variables later in the chain have greater policy or societal relevance, they are also subject to greater uncertainty because each step in the chain includes more modelling systems, each of which brings its own uncertainty (Balcombe et al., 2018; Chapter 1, Figure 1.15).

Since AR5, understanding of the radiative effects of emitted compounds has continued to evolve and these changes are assessed in Section 7.6.1.1. Metrics relating to precipitation and sea level have also been quantified (Section 7.6.1.2). Understanding of how the carbon-cycle response to temperature effects emission metrics has improved. This allows the carbon cycle response to temperature to be more fully included in the emission metrics presented here (Section 7.6.1.3). There have also been developments in approaches for comparing short-lived greenhouse gases to CO_2 in the context of mitigation and global surface temperature change (Section 7.6.1.4). Emission metrics for selected key compounds are presented in Section 7.6.1.5.

7.6.1.1 Radiative properties and lifetimes.

The radiative properties and lifetimes of compounds are the fundamental component of all emission metrics. Since AR5, there have been advances in the understanding of the radiative properties of various compounds (see Sections 7.3.1, 7.3.2 and 7.3.3), and hence their effective radiative efficiencies (ERFs per unit change in concentration). For CO_2, CH_4 and N_2O, better accounting of the spectral properties of these gases has led to re-evaluation of their SARF radiative efficiencies and their dependence on the background gas concentrations (Section 7.3.2). For CO_2, CH_4, N_2O, CFC-11 and CFC-12 the tropospheric adjustments (Sections 7.3.1 and 7.3.2) are assessed to make a non-zero contribution to ERF. There is insufficient evidence to include tropospheric adjustments for other halogenated compounds. The re-evaluated effective radiative efficiency for CO_2 will affect all emission metrics relative to CO_2.

The effective radiative efficiencies (including adjustments from Section 7.3.2) for 2019 background concentrations for CO_2, CH_4 and N_2O are assessed to be 1.36×10^{-5}, 3.77×10^{-4} and 3.11×10^{-3} W m^{-2} ppb^{-1} respectively (see Table 7.15 for uncertainties), compared to AR5 assessments of 1.37×10^{-5}, 3.63×10^{-4} and 3.00×10^{-3} W m^{-2} ppb^{-1}. For CO_2, increases due to the re-evaluated radiative properties and adjustments balance the decreases due to the increasing background concentration. For CH_4, increases due to the re-evaluated radiative properties more than offset the decreases due to the increasing background concentration. For N_2O the addition of tropospheric adjustments increases the effective radiative efficiency. Radiative efficiencies of halogenated species have been revised slightly (Section 7.3.2.4) and for CFCs include tropospheric adjustments.

The perturbation lifetimes of CH_4 (Chapter 6, Section 6.3.1). and N_2O (Chapter 5, Section 5.2.3.1) have been slightly revised since AR5 to be 11.8 ± 1.8 years and 109 ± 10 years (Table 7.15). The lifetimes of halogenated compounds have also been slightly revised (Hodnebrog et al., 2020a).

Although there has been greater understanding since AR5 of the carbon cycle responses to CO_2 emissions (Chapter 5, Sections 5.4 and 5.5), there has been no new quantification of the response of the carbon-cycle to an instantaneous pulse of CO_2 emission since Joos et al. (2013).

7.6.1.2 Physical indicators

The basis of all the emission metrics is the time profile of effective radiative forcing (ERF) following the emission of a particular compound. The emission metrics are then built up by relating the forcing to the desired physical indicators. These forcing-response relationships can either be generated from emulators (Tanaka et al., 2013; Gasser et al., 2017b; Cross-Chapter Box 7.1), or from analytical expressions based on parametric equations (response functions) derived from more complex models (Myhre et al., 2013b).

To illustrate the analytical approach, the ERF time evolution following a pulse of emission can be considered an Absolute Global Forcing Potential AGFP (similar to the Instantaneous Climate Impact of Edwards and Trancik (2014)). This can be transformed into an Absolute Global Temperature Potential (AGTP) by combining the radiative forcing with a global surface temperature response function. This temperature response is typically derived from a two-layer energy balance emulator (Supplementary Material 7.SM.5; Myhre et al., 2013b). For further physical indicators further response functions are needed based on the radiative forcing or temperature, for instance. Sterner et al. (2014) used an upwelling-diffusion energy balance model to derive the thermosteric component of sea level rise (SLR) as response functions to radiative forcing or global surface temperature. A metric for precipitation combines both the radiative forcing (AGFP) and temperature (AGTP) responses to derive an Absolute Global Precipitation Potential AGPP (Shine et al., 2015). The equations relating these metrics are given in the Supplementary Material 7.SM.5.

The physical emission metrics described above are functions of time since typically the physical effects reach a peak and then decrease in the period after a pulse emission as the concentrations of the emitted compound decay. The value of the metrics can therefore be strongly dependent on the time horizon of interest. All relative metrics (GWP, GTP etc) are also affected by the time dependence of the CO_2 metrics in the denominator. Instantaneous or endpoint metrics quantify the change (in radiative forcing, global surface temperature, global mean sea level) at a particular time after the emission. These can be appropriate when the goal is to not exceed a fixed target such as a temperature or global mean sea-level rise level at a specific time. Emission metrics can also be integrated from the time of emission. The most common of these is the Absolute Global Warming Potential (AGWP), which is the integral of the AGFP. The physical effect is then in units of forcing-years, degree-years or metre-years for forcing, temperature, or sea-level rise, respectively. These can be appropriate for trying to reduce the overall damage potential when the effect depends on how long the change occurs for, not just how large the change is. The integrated metrics still depend on the time horizon, though for the shorter-lived compounds this dependence is somewhat smoothed by the integration. The integrated version of a metric is often denoted as iAGxx, although the integral of the forcing-based metric (iAGFP) is known as the AGWP. Both the endpoint and integrated absolute metrics for non-CO_2 species can be divided by the equivalent for CO_2 to give relative emission metrics (e.g., GWP (=iGFP), GTP, iGTP).

Each step from radiative forcing to global surface temperature to SLR introduces longer timescales and therefore prolongs further the contributions to climate change of short-lived greenhouse gases (Myhre et al., 2013b). Thus, short-lived greenhouse gases become more important (relative to CO_2) for SLR than for temperature or radiative forcing (Zickfeld et al., 2017). Integrated metrics include the effects of a pulse emission from the time of emission up to the time horizon, whereas endpoint metrics only include the effects that persist out to the time horizon. Because the largest effects of short-lived greenhouse gases occur shortly after their emission and decline towards the end of the time period, short-lived greenhouse gases have relatively higher integrated metrics than their corresponding endpoint metrics (Peters et al., 2011; Levasseur et al., 2016).

For species perturbations that lead to a strong regional variation in forcing pattern, the regional temperature response can be different to that for CO_2. Regional equivalents to the global metrics can be derived by replacing the global surface temperature response function with a regional response matrix relating forcing changes in one region to temperature changes in another (Collins et al., 2013b; Aamaas et al., 2017; Lund et al., 2017).

For the research discussed above, metrics for several physical variables can be constructed that are linear functions of radiative forcing. Similar metrics could be devised for other climate variables provided they can be related by response functions to radiative forcing or global surface temperature change. The radiative forcing does not increase linearly with emissions for any species, but the non-linearities (for instance changes in CO_2 radiative efficiency) are small compared to other uncertainties.

7.6.1.3 Carbon cycle responses and other indirect contributions

The effect of a compound on climate is not limited to its direct radiative forcing. Compounds can perturb the carbon cycle affecting atmospheric CO_2 concentrations. Chemical reactions from emitted compounds can produce or destroy other greenhouse gases or aerosols.

Any agent that warms the surface perturbs the terrestrial and oceanic carbon fluxes (Chapter 5, Sections 5.4.3 and 5.4.4), typically causing a net flux of CO_2 into the atmosphere and hence further warming. This aspect is already included in the carbon cycle models that are used to generate the radiative effects of a pulse of CO_2 (Joos et al., 2013), but was neglected for non-CO_2 compounds in the conventional metrics so this introduces an inconsistency and bias in the metric values (Gillett and Matthews, 2010; MacDougall et al., 2015; Tokarska et al., 2018). A simplistic account of the carbon cycle response was tentatively included in AR5 based on a single study (Collins et al., 2013b). Since AR5 this understanding has been revised (Gasser et al., 2017b; Sterner and Johansson, 2017) using simple parameterised carbon cycle models to derive the change in CO_2 surface flux for a unit temperature pulse as an impulse response function to temperature. In Collins et al. (2013a) this response function was assumed to be simply a delta function, whereas the newer studies include a more complete functional form accounting for subsequent re-uptake of CO_2 after the removal of the temperature increase. Accounting for re-uptake has the effect of reducing the carbon-cycle responses associated with the metrics compared to AR5, particularly at large time horizons. The increase in any metric due to the carbon cycle response can be derived from the convolution of the global surface temperature response with the CO_2 flux response to temperature and the equivalent metric for CO_2 (equation 7.SM.5.5 in the Supplementary Material). Including this response also increases the duration of the effect of short-lived greenhouse gases on climate (Fu et al., 2020). An alternative way of accounting for the carbon cycle temperature response would be to incorporate it into the temperature response function (the response functions used here and given in Supplementary Material 7.SM.5.2 do not explicitly do this). If this were done, the correction could be excluded from both the CO_2 and non-CO_2 forcing responses as in Hodnebrog et al. (2020a).

Including the carbon cycle response for non-CO_2 treats CO_2 and non-CO_2 compounds consistently and therefore we assess that its inclusion more accurately represents the climate effects of non-CO_2 species. There is *high confidence* in the methodology of using carbon cycle models for calculating the carbon cycle response. The magnitude of the carbon cycle response contributions to the emission metrics vary by a factor of two between Sterner and Johansson (2017) and Gasser et al. (2017b). The central values are taken from Gasser et al. (2017b) as the OSCAR 2.2 model used is based on parameters derived from CMIP5 models, and the climate-carbon feedback magnitude is therefore similar to the CMIP5 multi-model mean (Arora et al., 2013; Lade et al., 2018). As values have only been calculated in two simple parameterised carbon cycle models the uncertainty is assessed to be ±100%. Due to few studies and a factor of two difference between them, there is *low confidence* that the magnitude of the carbon cycle response is within the higher end of this uncertainty range, but *high confidence* that the sign is positive. Carbon cycle responses are included in all the metrics presented in Tables 7.15 and Supplementary Table 7.SM.7. The carbon cycle contribution is lower than in AR5, but there is *high confidence* in the need for its inclusion and the method by which it is quantified.

Emissions of non-CO_2 species can affect the carbon cycle in other ways: emissions of ozone precursors can reduce the carbon uptake by plants (Collins et al., 2013b); emissions of reactive nitrogen species can fertilize plants and hence increase the carbon uptake (Zaehle et al., 2015); and emissions of aerosols or their precursors can affect the utilisation of light by plants (Cohan et al., 2002; Mercado et al., 2009; Mahowald et al., 2017) (see Chapter 6, Section 6.4.4 for further discussion). There is *robust evidence* that these processes occur and are important, but *insufficient evidence* to determine the magnitude of their contributions to emission metrics. Ideally, emission metrics should include all indirect effects to be consistent, but limits to our knowledge restrict how much can be included in practice.

Indirect contributions from chemical production or destruction of other greenhouse gases are quantified in Chapter 6, Section 6.4. For methane, AR5 (Myhre et al., 2013b) assessed that the contributions from effects on ozone and stratospheric water vapour add 50% ± 30% and 15% ± 11% to the emission-based ERF, which were equivalent to $1.8 \pm 0.7 \times 10^{-4}$ and $0.5 \pm 0.4 \times 10^{-4}$ W m^{-2} ppb (CH_4)$^{-1}$. In AR6 the radiative efficiency formulation is preferred as it is independent of the assumed radiative efficiency for methane. The assessed contributions to the radiative efficiency for methane due to ozone are $1.4 \pm 0.7 \times 10^{-4}$ W m^{-2} ppb (CH_4)$^{-1}$, based on 0.14 W m^{-2} forcing from a 1023 ppb (1850 to 2014) methane change (Thornhill et al., 2021b). The contribution from stratospheric water vapour is $0.4 \pm 0.4 \times 10^{-4}$ W m^{-2} ppb (CH_4)$^{-1}$, based on 0.05 W m^{-2} forcing from a 1137 ppb (1750 to 2019) methane change (Section 7.3.2.6). N_2O depletes upper stratospheric ozone (a positive forcing) and reduces the methane lifetime. In AR5 the methane lifetime effect was assessed to reduce methane concentrations by 0.36 ppb per ppb increase in N_2O, with no assessment of the effective radiative forcing from ozone. This is now increased to –1.7 ppb methane per ppb N_2O (based on a methane lifetime decrease of 4% ± 4% for a 55 ppb increase in N_2O (Thornhill et al., 2021b) and a radiative efficiency of $5.5 \pm 0.4 \times 10^{-4}$ W m^{-2} ppb (N_2O)$^{-1}$ through ozone (Thornhill et al., 2021b). In summary, GWPs and GTPs for methane and nitrous oxide are slightly lower than in AR5 (*medium confidence*) due to revisions in their lifetimes and updates to their indirect chemical effects.

Methane can also affect the oxidation pathways of aerosol formation (Shindell et al., 2009) but the available literature is insufficient to make a robust assessment of this. Hydrocarbon and molecular hydrogen oxidation also leads to tropospheric ozone production and change in methane lifetime (Collins et al., 2002; Hodnebrog et al., 2018). For reactive species the emission metrics can depend on where the emissions occur, and the season of emission (Aamaas et al., 2016; Lund et al., 2017; Persad and Caldeira, 2018). AR5 included a contribution to the emission metrics for ozone-depleting substances (ODSs) from the loss of stratospheric ozone. The assessment of ERFs from ODSs in Chapter 6 (Section 6.4.2) suggests the quantification of these terms may be more uncertain than the formulation in AR5 so these are not included here.

Oxidation of methane leads ultimately to the net production of atmospheric CO_2 (Boucher et al., 2009). This yield is less than 100% (on a molar basis) due to uptake by soils and some of the reaction products (mainly formaldehyde) being directly removed from the atmosphere before being completely oxidised. Estimates of the yield are 61% (Boucher et al., 2009) and 88% (Shindell et al., 2017), so the assessed range is 50-100% with a central value of 75% *(low confidence).* For methane and hydrocarbons from fossil sources, this will lead to additional fossil CO_2 in the atmosphere whereas for biogenic sources of methane or hydrocarbons, this replaces CO_2 that has been recently removed from the atmosphere. Since the ratio of molar masses is 2.75, 1 kg of methane generates 2.1± 0.7 kg CO_2 for a 75% yield. For biogenic methane the soil uptake and removal of partially-oxidised products is equivalent to a sink of atmospheric CO_2 of 0.7 ± 0.7 kg per kg methane. The contributions of this oxidation effect to the methane metric values allow for the time delay in the oxidation of methane. Methane from fossil fuel sources has therefore slightly higher emission metric values than those from biogenic sources (*high confidence*). The CO_2 can already be included in carbon emission totals (Muñoz and Schmidt, 2016) so care needs to be taken when applying the fossil correction to avoid double counting.

7.6.1.4 Comparing long-lived with short-lived greenhouse gases

Since AR5 there have been developments in how to account for the different behaviours of short-lived and long-lived compounds. Pulse-based emission metrics for short-lived greenhouse gases with lifetimes less than twenty years are very sensitive to the choice of time horizon (e.g. Pierrehumbert, 2014). Global surface temperature changes following a pulse of CO_2 emissions are roughly constant in time (the principle behind TCRE, Figure 7.21b, Chapter 5, Section 5.5.1) whereas the temperature change following a pulse of short-lived greenhouse gas emission declines with time. In contrast to a one-off pulse, a step change in short-lived greenhouse gas emissions that is maintained indefinitely causes a concentration increase that eventually equilibrates to a steady state in a way that is more comparable to a pulse of CO_2. Similarly the resulting change in global surface temperature from a step change in short-lived greenhouse gases (Figure 7.21a) after a few decades increases only slowly (due to accumulation of heat in the deep ocean) and hence its effects are more similar to a pulse of CO_2 (Smith et al., 2012; Lauder et al., 2013; Allen et al., 2016, 2018b). The different time dependence of short-lived and long-lived compounds can be accounted for exactly with the CO_2 forcing equivalent metric (Wigley, 1998; Allen et al., 2018b; Jenkins et al., 2018) that produces a CO_2 emission time profile such that the radiative forcing matches the time evolution of that from the non-CO_2 emissions. But other metric approaches can approximate this exact approach.

The similarity in behaviour of step changes in short-lived greenhouse gas emissions and pulses of CO_2 emissions has recently been used to formulate new emissions metric concepts (Collins et al., 2020). For short-lived greenhouse gases, these new concepts use a step change in the rate of emissions, in contrast to an instantaneous pulse in a given year that is typically used (e.g. Myhre et al., 2013b). Metrics for step emission changes are denoted here by a superscript "*S*" (e.g., $AGTP_X^S$ is the absolute global surface temperature change potential from a unit step change in emissions of species "*X*"). These can be derived by integrating the more standard pulse emission changes up to the time horizon. The response to a step emission change is therefore equivalent to the integrated response to a pulse emission ($AGTP_X^S = iAGTP_X$); and the radiative forcing response to a step emission change $AGFP_X^S$ is equivalent to the integrated forcing response $iAGFP_X$which is the AGWP. The step metric for short-lived greenhouse gases can then be compared with the pulse metric for CO_2 in a ratio $AGTP_X^S/AGTP_{CO2}$ (Collins et al., 2020). This is referred to as a combined-GTP (CGTP) in Collins et al. (2020), and has units of years (the standard GTP is dimensionless). This CGTP shows less variation with time than the standard GTP (comparing Figure 7.21c with Figure 7.21d) and provides a scaling for comparing a change in emission rate (in kg yr^{-1}) of short-lived greenhouse gases with a pulse emission or change in cumulative CO_2 emissions (in kg). Cumulative CO_2 equivalent emissions are given by CGTP × emission rate of short-lived greenhouse gases. The CGTP can be calculated for any species, but it is least dependent on the chosen time horizon for species with lifetimes less than half the time horizon of the metric (Collins et al., 2020). Pulse-step metrics can therefore be useful where time dependence of pulse metrics, like GWP or GTP, complicates their use (see Box 7.3).

For a stable global warming from non-CO_2 climate agents (gas or aerosol) their effective radiative forcing needs to gradually decrease (Tanaka and O'Neill, 2018). Cain et al. (2019) find this decrease to be around 0.3% yr^{-1} for the climate response function in AR5 (Myhre et al., 2013b). To account for this, a quantity referred to as GWP* has been defined that combines emissions (pulse) and changes in emission levels (step) approaches (Cain et al., 2019; Smith et al., 2021)[2]. The emission component accounts for the need for emissions to decrease to deliver a stable warming. The step (sometimes referred to as flow or rate) term in GWP* accounts for the change in global surface temperature that arises in from a change in short-lived greenhouse gas emission rate, as in CGTP, but here approximated by the change in emissions over the previous 20 years.

Cumulative CO_2 emissions and GWP*-based cumulative CO_2 equivalent greenhouse gas (GHG) emissions multiplied by TCRE closely approximate the global warming associated with emissions timeseries (of CO_2 and GHG, respectively) from the start of the time-series (Lynch et al., 2020). Both the CGTP and GWP* convert short-lived greenhouse gas emission rate changes into cumulative CO_2 equivalent emissions, hence scaling these by TCRE gives a direct conversion from short-lived greenhouse gas emission to global surface temperature change. By comparison expressing methane emissions as CO_2 equivalent emissions using GWP-100 overstates the effect of constant methane emissions on global surface temperature by a factor of 3-4 over a 20-year time horizon (Lynch et al., 2020, their Figure 5), while understating the effect of any new methane emission source by a factor of 4-5 over the 20 years following the introduction of the new source (Lynch et al., 2020, their Figure 4).

[START FIGURE 7.21 HERE]

Figure 7.21: Emission metrics for two short-lived greenhouse gases: HFC-32 and CH_4, (lifetimes of 5.4 and 11.8 years). The temperature response function comes from Supplementary Material 7.SM.5.2. Values for non-CO_2 species include the carbon cycle response (Section 7.6.1.3). Results for HFC-32 have been divided by 100 to show on the same scale. (a) temperature response to a step change in short-lived greenhouse gas emission. (b) temperature response to a pulse CO_2 emission. (c) conventional GTP metrics (pulse vs pulse). (d) combined-GTP metric (step versus pulse). Further details on data sources and processing are available in the chapter data table (Table 7.SM.14).

[END FIGURE 7.21 HERE]

Figure 7.22 explores how cumulative CO_2 equivalent emissions estimated for methane vary under different emission metric choices and how estimates of the global surface air temperature (GSAT) change deduced from these cumulative emissions compare to the actual temperature response computed with the two-layer emulator. Note that GWP and GTP metrics were not designed for use under a cumulative carbon dioxide equivalent emission framework (Shine et al., 1990, 2005), even if they sometimes are (e.g. Cui et al., 2017; Howard et al., 2018) and analysing them in this way can give useful insights into their physical properties. Using these standard metrics under such frameworks, the cumulative CO_2 equivalent emission associated with methane emissions would continue to rise if methane emissions were substantially reduced but remained above zero. In reality, a decline in methane emissions to a smaller but still positive value could cause a declining warming. GSAT changes estimated with cumulative CO_2 equivalent emissions computed with GWP-20 matches the warming trend for a few decades but quickly overestimates the response. Cumulative emissions using GWP-100 perform well when emissions are increasing but not when they are stable or decreasing. Cumulative emissions using GTP-100 consistently underestimate the warming. Cumulative emissions using either CGTP or GWP* approaches can more closely match the GSAT evolution (Allen et al., 2018b; Cain et al., 2019; Collins et al., 2020; Lynch et al., 2020).

[2] To calculate CO_2 equivalent emissions under GWP*, the short-lived greenhouse gas emissions are multiplied by GWP100 × 0.28 and added to the net emission increase or decrease over the previous 20 years multiplied by GWP100 x 4.24 (Smith et al., 2021).

In summary, new emission metric approaches such as GWP* and CGTP are designed to relate emission changes in short-lived greenhouse gases to emissions of CO_2 as they better account for the different physical behaviours of short and long-lived gases. Through scaling the corresponding cumulative CO_2 equivalent emissions by the TCRE, the GSAT response from emissions over time of an aggregated set of gases can be estimated. Using either these new approaches, or treating short and long-lived GHG emission pathways separately, can improve the quantification of the contribution of emissions to global warming within a cumulative emission framework, compared to approaches that aggregate emissions of GHGs using standard CO_2 equivalent emission metrics. As discussed in Box 7.3, there is *high confidence* that multi-gas emission pathways with the same time dependence of aggregated CO_2 equivalent emissions estimated from standard approaches, such as weighting emissions by their GWP-100 values, rarely lead to the same estimated temperature outcomes..

[START FIGURE 7.22 HERE]

Figure 7.22: Explores how cumulative carbon dioxide equivalent emissions estimated for methane vary under different emission metric choices and how estimates of the global surface air temperature (GSAT) change deduced from these cumulative emissions compare to the actual temperature response computed with the two-layer emulator (solid black lines). Panels a) and b) show the SSP4-6.0 and SSP1-2.6 scenarios respectively. The panels show annual methane emissions as the dotted lines (left axis) from 1750–2100. The solid lines can be read as either estimates of GSAT change or estimates of the cumulative carbon dioxide equivalent emissions. This is because they are related by a constant factor, the TCRE. Thus, values can be read using either of the right hand axes. Emission metric values are taken from Table 7.15. The GWP* calculation is given in Section 7.6.1.4. The two-layer emulator has been calibrated to the central values of the report's assessment (see Supplementary Material 7.SM.5.2). Further details on data sources and processing are available in the chapter data table (Table 7.SM.14).

[END FIGURE 7.22 HERE]

7.6.1.5 Emission metrics by compounds

Emission metrics for selected compounds are presented in Table 7.15, with further compounds presented in the Supplementary Material Table 7.SM.7. The evolution of the CO_2 concentrations in response to a pulse emission is as in AR5 (Joos et al., 2013; Myhre et al., 2013b), the perturbation lifetimes for CH_4 and N_2O are from Section 7.6.1.1. The lifetimes and radiative efficiencies for halogenated compounds are taken from Hodnebrog et al. (2020a). Combined metrics (CGTPs) are presented for compounds with lifetimes less than 20 years. Note CGTP has units of years and is applied to a change in emission rate rather than a change in emission amount. Changes since AR5 are due to changes in radiative properties and lifetimes (Section 7.6.1.1), and indirect contributions (Section 7.6.1.3). Table 7.15 also gives overall emission uncertainties in the emission metrics due to uncertainties in radiative efficiencies, lifetimes and the climate response function (Supplementary Material Tables 7.SM.8 to 7.SM.13)

Following their introduction in AR5 the assessed metrics now routinely include the carbon-cycle response for non-CO_2 gases (Section 7.6.1.3). As assessed in this earlier section, the carbon cycle contribution is lower than in AR5. Contributions to CO_2 formation are included for methane depending on whether or not the source originates from fossil carbon, thus methane from fossil fuel sources has slightly higher emission metric values than that from non-fossil sources.

[START TABLE 7.15 HERE]

Table 7.15: Emission metrics for selected species: Global Warming Potential (GWP), Global Temperature-change Potential (GTP). All values include carbon cycle responses as described in Section 7.6.1.3. Combined-GTPs (CGTPs) are shown only for species with a lifetime less than 20 years (see Section 7.6.1.4). Note CGTP has units of years and is applied to a change in emission rate rather than a change in emission

amount. The radiative efficiencies are as described in Section 7.3.2 and include tropospheric adjustments where assessed to be non-zero in Section 7.6.1.1. The climate response function is from Supplementary Material 7.SM.5.2. Uncertainty calculations are presented in Supplementary Tables 7.SM.8 to 7.SM.13. Chemical effects of CH_4 and N_2O are included (Section 7.6.1.3). Contributions from stratospheric ozone depletion to halogenated species metrics are not included. Supplementary Table 7.SM.7 presents the full table.

# Species	Lifetime (years)	Radiative efficiency (W m^{-2} ppb^{-1})	GWP-20	GWP-100	GWP-500	GTP-50	GTP-100	CGTP-50 (years)	CGTP-100 (years)
CO2	Multiple	1.33±0.16 ×10^{-5}	1.	1.000	1.000	1.000	1.000		
CH_4-fossil	11.8 ±1.8	5.7±1.4×10^{-4}	82.5 ±25.8	29.8 ±11	10.0 ±3.8	13.2 ±6.1	7.5 ±2.9	2823 ±1060	3531 ±1385
CH_4-non fossil	11.8 ±1.8	5.7±1.4×10^{-4}	80.8 ±25.8	27.2 ±11	7.3 ±3.8	10.3 ±6.1	4.7 ±2.9	2701 ±1057	3254 ±1364
N_2O	109 ±10	2.8±1.1 ×10^{-3}	273 ±118	273 ±130	130 ±64	290 ±140	233 ±110		
HFC-32	5.4 ±1.1	1.1±0.2 ×10^{-1}	2693 ±842	771 ±292	220 ±87	181 ±83	142 ±51	78175 ±29402	92888 ±36534
HFC-134a	14.0 ±2.8	1.67±0.32 ×10^{-1}	4144 ±1160	1526 ±577	436 ±173	733 ±410	306 ±119	146670 ±53318	181408 ±71365
CFC-11	52.0 ±10.4	2.91±0.65 ×10^{-1}	8321 ±2419	6226 ±2297	2093 ±865	6351 ±2342	3536 ±1511		
PFC-14	50000	9.89±0.19 ×10^{-2}	5301 ±1395	7380 ±2430	10587 ±3692	7660 ±2464	9055 ±3128		

[END TABLE 7.15 HERE]

[START BOX 7.3 HERE]

BOX 7.3: Physical considerations in emission-metric choice

Following AR5, this report does not recommend an emission metric because the appropriateness of the choice depends on the purposes for which gases or forcing agents are being compared. Emission metrics can facilitate the comparison of effects of emissions in support of policy goals. They do not define policy goals or targets but can support the evaluation and implementation of choices within multi-component policies (e.g., they can help prioritise which emissions to abate). The choice of metric will depend on which aspects of climate change are most important to a particular application or stakeholder and over which time-horizons. Different international and national climate policy goals may lead to different conclusions about what is the most suitable emission metric (Myhre et al., 2013b).

GWP and GTP give the relative effect of pulse emissions, i.e. how much more energy is trapped (GWP) or how much warmer (GTP) the climate would be when unit emissions of different compounds are compared (Section 7.6.1.2). Consequently, these metrics provide information on how much energy accumulation (GWP) or how much global warming (GTP) could be avoided (over a given time period, or at a given future point in time) by avoiding the emission of a unit of a short-lived greenhouse gas compared to avoiding a unit of CO_2. By contrast, the new metric approaches of Combined-GTP and GWP* closely approximate the additional effect on climate from a time-series of short-lived greenhouse gas emissions, and can be used to compare this to the effect on temperature from the emission or removal of a unit of CO_2 (Allen et al., 2018b; Collins et al., 2020; Section 7.6.1.4).

If global surface temperature stabilization goals are considered, cumulative CO_2 equivalent emissions computed with the GWP-100 emission metric would continue to rise when short-lived greenhouse gas emissions are reduced but remain above zero (Figure 7.22b). Such as rise would not match the expected global surface temperature stabilization or potential decline in warming that comes from a reduction in emissions of short-lived greenhouse gases (Pierrehumbert, 2014; Allen et al., 2018b; Cain et al., 2019; Collins et al., 2020; Lynch et al., 2020, 2021). This is relevant to net zero greenhouse gas emission goals (See Section 7.6.2 and Chapter 1, Box 1.4).

When individual gases are treated separately in climate model emulators (Cross-Chapter Box 7.1), or weighted and aggregated using an emission metric approach (such as CGTP or GWP*) which translate the distinct behaviour from cumulative emissions of short-lived gases, ambiguity in the future warming trajectory of a given emission scenario can be substantially reduced (Cain et al., 2019; Denison et al., 2019; Collins et al., 2020; Lynch et al., 2021). The degree of ambiguity varies with the emissions scenario. For mitigation pathways that limit warming to 2°C with an even chance, the ambiguity arising from using GWP-100 as sole constraint on emissions of a mix of greenhouse gases (without considering their economic implications or feasibility) could be as much as 0.17°C, which represents about one fifth of the remaining global warming in those pathways (Denison et al., 2019). If the evolution of the individual GHGs are not known, this can make it difficult to evaluate how a given global multi-gas emission pathway specified only in CO_2 equivalent emissions would achieve (or not) global surface temperature goals. This is potentially an issue as Nationally Determined Contributions frequently make commitments in terms of GWP-100 based CO_{2}- equivalent emissions at 2030 without specifying individual gases (Denison et al., 2019). Clear and transparent representation of the global warming implications of future emission pathways including Nationally Determined Contributions could be achieved either by their detailing pathways for multiple gases or by detailing a pathway of cumulative carbon dioxide equivalent emission approach aggregated across greenhouse gases evaluated by either GWP* or CGTP metric approaches (Cain et al., 2019; Collins et al., 2020; Lynch et al., 2021). Note that although the Paris Agreement Rulebook asks countries to report emissions of individual greenhouse gases separately for the global stocktake (Decision 18/CMA.1, annex, paragraph 38) which can allow the current effects of their emissions on global surface temperature to be accurately estimated, estimates of future warming are potentially ambiguous where emissions are aggregated using GWP-100 or other pulse metrics.

Although there is significant history of using single-basket approaches, supported by emission metrics such as GWP-100, in climate policies such as the Kyoto Protocol, multi-basket approaches also have many precedents in environmental management, including the Montreal Protocol (Daniel et al., 2012). Further assessment of the performance of physical and economics-based metrics in the context of climate change mitigation is provided in the contribution of Working Group III to the AR6.

[END BOX 7.3 HERE]

7.6.2 Applications of emission metrics

One prominent use of emission metrics is for comparison of efforts measured against climate change goals or targets. One of the most commonly discussed goals are in Article 2 of the Paris Agreement which aims to limit the risks and impacts of climate change by setting temperature goals. In addition, the Paris Agreement has important provisions which relate to how the goals are to be achieved, including making emissions reductions in a manner that does not threaten food production (Article 2), an early emissions peaking target, and the aim to “achieve a balance between anthropogenic emissions by sources and removals by sinks of greenhouse gases in the second half of this century” (Article 4). Article 4 also contains important context regarding international equity, sustainable development, and poverty reduction. Furthermore, the United Nations Framework Convention on Climate Change (UNFCCC) sets out as its ultimate objective, the “stabilization of greenhouse gas concentrations in the atmosphere at a level that would prevent dangerous anthropogenic interference with the climate system."

How the interpretation of the Paris Agreement and the meaning of "net zero" emissions, reflects on the appropriate choice of metric is an active area of research (Schleussner et al., 2016, 2019; Fuglestvedt et al., 2018; Collins et al., 2020). Several possible scientific interpretations of the Article 2 and 4 goals can be devised, and these along with emission metric choice have implications both for when a balance in GHG emissions, net zero CO_2 emissions or net zero GHG emissions are achieved, and for their meaning in terms of temperature outcome (Fuglestvedt et al., 2018; Rogelj et al., 2018; Wigley, 2018). In AR6 net zero greenhouse gas emissions is defined as the condition in which metric-weighted anthropogenic GHG emissions are balanced by metric-weighted anthropogenic GHG removals over a specified period (see Chapter 1, Box 1.4, Appendix VII: Glossary). The quantification of net zero GHG emissions depends on the GHG emission metric chosen to compare emissions and removals of different gases, as well as the time horizon chosen for that metric. As the choice of emission metric affects the quantification of net zero GHG emissions, it therefore affects the resulting temperature outcome after net zero emissions are achieved (Lauder et al., 2013; Rogelj et al., 2015; Fuglestvedt et al., 2018; Schleussner et al., 2019). Schleussner et al.(2019) note that declining temperatures may be a desirable outcome of net zero. Rogelj and Schleussner (2019) also point out that the physical metrics raise questions of equity and fairness between developed and developing countries.

Based on SR1.5 (Allen et al., 2018a), there is *high confidence* that achieving net zero CO_2 emissions and declining non-CO_2 radiative forcing would halt human-induced warming. Based on (Bowerman et al., 2013; Pierrehumbert, 2014; Fuglestvedt et al., 2018; Tanaka and O'Neill, 2018; Schleussner et al., 2019) there is also *high confidence* that reaching net zero GHG emissions as quantified by GWP-100 typically leads to reductions from peak global surface temperature after net zero GHGs emissions are achieved, depending on the relative sequencing of mitigation of short-lived and long-lived species. If both short- and long-lived species are mitigated together, then temperatures peak and decline. If mitigation of short-lived species occurs much earlier than that of long-lived species, then temperatures stabilise very near peak values, rather than decline. Temperature targets can be met even with positive net GHG emissions based on GWP-100 (Tanaka and O'Neill, 2018). As demonstrated by Allen et al. (2018b), Cain et al. (2019), Schleussner et al. (2019) and Collins et al. (2020) reaching net zero GHG emissions when quantified using the new emission metric approaches such as CGTP or GWP* would lead to an approximately similar temperature evolution as achieving net zero CO_2. Hence, net zero CO_2 and net zero GHG quantified using these new approaches would both lead to approximately stable contributions to temperature change after net zero emissions are achieved (*high confidence*).

Comparisons with emission or global surface temperature stabilisation goals are not the only role for emissions metrics. Other important roles include those in pricing approaches where policymakers choose to compare short-lived and long-lived climate forcers (e.g. Manne and Richels, 2001), and in life cycle analyses (e.g. Hellweg and Milà i Canals, 2014). Several papers have reviewed the issue of metric choice for life cycle analyses, noting that analysts should be aware of the challenges and value judgements inherent in attempting to aggregate the effects of forcing agents with different timescales onto a common scale (e.g. Mallapragada and Mignone, 2017) and recommend aligning metric choice with policy goals as well as testing sensitivities of results to metric choice (Cherubini et al., 2016). Furthermore, life cycle analyses approaches which are sensitive to choice of emission metric benefit from careful communication of the reasons for the sensitivity (Levasseur et al., 2016).

Frequently Asked Questions

[START FAQ7.1 HERE]

FAQ 7.1: What is the Earth's energy budget, and what does it tell us about climate change?

The Earth's energy budget describes the flow of energy within the climate system. Since at least 1970 there has been a persistent imbalance in the energy flows that has led to excess energy being absorbed by the climate system. By measuring and understanding these energy flows and the role that human activities play in changing them, we are better able to understand the causes of climate change and project future climate change more accurately.

Our planet receives vast amounts of energy every day in the form of sunlight. Around a third of the sunlight is reflected back to space by clouds, by tiny particles called *aerosols*, and by bright surfaces such as snow and ice. The rest is absorbed by the ocean, land, ice, and atmosphere. The planet then emits energy back out to space in the form of thermal radiation. In a world that was not warming or cooling, these energy flows would balance. Human activity has caused an imbalance in these energy flows.

We measure the influence of various human and natural factors on the energy flows at the top of our atmosphere in terms of *radiative forcings*, where a positive radiative forcing has a warming effect and a negative radiative forcing has a cooling effect. In response to these forcings, the Earth system will either warm or cool, so as to restore balance through changes in the amount of outgoing thermal radiation (the warmer the Earth, the more radiations it emits). Changes in Earth's temperature in turn lead to additional changes in the climate system (known as *climate feedbacks*) that either amplify or dampen the original effect. For example, Arctic sea-ice has been melting as the Earth warms, reducing the amount of reflected sunlight and adding to the initial warming (an amplifying feedback). The most uncertain of those climate feedbacks are clouds, as they respond to warming in complex ways that affect both the emission of thermal radiation and the reflection of sunlight. However, we are now more confident that cloud changes, taken together, will amplify climate warming (see FAQ 7.2).

Human activities have unbalanced these energy flows in two main ways. First, increases in greenhouse gas levels have led to more of the emitted thermal radiation being absorbed by the atmosphere, instead of being released to space. Second, increases in pollutants have increased the amount of aerosols such as sulphates in the atmosphere (see FAQ 6.1). This has led to more incoming sunlight being reflected away, by the aerosols themselves and through the formation of more cloud drops, which increases the reflectivity of clouds (see FAQ 7.2).

Altogether, the global energy flow imbalance since the 1970s has been just over half a watt per square metre of the Earth's surface. This sounds small, but because the imbalance is persistent and because Earth's surface is large, this adds up to about 25 times the total amount of primary energy consumed by human society, compared over 1971 to 2018. Compared to the IPCC Fifth Assessment Report, we are now better able to quantify and track these energy flows from multiple lines of evidence, including satellite data, direct measurements of ocean temperatures, and a wide variety of other Earth system observations (see FAQ 1.1). We also have a better understanding of the processes contributing to this imbalance, including the complex interactions between aerosols, clouds and radiation.

Research has shown that the excess energy since the 1970s has mainly gone into warming the ocean (91%), followed by the warming of land (5%) and the melting ice sheets and glaciers (3%). The atmosphere has warmed substantially since 1970, but because it is comprised of thin gases it has absorbed only 1% of the excess energy (FAQ 7.1, Figure 1). As the ocean has absorbed the vast majority of the excess energy, especially within their top two kilometres, the deep ocean is expected to continue to warm and expand for centuries to millennia, leading to long-term sea level rise – even if atmospheric greenhouse gas levels were to decline (see FAQ 5.3). This is in addition to the sea level rise expected from melting ice sheets and glaciers.

Understanding the Earth's energy budget also helps to narrow uncertainty in future projections of climate. By testing climate models against what we know about the Earth's energy budget, we can make more confident projections of surface temperature changes we might expect this century and beyond.

[START FAQ7.1, FIGURE 1 HERE]

FAQ7.1, Figure 1: The Earth's energy budget compares the flows of incoming and outgoing of energy that are relevant for the climate system. Since the at least the 1970s, less energy is flowing out than is flowing in, which leads to excess energy being absorbed by the ocean, land, ice and atmosphere, with the ocean absorbing 91%.

[END FIGURE FAQ7.1, FIGURE 1 HERE]

[END FAQ 7.1 HERE]

[START FAQ 7.2 HERE]

FAQ 7.2: Clouds – What is the role in a warming climate?

One of the biggest challenges in climate science has been to predict how clouds will change in a warming world and whether those changes will amplify or partially offset the warming caused by increasing concentrations of greenhouse gases and other human activities. Scientists have made significant progress over the past decade and are now more confident that changes in clouds will amplify, rather than offset, global warming in the future.

Clouds cover roughly two thirds of the Earth's surface. They consist of small droplets and/or ice crystals, which form when water vapour condenses or deposits around tiny particles called *aerosols* (such as salt, dust, or smoke). Clouds play a critical role in the Earth's *energy budget* at the top of atmosphere and therefore influence Earth's surface temperature (see FAQ 7.1) . The interactions between clouds and the climate are complex and varied. Clouds at low altitudes tend to reflect incoming solar energy back to space, preventing this energy from reaching and warming the Earth and causing a cooling effect. On the other hand, higher clouds tend to trap (i.e., absorb and then emit at a lower temperature) some of the energy leaving the Earth, leading to a warming effect. On average, clouds reflect back more incoming energy than the amount of outgoing energy they trap, resulting in an overall net cooling effect on the present climate. Human activities since the pre-industrial era have altered this climate effect of clouds in two different ways: by changing the abundance of the aerosol particles in the atmosphere and by warming the Earth's surface, primarily as a result of increases in greenhouse gas emissions.

The concentration of aerosols in the atmosphere has markedly increased since the pre-industrial era, and this has had two important effects on clouds. First, clouds now reflect more incoming energy because cloud droplets have become more numerous and smaller. Second, smaller droplets may delay rain formation, thereby making the clouds last longer, although this effect remains uncertain. Hence, aerosols released by human activities have had a cooling effect, counteracting a considerable portion of the warming caused by increases in greenhouse gases over the last century (see FAQ 3.1). Nevertheless, this cooling effect is expected to diminish in the future, as air pollution policies progress worldwide, reducing the amount of aerosols released into the atmosphere.

Since the pre-industrial period, the Earth's surface and atmosphere have warmed, altering the properties of clouds, such as their altitude, amount, and composition (water or ice), thereby affecting the Earth's energy budget and, in turn, changing temperature. This cascading effect of clouds, known as the *cloud feedback,* could either amplify or offset some of the future warming and has long been the biggest source of uncertainty in climate projections. The problem stems from the fact that clouds can change in many ways and that their processes occur on much smaller scales than what global climate models can explicitly represent. As a result, global climate models have disagreed on how clouds, particularly over the subtropical ocean, will change in the future and whether the change will amplify or suppress the global warming.

Since the last IPCC Report in 2013, understanding of cloud processes has advanced with better observations, new analysis approaches and explicit high-resolution numerical simulation of clouds. Also, current global climate models simulate cloud behaviour better than previous models, due both to advances in computational capabilities and process understanding. Altogether, this has helped to build a more complete picture of how clouds will change as the climate warms (FAQ 7.2, Figure 1). For example, the amount of low clouds will reduce over the subtropical ocean, leading to less reflection of incoming solar energy, and the altitude of high clouds will rise, making them more prone to trapping outgoing energy; both processes have a warming effect. In contrast, clouds in high latitudes will be increasingly made of water droplets rather than ice crystals. This shift from fewer, larger ice crystals to smaller but more numerous water droplets will result in more of the incoming solar energy being reflected back to space and produce a cooling effect. Better understanding of how clouds respond to warming has led to more confidence than before that future changes in clouds will, overall, cause additional warming (i.e., by weakening the current cooling effect of clouds). This is called a *positive net cloud feedback.*

In summary, clouds will amplify rather than suppress the warming of the climate system in the future, as more greenhouse gases and fewer aerosols are released to the atmosphere by human activities.

[START FAQ7.2, FIGURE 1 HERE]

FAQ7.2, Figure 1: Interactions between clouds and the climate today and in a warmer future. Global warming is expected to alter the altitude (left) and the amount (centre) of clouds, which will amplify warming. On the other hand, cloud composition will change (right), offsetting some of the warming. Overall clouds are expected to amplify future warming.

[END FAQ7.2, FIGURE 1 HERE]

[END FAQ 7.2 HERE]

FAQ 7.3: What is equilibrium climate sensitivity and how does it relate to future warming?

For a given future scenario, climate models project a range of changes in global surface temperature. This range is closely related to equilibrium climate sensitivity, or ECS, which measures how climate models respond to a doubling of carbon dioxide in the atmosphere. Models with high climate sensitivity project stronger future warming. Some climate models of the new generation are more sensitive than the range assessed in the IPCC Sixth Assessment Report. This leads to end-of-century global warming in some simulations of up to 2°C–3°C above the current IPCC best estimate. Although these higher warming levels are not expected to occur, high-ECS models are useful for exploring high impact, low-likelihood futures.

The *equilibrium climate sensitivity* (ECS) is defined as the long-term global warming caused by a doubling of carbon dioxide above its pre-industrial concentration. For a given emission scenario, much of the uncertainty in projections of future warming can be explained by the uncertainty in ECS (FAQ 7.3, Figure 1). The significance of equilibrium climate sensitivity has long been recognised, and the first estimate was presented by Swedish scientist Svante Arrhenius in 1896.

This Sixth Assessment Report concludes that there is a 90% or more chance (*very likely*) that the ECS is between 2°C and 5°C. This represents a significant reduction in uncertainty compared to the Fifth Assessment Report, which gave a 66% chance (*likely*) of ECS being between 1.5°C and 4.5°C. This reduction in uncertainty has been possible not through a single breakthrough or discovery but instead by combining evidence from many different sources and by better understanding their strengths and weaknesses.

There are four main lines of evidence for ECS. First, the self-reinforcing processes, called *feedback loops,* that amplify or dampen the warming in response to increasing carbon dioxide are now better understood. For example, warming in the Arctic melts sea ice, resulting in more open ocean area, which is darker and therefore absorbs more sunlight, further intensifying the initial warming. It remains challenging to represent realistically all the processes involved in these feedback loops, particularly those related to clouds (see FAQ 7.2). Such identified model errors are now taken into account, and other known, but generally weak, feedback loops that are usually not included in models are now included in the assessment of ECS.

Second, historical warming since early industrialisation provides strong evidence that climate sensitivity is not small. Since 1850, the concentration of carbon dioxide and other greenhouse gases have increased, and as a result the Earth has warmed by about 1.1ºC. However, relying on this industrial-era warming to estimate ECS is challenging, partly because some of the warming from greenhouse gases was offset by cooling from aerosol particles and partly because the ocean are still responding to past increases in carbon dioxide.

Third, evidence from ancient climates that had reached equilibrium with greenhouse gas concentrations, such as the coldest period of the last ice age around 20,000 years ago, or warmer periods further back in time, provide useful data on the ECS of the climate system (see FAQ 1.3). Fourth, statistical approaches linking model ECS values with observed changes, such as global warming since the 1970s, provide complementary evidence.

All four lines of evidence rely, to some extent, on climate models, and interpreting the evidence often benefits from model diversity and spread in modelled climate sensitivity. Furthermore, high-sensitivity models can provide important insights into futures that have a low likelihood of occurring but that could result in large impacts. But, unlike in previous assessments, climate models are not considered a line of evidence in their own right in the IPCC Sixth Assessment Report.

The ECS of the latest climate models is, on average, higher than that of the previous generation of models and also higher than this report's best estimate of 3.0°C. Furthermore, the ECS values in some of the new models are both above and below the 2°C to 5°C *very likely* range, and although such models cannot be ruled out as implausible solely based on their ECS, some of them do display climate change that is inconsistent with the observed when tested with ancient climates. A slight mismatch with models is only natural because the IPCC Sixth Assessment Report is based on observations and an improved understanding of the climate system.

[START FAQ 7.3, FIGURE 1 HERE]

FAQ7.3, Figure 1: Equilibrium climate sensitivity and future warming. (left) Equilibrium climate sensitivities for the current generation (sixth climate model intercomparison project, CMIP6) climate models, and the previous (CMIP5) generation. The assessed range in this report (AR6) is also shown. (right) Climate projections of CMIP5, CMIP6, and AR6 for the very high-emission scenarios RCP8.5, and SSP5-8.5, respectively. The thick horizontal lines represent the multi-model average and the thin horizontal lines the results of individual models. The boxes represent the model ranges for CMIP5 and CMIP6 and the range assessed in AR6.

[END FAQ 7.3, FIGURE 1 HERE]

[END FAQ 7.3 HERE]

References

Aamaas, B., T.K. Berntsen, J.S. Fuglestvedt, K.P. Shine, and N. Bellouin, 2016: Regional emission metrics for short-lived climate forcers from multiple models. *Atmospheric Chemistry and Physics*, doi:10.5194/acp-16-7451-2016.

Aamaas, B., T.K. Berntsen, J.S. Fuglestvedt, K.P. Shine, and W.J. Collins, 2017: Regional temperature change potentials for short-lived climate forcers based on radiative forcing from multiple models. *Atmospheric Chemistry and Physics*, doi:10.5194/acp-17-10795-2017.

Abe-Ouchi, A. et al., 2013: Insolation-driven 100,000-year glacial cycles and hysteresis of ice-sheet volume. *Nature*, **500(7461)**, 190–193, doi:10.1038/nature12374.

Abe-Ouchi, A. et al., 2015: Ice-sheet configuration in the CMIP5/PMIP3 Last Glacial Maximum experiments. *Geoscientific Model Development*, **8(11)**, 3621–3637, doi:10.5194/gmd-8-3621-2015.

Ackerley, D. and D. Dommenget, 2016: Atmosphere-only GCM (ACCESS1.0) simulations with prescribed land surface temperatures. *Geoscientific Model Development*, doi:10.5194/gmd-9-2077-2016.

Albrecht, B.A., 1989: Aerosols, cloud microphysics, and fractional cloudiness.. *Science (New York, N.Y.)*, **245(4923)**, 1227–30, doi:10.1126/science.245.4923.1227.

Aldrin, M. et al., 2012: Bayesian estimation of climate sensitivity based on a simple climate model fitted to observations of hemispheric temperatures and global ocean heat content. *Environmetrics*, **23(3)**, 253–271, doi:10.1002/env.2140.

Alexeev, V.A. and C.H. Jackson, 2013: Polar amplification: is atmospheric heat transport important? *Climate Dynamics*, **41(2)**, 533–547, doi:10.1007/s00382-012-1601-z.

Alexeev, V.A., P.L. Langen, and J.R. Bates, 2005: Polar amplification of surface warming on an aquaplanet in ”ghost forcing” experiments without sea ice feedbacks. *Climate Dynamics*, **24(7)**, 655–666, doi:10.1007/s00382-005-0018-3.

Allan, R.P. et al., 2014: Changes in global net radiative imbalance 1985–2012. *Geophysical Research Letters*, **41(15)**, 5588–5597, doi:10.1002/2014gl060962.

Allen, M.R. et al., 2016: New use of global warming potentials to compare cumulative and short-lived climate pollutants. *Nature Climate Change*, **6(8)**, 773–776, doi:10.1038/nclimate2998.

Allen, M.R. et al., 2018a: Framing and Context. In: *Global Warming of 1.5°C. An IPCC Special Report on the impacts of global warming of 1.5°C above pre-industrial levels and related global greenhouse gas emission pathways, in the context of strengthening the global response to the threat of climate change,* [Masson-Delmotte, V., P. Zhai, H.-O. Pörtner, D. Roberts, J. Skea, P.R. Shukla, A. Pirani, W. Moufouma-Okia, C. Péan, R. Pidcock, S. Connors, J.B.R. Matthews, Y. Chen, X. Zhou, M.I. Gomis, E. Lonnoy, T. Maycock, M. Tignor, and T. Waterfield (eds.)]. In Press, pp. 49–91.

Allen, M.R. et al., 2018b: A solution to the misrepresentations of CO2-equivalent emissions of short-lived climate pollutants under ambitious mitigation. *npj Climate and Atmospheric Science*, **1(1)**, doi:10.1038/s41612-018-0026-8.

Allen, R.J., J.R. Norris, and M. Wild, 2013: Evaluation of multidecadal variability in CMIP5 surface solar radiation and inferred underestimation of aerosol direct effects over Europe, China, Japan, and India. *Journal of Geophysical Research-Atmospheres*, **118(12)**, 6311–6336, doi:10.1002/jgrd.50426.

Allen, R.J. et al., 2019: Observationally constrained aerosol–cloud semi-direct effects. *npj Climate and Atmospheric Science*, **2(1)**, 1–12, doi:10.1038/s41612-019-0073-9.

Allison, L.C. et al., 2019: Towards quantifying uncertainty in ocean heat content changes using synthetic profiles. *Environmental Research Letters*, **14(8)**, 84037, doi:10.1088/1748-9326/ab2b0b.

Allison, L.C. et al., 2020a: Observations of planetary heating since the 1980s from multiple independent datasets. *Environmental Research Communications*, doi:10.1088/2515-7620/abbb39.

Allison, L.C. et al., 2020b: Observations of planetary heating since the 1980s from multiple independent datasets. *Environmental Research Communications*, doi:10.1088/2515-7620/abbb39.

Alo, C.A. and E.N. Anagnostou, 2017: A sensitivity study of the impact of dynamic vegetation on simulated future climate change over Southern Europe and the Mediterranean. *International Journal of Climatology*, **37(4)**, 2037–2050, doi:10.1002/joc.4833.

Anagnostou, E. et al., 2016: Changing atmospheric CO2 concentration was the primary driver of early Cenozoic climate. *Nature*, **533**, 380–384, doi:10.1038/nature17423.

Anagnostou, E. et al., 2020: Proxy evidence for state-dependence of climate sensitivity in the Eocene greenhouse. *Nature Communications*, **11(1)**, 4436, doi:10.1038/s41467-020-17887-x.

Andrews, E., J.A. Ogren, S. Kinne, and B. Samset, 2017: Comparison of AOD, AAOD and column single scattering albedo from AERONET retrievals and in situ profiling measurements. *Atmospheric Chemistry and Physics*, **17(9)**, 6041–6072, doi:10.5194/acp-17-6041-2017.

Andrews, M.B. et al., 2020: Historical Simulations With HadGEM3-GC3.1 for CMIP6. *Journal of Advances in Modeling Earth Systems*, **12(6)**, 1–34, doi:10.1029/2019ms001995.

Andrews, T. and M.J. Webb, 2018: The dependence of global cloud and lapse rate feedbacks on the spatial structure of tropical pacific warming. *Journal of Climate*, doi:10.1175/jcli-d-17-0087.1.
Andrews, T. and P.M. Forster, 2020: Energy budget constraints on historical radiative forcing. *Nature Climate Change*, **10**, 313–316, doi:10.1038/s41558-020-0696-1.
Andrews, T., J.M. Gregory, and M.J. Webb, 2015: The Dependence of Radiative Forcing and Feedback on Evolving Patterns of Surface Temperature Change in Climate Models. *Journal of Climate*, **28(4)**, 1630–1648, doi:10.1175/jcli-d-14-00545.1.
Andrews, T., J.M. Gregory, M.J. Webb, and K.E. Taylor, 2012: Forcing, feedbacks and climate sensitivity in CMIP5 coupled atmosphere-ocean climate models. *Geophysical Research Letters*, **39(9)**, L09712, doi:10.1029/2012gl051607.
Andrews, T., R.A. Betts, B.B.B. Booth, C.D. Jones, and G.S. Jones, 2017: Effective radiative forcing from historical land use change. *Climate Dynamics*, **48(11–12)**, 3489–3505, doi:10.1007/s00382-016-3280-7.
Andrews, T. et al., 2018: Accounting for Changing Temperature Patterns Increases Historical Estimates of Climate Sensitivity. *Geophysical Research Letters*, **45(16)**, 8490–8499, doi:10.1029/2018gl078887.
Andrews, T. et al., 2019: Forcings, feedbacks and climate sensitivity in HadGEM3-GC3.1 and UKESM1. *Journal of Advances in Modeling Earth Systems*, doi:10.1029/2019ms001866.
Andrews, T. et al., 2021: Effective radiative forcing in a GCM with fixed surface temperatures. *Journal of Geophysical Research: Atmospheres*, doi:10.1029/2020jd033880.
Ångström, K., 1900: Ueber die Bedeutung des Wasserdampfes und der Kohlensäure bei der Absorption der Erdatmosphäre. *Annalen der Physik*, **308(12)**, 720–732, doi:10.1002/andp.19003081208.
Annan, J.D. and J.C. Hargreaves, 2006: Using multiple observationally-based constraints to estimate climate sensitivity. *Geophysical Research Letters*, **33(6)**, doi:10.1029/2005gl025259.
Annan, J.D., J.C. Hargreaves, T. Mauritsen, and B. Stevens, 2020a: What could we learn about climate sensitivity from variability in the surface temperature record? *Earth System Dynamics*, **11**, 709–719, doi:10.5194/esd-11-709-2020.
Annan, J.D., J.C. Hargreaves, T. Mauritsen, and B. Stevens, 2020b: What could we learn about climate sensitivity from variability in the surface temperature record? *Earth System Dynamics*, **11**, 709–719, doi:10.5194/esd-11-709-2020.
Antuña-Marrero, J.C., F. García, R. Estevan, B. Barja, and A. Sánchez-Lorenzo, 2019: Simultaneous dimming and brightening under all and clear sky at Camagüey, Cuba (1981–2010). *Journal of Atmospheric and Solar-Terrestrial Physics*, **190**, 45–53, doi:10.1016/j.jastp.2019.05.004.
Armour, K.C., 2017: Energy budget constraints on climate sensitivity in light of inconstant climate feedbacks. *Nature Climate Change*, doi:10.1038/nclimate3278.
Armour, K.C. and G.H. Roe, 2011: Climate commitment in an uncertain world. *Geophysical Research Letters*, **38(1)**, doi:10.1029/2010gl045850.
Armour, K.C., C.M. Bitz, and G.H. Roe, 2013: Time-Varying Climate Sensitivity from Regional Feedbacks. *Journal of Climate*, doi:10.1175/jcli-d-12-00544.1.
Armour, K.C., N. Siler, A. Donohoe, and G.H. Roe, 2019: Meridional Atmospheric Heat Transport Constrained by Energetics and Mediated by Large-Scale Diffusion. *Journal of Climate*, **32(12)**, 3655–3680, doi:10.1175/jcli-d-18-0563.1.
Armour, K.C., J. Marshall, J.R. Scott, A. Donohoe, and E.R. Newsom, 2016: Southern Ocean warming delayed by circumpolar upwelling and equatorward transport. *Nature Geoscience*, doi:10.1038/ngeo2731.
Armstrong, E., P. Valdes, J. House, and J. Singarayer, 2019: Investigating the feedbacks between CO2, vegetation and the AMOC in a coupled climate model. *Climate Dynamics*, **53(5–6)**, 2485–2500, doi:10.1007/s00382-019-04634-2.
Arora, V.K. et al., 2013: Carbon-concentration and carbon-climate feedbacks in CMIP5 earth system models. *Journal of Climate*, **26(15)**, 5289–5314, doi:10.1175/jcli-d-12-00494.1.
Arora, V.K. et al., 2020: Carbon-concentration and carbon-climate feedbacks in CMIP6 models and their comparison to CMIP5 models. *Biogeosciences*, **17(16)**, 4173–4222, doi:10.5194/bg-17-4173-2020.
Arrhenius, S., 1896: On the Influence of Carbonic Acid in the Air upon the Temperature of the Ground. *Philosophocal Magazine and Journal of Science*, **41(page 270)**, 237–279.
Ashwin, P. and A.S. von der Heydt, 2020: Extreme Sensitivity and Climate Tipping Points. *Journal of Statistical Physics*, **179(5)**, 1531–1552, doi:10.1007/s10955-019-02425-x.
Augustine, J.A. and E.G. Dutton, 2013: Variability of the surface radiation budget over the United States from 1996 through 2011 from high-quality measurements. *Journal of Geophysical Research-Atmospheres*, **118(1)**, 43–53, doi:10.1029/2012jd018551.
Baggenstos, D. et al., 2019: Earth's radiative imbalance from the Last Glacial Maximum to the present. *Proceedings of the National Academy of Sciences of the United States of America*, **116(30)**, 14881–14886, doi:10.1073/pnas.1905447116.
Balcombe, P., J.F. Speirs, N.P. Brandon, and A.D. Hawkes, 2018: Methane emissions: choosing the right climate metric and time horizon. *Environmental Science: Processes & Impacts*, **20(10)**, 1323–1339,

doi:10.1039/c8em00414e.
Banerjee, A. et al., 2019: Stratospheric water vapor: an important climate feedback. *Climate Dynamics*, **53(3)**, 1697–1710, doi:10.1007/s00382-019-04721-4.
Barreiro, M. and S.G. Philander, 2008: Response of the tropical Pacific to changes in extratropical clouds. *Climate Dynamics*, doi:10.1007/s00382-007-0363-5.
Bartlein, P.J. et al., 2011: Pollen-based continental climate reconstructions at 6 and 21 ka: a global synthesis. *Climate Dynamics*, **37(3)**, 775–802, doi:10.1007/s00382-010-0904-1.
Bauer, S.E. et al., 2013: Historical and future black carbon deposition on the three ice caps: Ice core measurements and model simulations from 1850 to 2100. *Journal of Geophysical Research: Atmospheres*, **118(14)**, 7948–7961, doi:10.1002/jgrd.50612.
Beerling, D.J. and D.L. Royer, 2011: Convergent Cenozoic CO2 history. *Nature Geoscience*, **4(7)**, 418–420, doi:10.1038/ngeo1186.
Bellouin, N., J. Quaas, J.-J. Morcrette, and O. Boucher, 2013a: Estimates of aerosol radiative forcing from the MACC re-analysis. *Atmospheric Chemistry and Physics*, **13(4)**, 2045–2062, doi:10.5194/acp-13-2045-2013.
Bellouin, N. et al., 2013b: Impact of the modal aerosol scheme GLOMAP-mode on aerosol forcing in the Hadley Centre Global Environmental Model. *Atmospheric Chemistry and Physics*, **13(6)**, 3027–3044, doi:10.5194/acp-13-3027-2013.
Bellouin, N. et al., 2019: Bounding global aerosol radiative forcing of climate change. *Reviews of Geophysics*, doi:10.1029/2019rg000660.
Bender, F.A.M., A.M.L. Ekman, and H. Rodhe, 2010: Response to the eruption of Mount Pinatubo in relation to climate sensitivity in the CMIP3 models. *Climate Dynamics*, **35(5)**, 875–886, doi:10.1007/s00382-010-0777-3.
Bender, F.A.M., V. Ramanathan, and G. Tselioudis, 2012: Changes in extratropical storm track cloudiness 1983-2008: Observational support for a poleward shift. *Climate Dynamics*, **38**, 2037–2053, doi:10.1007/s00382-011-1065-6.
Bender, F.A.M., L. Frey, D.T. McCoy, D.P. Grosvenor, and J.K. Mohrmann, 2019: Assessment of aerosol–cloud–radiation correlations in satellite observations, climate models and reanalysis. *Climate Dynamics*, **52(7–8)**, 4371–4392, doi:10.1007/s00382-018-4384-z.
Bender, F.A.-M., 2011: Planetary albedo in strongly forced climate, as simulated by the CMIP3 models. *Theoretical and Applied Climatology*, **105(3–4)**, 529–535, doi:10.1007/s00704-011-0411-2.
Bengtsson, L. and S.E. Schwartz, 2013: Determination of a lower bound on Earth's climate sensitivity. *Tellus B*, **1**, 1–16, doi:10.3402/tellusb.v65i0.21533.
Bentamy, A. et al., 2017: Review and assessment of latent and sensible heat flux accuracy over the global oceans. *REMOTE SENSING OF ENVIRONMENT*, **201**, 196–218, doi:10.1016/j.rse.2017.08.016.
Bilbao, R.A.F., J.M. Gregory, and N. Bouttes, 2015: Analysis of the regional pattern of sea level change due to ocean dynamics and density change for 1993–2099 in observations and CMIP5 AOGCMs. *Climate Dynamics*, **45(9–10)**, 2647–2666, doi:10.1007/s00382-015-2499-z.
Bindoff, N.L. et al., 2013: Detection and Attribution of Climate Change, from Global to Regional. In: *Climate Change 2013: The Physical Science Basis. Contribution of Working Group I to the Fifth Assessment Report of the Intergovernmental Panel on Climate Change* [Stocker, T.F., D. Qin, G.-K. Plattner, M. Tignor, S.K. Allen, J. Boschung, A. Nauels, Y. Xia, V. Bex, and P.M. Midgley (eds.)]. Cambridge University Press, Cambridge, United Kingdom and New York, NY, USA, pp. 867–952, doi:10.1017/cbo9781107415324.022.
Bintanja, R., E.C. Van Der Linden, and W. Hazeleger, 2012: Boundary layer stability and Arctic climate change: a feedback study using EC-Earth. *Climate Dynamics*, **39(11)**, 2659–2673, doi:10.1007/s00382-011-1272-1.
Bintanja, R., G.J. Van Oldenborgh, S.S. Drijfhout, B. Wouters, and C.A. Katsman, 2013: Important role for ocean warming and increased ice-shelf melt in Antarctic sea-ice expansion. *Nature Geoscience*, doi:10.1038/ngeo1767.
Bjordal, J., T. Storelvmo, K. Alterskjær, and T. Carlsen, 2020: Equilibrium climate sensitivity above 5°C plausible due to state-dependent cloud feedback. *Nature Geoscience*, **13**, 718–721, doi:10.1038/s41561-020-00649-1.
Bloch-Johnson, J., R.T. Pierrehumbert, and D.S. Abbot, 2015: Feedback temperature dependence determines the risk of high warming. *Geophysical Research Letters*, **42(12)**, 4973–4980, doi:10.1002/2015gl064240.
Bloch-Johnson, J. et al., 2020: Climate Sensitivity Increases Under Higher CO2 Levels Due to Feedback Temperature Dependence. *Geophysical Research Letters*, **48(4)**, e2020GL089074, doi:10.1029/2020gl089074.
Block, K. and T. Mauritsen, 2013: Forcing and feedback in the MPI-ESM-LR coupled model under abruptly quadrupled CO2. *Journal of Advances in Modeling Earth Systems*, **5(4)**, 676–691, doi:10.1002/jame.20041.
Bodas-Salcedo, A. et al., 2019: Strong Dependence of Atmospheric Feedbacks on Mixed-Phase Microphysics and Aerosol-Cloud Interactions in HadGEM3. *Journal of Advances in Modeling Earth Systems*, **11(6)**, 1735–1758, doi:10.1029/2019ms001688.
Boeke, R.C. and P.C. Taylor, 2016: Evaluation of the Arctic surface radiation budget in CMIP5 models. *JOURNAL OF GEOPHYSICAL RESEARCH-ATMOSPHERES*, **121(14)**, 8525–8548, doi:10.1002/2016jd025099.
Boeke, R.C. and P.C. Taylor, 2018: Seasonal energy exchange in sea ice retreat regions contributes to differences in projected Arctic warming. *Nature Communications*, **9(1)**, doi:10.1038/s41467-018-07061-9.

Boisier, J.P., N. De Noblet-Ducoudré, and P. Ciais, 2013: Inferring past land use-induced changes in surface albedo from satellite observations: A useful tool to evaluate model simulations. *Biogeosciences*, doi:10.5194/bg-10-1501-2013.

Bonan, D.B., K.C. Armour, G.H. Roe, N. Siler, and N. Feldl, 2018: Sources of Uncertainty in the Meridional Pattern of Climate Change. *Geophysical Research Letters*, **45(17)**, 9131–9140, doi:10.1029/2018gl079429.

Bond, T.C. et al., 2013: Bounding the role of black carbon in the climate system: A scientific assessment. *Journal of Geophysical Research: Atmospheres*, **118(11)**, 5380–5552, doi:10.1002/jgrd.50171.

Bony, S. and J.L. Dufresne, 2005: Marine boundary layer clouds at the heart of tropical cloud feedback uncertainties in climate models.. *Geophysical Research Letters*, **32**, L20806, doi:10.1029/2005gl023851.

Bony, S. et al., 2006: How Well do we Understand and Evaluate Climate Change Feedback Processes? *Journal of Climate*, **19(15)**, 3445–3482, doi: 10.1175/JCLI3819.1.

Bony, S. et al., 2015: Clouds, circulation and climate sensitivity. *Nature Geoscience*, **8(4)**, 261–268, doi:10.1038/ngeo2398.

Bony, S. et al., 2016: Thermodynamic control of anvil cloud amount. *Proceedings of the National Academy of Sciences of the United States of America*, **113(32)**, 8927–8932, doi:10.1073/pnas.1601472113.

Bony, S. et al., 2020: Observed Modulation of the Tropical Radiation Budget by Deep Convective Organization and Lower-Tropospheric Stability. *AGU Advances*, **1(3)**, e2019AV000155, doi:10.1029/2019av000155.

Booth, B.B.B. et al., 2018: Comments on "Rethinking the Lower Bound on Aerosol Radiative Forcing". *Journal of Climate*, **31(22)**, 9407–9412, doi:10.1175/jcli-d-17-0369.1.

Boucher, O., 2012: Comparison of physically- and economically-based CO2- equivalences for methane. *Earth System Dynamics*, doi:10.5194/esd-3-49-2012.

Boucher, O., P. Friedlingstein, B. Collins, and K.P. Shine, 2009: The indirect global warming potential and global temperature change potential due to methane oxidation. *Environmental Research Letters*, **4(4)**, doi:10.1088/1748-9326/4/4/044007.

Boucher, O. et al., 2013: Clouds and Aerosols. In: *Climate Change 2013: The Physical Science Basis. Contribution of Working Group I to the Fifth Assessment Report of the Intergovernmental Panel on Climate Change* [Stocker, T.F., D. Qin, G.-K. Plattner, M. Tignor, S.K. Allen, J. Boschung, A. Nauels, Y. Xia, V. Bex, and P.M. Midgley (eds.)]. Cambridge Univeristy Press, Cambridge, United Kingdom and New York, NY, USA, pp. 571–657, doi:10.1017/cbo9781107415324.016.

Bowerman, N.H.A. et al., 2013: The role of short-lived climate pollutants in meeting temperature goals. *Nature Climate Change*, **3(12)**, 1021–1024, doi:10.1038/nclimate2034.

Brantley, S.L., 2008: Understanding Soil Time. *Science*, **321(5895)**, 1454–1455, doi:10.1126/science.1161132.

Brenguier, J.-L. et al., 2000: Radiative Properties of Boundary Layer Clouds: Droplet Effective Radius versus Number Concentration. *Journal of the Atmospheric Sciences*, **57(6)**, 803–821, doi:10.1175/1520-0469(2000)057<0803:rpoblc>2.0.co;2.

Bretherton, C.S., 2015: Insights into low-latitude cloud feedbacks from high-resolution models. *Philosophical Transactions of the Royal Society A: Mathematical, Physical and Engineering Sciences*, **373(2054)**, doi:10.1098/rsta.2014.0415.

Bretherton, C.S., P.N. Blossey, and C.R. Jones, 2013: Mechanisms of marine low cloud sensitivity to idealized climate perturbations: A single-LES exploration extending the CGILS cases. *Journal of Advances in Modeling Earth Systems*, doi:10.1002/jame.20019.

Bretherton, C.S., P.N. Blossey, and C. Stan, 2014: Cloud feedbacks on greenhouse warming in the superparameterized climate model SP-CCSM4. *Journal of Advances in Modeling Earth Systems*, **6(4)**, 1185–1204, doi:10.1002/2014ms000355.

Brient, F. and T. Schneider, 2016: Constraints on climate sensitivity from space-based measurements of low-cloud reflection. *Journal of Climate*, **29(16)**, 5821–5835, doi:10.1175/jcli-d-15-0897.1.

Brient, F. et al., 2016: Shallowness of tropical low clouds as a predictor of climate models' response to warming. *Climate Dynamics*, **47(1–2)**, 433–449, doi:10.1007/s00382-015-2846-0.

Brierley, C., N. Burls, C. Ravelo, and A. Fedorov, 2015: Pliocene warmth and gradients. *Nature Geoscience*, **8(6)**, 419–420, doi:10.1038/ngeo2444.

Bronselaer, B. et al., 2018: Change in future climate due to Antarctic meltwater. *Nature*, **564(7734)**, 53–58, doi:10.1038/s41586-018-0712-z.

Brovkin, V., T. Raddatz, C.H. Reick, M. Claussen, and V. Gayler, 2009: Global biogeophysical interactions between forest and climate. *Geophysical Research Letters*, **36(7)**, doi:10.1029/2009gl037543.

Brown, P.T. and K. Caldeira, 2017: Greater future global warming inferred from Earth's recent energy budget. *Nature*, **552(7683)**, 45–50, doi:10.1038/nature24672.

Brown, P.T., M.B. Stolpe, and K. Caldeira, 2018: Assumptions for emergent constraints. *Nature*, **563(7729)**, E1–E3, doi:10.1038/s41586-018-0638-5.

Brown, P.T., W. Li, L. Li, and Y. Ming, 2014: Top-of-atmosphere radiative contribution to unforced decadal global temperature variability in climate models. *Geophysical Research Letters*, **41(14)**, 5175–5183, doi:10.1002/2014gl060625.

Buchard, V. et al., 2017: The MERRA-2 Aerosol Reanalysis, 1980 Onward. Part II: Evaluation and Case Studies. *JOURNAL OF CLIMATE*, **30(17)**, 6851–6872, doi:10.1175/jcli-d-16-0613.1.
Burke, K.D. et al., 2018: Pliocene and Eocene provide best analogs for near-future climates. *Proceedings of the National Academy of Sciences*, **115(52)**, 13288–13293, doi:10.1073/pnas.1809600115.
Burls, N.J. and A. Fedorov, 2014a: Simulating Pliocene warmth and a permanent El Niño-like state: The role of cloud albedo. *Paleoceanography*, **29(10)**, 893–910, doi:10.1002/2014pa002644.
Burls, N.J. and A. Fedorov, 2014b: What controls the mean east-west sea surface temperature gradient in the equatorial pacific: The role of cloud albedo. *Journal of Climate*, **27(7)**, 2757–2778, doi:10.1175/jcli-d-13-00255.1.
Burt, M.A., D.A. Randall, and M.D. Branson, 2016: Dark warming. *Journal of Climate*, doi:10.1175/jcli-d-15-0147.1.
Caballero, R. and M. Huber, 2013: State-dependent climate sensitivity in past warm climates and its implications for future climate projections. *Proceedings of the National Academy of Sciences*, **110(35)**, 14162–14167, doi:10.1073/pnas.1303365110.
Cain, M. et al., 2019: Improved calculation of warming-equivalent emissions for short-lived climate pollutants. *NPJ climate and atmospheric science*, **2(1)**, 1–7, doi:10.1038/s41612-019-0086-4.
Caldwell, P.M., M.D. Zelinka, and S.A. Klein, 2018: Evaluating Emergent Constraints on Equilibrium Climate Sensitivity. *Journal of Climate*, **31(10)**, 3921–3942, doi:10.1175/jcli-d-17-0631.1.
Caldwell, P.M., M.D. Zelinka, K.E. Taylor, and K. Marvel, 2016: Quantifying the sources of intermodel spread in equilibrium climate sensitivity. *Journal of Climate*, **29(2)**, 513–524, doi:10.1175/jcli-d-15-0352.1.
Caldwell, P.M. et al., 2014: Statistical significance of climate sensitivity predictors obtained by data mining. *Geophysical Research Letters*, **41(5)**, 1803–1808, doi:10.1002/2014gl059205.
Calisto, M., D. Folini, M. Wild, and L. Bengtsson, 2014: Cloud radiative forcing intercomparison between fully coupled CMIP5 models and CERES satellite data. *Ann. Geophys.*, **32(7)**, 793–807, doi:10.5194/angeo-32-793-2014.
Calogovic, J. et al., 2010: Sudden cosmic ray decreases: No change of global cloud cover. *Geophysical Research Letters*, **37(3)**, doi:10.1029/2009gl041327.
Cane, M.A. et al., 1997: Twentieth-Century Sea Surface Temperature Trends. *Science*, **275(5302)**, 957–960, doi:10.1126/science.275.5302.957.
Cao, L., G. Bala, K. Caldeira, R. Nemani, and G. Ban-Weiss, 2010: Importance of carbon dioxide physiological forcing to future climate change. *Proceedings of the National Academy of Sciences of the United States of America*, **107(21)**, doi:10.1073/pnas.0913000107.
Cao, Y., S. Liang, X. Chen, and T. He, 2015: Assessment of Sea Ice Albedo Radiative Forcing and Feedback over the Northern Hemisphere from 1982 to 2009 Using Satellite and Reanalysis Data. *J. Climate*, **28(3)**, 1248–1259, doi:10.1175/jcli-d-14-00389.1.
Ceppi, P. and D.L. Hartmann, 2015: Connections between clouds, radiation, and midlatitude dynamics: A review.. *Curr. Clim. Change Rep.*, **1**, 94–102, doi:10.1007/s40641-015-0010-x.
Ceppi, P. and J.M. Gregory, 2017: Relationship of tropospheric stability to climate sensitivity and Earth's observed radiation budget. *Proceedings of the National Academy of Sciences*, **114(50)**, 13126–13131, doi:10.1073/pnas.1714308114.
Ceppi, P. and J.M. Gregory, 2019: A refined model for the Earth's global energy balance. *Climate Dynamics*, **53(7–8)**, 4781–4797, doi:10.1007/s00382-019-04825-x.
Ceppi, P., D.T. McCoy, and D.L. Hartmann, 2016: Observational evidence for a negative shortwave cloud feedback in middle to high latitudes. *Geophysical Research Letters*, **43(3)**, 1331–1339, doi:10.1002/2015gl067499.
Cesana, G. and T. Storelvmo, 2017: Improving climate projections by understanding how cloud phase affects radiation. *Journal of Geophysical Research: Atmospheres*, **122(8)**, 4594–4599, doi:10.1002/2017jd026927.
Cesana, G. et al., 2019: Evaluating models' response of tropical low clouds to SST forcings using CALIPSO observations. *Atmos. Chem. Phys.*, **19(5)**, 2813–2832, doi:10.5194/acp-19-2813-2019.
Cess, R.D. et al., 1990: Intercomparison and interpretation of climate feedback processes in 19 atmospheric general circulation models. *Journal of Geophysical Research*, **95**, 16601–16615, doi:10.1029/jd095id10p16601.
Chafik, L. et al., 2016: Global linkages originating from decadal oceanic variability in the subpolar North Atlantic. *Geophysical Research Letters*, **43(20)**, 10,909–10,919, doi:10.1002/2016gl071134.
Chandan, D. and R.W. Peltier, 2018: On the mechanisms of warming the mid-Pliocene and the inference of a hierarchy of climate sensitivities with relevance to the understanding of climate futures. *Climate of the Past*, **14(6)**, 825–856, doi:10.5194/cp-14-825-2018.
Charney, J.G. et al., 1979: *Carbon Dioxide and Climate: A Scientific Assessment*. National Research Council (NRC). The National Academies Press, Washington, DC, USA, 34 pp., doi:10.17226/12181.
Checa-Garcia, R., M.I. Hegglin, D. Kinnison, D.A. Plummer, and K.P. Shine, 2018: Historical Tropospheric and Stratospheric Ozone Radiative Forcing Using the CMIP6 Database. *Geophysical Research Letters*, **45(7)**, 3264–3273, doi:10.1002/2017gl076770.
Chen, X., S. Liang, and Y. Cao, 2016: Satellite observed changes in the Northern Hemisphere snow cover phenology and the associated radiative forcing and feedback between 1982 and 2013. *Environ. Res. Lett.*, **11(8)**, 84002, doi:10.1088/1748-9326/11/8/084002.

Chen, Y.-C., M.W. Christensen, G.L. Stephens, and J.H. Seinfeld, 2014: Satellite-based estimate of global aerosol–cloud radiative forcing by marine warm clouds. *Nature Geoscience*, **7(9)**, 643–646, doi:10.1038/ngeo2214.
Cheng, L. et al., 2017: Improved estimates of ocean heat content from 1960 to 2015. *Science Advances*, **3(3)**, doi:10.1126/sciadv.1601545.
Cheng, L. et al., 2018: Taking the pulse of the planet. *Eos*, **99(1)**, 14–16, doi:10.1029/2017eo081839.
Chepfer, H., V. Noel, D. Winker, and M. Chiriaco, 2014: Where and when will we observe cloud changes due to climate warming? *Geophysical Research Letters*, **41(23)**, 8387–8395, doi:10.1002/2014gl061792.
Cherian, R., J. Quaas, M. Salzmann, and M. Wild, 2014: Pollution trends over Europe constrain global aerosol forcing as simulated by climate models. *Geophysical Research Letters*, doi:10.1002/2013gl058715.
Cherubini, F. et al., 2016: Bridging the gap between impact assessment methods and climate science. *Environmental Science & Policy*, **64(C)**, 129–140, doi:10.1016/j.envsci.2016.06.
Christensen, M.W. and G.L. Stephens, 2011: Microphysical and macrophysical responses of marine stratocumulus polluted by underlying ships: Evidence of cloud deepening. *Journal of Geophysical Research*, **116(D3)**, D03201, doi:10.1029/2010jd014638.
Christensen, M.W., Y.C. Chen, and G.L. Stephens, 2016a: Aerosol indirect effect dictated by liquid clouds. *Journal of Geophysical Research*, **121(24)**, doi:10.1002/2016jd025245.
Christensen, M.W. et al., 2016b: Arctic Observation and Reanalysis Integrated System: A New Data Product for Validation and Climate Study. *BULLETIN OF THE AMERICAN METEOROLOGICAL SOCIETY*, **97(6)**, 907–915, doi:10.1175/bams-d-14-00273.1.
Christensen, M.W. et al., 2017: Unveiling aerosol–cloud interactions – Part 1: Cloud contamination in satellite products enhances the aerosol indirect forcing estimate. *Atmospheric Chemistry and Physics*, **17(21)**, 13151–13164, doi:10.5194/acp-17-13151-2017.
Chung, E.S., B.J. Soden, and B.J. Sohn, 2010: Revisiting the determination of climate sensitivity from relationships between surface temperature and radiative fluxes. *Geophysical Research Letters*, doi:10.1029/2010gl043051.
Chung, E.S. et al., 2019: Reconciling opposing Walker circulation trends in observations and model projections. *Nature Climate Change*, **9(5)**, 405–412, doi:10.1038/s41558-019-0446-4.
Chung, E.-S. and B.J. Soden, 2015: An assessment of methods for computing radiative forcing in climate models. *Environmental Research Letters*, **10(7)**, 074004, doi:10.1088/1748-9326/10/7/074004.
Chung, E.-S. and B.J. Soden, 2018: On the compensation between cloud feedback and cloud adjustment in climate models. *Climate Dynamics*, **50(3)**, 1267–1276, doi:10.1007/s00382-017-3682-1.
Chung, E.-S., B. Soden, B.J. Sohn, and L. Shi, 2014: Upper-tropospheric moistening in response to anthropogenic warming. *Proceedings of the National Academy of Sciences*, **111(32)**, 11636–11641, doi:10.1073/pnas.1409659111.
Church, J.A. et al., 2013: Sea Level Change. In: *Climate Change 2013: The Physical Science Basis. Contribution of Working Group I to the Fifth Assessment Report of the Intergovernmental Panel on Climate Change* [Stocker, T.F., D. Qin, G.-K. Plattner, M. Tignor, S.K. Allen, J. Boschung, A. Nauels, Y. Xia, V. Bex, and P.M. Midgley (eds.)]. Cambridge University Press, Cambridge, United Kingdom and New York, NY, USA, pp. 1137–1216, doi:10.1017/cbo9781107415315.026.
Clark, P.U. et al., 2016: Consequences of twenty-first-century policy for multi-millennial climate and sea-level change. *Nature Climate Change*, **6(4)**, 360–369, doi:10.1038/nclimate2923.
Clarke, L. et al., 2014: Assessing Transformation Pathways. In: *Climate Change 2014: Mitigation of Climate Change. Contribution of Working Group III to the Fifth Assessment Report of the Intergovernmental Panel on Climate Change* [Edenhofer, O., R. Pichs-Madruga, Y. Sokona, E. Farahani, S. Kadner, K. Seyboth, A. Adler, I. Baum, S. Brunner, P. Eickemeier, B. Kriemann, J. Savolainen, S. Schlömer, C. von Stechow, T. Zwickel, and J.C. Minx (eds.)]. Cambridge University Press, Cambridge, United Kingdom and New York, USA, pp. 413–510, doi:10.1017/cbo9781107415416.012.
Cleator, S.F., S.P. Harrison, N.K. Nichols, I.C. Prentice, and I. Roulstone, 2020: A new multivariable benchmark for Last Glacial Maximum climate simulations. *Climate of the Past*, **16(2)**, 699–712, doi:10.5194/cp-16-699-2020.
Clement, A.C., R. Seager, M.A. Cane, and S.E. Zebiak, 1996: An ocean dynamical thermostat. *Journal of Climate*, doi:10.1175/1520-0442(1996)009<2190:aodt>2.0.co;2.
Coats, S. and K.B. Karnauskas, 2017: Are Simulated and Observed Twentieth Century Tropical Pacific Sea Surface Temperature Trends Significant Relative to Internal Variability? *Geophysical Research Letters*, **44(19)**, 9928–9937, doi:10.1002/2017gl074622.
Coddington, O., J.L. Lean, P. Pilewskie, M. Snow, and D. Lindholm, 2016: A solar irradiance climate data record. *Bulletin of the American Meteorological Society*, **97(7)**, 1265–1282, doi:10.1175/bams-d-14-00265.1.
Cohan, D.S., J. Xu, R. Greenwald, M.H. Bergin, and W.L. Chameides, 2002: Impact of atmospheric aerosol light scattering and absorption on terrestrial net primary productivity. *Global Biogeochemical Cycles*, **16(4)**, 37–1–37–12, doi:10.1029/2001gb001441.
Collins, M. et al., 2013: Long-term Climate Change: Projections, Commitments and Irreversibility. In: *Climate Change 2013: The Physical Science Basis. Contribution of Working Group I to the Fifth Assessment Report of the Intergovernmental Panel on Climate Change* [Stocker, T.F., D. Qin, G.-K. Plattner, M. Tignor, S.K. Allen, J.

Boschung, A. Nauels, Y. Xia, V. Bex, and P.M. Midgley (eds.)]. Cambridge University Press, Cambridge, United Kingdom and New York, NY, USA, pp. 1029–1136, doi:10.1017/cbo9781107415324.024.
Collins, W.D., D.R. Feldman, C. Kuo, and N.H. Nguyen, 2018: Large regional shortwave forcing by anthropogenic methane informed by Jovian observations. *Science Advances*, **4(9)**, doi:10.1126/sciadv.aas9593.
Collins, W.J., R.G. Derwent, C.E. Johnson, and D.S. Stevenson, 2002: The oxidation of organic compounds in the troposphere and their global warming potentials. *Climatic Change*, **52**, 453–479, doi:10.1023/a:1014221225434.
Collins, W.J., D.J. Frame, J.S. Fuglestvedt, and K.P. Shine, 2020: Stable climate metrics for emissions of short and long-lived species-combining steps and pulses. *Environmental Research Letters*, **15(2)**, doi:10.1088/1748-9326/ab6039.
Collins, W.J. et al., 2011: Development and evaluation of an Earth-System model – HadGEM2. *Geoscientific Model Development*, **4**, 1051–1075, doi:10.5194/gmd-4-1051-2011.
Collins, W.J. et al., 2013: Global and regional temperature-change potentials for near-term climate forcers. *Atmospheric Chemistry and Physics*, **13**, 2471–2485, doi:10.5194/acp-13-2471-2013.
Collins, W.J. et al., 2017: AerChemMIP: Quantifying the effects of chemistry and aerosols in CMIP6. *Geoscientific Model Development*, **10(2)**, 585–607, doi:10.5194/gmd-10-585-2017.
Colman, R. and B. McAvaney, 2009: Climate feedbacks under a very broad range of forcing. *Geophysical Research Letters*, **36(1)**, 1–5, doi:10.1029/2008gl036268.
Colman, R. and L. Hanson, 2017: On the relative strength of radiative feedbacks under climate variability and change. *Climate Dynamics*, **49(5–6)**, 2115–2129, doi:10.1007/s00382-016-3441-8.
Colman, R.A., 2015: Climate radiative feedbacks and adjustments at the Earth's surface. *Journal of Geophysical Research*, **120(8)**, 3173–3182, doi:10.1002/2014jd022896.
Covey, C. et al., 2000: The seasonal cycle in coupled ocean-atmosphere general circulation models. *Climate Dynamics*, **16(10)**, 775–787, doi:10.1007/s003820000081.
Cox, P.M., C. Huntingford, and M.S. Williamson, 2018a: Emergent constraint on equilibrium climate sensitivity from global temperature variability. *Nature*, **553(7688)**, 319–322, doi:10.1038/nature25450.
Cox, P.M., M.S. Williamson, F.J.M.M. Nijsse, and C. Huntingford, 2018b: Cox et al. reply. *Nature*, **563(7729)**, E10–E15, doi:10.1038/s41586-018-0641-x.
Crook, J.A. and P.M. Forster, 2014: Comparison of surface albedo feedback in climate models and observations. *Geophysical Research Letters*, **41**, 1717–1723, doi:10.1002/2014gl059280.
Crook, J.A., P.M. Forster, and N. Stuber, 2011: Spatial patterns of modeled climate feedback and contributions to temperature response and polar amplification. *Journal of Climate*, **24(14)**, 3575–3592, doi:10.1175/2011jcli3863.1.
Cuesta-Valero, F.J., A. García-García, H. Beltrami, J.F. González-Rouco, and E. García-Bustamante, 2021: Long-term Global Ground Heat Flux and Continental Heat Storage from Geothermal Data. *Clim. Past*, **17(1)**, 451–468, doi:10.5194/cp-17-451-2021.
Cui, Y.F. et al., 2017: Effects of straw and biochar addition on soil nitrogen, carbon, and super rice yield in cold waterlogged paddy soils of North China. *Journal of Integrative Agriculture*, **16(5)**, 1064–1074, doi:10.1016/s2095-3119(16)61578-2.
Dai, A., D. Luo, M. Song, and J. Liu, 2019: Arctic amplification is caused by sea-ice loss under increasing CO2. *Nature Communications*, **10(1)**, 121, doi:10.1038/s41467-018-07954-9.
Daniel, J.S. et al., 2012: Limitations of single-basket trading: Lessons from the Montreal Protocol for climate policy. *Climatic Change*, **111(2)**, 241–248, doi:10.1007/s10584-011-0136-3.
Davies, R., V.M. Jovanovic, and C.M. Moroney, 2017: Cloud heights measured by MISR from 2000 to 2015. *Journal of Geophysical Research: Atmospheres*, **122(7)**, 3975–3986, doi:10.1002/2017jd026456.
Davies-Barnard, T., P.J. Valdes, J.S. Singarayer, A.J. Wiltshire, and C.D. Jones, 2015: Quantifying the relative importance of land cover change from climate and land use in the representative concentration pathways. *Global Biogeochemical Cycles*, **29(6)**, 842–853, doi:10.1002/2014gb004949.
de la Vega, E., T.B. Chalk, P.A. Wilson, R.P. Bysani, and G.L. Foster, 2020: Atmospheric CO2 during the Mid-Piacenzian Warm Period and the M2 glaciation. *Scientific Reports*, **10(1)**, 11002, doi:10.1038/s41598-020-67154-8.
Dekens, P.S., A.C. Ravelo, M.D. McCarthy, and C.A. Edwards, 2008: A 5 million year comparison of Mg/Ca and alkenone paleothermometers. *Geochemistry, Geophysics, Geosystems*, **9(10)**, doi:10.1029/2007gc001931.
Denison, S., P.M. Forster, and C.J. Smith, 2019: Guidance on emissions metrics for nationally determined contributions under the Paris Agreement. *Environmental Research Letters*, **14(12)**, 124002, doi:10.1088/1748-9326/ab4df4.
Deser, C., R. Knutti, S. Solomon, and A.S. Phillips, 2012: Communication of the role of natural variability in future North American climate. *Nature Clim Change*, **2**, 775–779, doi:10.1038/nclimate1562.
Dessler, A.E., 2011: Cloud variations and the Earth's energy budget. *Geophysical Research Letters*, **38(19)**, doi:10.1029/2011gl049236.
Dessler, A.E. and P.M. Forster, 2018: An estimate of equilibrium climate sensitivity from interannual variability. *Journal of Geophysical Research: Atmospheres*, **123(16)**, 8634–8645, doi:10.1029/2018jd028481.

Dessler, A.E., T. Mauritsen, and B. Stevens, 2018: The influence of internal variability on Earth's energy balance framework and implications for estimating climate sensitivity. *Atmospheric Chemistry and Physics*, **18(7)**, 5147–5155, doi:10.5194/acp-18-5147-2018.

Dessler, A.E., M.R. Schoeberl, T. Wang, S.M. Davis, and K.H. Rosenlof, 2013: Stratospheric water vapor feedback. *Proceedings of the National Academy of Sciences*, **110(45)**, 18087–18091, doi:10.1073/pnas.1310344110.

Dessler, A.E.E., 2013: Observations of climate feedbacks over 2000-10 and comparisons to climate models. *Journal of Climate*, **26(1)**, 333–342, doi:10.1175/jcli-d-11-00640.1.

Devaraju, N., G. Bala, and R. Nemani, 2015: Modelling the influence of land-use changes on biophysical and biochemical interactions at regional and global scales. *Plant, Cell and Environment*, **38(9)**, 1931–1946, doi:10.1111/pce.12488.

Diamond, M., H.M. Director, R. Eastman, A. Possner, and R. Wood, 2020: Substantial Cloud Brightening From Shipping in Subtropical Low Clouds. *AGU Advances*, **1(1)**, e2019AV000111, doi:10.1029/2019av000111.

Dickinson, R.E., 1975: Solar Variability and the Lower Atmosphere. *Bulletin of the American Meteorological Society*, **56(12)**, 1240–1248, doi:10.1175/1520-0477(1975)056<1240:svatla>2.0.co;2.

DiNezio, P.N. et al., 2009: Climate Response of the Equatorial Pacific to Global Warming. *Journal of Climate*, **22(18)**, 4873–4892, doi:10.1175/2009jcli2982.1.

Dinh, T. and S. Fueglistaler, 2019: On the Causal Relationship between the Moist Diabatic Circulation and Cloud Rapid Adjustment to Increasing CO_2. *Journal of Advances in Modeling Earth Systems*, **11(11)**, 3836–3851, doi:10.1029/2019ms001853.

Doherty, S.J. et al., 2013: Observed vertical redistribution of black carbon and other insoluble light-absorbing particles in melting snow. *J. Geophys. Res. Atmos*, **118(11)**, 5553–5569, doi:10.1002/jgrd.50235.

Dolinar, E.K., X. Dong, B. Xi, J.H. Jiang, and H. Su, 2015: Evaluation of CMIP5 simulated clouds and TOA radiation budgets using NASA satellite observations. *CLIMATE DYNAMICS*, **44(7–8)**, 2229–2247, doi:10.1007/s00382-014-2158-9.

Dong, L. and M.J. McPhaden, 2017: The effects of external forcing and internal variability on the formation of interhemispheric sea surface temperature gradient trends in the Indian Ocean. *Journal of Climate*, **30(22)**, 9077–9095, doi:10.1175/jcli-d-17-0138.1.

Dong, Y., K.C. Armour, C. Proistosescu, and D.S. Battisti, 2019: Attributing Historical and Future Evolution of Radiative Feedbacks to Regional Warming. *Journal of Climate*, **32(17)**, 9, doi:10.1175/jcli-d-18-0843.1.

Dong, Y. et al., 2020: Inter-model spread in the sea-surface temperature pattern effect and its contribution to climate sensitivity in CMIP5 and CMIP6 models. *Journal of Climate*, **33**, 7755–7775, doi:10.1175/jcli-d-19-1011.1.

Donohoe, A. and D.S. Battisti, 2011: Atmospheric and Surface Contributions to Planetary Albedo. *Journal of Climate*, **24(16)**, 4402–4418, doi:10.1175/2011jcli3946.1.

Donohoe, A. and D.S. Battisti, 2012: What determines meridional heat transport in climate models? *Journal of Climate*, **25(11)**, 3832–3850, doi:10.1175/jcli-d-11-00257.1.

Donohoe, A., K.C. Armour, A.G. Pendergrass, and D.S. Battisti, 2014: Shortwave and longwave radiative contributions to global warming under increasing CO_2. *Proceedings of the National Academy of Sciences*, **111(47)**, 16700–16705, doi:10.1073/pnas.1412190111.

Donohoe, A., K.C. Armour, G.H. Roe, D.S. Battisti, and L. Hahn, 2020: The partitioning of meridional heat transport from the Last Glacial Maximum to CO_2 quadrupling in coupled climate models. *Journal of Climate*, **33**, 4141–4165, doi:10.1175/jcli-d-19-0797.1.

Dorheim, K., R. Link, C. Hartin, B. Kravitz, and A. Snyder, 2020: Calibrating Simple Climate Models to Individual Earth System Models: Lessons Learned From Calibrating Hector. *Earth and Space Science*, **7(11)**, e2019EA000980, doi:10.1029/2019ea000980.

Doutriaux-Boucher, M., M.J. Webb, J.M. Gregory, and O. Boucher, 2009: Carbon dioxide induced stomatal closure increases radiative forcing via a rapid reduction in low cloud. *Geophysical Research Letters*, **36(2)**, 1–5, doi:10.1029/2008gl036273.

Dowsett, H.J. et al., 2012: Assessing confidence in Pliocene sea surface temperatures to evaluate predictive models. *Nature Climate Change*, **2(5)**, 365–371, doi:10.1038/nclimate1455.

Du, J., K. Wang, J. Wang, and Q. Ma, 2017: Contributions of surface solar radiation and precipitation to the spatiotemporal patterns of surface and air warming in China from 1960 to 2003. *ATMOSPHERIC CHEMISTRY AND PHYSICS*, **17(8)**, 4931–4944, doi:10.5194/acp-17-4931-2017.

Duan, L., L. Cao, and K. Caldeira, 2019: Estimating Contributions of Sea Ice and Land Snow to Climate Feedback. *Journal of Geophysical Research: Atmospheres*, **124(1)**, 199–208, doi:10.1029/2018jd029093.

Duan, L., L. Cao, G. Bala, and K. Caldeira, 2018: Comparison of the Fast and Slow Climate Response to Three Radiation Management Geoengineering Schemes. *Journal of Geophysical Research: Atmospheres*, **123(21)**, 11,980–12,001, doi:10.1029/2018jd029034.

Dufresne, J.L. and S. Bony, 2008: An assessment of the primary sources of spread of global warming estimates from coupled atmosphere-ocean models. *Journal of Climate*, **21(19)**, 5135–5144, doi:10.1175/2008jcli2239.1.

Dufresne, J.-L. and M. Saint-Lu, 2016: Positive feedback in climate: stabilization or runaway, illustrated by a simple experiment. *Bull. Am. Meteorol. Soc.*, **97(5)**, 755–765, doi:10.1175/bams-d-14-00022.1.

Dunne, E.M. et al., 2016: Global atmospheric particle formation from CERN CLOUD measurements. *Science*, **354(6316)**, 1119–1124, doi:10.1126/science.aaf2649.

Durack, P.J., P.J. Gleckler, F.W. Landerer, and K.E. Taylor, 2014: Quantifying underestimates of long-term upper-ocean warming. *Nature Climate Change*, **4**, 999–1005, doi:10.1038/nclimate2389.

Eastman, R. and S.G. Warren, 2013: A 39-yr survey of cloud changes from land stations worldwide 1971-2009: Long-term trends, relation to aerosols, and expansion of the tropical belt. *Journal of Climate*, **26(4)**, 1286–1303, doi:10.1175/jcli-d-12-00280.1.

Ebmeier, S.K., A.M. Sayer, R.G. Grainger, T.A. Mather, and E. Carboni, 2014: Systematic satellite observations of the impact of aerosols from passive volcanic degassing on local cloud properties. *Atmospheric Chemistry and Physics*, **14(19)**, 10601–10618, doi:10.5194/acp-14-10601-2014.

Edwards, M.R. and J.E. Trancik, 2014: Climate impacts of energy technologies depend on emissions timing. *Nature Climate Change*, **4**, 347–352, doi:10.1038/nclimate2204.

Egorova, T. et al., 2018: Revised historical solar irradiance forcing. *Astronomy & Astrophysics*, **615**, A85, doi:10.1051/0004-6361/201731199.

Einstein, A., 1905: Über die von der molekularkinetischen Theorie der Wärme geforderte Bewegung von in ruhenden Flüssigkeiten suspendierten Teilchen. *Annalen der Physik*, **322(8)**, 549–560, doi:10.1002/andp.19053220806.

Elagib, N.A. and S.H. Alvi, 2013: Moderate solar dimming in an accelerating warming climate of Bahrain. *International Journal of Global Warming*, **5(1)**, 96–107, doi:10.1504/ijgw.2013.051487.

Emanuel, K., A.A. Wing, and E.M. Vincent, 2014: Radiative-convective instability. *Journal of Advances in Modeling Earth Systems*, **6(1)**, 75–90, doi:10.1002/2013ms000270.

England, M.H. et al., 2014: Recent intensification of wind-driven circulation in the Pacific and the ongoing warming hiatus. *Nature Climate Change*, **4(3)**, 222–227, doi:10.1038/nclimate2106.

Erfani, E. and N.J. Burls, 2019: The Strength of Low-Cloud Feedbacks and Tropical Climate: A CESM Sensitivity Study. *Journal of Climate*, JCLI–D–18–0551.1, doi:10.1175/jcli-d-18-0551.1.

Etminan, M., G. Myhre, E.J. Highwood, and K.P. Shine, 2016: Radiative forcing of carbon dioxide, methane, and nitrous oxide: A significant revision of the methane radiative forcing. *Geophysical Research Letters*, **43(24)**, 12,614–12,623, doi:10.1002/2016gl071930.

Exarchou, E., T. Kuhlbrodt, J.M. Gregory, and R.S. Smith, 2014: Ocean Heat Uptake Processes: A Model Intercomparison. *Journal of Climate*, **28(2)**, 887–908, doi:10.1175/jcli-d-14-00235.1.

Farnsworth, A. et al., 2019: Climate Sensitivity on Geological Timescales Controlled by Nonlinear Feedbacks and Ocean Circulation. *Geophysical Research Letters*, **46(16)**, 9880–9889, doi:10.1029/2019gl083574.

Fedorov, A., N.J. Burls, K.T. Lawrence, and L.C. Peterson, 2015: Tightly linked zonal and meridional sea surface temperature gradients over the past five million years. *Nature Geoscience*, **8**, 975–980, doi:10.1038/ngeo2577.

Fedorov, A. et al., 2013: Patterns and mechanisms of early Pliocene warmth. *Nature*, **496(7443)**, 43–49, doi:10.1038/nature12003.

Feldl, N. and G.H. Roe, 2013: The nonlinear and nonlocal nature of climate feedbacks. *Journal of Climate*, doi:10.1175/jcli-d-12-00631.1.

Feldl, N., B.T. Anderson, and S. Bordoni, 2017a: Atmospheric eddies mediate lapse rate feedback and arctic amplification. *Journal of Climate*, **30(22)**, 9213–9224, doi:10.1175/jcli-d-16-0706.1.

Feldl, N., S. Bordoni, and T.M. Merlis, 2017b: Coupled high-latitude climate feedbacks and their impact on atmospheric heat transport. *Journal of Climate*, **30(1)**, 189–201, doi:10.1175/jcli-d-16-0324.1.

Feldl, N., S. Po-Chedley, H.K.A. Singh, S. Hay, and P.J. Kushner, 2020: Sea ice and atmospheric circulation shape the high-latitude lapse rate feedback. *npj Climate and Atmospheric Science*, **3(1)**, doi:10.1038/s41612-020-00146-7.

Feng, F. and K. Wang, 2019: Does the modern-era retrospective analysis for research and applications-2 aerosol reanalysis introduce an improvement in the simulation of surface solar radiation over China? *INTERNATIONAL JOURNAL OF CLIMATOLOGY*, **39(3)**, 1305–1318, doi:10.1002/joc.5881.

Feng, R., B.L. Otto-Bliesner, E.C. Brady, and N. Rosenbloom, 2020: Increased Climate Response and Earth System Sensitivity From CCSM4 to CESM2 in Mid-Pliocene Simulations. *Journal of Advances in Modeling Earth Systems*, **12(8)**, doi:10.1029/2019ms002033.

Feng, R. et al., 2019: Contributions of aerosol-cloud interactions to mid-Piacenzian seasonally sea ice-free Arctic Ocean. *Geophysical Research Letters*, **46(16)**, 9920–9929, doi:10.1029/2019gl083960.

Fiedler, S., B. Stevens, and T. Mauritsen, 2017: On the sensitivity of anthropogenic aerosol forcing to model-internal variability and parameterizing a Twomey effect. *Journal of Advances in Modeling Earth Systems*, **9(2)**, 1325–1341, doi:10.1002/2017ms000932.

Fiedler, S. et al., 2019: Anthropogenic aerosol forcing-insights from multiple estimates from aerosol-climate models with reduced complexity. *Atmospheric Chemistry and Physics*, **19(10)**, 6821–6841, doi:10.5194/acp-19-6821-2019.

Fisher, J.B. et al., 2017: The future of evapotranspiration: Global requirements for ecosystem functioning, carbon and climate feedbacks, agricultural management, and water resources. *Water Resources Research*, **53(4)**, 2618–2626, doi:10.1002/2016wr020175.

Flanner, M.G. and C.S. Zender, 2006: Linking snowpack microphysics and albedo evolution. *J. Geophys. Res.*, **111**, doi:10.1029/2005jd006834.

Flanner, M.G., K.M. Shell, M. Barlage, D.K. Perovich, and M.A. Tschudi, 2011: Radiative forcing and albedo feedback from the Northern Hemisphere cryosphere between 1979 and 2008. *Nature Geosci.*, **4**, 151–155, doi:10.1038/ngeo1062.

Flannery, B.P., 1984: Energy Balance Models Incorporating Transport of Thermal and Latent Energy. *Journal of the Atmospheric Sciences*, **41(3)**, doi:10.1175/1520-0469(1984)041<0414:ebmito>2.0.co;2.

Flato, G. et al., 2013: Evaluation of Climate Models. In: *Climate Change 2013: The Physical Science Basis. Contribution of Working Group I to the Fifth Assessment Report of the Intergovernmental Panel on Climate Change* [Stocker, T.F., D. Qin, G.-K. Plattner, M. Tignor, S.K. Allen, J. Boschung, A. Nauels, Y. Xia, V. Bex, and P.M. Midgley (eds.)]. Cambridge University Press, Cambridge, United Kingdom and New York, NY, USA, pp. 741–866, doi:10.1017/cbo9781107415324.020.

Flynn, C.M. and T. Mauritsen, 2020: On the climate sensitivity and historical warming evolution in recent coupled model ensembles. *Atmospheric Chemistry and Physics*, **20(13)**, 7829–7842, doi:10.5194/acp-20-7829-2020.

Folini, D. and M. Wild, 2015: The effect of aerosols and sea surface temperature on China's climate in the late twentieth century from ensembles of global climate simulations. *J. Geophys. Res.*, **120** , 2261–2279, doi:10.1002/2014jd022851.

Ford, H.L., A.C. Ravelo, P.S. Dekens, J.P. LaRiviere, and M.W. Wara, 2015: The evolution of the equatorial thermocline and the early Pliocene El Padre mean state. *Geophysical Research Letters*, **42(12)**, 4878–4887, doi:10.1002/2015gl064215.

Forest, C.E., 2002: Quantifying Uncertainties in Climate System Properties with the Use of Recent Climate Observations. *Science*, **295(5552)**, 113–117, doi:10.1126/science.1064419.

Forest, C.E., 2018: Inferred Net Aerosol Forcing Based on Historical Climate Changes: a Review. *Current Climate Change Reports*, **4(1)**, 11–22, doi:10.1007/s40641-018-0085-2.

Forster, P. et al., 2007: Changes in Atmospheric Constituents and in Radiative Forcing. In: *Climate Change 2007: The Physical Science Basis. Contribution of Working Group I to the Fourth Assessment Report of the Intergovernmental Panel on Climate Change* [Solomon, S., D. Qin, M. Manning, Z. Chen, M. Marquis, K.B. Averyt, M. Tignor, and H.L. Miller (eds.)]. Cambridge University Press, Cambridge, United Kingdom and New York, NY, USA, pp. 129–234.

Forster, P. et al., 2018: Mitigation Pathways Compatible with 1.5°C in the Context of Sustainable Development Supplementary Material. In: *Global Warming of 1.5°C. An IPCC Special Report on the impacts of global warming of 1.5°C above pre-industrial levels and related global greenhouse gas emission pathways, in the context of strengthening the global response to the threat of climate change,* [Masson-Delmotte, V., P. Zhai, H.-O. Pörtner, D. Roberts, J. Skea, P.R. Shukla, A. Pirani, W. Moufouma-Okia, C. Péan, R. Pidcock, S. Connors, J.B.R. Matthews, Y. Chen, X. Zhou, M.I. Gomis, E. Lonnoy, T. Maycock, M. Tignor, and T. Waterfield (eds.)]. In Press, pp. 2SM: 1–50.

Forster, P.M., 2016: Inference of Climate Sensitivity from Analysis of Earth's Energy Budget. *Annual Review of Earth and Planetary Sciences*, **44(1)**, 85–106, doi:10.1146/annurev-earth-060614-105156.

Forster, P.M., A.C. Maycock, C.M. McKenna, and C.J. Smith, 2019: Latest climate models confirm need for urgent mitigation. *Nature Climate Change*, doi:10.1038/s41558-019-0660-0.

Forster, P.M. et al., 2013: Evaluating adjusted forcing and model spread for historical and future scenarios in the CMIP5 generation of climate models. *Journal of Geophysical Research Atmospheres*, **118(3)**, 1139–1150, doi:10.1002/jgrd.50174.

Forster, P.M. et al., 2016: Recommendations for diagnosing effective radiative forcing from climate models for CMIP6. *Journal of Geophysical Research*, doi:10.1002/2016jd025320.

Forster, P.M.D.F. and M. Joshi, 2005: The role of halocarbons in the climate change of the troposphere and stratosphere. *Climatic Change*, doi:10.1007/s10584-005-5955-7.

Foster, G., J.D. Annan, G.A. Schmidt, and M.E. Mann, 2008: Comment on "Heat capacity, time constant, and sensitivity of Earth's climate system" by S. E. Schwartz. *Journal of Geophysical Research Atmospheres*, **113(15)**, doi:10.1029/2007jd009373.

Foster, G.L. and J.W.B. Rae, 2016: Reconstructing Ocean pH with Boron Isotopes in Foraminifera. *Annual Review of Earth and Planetary Sciences*, **44(1)**, 207–237, doi:10.1146/annurev-earth-060115-012226.

Frame, D.J., D.A. Stone, P.A. Stott, and M.R. Allen, 2006: Alternatives to stabilization scenarios. *Geophysical Research Letters*, doi:10.1029/2006gl025801.

Frame, D.J. et al., 2005: Constraining climate forecasts: The role of prior assumptions. *Geophysical Research Letters*, **32(9)**, doi:10.1029/2004gl022241.

Frey, W.R. and J.E. Kay, 2018: The influence of extratropical cloud phase and amount feedbacks on climate sensitivity. *Climate Dynamics*, **50(7)**, 3097–3116, doi:10.1007/s00382-017-3796-5.

Friberg, J. et al., 2015: Influence of volcanic eruptions on midlatitude upper tropospheric aerosol and consequences for cirrus clouds. *Earth and Space Science*, **2**, 285–300, doi:10.1002/2015ea000110.

Friedrich, T. and A. Timmermann, 2020: Using Late Pleistocene sea surface temperature reconstructions to constrain

future greenhouse warming. *Earth and Planetary Science Letters*, **530**, 115911, doi:10.1016/j.epsl.2019.115911.
Friedrich, T., A. Timmermann, M. Tigchelaar, O.E. Timm, and A. Ganopolski, 2016: Nonlinear climate sensitivity and its implications for future greenhouse warming. *Science Advances*, **2(11)**, doi:10.1126/sciadv.1501923.
Frouin, R. and S.F. Iacobellis, 2002: Influence of phytoplankton on the global radiation budget. *Journal of Geophysical Research*, **107(D19)**, 4377, doi:10.1029/2001jd000562.
Fu, B. et al., 2020: Short-lived climate forcers have long-term climate impacts via the carbon–climate feedback. *Nature Climate Change*, **10(9)**, 851–855, doi:10.1038/s41558-020-0841-x.
Fueglistaler, S., 2019: Observational Evidence for Two Modes of Coupling Between Sea Surface Temperatures, Tropospheric Temperature Profile, and Shortwave Cloud Radiative Effect in the Tropics. *Geophysical Research Letters*, **46(16)**, 9890–9898, doi:10.1029/2019gl083990.
Fueglistaler, S. and L.G. Silvers, 2021: The Peculiar Trajectory of Global Warming. *Journal of Geophysical Research: Atmospheres*, **126(4)**, e2020JD033629, doi:10.1029/2020jd033629.
Fuglestvedt, J. et al., 2018: Implications of possible interpretations of 'greenhouse gas balance' in the Paris Agreement. *Philosophical Transactions of the Royal Society A: Mathematical, Physical and Engineering Sciences*, **376(2119)**, doi:10.1098/rsta.2016.0445.
Fuglestvedt, J.S. et al., 2003: Metrics of climate change: Assessing radiative forcing and emission indices. *Climatic Change*, **58(3)**, 267–331, doi:10.1023/a:1023905326842.
Fyke, J., O. Sergienko, M. Löfverström, S. Price, and J.T.M. Lenaerts, 2018: An Overview of Interactions and Feedbacks Between Ice Sheets and the Earth System. *Reviews of Geophysics*, **56(2)**, 361–408, doi:10.1029/2018rg000600.
Gan, C.M. et al., 2014: Assessment of the effect of air pollution controls on trends in shortwave radiation over the United States from 1995 through 2010 from multiple observation networks. *Atmospheric Chemistry and Physics*, **14(3)**, 1701–1715, doi:10.5194/acp-14-1701-2014.
Garcia, R.D. et al., 2014: Reconstruction of global solar radiation time series from 1933 to 2013 at the Izana Atmospheric Observatory. *Atmospheric Measurement Techniques*, **7(9)**, 3139–3150, doi:10.5194/amt-7-3139-2014.
Garuba, O.A., J. Lu, F. Liu, and H.A. Singh, 2018: The Active Role of the Ocean in the Temporal Evolution of Climate Sensitivity. *Geophysical Research Letters*, doi:10.1002/2017gl075633.
Gasser, T. et al., 2017a: The compact Earth system model OSCAR v2.2: Description and first results. *Geoscientific Model Development*, **10(1)**, 271–319, doi:10.5194/gmd-10-271-2017.
Gasser, T. et al., 2017b: Accounting for the climate–carbon feedback in emission metric. *Earth System Dynamics*, **8(2)**, 235–253, doi:10.5194/esd-8-235-2017.
Gasser, T. et al., 2020: Historical CO2 emissions from land use and land cover change and their uncertainty. *Biogeosciences*, **17(15)**, 4075–4101, doi:10.5194/bg-17-4075-2020.
Gassó, S., 2008: Satellite observations of the impact of weak volcanic activity on marine clouds. *Journal of Geophysical Research*, **113(D14)**, D14S19, doi:10.1029/2007jd009106.
Gebbie, G. and P. Huybers, 2019: The Little Ice Age and 20th Century Deep Pacific Cooling. *Science*, **363(6422)**, 70–74, doi:10.1126/science.aar8413.
Geoffroy, O., D. Saint-Martin, and A. Ribes, 2012: Quantifying the sources of spread in climate change experiments. *Geophysical Research Letters*, **39(24)**, doi:10.1029/2012gl054172.
Geoffroy, O. et al., 2013a: Transient Climate Response in a Two-Layer Energy-Balance Model. Part II: Representation of the Efficacy of Deep-Ocean Heat Uptake and Validation for CMIP5 AOGCMs. *Journal of Climate*, **26(6)**, 1859–1876, doi:10.1175/jcli-d-12-00196.1.
Geoffroy, O. et al., 2013b: Transient climate response in a two-layer energy-balance model. Part I: Analytical solution and parameter calibration using CMIP5 AOGCM experiments. *Journal of Climate*, **26(6)**, 1841–1857, doi:10.1175/jcli-d-12-00195.1.
Gettelman, A. and S.C. Sherwood, 2016: Processes Responsible for Cloud Feedback. *Current Climate Change Reports*, **2(4)**, 179–189, doi:10.1007/s40641-016-0052-8.
Gettelman, A., J.E. Kay, and K.M. Shell, 2012: The evolution of climate sensitivity and climate feedbacks in the Community Atmosphere Model.. *Journal of Climate*, **25(5)**, 1453–1469, doi:10.1175/jcli-d-11-00197.1.
Gettelman, A., A. Schmidt, and J.E. Kristjánsson, 2015: Icelandic volcanic emissions and climate. *Nature Geoscience*, **8(4)**, 243, doi:10.1038/ngeo2376.
Gettelman, A. et al., 2019: High Climate Sensitivity in the Community Earth System Model Version 2 (CESM2). *Geophysical Research Letters*, **46(14)**, 8329–8337, doi:10.1029/2019gl083978.
Ghan, S. et al., 2016: Challenges in constraining anthropogenic aerosol effects on cloud radiative forcing using present-day spatiotemporal variability.. *Proceedings of the National Academy of Sciences of the United States of America*, **113(21)**, 5804–11, doi:10.1073/pnas.1514036113.
Ghimire, B. et al., 2014: Global albedo change and radiative cooling from anthropogenic land cover change, 1700 to 2005 based on MODIS, land use harmonization, radiative kernels, and reanalysis. *Geophysical Research Letters*, doi:10.1002/2014gl061671.

Gilgen, A., W.T.K. Huang, L. Ickes, D. Neubauer, and U. Lohmann, 2018: How important are future marine and shipping aerosol emissions in a warming Arctic summer and autumn? *Atmospheric Chemistry and Physics*, **18(14)**, 10521–10555, doi:10.5194/acp-18-10521-2018.
Gillett, N.P. and H.D. Matthews, 2010: Accounting for carbon cycle feedbacks in a comparison of the global warming effects of greenhouse gases. *Environmental Research Letters*, **5(3)**, doi:10.1088/1748-9326/5/3/034011.
Gillett, N.P., V.K. Arora, D. Matthews, and M.R. Allen, 2013: Constraining the ratio of global warming to cumulative CO2 emissions using CMIP5 simulations. *Journal of Climate*, **26(18)**, 6844–6858, doi:10.1175/jcli-d-12-00476.1.
Gillett, N.P., V.K. Arora, G.M. Flato, J.F. Scinocca, and K. Von Salzen, 2012: Improved constraints on 21st-century warming derived using 160 years of temperature observations. *Geophysical Research Letters*, **39(1)**, 1–5, doi:10.1029/2011gl050226.
Giorgetta, M.A. et al., 2013: Climate and carbon cycle changes from 1850 to 2100 in MPI-ESM simulations for the Coupled Model Intercomparison Project phase 5. *Journal of Advances in Modeling Earth Systems*, **5(3)**, 572–597, doi:10.1002/jame.20038.
Goelzer, H. et al., 2011: Impact of Greenland and Antarctic ice sheet interactions on climate sensitivity. *Climate Dynamics*, **37(5)**, 1005–1018, doi:10.1007/s00382-010-0885-0.
Golaz, J.C., J.C. Golaz, and H. Levy, 2013: Cloud tuning in a coupled climate model: Impact on 20th century warming. *Geophysical Research Letters*, **40(10)**, 2246–2251, doi:10.1002/grl.50232.
Golaz, J.C. et al., 2019a: The DOE E3SM Coupled Model Version 1: Overview and Evaluation at Standard Resolution. *Journal of Advances in Modeling Earth Systems*, **11(7)**, 2089–2129, doi:10.1029/2018ms001603.
Golaz, J.C. et al., 2019b: The DOE E3SM Coupled Model Version 1: Overview and Evaluation at Standard Resolution. *Journal of Advances in Modeling Earth Systems*, **11(7)**, 2089–2129, doi:10.1029/2018ms001603.
Goldner, A., N. Herold, and M. Huber, 2014a: Antarctic glaciation caused ocean circulation changes at the Eocene-Oligocene transition. *Nature*, **511(7511)**, 574–577, doi:10.1038/nature13597.
Goldner, A., N. Herold, and M. Huber, 2014b: The challenge of simulating the warmth of the mid-Miocene climatic optimum in CESM1. *Climate of the Past*, **10(2)**, 523–536, doi:10.5194/cp-10-523-2014.
Golledge, N.R. et al., 2019: Global environmental consequences of twenty-first-century ice-sheet melt. *Nature*, **566(7742)**, 65–72, doi:10.1038/s41586-019-0889-9.
Gong, T., S. Feldstein, and S. Lee, 2017: The role of downward infrared radiation in the recent arctic winter warming trend. *Journal of Climate*, doi:10.1175/jcli-d-16-0180.1.
Good, P., J.M. Gregory, and J.A. Lowe, 2011: A step-response simple climate model to reconstruct and interpret AOGCM projections. *Geophysical Research Letters*, **38(1)**, doi:10.1029/2010gl045208.
Good, P., J.M. Gregory, J.A. Lowe, and T. Andrews, 2013: Abrupt CO2 experiments as tools for predicting and understanding CMIP5 representative concentration pathway projections. *Climate Dynamics*, **40(3)**, 1041–1053, doi:10.1007/s00382-012-1410-4.
Good, P. et al., 2015: Nonlinear regional warming with increasing CO2 concentrations. *Nature Climate Change*, **5(2)**, 138–142, doi:10.1038/nclimate2498.
Good, P. et al., 2016: NonlinMIP contribution to CMIP6: Model intercomparison project for non-linear mechanisms: Physical basis, experimental design and analysis principles (v1.0). *Geoscientific Model Development*, **9(11)**, 4019–4028, doi:10.5194/gmd-9-4019-2016.
Good, S.A., 2017: The impact of observational sampling on time series of global 0–700 m ocean average temperature: a case study. *International Journal of Climatology*, **37(5)**, 2260–2268, doi:10.1002/joc.4654.
Goodwin, P., 2016: How historic simulation–observation discrepancy affects future warming projections in a very large model ensemble. *Climate Dynamics*, **47(7–8)**, 2219–2233, doi:10.1007/s00382-015-2960-z.
Goodwin, P., 2018: On the Time Evolution of Climate Sensitivity and Future Warming. *Earth's Future*, **6(9)**, 1336–1348, doi:10.1029/2018ef000889.
Goosse, H. et al., 2018: Quantifying climate feedbacks in polar regions. *Nature Communications*, doi:10.1038/s41467-018-04173-0.
Gordon, H. et al., 2016: Reduced anthropogenic aerosol radiative forcing caused by biogenic new particle formation. *Proceedings of the National Academy of Sciences of the United States of America*, **113(43)**, 12053–12058, doi:10.1073/pnas.1602360113.
Gordon, H. et al., 2017: Causes and importance of new particle formation in the present-day and preindustrial atmospheres. *Journal of Geophysical Research: Atmospheres*, **122(16)**, 8739–8760, doi:10.1002/2017jd026844.
Gordon, N.D. and S.A. Klein, 2014: Low-cloud optical depth feedback in climate models. *Journal of Geophysical Research: Atmospheres*, **119(10)**, 6052–6065, doi:10.1002/2013jd021052.
Gordon, N.D., A.K. Jonko, P.M. Forster, and K.M. Shell, 2013: An observationally based constraint on the water-vapor feedback. *Journal of Geophysical Research Atmospheres*, **118(22)**, 12435–12443, doi:10.1002/2013jd020184.
Goren, T. and D. Rosenfeld, 2014: Decomposing aerosol cloud radiative effects into cloud cover, liquid water path and Twomey components in marine stratocumulus. *Atmospheric Research*, **138**, 378–393, doi:10.1016/j.atmosres.2013.12.008.

Grandey, B.S., P. Stier, and T.M. Wagner, 2013: Investigating relationships between aerosol optical depth and cloud fraction using satellite, aerosol reanalysis and general circulation model data. *Atmospheric Chemistry and Physics*, **13(6)**, 3177–3184, doi:10.5194/acp-13-3177-2013.

Grandey, B.S. et al., 2018: Effective radiative forcing in the aerosol-climate model CAM5.3-MARC-ARG. *Atmospheric Chemistry and Physics*, **18(21)**, 15783–15810, doi:10.5194/acp-18-15783-2018.

Graversen, R.G. and M. Wang, 2009: Polar amplification in a coupled climate model with locked albedo. *Climate Dynamics*, doi:10.1007/s00382-009-0535-6.

Graversen, R.G. and M. Burtu, 2016: Arctic amplification enhanced by latent energy transport of atmospheric planetary waves. *Quarterly Journal of the Royal Meteorological Society*, **142(698)**, 2046–2054, doi:10.1002/qj.2802.

Graversen, R.G., P.L. Langen, and T. Mauritsen, 2014: Polar Amplification in CCSM4: Contributions from the Lapse Rate and Surface Albedo Feedbacks. *Journal of Climate*, **27(12)**, 4433–4450, doi:10.1175/jcli-d-13-00551.1.

Gray, L.J., S.T. Rumbold, and K.P. Shine, 2009: Stratospheric Temperature and Radiative Forcing Response to 11-Year Solar Cycle Changes in Irradiance and Ozone. *Journal of the Atmospheric Sciences*, **66(8)**, 2402–2417, doi:10.1175/2009jas2866.1.

Gregory, J.M., 2000: Vertical heat transports in the ocean and their effect on time-dependent climate change. *Climate Dynamics*, doi:10.1007/s003820000059.

Gregory, J.M. and T. Andrews, 2016: Variation in climate sensitivity and feedback parameters during the historical period. *Geophysical Research Letters*, doi:10.1002/2016gl068406.

Gregory, J.M., T. Andrews, and P. Good, 2015: The inconstancy of the transient climate response parameter under increasing CO2. *Philosophical Transactions of the Royal Society A: Mathematical, Physical and Engineering Sciences*, **373(2054)**, doi:10.1098/rsta.2014.0417.

Gregory, J.M., C.D. Jones, P. Cadule, and P. Friedlingstein, 2009: Quantifying carbon cycle feedbacks. *Journal of Climate*, **22(19)**, 5232–5250, doi:10.1175/2009jcli2949.1.

Gregory, J.M., R.J. Stouffer, S.C.B. Raper, P.A. Stott, and N.A. Rayner, 2002: An observationally based estimate of the climate sensitivity. *Journal of Climate*, **15(22)**, 3117–3121, doi:10.1175/1520-0442(2002)015<3117:aobeot>2.0.co;2.

Gregory, J.M., T. Andrews, P. Good, T. Mauritsen, and P.M. Forster, 2016: Small global-mean cooling due to volcanic radiative forcing. *Climate Dynamics*, **47(12)**, 3979–3991, doi:10.1007/s00382-016-3055-1.

Gregory, J.M., T. Andrews, P. Ceppi, T. Mauritsen, and M.J. Webb, 2020: How accurately can the climate sensitivity to CO2 be estimated from historical climate change? *Climate Dynamics*, **54**, 129–157, doi:10.1007/s00382-019-04991-y.

Gregory, J.M. et al., 2004: A new method for diagnosing radiative forcing and climate sensitivity. *Geophysical Research Letters*, **31(3)**, L03205, doi:10.1029/2003gl018747.

Grise, K.M. and B. Medeiros, 2016: Understanding the Varied Influence of Midlatitude Jet Position on Clouds and Cloud Radiative Effects in Observations and Global Climate Models. *Journal of Climate*, **29(24)**, 9005–9025, doi:10.1175/jcli-d-16-0295.1.

Grise, K.M., S.W. Son, G.J.P. Correa, and L.M. Polvani, 2014: The response of extratropical cyclones in the Southern Hemisphere to stratospheric ozone depletion in the 20th century. *Atmospheric Science Letters*, doi:10.1002/asl2.458.

Grise, K.M., L.M. Polvani, G. Tselioudis, Y. Wu, and M.D. Zelinka, 2013: The ozone hole indirect effect: Cloud-radiative anomalies accompanying the poleward shift of the eddy-driven jet in the Southern Hemisphere. *Geophysical Research Letters*, doi:10.1002/grl.50675.

Grose, M.R., J. Gregory, R. Colman, and T. Andrews, 2018: What Climate Sensitivity Index Is Most Useful for Projections? *Geophysical Research Letters*, **45(3)**, 1559–1566, doi:10.1002/2017gl075742.

Grosvenor, D.P. et al., 2018: Remote Sensing of Droplet Number Concentration in Warm Clouds: A Review of the Current State of Knowledge and Perspectives. *Reviews of Geophysics*, **56(2)**, 409–453, doi:10.1029/2017rg000593.

Gryspeerdt, E., P. Stier, and B.S. Grandey, 2014a: Cloud fraction mediates the aerosol optical depth-cloud top height relationship. *Geophysical Research Letters*, **41(10)**, 3622–3627, doi:10.1002/2014gl059524.

Gryspeerdt, E., P. Stier, and D.G. Partridge, 2014b: Satellite observations of cloud regime development: the role of aerosol processes. *Atmospheric Chemistry and Physics*, **14(3)**, 1141–1158, doi:10.5194/acp-14-1141-2014.

Gryspeerdt, E., J. Quaas, and N. Bellouin, 2016: Constraining the aerosol influence on cloud fraction. *Journal of Geophysical Research: Atmospheres*, **121(7)**, 3566–3583, doi:10.1002/2015jd023744.

Gryspeerdt, E. et al., 2017: Constraining the instantaneous aerosol influence on cloud albedo.. *Proceedings of the National Academy of Sciences of the United States of America*, **114(19)**, 4899–4904, doi:10.1073/pnas.1617765114.

Gryspeerdt, E. et al., 2018: Ice crystal number concentration estimates from lidar–radar satellite remote sensing – Part 2: Controls on the ice crystal number concentration. *Atmospheric Chemistry and Physics*, **18(19)**, 14351–14370, doi:10.5194/acp-18-14351-2018.

Gryspeerdt, E. et al., 2019: Constraining the aerosol influence on cloud liquid water path. *Atmospheric Chemistry and Physics*, **19**, 5331–5347, doi:10.5194/acp-19-5331-2019.

Gryspeerdt, E. et al., 2020: Surprising similarities in model and observational aerosol radiative forcing estimates. *Atmospheric Chemistry and Physics*, **20(1)**, 613–623, doi:10.5194/acp-20-613-2020.

Gulev, S.K. and K. Belyaev, 2012: Probability Distribution Characteristics for Surface Air-Sea Turbulent Heat Fluxes over the Global Ocean. *JOURNAL OF CLIMATE*, **25(1)**, 184–206, doi:10.1175/2011jcli4211.1.

Hahn, L.C. et al., 2020: Antarctic Elevation Drives Hemispheric Asymmetry in Polar Lapse Rate Climatology and Feedback. *Geophysical Research Letters*, **47(16)**, doi:10.1029/2020gl088965.

Hakuba, M.Z., D. Folini, A. Sanchez-Lorenzo, and M. Wild, 2014: Spatial representativeness of ground-based solar radiation measurements-Extension to the full Meteosat disk. *JOURNAL OF GEOPHYSICAL RESEARCH-ATMOSPHERES*, **119(20)**, 11760–11771, doi:10.1002/2014jd021946.

Hall, A., 2004: The role of surface albedo feedback in climate. *Journal of Climate*, **17(7)**, 1550–1568, doi:10.1175/1520-0442(2004)017<1550:trosaf>2.0.co;2.

Hall, A. and X. Qu, 2006: Using the current seasonal cycle to constrain snow albedo feedback in future climate change. *Geophysical Research Letters*, **33(3)**, 1–4, doi:10.1029/2005gl025127.

Hansen, J., M. Sato, G. Russell, and P. Kharecha, 2013: Climate sensitivity, sea level and atmospheric carbon dioxide. *Philosophical Transactions of the Royal Society A: Mathematical, Physical and Engineering Sciences*, **371(2001)**, doi:10.1098/rsta.2012.0294.

Hansen, J. et al., 1984: Climate sensitivity: Analysis of feedback mechanisms. In: *Climate Processes and Climate Sensitivity, AGU Geophysical Monograph 29, Maurice Ewing Volume 5* [Hansen, J.E. and T. Takahashi (eds.)]. American Geophysical Union (AGU), Washington, DC, USA, pp. 130–163.

Hansen, J. et al., 1985: Climate Response Times: Dependence on Climate Sensitivity and Ocean Mixing. *Science*, **229(4716)**, 857–859, doi:10.1126/science.229.4716.857.

Hansen, J. et al., 2005a: Earth's energy imbalance: Confirmation and implications. *SCIENCE*, **308(5727)**, 1431–1435, doi:10.1126/science.1110252.

Hansen, J. et al., 2005b: Efficacy of climate forcings. *Journal of Geophysical Research*, **110(18)**, 1–45, doi:10.1029/2005jd005776.

Hargreaves, J.C. and J.D. Annan, 2016: Could the Pliocene constrain the equilibrium climate sensitivity? *Climate of the Past*, **12(8)**, 1591–1599, doi:10.5194/cp-12-1591-2016.

Hargreaves, J.C., J.D. Annan, M. Yoshimori, and A. Abe-Ouchi, 2012: Can the Last Glacial Maximum constrain climate sensitivity? *Geophysical Research Letters*, **39(24)**, 1–5, doi:10.1029/2012gl053872.

Harper, A.B. et al., 2018: Vegetation distribution and terrestrial carbon cycle in a carbon cycle configuration of JULES4.6 with new plant functional types. *Geoscientific Model Development*, **11(7)**, 2857–2873, doi:10.5194/gmd-11-2857-2018.

Hartmann, D.J. et al., 2013: Observations: Atmosphere and Surface. In: *Climate Change 2013: The Physical Science Basis. Contribution of Working Group I to the Fifth Assessment Report of the Intergovernmental Panel on Climate Change* [Stocker, T.F., D. Qin, G.-K. Plattner, M. Tignor, S.K. Allen, J. Boschung, A. Nauels, Y. Xia, V. Bex, and P.M. Midgley (eds.)]. Cambridge University Press, Cambridge, United Kingdom and New York, NY, USA, pp. 159–254, doi:10.1017/cbo9781107415324.008.

Hartmann, D.L. and K. Larson, 2002: An important constraint on tropical cloud - climate feedback. *Geophysical Research Letters*, **29**, 1951, doi:10.1029/2002gl015835.

Hartmann, D.L., L.A. Moy, and Q. Fu, 2001: Tropical Convection and the Energy Balance at the Top of the Atmosphere. *Journal of Climate*, **14(24)**, 4495–4511, doi:10.1175/1520-0442(2001)014<4495:tcateb>2.0.co;2.

Hasekamp, O.P., E. Gryspeerdt, and J. Quaas, 2019: Analysis of polarimetric satellite measurements suggests stronger cooling due to aerosol-cloud interactions. *Nature Communications*, **10(1)**, 1–7, doi:10.1038/s41467-019-13372-2.

Hasselmann, K., 1976: Stochastic climate models Part I. Theory. *Tellus*, **28(6)**, 473–485, doi:10.1111/j.2153-3490.1976.tb00696.x.

Haugstad, A.D., K.C. Armour, D.S. Battisti, and B.E.J. Rose, 2017: Relative roles of surface temperature and climate forcing patterns in the inconstancy of radiative feedbacks. *Geophysical Research Letters*, **44(14)**, 7455–7463, doi:10.1002/2017gl074372.

Hawkins, E. and R. Sutton, 2012: Time of emergence of climate signals. *Geophysical Research Letters*, **39(1)**, doi:10.1029/2011gl050087.

Haywood, A.M., H.J. Dowsett, and A.M. Dolan, 2016a: Integrating geological archives and climate models for the mid-Pliocene warm period. *Nature Communications*, **7(1)**, 10646, doi:10.1038/ncomms10646.

Haywood, A.M. et al., 2013: On the identification of a Pliocene time slice for data model comparison. *Philosophical Transactions of the Royal Society of London A: Mathematical, Physical and Engineering Sciences*, **371(2001)**, doi:10.1098/rsta.2012.0515.

Haywood, A.M. et al., 2016b: The Pliocene Model Intercomparison Project (PlioMIP) Phase 2: scientific objectives and experimental design. *Climate of the Past*, **12(3)**, 663–675, doi:10.5194/cp-12-663-2016.

Haywood, A.M. et al., 2020: The Pliocene Model Intercomparison Project Phase 2: large-scale climate features and climate sensitivity. *Climate of the Past*, **16(6)**, 2095–2123, doi:10.5194/cp-16-2095-2020.

He, C. et al., 2018: Black carbon-induced snow albedo reduction over the Tibetan Plateau: Uncertainties from snow

grain shape and aerosol-snow mixing state based on an updated SNICAR model. *Atmospheric Chemistry and Physics*, **18(15)**, 11507–11527, doi:10.5194/acp-18-11507-2018.
He, Y., K. Wang, C. Zhou, and M. Wild, 2018: A Revisit of Global Dimming and Brightening Based on the Sunshine Duration. *GEOPHYSICAL RESEARCH LETTERS*, **45(9)**, 4281–4289, doi:10.1029/2018gl077424.
Hedemann, C., T. Mauritsen, J. Jungclaus, and J. Marotzke, 2017: The subtle origins of surface-warming hiatuses. *Nature Climate Change*, **7(5)**, 336–339, doi:10.1038/nclimate3274.
Heede, U.K., A. Fedorov, and N. Burls, 2020: Time Scales and Mechanisms for the Tropical Pacific Response to Global Warming: A Tug of War between the Ocean Thermostat and Weaker Walker. *Journal of Climate*, **33(14)**, 6101–6118, doi:10.1175/jcli-d-19-0690.1.
Held, I.M. and B.J. Soden, 2006: Robust Responses of the Hydrological Cycle to Global Warming. *Journal of Climate*, **19(21)**, 5686–5699, doi:10.1175/jcli3990.1.
Held, I.M. and K.M. Shell, 2012: Using Relative Humidity as a State Variable in Climate Feedback Analysis. , **25(8)**, 2578–2582, doi:10.1175/jcli-d-11-00721.1.
Held, I.M. et al., 2010: Probing the Fast and Slow Components of Global Warming by Returning Abruptly to Preindustrial Forcing. *Journal of Climate*, **23(9)**, 2418–2427, doi:10.1175/2009jcli3466.1.
Hellweg, S. and L. Milà i Canals, 2014: Emerging approaches, challenges and opportunities in life cycle assessment. *Science*, **344(6188)**, 1109–1113, doi:10.1126/science.1248361.
Heyn, I. et al., 2017: Assessment of simulated aerosol effective radiative forcings in the terrestrial spectrum. *Geophysical Research Letters*, doi:10.1002/2016gl071975.
Hock, R. et al., 2019: High Mountain Areas. In: *IPCC Special Report on the Ocean and Cryosphere in a Changing Climate* [Pörtner, H.-O., D.C. Roberts, V. Masson-Delmotte, P. Zhai, M. Tignor, E. Poloczanska, K. Mintenbeck, A. Alegría, M. Nicolai, A. Okem, J. Petzold, B. Rama, and N.M. Weyer (eds.)]. In Press, pp. 131–202.
Hodnebrog, S.B. Dalsøren, and G. Myhre, 2018: Lifetimes, direct and indirect radiative forcing, and global warming potentials of ethane (C2H6), propane (C3H8), and butane (C4H10). *Atmospheric Science Letters*, **19(2)**, doi:10.1002/asl.804.
Hodnebrog et al., 2020a: Updated global warming potentials and radiative efficiencies of halocarbons and other weak atmospheric absorbers. *Reviews of Geophysics*, doi:10.1029/2019rg000691.
Hodnebrog et al., 2020b: The effect of rapid adjustments to halocarbons and N2O on radiative forcing. *npj Climate and Atmospheric Science*, **3(43)**, doi:10.1038/s41612-020-00150-x.
Hoesly, R.M. et al., 2018: Historical (1750–2014) anthropogenic emissions of reactive gases and aerosols from the Community Emissions Data System (CEDS). *Geoscientific Model Development*, **11(1)**, 369–408, doi:10.5194/gmd-11-369-2018.
Holland, M.M. and C.M. Bitz, 2003: Polar amplification of climate change in coupled models. *Climate Dynamics*, doi:10.1007/s00382-003-0332-6.
Hollis, C.J. et al., 2019: The DeepMIP contribution to PMIP4: methodologies for selection, compilation and analysis of latest Paleocene and early Eocene climate proxy data, incorporating version 0.1 of the DeepMIP database. *Geoscientific Model Development*, **12(7)**, 3149–3206, doi:10.5194/gmd-12-3149-2019.
Holloway, C.E. et al., 2017: Observing Convective Aggregation. *Surveys in Geophysics*, **38(6)**, 1199–1236, doi:10.1007/s10712-017-9419-1.
Hopcroft, P.O. and P.J. Valdes, 2015: How well do simulated last glacial maximum tropical temperatures constrain equilibrium climate sensitivity? *Geophysical Research Letters*, **42(13)**, 5533–5539, doi:10.1002/2015gl064903.
Hourdin, F. et al., 2017: The Art and Science of Climate Model Tuning. *Bulletin of the American Meteorological Society*, **98(3)**, 589–602, doi:10.1175/bams-d-15-00135.1.
Howard, B.S., N.E. Hamilton, M. Diesendorf, and T. Wiedmann, 2018: Modeling the carbon budget of the Australian electricity sector's transition to renewable energy. *Renewable Energy*, **125**, 712–728, doi:10.1016/j.renene.2018.02.013.
Hua, W., A. Dai, and M. Qin, 2018: Contributions of Internal Variability and External Forcing to the Recent Pacific Decadal Variations. *Geophysical Research Letters*, **45(14)**, 7084–7092, doi:10.1029/2018gl079033.
Huang, G. et al., 2019: Estimating surface solar irradiance from satellites: Past, present, and future perspectives. *Remote Sensing of Environment*, **233**, 111371, doi:10.1016/j.rse.2019.111371.
Huang, Y. and M. Zhang, 2014: The implication of radiative forcing and feedback for meridional energy transport. *Geophysical Research Letters*, doi:10.1002/2013gl059079.
Huang, Y., Y. Xia, and X. Tan, 2017: On the pattern of CO2 radiative forcing and poleward energy transport. *Journal of Geophysical Research: Atmospheres*, **122(20)**, 10,578–10,593, doi:10.1002/2017jd027221.
Huang, Y., Y. Wang, and H. Huang, 2020: Stratospheric Water Vapor Feedback Disclosed by a Locking Experiment. *Geophysical Research Letters*, **47(12)**, e2020GL087987, doi:10.1029/2020gl087987.
Huang, Y., M. Zhang, Y. Xia, Y. Hu, and S.-W. Son, 2016: Is there a stratospheric radiative feedback in global warming simulations? *Climate Dynamics*, **46(1)**, 177–186, doi:10.1007/s00382-015-2577-2.
Huber, M. and R. Caballero, 2011: The early Eocene equable climate problem revisited. *Climate of the Past*, **7(2)**, 603–

633, doi:10.5194/cp-7-603-2011.
Huber, M., I. Mahlstein, M. Wild, J. Fasullo, and R. Knutti, 2010: Constraints on Climate Sensitivity from Radiation Patterns in Climate Models. *Journal of Climate*, **24(4)**, 1034–1052, doi:10.1175/2010jcli3403.1.
Hurtt, G.C. et al., 2011: Harmonization of land-use scenarios for the period 1500-2100: 600 years of global gridded annual land-use transitions, wood harvest, and resulting secondary lands. *Climatic Change*, doi:10.1007/s10584-011-0153-2.
Huss, M., M. Funk, and A. Ohmura, 2009: Strong Alpine glacier melt in the 1940s due to enhanced solar radiation. *GEOPHYSICAL RESEARCH LETTERS*, **36**, doi:10.1029/2009gl040789.
Huybers, P., 2010: Compensation between Model Feedbacks and Curtailment of Climate Sensitivity. *Journal of Climate*, **23(11)**, 3009–3018, doi:10.1175/2010jcli3380.1.
Hwang, Y.T. and D.M.W. Frierson, 2010: Increasing atmospheric poleward energy transport with global warming. *Geophysical Research Letters*, doi:10.1029/2010gl045440.
Hwang, Y.T., D.M.W. Frierson, and J.E. Kay, 2011: Coupling between Arctic feedbacks and changes in poleward energy transport. *Geophysical Research Letters*, doi:10.1029/2011gl048546.
Hwang, Y.T., S.P. Xie, C. Deser, and S.M. Kang, 2017: Connecting tropical climate change with Southern Ocean heat uptake. *Geophysical Research Letters*, **44(18)**, 9449–9457, doi:10.1002/2017gl074972.
Hwang, Y.-T. and D.M.W. Frierson, 2013: Link between the double-Intertropical Convergence Zone problem and cloud biases over the Southern Ocean. *Proceedings of the National Academy of Sciences*, doi:10.1073/pnas.1213302110.
Hyder, P. et al., 2018: Critical Southern Ocean climate model biases traced to atmospheric model cloud errors. *Nature Communications*, **9(1)**, 1–17, doi:10.1038/s41467-018-05634-2.
Imamovic, A., K. Tanaka, D. Folini, and M. Wild, 2016: Global dimming and urbanization: did stronger negative SSR trends collocate with regions of population growth? *Atmospheric Chemistry and Physics*, **16(5)**, 2719–2725, doi:10.5194/acp-16-2719-2016.
Inglis, G.N. et al., 2020: Global mean surface temperature and climate sensitivity of the early Eocene Climatic Optimum (EECO), Paleocene--Eocene Thermal Maximum (PETM), and latest Paleocene. *Climate of the Past*, **16(5)**, 1953–1968, doi:10.5194/cp-16-1953-2020.
Ingram, W., 2010: A very simple model for the water vapour feedback on climate change. *Quarterly Journal of the Royal Meteorological Society*, **136(646)**, 30–40, doi:10.1002/qj.546.
Ingram, W., 2013: A new way of quantifying GCM water vapour feedback. *Climate Dynamics*, **40(3)**, 913–924, doi:10.1007/s00382-012-1294-3.
IPCC, 2014: Climate Change 2014: Synthesis Report. Contribution of Working Groups I, II and III to the Fifth Assessment Report of the Intergovernmental Panel on Climate Change. [Core Writing Team, R.K. Pachauri, and L.A. Meyer (eds.)]. IPCC, Geneva, Switzerland, 151 pp.
IPCC, 2018: Summary for Policymakers. In: *Global Warming of 1.5°C. An IPCC Special Report on the impacts of global warming of 1.5°C above pre-industrial levels and related global greenhouse gas emission pathways, in the context of strengthening the global response to the threat of climate change,* [Masson-Delmotte, V., P. Zhai, H.-O. Pörtner, D. Roberts, J. Skea, P.R. Shukla, A. Pirani, W. Moufouma-Okia, C. Péan, R. Pidcock, S. Connors, J.B.R. Matthews, Y. Chen, X. Zhou, M.I. Gomis, E. Lonnoy, T. Maycock, M. Tignor, and T. Waterfield (eds.)]. In Press, pp. 3–24.
IPCC, 2019a: IPCC Special Report on the Ocean and Cryosphere in a Changing Climate. [Pörtner, H.-O., D.C. Roberts, V. Masson-Delmotte, P. Zhai, M. Tignor, E. Poloczanska, K. Mintenbeck, A. Alegría, M. Nicolai, A. Okem, J. Petzold, B. Rama, and N.M. Weyer (eds.)]. In Press, 755 pp.
IPCC, 2019b: Summary for Policymakers. In: *Climate Change and Land: an IPCC special report on climate change, desertification, land degradation, sustainable land management, food security, and greenhouse gas fluxes in terrestrial ecosystems* [Shukla, P.R., J. Skea, E.C. Buendia, V. Masson-Delmotte, H.-O. Pörtner, D.C. Roberts, P. Zhai, R. Slade, S. Connors, R. Diemen, M. Ferrat, E. Haughey, S. Luz, S. Neogi, M. Pathak, J. Petzold, J.P. Pereira, P. Vyas, E. Huntley, K. Kissick, M. Belkacemi, and J. Malley (eds.)]. In Press, pp. 3–36.
Ishii, M. et al., 2017: Accuracy of Global Upper Ocean Heat Content Estimation Expected from Present Observational Data Sets. *SOLA*, **13**, 163–167, doi:10.2151/sola.2017-030.
Jahani, B., Y. Dinpashoh, and M. Wild, 2018: Dimming in Iran since the 2000s and the potential underlying causes. *INTERNATIONAL JOURNAL OF CLIMATOLOGY*, **38(3)**, 1543–1559, doi:10.1002/joc.5265.
Jenkins, S., R.J. Millar, N. Leach, and M.R. Allen, 2018: Framing Climate Goals in Terms of Cumulative CO2-Forcing-Equivalent Emissions. *Geophysical Research Letters*, doi:10.1002/2017gl076173.
Jia, G., E. Shevliakova, P. Artaxo, N. De Noblt-Ducoudre, and R. Houghton, 2019: Land–climate interactions. In: *Climate Change and Land: an IPCC special report on climate change, desertification, land degradation, sustainable land management, food security, and greenhouse gas fluxes in terrestrial ecosystems* [Shukla, P.R., J. Skea, E. Calvo Buendia, V. Masson-Delmotte, H.-O. Pörtner, D.C. Roberts, P. Zhai, R. Slade, S. Connors, R. van Diemen, M. Ferrat, E. Haughey, S. Luz, S. Neogi, M. Pathak, J. Petzold, and J.M. J. Portugal Pereira, P. Vyas, E. Huntley, K. Kissick, M, Belkacemi (eds.)]. In Press, pp. 131–247.
Jiménez-de-la-Cuesta, D. and T. Mauritsen, 2019: Emergent constraints on Earth's transient and equilibrium response

to doubled CO2 from post-1970s global warming. *Nature Geoscience*, **2015**, doi:10.1038/s41561-019-0463-y.
Johansson, D.J.A., B.C. O'Neill, C. Tebaldi, and O. Häggström, 2015: Equilibrium climate sensitivity in light of observations over the warming hiatus. *Nature Climate Change*, **5**, 449, doi:10.1038/nclimate2573.
Johnson, G.C., J.M. Lyman, and N.G. Loeb, 2016: Improving estimates of Earth's energy imbalance. *Nature Climate Change*, **6(7)**, 639–640, doi:10.1038/nclimate3043.
Jonko, A.K., K.M. Shell, B.M. Sanderson, and G. Danabasoglu, 2013: Climate Feedbacks in CCSM3 under Changing CO2 Forcing. Part II: Variation of Climate Feedbacks and Sensitivity with Forcing. *Journal of Climate*, **26(9)**, 2784–2795, doi:10.1175/jcli-d-12-00479.1.
Joos, F. et al., 2013: Carbon dioxide and climate impulse response functions for the computation of greenhouse gas metrics: A multi-model analysis. *Atmospheric Chemistry and Physics*, **13(5)**, 2793–2825, doi:10.5194/acp-13-2793-2013.
Joshi, M.M., M.J. Webb, A.C. Maycock, and M. Collins, 2010: Stratospheric water vapour and high climate sensitivity in a version of the HadSM3 climate model. *Atmospheric Chemistry and Physics*, **10(15)**, 7161–7167, doi:10.5194/acp-10-7161-2010.
Jungclaus, J.H., K. Lohmann, and D. Zanchettin, 2014: Enhanced 20th century heat transfer to the Arctic simulated in the context of climate variations over the last millennium. *Climate of the Past*, **10**, 2201–2213, doi:10.5194/cp-10-2201-2014.
Jungclaus, J.H. et al., 2017: The PMIP4 contribution to CMIP6 Part 3: The last millennium, scientific objective, and experimental design for PMIP4 simulations. *Geoscientific Model Development*, **10(11)**, 4005–4033, doi:10.5194/gmd-10-4005-2017.
Kageyama, M. et al., 2021: The PMIP4-CMIP6 Last Glacial Maximum experiments: preliminary results and comparison with the PMIP3-CMIP5 simulations. *Climate of the Past*, 1–37, doi:10.5194/cp-2019-169.
Kajtar, J.B., A. Santoso, M.H. England, and W. Cai, 2017: Tropical climate variability: interactions across the Pacific, Indian, and Atlantic Oceans. *Climate Dynamics*, **48(7–8)**, 2173–2190, doi:10.1007/s00382-016-3199-z.
Kajtar, J.B., A. Santoso, S. McGregor, M.H. England, and Z. Baillie, 2018: Model under-representation of decadal Pacific trade wind trends and its link to tropical Atlantic bias. *Climate Dynamics*, **50(3–4)**, 1471–1484, doi:10.1007/s00382-017-3699-5.
Kamae, Y., T. Ogura, M. Watanabe, S.P. Xie, and H. Ueda, 2016: Robust cloud feedback over tropical land in a warming climate. *Journal of Geophysical Research*, **121**, 2593–2609, doi:10.1002/2015jd024525.
Kang, S.M. and S.P. Xie, 2014: Dependence of climate response on meridional structure of external thermal forcing. *Journal of Climate*, **27(14)**, 5593–5600, doi:10.1175/jcli-d-13-00622.1.
Kanji, Z.A. et al., 2017: Overview of Ice Nucleating Particles. *Meteorological Monographs*, **58**, 1.1–1.33, doi:10.1175/amsmonographs-d-16-0006.1.
Karset, I.H.H. et al., 2018: Strong impacts on aerosol indirect effects from historical oxidant changes. *Atmospheric Chemistry and Physics*, **18(10)**, 7669–7690, doi:10.5194/acp-18-7669-2018.
Kato, S. et al., 2016: Investigation of the Residual in Column-Integrated Atmospheric Energy Balance Using Cloud Objects. *JOURNAL OF CLIMATE*, **29(20)**, 7435–7452, doi:10.1175/jcli-d-15-0782.1.
Kato, S. et al., 2018: Surface Irradiances of Edition 4.0 Clouds and the Earth's Radiant Energy System (CERES) Energy Balanced and Filled (EBAF) Data Product. *Journal of Climate*, **31(11)**, 4501–4527, doi:10.1175/jcli-d-17-0523.1.
Kaufman, Y.J. and I. Koren, 2006: Smoke and pollution aerosol effect on cloud cover.. *Science (New York, N.Y.)*, **313(5787)**, 655–8, doi:10.1126/science.1126232.
Kawai, H., T. Koshiro, and M.J. Webb, 2017: Interpretation of Factors Controlling Low Cloud Cover and Low Cloud Feedback Using a Unified Predictive Index. *Journal of Climate*, **30(22)**, 9119–9131, doi:10.1175/jcli-d-16-0825.1.
Kay, J.E. and A. Gettelman, 2009: Cloud influence on and response to seasonal Arctic sea ice loss. *Journal of Geophysical Research: Atmospheres*, **114(D18)**, doi:10.1029/2009jd011773.
Kay, J.E. et al., 2012: The Influence of Local Feedbacks and Northward Heat Transport on the Equilibrium Arctic Climate Response to Increased Greenhouse Gas Forcing. *Journal of Climate*, **25(16)**, 5433–5450, doi:10.1175/jcli-d-11-00622.1.
Kay, J.E. et al., 2016a: Evaluating and improving cloud phase in the Community Atmosphere Model version 5 using spaceborne lidar observations. *Journal of Geophysical Research: Atmospheres*, **121(8)**, 4162–4176, doi:10.1002/2015jd024699.
Kay, J.E. et al., 2016b: Recent Advances in Arctic Cloud and Climate Research. *Current Climate Change Reports*, **2(4)**, 159–169, doi:10.1007/s40641-016-0051-9.
Kazadzis, S. et al., 2018: Long-term series and trends in surface solar radiation in Athens, Greece. *ATMOSPHERIC CHEMISTRY AND PHYSICS*, **18(4)**, 2395–2411, doi:10.5194/acp-18-2395-2018.
Kennedy-Asser, A.T., D.J. Lunt, A. Farnsworth, and P.J. Valdes, 2019: Assessing Mechanisms and Uncertainty in Modeled Climatic Change at the Eocene-Oligocene Transition. *Paleoceanography and Paleoclimatology*, doi:10.1029/2018pa003380.
Khairoutdinov, M. and K. Emanuel, 2013: Rotating radiative-convective equilibrium simulated by a cloud-resolving

model. *Journal of Advances in Modeling Earth Systems*, **5(4)**, 816–825, doi:10.1002/2013ms000253.
Kiehl, J.T., 2007: Twentieth century climate model response and climate sensitivity. *Geophysical Research Letters*, **34(22)**, 1–4, doi:10.1029/2007gl031383.
Kiehl, J.T. and C.A. Shields, 2013: Sensitivity of the Palaeocene-Eocene Thermal Maximum climate to cloud properties. *Philosophical Transactions of the Royal Society of London A: Mathematical, Physical and Engineering Sciences*, **371(2001)**, doi:10.1098/rsta.2013.0093.
Kim, K.Y. et al., 2019: Vertical Feedback Mechanism of Winter Arctic Amplification and Sea Ice Loss. *Scientific Reports*, **9(1)**, doi:10.1038/s41598-018-38109-x.
Kinne, S., 2019: Aerosol radiative effects with MACv2. *Atmospheric Chemistry and Physics*, **19**, 10919–10959, doi:10.5194/acp-19-10919-2019.
Kirkby, J., 2007: Cosmic rays and climate. *Surveys in Geophysics*, **28(5–6)**, 333–375, doi:10.1007/s10712-008-9030-6.
Kirkby, J. et al., 2016: Ion-induced nucleation of pure biogenic particles. *Nature*, **533(7604)**, 521–526, doi:10.1038/nature17953.
Klein, S.A. and A. Hall, 2015: Emergent Constraints for Cloud Feedbacks. *Current Climate Change Reports*, **1(4)**, 276–287, doi:10.1007/s40641-015-0027-1.
Klein, S.A., A. Hall, J.R. Norris, and R. Pincus, 2017: Low-cloud feedbacks from cloud-controlling factors: A review. *Surveys in Geophysics*, **38(6)**, 1307–1329, doi:10.1007/s10712-017-9433-3.
Knutti, R., 2010: The end of model democracy? *Climatic Change*, **102(3)**, 395–404, doi:10.1007/s10584-010-9800-2.
Knutti, R. and G.C. Hegerl, 2008: The equilibrium sensitivity of the Earth's temperature to radiation changes. *Nature Geoscience*, **1**, 735, doi:10.1038/ngeo337.
Knutti, R., D. Masson, and A. Gettelman, 2013: Climate model genealogy: Generation CMIP5 and how we got there. *Geophysical Research Letters*, **40(6)**, 1194–1199, doi:10.1002/grl.50256.
Knutti, R., M.A.A. Rugenstein, and G.C. Hegerl, 2017: Beyond equilibrium climate sensitivity. *Nature Geoscience*, **10(10)**, 727–736, doi:10.1038/ngeo3017.
Knutti, R., T.F. Stocker, F. Joos, and G.-K. Plattner, 2002: Constraints on radiative forcing and future climate change from observations and climate model ensembles. *Nature*, **416(6882)**, 719–723, doi:10.1038/416719a.
Knutti, R., G.A. Meehl, M.R. Allen, and D.A. Stainforth, 2006: Constraining Climate Sensitivity from the Seasonal Cycle in Surface Temperature. *Journal of Climate*, **19(17)**, 4224–4233, doi:10.1175/jcli3865.1.
Knutti, R., S. Krähenmann, D.J. Frame, and M.R. Allen, 2008: Comment on "Heat capacity, time constant, and sensitivity of Earth's climate system" by S. E. Schwartz. *Journal of Geophysical Research Atmospheres*, **113(15)**, 1–6, doi:10.1029/2007jd009473.
Knutti, R., F. Joos, S.A. Müller, G.K. Plattner, and T.F. Stocker, 2005: Probabilistic climate change projections for CO2 stabilization profiles. *Geophysical Research Letters*, **32(20)**, 1–4, doi:10.1029/2005gl023294.
Koenigk, T. and L. Brodeau, 2014: Ocean heat transport into the Arctic in the twentieth and twenty-first century in EC-Earth. *Climate Dynamics*, doi:10.1007/s00382-013-1821-x.
Köhler, P., B. De Boer, A.S. Von Der Heydt, L.B. Stap, and R.S.W. Van De Wal, 2015: On the state dependency of the equilibrium climate sensitivity during the last 5 million years. *Climate of the Past*, **11(12)**, 1801–1823, doi:10.5194/cp-11-1801-2015.
Köhler, P. et al., 2017: A state-dependent quantification of climate sensitivity based on paleo data of the last 2.1 million years. *Paleoceanography*, 1–13, doi:10.1002/2017pa003190.
Köhler, P. et al., 2018: The Effect of Obliquity-Driven Changes on Paleoclimate Sensitivity During the Late Pleistocene. *Geophysical Research Letters*, **45**, doi:10.1029/2018gl077717.
Kohyama, T., D.L. Hartmann, and D.S. Battisti, 2017: La Niña-like mean-state response to global warming and potential oceanic roles. *Journal of Climate*, **30(11)**, 4207–4225, doi:10.1175/jcli-d-16-0441.1.
Kooperman, G.J. et al., 2012: Constraining the influence of natural variability to improve estimates of global aerosol indirect effects in a nudged version of the Community Atmosphere Model 5. *Journal of Geophysical Research Atmospheres*, doi:10.1029/2012jd018588.
Koren, I., G. Feingold, and L.A. Remer, 2010: The invigoration of deep convective clouds over the Atlantic: aerosol effect, meteorology or retrieval artifact? *Atmospheric Chemistry and Physics*, **10(18)**, 8855–8872, doi:10.5194/acp-10-8855-2010.
Koren, I., Y.J. Kaufman, D. Rosenfeld, L.A. Remer, and Y. Rudich, 2005: Aerosol invigoration and restructuring of Atlantic convective clouds. *Geophysical Research Letters*, **32(14)**, doi:10.1029/2005gl023187.
Kostov, Y., K.C. Armour, and J. Marshall, 2014: Impact of the Atlantic meridional overturning circulation on ocean heat storage and transient climate change. *Geophysical Research Letters*, doi:10.1002/2013gl058998.
Kostov, Y., D. Ferreira, K.C. Armour, and J. Marshall, 2018: Contributions of Greenhouse Gas Forcing and the Southern Annular Mode to Historical Southern Ocean Surface Temperature Trends. *Geophysical Research Letters*, doi:10.1002/2017gl074964.
Kostov, Y. et al., 2017: Fast and slow responses of Southern Ocean sea surface temperature to SAM in coupled climate models. *Climate Dynamics*, doi:10.1007/s00382-016-3162-z.
Kramer, R.J., A. Matus, B.J. Soden, and T.S. L'Ecuyer, 2019: Observation-Based Radiative Kernels From CloudSat/CALIPSO. *Journal of Geophysical Research: Atmospheres*, **124(10)**, 5431–5444,

doi:10.1029/2018jd029021.
Krasting, J.P. et al., 2018: Role of Ocean Model Formulation in Climate Response Uncertainty. *Journal of Climate*, doi:10.1175/jcli-d-18-0035.1.
Kretzschmar, J., M. Salzmann, J. Mülmenstädt, O. Boucher, and J. Quaas, 2017: Comment on "Rethinking the Lower Bound on Aerosol Radiative Forcing". *Journal of Climate*, **30(16)**, 6579–6584, doi:10.1175/jcli-d-16-0668.1.
Krishnamohan, K.S., G. Bala, L. Cao, L. Duan, and K. Caldeira, 2019: Climate System Response to Stratospheric Sulfate Aerosols: Sensitivity to Altitude of Aerosol Layer. *Earth System Dynamics*, **10(4)**, 885–900, doi:10.5194/esd-10-885-2019.
Kristjánsson, J.E. et al., 2008: Cosmic rays, cloud condensation nuclei and clouds – a reassessment using MODIS data. *Atmospheric Chemistry and Physics*, **8(24)**, 7373–7387, doi:10.5194/acp-8-7373-2008.
Krivova, N.A., S.K. Solanki, and L. Floyd, 2006: Reconstruction of solar UV irradiance in cycle 23. *Astronomy & Astrophysics*, **452(2)**, 631–639, doi:10.1051/0004-6361:20064809.
Kucharski, F., I.-S.S. Kang, R. Farneti, and L. Feudale, 2011: Tropical Pacific response to 20th century Atlantic warming. *Geophysical Research Letters*, **38(3)**, doi:10.1029/2010gl046248.
Kucharski, F., F.S. Syed, A. Burhan, I. Farah, and A. Gohar, 2014: Tropical Atlantic influence on Pacific variability and mean state in the twentieth century in observations and CMIP5. *Climate Dynamics*, **44(3–4)**, 881–896, doi:10.1007/s00382-014-2228-z.
Kucharski, F. et al., 2015: Atlantic forcing of Pacific decadal variability. *Climate Dynamics*, **46(7–8)**, 2337–2351, doi:10.1007/s00382-015-2705-z.
Kuhlbrodt, T., J.M. Gregory, and L.C. Shaffrey, 2015: A process-based analysis of ocean heat uptake in an AOGCM with an eddy-permitting ocean component. *Climate Dynamics*, **45(11)**, 3205–3226, doi:10.1007/s00382-015-2534-0.
Kummer, J.R. and A.E. Dessler, 2014: The impact of forcing efficacy on the equilibrium climate sensitivity. *Geophysical Research Letters*, **41(10)**, 3565–3568, doi:10.1002/2014gl060046.
Kutzbach, J.E., F. He, S.J. Vavrus, and W.F. Ruddiman, 2013: The dependence of equilibrium climate sensitivity on climate state: Applications to studies of climates colder than present. *Geophysical Research Letters*, **40(14)**, 3721–3726, doi:10.1002/grl.50724.
L'Ecuyer, T.S. et al., 2015: The Observed State of the Energy Budget in the Early Twenty-First Century. *Journal of Climate*, **28(21)**, 8319–8346, doi:10.1175/jcli-d-14-00556.1.
Lade, S.J. et al., 2018: Analytically tractable climate-carbon cycle feedbacks under 21st century anthropogenic forcing. *Earth System Dynamics*, doi:10.5194/esd-9-507-2018.
Laepple, T. and P. Huybers, 2014: Ocean surface temperature variability: Large model-data differences at decadal and longer periods. *Proceedings of the National Academy of Sciences of the United States of America*, **111(47)**, 16682–16687, doi:10.1073/pnas.1412077111.
Lago, V. and M.H. England, 2019: Projected slowdown of antarctic bottom water formation in response to amplified meltwater contributions. *Journal of Climate*, **32(19)**, 6319–6335, doi:10.1175/jcli-d-18-0622.1.
Laîné, A., M. Yoshimori, and A. Abe-Ouchi, 2016: Surface Arctic Amplification Factors in CMIP5 Models: Land and Oceanic Surfaces and Seasonality. *Journal of Climate*, **29(9)**, 3297–3316, doi:10.1175/jcli-d-15-0497.1.
Laken, B.A., 2016: Can Open Science save us from a solar-driven monsoon? *Journal of Space Weather and Space Climate*, **6**, A11, doi:10.1051/swsc/2016005.
Larson, E.J.L. and R.W. Portmann, 2016: A temporal kernel method to compute effective radiative forcing in CMIP5 transient simulations. *Journal of Climate*, doi:10.1175/jcli-d-15-0577.1.
Lauder, A.R. et al., 2013: Offsetting methane emissions - An alternative to emission equivalence metrics. *International Journal of Greenhouse Gas Control*, **12**, 419–429, doi:10.1016/j.ijggc.2012.11.028.
Lean, J.L., 2018: Estimating Solar Irradiance Since 850 CE. *Earth and Space Science*, **5(4)**, 133–149, doi:10.1002/2017ea000357.
Lebsock, M.D., G.L. Stephens, and C. Kummerow, 2008: Multisensor satellite observations of aerosol effects on warm clouds. *Journal of Geophysical Research*, **113(D15)**, D15205, doi:10.1029/2008jd009876.
Lee, D.S.S. et al., 2020: The contribution of global aviation to anthropogenic climate forcing for 2000 to 2018. *Atmospheric Environment*, **244(117834)**, doi:10.1016/j.atmosenv.2020.117834.
Lee, S., T. Gong, S.B. Feldstein, J.A. Screen, and I. Simmonds, 2017: Revisiting the Cause of the 1989–2009 Arctic Surface Warming Using the Surface Energy Budget: Downward Infrared Radiation Dominates the Surface Fluxes. *Geophysical Research Letters*, doi:10.1002/2017gl075375.
Lee, S.H. et al., 2019: New Particle Formation in the Atmosphere: From Molecular Clusters to Global Climate. *Journal of Geophysical Research: Atmospheres*, **124(13)**, 7098–7146, doi:10.1029/2018jd029356.
Lejeune, Q. et al., 2020: Biases in the albedo sensitivity to deforestation in CMIP5 models and their impacts on the associated historical Radiative Forcing. *Earth System Dynamics*, **11**, 1209–1232, doi:10.5194/esd-11-1209-2020.
Levasseur, A. et al., 2016: Enhancing life cycle impact assessment from climate science: Review of recent findings and recommendations for application to LCA. *Ecological Indicators*, doi:10.1016/j.ecolind.2016.06.049.
Lewis, N., 2013: An objective bayesian improved approach for applying optimal fingerprint techniques to estimate

climate sensitivity. *Journal of Climate*, **26(19)**, 7414–7429, doi:10.1175/jcli-d-12-00473.1.

Lewis, N. and J.A. Curry, 2015: The implications for climate sensitivity of AR5 forcing and heat uptake estimates. *Climate Dynamics*, **45(3–4)**, 1009–1023, doi:10.1007/s00382-014-2342-y.

Lewis, N. and J. Curry, 2018: The impact of recent forcing and ocean heat uptake data on estimates of climate sensitivity. *Journal of Climate*, JCLI–D–17–0667.1, doi:10.1175/jcli-d-17-0667.1.

Lewis, N. and T. Mauritsen, 2020: Negligible unforced historical pattern effect on climate feedback strength found in HadISST-based AMIP simulations. *Journal of Climate*, doi:10.1175/jcli-d-19-0941.1.

Li, C., J.S. von Storch, and J. Marotzke, 2013: Deep-ocean heat uptake and equilibrium climate response. *Climate Dynamics*, **40(5–6)**, 1071–1086, doi:10.1007/s00382-012-1350-z.

Li, F. and P. Newman, 2020: Stratospheric water vapor feedback and its climate impacts in the coupled atmosphere-ocean Goddard Earth Observing System Chemistry-Climate Model. *Climate Dynamics*, **55(5–6)**, 1585–1595, doi:10.1007/s00382-020-05348-6.

Li, J., Y. Jiang, X. Xia, and Y. Hu, 2018: Increase of surface solar irradiance across East China related to changes in aerosol properties during the past decade. *Environmental Research Letters*, **13(3)**, 034006, doi:10.1088/1748-9326/aaa35a.

Li, J.-L.F. et al., 2013: Characterizing and understanding radiation budget biases in CMIP3/CMIP5 GCMs, contemporary GCM, and reanalysis. *JOURNAL OF GEOPHYSICAL RESEARCH-ATMOSPHERES*, **118(15)**, 8166–8184, doi:10.1002/jgrd.50378.

Li, R.L., T. Storelvmo, A. Fedorov, and Y.-S. Choi, 2019: A Positive Iris Feedback: Insights from Climate Simulations with Temperature-Sensitive Cloud–Rain Conversion. *Journal of Climate*, **32(16)**, 5305–5324, doi:10.1175/jcli-d-18-0845.1.

Li, X., S.-P.P. Xie, S.T. Gille, and C. Yoo, 2016: Atlantic-induced pan-tropical climate change over the past three decades. *Nature Climate Change*, **6(3)**, 275–279, doi:10.1038/nclimate2840.

Li, Y., W. Han, and L. Zhang, 2017: Enhanced Decadal Warming of the Southeast Indian Ocean During the Recent Global Surface Warming Slowdown. *Geophysical Research Letters*, **44(19)**, 9876–9884, doi:10.1002/2017gl075050.

Li, Y., D.W.J. Thompson, S. Bony, and T.M. Merlis, 2018: Thermodynamic Control on the Poleward Shift of the Extratropical Jet in Climate Change Simulations: The Role of Rising High Clouds and Their Radiative Effects. *Journal of Climate*, **32(3)**, 917–934, doi:10.1175/jcli-d-18-0417.1.

Li, Z. et al., 2016: Aerosol and monsoon climate interactions over Asia. *REVIEWS OF GEOPHYSICS*, **54(4)**, 866–929, doi:10.1002/2015rg000500.

Lin, G. et al., 2014: Radiative forcing of organic aerosol in the atmosphere and on snow: Effects of SOA and brown carbon. *Journal of Geophysical Research: Atmospheres*, **119(12)**, 7453–7476, doi:10.1002/2013jd021186.

Lindzen, R.S., M.D. Chou, and A.Y. Hou, 2001: Does the Earth Have an Adaptive Infrared Iris? *Bulletin of the American Meteorological Society*, **82(3)**, 417–432, doi:10.1175/1520-0477(2001)082<0417:dtehaa>2.3.co;2.

Lipat, B.R., G. Tselioudis, K.M. Grise, and L.M. Polvani, 2017: CMIP5 models' shortwave cloud radiative response and climate sensitivity linked to the climatological Hadley cell extent. *Geophysical Research Letters*, **44(11)**, 5739–5748, doi:10.1002/2017gl073151.

Lisiecki, L.E. and M.E. Raymo, 2005: A Pliocene-Pleistocene stack of 57 globally distributed benthic δ18O records. *Paleoceanography*, **20(1)**, doi:10.1029/2004pa001071.

Liu, C. et al., 2020: Variability in the global energy budget and transports 1985-2017. *CLIMATE DYNAMICS*, **55(11–12)**, 3381–3396, doi:10.1007/s00382-020-05451-8.

Liu, J. et al., 2019: Eastern equatorial Pacific cold tongue evolution since the late Miocene linked to extratropical climate. *Science Advances*, **5(4)**, doi:10.1126/sciadv.aau6060.

Liu, R. et al., 2018: An Assessment of Tropospheric Water Vapor Feedback Using Radiative Kernels. *Journal of Geophysical Research: Atmospheres*, **123(3)**, 1499–1509, doi:10.1002/2017jd027512.

Liu, W., S.P. Xie, Z. Liu, and J. Zhu, 2017: Overlooked possibility of a collapsed atlantic meridional overturning circulation in warming climate. *Science Advances*, doi:10.1126/sciadv.1601666.

Liu, Y. et al., 2017: Climate response to the meltwater runoff from Greenland ice sheet: evolving sensitivity to discharging locations. *Climate Dynamics*, doi:10.1007/s00382-017-3980-7.

Liu, Z. and B. Huang, 1997: A coupled theory of tropical climatology: Warm pool, cold tongue, and walker circulation. *Journal of Climate*, **10(7)**, 1662–1679, doi:10.1175/1520-0442(1997)010<1662:actotc>2.0.co;2.

Liu, Z., S. Vavrus, F. He, N. Wen, and Y. Zhong, 2005: Rethinking Tropical Ocean Response to Global Warming: The Enhanced Equatorial Warming. *Journal of Climate*, **18(22)**, 4684–4700, doi:10.1175/jcli3579.1.

Liu, Z. et al., 2014: The Holocene temperature conundrum. *Proceedings of the National Academy of Sciences*, **111(34)**, E3501–E3505, doi:10.1073/pnas.1407229111.

Lockwood, M. and W.T. Ball, 2020: Placing limits on long-term variations in quiet-Sun irradiance and their contribution to total solar irradiance and solar radiative forcing of climate. *Proceedings of the Royal Society A: Mathematical, Physical and Engineering Sciences*, **476(2238)**, 20200077, doi:10.1098/rspa.2020.0077.

Loeb, N.G., D.A. Rutan, S. Kato, and W. Wang, 2014: Observing Interannual Variations in Hadley Circulation Atmospheric Diabatic Heating and Circulation Strength. *JOURNAL OF CLIMATE*, **27(11)**, 4139–4158,

doi:10.1175/jcli-d-13-00656.1.
Loeb, N.G., T.J. Thorsen, J.R. Norris, H. Wang, and W. Su, 2018a: Changes in Earth's Energy Budget during and after the "Pause" in Global Warming: An Observational Perspective. *Climate*, **6(3)**, 62, doi:10.3390/cli6030062.
Loeb, N.G. et al., 2012: Observed changes in top-of-the-atmosphere radiation and upper-ocean heating consistent within uncertainty. *Nature Geoscience*, doi:10.1038/ngeo1375.
Loeb, N.G. et al., 2016: Observational constraints on atmospheric and oceanic cross-equatorial heat transports: revisiting the precipitation asymmetry problem in climate models. *CLIMATE DYNAMICS*, **46(9–10)**, 3239–3257, doi:10.1007/s00382-015-2766-z.
Loeb, N.G. et al., 2018b: Clouds and the Earth's Radiant Energy System (CERES) Energy Balanced and Filled (EBAF) Top-of-Atmosphere (TOA) Edition-4.0 Data Product. *Journal of Climate*, **31(2)**, 895–918, doi:10.1175/jcli-d-17-0208.1.
Loeb, N.G. et al., 2020: New Generation of Climate Models Track Recent Unprecedented Changes in Earth's Radiation Budget Observed by CERES. *Geophysical Research Letters*, **47(5)**, doi:10.1029/2019gl086705.
Lohmann, U. and D. Neubauer, 2018: The importance of mixed-phase and ice clouds for climate sensitivity in the global aerosol–climate model ECHAM6-HAM2. *Atmos. Chem. Phys.*, **18(12)**, 8807–8828, doi:10.5194/acp-18-8807-2018.
Longman, R.J., T.W. Giambelluca, R.J. Alliss, and M.L. Barnes, 2014: Temporal solar radiation change at high elevations in Hawai'i. *Journal of Geophysical Research-Atmospheres*, **119(10)**, 6022–6033, doi:10.1002/2013jd021322.
Lund, M.T. et al., 2017: Emission metrics for quantifying regional climate impacts of aviation. *Earth System Dynamics*, doi:10.5194/esd-8-547-2017.
Lund, M.T. et al., 2018a: Concentrations and radiative forcing of anthropogenic aerosols from 1750 to 2014 simulated with the Oslo CTM3 and CEDS emission inventory. *Geoscientific Model Development*, **11(12)**, 4909–4931, doi:10.5194/gmd-11-4909-2018.
Lund, M.T. et al., 2018b: Short Black Carbon lifetime inferred from a global set of aircraft observations. *npj Climate and Atmospheric Science*, **1(1)**, 31, doi:10.1038/s41612-018-0040-x.
Lunt, D.J. et al., 2010: Earth system sensitivity inferred from Pliocene modelling and data. *Nature Geoscience*, **3(1)**, 60–64, doi:10.1038/ngeo706.
Lunt, D.J. et al., 2012a: A model–data comparison for a multi-model ensemble of early Eocene atmosphere–ocean simulations: EoMIP. *Climate of the Past*, **8(5)**, 1717–1736, doi:10.5194/cp-8-1717-2012.
Lunt, D.J. et al., 2012b: On the causes of mid-Pliocene warmth and polar amplification. *Earth and Planetary Science Letters*, **321–322**, 128–138, doi:10.1016/j.epsl.2011.12.042.
Lunt, D.J. et al., 2021: DeepMIP: Model intercomparison of early Eocene climatic optimum (EECO) large-scale climate features and comparison with proxy data. *Climate of the Past*, **17(1)**, 203–227, doi:10.5194/cp-17-203-2021.
Luo, B., D. Luo, L. Wu, L. Zhong, and I. Simmonds, 2017: Atmospheric circulation patterns which promote winter Arctic sea ice decline. *Environmental Research Letters*, **12(5)**, doi:10.1088/1748-9326/aa69d0.
Luo, J.J., W. Sasaki, and Y. Masumoto, 2012: Indian Ocean warming modulates Pacific climate change. *Proceedings of the National Academy of Sciences of the United States of America*, **109(46)**, 18701–18706, doi:10.1073/pnas.1210239109.
Luo, J.J., G. Wang, and D. Dommenget, 2018: May common model biases reduce CMIP5's ability to simulate the recent Pacific La Niña-like cooling? *Climate Dynamics*, **50(3–4)**, 1335–1351, doi:10.1007/s00382-017-3688-8.
Luo, Y., J. Lu, F. Liu, and W. Liu, 2015: Understanding the El Niño-like oceanic response in the tropical Pacific to global warming. *Climate Dynamics*, doi:10.1007/s00382-014-2448-2.
Luo, Y., J. Lu, F. Liu, and O. Garuba, 2017: The role of ocean dynamical thermostat in delaying the El Niño-Like response over the equatorial Pacific to climate warming. *Journal of Climate*, **30(8)**, 2811–2827, doi:10.1175/jcli-d-16-0454.1.
Lurton, T. et al., 2020: Implementation of the CMIP6 Forcing Data in the IPSL-CM6A-LR Model. *Journal of Advances in Modeling Earth Systems*, **12(4)**, 1–22, doi:10.1029/2019ms001940.
Lutsko, N.J. and K. Takahashi, 2018: What Can the Internal Variability of CMIP5 Models Tell Us about Their Climate Sensitivity? *Journal of Climate*, **31(13)**, 5051–5069, doi:10.1175/jcli-d-17-0736.1.
Lutsko, N.J. and M. Popp, 2019: Probing the Sources of Uncertainty in Transient Warming on Different Timescales. *Geophysical Research Letters*, **46(20)**, 11367–11377, doi:10.1029/2019gl084018.
Luyssaert, S. et al., 2014: Land management and land-cover change have impacts of similar magnitude on surface temperature. *Nature Climate Change*, doi:10.1038/nclimate2196.
Lyman, J.M. and G.C. Johnson, 2008: Estimating Annual Global Upper-Ocean Heat Content Anomalies despite Irregular In Situ Ocean Sampling. *Journal of Climate*, **21(21)**, 5629–5641, doi:10.1175/2008jcli2259.1.
Lynch, J., M. Cain, R. Pierrehumbert, and M. Allen, 2020: Demonstrating GWP*: A means of reporting warming-equivalent emissions that captures the contrasting impacts of short- and long-lived climate pollutants. *Environmental Research Letters*, **15(4)**, 044023, doi:10.1088/1748-9326/ab6d7e.
Lynch, J., M. Cain, D. Frame, and R. Pierrehumbert, 2021: Agriculture's Contribution to Climate Change and Role in Mitigation Is Distinct From Predominantly Fossil CO2-Emitting Sectors. *Frontiers in Sustainable Food*

Systems, **4**, 518039, doi:10.3389/fsufs.2020.518039.
Ma, X., F. Yu, and J. Quaas, 2014: Reassessment of satellite-based estimate of aerosol climate forcing. *Journal of Geophysical Research: Atmospheres*, **119(17)**, 10,310–394,409, doi:10.1002/2014jd021670.
MacDougall, A.H., K. Zickfeld, R. Knutti, and H.D. Matthews, 2015: Sensitivity of carbon budgets to permafrost carbon feedbacks and non-CO2 forcings. *Environmental Research Letters*, doi:10.1088/1748-9326/10/12/125003.
MacIntosh, C.R.R. et al., 2016: Contrasting fast precipitation responses to tropospheric and stratospheric ozone forcing. *Geophysical Research Letters*, **43(3)**, 1263–1271, doi:10.1002/2015gl067231.
Maher, N., M.H. England, A. Gupta, and P. Spence, 2018: Role of Pacific trade winds in driving ocean temperatures during the recent slowdown and projections under a wind trend reversal. *Climate Dynamics*, **51(1–2)**, 321–336, doi:10.1007/s00382-017-3923-3.
Mahlstein, I. and R. Knutti, 2011: Ocean heat transport as a cause for model uncertainty in projected arctic warming. *Journal of Climate*, doi:10.1175/2010jcli3713.1.
Mahowald, N.M. et al., 2017: Aerosol Deposition Impacts on Land and Ocean Carbon Cycles. *Current Climate Change Reports*, doi:10.1007/s40641-017-0056-z.
Mahrt, F. et al., 2018: Ice nucleation abilities of soot particles determined with the Horizontal Ice Nucleation Chamber. *Atmospheric Chemistry and Physics*, **18(18)**, 13363–13392, doi:10.5194/acp-18-13363-2018.
Malavelle, F.F. et al., 2017: Strong constraints on aerosol-cloud interactions from volcanic eruptions. *Nature*, **546(7659)**, 485–491, doi:10.1038/nature22974.
Mallapragada, D. and B.K. Mignone, 2017: A consistent conceptual framework for applying climate metrics in technology life cycle assessment. *Environmental Research Letters*, doi:10.1088/1748-9326/aa7397.
Mallick, K. et al., 2016: Canopy-scale biophysical controls of transpiration and evaporation in the Amazon Basin. *Hydrology and Earth System Sciences*, **20(10)**, 4237–4264, doi:10.5194/hess-20-4237-2016.
Manabe, S. and R.T. Wetherald, 1975: The Effects of Doubling the CO2 Concentration on the climate of a General Circulation Model. *Journal of the Atmospheric Sciences*, **32(1)**, 3–15, doi:10.1175/1520-0469(1975)032<0003:teodtc>2.0.co;2.
Manabe, S. and K. Bryan, 1985: CO2-induced change in a coupled ocean-atmosphere model and its paleoclimatic implications. *Journal of Geophysical Research*, **90(5)**, 11,611–689,707, doi:10.1029/jc090ic06p11689.
Manara, V. et al., 2015: Sunshine duration variability and trends in Italy from homogenized instrumental time series (1936-2013). *Journal of Geophysical Research-Atmospheres*, **120(9)**, 3622–3641, doi:10.1002/2014jd022560.
Manara, V. et al., 2016: Detection of dimming/brightening in Italy from homogenized all-sky and clear-sky surface solar radiation records and underlying causes (1959-2013). *Atmospheric Chemistry and Physics*, **16(17)**, 11145–11161, doi:10.5194/acp-16-11145-2016.
Manaster, A., C.W. O'Dell, and G. Elsaesser, 2017: Evaluation of Cloud Liquid Water Path Trends Using a Multidecadal Record of Passive Microwave Observations. *Journal of Climate*, **30(15)**, 5871–5884, doi:10.1175/jcli-d-16-0399.1.
Manne, A.S. and R.G. Richels, 2001: An alternative approach to establishing trade-offs among greenhouse gases. *Nature*, **410(6829)**, 675–677, doi:10.1038/35070541.
Marotzke, J., 2019: Quantifying the irreducible uncertainty in near-term climate projections. *Wiley Interdisciplinary Reviews: Climate Change*, **10(1)**, e563, doi:10.1002/wcc.563.
Marotzke, J. and P.M. Forster, 2015: Forcing, feedback and internal variability in global temperature trends. *Nature*, **517(7536)**, 565–570, doi:10.1038/nature14117.
Marshall, J. et al., 2015: The ocean's role in the transient response of climate to abrupt greenhouse gas forcing. *Climate Dynamics*, doi:10.1007/s00382-014-2308-0.
Marshall, L.R. et al., 2020: Large Variations in Volcanic Aerosol Forcing Efficiency Due to Eruption Source Parameters and Rapid Adjustments. *Geophysical Research Letters*, **47(19)**, doi:10.1029/2020gl090241.
Martínez-Botí, M.A. et al., 2015: Plio-Pleistocene climate sensitivity evaluated using high-resolution CO2 records. *Nature*, **518**, 49–54, doi:10.1038/nature14145.
Marvel, K., G.A. Schmidt, R.L. Miller, and L.S. Nazarenko, 2016: Implications for climate sensitivity from the response to individual forcings. *Nature Climate Change*, **6(4)**, 386–389, doi:10.1038/nclimate2888.
Marvel, K., R. Pincus, G.A. Schmidt, and R.L. Miller, 2018: Internal Variability and Disequilibrium Confound Estimates of Climate Sensitivity From Observations. *Geophysical Research Letters*, **45(3)**, 1595–1601, doi:10.1002/2017gl076468.
Marvel, K. et al., 2015: External influences on modeled and observed cloud trends. *Journal of Climate*, **28(12)**, 4820–4840, doi:10.1175/jcli-d-14-00734.1.
Masson-Delmotte, V. et al., 2013: Information from Paleoclimate Archives. In: *Climate Change 2013: The Physical Science Basis. Contribution of Working Group I to the Fifth Assessment Report of the Intergovernmental Panel on Climate Change* [Stocker, T.F., D. Qin, G.-K. Plattner, M. Tignor, S.K. Allen, J. Boschung, A. Nauels, Y. Xia, V. Bex, and P.M. Midgley (eds.)]. Cambridge University Press, Cambridge, United Kingdom and New York, NY, USA, pp. 383–464, doi:10.1017/cbo9781107415324.013.
Mateos, D., M. Anton, A. Sanchez-Lorenzo, J. Calbo, and M. Wild, 2013: Long-term changes in the radiative effects of

aerosols and clouds in a mid-latitude region (1985-2010). *Global and Planetary Change*, **111**, 288–295, doi:10.1016/j.gloplacha.2013.10.004.
Matus, A. and T.S. L'Ecuyer, 2017: The role of cloud phase in Earth's radiation budget. *Journal of Geophysical Research: Atmospheres*, **122(5)**, 2559–2578, doi:10.1002/2016jd025951.
Mauritsen, T., 2016: Global warming: Clouds cooled the Earth. *Nature Geoscience*, **9(12)**, 865–867, doi:10.1038/ngeo2838.
Mauritsen, T. and B. Stevens, 2015: Missing iris effect as a possible cause of muted hydrological change and high climate sensitivity in models. *Nature Geoscience*, **8(5)**, 346–351, doi:10.1038/ngeo2414.
Mauritsen, T. and R. Pincus, 2017: Committed warming inferred from observations. *Nature Climate Change*, **7(9)**, 652–655, doi:10.1038/nclimate3357.
Mauritsen, T. and E. Roeckner, 2020: Tuning the MPI-ESM1.2 Global Climate Model to Improve the Match With Instrumental Record Warming by Lowering Its Climate Sensitivity. *Journal of Advances in Modeling Earth Systems*, **12(5)**, doi:10.1029/2019ms002037.
Mauritsen, T. et al., 2012: Tuning the climate of a global model. *Journal of Advances in Modeling Earth Systems*, **4(8)**, 1–18, doi:10.1029/2012ms000154.
Mauritsen, T. et al., 2013: Climate feedback efficiency and synergy. *Climate Dynamics*, **41(9–10)**, 2539–2554, doi:10.1007/s00382-013-1808-7.
Mauritsen, T. et al., 2019: Developments in the MPI-M Earth System Model version 1.2 (MPI-ESM 1.2) and its response to increasing CO2. *Journal of Advances in Modeling Earth Systems*, doi:10.1029/2018ms001400.
McCabe, M.F., B. Aragon, R. Houborg, and J. Mascaro, 2017a: CubeSats in Hydrology: Ultrahigh-Resolution Insights Into Vegetation Dynamics and Terrestrial Evaporation. *Water Resources Research*, **53(12)**, 10017–10024, doi:10.1002/2017wr022240.
McCabe, M.F. et al., 2017b: The future of Earth observation in hydrology. *Hydrology and Earth System Sciences*, **21(7)**, 3879–3914, doi:10.5194/hess-21-3879-2017.
McClymont, E.L. et al., 2020: Lessons from a high-CO2 world: an ocean view from ~3 million years ago. *Climate of the Past*, **16(4)**, 1599–1615, doi:10.5194/cp-16-1599-2020.
McComiskey, A. and G. Feingold, 2012: The scale problem in quantifying aerosol indirect effects. *Atmospheric Chemistry and Physics*, **12(2)**, 1031–1049, doi:10.5194/acp-12-1031-2012.
McCoy, D.T., D.L. Hartmann, and D.P. Grosvenor, 2014a: Observed Southern Ocean Cloud Properties and Shortwave Reflection. Part I: Calculation of SW Flux from Observed Cloud Properties. *Journal of Climate*, **27(23)**, 8836–8857, doi:10.1175/jcli-d-14-00287.1.
McCoy, D.T., D.L. Hartmann, and D.P. Grosvenor, 2014b: Observed Southern Ocean Cloud Properties and Shortwave Reflection. Part II: Phase Changes and Low Cloud Feedback. *Journal of Climate*, **27(23)**, 8858–8868, doi:10.1175/jcli-d-14-00288.1.
McCoy, D.T., R. Eastman, D.L. Hartmann, and R. Wood, 2017a: The Change in Low Cloud Cover in a Warmed Climate Inferred from AIRS, MODIS, and ERA-Interim. *Journal of Climate*, **30(10)**, 3609–3620, doi:10.1175/jcli-d-15-0734.1.
McCoy, D.T., I. Tan, D.L. Hartmann, M.D. Zelinka, and T. Storelvmo, 2016: On the relationships among cloud cover, mixed-phase partitioning, and planetary albedo in GCMs.. *Journal of Advances in Modeling Earth Systems*, **8**, 650–668, doi:10.1002/2015ms000589.
McCoy, D.T. et al., 2017b: The global aerosol-cloud first indirect effect estimated using MODIS, MERRA, and AeroCom. *Journal of Geophysical Research: Atmospheres*, **122(3)**, 1779–1796, doi:10.1002/2016jd026141.
McCoy, D.T. et al., 2018: Aerosol midlatitude cyclone indirect effects in observations and high-resolution simulations. *Atmospheric Chemistry and Physics*, **18(8)**, 5821–5846, doi:10.5194/acp-18-5821-2018.
McCoy, D.T. et al., 2019: Cloud feedbacks in extratropical cyclones: Insight from long-term satellite data and high-resolution global simulations. *Atmospheric Chemistry and Physics*, doi:10.5194/acp-19-1147-2019.
McCoy, I.L. et al., 2020a: The hemispheric contrast in cloud microphysical properties constrains aerosol forcing. *Proceedings of the National Academy of Sciences of the United States of America*, **117(32)**, 18998–19006, doi:10.1073/pnas.1922502117.
McCoy, I.L. et al., 2020b: The hemispheric contrast in cloud microphysical properties constrains aerosol forcing. *Proceedings of the National Academy of Sciences of the United States of America*, **117(32)**, 18998–19006, doi:10.1073/pnas.1922502117.
McGraw, Z., T. Storelvmo, B.H. Samset, and C.W. Stjern, 2020: Global Radiative Impacts of Black Carbon Acting as Ice Nucleating Particles. *Geophysical Research Letters*, **47(20)**, 1–9, doi:10.1029/2020gl089056.
McGregor, S., M.F. Stuecker, J.B. Kajtar, M.H. England, and M. Collins, 2018: Model tropical Atlantic biases underpin diminished Pacific decadal variability. *Nature Climate Change*, **8(6)**, 493–498, doi:10.1038/s41558-018-0163-4.
McGregor, S. et al., 2014: Recent Walker circulation strengthening and Pacific cooling amplified by Atlantic warming. *Nature Climate Change*, **4(10)**, 888–892, doi:10.1038/nclimate2330.
Meehl, G.A. et al., 2020: Context for interpreting equilibrium climate sensitivity and transient climate response from the CMIP6 Earth system models. *Science Advances*, **6(26)**, doi:10.1126/sciadv.aba1981.

Meinshausen, M., S.C.B.B. Raper, and T.M.L.L. Wigley, 2011a: Emulating coupled atmosphere-ocean and carbon cycle models with a simpler model, MAGICC6 – Part 1: Model description and calibration. *Atmospheric Chemistry and Physics*, **11(4)**, 1417–1456, doi:10.5194/acp-11-1417-2011.
Meinshausen, M., T.M.L. Wigley, and S.C.B. Raper, 2011b: Emulating atmosphere-ocean and carbon cycle models with a simpler model, MAGICC6 - Part 2: Applications. *Atmospheric Chemistry and Physics*, **11(4)**, 1457–1471, doi:10.5194/acp-11-1457-2011.
Meinshausen, M. et al., 2009: Greenhouse-gas emission targets for limiting global warming to 2 °C. *Nature*, **458(7242)**, 1158–1162, doi:10.1038/nature08017.
Meinshausen, M. et al., 2020: The shared socio-economic pathway (SSP) greenhouse gas concentrations and their extensions to 2500. *Geoscientific Model Development*, **13(8)**, 3571–3605, doi:10.5194/gmd-13-3571-2020.
Meraner, K., T. Mauritsen, and A. Voigt, 2013: Robust increase in equilibrium climate sensitivity under global warming. *Geophysical Research Letters*, **40(22)**, 5944–5948, doi:10.1002/2013gl058118.
Mercado, L.M. et al., 2009: Impact of changes in diffuse radiation on the global land carbon sink. *Nature*, doi:10.1038/nature07949.
Meredith, M. et al., 2019: Polar Regions. In: *IPCC Special Report on the Ocean and Cryosphere in a Changing Climate* [Pörtner, H.-O., D.C. Roberts, V. Masson-Delmotte, P. Zhai, M. Tignor, E. Poloczanska, K. Mintenbeck, A. Alegría, M. Nicolai, A. Okem, J. Petzold, B. Rama, and N.M. Weyer (eds.)]. In Press, pp. 203–320.
Merlis, T.M., 2014: Interacting components of the top-of-atmosphere energy balance affect changes in regional surface temperature. *Geophysical Research Letters*, **41(20)**, 7291–7297, doi:10.1002/2014gl061700.
Merlis, T.M. and T. Schneider, 2011: Changes in zonal surface temperature gradients and Walker circulations in a wide range of climates. *Journal of Climate*, **24(17)**, 4757–4768, doi:10.1175/2011jcli4042.1.
Merlis, T.M. and M. Henry, 2018: Simple estimates of polar amplification in moist diffusive energy balance models. *Journal of Climate*, doi:10.1175/jcli-d-17-0578.1.
Merlis, T.M., I.M. Held, G.L. Stenchikov, F. Zeng, and L.W. Horowitz, 2014: Constraining transient climate sensitivity using coupled climate model simulations of volcanic eruptions. *Journal of Climate*, doi:10.1175/jcli-d-14-00214.1.
Meyer, A., J.P. Vernier, B. Luo, U. Lohmann, and T. Peter, 2015: Did the 2011 Nabro eruption affect the optical properties of ice clouds? *Journal of Geophysical Research*, **120(18)**, 9500–9513, doi:10.1002/2015jd023326.
Meyssignac, B. et al., 2019: Measuring Global Ocean Heat Content to Estimate the Earth Energy Imbalance. *Frontiers in Marine Science*, **6**, 432, doi:10.3389/fmars.2019.00432.
Michibata, T., K. Suzuki, Y. Sato, and T. Takemura, 2016: The source of discrepancies in aerosol–cloud–precipitation interactions between GCM and A-Train retrievals. *Atmospheric Chemistry and Physics*, **16(23)**, 15413–15424, doi:10.5194/acp-16-15413-2016.
Millar, J.R., Z.R. Nicholls, P. Friedlingstein, and M.R. Allen, 2017: A modified impulse-response representation of the global near-surface air temperature and atmospheric concentration response to carbon dioxide emissions. *Atmospheric Chemistry and Physics*, **17(11)**, 7213–7228, doi:10.5194/acp-17-7213-2017.
Millar, R.J. et al., 2015: Model structure in observational constraints on transient climate response. *Climatic Change*, **131(2)**, 199–211, doi:10.1007/s10584-015-1384-4.
Mlynczak, M.G. et al., 2016: The spectroscopic foundation of radiative forcing of climate by carbon dioxide. *Geophysical Research Letters*, doi:10.1002/2016gl068837.
Modak, A. and G. Bala, 2019: Efficacy of black carbon aerosols: The role of shortwave cloud feedback. *Environmental Research Letters*, doi:10.1088/1748-9326/ab21e7.
Modak, A., G. Bala, L. Cao, and K. Caldeira, 2016: Why must a solar forcing be larger than a CO2 forcing to cause the same global mean surface temperature change? *Environmental Research Letters*, **11(4)**, doi:10.1088/1748-9326/11/4/044013.
Modak, A., G. Bala, K. Caldeira, and L. Cao, 2018: Does shortwave absorption by methane influence its effectiveness? *Climate Dynamics*, 1–20, doi:10.1007/s00382-018-4102-x.
Morgenstern, O. et al., 2017: Review of the global models used within phase 1 of the Chemistry-Climate Model Initiative (CCMI). *Geoscientific Model Development*, doi:10.5194/gmd-10-639-2017.
Morgenstern, O. et al., 2020: Reappraisal of the climate impacts of ozone-depleting substances. *Earth and Space Science Open Archive*, doi:10.1002/essoar.10502742.1.
Morrison, A.L., J.E. Kay, W.R. Frey, H. Chepfer, and R. Guzman, 2018: Cloud Response to Arctic Sea Ice Loss and Implications for Future Feedbacks in the CESM1 Climate Model. *Journal of Geophysical Research: Atmospheres*, doi:10.1029/2018jd029142.
Moseid, K.O. et al., 2020: Bias in CMIP6 models compared to observed regional dimming and brightening trends (1961-2014). *Atmospheric Chemistry and Physics*, 1–20, doi:10.5194/acp-2019-1210.
Mueller, B. et al., 2013: Benchmark products for land evapotranspiration: LandFlux-EVAL multi-data set synthesis. *Hydrology and Earth System Sciences*, **17(10)**, 3707–3720, doi:10.5194/hess-17-3707-2013.
Mülmenstädt, J. et al., 2019: Separating radiative forcing by aerosol-cloud interactions and fast cloud adjustments in the ECHAM-HAMMOZ aerosol-climate model using the method of partial radiative perturbations. *Atmospheric Chemistry and Physics*, **19**, 15415–15429, doi:10.5194/acp-19-15415-2019.

Muñoz, I. and J.H. Schmidt, 2016: Methane oxidation, biogenic carbon, and the IPCC's emission metrics. Proposal for a consistent greenhouse-gas accounting. *International Journal of Life Cycle Assessment*, doi:10.1007/s11367-016-1091-z.

Murphy, D.M. and P.M. Forster, 2010: On the accuracy of deriving climate feedback parameters from correlations between surface temperature and outgoing radiation. *Journal of Climate*, doi:10.1175/2010jcli3657.1.

Murphy, J.M., 1995: Transient Response of the Hadley Centre Coupled Ocean-Atmosphere Model to Increasing Carbon Dioxide. Part III: Analysis of Global-Mean Response Using Simple Models. *Journal of Climate*, doi:10.1175/1520-0442(1995)008<0496:trothc>2.0.co;2.

Myers, T.A. and J.R. Norris, 2016: Reducing the uncertainty in subtropical cloud feedback. *Geophysical Research Letters*, **43(5)**, 2144–2148, doi:10.1002/2015gl067416.

Myhre, G., E.J. Highwood, K.P. Shine, and F. Stordal, 1998: New estimates of radiative forcing due to well mixed greenhouse gases. *Geophysical Research Letters*, **25(14)**, 2715–2718, doi:10.1029/98gl01908.

Myhre, G. et al., 2013a: Radiative forcing of the direct aerosol effect from AeroCom Phase II simulations. *Atmospheric Chemistry and Physics*, **13(4)**, 1853–1877, doi:10.5194/acp-13-1853-2013.

Myhre, G. et al., 2013b: Anthropogenic and Natural Radiative Forcing. In: *Climate Change 2013: The Physical Science Basis. Contribution of Working Group I to the Fifth Assessment Report of the Intergovernmental Panel on Climate Change* [Stocker, T.F., D. Qin, G.-K. Plattner, M. Tignor, S.K. Allen, J. Boschung, A. Nauels, Y. Xia, V. Bex, and P.M. Midgley (eds.)]. Cambridge University Press, Cambridge, United Kingdom and New York, NY, USA, pp. 659–740, doi:10.1017/ cbo9781107415324.018.

Myhre, G. et al., 2017: Multi-model simulations of aerosol and ozone radiative forcing due to anthropogenic emission changes during the period 1990-2015. *Atmospheric Chemistry and Physics*, doi:10.5194/acp-17-2709-2017.

Nabat, P., S. Somot, M. Mallet, A. Sanchez-Lorenzo, and M. Wild, 2014: Contribution of anthropogenic sulfate aerosols to the changing Euro-Mediterranean climate since 1980. *Geophysical Research Letters*, **41(15)**, 5605–5611, doi:10.1002/2014gl060798.

Nakajima, T., A. Higurashi, K. Kawamoto, and J.E. Penner, 2001: A possible correlation between satellite-derived cloud and aerosol microphysical parameters. *Geophysical Research Letters*, **28(7)**, 1171–1174, doi:10.1029/2000gl012186.

Namazi, M., K. von Salzen, and J.N.S. Cole, 2015: Simulation of black carbon in snow and its climate impact in the Canadian Global Climate Model. *Atmospheric Chemistry and Physics*, **15(18)**, 10887–10904, doi:10.5194/acp-15-10887-2015.

Narenpitak, P., C.S. Bretherton, and M.F. Khairoutdinov, 2017: Cloud and circulation feedbacks in a nearglobal aquaplanet cloudresolving model.. *Journal of Advances in Modeling Earth Systems*, **9**, 1069–1090.

Nazarenko, L. et al., 2017: Interactive nature of climate change and aerosol forcing. *Journal of Geophysical Research: Atmospheres*, **122(6)**, 3457–3480, doi:10.1002/2016jd025809.

Neubauer, D., M.W. Christensen, C.A. Poulsen, and U. Lohmann, 2017: Unveiling aerosol–cloud interactions – Part 2: Minimising the effects of aerosol swelling and wet scavenging in ECHAM6-HAM2 for comparison to satellite data. *Atmospheric Chemistry and Physics*, **17(21)**, 13165–13185, doi:10.5194/acp-17-13165-2017.

Newsom, E., L. Zanna, S. Khatiwala, and J.M. Gregory, 2020: The Influence of Warming Patterns on Passive Ocean Heat Uptake. *Geophysical Research Letters*, **47(18)**, doi:10.1029/2020gl088429.

Nicholls, Z.R.J. et al., 2020: Reduced Complexity Model Intercomparison Project Phase 1: introduction and evaluation of global-mean temperature response. *Geoscientific Model Development*, **13(11)**, 5175–5190, doi:10.5194/gmd-13-5175-2020.

Nijsse, F., P. Cox, and M. Williamson, 2020: An emergent constraint on Transient Climate Response from simulated historical warming in CMIP6 models. *Earth System Dynamics*, 1–14, doi:10.5194/esd-2019-86.

Norris, J.R. et al., 2016: Evidence for climate change in the satellite cloud record. *Nature*, **536(7614)**, 72, doi:10.1038/nature18273.

Notaro, M., S. Vavrus, and Z. Liu, 2007: Global vegetation and climate change due to future increases in CO_2 as projected by a fully coupled model with dynamic vegetation. *Journal of Climate*, **20(1)**, 70–90, doi:10.1175/jcli3989.1.

Notz, D., 2015: How well must climate models agree with observations? *Philosophical Transactions of the Royal Society A: Mathematical, Physical and Engineering Sciences*, **373(2052)**, 20140164, doi:10.1098/rsta.2014.0164.

Nummelin, A., C. Li, and P.J. Hezel, 2017: Connecting ocean heat transport changes from the midlatitudes to the Arctic Ocean. *Geophysical Research Letters*, doi:10.1002/2016gl071333.

O'Brien, C.L. et al., 2014: High sea surface temperatures in tropical warm pools during the Pliocene. *Nature Geoscience*, **7(8)**, 606–611, doi:10.1038/ngeo2194.

O'Connor, F.M. et al., 2021: Assessment of pre-industrial to present-day anthropogenic climate forcing in UKESM1. *Atmospheric Chemistry and Physics*, **21(2)**, 1211–1243, doi:10.5194/acp-21-1211-2021.

O'Gorman, P.A. and M.S. Singh, 2013: Vertical structure of warming consistent with an upward shift in the middle and upper troposphere. *Geophysical Research Letters*, **40(9)**, 1838–1842, doi:10.1002/grl.50328.

O'ishi, R., A. Abe-Ouchi, I.C. Prentice, and S. Sitch, 2009: Vegetation dynamics and plant CO_2 responses as positive feedbacks in a greenhouse world. *Geophysical Research Letters*, **36(11)**, 1–5, doi:10.1029/2009gl038217.

Ohmura, A., A. Bauder, H. Mueller, and G. Kappenberger, 2007: Long-term change of mass balance and the role of radiation. *Annals of Glaciology*, **46**, 367–374, doi:10.3189/172756407782871297.

Ohno, T., M. Satoh, and A. Noda, 2019: Fine Vertical Resolution Radiative-Convective Equilibrium Experiments: Roles of Turbulent Mixing on the High-Cloud Response to Sea Surface Temperatures. *Journal of Advances in Modeling Earth Systems*, **11(6)**, 1637–1654, doi:10.1029/2019ms001704.

Oldenburg, D., K.C. Armour, L.A. Thompson, and C.M. Bitz, 2018: Distinct mechanisms of ocean heat transport into the Arctic under internal variability and climate change. *Geophysical Research Letters*, doi:10.1029/2018gl078719.

Olonscheck, D., T. Mauritsen, and D. Notz, 2019: Arctic sea-ice variability is primarily driven by atmospheric temperature fluctuations. *Nature Geoscience*, **12(6)**, 430–434, doi:10.1038/s41561-019-0363-1.

Olonscheck, D., M. Rugenstein, and J. Marotzke, 2020: Broad Consistency Between Observed and Simulated Trends in Sea Surface Temperature Patterns. *Geophysical Research Letters*, **47(10)**, doi:10.1029/2019gl086773.

Otto, A. et al., 2013: Energy budget constraints on climate response. *Nature Geoscience*, **6(6)**, 415–416, doi:10.1038/ngeo1836.

Otto-Bliesner, B.L. et al., 2017: Amplified North Atlantic warming in the late Pliocene by changes in Arctic gateways. *Geophysical Research Letters*, **44(2)**, 957–964, doi:10.1002/2016gl071805.

Padilla, L.E., G.K. Vallis, and C.W. Rowley, 2011: Probabilistic estimates of transient climate sensitivity subject to uncertainty in forcing and natural variability. *Journal of Climate*, doi:10.1175/2011jcli3989.1.

Palmer, M.D., 2017: Reconciling Estimates of Ocean Heating and Earth's Radiation Budget. *Current Climate Change Reports*, **3(1)**, 78–86, doi:10.1007/s40641-016-0053-7.

Palmer, M.D. and D.J. McNeall, 2014: Internal variability of Earth's energy budget simulated by CMIP5 climate models. *Environmental Research Letters*, **9(3)**, 34016, doi:10.1088/1748-9326/9/3/034016.

Palmer, M.D., G.R. Harris, and J.M. Gregory, 2018: Extending CMIP5 projections of global mean temperature change and sea level rise due to thermal expansion using a physically-based emulator. *Environmental Research Letters*, **13(8)**, 84003, doi:10.1088/1748-9326/aad2e4.

Palmer, M.D., C.M. Domingues, A.B.A. Slangen, and F. Boeira Dias, 2021: An ensemble approach to quantify global mean sea-level rise over the 20th century from tide gauge reconstructions. *Environ. Res. Lett*, doi:10.1088/1748-9326/abdaec.

Parding, K., J.A. Olseth, K.F. Dagestad, and B.G. Liepert, 2014: Decadal variability of clouds, solar radiation and temperature at a high-latitude coastal site in Norway. *Tellus Series B-Chemical and Physical Meteorology*, **66**, doi:10.3402/tellusb.v66.25897.

Park, J.-Y., J.-S. Kug, J. Bader, R. Rolph, and M. Kwon, 2015: Amplified Arctic warming by phytoplankton under greenhouse warming. *Proceedings of the National Academy of Sciences*, **112(19)**, 5921–5926, doi:10.1073/pnas.1416884112.

Pattyn, F. et al., 2018: The Greenland and Antarctic ice sheets under 1.5°C global warming. *Nature Climate Change*, **8(12)**, 1053–1061, doi:10.1038/s41558-018-0305-8.

Pauling, A.G., I.J. Smith, P.J. Langhorne, and C.M. Bitz, 2017: Time-Dependent Freshwater Input From Ice Shelves: Impacts on Antarctic Sea Ice and the Southern Ocean in an Earth System Model. *Geophysical Research Letters*, doi:10.1002/2017gl075017.

Paulot, F., D. Paynter, P. Ginoux, V. Naik, and L.W. Horowitz, 2018: Changes in the aerosol direct radiative forcing from 2001 to 2015: Observational constraints and regional mechanisms. *Atmospheric Chemistry and Physics*, **18(17)**, 13265–13281, doi:10.5194/acp-18-13265-2018.

Payne, A.E., M.F. Jansen, and T.W. Cronin, 2015: Conceptual model analysis of the influence of temperature feedbacks on polar amplification. *Geophysical Research Letters*, **42(21)**, 9561–9570, doi:10.1002/2015gl065889.

Paynter, D., T.L. Frölicher, L.W. Horowitz, and L.G. Silvers, 2018: Equilibrium Climate Sensitivity Obtained From Multimillennial Runs of Two GFDL Climate Models. *Journal of Geophysical Research: Atmospheres*, **123(4)**, 1921–1941, doi:10.1002/2017jd027885.

Peng, J. et al., 2016: Markedly enhanced absorption and direct radiative forcing of black carbon under polluted urban environments.. *Proceedings of the National Academy of Sciences of the United States of America*, **113(16)**, 4266–71, doi:10.1073/pnas.1602310113.

Penner, J.E., L. Xu, and M. Wang, 2011: Satellite methods underestimate indirect climate forcing by aerosols.. *Proceedings of the National Academy of Sciences of the United States of America*, **108(33)**, 13404–8, doi:10.1073/pnas.1018526108.

Penner, J.E., C. Zhou, A. Garnier, and D.L. Mitchell, 2018: Anthropogenic Aerosol Indirect Effects in Cirrus Clouds. *Journal of Geophysical Research: Atmospheres*, **123(20)**, 11,652–11,677, doi:10.1029/2018jd029204.

Persad, G.G. and K. Caldeira, 2018: Divergent global-scale temperature effects from identical aerosols emitted in different regions. *Nature Communications*, doi:10.1038/s41467-018-05838-6.

Persad, G.G., Y. Ming, and V. Ramaswamy, 2014: The role of aerosol absorption in driving clear-sky solar dimming over East Asia. *Journal of Geophysical Research-Atmospheres*, **119(17)**, 10,410–10,424, doi:10.1002/2014jd021577.

Peters, G.P., B. Aamaas, T. Berntsen, and J.S. Fuglestvedt, 2011: The integrated global temperature change potential (iGTP) and relationships between emission metrics. *Environmental Research Letters*, doi:10.1088/1748-9326/6/4/044021.
Petersik, P. et al., 2018: Subgrid-scale variability in clear-sky relative humidity and forcing by aerosol–radiation interactions in an atmosphere model. *Atmospheric Chemistry and Physics*, **18(12)**, 8589–8599, doi:10.5194/acp-18-8589-2018.
Pfeifroth, U., A. Sanchez-Lorenzo, V. Manara, J. Trentmann, and R. Hollmann, 2018: Trends and Variability of Surface Solar Radiation in Europe Based On Surface- and Satellite-Based Data Records. *JOURNAL OF GEOPHYSICAL RESEARCH-ATMOSPHERES*, **123(3)**, 1735–1754, doi:10.1002/2017jd027418.
Pfister, P.L. and T.F. Stocker, 2017: State-Dependence of the Climate Sensitivity in Earth System Models of Intermediate Complexity. *Geophysical Research Letters*, **44(20)**, 10,643–10,653, doi:10.1002/2017gl075457.
Pierce, J.R., 2017: Cosmic rays, aerosols, clouds, and climate: Recent findings from the CLOUD experiment. *Journal of Geophysical Research: Atmospheres*, **122(15)**, 8051–8055, doi:10.1002/2017jd027475.
Pierrehumbert, R.T., 2014: Short-Lived Climate Pollution. *Annual Review of Earth and Planetary Sciences*, **42(1)**, 341–379, doi:10.1146/annurev-earth-060313-054843.
Pincus, R., P.M. Forster, and B. Stevens, 2016: The Radiative Forcing Model Intercomparison Project (RFMIP): Experimental protocol for CMIP6. *Geoscientific Model Development*, **9(9)**, 3447–3460, doi:10.5194/gmd-9-3447-2016.
Pincus, R. et al., 2015: Radiative flux and forcing parameterization error in aerosol-free clear skies. *Geophysical Research Letters*, **42(13)**, 5485–5492, doi:10.1002/2015gl064291.
Pincus, R. et al., 2020: Benchmark Calculations of Radiative Forcing by Greenhouse Gases. *Journal of Geophysical Research: Atmospheres*, **125(23)**, 1–15, doi:10.1029/2020jd033483.
Pistone, K., I. Eisenman, and V. Ramanathan, 2014: Observational determination of albedo decrease caused by vanishing Arctic sea ice. *Proc. Natl. Acad. Sci.*, **111(9)**, 3322–3326, doi:10.1073/pnas.1318201111.
Pithan, F. and T. Mauritsen, 2014: Arctic amplification dominated by temperature feedbacks in contemporary climate models. *Nature Geoscience*, **7(3)**, 181–184, doi:10.1038/ngeo2071.
Po-Chedley, S., C. Proistosescu, K.C. Armour, and B.D. Santer, 2018a: Climate constraint reflects forced signal. *Nature*, **563(7729)**, E6–E9, doi:10.1038/s41586-018-0640-y.
Po-Chedley, S., K.C. Armour, C.M. Bitz, M.D. Zelinka, and B.D. Santer, 2018b: Sources of intermodel spread in the lapse rate and water vapor feedbacks. *Journal of Climate*, doi:10.1175/jcli-d-17-0674.1.
Po-Chedley, S., M.D. Zelinka, N. Jeevanjee, T.J. Thorsen, and B.D. Santer, 2019: Climatology explains intermodel spread in tropical upper tropospheric cloud and relative humidity response to greenhouse warming. *Geophysical Research Letters*, doi:10.1029/2019gl084786.
Popp, M., H. Schmidt, and J. Marotzke, 2016: Transition to a Moist Greenhouse with CO2 and solar forcing. *Nature Communications*, **7**, 10627, doi:10.1038/ncomms10627.
Port, U., V. Brovkin, and M. Claussen, 2012: The influence of vegetation dynamics on anthropogenic climate change. *Earth System Dynamics*, **3(2)**, 233–243, doi:10.5194/esd-3-233-2012.
Posselt, R., R. Mueller, J. Trentmann, R. Stockli, and M.A. Liniger, 2014: A surface radiation climatology across two Meteosat satellite generations. *Remote Sensing of Environment*, **142**, 103–110, doi:10.1016/j.rse.2013.11.007.
Previdi, M., K.L. Smith, and L.M. Polvani, 2015: How Well Do the CMIP5 Models Simulate the Antarctic Atmospheric Energy Budget? *JOURNAL OF CLIMATE*, **28(20)**, 7933–7942, doi:10.1175/jcli-d-15-0027.1.
Proistosescu, C. and P.J. Huybers, 2017: Slow climate mode reconciles historical and model-based estimates of climate sensitivity. *Science Advances*, **3(7)**, 1–7, doi:10.1126/sciadv.1602821.
Proistosescu, C. et al., 2018: Radiative Feedbacks From Stochastic Variability in Surface Temperature and Radiative Imbalance. *Geophysical Research Letters*, doi:10.1029/2018gl077678.
Purich, A., M.H. England, W. Cai, A. Sullivan, and P.J. Durack, 2018: Impacts of broad-scale surface freshening of the Southern Ocean in a coupled climate model. *Journal of Climate*, doi:10.1175/jcli-d-17-0092.1.
Qian, Y. et al., 2015: Light-absorbing particles in snow and ice: Measurement and modeling of climatic and hydrological impact. *Advances in Atmospheric Sciences*, **32(1)**, 64–91, doi:10.1007/s00376-014-0010-0.
Qu, X. and A. Hall, 2007: What controls the strength of snow-albedo feedback? *J. Climate*, **20(15)**, 3971–3981, doi:10.1175/jcli4186.1.
Qu, X. and A. Hall, 2014: On the persistent spread in snow-albedo feedback. *Clim. Dyn.*, **42**, 69–81, doi:10.1007/s00382-013-1774-0.
Qu, X., A. Hall, S.A. Klein, and P.M. Caldwell, 2014: On the spread of changes in marine low cloud cover in climate model simulations of the 21st century. *Climate Dynamics*, doi:10.1007/s00382-013-1945-z.
Qu, X., A. Hall, S.A. Klein, and A.M. DeAngelis, 2015: Positive tropical marine low-cloud cover feedback inferred from cloud-controlling factors.. *Geophysical Research Letters*, **42**, 7767–7775, doi:10.1002/2015gl065627.
Qu, X. et al., 2018: On the emergent constraints of climate sensitivity. *Journal of Climate*, **31(2)**, 863–875, doi:10.1175/jcli-d-17-0482.1.
Quaas, J., O. Boucher, N. Bellouin, and S. Kinne, 2008: Satellite-based estimate of the direct and indirect aerosol climate forcing. *Journal of Geophysical Research: Atmospheres*, **113(D5)**, doi:10.1029/2007jd008962.

Quaas, J. et al., 2009: Aerosol indirect effects – general circulation model intercomparison and evaluation with satellite data. *Atmospheric Chemistry and Physics*, **9(22)**, 8697–8717, doi:10.5194/acp-9-8697-2009.
Radtke, J., T. Mauritsen, and C. Hohenegger, 2020: Shallow cumulus cloud feedback in large eddy simulations - Bridging the gap to storm resolving models. *Atmospheric Chemistry and Physics*, 1–19, doi:10.5194/acp-2020-1160.
Raes, F., H. Liao, W.-T. Chen, and J.H. Seinfeld, 2010: Atmospheric chemistry-climate feedbacks. *Journal of Geophysical Research (Atmospheres)*, **115(D12)**, D12121, doi:10.1029/2009jd013300.
Raghuraman, S.P., D. Paynter, and V. Ramaswamy, 2019: Quantifying the Drivers of the Clear Sky Greenhouse Effect, 2000-2016. *JOURNAL OF GEOPHYSICAL RESEARCH-ATMOSPHERES*, **124(21)**, 11354–11371, doi:10.1029/2019jd031017.
Rahimzadeh, F., A. Sanchez-Lorenzo, M. Hamedi, M.C. Kruk, and M. Wild, 2015: New evidence on the dimming/brightening phenomenon and decreasing diurnal temperature range in Iran (1961-2009). *Int. J. Climatol.*, **35**, 2065–2079, doi:10.1002/joc.4107.
Ramaswamy, V. et al., 2019: Radiative Forcing of Climate: The Historical Evolution of the Radiative Forcing Concept, the Forcing Agents and their Quantification, and Applications. *Meteorological Monographs*, **59**, 14.1–14.101, doi:10.1175/amsmonographs-d-19-0001.1.
Randall, D.A. et al., 2007: Climate Models and Their Evaluation. In: *Climate Change 2007: The Scientific Basis. Contribution of Working Group I to the Fourth Assessment Report of the Intergovernmental Panel on Climate Change* [Solomon, S., D. Qin, M. Manning, Z. Chen, M. Marquis, K.B. Averyt, M. Tignor, and H.L. Miller (eds.)]. Cambridge University Press, Cambridge, United Kingdom and New York, USA, pp. 589–662.
Randles, C.A. et al., 2017: The MERRA-2 Aerosol Reanalysis, 1980 Onward. Part I: System Description and Data Assimilation Evaluation. *Journal of Climate*, **30(17)**, 6823–6850, doi:10.1175/jcli-d-16-0609.1.
Raschke, E., S. Kinne, W.B. Rossow, P.W. Stackhouse, and M. Wild, 2016: Comparison of Radiative Energy Flows in Observational Datasets and Climate Modeling. *Journal of Applied Meteorology and Climatology*, **55(1)**, 93–117, doi:10.1175/jamc-d-14-0281.1.
Raval, A. and V. Ramanathan, 1989: Observational determination of the greenhouse effect. *Nature*, **342**, 758–761, doi:10.1038/342758a0.
Ravelo, A.C., K.T. Lawrence, A. Fedorov, and H.L. Ford, 2014: Comment on "A 12-million-year temperature history of the tropical Pacific Ocean". *Science*, **346(6216)**, 1467, doi:10.1126/science.1257618.
Rayner, N.A. et al., 2003: Global analyses of sea surface temperature, sea ice, and night marine air temperature since the late nineteenth century. *Journal of Geophysical Research*, **108(D14)**, 4407, doi:10.1029/2002jd002670.
Regayre, L.A. et al., 2018: Aerosol and physical atmosphere model parameters are both important sources of uncertainty in aerosol ERF. *Atmospheric Chemistry and Physics*, **18(13)**, 9975–10006, doi:10.5194/acp-18-9975-2018.
Reick, C.H., T. Raddatz, V. Brovkin, and V. Gayler, 2013: Representation of natural and anthropogenic land cover change in MPI-ESM. *Journal of Advances in Modeling Earth Systems*, **5(3)**, 459–482, doi:10.1002/jame.20022.
Rémy, S., N. Bellouin, A. Benedetti, and O. Boucher, 2018: Aerosols [in "State of the Climate in 2017"].. *Bull. Amer. Meteor. Soc.,*, **99(8)**, S49–S51, doi:10.1175/2018bamsstateoftheclimate.1.
Renoult, M. et al., 2020: A Bayesian framework for emergent constraints: case studies of climate sensitivity with PMIP. *Climate of The Past*, **16**, 1715–1735, doi:10.5194/cp-16-1715-2020.
Rhein, M. et al., 2013: Observations: Ocean. In: *Climate Change 2013: The Physical Science Basis. Contribution of Working Group I to the Fifth Assessment Report of the Intergovernmental Panel on Climate Change* [Stocker, T.F., D. Qin, G.-K. Plattner, M. Tignor, S.K. Allen, J. Boschung, A. Nauels, Y. Xia, V. Bex, and P.M. Midgley (eds.)]. Cambridge University Press, Cambridge, United Kingdom and New York, NY, USA, pp. 255–316, doi:10.1017/cbo9781107415324.010.
Ribes, A., S. Qasmi, and N. Gillett, 2021: Making climate projections conditional on historical observations. *Science Advances*, **7(4)**, eabc0671, doi:10.1126/sciadv.abc0671.
Richardson, M., K. Cowtan, and R.J. Millar, 2018: Global temperature definition affects achievement of long-term climate goals. *Environmental Research Letters*, **13(5)**, 054004, doi:10.1088/1748-9326/aab305.
Richardson, M., K. Cowtan, E. Hawkins, and M.B. Stolpe, 2016: Reconciled climate response estimates from climate models and the energy budget of Earth. *Nature Climate Change*, **6(10)**, 931–935, doi:10.1038/nclimate3066.
Richardson, T.B. et al., 2018: Carbon Dioxide Physiological Forcing Dominates Projected Eastern Amazonian Drying. *Geophysical Research Letters*, doi:10.1002/2017gl076520.
Richardson, T.B. et al., 2019: Efficacy of climate forcings in PDRMIP models. *Journal of Geophysical Research: Atmospheres*, **124**, 12,824–12,844, doi:10.1029/2019jd030581.
Richter, K. et al., 2020: Detecting a forced signal in satellite-era sea-level change. *Environmental Research Letters*, **15(9)**, doi:10.1088/1748-9326/ab986e.
Rienecker, M.M. et al., 2011: MERRA: NASA's Modern-Era Retrospective Analysis for Research and Applications. *Journal of Climate*, **24(14)**, 3624–3648, doi:10.1175/jcli-d-11-00015.1.
Ringer, M.A., T. Andrews, and M.J. Webb, 2014: Global-mean radiative feedbacks and forcing in atmosphere-only and

coupled atmosphere-ocean climate change experiments. *Geophysical Research Letters*, **41**, 4035–4042, doi:10.1002/ 2014gl060347.

Riser, S.C. et al., 2016: Fifteen years of ocean observations with the global Argo array. *Nature Climate Change*, **6(2)**, 145–153, doi:10.1038/nclimate2872.

Roberts, C.D., M.D. Palmer, D. McNeall, and M. Collins, 2015: Quantifying the likelihood of a continued hiatus in global warming. *Nature Climate Change*, **5(4)**, 337–342, doi:10.1038/nclimate2531.

Rodell, M. et al., 2018: Emerging trends in global freshwater availability. *Nature*, **557(7707)**, 651–659, doi:10.1038/s41586-018-0123-1.

Roe, G., 2009: Feedbacks, Timescales, and Seeing Red. *Annual Review of Earth and Planetary Sciences*, **37(1)**, 93–115, doi:10.1146/annurev.earth.061008.134734.

Roe, G.H. and M.B. Baker, 2007: Why Is Climate Sensitivity So Unpredictable? *Science*, **318(5850)**, 629–632, doi:10.1126/science.1144735.

Roe, G.H. and K.C. Armour, 2011: How sensitive is climate sensitivity? *Geophysical Research Letters*, **38(14)**, n/a–n/a, doi:10.1029/2011gl047913.

Roe, G.H., N. Feldl, K.C. Armour, Y.T. Hwang, and D.M.W. Frierson, 2015: The remote impacts of climate feedbacks on regional climate predictability. *Nature Geoscience*, doi:10.1038/ngeo2346.

Rogelj, J. and C.F. Schleussner, 2019: Unintentional unfairness when applying new greenhouse gas emissions metrics at country level. *Environmental Research Letters*, **14(11)**, 114039, doi:10.1088/1748-9326/ab4928.

Rogelj, J. et al., 2015: Zero emission targets as long-term global goals for climate protection. *Environmental Research Letters*, **10(10)**, 105007, doi:10.1088/1748-9326/10/10/105007.

Rogelj, J. et al., 2018: Mitigation Pathways Compatible with 1.5°C in the Context of Sustainable Development. In: *Global Warming of 1.5°C. An IPCC Special Report on the impacts of global warming of 1.5°C above pre-industrial levels and related global greenhouse gas emission pathways, in the context of strengthening the global response to the threat of climate change,* [Masson-Delmotte, V., P. Zhai, H.-O. Pörtner, D. Roberts, J. Skea, P.R. Shukla, A. Pirani, W. Moufouma-Okia, C. Péan, R. Pidcock, S. Connors, J.B.R. Matthews, Y. Chen, X. Zhou, M.I. Gomis, E. Lonnoy, T. Maycock, M. Tignor, and T. Waterfield (eds.)]. In Press, pp. 93–174.

Rohling, E.J. et al., 2012: Making sense of palaeoclimate sensitivity. *Nature*, **491(7426)**, 683–691, doi:10.1038/nature11574.

Rohrschneider, T., B. Stevens, and T. Mauritsen, 2019: On simple representations of the climate response to external radiative forcing. *Climate Dynamics*, doi:10.1007/s00382-019-04686-4.

Romps, D.M., 2014: An Analytical Model for Tropical Relative Humidity. *Journal of Climate*, **27(19)**, 7432–7449, doi:10.1175/jcli-d-14-00255.1.

Rose, B.E.J. and L. Rayborn, 2016: The Effects of Ocean Heat Uptake on Transient Climate Sensitivity. *Current Climate Change Reports*, doi:10.1007/s40641-016-0048-4.

Rose, B.E.J. and M.C. Rencurrel, 2016: The Vertical Structure of Tropospheric Water Vapor: Comparing Radiative and Ocean-Driven Climate Changes. *Journal of Climate*, **29(11)**, 4251–4268, doi:10.1175/jcli-d-15-0482.1.

Rose, B.E.J., K.C. Armour, D.S. Battisti, N. Feldl, and D.D.B. Koll, 2014: The dependence of transient climate sensitivity and radiative feedbacks on the spatial pattern of ocean heat uptake. *Geophysical Research Letters*, doi:10.1002/2013gl058955.

Rosenfeld, D. et al., 2019: Aerosol-driven droplet concentrations dominate coverage and water of oceanic low level clouds.. *Science (New York, N.Y.)*, doi:10.1126/science.aav0566.

Rostron, J.W. et al., 2020: The impact of performance filtering on climate feedbacks in a perturbed parameter ensemble. *Climate Dynamics*, **55(3–4)**, 521–551, doi:10.1007/s00382-020-05281-8.

Rotstayn, L.D. and J.E. Penner, 2001: Indirect aerosol forcing, quasi forcing, and climate response. *Journal of Climate*, doi:10.1175/1520-0442(2001)014<2960:iafqfa>2.0.co;2.

Rotstayn, L.D., M.A. Collier, D.T. Shindell, and O. Boucher, 2015: Why does aerosol forcing control historical global-mean surface temperature change in CMIP5 models? *Journal of Climate*, **28(17)**, 6608–6625, doi:10.1175/jcli-d-14-00712.1.

Rowlands, D.J. et al., 2012: Broad range of 2050 warming from an observationally constrained large climate model ensemble. *Nature Geoscience*, doi:10.1038/ngeo1430.

Rowlinson, M. et al., 2020: Tropospheric ozone radiative forcing uncertainty due to pre-industrial fire and biogenic emissions. *Atmospheric Chemistry and Physics*, doi:10.5194/acp-2019-1065.

Royer, D.L., 2016: Climate Sensitivity in the Geologic Past. *Annual Review of Earth and Planetary Sciences*, **44(1)**, 277–293, doi:10.1146/annurev-earth-100815-024150.

Rugenstein, M. et al., 2019a: LongRunMIP – motivation and design for a large collection of millennial-length AO-GCM simulations. *Bulletin of the American Meteorological Society*, doi:10.1175/bams-d-19-0068.1.

Rugenstein, M. et al., 2019b: Equilibrium climate sensitivity estimated by equilibrating climate models. *Geophysical Research Letters*, 2019GL083898, doi:10.1029/2019gl083898.

Rugenstein, M.A.A., K. Caldeira, and R. Knutti, 2016a: Dependence of global radiative feedbacks on evolving patterns of surface heat fluxes. *Geophysical Research Letters*, doi:10.1002/2016gl070907.

Rugenstein, M.A.A., M. Winton, R.J. Stouffer, S.M. Griffies, and R. Hallberg, 2013: Northern High-Latitude Heat Budget Decomposition and Transient Warming. *Journal of Climate*, **26(2)**, 609–621, doi:10.1175/jcli-d-11-00695.1.
Rugenstein, M.A.A., J.M. Gregory, N. Schaller, J. Sedlácek, and R. Knutti, 2016b: Multiannual ocean-atmosphere adjustments to radiative forcing. *Journal of Climate*, **29(15)**, 5643–5659, doi:10.1175/jcli-d-16-0312.1.
Russotto, R.D. and M. Biasutti, 2020: Polar Amplification as an Inherent Response of a Circulating Atmosphere: Results From the TRACMIP Aquaplanets. *Geophysical Research Letters*, **47(6)**, doi:10.1029/2019gl086771.
Rypdal, M., H.-B. Fredriksen, K. Rypdal, and R.J. Steene, 2018: Emergent constraints on climate sensitivity. *Nature*, **563(7729)**, E4–E5, doi:10.1038/s41586-018-0639-4.
Sagoo, N., P. Valdes, R. Flecker, L.J. Gregoire, and P.T.R.S. A, 2013: The Early Eocene equable climate problem: can perturbations of climate model parameters identify possible solutions? *Philosophical Transactions of the Royal Society of London A: Mathematical, Physical and Engineering Sciences*, **371(2001)**, doi:10.1098/rsta.2013.0123.
Saint-Lu, M., S. Bony, and J.-L. Dufresne, 2020: Observational Evidence for a Stability Iris Effect in the Tropics. *Geophysical Research Letters*, **47(14)**, e2020GL089059, doi:10.1029/2020gl089059.
Salzmann, M., 2017: The polar amplification asymmetry: role of Antarctic surface height. *Earth System Dynamics*, **8(2)**, 323–336, doi:10.5194/esd-8-323-2017.
Salzmann, U. et al., 2013: Challenges in quantifying Pliocene terrestrial warming revealed by data-model discord. *Nature Climate Change*, **3(11)**, 969–974, doi:10.1038/nclimate2008.
Sanchez-Lorenzo, A., J. Calbo, and M. Wild, 2013: Global and diffuse solar radiation in Spain: Building a homogeneous dataset and assessing their trends. *Global and Planetary Change*, **100**, 343–352, doi:10.1016/j.gloplacha.2012.11.010.
Sanchez-Lorenzo, A. et al., 2015: Reassessment and update of long-term trends in downward surface shortwave radiation over Europe (1939-2012). *Journal of Geophysical Research-Atmospheres*, **120(18)**, 9555–9569, doi:10.1002/2015jd023321.
Santer, B.D. et al., 2005: Amplification of Surface Temperature Trends and Variability in the Tropical Atmosphere. *Science*, **309(5740)**, 1551–1556, doi:10.1126/science.1114867.
Sato, Y. et al., 2018: Aerosol effects on cloud water amounts were successfully simulated by a global cloud-system resolving model. *Nature Communications*, **9(1)**, 985, doi:10.1038/s41467-018-03379-6.
Schleussner, C.F. et al., 2016: Science and policy characteristics of the Paris Agreement temperature goal. *Nature Climate Change*, **6(9)**, 827–835, doi:10.1038/nclimate3096.
Schleussner, C.-F., A. Nauels, M. Schaeffer, W. Hare, and J. Rogelj, 2019: Inconsistencies when applying novel metrics for emissions accounting to the Paris Agreement. *Environmental Research Letters*, doi:10.1088/1748-9326/ab56e7.
Schlund, M., A. Lauer, P. Gentine, S. Sherwood, and V. Eyring, 2020: Emergent constraints on Equilibrium Climate Sensitivity in CMIP5: do they hold for CMIP6? *Earth System Dynamics*, **11**, 1233–1258, doi:10.5194/esd-11-1233-2020.
Schmidt, A. et al., 2018: Volcanic Radiative Forcing From 1979 to 2015. *Journal of Geophysical Research: Atmospheres*, doi:10.1029/2018jd028776.
Schmidt, G.A. et al., 2014: Using palaeo-climate comparisons to constrain future projections in CMIP5. *Climate of the Past*, **10(1)**, 221–250, doi:10.5194/cp-10-221-2014.
Schmidt, G.A. et al., 2017a: Practice and philosophy of climate model tuning across six US modeling centers. *Geoscientific Model Development*, **10(9)**, 3207–3223, doi:10.5194/gmd-10-3207-2017.
Schmidt, G.A. et al., 2017b: Overestimate of committed warming. *Nature*, **547(7662)**, E16–E17, doi:10.1038/nature22803.
Schneider, A., M. Flanner, and J. Perket, 2018: Multidecadal Variability in Surface Albedo Feedback Across CMIP5 Models. *Geophysical Research Letters*, **45(4)**, 1972–1980, doi:10.1002/2017gl076293.
Schneider, T., C.M. Kaul, and K.G. Pressel, 2019: Possible climate transitions from breakup of stratocumulus decks under greenhouse warming. *Nature Geoscience*, **12(3)**, 163–167, doi:10.1038/s41561-019-0310-1.
Schneider von Deimling, T. et al., 2012: Estimating the near-surface permafrost-carbon feedback on global warming. *Biogeosciences*, **9(2)**, 649–665, doi:10.5194/bg-9-649-2012.
Schneider von Deimling, T. et al., 2015: Observation-based modelling of permafrost carbon fluxes with accounting for deep carbon deposits and thermokarst activity. *Biogeosciences*, **12**, 3469–3488, doi:10.5194/bg-12-3469-2015.
Schröder, M. et al., 2019: The GEWEX Water Vapor Assessment: Overview and Introduction to Results and Recommendations. *Remote Sensing*, **11(3)**, 251, doi:10.3390/rs11030251.
Schulz, M. et al., 2006: Radiative forcing by aerosols as derived from the AeroCom present-day and pre-industrial simulations. *Atmospheric Chemistry and Physics*, **6(12)**, 5225–5246, doi:10.5194/acp-6-5225-2006.
Schurer, A. et al., 2018: Estimating the Transient Climate Response from Observed Warming. *Journal of Climate*, **31(20)**, 8645–8663, doi:10.1175/jcli-d-17-0717.1.
Schwartz, S.E., 2007: Heat capacity, time constant, and sensitivity of Earth's climate system. *Journal of Geophysical Research Atmospheres*, **112(24)**, 1–12, doi:10.1029/2007jd008746.

Schwartz, S.E., 2012: Determination of Earth's Transient and Equilibrium Climate Sensitivities from Observations Over the Twentieth Century: Strong Dependence on Assumed Forcing. *Surveys in Geophysics*, **33(3–4)**, 745–777, doi:10.1007/s10712-012-9180-4.
Schwartz, S.E., 2018: Unrealized Global Temperature Increase: Implications of Current Uncertainties. *Journal of Geophysical Research: Atmospheres*, **123(7)**, 3462–3482, doi:10.1002/2017jd028121.
Schwarz, M., D. Folini, M.Z. Hakuba, and M. Wild, 2018: From Point to Area: Worldwide Assessment of the Representativeness of Monthly Surface Solar Radiation Records. *JOURNAL OF GEOPHYSICAL RESEARCH-ATMOSPHERES*, **123(24)**, 13857–13874, doi:10.1029/2018jd029169.
Schwarz, M., D. Folini, S. Yang, R.P. Allan, and M. Wild, 2020: Changes in atmospheric shortwave absorption as important driver of dimming and brightening. *Nature Geoscience*, **13(2)**, 110–115, doi:10.1038/s41561-019-0528-y.
Schweiger, A. et al., 2011: Uncertainty in modeled Arctic sea ice volume. *Journal of Geophysical Research: Oceans*, **116(C8)**, doi:10.1029/2011jc007084.
Scott, C.E. et al., 2017: Impact on short-lived climate forcers (SLCFs) from a realistic land-use change scenario via changes in biogenic emissions. *Faraday Discussions*, doi:10.1039/c7fd00028f.
Screen, J.A., C. Deser, and I. Simmonds, 2012: Local and remote controls on observed Arctic warming. *Geophysical Research Letters*, **39(10)**, doi:10.1029/2012gl051598.
Seager, R. et al., 2019: Strengthening tropical Pacific zonal sea surface temperature gradient consistent with rising greenhouse gases. *Nature Climate Change*, **9(7)**, 517–522, doi:10.1038/s41558-019-0505-x.
Seeley, J.T. and N. Jeevanjee, 2021: H2O Windows and CO2 Radiator Fins: A Clear-Sky Explanation for the Peak in Equilibrium Climate Sensitivity. *Geophysical Research Letters*, **48(4)**, e2020GL089609, doi:10.1029/2020gl089609.
Séférian, R. et al., 2019: Evaluation of CNRM Earth-System model, CNRM-ESM2-1: role of Earth system processes in present-day and future climate. *Journal of Advances in Modeling Earth Systems*, **11**, 2019MS001791, doi:10.1029/2019ms001791.
Seifert, A., T. Heus, R. Pincus, and B. Stevens, 2015: Large-eddy simulation of the transient and near-equilibrium behavior of precipitating shallow convection. *Journal of Advances in Modeling Earth Systems*, **7(4)**, 1918–1937, doi:10.1002/2015ms000489.
Seneviratne, S.I., M.G. Donat, A.J. Pitman, R. Knutti, and R.L. Wilby, 2016: Allowable CO2 emissions based on regional and impact-related climate targets. *Nature*, **529**, 477–483, doi:10.1038/nature16542.
Shaffer, G., M. Huber, R. Rondanelli, and J.O. Pepke Pedersen, 2016: Deep time evidence for climate sensitivity increase with warming. *Geophysical Research Letters*, **43(12)**, 6538–6545, doi:10.1002/2016gl069243.
Shapiro, A.V.A.I. et al., 2011: A new approach to the long-term reconstruction of the solar irradiance leads to large historical solar forcing. *Astronomy & Astrophysics*, **529**, A67, doi:10.1051/0004-6361/201016173.
Sherwood, S. et al., 2020a: An assessment of Earth's climate sensitivity using multiple lines of evidence. *Reviews of Geophysics*, **58(4)**, doi:10.1029/2019rg000678.
Sherwood, S. et al., 2020b: An assessment of Earth's climate sensitivity using multiple lines of evidence. *Reviews of Geophysics*, **58(4)**, doi:10.1029/2019rg000678.
Sherwood, S.C., S. Bony, and J.-L. Dufresne, 2014: Spread in model climate sensitivity traced to atmospheric convective mixing. *Nature*, **505(7481)**, 37–42, doi:10.1038/nature12829.
Sherwood, S.C., V. Dixit, and C. Salomez, 2018: The global warming potential of near-surface emitted water vapour. *Environmental Research Letters*, doi:10.1088/1748-9326/aae018.
Sherwood, S.C., R. Roca, T.M. Weckwerth, and N.G. Andronova, 2010a: Tropospheric water vapor, convection, and climate. *Reviews of Geophysics*, **48(2)**, doi:10.1029/2009rg000301.
Sherwood, S.C. et al., 2010b: Relative humidity changes in a warmer climate. *Journal of Geophysical Research: Atmospheres*, **115(D9)**, doi:10.1029/2009jd012585.
Sherwood, S.C. et al., 2015: Adjustments in the forcing-feedback framework for understanding climate change. *Bulletin of the American Meteorological Society*, **96(2)**, 217–228, doi:10.1175/bams-d-13-00167.1.
Shindell, D.T., 2014: Inhomogeneous forcing and transient climate sensitivity. *Nature Climate Change*, **4**, 274–277, doi:10.1038/nclimate2136.
Shindell, D.T., J.S. Fuglestvedt, and W.J. Collins, 2017: The social cost of methane: Theory and applications. *Faraday Discussions*, doi:10.1039/c7fd00009j.
Shindell, D.T. et al., 2009: Improved attribution of climate forcing to emissions. *Science*, doi:10.1126/science.1174760.
Shindell, D.T. et al., 2013: Radiative forcing in the ACCMIP historical and future climate simulations. *Atmospheric Chemistry and Physics*, **13(6)**, 2939–2974, doi:10.5194/acp-13-2939-2013.
Shindell, D.T.D.T., G. Faluvegi, L. Rotstayn, and G. Milly, 2015: Spatial patterns of radiative forcing and surface temperature response. *Journal of Geophysical Research: Atmospheres*, **120**, 1–19, doi:10.1002/2014jd022752.
Shine, K.P., R.G. Derwent, D.J. Wuebbles, and J.-J. Morcrette, 1990: Radiative Forcing of Climate. In: *Climate Change: The IPCC Scientific Assessment* [Houghton, J.T., J.G. Jenkins, and J.J. Ephraums (eds.)]. Cambridge University Press, Cambridge, United Kingdom and New York, NY, USA, pp. 41–68.
Shine, K.P., J. Cook, E.J. Highwood, and M.M. Joshi, 2003: An alternative to radiative forcing for estimating the

relative importance of climate change mechanisms. *Geophysical Research Letters*, doi:10.1029/2003gl018141.
Shine, K.P., J.S. Fuglestvedt, K. Hailemariam, and N. Stuber, 2005: Alternatives to the Global Warming Potential for comparing climate impacts of emissions of greenhouse gases. *Climatic Change*, **68(3)**, 281–302, doi:10.1007/s10584-005-1146-9.
Shine, K.P.P., R.P.P. Allan, W.J.J. Collins, and J.S.S. Fuglestvedt, 2015: Metrics for linking emissions of gases and aerosols to global precipitation changes. *Earth System Dynamics*, **6(2)**, 525–540, doi:10.5194/esd-6-525-2015.
Siler, N., S. Po-Chedley, and C.S. Bretherton, 2018a: Variability in modeled cloud feedback tied to differences in the climatological spatial pattern of clouds. *Climate Dynamics*, **50(3)**, 1209–1220, doi:10.1007/s00382-017-3673-2.
Siler, N., G.H. Roe, and K.C. Armour, 2018b: Insights into the zonal-mean response of the hydrologic cycle to global warming from a diffusive energy balance model. *Journal of Climate*, doi:10.1175/jcli-d-18-0081.1.
Silvers, L.G., D. Paynter, and M. Zhao, 2018: The Diversity of Cloud Responses to Twentieth Century Sea Surface Temperatures. *Geophysical Research Letters*, **45(1)**, 391–400, doi:10.1002/2017gl075583.
Singarayer, J.S., P.J. Valdes, P. Friedlingstein, S. Nelson, and D.J. Beerling, 2011: Late Holocene methane rise caused by orbitally controlled increase in tropical sources. *Nature*, **470(7332)**, 82–85, doi:10.1038/nature09739.
Singh, H.A., P.J. Rasch, and B.E.J. Rose, 2017: Increased Ocean Heat Convergence Into the High Latitudes With CO2 Doubling Enhances Polar-Amplified Warming. *Geophysical Research Letters*, doi:10.1002/2017gl074561.
Sitch, S. et al., 2008: Evaluation of the terrestrial carbon cycle, future plant geography and climate-carbon cycle feedbacks using five Dynamic Global Vegetation Models (DGVMs). *Global Change Biology*, **14(9)**, 2015–2039, doi:10.1111/j.1365-2486.2008.01626.x.
Skeie, R.B., G.P. Peters, J. Fuglestvedt, and R. Andrew, 2021: A future perspective of historical contributions to climate change. *Climatic Change*, **164(1–2)**, 1–13, doi:10.1007/s10584-021-02982-9.
Skeie, R.B., T. Berntsen, M. Aldrin, M. Holden, and G. Myhre, 2018: Climate sensitivity estimates - Sensitivity to radiative forcing time series and observational data. *Earth System Dynamics*, **9(2)**, 879–894, doi:10.5194/esd-9-879-2018.
Skeie, R.B. et al., 2017: Perspective has a strong effect on the calculation of historical contributions to global warming. *Environmental Research Letters*, **12(2)**, 024022, doi:10.1088/1748-9326/aa5b0a.
Skeie, R.B. et al., 2020: Historical total ozone radiative forcing derived from CMIP6 simulations. *npj Climate and Atmospheric Science*, doi:10.1038/s41612-020-00131-0.
Skinner, L., 2012: A Long View on Climate Sensitivity. *Science*, **337(6097)**, 917–919, doi:10.1126/science.1224011.
Slater, T. et al., 2021: Review article: Earth's ice imbalance. *The Cryosphere*, **15(1)**, 233–246, doi:10.5194/tc-15-233-2021.
Smith, C.J., R.J. Kramer, and A. Sima, 2020a: The HadGEM3-GA7.1 radiative kernel: The importance of a well-resolved stratosphere. *Earth System Science Data*, **12(3)**, 2157–2168, doi:10.5194/essd-12-2157-2020.
Smith, C.J. et al., 2018a: FAIR v1.3: A simple emissions-based impulse response and carbon cycle model. *Geoscientific Model Development*, doi:10.5194/gmd-11-2273-2018.
Smith, C.J. et al., 2018b: Understanding Rapid Adjustments to Diverse Forcing Agents. *Geophysical Research Letters*, **45(21)**, doi:10.1029/2018gl079826.
Smith, C.J. et al., 2019: Current fossil fuel infrastructure does not yet commit us to 1.5°C warming. *Nature Communications*, doi:10.1038/s41467-018-07999-w.
Smith, C.J. et al., 2020b: Effective radiative forcing and adjustments in CMIP6 models. *Atmospheric Chemistry and Physics*, **20(16)**, 9591–9618, doi:10.5194/acp-20-9591-2020.
Smith, D.M. et al., 2016: Role of volcanic and anthropogenic aerosols in the recent global surface warming slowdown. *Nature Climate Change*, **6(10)**, 936–940, doi:10.1038/nclimate3058.
Smith, M.A., M. Cain, and M.R. Allen, 2021: Further improvement of warming-equivalent emissions calculation. *npj Climate and Atmospheric Science*, **accepted**, doi:10.1038/s41612-021-00169-8.
Smith, S.M. et al., 2012: Equivalence of greenhouse-gas emissions for peak temperature limits. *Nature Climate Change*, **2(7)**, 535–538, doi:10.1038/nclimate1496.
Snyder, C.W., 2016: Evolution of global temperature over the past two million years. *Nature*, **538(7624)**, 226–228, doi:10.1038/nature19798.
Snyder, C.W., 2019: Revised estimates of paleoclimate sensitivity over the past 800,000 years. *Climatic Change*, **156(1)**, 121–138, doi:10.1007/s10584-019-02536-0.
Soden, B.J. and I.M. Held, 2006: An Assessment of Climate Feedbacks in Coupled Ocean–Atmosphere Models. *Journal of Climate*, **19(14)**, 3354–3360, doi:10.1175/jcli3799.1.
Soden, B.J., D.L. Jackson, V. Ramaswamy, M.D. Schwarzkopf, and X. Huang, 2005: The Radiative Signature of Upper Tropospheric Moistening. *Science*, **310(5749)**, 841–844, doi:10.1126/science.1115602.
Soden, B.J. et al., 2008: Quantifying climate feedbacks using radiative kernels. *Journal of Climate*, **21(14)**, 3504–3520, doi:10.1175/2007jcli2110.1.
Soden, B.J.J., W.D.D. Collins, and D.R.R. Feldman, 2018: Reducing uncertainties in climate models. *Science*, **361(6400)**, 326–327, doi:10.1126/science.aau1864.
Sohn, B.J., S.W. Yeh, J. Schmetz, and H.J. Song, 2013: Observational evidences of Walker circulation change over the

last 30 years contrasting with GCM results. *Climate Dynamics*, **40(7–8)**, 1721–1732, doi:10.1007/s00382-012-1484-z.
Soni, V.K., G. Pandithurai, and D.S. Pai, 2016: Is there a transition of solar radiation from dimming to brightening over India? *ATMOSPHERIC RESEARCH*, **169(A)**, 209–224, doi:10.1016/j.atmosres.2015.10.010.
Spencer, R.W. and W.D. Braswell, 2010: On the diagnosis of radiative feedback in the presence of unknown radiative forcing. *Journal of Geophysical Research Atmospheres*, doi:10.1029/2009jd013371.
Spencer, R.W. and W.D. Braswell, 2011: On the misdiagnosis of surface temperature feedbacks from variations in Earth's radiant energy balance. *Remote Sensing*, doi:10.3390/rs3081603.
Stanhill, G., O. Achiman, R. Rosa, and S. Cohen, 2014: The cause of solar dimming and brightening at the Earth's surface during the last half century: Evidence from measurements of sunshine duration. *JOURNAL OF GEOPHYSICAL RESEARCH-ATMOSPHERES*, **119(18)**, 10902–10911, doi:10.1002/2013jd021308.
Stap, L.B., P. Köhler, and G. Lohmann, 2019: Including the efficacy of land ice changes in deriving climate sensitivity from paleodata. *Earth System Dynamics*, **10(2)**, 333–345, doi:10.5194/esd-10-333-2019.
Steffen, W. et al., 2018: Trajectories of the Earth System in the Anthropocene. *Proceedings of the National Academy of Sciences*, **115(33)**, 8252–8259, doi:10.1073/pnas.1810141115.
Stein, T.H.M., C.E. Holloway, I. Tobin, and S. Bony, 2017: Observed Relationships between Cloud Vertical Structure and Convective Aggregation over Tropical Ocean. *Journal of Climate*, **30(6)**, 2187–2207, doi:10.1175/jcli-d-16-0125.1.
Steiner, A.K. et al., 2020: Observed temperature changes in the troposphere and stratosphere from 1979 to 2018. *Journal of Climate*, doi:10.1175/jcli-d-19-0998.1.
Steinhilber, F. et al., 2012: 9,400 years of cosmic radiation and solar activity from ice cores and tree rings. *Proceedings of the National Academy of Sciences*, **109(16)**, 5967–5971, doi:10.1073/pnas.1118965109.
Steinthorsdottir, M. et al., 2020: The Miocene: the Future of the Past. *Paleoceanography and Paleoclimatology*, e2020PA004037, doi:10.1029/2020pa004037.
Stephens, G.L. et al., 2015: The albedo of Earth. *Reviews of Geophysics*, **53(1)**, 141–163, doi:10.1002/2014rg000449.
Sterner, E., D.J.A. Johansson, and C. Azar, 2014: Emission metrics and sea level rise. *Climatic Change*, **127(2)**, 335–351, doi:10.1007/s10584-014-1258-1.
Sterner, E.O. and D.J.A. Johansson, 2017: The effect of climate-carbon cycle feedbacks on emission metrics. *Environmental Research Letters*, doi:10.1088/1748-9326/aa61dc.
Stevens, B., 2015: Rethinking the lower bound on aerosol radiative forcing. *Journal of Climate*, **28(12)**, 4794–4819, doi:10.1175/jcli-d-14-00656.1.
Stevens, B. and G. Feingold, 2009: Untangling aerosol effects on clouds and precipitation in a buffered system. *Nature*, **461(7264)**, 607–613, doi:10.1038/nature08281.
Stevens, B., S.C. Sherwood, S. Bony, and M.J. Webb, 2016: Prospects for narrowing bounds on Earth's equilibrium climate sensitivity. *Earth's Future*, **4(11)**, 512–522, doi:10.1002/2016ef000376.
Stier, P., 2016: Limitations of passive remote sensing to constrain global cloud condensation nuclei. *Atmospheric Chemistry and Physics*, **16(10)**, 6595–6607, doi:10.5194/acp-16-6595-2016.
Stjern, C.W. et al., 2017: Rapid Adjustments Cause Weak Surface Temperature Response to Increased Black Carbon Concentrations. *Journal of Geophysical Research: Atmospheres*, doi:10.1002/2017jd027326.
Stjern, C.W. et al., 2019: Arctic Amplification Response to Individual Climate Drivers. *Journal of Geophysical Research: Atmospheres*, **124(13)**, 6698–6717, doi:10.1029/2018jd029726.
Stocker, B.D. et al., 2013: Multiple greenhouse-gas feedbacks from the land biosphere under future climate change scenarios. *Nature Climate Change*, **3(7)**, 666–672, doi:10.1038/nclimate1864.
Stolpe, M.B., I. Medhaug, U. Beyerle, and R. Knutti, 2019: Weak dependence of future global mean warming on the background climate state. *Climate Dynamics*, **53(7)**, 5079–5099, doi:10.1007/s00382-019-04849-3.
Storelvmo, T., 2017: Aerosol Effects on Climate via Mixed-Phase and Ice Clouds. *Annual Review of Earth and Planetary Sciences*, doi:10.1146/annurev-earth-060115-012240.
Storelvmo, T., T. Leirvik, U. Lohmann, P.C.B. Phillips, and M. Wild, 2016: Disentangling greenhouse warming and aerosol cooling to reveal Earth's climate sensitivity. *Nature Geoscience*, **9(4)**, 286–289, doi:10.1038/ngeo2670.
Storelvmo, T. et al., 2018: Lethargic response to aerosol emissions in current climate models. *Geophysical Research Letters*, **45(18)**, 9, doi:10.1029/2018gl078298.
Stouffer, R.J. and S. Manabe, 2003: Equilibrium response of thermohaline circulation to large changes in atmospheric CO2 concentration. *Climate Dynamics*, **20(7–8)**, 759–773, doi:10.1007/s00382-002-0302-4.
Streets, D.G., Y. Wu, and M. Chin, 2006: Two-decadal aerosol trends as a likely explanation of the global dimming/brightening transition. *GEOPHYSICAL RESEARCH LETTERS*, **33(15)**, doi:10.1029/2006gl026471.
Stroeve, J.C. et al., 2012: Trends in Arctic sea ice extent from CMIP5, CMIP3 and observations. *Geophys. Res. Lett.*, **39(16)**, doi:10.1029/2012gl052676.
Stuber, N., M. Ponater, and R. Sausen, 2005: Why radiative forcing might fail as a predictor of climate change. *Climate Dynamics*, doi:10.1007/s00382-004-0497-7.
Stuecker, M.F. et al., 2018: Polar amplification dominated by local forcing and feedbacks. *Nature Climate Change*,

8(12), 1076–1081, doi:10.1038/s41558-018-0339-y.
Su, H. et al., 2014: Weakening and strengthening structures in the Hadley Circulation change under global warming and implications for cloud response and climate sensitivity. *Journal of Geophysical Research: Atmospheres*, **119(10)**, 5787–5805, doi:10.1002/2014jd021642.
Su, H. et al., 2017: Tightening of tropical ascent and high clouds key to precipitation change in a warmer climate. *Nature Communications*, **8(1)**, 15771, doi:10.1038/ncomms15771.
Sun, C. et al., 2017: Western tropical Pacific multidecadal variability forced by the Atlantic multidecadal oscillation. *Nature Communications*, **8**, doi:10.1038/ncomms15998.
Super, J.R. et al., 2018: North Atlantic temperature and pCO2 coupling in the early-middle Miocene. *Geology*, **46(6)**, 519–522, doi:10.1130/g40228.1.
Sutton, R.T., 2018: ESD Ideas: A simple proposal to improve the contribution of IPCC WGI to the assessment and communication of climate change risks. *Earth System Dynamics*, **9(4)**, 1155–1158, doi:10.5194/esd-9-1155-2018.
Svensmark, H., 1998: Influence of Cosmic Rays on Earth's Climate. *Phys. Rev. Lett.*, **81(22)**, 5027–5030, doi:10.1103/physrevlett.81.5027.
Svensmark, H., T. Bondo, and J. Svensmark, 2009: Cosmic ray decreases affect atmospheric aerosols and clouds. *Geophysical Research Letters*, **36(15)**, doi:10.1029/2009gl038429.
Svensmark, H., M.B. Enghoff, N.J. Shaviv, and J. Svensmark, 2017: Increased ionization supports growth of aerosols into cloud condensation nuclei. *Nature Communications*, **8(1)**, 1–9, doi:10.1038/s41467-017-02082-2.
Svensmark, J., M.B. Enghoff, N.J. Shaviv, and H. Svensmark, 2016: The response of clouds and aerosols to cosmic ray decreases. *Journal of Geophysical Research: Space Physics*, **121(9)**, 8152–8181, doi:10.1002/2016ja022689.
Swingedouw, D. et al., 2008: Antarctic ice-sheet melting provides negative feedbacks on future climate warming. *Geophysical Research Letters*, **35(17)**, doi:10.1029/2008gl034410.
Takahashi, C. and M. Watanabe, 2016: Pacific trade winds accelerated by aerosol forcing over the past two decades. *Nature Climate Change*, **6(8)**, 768–772, doi:10.1038/nclimate2996.
Takahashi, H., H. Su, and J.H. Jiang, 2016: Water vapor changes under global warming and the linkage to present-day interannual variabilities in CMIP5 models. *Climate Dynamics*, **47(12)**, 3673–3691, doi:10.1007/s00382-016-3035-5.
Takemura, T. and K. Suzuki, 2019: Weak global warming mitigation by reducing black carbon emissions. *Scientific Reports*, **9(1)**, doi:10.1038/s41598-019-41181-6.
Tan, I., T. Storelvmo, and M.D. Zelinka, 2016: Observational constraints on mixed-phase clouds imply higher climate sensitivity. *Science*, **352(6282)**, 224–227, doi:10.1126/science.aad5300.
Tan, I., L. Oreopoulos, and N. Cho, 2019: The Role of Thermodynamic Phase Shifts in Cloud Optical Depth Variations With Temperature. *Geophysical Research Letters*, **46(8)**, 4502–4511, doi:10.1029/2018gl081590.
Tanaka, K. and B.C. O'Neill, 2018: The Paris Agreement zero-emissions goal is not always consistent with the 1.5°C and 2°C temperature targets. *Nature Climate Change*, doi:10.1038/s41558-018-0097-x.
Tanaka, K., D.J.A. Johansson, B.C. O'Neill, and J.S. Fuglestvedt, 2013: Emission metrics under the 2°C climate stabilization target. *Climatic Change*, doi:10.1007/s10584-013-0693-8.
Tanaka, K., A. Ohmura, D. Folini, M. Wild, and N. Ohkawara, 2016: Is global dimming and brightening in Japan limited to urban areas? *ATMOSPHERIC CHEMISTRY AND PHYSICS*, **16(21)**, 13969–14001, doi:10.5194/acp-16-13969-2016.
Tang, T. et al., 2019: Comparison of Effective Radiative Forcing Calculations Using Multiple Methods, Drivers, and Models. *Journal of Geophysical Research: Atmospheres*, **124(8)**, 4382–4394, doi:10.1029/2018jd030188.
Tao, W.K., J.P. Chen, Z. Li, C. Wang, and C. Zhang, 2012: Impact of aerosols on convective clouds and precipitation. *Reviews of Geophysics*, doi:10.1029/2011rg000369.
Taylor, P.C., S. Kato, K.-M. Xu, and M. Cai, 2015: Covariance between Arctic sea ice and clouds within atmospheric state regimes at the satellite footprint level. *Journal of Geophysical Research: Atmospheres*, **120(24)**, 12656–12678, doi:10.1002/2015jd023520.
Taylor, P.C. et al., 2013: A Decomposition of Feedback Contributions to Polar Warming Amplification. *Journal of Climate*, **26(18)**, 7023–7043, doi:10.1175/jcli-d-12-00696.1.
Tebaldi, C. and J.M. Arblaster, 2014: Pattern scaling: Its strengths and limitations, and an update on the latest model simulations. *Climatic Change*, doi:10.1007/s10584-013-1032-9.
Tebaldi, C. and R. Knutti, 2018: Evaluating the accuracy of climate change pattern emulation for low warming targets. *Environmental Research Letters*, **13(5)**, 55006, doi:10.1088/1748-9326/aabef2.
Terai, C.R., S.A. Klein, and M.D. Zelinka, 2016: Constraining the lowcloud optical depth feedback at middle and high latitudes using satellite observations.. *Journal of Geophysical Research*, **121**, 9696–9716, doi:10.1002/2016jd025233.
Terai, C.R. et al., 2019: Mechanisms Behind the Extratropical Stratiform Low-Cloud Optical Depth Response to Temperature in ARM Site Observations. *Journal of Geophysical Research: Atmospheres*, **124(4)**, 2127–2147, doi:10.1029/2018jd029359.
Thackeray, C.W. and A. Hall, 2019: An emergent constraint on future Arctic sea-ice albedo feedback. *Nature Climate*

Change, doi:10.1038/s41558-019-0619-1.
Thomas, C.M., B. Dong, and K. Haines, 2020: Inverse modeling of global and regional energy and water cycle fluxes using earth observation data. *Journal of Climate*, **33(5)**, 1707–1723, doi:10.1175/jcli-d-19-0343.1.
Thompson, D.W.J., S. Bony, and Y. Li, 2017: Thermodynamic constraint on the depth of the global tropospheric circulation. *Proceedings of the National Academy of Sciences*, **114(31)**, 8181 LP – 8186, doi:10.1073/pnas.1620493114.
Thornhill, G. et al., 2021: Climate-driven chemistry and aerosol feedbacks in CMIP6 Earth system models. *Atmospheric Chemistry and Physics*, **21(2)**, 1105–1126, doi:10.5194/acp-21-1105-2021.
Thornhill, G.D. et al., 2021: Effective radiative forcing from emissions of reactive gases and aerosols-A multi-model comparison. *Atmospheric Chemistry and Physics*, **21(2)**, 853–874, doi:10.5194/acp-21-853-2021.
Tian, B., 2015: Spread of model climate sensitivity linked to double-Intertropical Convergence Zone bias. *Geophysical Research Letters*, **42(10)**, 4133–4141, doi:10.1002/2015gl064119.
Tierney, J.E., A.M. Haywood, R. Feng, T. Bhattacharya, and B.L. Otto-Bliesner, 2019: Pliocene Warmth Consistent With Greenhouse Gas Forcing. *Geophysical Research Letters*, **46(15)**, 9136–9144, doi:10.1029/2019gl083802.
Tierney, J.E. et al., 2020a: Past climates inform our future. *Science*, **370(6517)**, doi:10.1126/science.aay3701.
Tierney, J.E. et al., 2020b: Glacial cooling and climate sensitivity revisited. *Nature*, **584(7822)**, 569–573, doi:10.1038/s41586-020-2617-x.
Tokarska, K.B., N.P. Gillett, V.K. Arora, W.G. Lee, and K. Zickfeld, 2018: The influence of non-CO2 forcings on cumulative carbon emissions budgets. *Environmental Research Letters*, **13**, 034039, doi:10.1088/1748-9326/aaafdd.
Tokarska, K.B. et al., 2020: Past warming trend constrains future warming in CMIP6 models. *Science Advances*, **6(12)**, 1–14, doi:10.1126/sciadv.aaz9549.
Toll, V., M. Christensen, S. Gassó, and N. Bellouin, 2017: Volcano and Ship Tracks Indicate Excessive Aerosol-Induced Cloud Water Increases in a Climate Model. *Geophysical Research Letters*, **44(24)**, 12,492–12,500, doi:10.1002/2017gl075280.
Toll, V., M. Christensen, J. Quaas, and N. Bellouin, 2019: Weak average liquid-cloud-water response to anthropogenic aerosols. *Nature*, **572(7767)**, 51–55, doi:10.1038/s41586-019-1423-9.
Tomassini, L., A. Voigt, and B. Stevens, 2015: On the connection between tropical circulation, convective mixing, and climate sensitivity. *Quarterly Journal of the Royal Meteorological Society*, **141(689)**, 1404–1416, doi:10.1002/qj.2450.
Toohey, M. and M. Sigl, 2017: Volcanic stratospheric sulfur injections and aerosol optical depth from 500 BCE to 1900 CE. *Earth System Science Data*, **9(2)**, 809–831, doi:10.5194/essd-9-809-2017.
Trenberth, K.E. and J.T. Fasullo, 2010: Simulation of Present-Day and Twenty-First-Century Energy Budgets of the Southern Oceans. *JOURNAL OF CLIMATE*, **23(2)**, 440–454, doi:10.1175/2009jcli3152.1.
Trenberth, K.E., J.T. Fasullo, and M.A. Balmaseda, 2014: Earth's Energy Imbalance. *JOURNAL OF CLIMATE*, **27(9)**, 3129–3144, doi:10.1175/jcli-d-13-00294.1.
Trenberth, K.E., Y. Zhang, J.T. Fasullo, and S. Taguchi, 2015: Climate variability and relationships between top-of-atmosphere radiation and temperatures on Earth. *Journal of Geophysical Research: Atmospheres*, **120(9)**, 3642–3659, doi:10.1002/2014jd022887.
Tselioudis, G., B.R. Lipat, D. Konsta, K.M. Grise, and L.M. Polvani, 2016: Midlatitude cloud shifts, their primary link to the Hadley cell, and their diverse radiative effects. *Geophys. Res. Lett.*, **43**, 4594–4601, doi:10.1002/2016gl068242.
Tsushima, Y. and S. Manabe, 2013: Assessment of radiative feedback in climate models using satellite observations of annual flux variation. *Proceedings of the National Academy of Sciences*, doi:10.1073/pnas.1216174110.
Tsushima, Y., M.A. Ringer, G.M. Martin, J.W. Rostron, and D.M.H. Sexton, 2020: Investigating physical constraints on climate feedbacks using a perturbed parameter ensemble. *Climate Dynamics*, **55(5–6)**, 1159–1185, doi:10.1007/s00382-020-05318-y.
Tsushima, Y. et al., 2014: High cloud increase in a perturbed SST experiment with a global nonhydrostatic model including explicit convective processes.. *Journal of Advances in Modeling Earth Systems*, **6**, 571–585, doi:10.1002/2013ms000301.
Tsutsui, J., 2020: Diagnosing Transient Response to CO2 Forcing in Coupled Atmosphere-Ocean Model Experiments Using a Climate Model Emulator. *Geophysical Research Letters*, **47(7)**, 1–12, doi:10.1029/2019gl085844.
Turnock, S.T. et al., 2015: Modelled and observed changes in aerosols and surface solar radiation over Europe between 1960 and 2009. *ATMOSPHERIC CHEMISTRY AND PHYSICS*, **15(16)**, 9477–9500, doi:10.5194/acp-15-9477-2015.
Tuzet, F. et al., 2017: A multilayer physically based snowpack model simulating direct and indirect radiative impacts of light-absorbing impurities in snow. *The Cryosphere*, **11(6)**, 2633–2653, doi:10.5194/tc-11-2633-2017.
Twomey, S., 1959: The nuclei of natural cloud formation part II: The supersaturation in natural clouds and the variation of cloud droplet concentration. *Geofisica Pura e Applicata*, **43(1)**, 243–249, doi:10.1007/bf01993560.
Ullrich, R. et al., 2017: A New Ice Nucleation Active Site Parameterization for Desert Dust and Soot. *Journal of the Atmospheric Sciences*, **74(3)**, 699–717, doi:10.1175/jas-d-16-0074.1.

Unger, N., 2014: Human land-use-driven reduction of forest volatiles cools global climate. *Nature Climate Change*, doi:10.1038/nclimate2347.
Usoskin, I.G. et al., 2015: The Maunder minimum (1645–1715) was indeed a grand minimum: A reassessment of multiple datasets. *Astronomy & Astrophysics*, **581**, A95, doi:10.1051/0004-6361/201526652.
Vaillant de Guélis, T. et al., 2018: Space lidar observations constrain longwave cloud feedback. *Scientific Reports*, **8(1)**, 16570, doi:10.1038/s41598-018-34943-1.
Vanderkelen, I. et al., 2020: Global Heat Uptake by Inland Waters. *Geophysical Research Letters*, **47(12)**, e2020GL087867, doi:10.1029/2020gl087867.
Vargas Zeppetello, L.R., A. Donohoe, and D.S. Battisti, 2019: Does Surface Temperature Respond to or Determine Downwelling Longwave Radiation? *Geophysical Research Letters*, **46(5)**, 2781–2789, doi:10.1029/2019gl082220.
Várnai, T. and A. Marshak, 2015: Effect of Cloud Fraction on Near-Cloud Aerosol Behavior in the MODIS Atmospheric Correction Ocean Color Product. *Remote Sensing*, **7(5)**, 5283–5299, doi:10.3390/rs70505283.
Vaughan, D.G. et al., 2013: Observations: Cryosphere. In: *Climate Change 2013: The Physical Science Basis. Contribution of Working Group I to the Fifth Assessment Report of the Intergovernmental Panel on Climate Change* [Stocker, T.F., D. Qin, G.K. Plattner, M. Tignor, S.K. Allen, J. Boschung, A. Nauels, Y. Xia, V. Bex, and P.M. Midgley (eds.)]. Cambridge University Press, Cambridge, United Kingdom and New York, NY, USA, pp. 317–382, doi:10.1017/cbo9781107415324.012.
Vecchi, G.A., A. Clement, and B.J. Soden, 2008: Examining the tropical Pacific's response to global warming. *Eos*, **89(9)**, 81–83, doi:10.1029/2008eo090002.
Vecchi, G.A. et al., 2006: Weakening of tropical Pacific atmospheric circulation due to anthropogenic forcing. *Nature*, **441(1)**, 73–76, doi:10.1038/nature04744.
Vergara-Temprado, J. et al., 2018: Is Black Carbon an Unimportant Ice-Nucleating Particle in Mixed-Phase Clouds? *Journal of Geophysical Research: Atmospheres*, doi:10.1002/2017jd027831.
Vial, J., J.-L.L. Dufresne, and S. Bony, 2013: On the interpretation of inter-model spread in CMIP5 climate sensitivity estimates. *Climate Dynamics*, **41(11–12)**, 3339–3362, doi:10.1007/s00382-013-1725-9.
Vieira, L.E.A., S.K. Solanki, N.A. Krivova, and I. Usoskin, 2011: Evolution of the solar irradiance during the Holocene. *Astronomy & Astrophysics*, **531**, A6, doi:10.1051/0004-6361/201015843.
Vieira, M., M.J. Pound, and D.I. Pereira, 2018: The late Pliocene palaeoenvironments and palaeoclimates of the western Iberian Atlantic margin from the Rio Maior flora. *Palaeogeography, Palaeoclimatology, Palaeoecology*, **495**, 245–258, doi:10.1016/j.palaeo.2018.01.018.
Vizcaíno, M., U. Mikolajewicz, J. Jungclaus, and G. Schurgers, 2010: Climate modification by future ice sheet changes and consequences for ice sheet mass balance. *Climate Dynamics*, **34(2)**, 301–324, doi:10.1007/s00382-009-0591-y.
Volodin, E.M., 2008: Relation between temperature sensitivity to doubled carbon dioxide and the distribution of clouds in current climate models. *Izvestiya, Atmospheric and Oceanic Physics*, **44(3)**, 288–299, doi:10.1134/s0001433808030043.
von der Heydt, A.S. and P. Ashwin, 2016: State dependence of climate sensitivity: attractor constraints and palaeoclimate regimes. *Dynamics and Statistics of the Climate System*, **1(1)**, 1–21, doi:10.1093/climsys/dzx001.
von der Heydt, A.S., H.A. Dijkstra, P. Köhler, and R. Wal, 2014: On the background state dependency of (palaeo) climate sensitivity. *Geophysical Research Letters*, **41(2)**, 6484–6492, doi:10.1002/2014gl061121.
von der Heydt, A.S. et al., 2016: Lessons on Climate Sensitivity From Past Climate Changes. *Current Climate Change Reports*, **2(4)**, 148–158, doi:10.1007/s40641-016-0049-3.
von Schuckmann, K. et al., 2016: An imperative to monitor Earth's energy imbalance. *Nature Climate Change*, **6(2)**, 138–144, doi:10.1038/nclimate2876.
von Schuckmann, K. et al., 2020: Heat stored in the Earth system: where does the energy go? *Earth System Science Data*, **12(3)**, 2013–2041, doi:10.5194/essd-12-2013-2020.
Voss, R. and U. Mikolajewicz, 2001: Long-term climate changes due to increased CO2 concentration in the coupled atmosphere-ocean general circulation model ECHAM3/LSG. *Climate Dynamics*, **17(1)**, 45–60, doi:10.1007/pl00007925.
Waelbroeck, C. et al., 2009: Constraints on the magnitude and patterns of ocean cooling at the Last Glacial Maximum. *Nature Geoscience*, **2(2)**, 127–132, doi:10.1038/ngeo411.
Wang, C., B.J.J. Soden, W. Yang, and G.A. Vecchi, 2021: Compensation between cloud feedback and aerosol-cloud interaction in CMIP6 models. *Geophysical Research Letters*, doi:10.1029/2020gl091024.
Wang, K., Q. Ma, Z. Li, and J. Wang, 2015: Decadal variability of surface incident solar radiation over China: Observations, satellite retrievals, and reanalyses. *JOURNAL OF GEOPHYSICAL RESEARCH-ATMOSPHERES*, **120(13)**, 6500–6514, doi:10.1002/2015jd023420.
Wang, K.C., Q. Ma, X.Y. Wang, and M. Wild, 2014: Urban impacts on mean and trend of surface incident solar radiation. *Geophysical Research Letters*, **41(13)**, 4664–4668, doi:10.1002/2014gl060201.
Wang, R. et al., 2016: Estimation of global black carbon direct radiative forcing and its uncertainty constrained by

observations. *Journal of Geophysical Research: Atmospheres*, **121(10)**, 5948–5971, doi:10.1002/2015jd024326.
Wang, R. et al., 2018: Spatial Representativeness Error in the Ground-Level Observation Networks for Black Carbon Radiation Absorption. *Geophysical Research Letters*, **45(4)**, 2106–2114, doi:10.1002/2017gl076817.
Wang, Y. and M. Wild, 2016: A new look at solar dimming and brightening in China. *GEOPHYSICAL RESEARCH LETTERS*, **43(22)**, 11777–11785, doi:10.1002/2016gl071009.
Wang, Y. and Y. Huang, 2020: The Surface Warming Attributable to Stratospheric Water Vapor in CO2-Caused Global Warming. *Journal of Geophysical Research: Atmospheres*, doi:10.1029/2020jd032752.
Wang, Y.W. and Y.H. Yang, 2014: China's dimming and brightening: evidence, causes and hydrological implications. *ANNALES GEOPHYSICAE*, **32(1)**, 41–55, doi:10.5194/angeo-32-41-2014.
Wara, M.W., A.C. Ravelo, and M.L. Delaney, 2005: Climate change: Permanent El Niño-like conditions during the Pliocene warm period. *Science*, **309(5735)**, 758–761, doi:10.1126/science.1112596.
Ward, D.S., N.M. Mahowald, and S. Kloster, 2014: Potential climate forcing of land use and land cover change. *Atmospheric Chemistry and Physics*, doi:10.5194/acp-14-12701-2014.
Watanabe, M., H. Tatebe, T. Suzuki, and K. Tachiiri, 2020a: Control of transient climate response and associated sea level rise by deep-ocean mixing. *Environmental Research Letters*, **15(9)**, 094001, doi:10.1088/1748-9326/ab8ca7.
Watanabe, M., Y. Kamae, H. Shiogama, A.M. DeAngelis, and K. Suzuki, 2018: Low clouds link equilibrium climate sensitivity to hydrological sensitivity. *Nature Climate Change*, **8(10)**, 901–906, doi:10.1038/s41558-018-0272-0.
Watanabe, M., J.-L. Dufresne, Y. Kosaka, T. Mauritsen, and H. Tatebe, 2020b: Enhanced warming constrained by past trends in equatorial Pacific sea surface temperature gradient. *Nature Climate Change*, doi:10.1038/s41558-020-00933-3.
Webb, M.J. and A.P. Lock, 2020: Testing a physical hypothesis for the relationship between climate sensitivity and double-ITCZ bias in climate models. *Journal of Advances in Modeling Earth Systems*, doi:10.1029/2019ms001999.
Webb, M.J., F.H. Lambert, and J.M. Gregory, 2013: Origins of differences in climate sensitivity, forcing and feedback in climate models. *Climate Dynamics*, **40(3)**, 677–707, doi:10.1007/s00382-012-1336-x.
Webb, M.J. et al., 2015: The impact of parametrized convection on cloud feedback. *Philosophical Transactions of the Royal Society A: Mathematical, Physical and Engineering Sciences*, **373(2054)**, doi:10.1098/rsta.2014.0414.
Wen, Q., J. Yao, K. Döös, and H. Yang, 2018: Decoding hosing and heating effects on global temperature and meridional circulations in a warming climate. *Journal of Climate*, doi:10.1175/jcli-d-18-0297.1.
Westerhold, T. et al., 2020: An astronomically dated record of Earth's climate and its predictability over the last 66 million years. *Science*, **369(6509)**, 1383–1388, doi:10.1126/science.aba6853.
Wigley, T.M.L., 1998: The Kyoto Protocol: CO2, CH4 and climate implications. *Geophysical Research Letters*, doi:10.1029/98gl01855.
Wigley, T.M.L., 2018: The Paris warming targets: emissions requirements and sea level consequences. *Climatic Change*, **147(1–2)**, 31–45, doi:10.1007/s10584-017-2119-5.
Wigley, T.M.L., C.M. Ammann, B.D. Santer, and S.C.B. Raper, 2005: Effect of climate sensitivity on the response to volcanic forcing. *Journal of Geophysical Research D: Atmospheres*, doi:10.1029/2004jd005557.
Wijffels, S., D. Roemmich, D. Monselesan, J. Church, and J. Gilson, 2016: Ocean temperatures chronicle the ongoing warming of Earth. *Nature Climate Change*, **6(2)**, 116–118, doi:10.1038/nclimate2924.
Wilcox, E.M. et al., 2016: Black carbon solar absorption suppresses turbulence in the atmospheric boundary layer. *Proceedings of the National Academy of Sciences of the United States of America*, **113(42)**, 11794–11799, doi:10.1073/pnas.1525746113.
Wild, M., 2009: Global dimming and brightening: A review. *JOURNAL OF GEOPHYSICAL RESEARCH-ATMOSPHERES*, **114**, doi:10.1029/2008jd011470.
Wild, M., 2012: Enlightening global dimming and brightening. *BULLETIN OF THE AMERICAN METEOROLOGICAL SOCIETY*, **93(1)**, 27–37, doi:10.1175/bams-d-11-00074.1.
Wild, M., 2016: Decadal changes in radiative fluxes at land and ocean surfaces and their relevance for global warming. *Wiley Interdisciplinary Reviews-Climate Change*, **7(1)**, 91–107, doi:10.1002/wcc.372.
Wild, M., 2017: Towards Global Estimates of the Surface Energy Budget. *Current Climate Change Reports*, **3(1)**, 87–97, doi:10.1007/s40641-017-0058-x.
Wild, M., 2020: The global energy balance as represented in CMIP6 climate models. *Climate Dynamics*, **55(3)**, 553–577, doi:10.3929/ethz-b-000418579.
Wild, M. and E. Schmucki, 2011: Assessment of global dimming and brightening in IPCC-AR4/CMIP3 models and ERA40. *Climate Dynamics*, **37(7–8)**, 1671–1688, doi:10.1007/s00382-010-0939-3.
Wild, M., S. Wacker, S. Yang, and A. Sanchez-Lorenzo, 2021: Evidence for Clear-Sky Dimming and Brightening in Central Europe. *Geophysical Research Letters*, **48(6)**, e2020GL092216, doi:10.1029/2020gl092216.
Wild, M. et al., 2013: The global energy balance from a surface perspective. *Climate Dynamics*, **40(11–12)**, 3107–3134, doi:10.1007/s00382-012-1569-8.

Wild, M. et al., 2015: The energy balance over land and oceans: an assessment based on direct observations and CMIP5 climate models. *Climate Dynamics*, **44(11–12)**, 3393–3429, doi:10.1007/s00382-014-2430-z.

Wild, M. et al., 2019: The cloud-free global energy balance and inferred cloud radiative effects: an assessment based on direct observations and climate models. *CLIMATE DYNAMICS*, doi:10.1007/s00382-018-4413-y.

Willeit, M., A. Ganopolski, and G. Feulner, 2014: Asymmetry and uncertainties in biogeophysical climate-vegetation feedback over a range of CO_2 forcings. *Biogeosciences*, **11(1)**, 17–32, doi:10.5194/bg-11-17-2014.

Williams, I.N. and R.T. Pierrehumbert, 2017: Observational evidence against strongly stabilizing tropical cloud feedbacks. *Geophysical Research Letters*, **44(3)**, 1503–1510, doi:10.1002/2016gl072202.

Williams, K.D., W.J. Ingram, and J.M. Gregory, 2008: Time variation of effective climate sensitivity in GCMs. *Journal of Climate*, doi:10.1175/2008jcli2371.1.

Williams, R.G., P. Ceppi, and A. Katavouta, 2020: Controls of the transient climate response to emissions by physical feedbacks, heat uptake and carbon cycling. *Environmental Research Letters*, **15(9)**, 0940c1, doi:10.1088/1748-9326/ab97c9.

Wing, A.A. and K.A. Emanuel, 2014: Physical mechanisms controlling self-aggregation of convection in idealized numerical modeling simulations. *Journal of Advances in Modeling Earth Systems*, **6(1)**, 59–74, doi:10.1002/2013ms000269.

Wing, A.A. et al., 2020: Clouds and Convective Self-Aggregation in a Multimodel Ensemble of Radiative-Convective Equilibrium Simulations. *Journal of Advances in Modeling Earth Systems*, **12(9)**, e2020MS002138, doi:10.1029/2020ms002138.

Winguth, A., C. Shellito, C. Shields, and C. Winguth, 2010: Climate Response at the Paleocene-Eocene Thermal Maximum to Greenhouse Gas Forcing – A Model Study with CCSM3. *Journal of Climate*, **23(10)**, 2562–2584, doi:10.1175/2009jcli3113.1.

Winterstein, F., F. Tanalski, P. Jöckel, M. Dameris, and M. Ponater, 2019: Implication of strongly increased atmospheric methane concentrations for chemistry-climate connections. *Atmospheric Chemistry and Physics*, doi:10.5194/acp-19-7151-2019.

Winton, M., K. Takahashi, and I.M. Held, 2010: Importance of Ocean Heat Uptake Efficacy to Transient Climate Change. *Journal of Climate*, **23(9)**, 2333–2344, doi:10.1175/2009jcli3139.1.

Winton, M. et al., 2013: Influence of ocean and atmosphere components on simulated climate sensitivities. *Journal of Climate*, doi:10.1175/jcli-d-12-00121.1.

Winton, M. et al., 2020: Climate Sensitivity of GFDL's CM4.0. *Journal of Advances in Modeling Earth Systems*, **12(1)**, 1–17, doi:10.1029/2019ms001838.

Witkowski, C.R., J.W.H. Weijers, B. Blais, S. Schouten, and J.S. Sinninghe Damsté, 2018: Molecular fossils from phytoplankton reveal secular PCO_2 trend over the Phanerozoic. *Science Advances*, **4(11)**, doi:10.1126/sciadv.aat4556.

WMO, 2018: *Scientific Assessment of Ozone Depletion: 2018*. Global Ozone Research and Monitoring Project – Report No. 58, World Meteorological Organization (WMO), Geneva, Switzerland, 588 pp.

Wohland, J., D. Brayshaw, H. Bloomfield, and M. Wild, 2020: European multidecadal solar variability badly captured in all centennial reanalyses except CERA20C. *Environmental Research Letters*, **15(10)**, 104021, doi:10.1088/1748-9326/aba7e6.

Wood, R. and C.S. Bretherton, 2006: On the relationship between stratiform low cloud cover and lower-tropospheric stability. *Journal of Climate*, doi:10.1175/jcli3988.1.

Woods, C. and R. Caballero, 2016: The role of moist intrusions in winter arctic warming and sea ice decline. *Journal of Climate*, doi:10.1175/jcli-d-15-0773.1.

Wyant, M.C. et al., 2006: A comparison of low-latitude cloud properties and their response to climate change in three AGCMs sorted into regimes using mid-tropospheric vertical velocity. *Clim Dyn*, **27(2–3)**, 261–279, doi:10.1007/s00382-006-0138-4.

Wycech, J.B., E. Gill, B. Rajagopalan, T.M. Marchitto Jr, and P.H. Molnar, 2020: Multiproxy Reduced-Dimension Reconstruction of Pliocene Equatorial Pacific Sea Surface Temperatures. *Paleoceanography and Paleoclimatology*, **35(1)**, e2019PA003685, doi:10.1029/2019pa003685.

Xia, Y., Y. Hu, and Y. Huang, 2016: Strong modification of stratospheric ozone forcing by cloud and sea-ice adjustments. *Atmospheric Chemistry and Physics*, doi:10.5194/acp-16-7559-2016.

Xia, Y. et al., 2020: Stratospheric Ozone-induced Cloud Radiative Effects on Antarctic Sea Ice. *Advances in Atmospheric Sciences*, doi:10.1007/s00376-019-8251-6.

Xie, B., H. Zhang, Z. Wang, S. Zhao, and Q. Fu, 2016: A Modeling Study of Effective Radiative Forcing and Climate Response Due to Tropospheric Ozone. , **33**, 819–828, doi:10.1007/s00376-016-5193-0.

Xie, S.P. et al., 2010: Global warming pattern formation: Sea surface temperature and rainfall. *Journal of Climate*, doi:10.1175/2009jcli3329.1.

Xu, J., C. Li, H. Shi, Q. He, and L. Pan, 2011: Analysis on the impact of aerosol optical depth on surface solar radiation in the Shanghai megacity, China. *ATMOSPHERIC CHEMISTRY AND PHYSICS*, **11(7)**, 3281–3289, doi:10.5194/acp-11-3281-2011.

Yan, X.-H. et al., 2016: The global warming hiatus: Slowdown or redistribution? *Earth's Future*, **4(11)**, 472–482, doi:10.1002/2016ef000417.

Yang, S., X.L. Wang, and M. Wild, 2018: Homogenization and Trend Analysis of the 1958-2016 In Situ Surface Solar Radiation Records in China. *JOURNAL OF CLIMATE*, **31(11)**, 4529–4541, doi:10.1175/jcli-d-17-0891.1.

Yang, S., X.L. Wang, and M. Wild, 2019: Causes of Dimming and Brightening in China Inferred from Homogenized Daily Clear-Sky and All-Sky in situ Surface Solar Radiation Records (1958-2016). *JOURNAL OF CLIMATE*, **32(18)**, 5901–5913, doi:10.1175/jcli-d-18-0666.1.

Yasunari, T.J., R.D. Koster, W.K.M. Lau, and K.-M. Kim, 2015: Impact of snow darkening via dust, black carbon, and organic carbon on boreal spring climate in the Earth system. *Journal of Geophysical Research: Atmospheres*, **120(11)**, 5485–5503, doi:10.1002/2014jd022977.

Yeo, K.L. et al., 2020: The Dimmest State of the Sun. *Geophysical Research Letters*, **47(19)**, doi:10.1029/2020gl090243.

Yoshimori, M., T. Yokohata, and A. Abe-Ouchi, 2009: A Comparison of Climate Feedback Strength between CO2 Doubling and LGM Experiments. *Journal of Climate*, **22(12)**, 3374–3395, doi:10.1175/2009jcli2801.1.

Yoshimori, M., A. Abe-Ouchi, and A. Laîné, 2017: The role of atmospheric heat transport and regional feedbacks in the Arctic warming at equilibrium. *Climate Dynamics*, doi:10.1007/s00382-017-3523-2.

Yoshimori, M., F.H. Lambert, M.J. Webb, and T. Andrews, 2020: Fixed Anvil Temperature Feedback: Positive, Zero, or Negative? *Journal of Climate*, **33(7)**, 2719–2739, doi:10.1175/jcli-d-19-0108.1.

Yoshimori, M., J.C. Hargreaves, J.D. Annan, T. Yokohata, and A. Abe-Ouchi, 2011: Dependency of feedbacks on forcing and climate state in physics parameter ensembles. *Journal of Climate*, **24(24)**, 6440–6455, doi:10.1175/2011jcli3954.1.

You, Q.L. et al., 2013: Decadal variation of surface solar radiation in the Tibetan Plateau from observations, reanalysis and model simulations. *Climate Dynamics*, **40(7–8)**, 2073–2086, doi:10.1007/s00382-012-1383-3.

Yu, F. and G. Luo, 2014: Effect of solar variations on particle formation and cloud condensation nuclei. *Environmental Research Letters*, **9(4)**, doi:10.1088/1748-9326/9/4/045004.

Yu, L., 2019: Global Air-Sea Fluxes of Heat, Fresh Water, and Momentum: Energy Budget Closure and Unanswered Questions. *Annual Review of Marine Science*, **11**, 227–248, doi:10.1146/annurev-marine-010816-060704.

Yuan, T., L.A. Remer, and H. Yu, 2011: Microphysical, macrophysical and radiative signatures of volcanic aerosols in trade wind cumulus observed by the A-Train. *Atmospheric Chemistry and Physics*, **11(14)**, 7119–7132, doi:10.5194/acp-11-7119-2011.

Zaehle, S., C.D. Jones, B. Houlton, J.F. Lamarque, and E. Robertson, 2015: Nitrogen availability reduces CMIP5 projections of twenty-first-century land carbon uptake. *Journal of Climate*, doi:10.1175/jcli-d-13-00776.1.

Zaliapin, I. and M. Ghil, 2010: Nonlinear Processes in Geophysics Another look at climate sensitivity. *Nonlin. Processes Geophys*, **17**, 113–122, doi:10.5194/npg-17-113-2010.

Zanatta, M. et al., 2016: A European aerosol phenomenology-5: Climatology of black carbon optical properties at 9 regional background sites across Europe. *Atmospheric Environment*, **145**, 346–364, doi:10.1016/j.atmosenv.2016.09.035.

Zanna, L., S. Khatiwala, J.M. Gregory, J. Ison, and P. Heimbach, 2019: Global reconstruction of historical ocean heat storage and transport. *Proceedings of the National Academy of Sciences*, **116(4)**, 1126–1131, doi:10.1073/pnas.1808838115.

Zarakas, C.M., A.L.S. Swann, M.M. Laguë, K.C. Armour, and J.T. Randerson, 2020: Plant Physiology Increases the Magnitude and Spread of the Transient Climate Response to CO2 in CMIP6 Earth System Models. *Journal of Climate*, doi:10.1175/jcli-d-20-0078.1.

Zelinka, M.D. and D.L. Hartmann, 2012: Climate feedbacks and their implications for poleward energy flux changes in a warming climate. *Journal of Climate*, doi:10.1175/jcli-d-11-00096.1.

Zelinka, M.D., C. Zhou, and S.A. Klein, 2016: Insights from a refined decomposition of cloud feedbacks. *Geophysical Research Letters*, **43**, 9259–9269, doi:10.1002/2016gl069917.

Zelinka, M.D., T. Andrews, P.M. Forster, and K.E. Taylor, 2014: Quantifying components of aerosol-cloud-radiation interactions in climate models. *Journal of Geophysical Research: Atmospheres*, **119(12)**, 7599–7615, doi:10.1002/2014jd021710.

Zelinka, M.D. et al., 2018: Drivers of the Low-Cloud Response to Poleward Jet Shifts in the North Pacific in Observations and Models. *Journal of Climate*, **31(19)**, 7925–7947, doi:10.1175/jcli-d-18-0114.1.

Zelinka, M.D. et al., 2020: Causes of higher climate sensitivity in CMIP6 models. *Geophysical Research Letters*, **46**, 2019GL085782, doi:10.1029/2019gl085782.

Zhai, C., J.H. Jiang, and H. Su, 2015: Long-term cloud change imprinted in seasonal cloud variation: More evidence of high climate sensitivity. *Geophysical Research Letters*, **42(20)**, 8729–8737, doi:10.1002/2015gl065911.

Zhang, C. et al., 2018: CAUSES: Diagnosis of the Summertime Warm Bias in CMIP5 Climate Models at the ARM Southern Great Plains Site. *JOURNAL OF GEOPHYSICAL RESEARCH-ATMOSPHERES*, **123(6)**, 2968–2992, doi:10.1002/2017jd027200.

Zhang, H., S. Zhao, Z. Wang, X. Zhang, and L. Song, 2016: The updated effective radiative forcing of major anthropogenic aerosols and their effects on global climate at present and in the future. *International Journal of Climatology*, **36(12)**, 4029–4044, doi:10.1002/joc.4613.

Zhang, M. and Y. Huang, 2014: Radiative Forcing of Quadrupling CO2. *Journal of Climate*, **27(7)**, 2496–2508, doi:10.1175/jcli-d-13-00535.1.
Zhang, R., H. Wang, Q. Fu, P.J. Rasch, and X. Wang, 2019: Unraveling driving forces explaining significant reduction in satellite-inferred Arctic surface albedo since the 1980s. *Proceedings of the National Academy of Sciences*, doi:10.1073/pnas.1915258116.
Zhang, R. et al., 2018: Local Radiative Feedbacks Over the Arctic Based on Observed Short-Term Climate Variations. *Geophysical Research Letters*, **45(11)**, 5761–5770, doi:10.1029/2018gl077852.
Zhang, W. et al., 2018: Self-Amplifying Feedbacks Accelerate Greening and Warming of the Arctic. *Geophysical Research Letters*, **45(14)**, 7102–7111, doi:10.1029/2018gl077830.
Zhang, X.T., S.L. Liang, M. Wild, and B. Jiang, 2015: Analysis of surface incident shortwave radiation from four satellite products. *Remote Sensing of Environment*, **165**, 186–202, doi:10.1016/j.rse2015.05.015.
Zhang, Y.G., M. Pagani, and Z. Liu, 2014: A 12-Million-Year Temperature History of the Tropical Pacific Ocean. *Science*, **344(6179)**, 84 LP – 87, doi:10.1126/science.1246172.
Zhang, Z. et al., 2021: Mid-Pliocene Atlantic Meridional Overturning Circulation simulated in PlioMIP2. *Climate of the Past*, **17(1)**, 529–543, doi:10.5194/cp-17-529-2021.
Zhao, B. et al., 2018: Impact of aerosols on ice crystal size. *Atmospheric Chemistry and Physics*, **18(2)**, 1065–1078, doi:10.5194/acp-18-1065-2018.
Zhao, M. et al., 2015: Uncertainty in Model Climate Sensitivity Traced to Representations of Cumulus Precipitation Microphysics. *Journal of Climate*, **29(2)**, 543–560, doi:10.1175/jcli-d-15-0191.1.
Zhao, S. and K. Suzuki, 2019: Differing Impacts of Black Carbon and Sulfate Aerosols on Global Precipitation and the ITCZ Location via Atmosphere and Ocean Energy Perturbations. *Journal of Climate*, **32(17)**, 5567–5582, doi:10.1175/jcli-d-18-0616.1.
Zhou, C., M.D. Zelinka, and S.A. Klein, 2016: Impact of decadal cloud variations on the Earth's energy budget. *Nature Geoscience*, **9(12)**, 871–874, doi:10.1038/ngeo2828.
Zhou, C., K. Wang, and Q. Ma, 2017a: Evaluation of Eight Current Reanalyses in Simulating Land Surface Temperature from 1979 to 2003 in China. *Journal of Climate*, **30(18)**, 7379–7398, doi:10.1175/jcli-d-16-0903.1.
Zhou, C., M.D. Zelinka, and S.A. Klein, 2017b: Analyzing the dependence of global cloud feedback on the spatial pattern of sea surface temperature change with a Green's function approach. *Journal of Advances in Modeling Earth Systems*, **9(5)**, 2174–2189, doi:10.1002/2017ms001096.
Zhou, C., Y. He, and K. Wang, 2018a: On the suitability of current atmospheric reanalyses for regional warming studies over China. *ATMOSPHERIC CHEMISTRY AND PHYSICS*, **18(11)**, 8113–8136, doi:10.5194/acp-18-8113-2018.
Zhou, C., M.D. Zelinka, A.E. Dessler, and S.A. Klein, 2015: The relationship between interannual and long-term cloud feedbacks. *Geophysical Research Letters*, doi:10.1002/2015gl066698.
Zhou, C., H. Zhang, S. Zhao, and J. Li, 2017c: Simulated effects of internal mixing of anthropogenic aerosols on the aerosol–radiation interaction and global temperature. *International Journal of Climatology*, **37**, 972–986, doi:10.1002/joc.5050.
Zhou, C., H. Zhang, S. Zhao, and J. Li, 2018b: On Effective Radiative Forcing of Partial Internally and Externally Mixed Aerosols and Their Effects on Global Climate. *Journal of Geophysical Research: Atmospheres*, **123(1)**, 401–423, doi:10.1002/2017jd027603.
Zhou, C., A.E. Dessler, M.D. Zelinka, P. Yang, and T. Wang, 2014: Cirrus feedback on interannual climate fluctuations. *Geophysical Research Letters*, **41(24)**, 9166–9173, doi:10.1002/2014gl062095.
Zhu, J. and J.E. Penner, 2020: Indirect Effects of Secondary Organic Aerosol on Cirrus Clouds. *Journal of Geophysical Research: Atmospheres*, doi:10.1029/2019jd032233.
Zhu, J. and C.J. Poulsen, 2021: Last Glacial Maximum (LGM) climate forcing and ocean dynamical feedback and their implications for estimating climate sensitivity. *Climate of the Past*, **17(1)**, 253–267, doi:10.5194/cp-17-253-2021.
Zhu, J., C.J. Poulsen, and J.E. Tierney, 2019a: Simulation of Eocene extreme warmth and high climate sensitivity through cloud feedbacks. *Science Advances*, **5(9)**, doi:10.1126/sciadv.aax1874.
Zhu, J., C.J. Poulsen, and B.L. Otto-Bliesner, 2020: High climate sensitivity in CMIP6 model not supported by paleoclimate. *Nature Climate Change*, **10(5)**, 378–379, doi:10.1038/s41558-020-0764-6.
Zhu, J. et al., 2019b: Decrease in radiative forcing by organic aerosol nucleation, climate, and land use change. *Nature Communications*, doi:10.1038/s41467-019-08407-7.
Zhu, J. et al., 2021: Assessment of Equilibrium Climate Sensitivity of the Community Earth System Model Version 2 Through Simulation of the Last Glacial Maximum. *Geophysical Research Letters*, **48(3)**, e2020GL091220, doi:10.1029/2020gl091220.
Zhu, Y., D. Rosenfeld, and Z. Li, 2018: Under What Conditions Can We Trust Retrieved Cloud Drop Concentrations in Broken Marine Stratocumulus? *Journal of Geophysical Research: Atmospheres*, **123(16)**, 8754–8767, doi:10.1029/2017jd028083.
Zickfeld, K., S. Solomon, and D.M. Gilford, 2017: Centuries of thermal sea-level rise due to anthropogenic emissions

of short-lived greenhouse gases.. *Proceedings of the National Academy of Sciences of the United States of America*, **114(4)**, 657–662, doi:10.1073/pnas.1612066114.

1 **Figures**

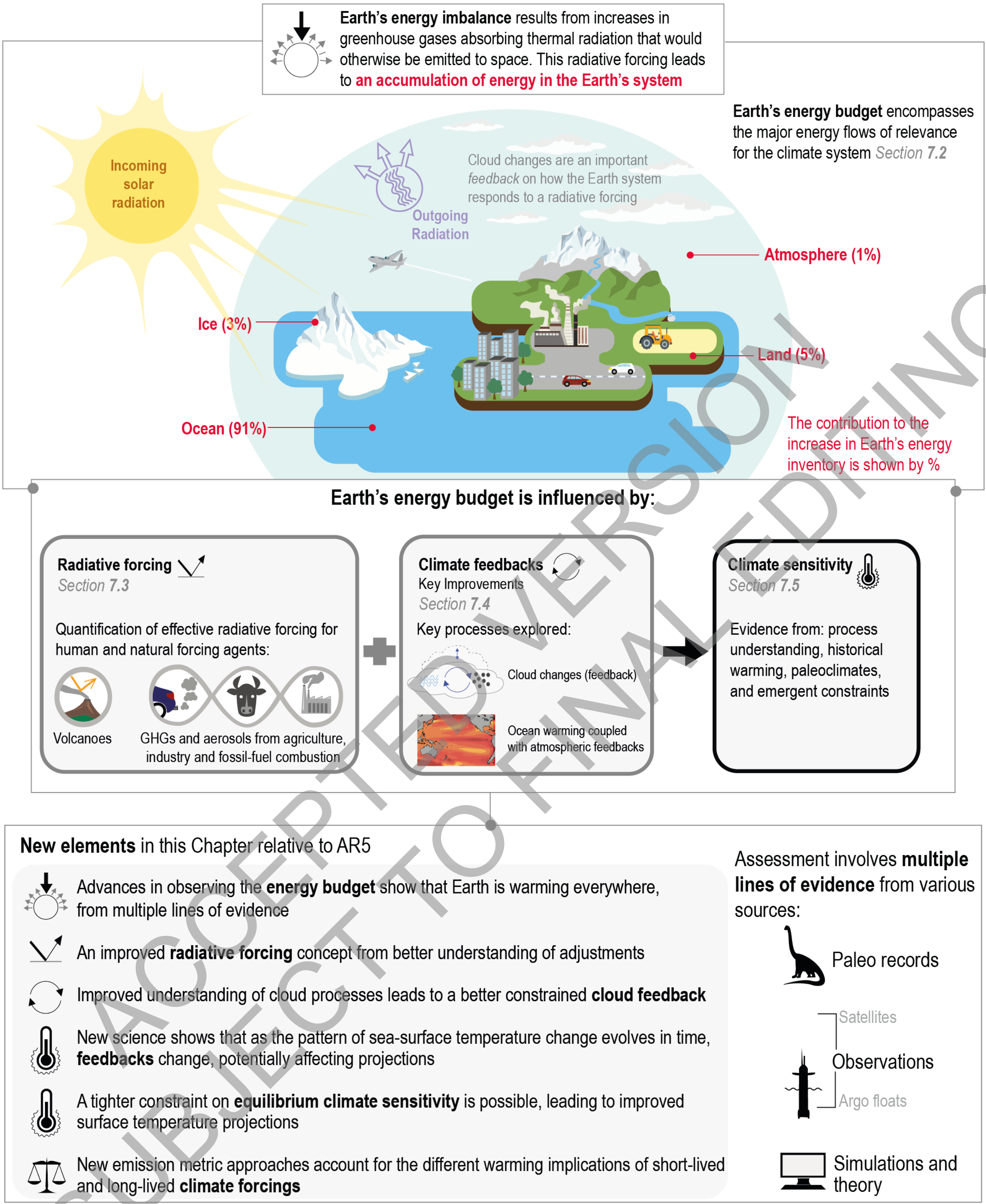

2
3
4 **Figure 7.1:** A visual abstract of the chapter, illustrating why the Earth's energy budget matters and how it relates to
5 the underlying chapter assessment. The methods used to assess processes and key new findings relative to
6 AR5 are highlighted.
7

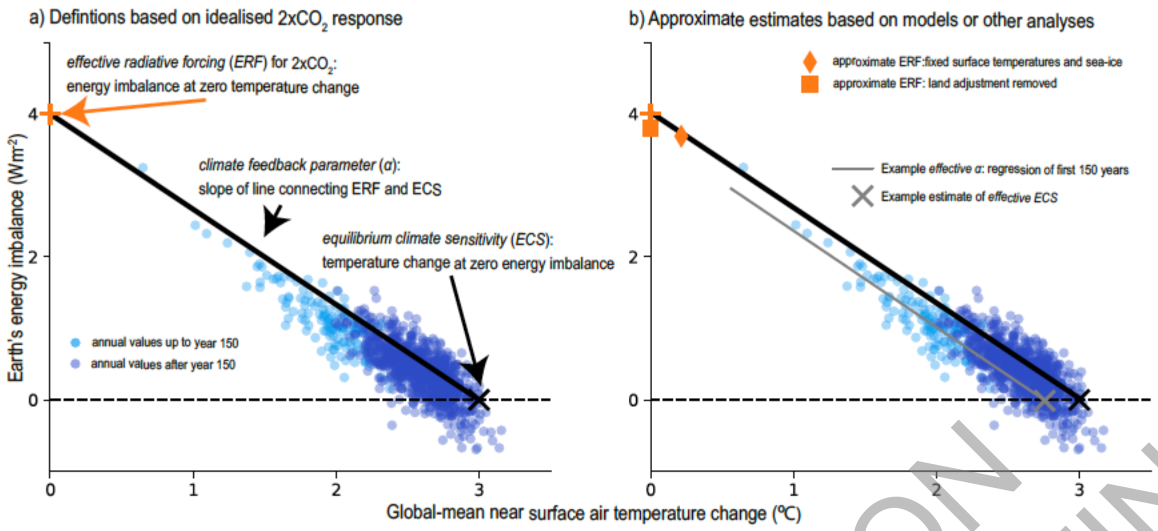

Box 7.1, Figure 1: Schematics of the forcing-feedback framework adopted within the assessment, following Equation 7.1. Illustrated is how the Earth's TOA net energy flux might evolve for a hypothetical doubling of atmospheric CO_2 concentration above preindustrial levels, where an initial positive energy imbalance (energy entering the Earth system, shown on the y-axis) is gradually restored towards equilibrium as the surface temperature warms (shown on the x-axis). a) illustrates the definitions of ERF for the special case of a doubling of atmospheric CO_2 concentration, the feedback parameter and the ECS. b) illustrates how approximate estimates of these metrics are made within the chapter and how these approximations might relate to the exact definitions adopted in panel a).

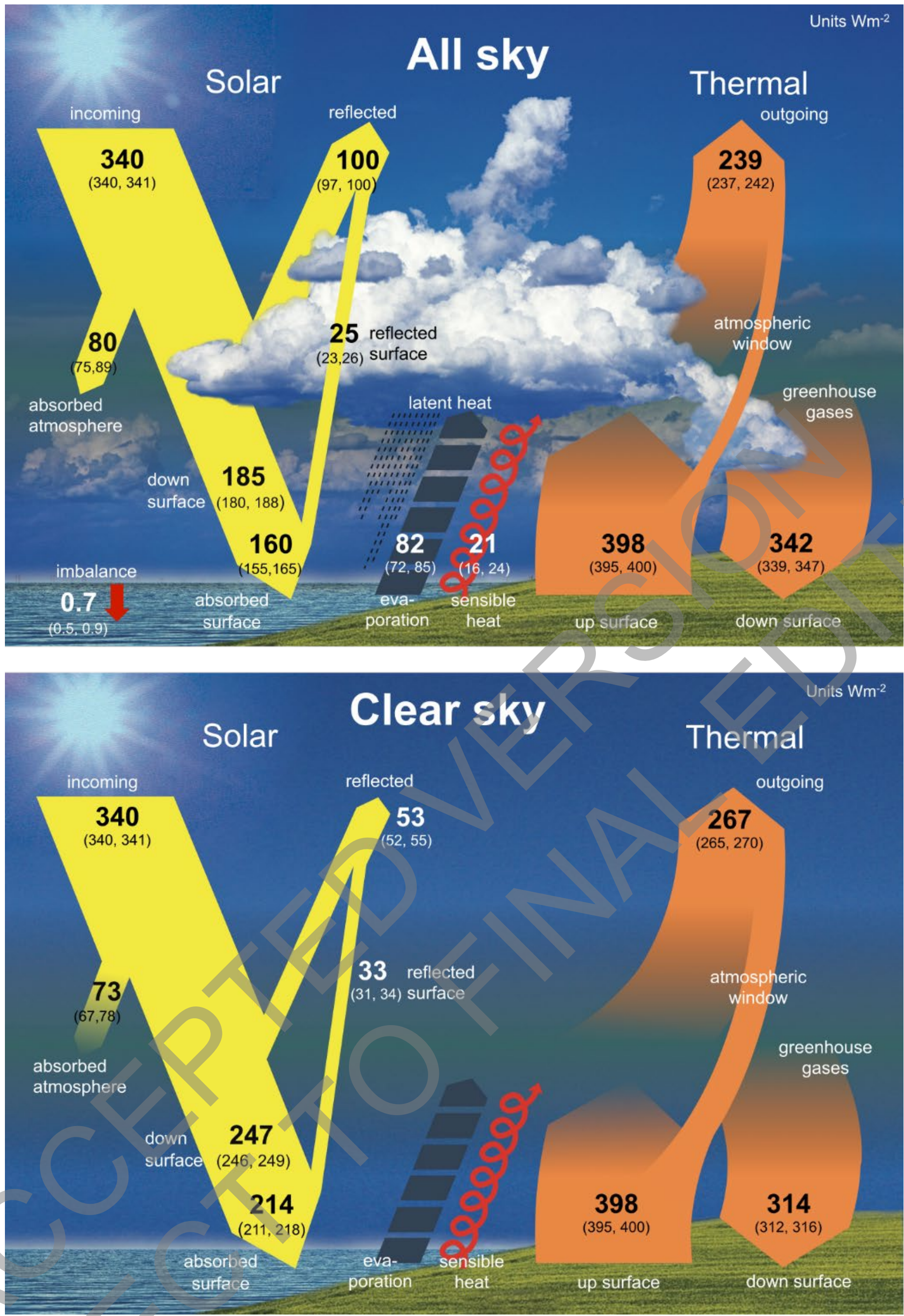

Figure 7.2: Schematic representation of the global mean energy budget of the Earth (upper panel), and its equivalent without considerations of cloud effects (lower panel). Numbers indicate best estimates for the magnitudes of the globally averaged energy balance components in W m^{-2} together with their uncertainty ranges in parentheses (5–95 % confidence range), representing climate conditions at the beginning of the 21st century. Note that the cloud-free energy budget shown in the lower panel is not the one that Earth would achieve in equilibrium when no clouds could form. It rather represents the global mean fluxes as determined solely by removing the clouds but otherwise retaining the entire atmospheric structure. This enables the quantification of the effects of clouds on the Earth energy budget and corresponds to the way clear-sky fluxes are calculated in climate models. Thus, the cloud-free energy budget is not closed and therefore the sensible and latent heat fluxes are not quantified in the lower panel. Adapted from Wild et al. (2015, 2019).

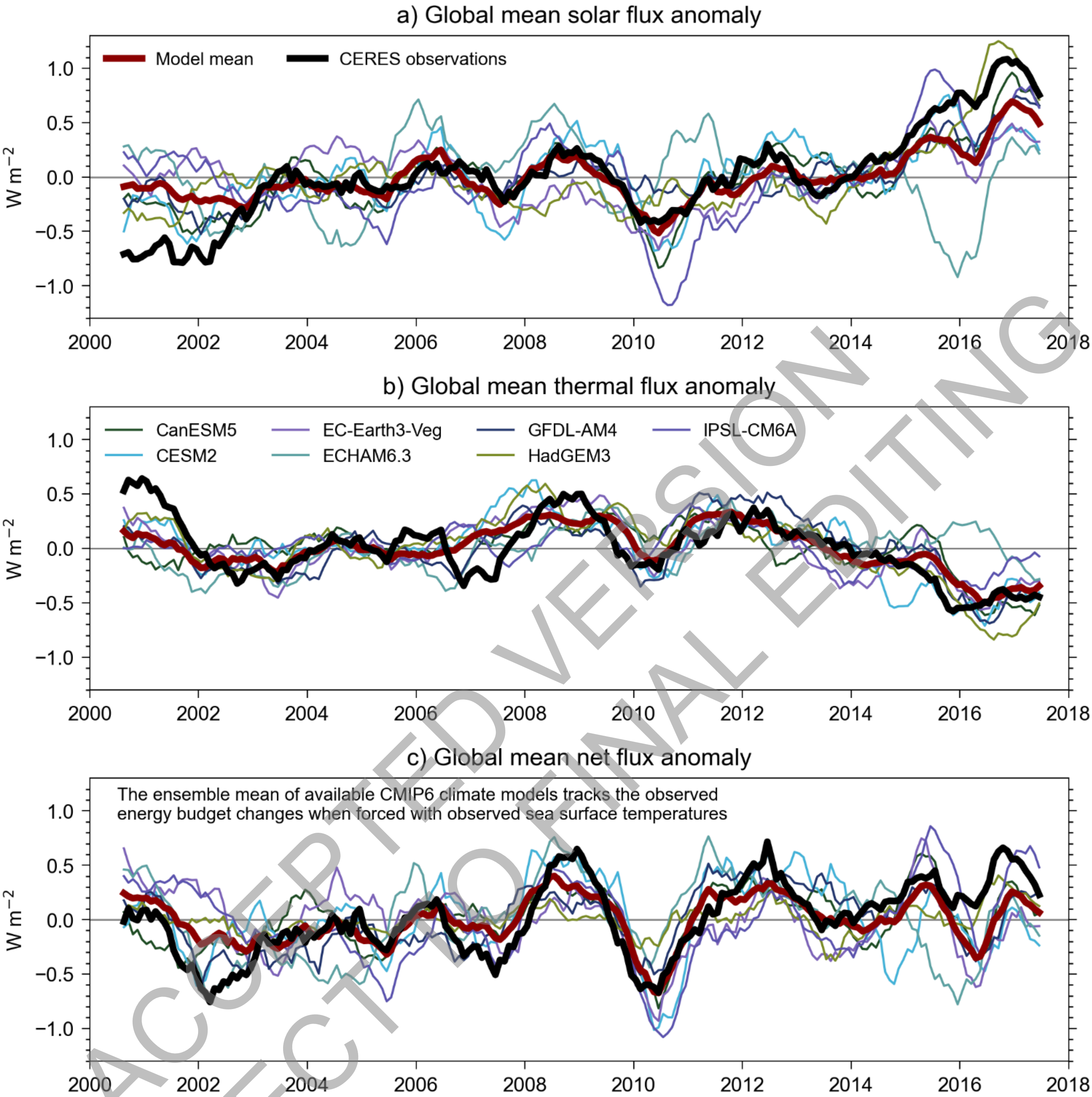

Figure 7.3: Anomalies in global mean all-sky TOA fluxes from EBAF Ed4.0 (solid black lines) and various CMIP6 climate models (coloured lines) in terms of (a) reflected solar, (b) emitted thermal and (c) net TOA fluxes. The multi-model means are additionally depicted as dotted black lines. Model fluxes stem from simulations driven with prescribed SSTs and all known anthropogenic and natural forcings. Shown are anomalies of 12-month running means. All flux anomalies are defined as positive downwards, consistent with the sign convention used throughout this chapter. The correlations between the multi-model means (dotted black lines) and the CERES records (solid black lines) for 12-month running means are 0.85, 0.73 and 0.81 for the global mean reflected solar, outgoing thermal and net TOA radiation, respectively. Adapted from Loeb et al. (2020). Further details on data sources and processing are available in the chapter data table (Table 7.SM.14).

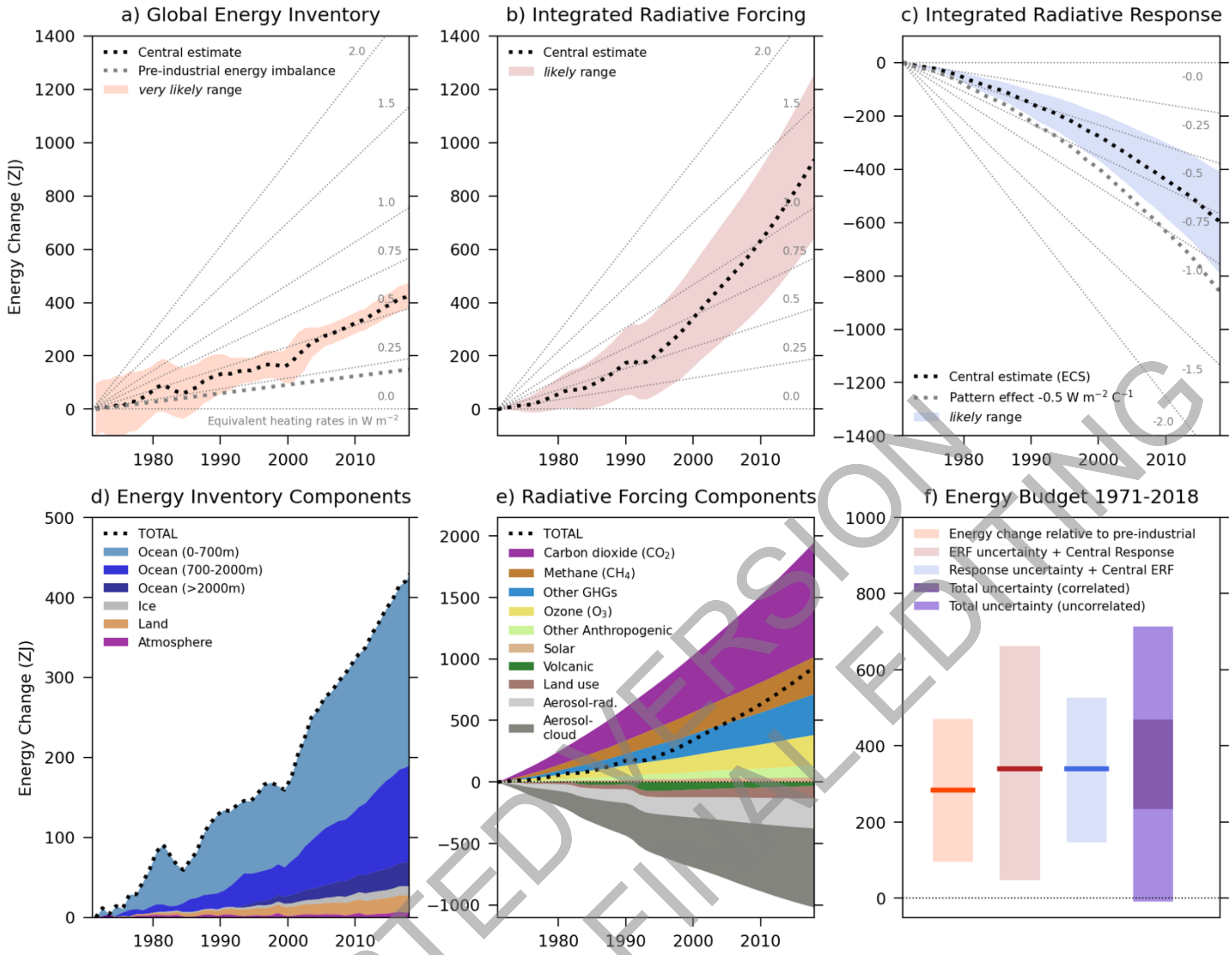

Box 7.2, Figure 1: Estimates of the net cumulative energy change (ZJ = 10^{21} Joules) for the period 1971–2018 associated with: (a) observations of changes in the Global Energy Inventory (b) Integrated Radiative Forcing; (c) Integrated Radiative Response. Black dotted lines indicate the central estimate with *likely* and *very likely* ranges as indicated in the legend. The grey dotted lines indicate the energy change associated with an estimated pre-industrial Earth energy imbalance of 0.2 W m^{-2} (panel a) and an illustration of an assumed pattern effect of –0.5 W m^{-2} $°C^{-1}$ (panel c). Background grey lines indicate equivalent heating rates in W m^{-2} per unit area of Earth's surface. Panels (d) and (e) show the breakdown of components, as indicated in the legend, for the Global Energy Inventory and Integrated Radiative Forcing, respectively. Panel (f) shows the Global Energy Budget assessed for the period 1971–2018, i.e. the consistency between the change in the Global Energy Inventory relative to pre-industrial and the implied energy change from Integrated Radiative Forcing plus Integrated Radiative Response under a number of different assumptions, as indicated in the figure legend, including assumptions of correlated and uncorrelated uncertainties in Forcing plus Response. Shading represents the *very likely* range for observed energy change relative to pre-industrial and *likely* range for all other quantities. Forcing and Response timeseries are expressed relative to a baseline period of 1850–1900. Further details on data sources and processing are available in the chapter data table (Table 7.SM.14).

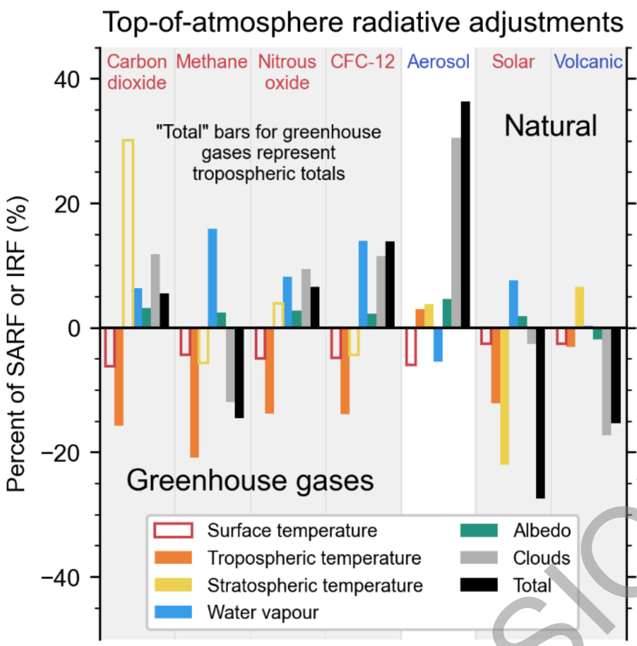

Figure 7.4: Radiative adjustments at top of atmosphere for seven different climate drivers as a proportion of forcing. Tropospheric temperature (orange), stratospheric temperature (yellow), water vapour (blue), surface albedo (green), clouds (grey) and the total adjustment (black) is shown. For the greenhouse gases (carbon dioxide, methane, nitrous oxide, CFC-12) the adjustments are expressed as a percentage of SARF, whereas for aerosol, solar and volcanic forcing they are expressed as a percentage of IRF. Land surface temperature response (outline red bar) is shown, but included in the definition of forcing. Data from Smith et al. (2018b) for carbon dioxide and methane, Smith et al. (2018b) and Gray et al. (2009) for solar, Hodnebrog et al. (2020b) for nitrous oxide and CFC-12, Smith et al. (2020a) for aerosol, and Marshall et al. (2020) for volcanic. Further details on data sources and processing are available in the chapter data table (Table 7.SM.14).

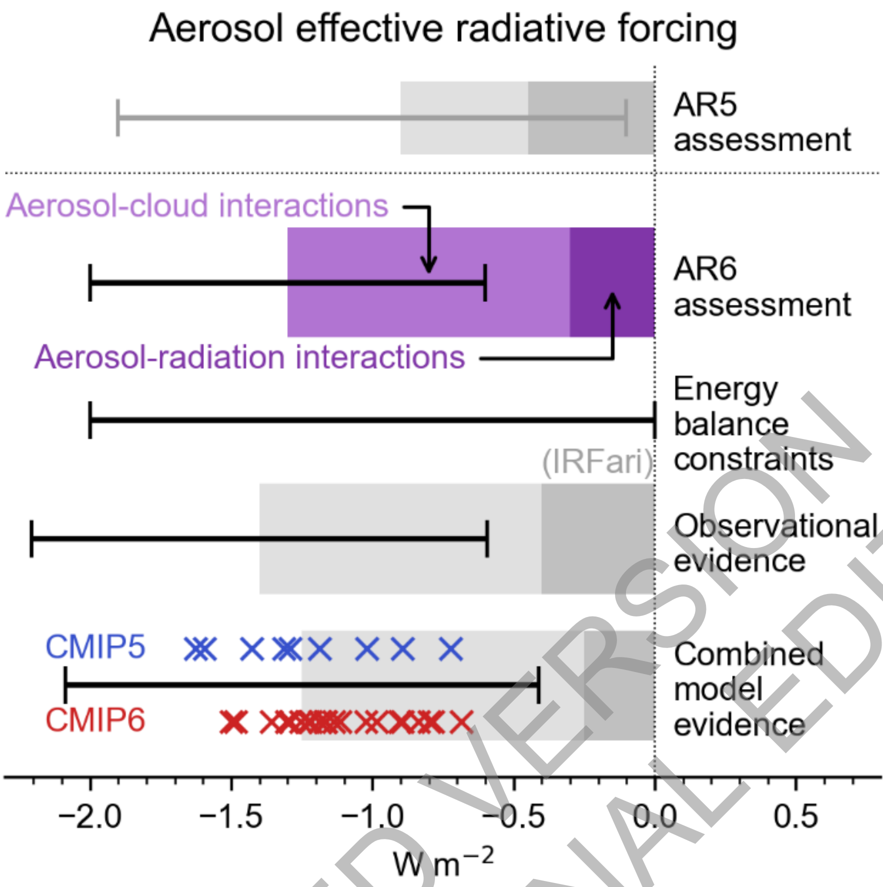

Figure 7.5: Net aerosol effective radiative forcing from different lines of evidence. The headline AR6 assessment of –1.3 [–2.0 to –0.6] W m^{-2} is highlighted in purple for 1750–2014 and compared to the AR5 assessment of –0.9 [–1.9 to –0.1] W m^{-2} for 1750–2011. The evidence comprising the AR6 assessment is shown below this: energy balance constraints [–2 to 0 W m^{-2} with no best estimate], observational evidence from satellite retrievals of –1.4 [–2.2 to –0.6] W m^{-2}, and climate model-based evidence of –1.25 [–2.1 to –0.4] W m^{-2}. Estimates from individual CMIP5 (Zelinka et al., 2014) and CMIP6 (Smith et al., 2020a and Table 7.6) models are depicted by blue and red crosses respectively. For each line of evidence the assessed best-estimate contributions from ERFari and ERFaci are shown with darker and paler shading respectively. The observational assessment for ERFari is taken from the IRFari. Uncertainty ranges are given in black bars for the total aerosol ERF and depict *very likely* ranges. Further details on data sources and processing are available in the chapter data table (Table 7.SM.14).

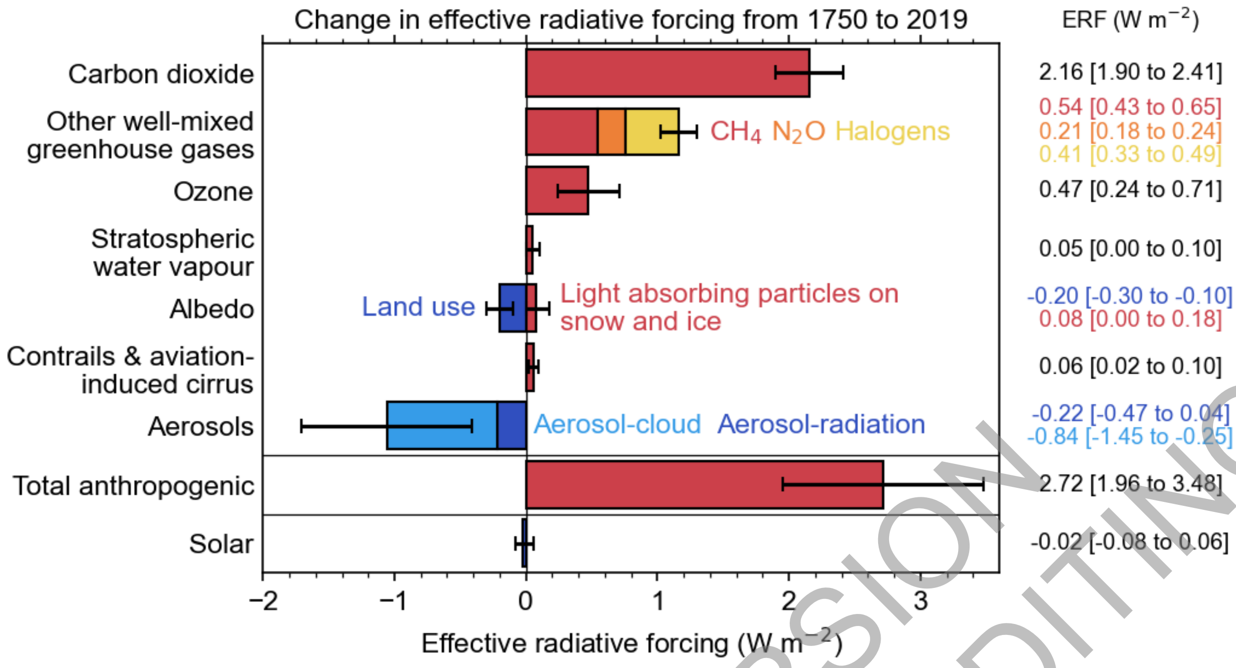

Figure 7.6: Change in effective radiative forcing from 1750 to 2019 by contributing forcing agents (carbon dioxide, other well-mixed greenhouse gases (WMGHGs), ozone, stratospheric water vapour, surface albedo, contrails and aviation-induced cirrus, aerosols, anthropogenic total, and solar). Solid bars represent best estimates, and *very likely* (5–95%) ranges are given by error bars. Non-CO_2 WMGHGs are further broken down into contributions from methane (CH_4), nitrous oxide (N_2O) and halogenated compounds. Surface albedo is broken down into land use changes and light absorbing particles on snow and ice. Aerosols are broken down into contributions from aerosol-cloud interactions (ERFaci) and aerosol-radiation interactions (ERFari). For aerosols and solar, the 2019 single-year values are given (Table 7.8) that differ from the headline assessments in both cases. Volcanic forcing is not shown due to the episodic nature of volcanic eruptions. Further details on data sources and processing are available in the chapter data table (Table 7.SM.14).

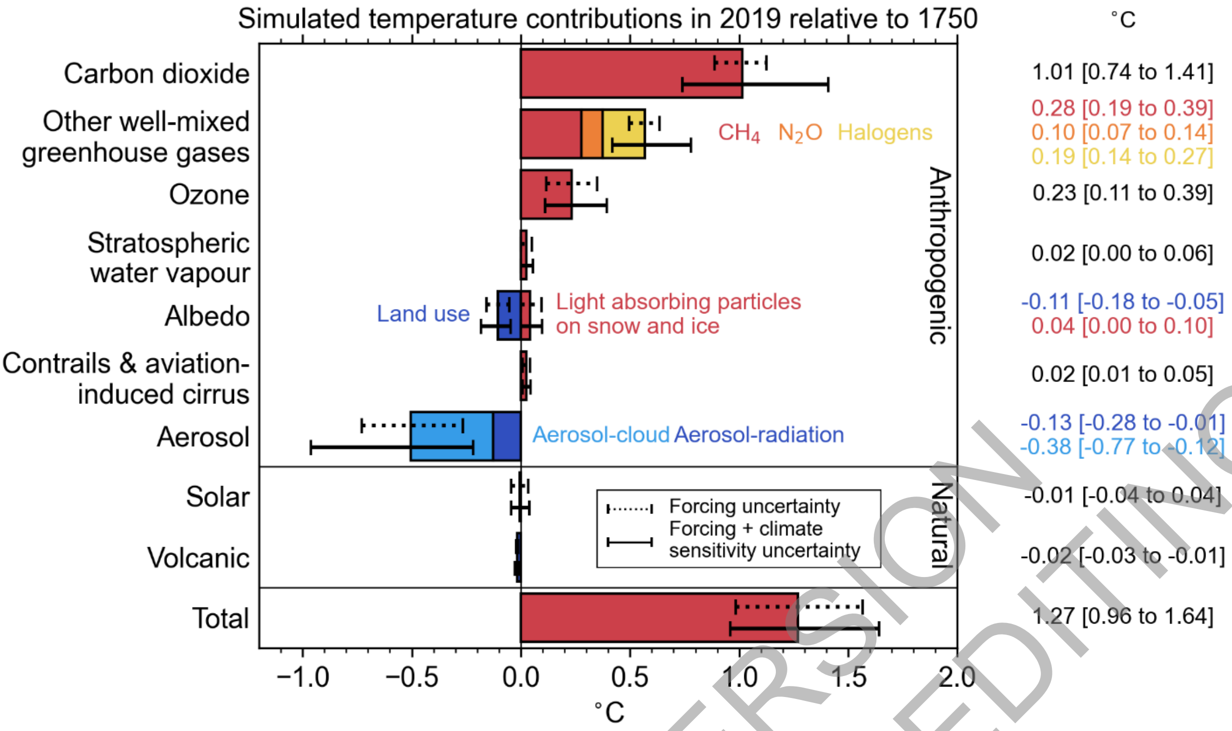

Figure 7.7: The contribution of forcing agents to 2019 temperature change relative to 1750 produced using the two-layer emulator (Supplementary Material 7.SM.2), constrained to assessed ranges for key climate metrics described in Cross-Chapter Box 7.1. The results are from a 2,237-member ensemble. Temperature contributions are expressed for carbon dioxide, other well-mixed greenhouse gases (WMGHGs), ozone, stratospheric water vapour, surface albedo, contrails and aviation-induced cirrus, aerosols, solar, volcanic, and total. Solid bars represent best estimates, and *very likely* (5–95%) ranges are given by error bars. Dashed error bars show the contribution of forcing uncertainty alone, using best estimates of ECS (3.0°C), TCR (1.8°C) and two-layer model parameters representing the CMIP6 multi-model mean. Solid error bars show the combined effects of forcing and climate response uncertainty using the distribution of ECS and TCR from Tables 7.13 and 7.14, and the distribution of calibrated model parameters from 44 CMIP6 models. Non-CO_2 WMGHGs are further broken down into contributions from methane (CH_4), nitrous oxide (N_2O) and halogenated compounds. Surface albedo is broken down into land use changes and light absorbing particles on snow and ice. Aerosols are broken down into contributions from aerosol-cloud interactions (ERFaci) and aerosol-radiation interactions (ERFari). Further details on data sources and processing are available in the chapter data table (Table 7.SM.14).

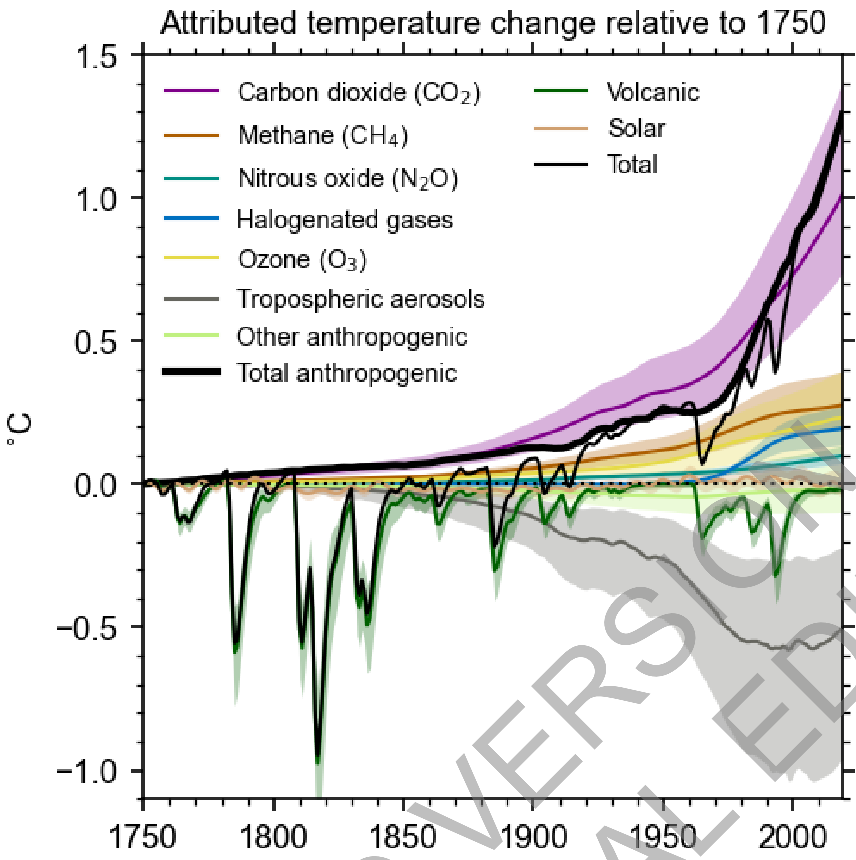

Figure 7.8: Attributed global near-surface air temperature change (GSAT) from 1750 to 2019 produced using the two-layer emulator (Supplementary Material 7.SM.2), forced with ERF derived in this chapter (displayed in Chapter 2, Figure 2.10) and climate response constrained to assessed ranges for key climate metrics described in Cross-Chapter Box 7.1. The results shown are the medians from a 2,237-member ensemble that encompasses uncertainty in forcing and climate response (year-2019 best estimates and uncertainties are shown in Figure 7.7 for several components). Temperature contributions are expressed for carbon dioxide, methane, nitrous oxide, other well-mixed greenhouse gases (WMGHGs), ozone, aerosols, other anthropogenic forcings, total anthropogenic, solar, volcanic, and total. Shaded uncertainty bands show *very likely* ranges. Further details on data sources and processing are available in the chapter data table (Table 7.SM.14).

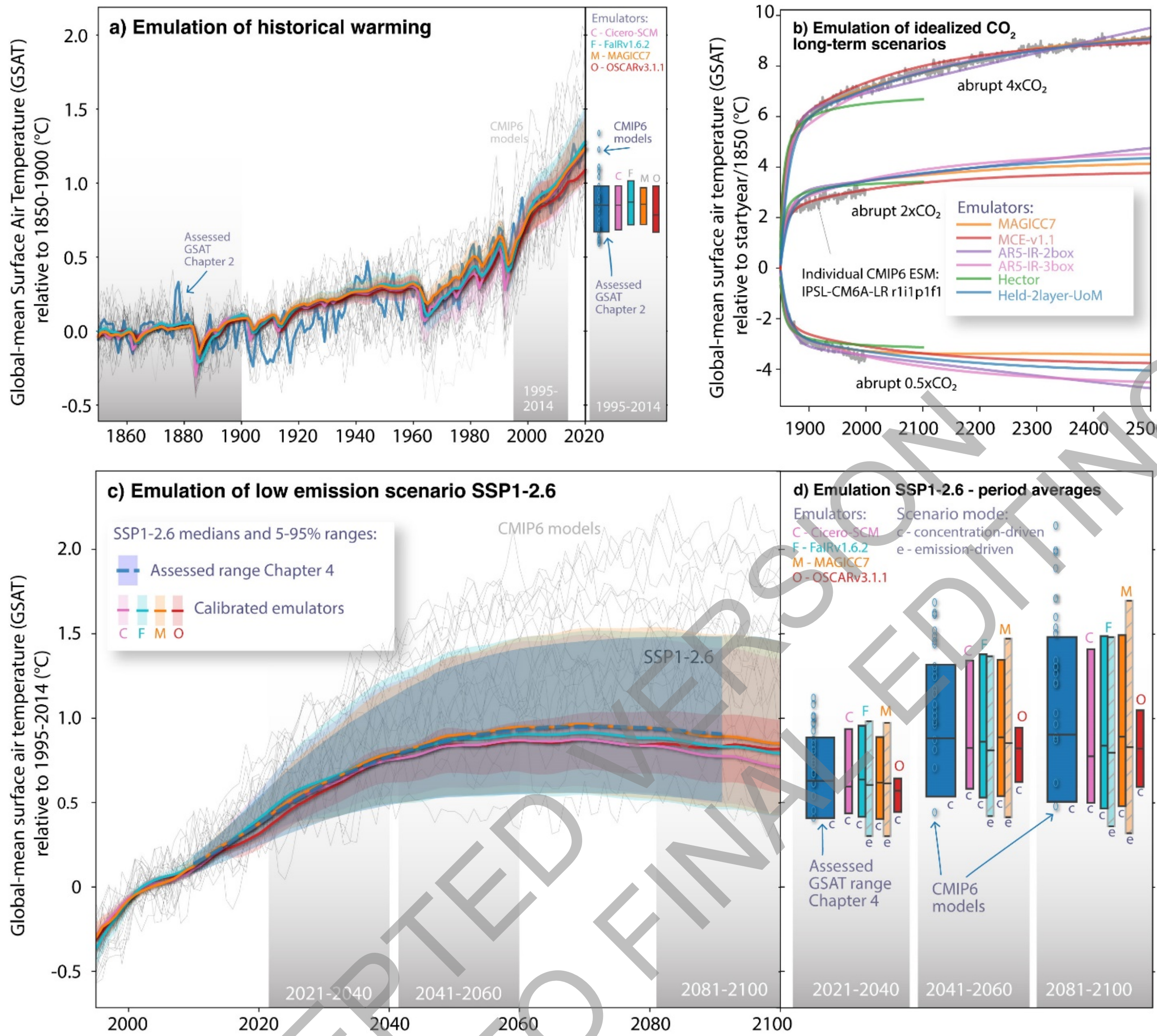

Cross-Chapter Box 7.1, Figure 1: A comparison between the global-mean surface air temperature response of various calibrated simple climate models, assessed ranges and Earth System Models. The top panels compare the assessed historical GSAT time series (Chapter 2, Section 2.3.1) with four multi-gas emulators calibrated to replicate numerous assessed ranges (Cross-Chapter Box 7.1, Table 2 below) (panel a) and also compares idealized CO_2-only concentration scenario response for one ESM (IPSL CM6A-LR) and multiple emulators which participated in RCMIP Phase 1 (Nicholls et al., 2020) calibrated to that single ESM (panel b). The bottom panels compare this report's assessed ranges for GSAT warming (Chapter 4, Box 4.1) under the multi-gas scenario SSP1-2.6 with the same calibrated emulators as in panel a (panel c and d). For context, a range of CMIP6 ESM results are also shown (thin lines in bottom-left panel c and open circles in bottom-right panel d). Panel b) adapted from Nicholls et al. (2020). Further details on data sources and processing are available in the chapter data table (Table 7.SM.14).

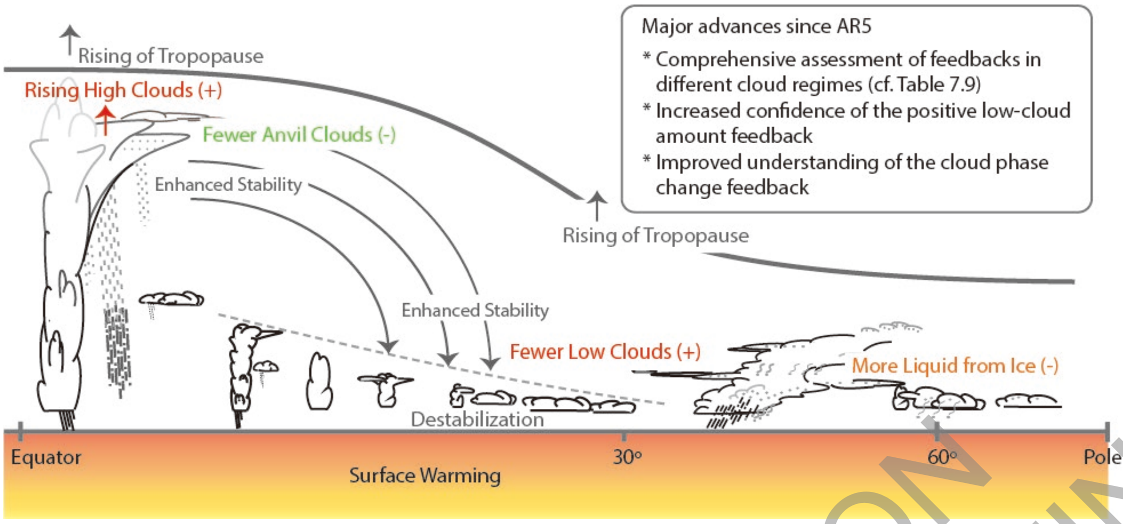

Figure 7.9: Schematic cross section of diverse cloud responses to surface warming from the tropics to polar regions. Thick solid and dashed curves indicate the tropopause and the subtropical inversion layer in the current climate, respectively. Thin grey text and arrows represent robust responses in the thermodynamic structure to greenhouse warming, of relevance to cloud changes. Text and arrows in red, orange and green show the major cloud responses assessed with *high*, *medium* and *low confidence*, respectively, and the sign of their feedbacks to the surface warming is indicated in the parenthesis. Major advances since AR5 are listed in a box.

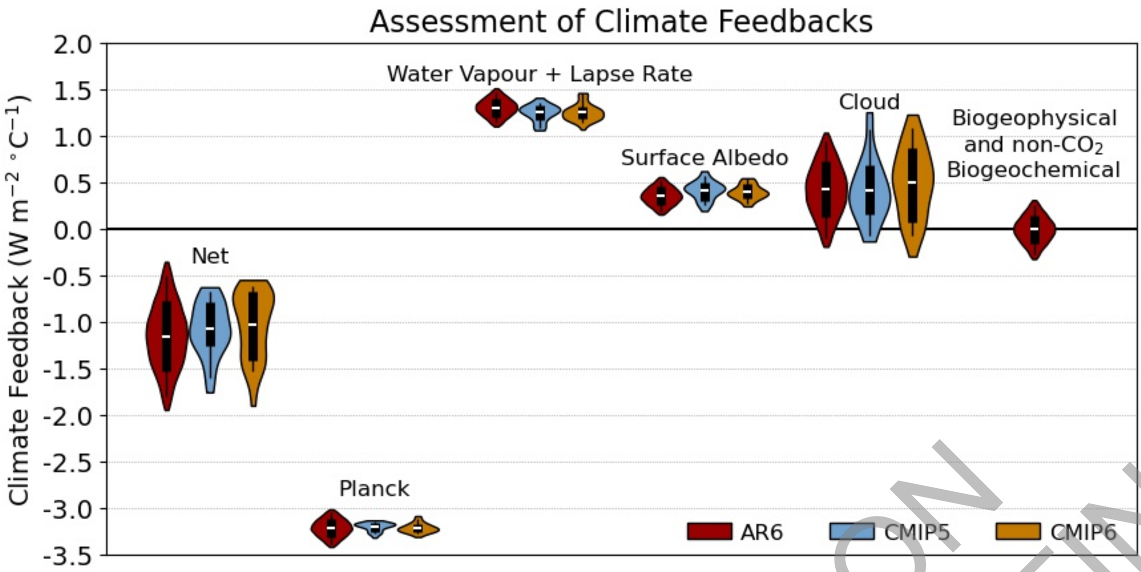

Figure 7.10: Global-mean climate feedbacks estimated in *abrupt4xCO2* simulations of 29 CMIP5 models (light blue) and 49 CMIP6 models (orange), compared with those assessed in this Report (red). Individual feedbacks for CMIP models are averaged across six radiative kernels as computed in Zelinka et al. (2020). The white line, black box and vertical line indicate the mean, 66% and 90% ranges, respectively. The shading represents the probability distribution across the full range of GCM/ESM values and for the 2.5–97.5 percentile range of the AR6 normal distribution. The unit is W m^{-2} °C^{-1}. Feedbacks associated with biogeophysical and non-CO_2 biogeochemical processes are assessed in AR6, but they are not explicitly estimated from GCMs/ESMs in CMIP5 and CMIP6. Further details on data sources and processing are available in the chapter data table (Table 7.SM.14).

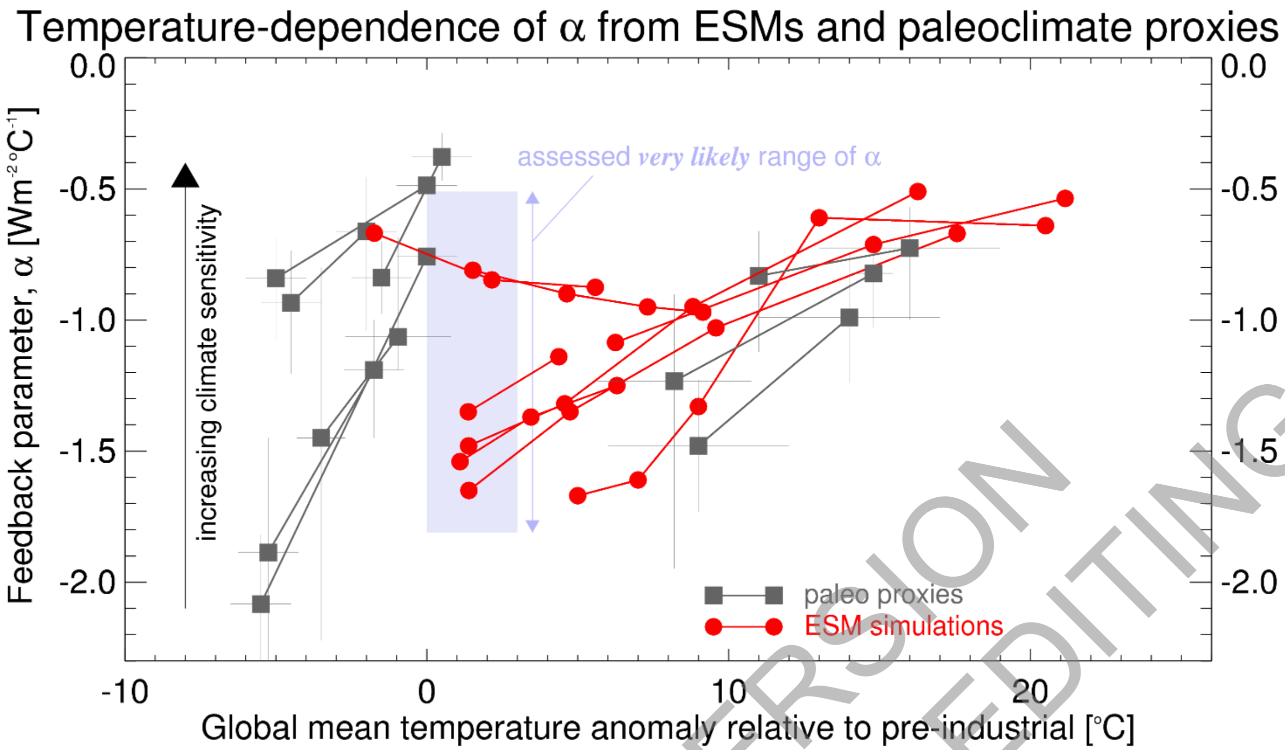

Figure 7.11: Feedback parameter, α (W m^{-2} °C^{-1}), as a function of global mean surface air temperature anomaly relative to preindustrial, for ESM simulations (red circles and lines) (Caballero and Huber, 2013; Jonko et al., 2013; Meraner et al., 2013; Good et al., 2015; Duan et al., 2019; Mauritsen et al., 2019; Stolpe et al., 2019; Zhu et al., 2019), **and derived from paleoclimate proxies (grey squares and lines)** (von der Heydt et al., 2014; Anagnostou et al., 2016, 2020; Friedrich et al., 2016; Royer, 2016; Shaffer et al., 2016; Köhler et al., 2017; Snyder, 2019; Stap et al., 2019). For the ESM simulations, the value on the *x*-axis refers to the average of the temperature before and after the system has equilibrated to a forcing (in most cases a CO_2 doubling), and is expressed as an anomaly relative to an associated pre-industrial global mean temperature from that model. The light blue shaded square extends across the assessed range of α (Table 7.10) on the *y*-axis, and on the *x*-axis extends across the approximate temperature range over which the assessment of α is based (taken as from zero to the assessed central value of ECS (Table 7.13). Further details on data sources and processing are available in the chapter data table (Table 7.SM.14).

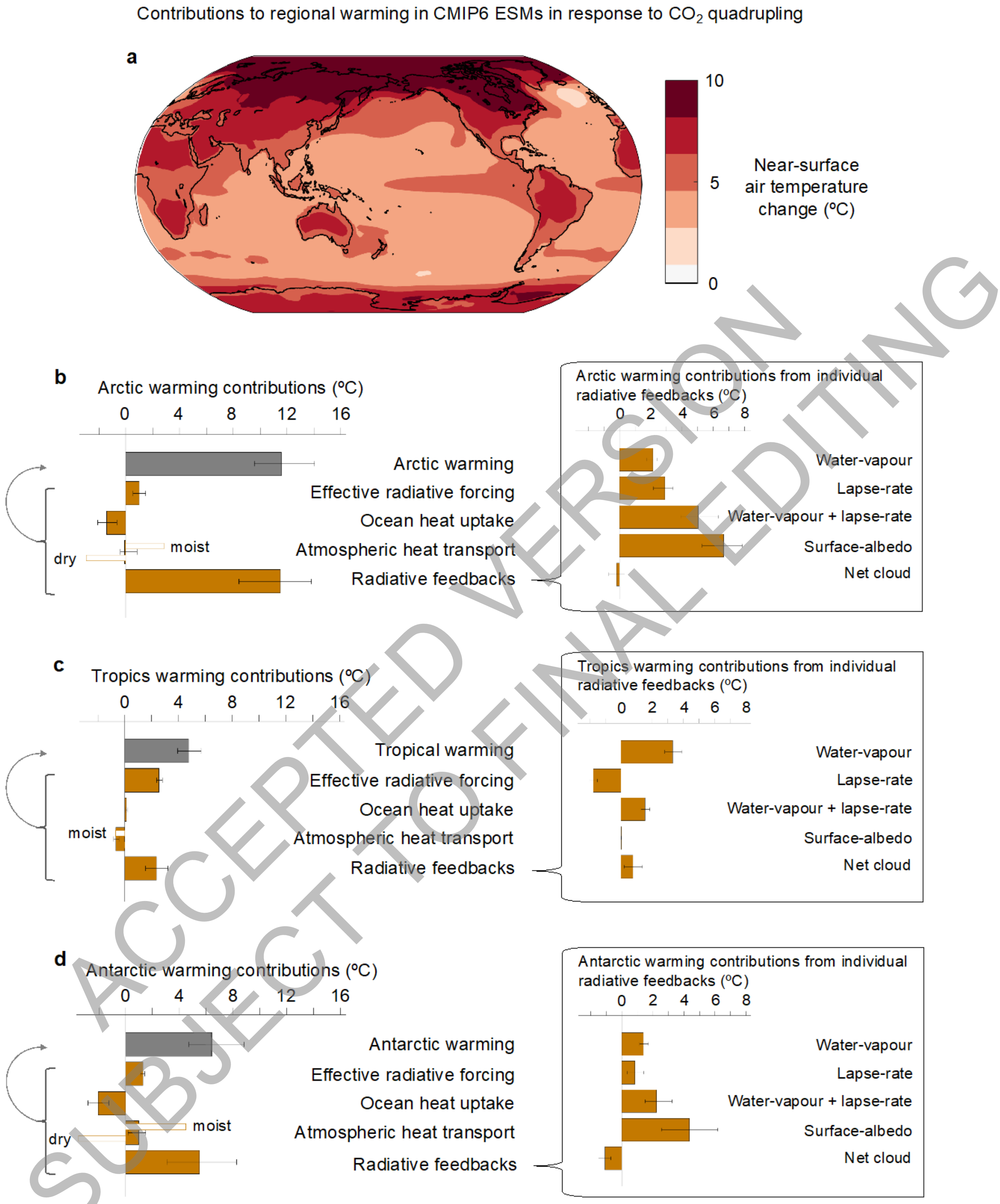

Figure 7.12: Contributions of effective radiative forcing, ocean heat uptake, atmospheric heat transport, and radiative feedbacks to regional surface temperature changes at year 100 of *abrupt4xCO2* simulations of CMIP6 ESMs. (a) Pattern of near-surface air temperature change. (b-d) Contributions to net Arctic (>60°N), tropical (30°S – 30°N), and Antarctic (<60°S) warming calculated by dividing regional-average energy inputs by the magnitude of the regional-average Planck response. The contributions from radiative forcing, changes in moist, dry-static, and total atmospheric energy transport, ocean heat uptake, and radiative feedbacks (orange bars) all sum to the value of net warming (grey bar).

Inset shows regional warming contributions associated with individual feedbacks, all summing to the total feedback contribution. Uncertainties show the interquartile range (25th and 75th percentiles) across models. The warming contributions (units of °C) for each process are diagnosed by calculating the energy flux (units of W m^{-2}) that each process contributes to the atmosphere over a given region, either at the TOA or surface, then dividing that energy flux by the magnitude of the regional Planck response (around 3.2 W m^{-2} $°C^{-1}$ but varying with region). By construction, the individual warming contributions sum to the total warming in each region. Radiative kernel methods (see Section 7.4.1) are used to decompose the net energy input from radiative feedbacks into contributions from changes in atmospheric water vapour, lapse-rate, clouds, and surface albedo (Zelinka et al. (2020) using the Huang et al. (2017) radiative kernel). The CMIP6 models included are those analysed by Zelinka et al. (2020) and the warming contribution analysis is based on that of Goosse et al. (2018). Further details on data sources and processing are available in the chapter data table (Table 7.SM.14).

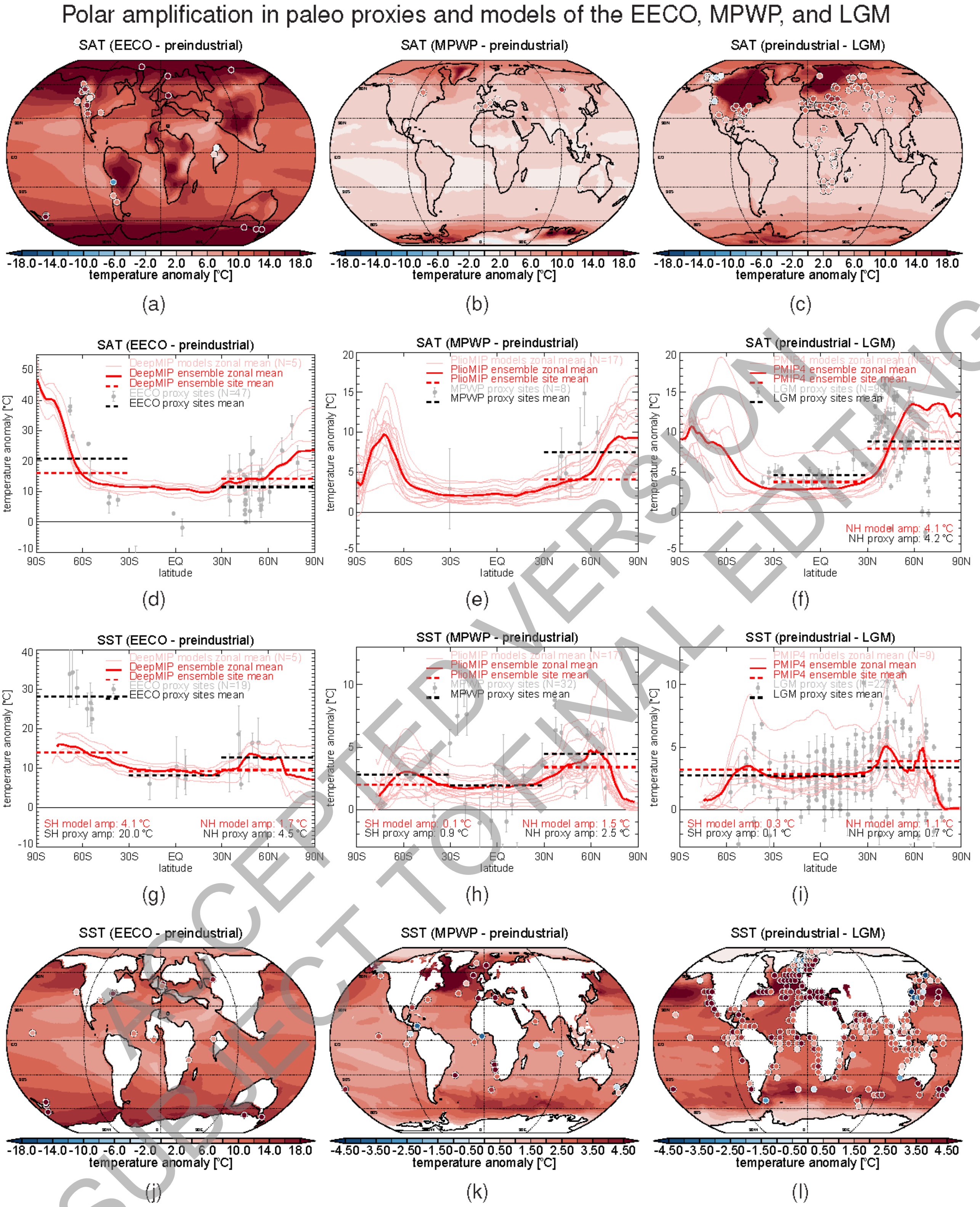

Figure 7.13: Polar amplification in paleo proxies and models of the early Eocene climatic optimum (EECO), the mid-Pliocene warm period (MPWP), and the Last Glacial Maximum (LGM). Temperature anomalies compared with pre-industrial (equivalent to CMIP6 simulation *piControl*) are shown for the high-CO_2 EECO and MPWP time periods, and for the low-CO_2 LGM (expressed as pre-industrial minus LGM). (a,b,c) Modelled near-surface air temperature anomalies for ensemble-mean simulations of the (a) EECO (Lunt et al., 2021), (b) MPWP (Haywood et al., 2020; Zhang et al., 2021), and (c) LGM (Kageyama et al., 2021; Zhu et al., 2021). Also shown are proxy near-surface air temperature anomalies (coloured circles). (d,e,f) Proxy near-surface air temperature anomalies (grey circles), including published

uncertainties (grey vertical bars), model ensemble mean zonal mean anomaly (solid red line) for the same model ensembles as in (a,b,c), light red lines show the modelled temperature anomaly for the individual models that make up each ensemble (LGM, N=9; MPWP, N=17; EECO, N=5). Black dashed lines show the average of the proxy values in each latitude bands 90°S to 30°S, 30°S to 30°N, and 30°N to 90°N. Red dashed lines show the same banded average in the model ensemble mean, calculated from the same locations as the proxies. Black and red dashed lines are only shown if there are 5 or more proxy points in that band. Mean differences between the 90°S/N to 30°S/N and 30°S to 30°N bands are quantified for the models and proxies in each plot. Panels (g,h,i) are like panels (d,e,f) but for SST instead of near-surface air temperature. Panels (j,k,l) are like panels (a,b,c) but for SST instead of near-surface air temperature. For the EECO maps (a,j), the anomalies are relative to the zonal mean of the pre-industrial, due to the different continental configuration. Proxy datasets are (a,d) Hollis et al. (2019), (b,e) Salzmann et al. (2013); Vieira et al. (2018), (c,f) Cleator et al. (2020) at the sites defined in Bartlein et al. (2011), (g,j)) Hollis et al. (2019), (h,k) McClymont et al. (2020) (i,l) Tierney et al. (2020b). Where there are multiple proxy estimations at a single site, a mean is taken. Model ensembles are (a,d,g,j) DeepMIP (only model simulations carried out with a mantle-frame paleogeography, and carried out under CO_2 concentrations within the range assessed in Chapter 2, Table 2.2, are shown), (b,e,h,k) PlioMIP, and (c,f,i,l) PMIP4. Further details on data sources and processing are available in the chapter data table (Table 7.SM.14).

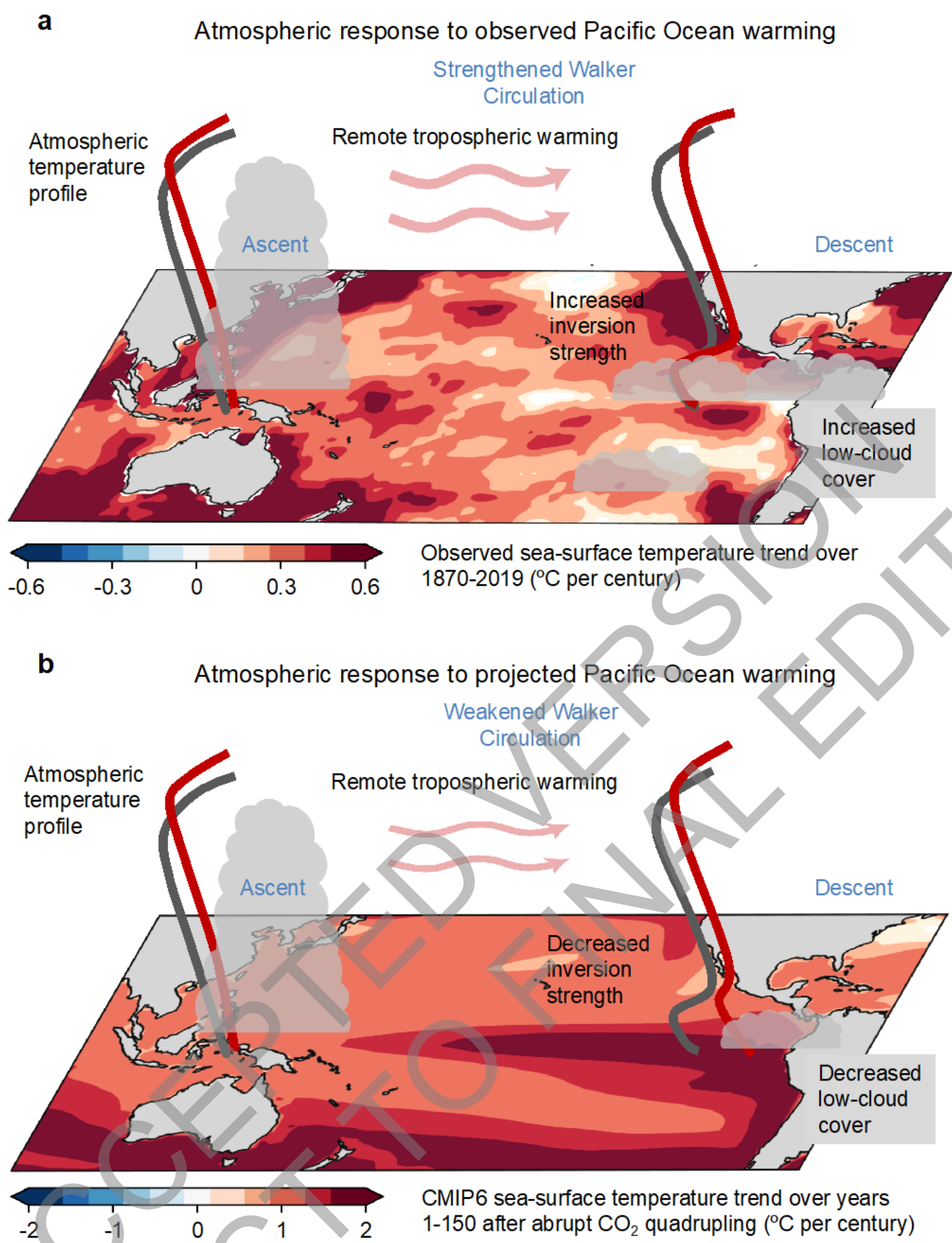

Figure 7.14: Illustration of tropospheric temperature and low-cloud response to observed and projected Pacific Ocean sea-surface temperature trends; adapted from Mauritsen (2016). (a) Atmospheric response to linear sea-surface temperature trend observed over 1870–2019 (HadISST1 dataset; Rayner et al., 2003). (b) Atmospheric response to linear sea-surface temperature trend over 150 years following *abrupt4xCO2* forcing as projected by CMIP6 ESMs (Dong et al., 2020). Relatively large historical warming in the western tropical Pacific has been communicated aloft (a shift from grey to red atmospheric temperature profile), remotely warming the tropical free troposphere and increasing the strength of the inversion in regions of the tropics where warming has been slower, such as the eastern equatorial Pacific. In turn, an increased inversion strength has increased the low-cloud cover (Zhou et al., 2016) causing an anomalously-negative cloud and lapse-rate feedbacks over the historical record (Andrews et al., 2018; Marvel et al., 2018). Relatively large projected warming in the eastern tropical Pacific is trapped near the surface (shift from grey to red atmospheric temperature profile), decreasing the strength of the inversion locally. In turn, a decreased inversion strength combined with surface warming is projected to decrease the low-cloud cover, causing the cloud and lapse-rate feedbacks to become less negative in the future. Further details on data sources and processing are available in the chapter data table (Table 7.SM.14).

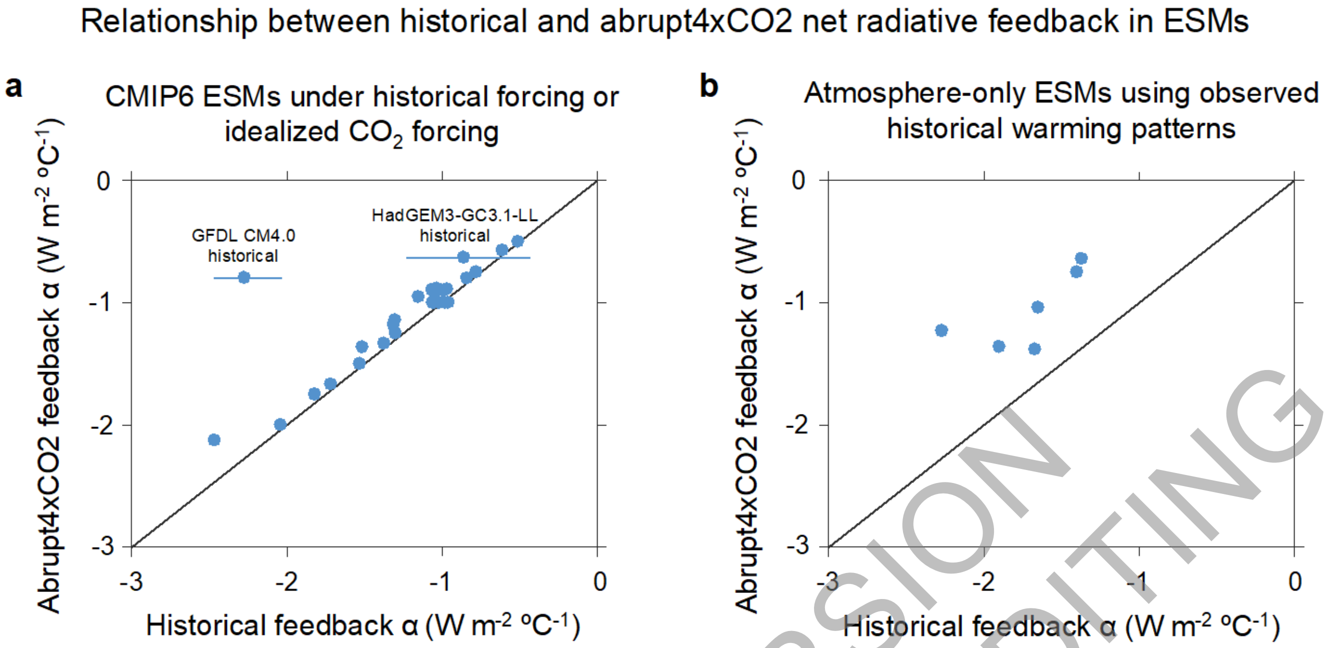

Figure 7.15: Relationship between *historical* and *abrupt4xCO2* net radiative feedbacks in ESMs. (a) Radiative feedbacks in CMIP6 ESMs estimated under historical forcing (values for GFDL CM4.0 and HadGEM3-CG3.1-LL from Winton et al. (2020) and Andrews et al. (2019), respectively); horizontal lines show the range across ensemble members. The other points show effective feedback values for 29 ESMs estimated using regression over the first 50 years of *abrupt4xCO2* simulations as an analogue for historical warming (Dong et al., 2020). (b) Historical radiative feedbacks estimated from atmosphere-only ESMs with prescribed observed sea-surface temperature and sea-ice concentration changes (Andrews et al. 2018) based on a linear regression of global TOA radiation against global near-surface air temperature over the period 1870–2010 (pattern of warming similar to Figure 7.14a) and compared with equilibrium feedbacks in a *abrupt4xCO2* simulations of coupled versions of the same ESMs (pattern of warming similar to Figure 7.14b). In all cases, the equilibrium feedback magnitudes are estimated as CO_2 ERF divided by ECS where ECS is derived from regression over years 1–150 of *abrupt4xCO2* simulations (Box 7.1); similar results are found if the equilibrium feedback is estimated directly from the slope of the linear regression. Further details on data sources and processing are available in the chapter data table (Table 7.SM.14).

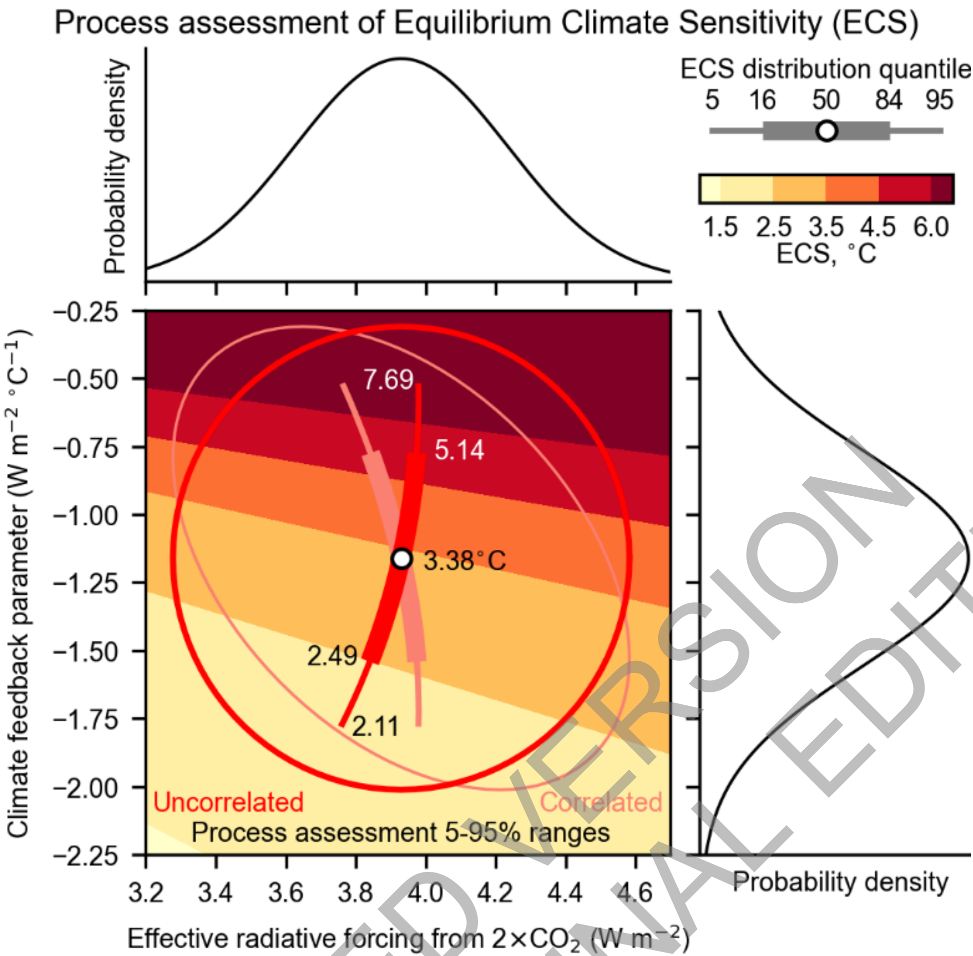

Figure 7.16: Probability distributions of ERF to CO_2 doubling ($\Delta F_{2\times CO2}$, top) and the net climate feedback (α, right), derived from process-based assessments in Sections 7.3.2 and 7.4.2. Middle panel shows the joint probability density function calculated on a two-dimensional plane of $\Delta F_{2\times CO2}$ and α (red), on which the 90% range shown by an ellipse is imposed to the background theoretical values of ECS (colour shading). The white dot, thick and thin curves in the ellipse represent the mean, *likely* and *very likely* ranges of ECS. An alternative estimation of the ECS range (pink) is calculated by assuming that $\Delta F_{2\times CO2}$ and α have a covariance. The assumption about the co-dependence between $\Delta F_{2\times CO2}$ and α does not alter the mean estimate of ECS but affects its uncertainty. Further details on data sources and processing are available in the chapter data table (Table 7.SM.14).

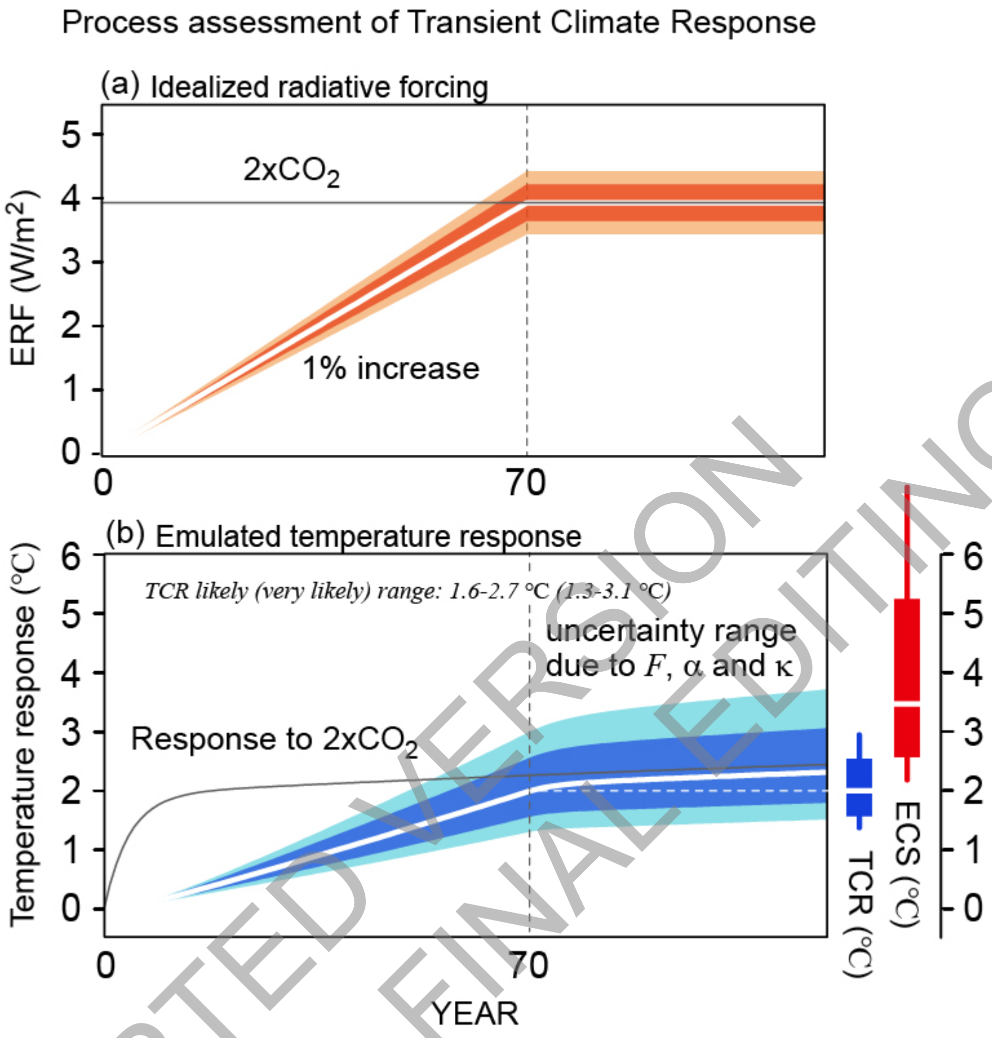

Figure 7.17: (a) Time evolution of the effective radiative forcing (ERF) to the CO_2 concentration increased by 1% per year until the year 70 (equal to the time of doubling) and kept fixed afterwards (white line). The *likely* and *very likely* ranges of ERF indicated by light and dark orange have been assessed in Section 7.3.2.1. (b) Surface temperature response to the CO_2 forcing calculated using the emulator with a given value of ECS, considering uncertainty in $\Delta F_{2\times CO2}$, α, and κ associated with the ocean heat uptake and efficacy (white line). The *likely* and *very likely* ranges are indicated by cyan and blue. For comparison, the temperature response to abrupt doubling of the CO_2 concentration is displayed by a grey curve. The mean, *likely* and *very likely* ranges of ECS and TCR are shown at the right (the values of TCR also presented in the panel). Further details on data sources and processing are available in the chapter data table (Table 7.SM.14).

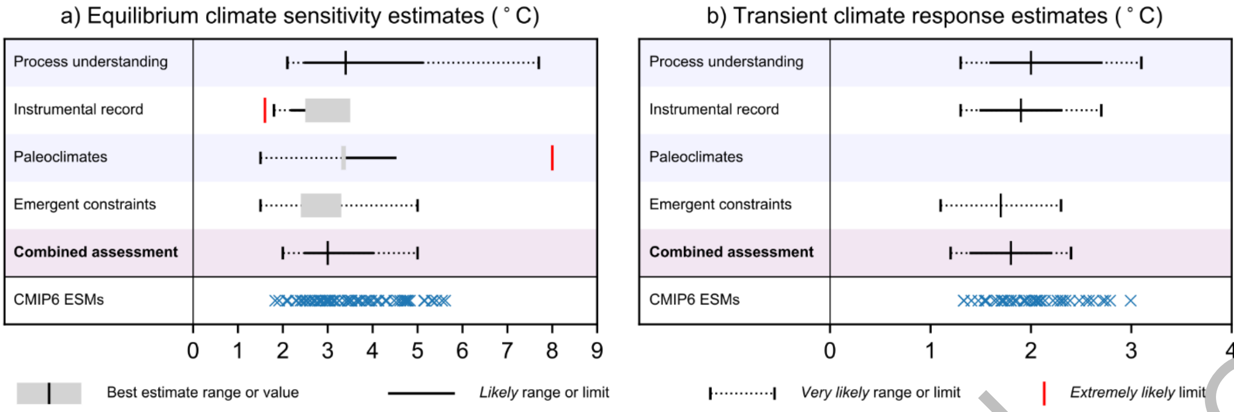

Figure 7.18: Summary of the equilibrium climate sensitivity (ECS) and transient climate response (TCR) assessments using different lines of evidence. Assessed ranges are taken from Tables 7.13 and 7.14 for ECS and TCR respectively. Note that for the ECS assessment based on both the instrumental record and paleoclimates, limits (i.e. one-sided distributions) are given, which have twice the probability of being outside the maximum/minimum value at a given end, compared to ranges (i.e. two tailed distributions) which are given for the other lines of evidence. For example, the *extremely likely* limit of greater than 95% probability corresponds to one side of the *very likely* (5% to 95%) range. Best estimates are given as either a single number or by a range represented by grey box. CMIP6 model values are not directly used as a line of evidence but presented on the Figure for comparison. ECS values are taken from Schlund et al. (2020) and TCR values from Meehl et al. (2020), see Supplementary Material 7.SM.4. Further details on data sources and processing are available in the chapter data table (Table 7.SM.14).

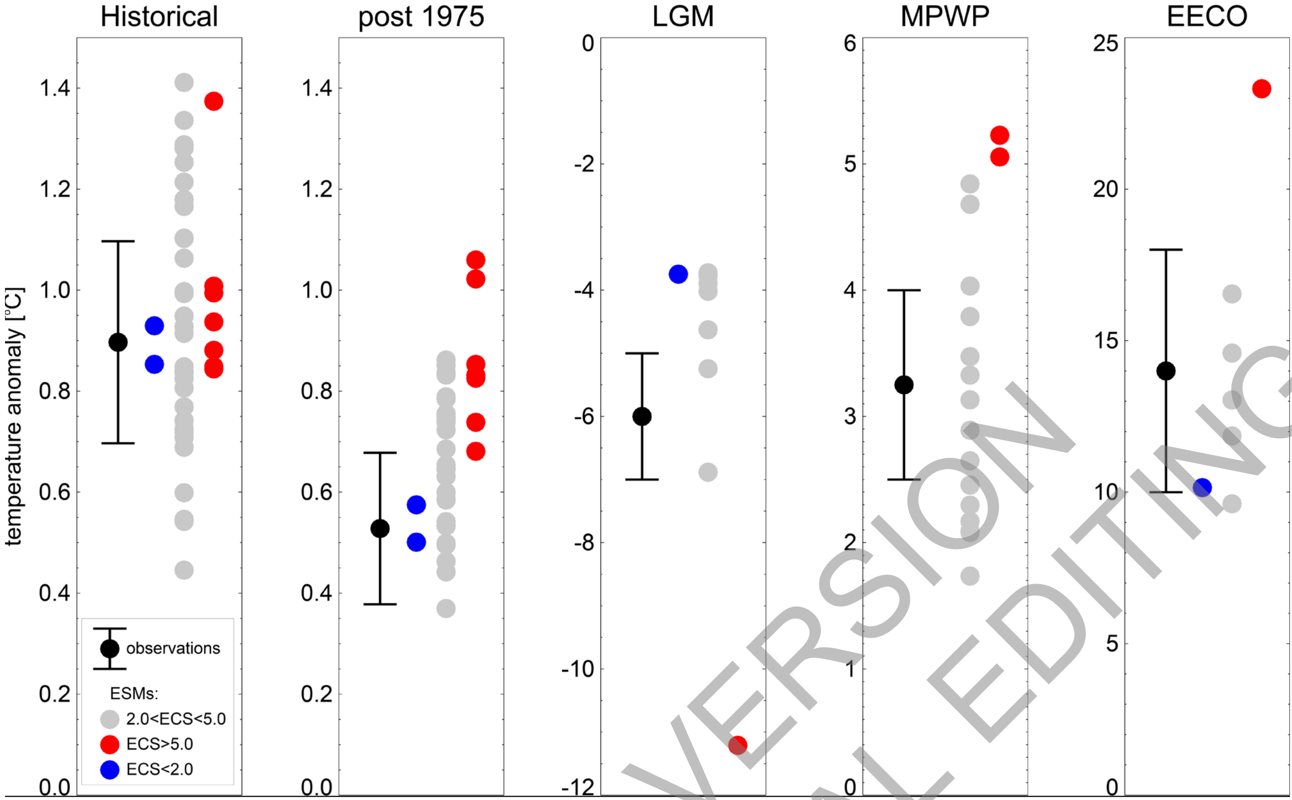

Figure 7.19: Global mean temperature anomaly in models and observations from 5 time periods. (a) Historical (CMIP6 models), (b) post 1975 (CMIP6 models), (c) Last Glacial Maximum (LGM; Cross-Chapter Box 2.1; PMIP4 models; (Kageyama et al., 2021; Zhu et al., 2021), (d) mid Pliocene warm period (MPWP; Cross-Chapter Box 2.4; PlioMIP models; Haywood et al., 2020; Zhang et al., 2021), (e) early Eocene climatic optimum (EECO; Cross-Chapter Box 2.1; DeepMIP models; Zhu et al., 2020; Lunt et al., 2021). Grey circles show models with ECS in the assessed *very likely* range; models in red have an ECS greater than the assessed *very likely* range (>5°C), models in blue have an ECS lower than the assessed *very likely* range (<2°C). Black ranges show the assessed temperature anomaly derived from observations (Chapter 2, Section 2.3). The Historical anomaly in models and observations is calculated as the difference between 2005–2014 and 1850–1900, and the post 1975 anomaly is calculated as the difference between 2005–2014 and 1975–1984. For the LGM, MPWP, and EECO, temperature anomalies are compared with pre-industrial (equivalent to CMIP6 simulation *piControl*). All model simulations of the MPWP and LGM were carried out with atmospheric CO_2 concentrations of 400 and 190 ppm respectively. However, CO_2 during the EECO is relatively more uncertain, and model simulations were carried out at either 1120ppm or 1680 ppm (except for the one high-ECS EECO simulation which was carried out at 560 ppm; Zhu et al., 2020). The one low-ECS EECO simulation was carried out at 1680 ppm. Further details on data sources and processing are available in the chapter data table (Table 7.SM.14).

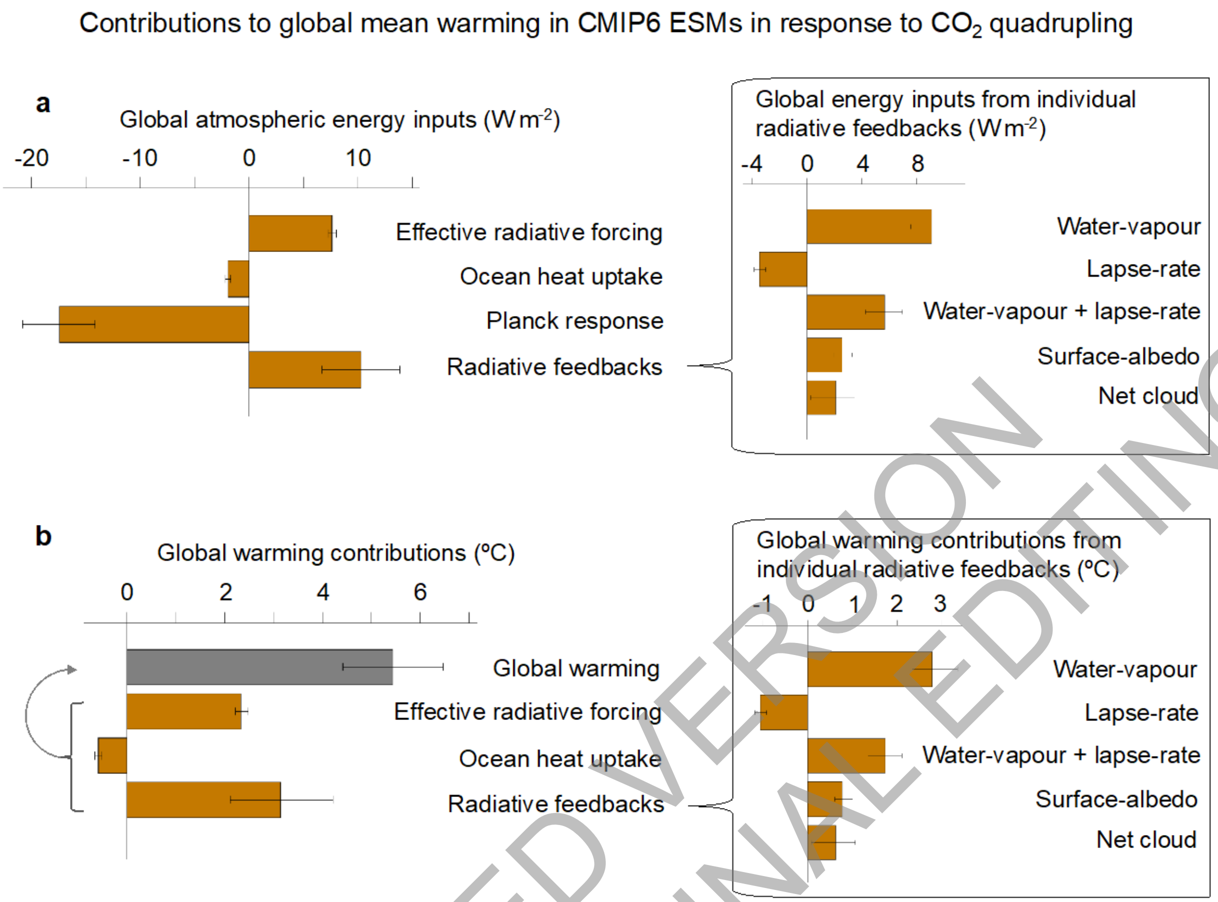

Figure 7.20: Contributions of effective radiative forcing, ocean heat uptake and radiative feedbacks to global atmospheric energy input and near-surface air temperature change at year 100 of *abrupt4xCO2* simulations of CMIP6 models. (a) The energy flux to the global atmosphere associated with the effective CO_2 forcing, global ocean heat uptake, Planck response, and radiative feedbacks, which together sum to zero. The inset shows energy input from individual feedbacks, summing to the total feedback energy input. (b) Contributions to net global warming are calculated by dividing the energy inputs by the *magnitude* of the global Planck response (3.2 W m^{-2} °C^{-1}), with the contributions from radiative forcing, ocean heat uptake, and radiative feedbacks (orange bars) summing to the value of net warming (grey bar). The inset shows warming contributions associated with individual feedbacks, summing to the total feedback contribution. Uncertainties show the interquartile range (25% and 75% percentiles) across models. Radiative kernel methods (see Section 7.4.1) were used to decompose the net energy input from radiative feedbacks into contributions from changes in atmospheric water vapour, lapse-rate, clouds, and surface albedo (Zelinka et al. (2020) using the Huang et al. (2017) radiative kernel). The CMIP6 models included are those analysed by Zelinka et al. (2020) and the warming contribution analysis is based on that of Goosse et al. (2018). Further details on data sources and processing are available in the chapter data table (Table 7.SM.14).

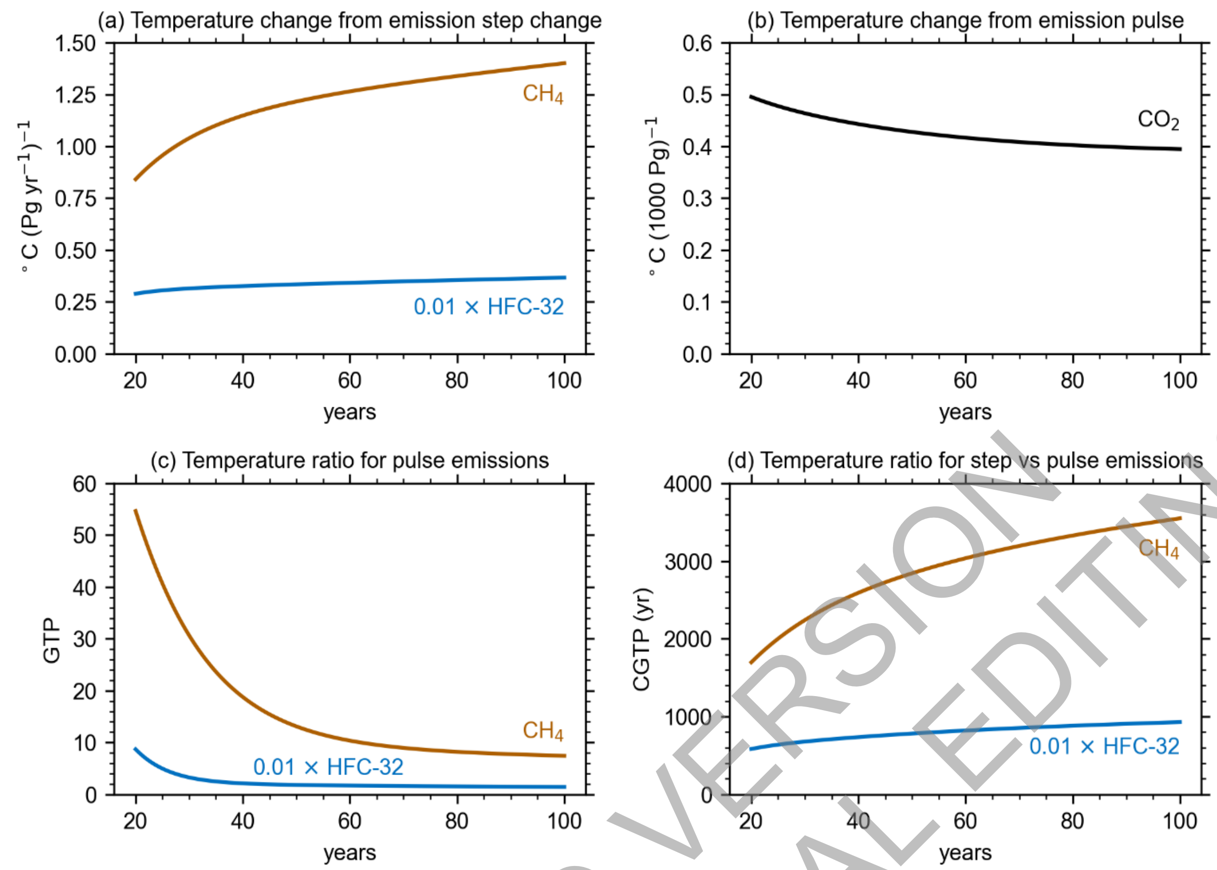

Figure 7.21: Emission metrics for two short-lived greenhouse gases: HFC-32 and CH_4, (lifetimes of 5.4 and 11.8 years). The temperature response function comes from Supplementary Material 7.SM.5.2. Values for non-CO_2 species include the carbon cycle response (Section 7.6.1.3). Results for HFC-32 have been divided by 100 to show on the same scale. (a) temperature response to a step change in short-lived greenhouse gas emission. (b) temperature response to a pulse CO_2 emission. (c) conventional GTP metrics (pulse vs pulse). (d) combined-GTP metric (step versus pulse). Further details on data sources and processing are available in the chapter data table (Table 7.SM.14).

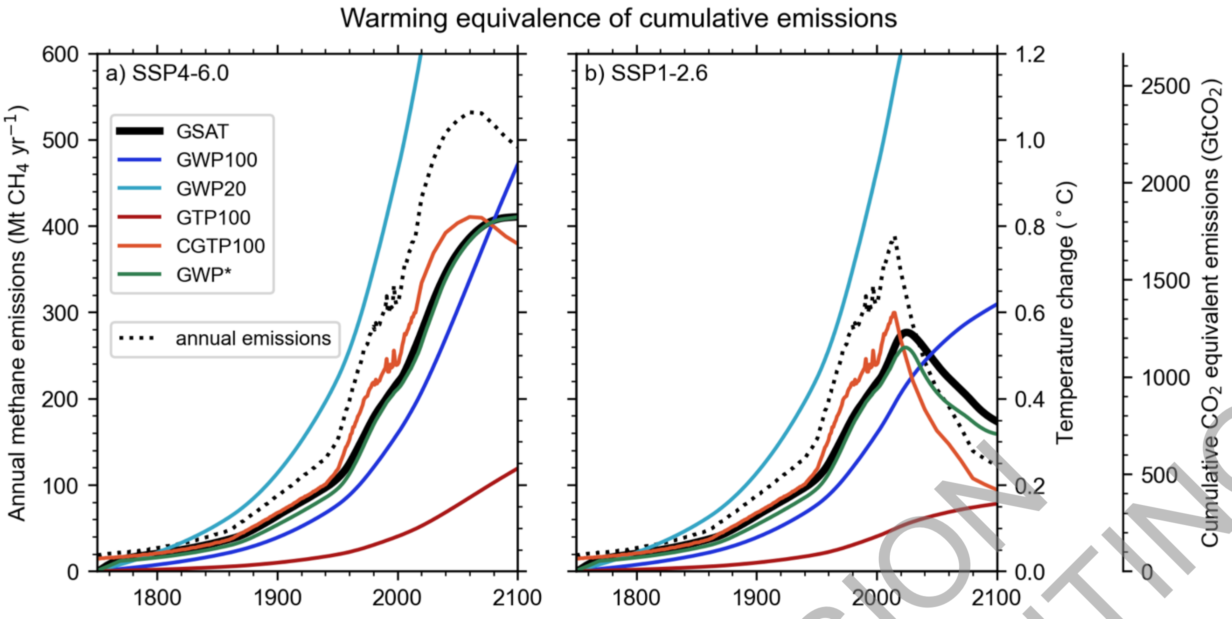

Figure 7.22: Explores how cumulative carbon dioxide equivalent emissions estimated for methane vary under different emission metric choices and how estimates of the surface temperature (GSAT) change deduced from these cumulative emissions compare to the actual temperature response computed with the two-layer emulator (solid black lines). Panels a) and b) show the SSP4-6.0 and SSP1-2.6 scenarios respectively. The panels show annual methane emissions as the dotted lines (left axis) from 1750–2100. The solid lines can be read as either estimates of GSAT change or estimates of the cumulative carbon dioxide equivalent emissions. This is because they are related by a constant factor, the TCRE. Thus, values can be read using either of the right hand axes. Emission metric values are taken from Table 7.15. The GWP* calculation is given in Section 7.6.1.4. The two-layer emulator has been calibrated to the central values of the report's assessment (see Supplementary Material 7.SM.5.2). Further details on data sources and processing are available in the chapter data table (Table 7.SM.14).

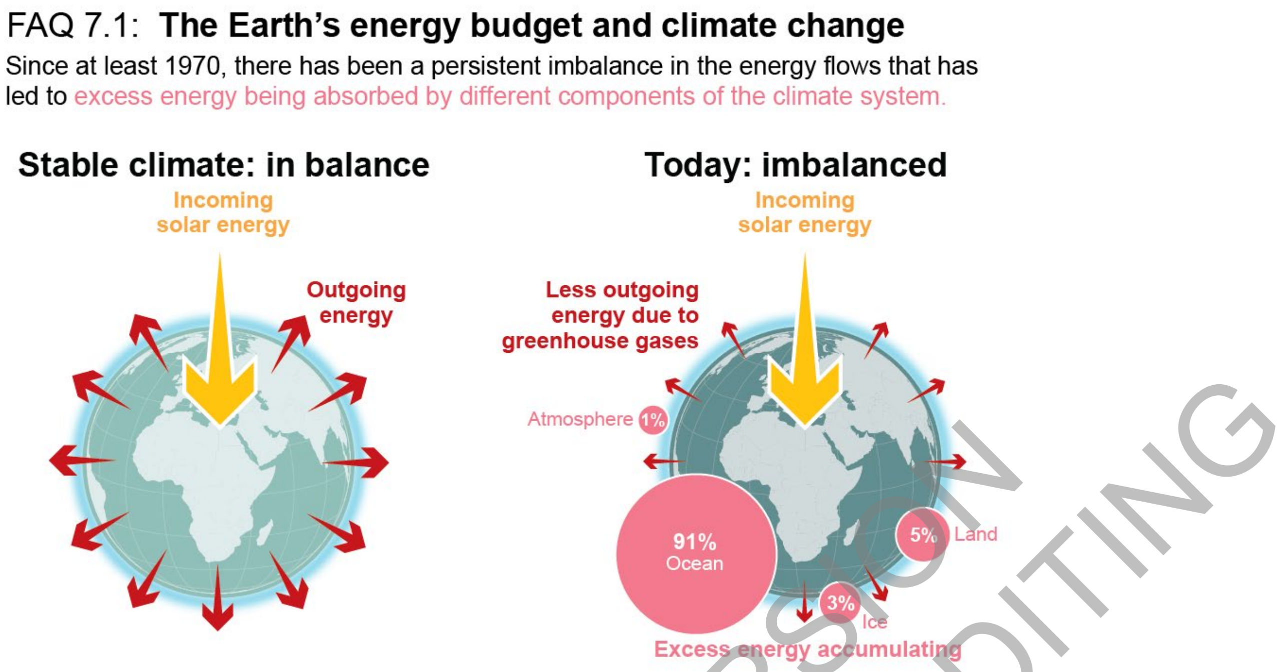

FAQ 7.1, Figure 1: **The Earth's energy budget compares the flows of incoming and outgoing of energy that are relevant for the climate system.** Since the at least the 1970s, less energy is flowing out than is flowing in, which leads to excess energy being absorbed by the ocean, land, ice and atmosphere, with the ocean absorbing 91%.

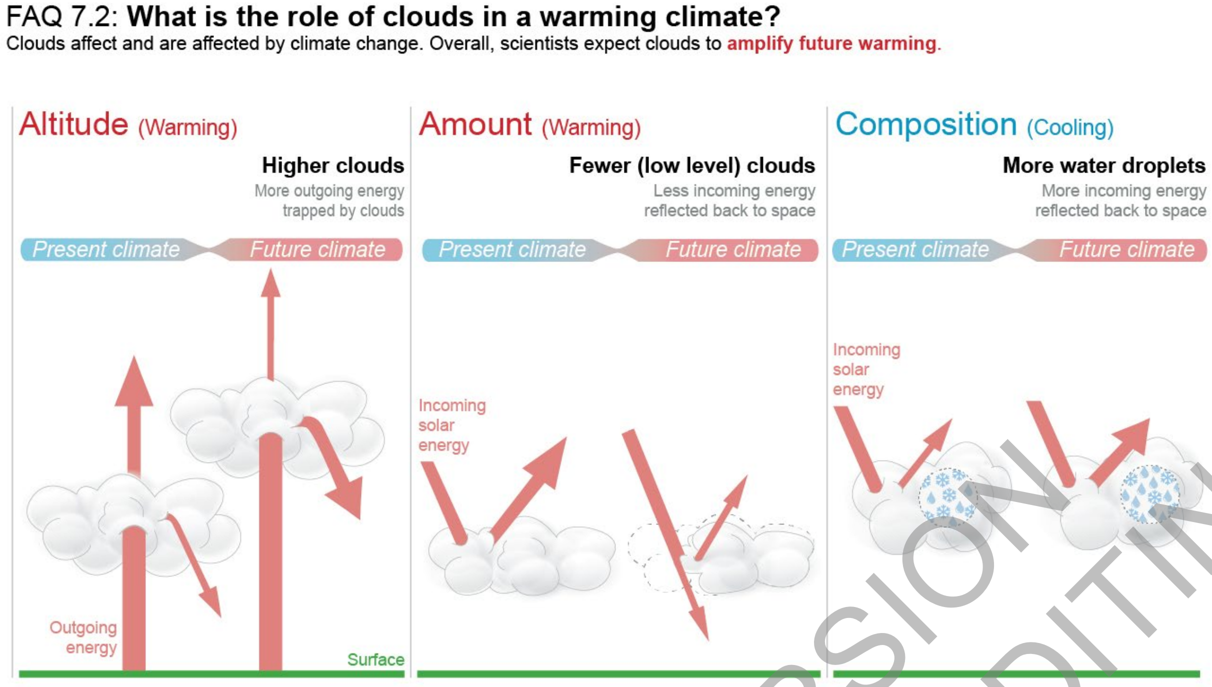

FAQ 7.2, Figure 1: **Interactions between clouds and the climate today and in a warmer future**. Global warming is expected to alter the altitude (left) and the amount (centre) of clouds, which will amplify warming. On the other hand, cloud composition will change (right), offsetting some of the warming. Overall clouds are expected to amplify future warming.

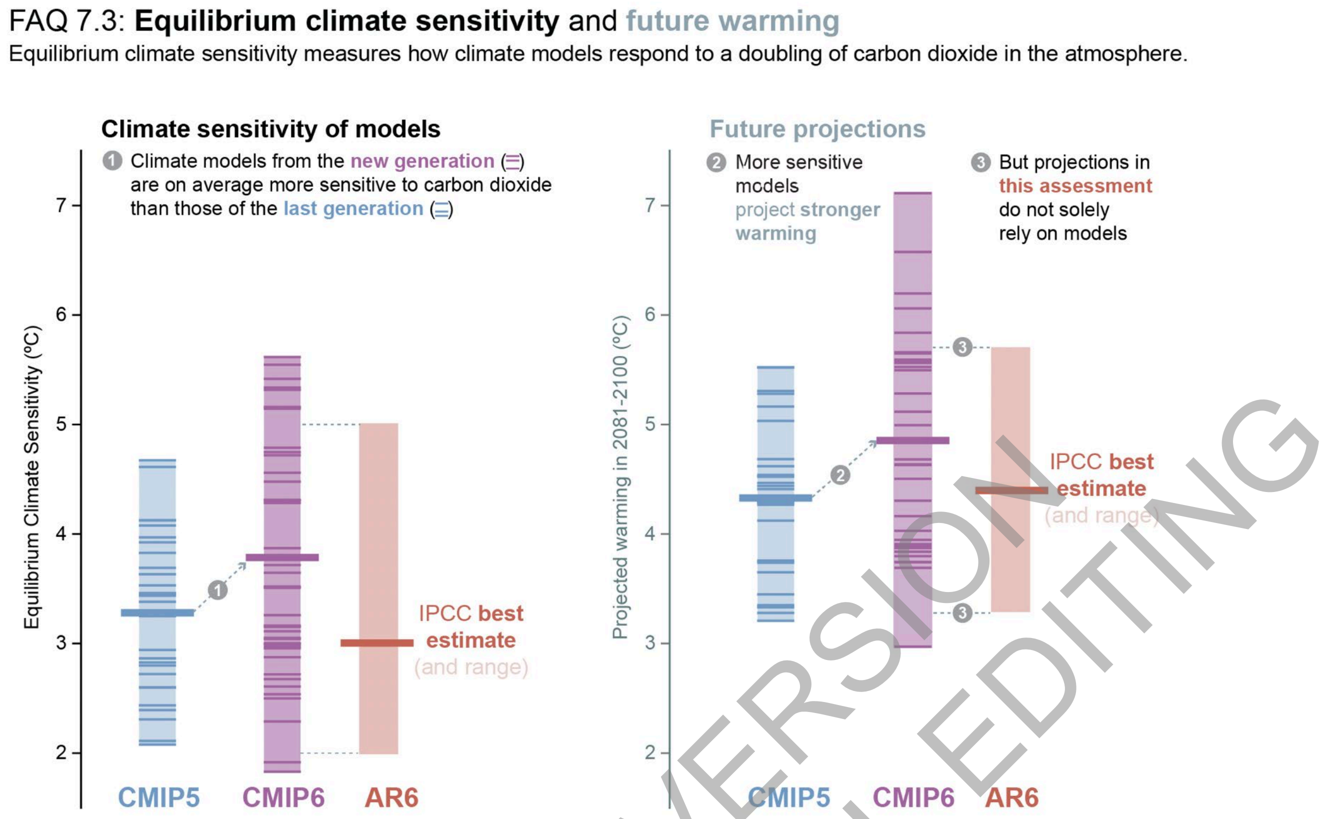

FAQ7.3, Figure 1: Equilibrium climate sensitivity and future warming. (left) Equilibrium climate sensitivities for the current generation (sixth climate model intercomparison project, CMIP6) climate models, and the previous (CMIP5) generation. The assessed range in this report (AR6) is also shown. (right) Climate projections of CMIP5, CMIP6, and AR6 for the very high-emission scenarios RCP8.5, and SSP5-8.5, respectively. The thick horizontal lines represent the multi-model average and the thin horizontal lines the results of individual models. The boxes represent the model ranges for CMIP5 and CMIP6 and the range assessed in AR6.